ADA279187

HANDBOOK OF SUPERSONIC AERODYNAMICS

SECTION 8

BODIES OF REVOLUTION

OCTOBER 1961

SERIES CONTENTS

PREFACE

The preface appearing in Volume 1 of the Handbook of Super-
sonic Aerodynamics defines the Handbook's purpose and also traces the
sequence of events leading to its undertaking. In accordance with the
criteria established at that time, the subject matter of the Handbook
is selected on the basis of anticipated usefulness to all who are ac-
tively concerned with the design and performance of supersonic vehicles.
Essential to this subject matter are the properties of fluids in which
a vehicle operates or is tested and the flight characteristics of the
vehicle itself. Each section of the Handbook therefore presents appro-
priate theory and relevant data which are basic to supersonic aerody-
namics and which conform to the practical requirements imposed by the
criteria.

A complete list of Handbook sections and their status appears
on the facing page. The unpublished sections, now being prepared by
individual authors and the Handbook Staff, will be published separately
as they become available.

Volume 3, presented in three Handbook sections, is devoted to
the theoretical and experimental investigations of the flow fields sur-
rounding aerodynamic surfaces and bodies as well as their aerodynamic
characteristics, such as lift, drag, and moments. The material on two-
and three-dimensional airfoils is contained in Sections 6 and 7, both
of which were published previously. Section 8, "Bodies of Revolution,"
is presented herewith. It should be noted that vehicle components and
their characteristics are considered separately in Volume 3. The in-
teraction effects of these components are treated in Volume 4.

Section 8 was prepared by D. Adamson, E. A. Bonney, and
I. D. V. Faro, each of whom was a member of the Handbook Staff at the
time of writing. Specific subsections of the manuscript were reviewed
by L. L. Cronvich, H. H. Hart, H. Ginsberg, P. T. Pilon, L. E. Tisserand,
and E. T. Marley, all aerodynamicists at the Applied Physics Laboratory.
Many of the excellent suggestions offered by these reviewers have been
incorporated in the final revision.

The subject matter appearing in the Handbook is selected and
reviewed by the Technical Reviewing Committee at the Applied Physics
Laboratory, headed by L. L. Cronvich. Constructive criticism or recom-
mendations relating to the inclusion of suitable material in the Hand-
book should be directed to:

> Editor, Aerodynamics Handbook Project
> Applied Physics Laboratory
> The Johns Hopkins University
> 8621 Georgia Avenue
> Silver Spring, Maryland

The Handbook is printed and distributed by the Bureau of Naval
Weapons, Department of the Navy. It is available for public sale (see
Title Page) and is also distributed without charge to an approved list

of facilities and institutions actively engaged in national defense re-
search and development. Correspondence relating to the distribution of
the Handbook should be directed to:

> Chief, Bureau of Naval Weapons
> Department of the Navy
> Washington 25, D. C.

Improvements in the format, adopted for Section 18 and con-
sisting for the most part of a more concise running head and consecu-
tively numbered pages, are continued herein. It has been judged that
these changes enhance the usefulness of the sections and offset any
sacrifice to uniformity in the whole series.

The Handbook of Supersonic Aerodynamics is edited and pro-
duced by the Handbook Staff, which includes Mrs. Doris McCeney, repro-
duction copy typist; Thomas Timer, Mathematical Assistant; and Anthony
Strank, Associate Editor.

Ione D. V. Faro, Editor

CONTENTS

LIST OF TABLES

LIST OF FIGURES

SYMBOLS

a	velocity of sound
A	axial force
A_p	planform area
c	chord length
c_f	local skin-friction coefficient
c_N	local normal-force coefficient
c.p.	center of pressure of all forces acting normal to the body
C_A	axial-force coefficient $= A/qS$
C_D	total drag coefficient $= D/qS$
C_{D_c}	cross-drag coefficient
C_{D_w}	wave-drag coefficient
C_f	mean skin-friction coefficient
C_{f_i}	incompressible skin-friction coefficient
C_L	lift coefficient $= L/qS$
C_m	pitching-moment coefficient
C_{m_α}	pitching-moment slope coefficient $= \dfrac{dC_m}{d\alpha}$
$C_{m_{p\alpha}}$	Magnus-moment slope coefficient
C_N	total normal-force coefficient $= N/qS$
C_{N_α}	normal-force slope coefficient $= \dfrac{dC_N}{d\alpha}$
C_p	pressure coefficient $= \dfrac{p - p_\infty}{q_\infty}$ or $\dfrac{\Delta p}{q}$
C_{p_b}	base-pressure coefficient $= \dfrac{p_b - p_\infty}{q_\infty}$ or $\dfrac{\Delta p_b}{q}$
$C_{y,p}$	Magnus-force coefficient
C_{y_p}	Magnus-force slope coefficient
d	diameter; maximum diameter
D	drag

G   heat capacity

h   heat-transfer coefficient

k   thermal conductivity

K   hypersonic similarity parameter, Md/ℓ; also $\sqrt{M^2 - 1}\ d/\ell$

ℓ total length; skin thickness

ℓ_a afterbody length

ℓ_N nose length

ℓ_t mean transition distance from nose

L   reference length; lift

M   Mach number

M_∞ free-stream Mach number

M_c cross-flow Mach number

N   force normal to body centerline

p   pressure; body spin rate

q   dynamic pressure $= \dfrac{\rho V^2}{2}$ or $\dfrac{\gamma}{2}\ pM^2$

r   radius; recovery factor

Re   Reynolds number

Re_c cross-flow Reynolds number

s   distance along a curved surface

S   reference area (generally taken at maximum diameter)

t   time; thickness

T   temperature

v   volume

V   velocity

w   upwash velocity

x   axial distance

x, r, θ cylindrical coordinates

x, y, z rectangular coordinates; x is generally taken along body axis
             of symmetry

α angle of attack

β $\sqrt{M^2 - 1}$

γ ratio of specific heats

δ boundary-layer thickness

ϵ error; eccentricity; slope of meridian contour

θ semi-vertex angle of cone; cowl angle through which flow is turned; local slope of body surface; boattail angle

θ_s shock angle

ν kinematic viscosity

ρ density

ϕ station around a body, in degrees

Φ perturbation velocity potential

ψ stream function

Ω velocity potential

Subscripts

b   base

c   cross flow; cone

cyl   cylinder

cg   center of gravity

c.p.   center of pressure

i   incompressible; inlet

r   recovery

s   secant

t   tangent

w   wall conditions; wetted area

BODIES OF REVOLUTION

1.   Introduction

This section of the Handbook presents data on the aerodynamic characteristics of bodies of revolution for an angle-of-attack range of zero to almost ninety degrees throughout the supersonic and hypersonic flight regimes.

Basic theories governing the pressure distributions on bodies of revolution and in their surrounding flow fields are discussed and evaluated. To provide a basis for the selection of theoretical methods to be used in specific calculation the reliability and accuracy of these theories are compared at different Mach and Reynolds numbers. Actual step-by-step development is omitted except where it is essential to an understanding of resultant expressions. In all cases, however, sources containing full derivations are referenced.

To permit comparison or extension of the theoretical methods, experimentally-derived data in many instances are also presented. For those cases in which there is discrepancy between theory and experiment, empirical formulae are given together with the limiting values of the parameters within which the particular formula is valid.

Techniques for incorporating the effects of skin friction and heat transfer (treated fully in Sections 13 and 14 of the Handbook) are also given.

No attempt has been made to extrapolate the data (gathered from unclassified literature) beyond the range for which they were initially obtained. In many areas, e.g., Magnus forces, too few references were available to establish appropriate generalizations. In such cases the material is merely presented and conclusions are left to the reader.

1.1   Organization

Each of the six following subsections are devoted to a particular characteristic of flow, i.e., pressure, normal force, drag, etc., with various body shapes serving as the parameters. Subsections 2 and 3 present the various theoretical methods available for the evaluation of flow fields about bodies at low and high angles of attack. Subsection 4 discusses the external surface pressure distribution of basic shapes, including solid and ducted bodies. Subsection 5 presents theory and corresponding data on normal force, pitching moment, and drag due to normal force for the same shapes. Subsection 6 deals with pressure drag and skin friction. The last part, Subsec. 7, presents available base drag information together with the effects of variations in the parameters which affect the afterbody drag.

Within each subsection, particularly in the last four, the development is introduced by a discussion of appropriate theories which are then compared with each other and with representative experimental data. Many references are made to appropriate literature on the development and application of relevant theories as well as to experimental results which supplement those presented herein.

2.   Flow Characteristics at Low Angles of Attack

The solution of complete differential equations of flow is a complex undertaking, even when the effects of viscosity and heat conduction are disregarded. By means of certain simplifying assumptions, however, it is possible to obtain both first and second-order solutions for slender bodies at small angles of attack. Solutions may also be obtained by means of numerical and graphical integration. The method of characteristics, generally accepted as the most accurate of the latter, is practicable only for the cases of two-dimensional and axially symmetric flows, but even these cases require the expenditure of much time for computations. Simplified techniques of flow evaluation will therefore be treated, and the accuracy of the various methods of solution will be evaluated by comparing their results with experimental data.

2.1   Mathematical Formulation of Problem

A convenient method for studying the inviscid flow past a body of revolution utilizes cylindrical coordinates (x, r, θ), wherein the x-axis is aligned along the body axis and the origin is located at the nose of the body as shown below.
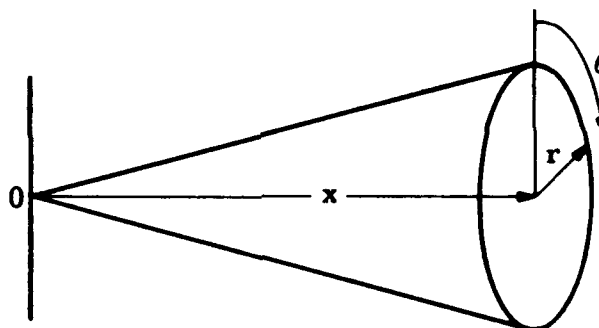
For the development of this method the following simplifying assumptions are made.

1. The body is slender, i.e., the slope of the meridian contour is nowhere greater than ϵ, where $\epsilon \ll 1$ (this implies that the body is either pointed or has a sharp lip);

2. The angle of attack is small;

3. The free-stream Mach number is moderately supersonic.

Subject to these assumptions, the flow can be shown (e.g., see Ref. 1) to be irrotational within the accuracy of the solutions being sought. The velocity potential, Ω, associated with the flow field is assumed to be made up of two parts: first, that associated with the uniform flow field in the absence of the body; and second, a perturbation velocity potential, Φ, induced by the presence of the body. Thus,

$$\Omega(x,r,\theta) = U\left[(x \cos \alpha + r \sin \alpha \cos \theta) + \Phi(x,r,\theta)\right] \qquad (2\text{-}1)$$

The perturbation potential, Φ, can be shown to satisfy the following differential equation (Ref. 2).

$$\Phi_{rr} + \frac{\Phi_r}{r} + \frac{\Phi_{\theta\theta}}{r^2} - \beta^2 \Phi_{xx} = M^2 \left\{ \frac{\gamma-1}{2} \left(\Phi_{xx} + \Phi_{rr} + \frac{\Phi_r}{r} + \frac{\Phi_{\theta\theta}}{r^2} \right) \right.$$

$$\times \left[2 \left(\Phi_x \cos\alpha + \Phi_r \sin\alpha \cos\theta - \frac{\Phi_\theta}{r} \sin\alpha \sin\theta \right) + \Phi_x^2 + \Phi_r^2 + \frac{\Phi_\theta^2}{r^2} \right]$$

$$+ \Phi_{xx} \left(2\Phi_x \cos\alpha + \Phi_x^2 - \sin^2\alpha \right) + \Phi_{rr} \left(\Phi_r + \sin\alpha \cos\theta \right)^2$$

$$+ \left(\frac{\Phi_{\theta\theta}}{r^2} - \frac{\Phi_r}{r} \right) \left(\frac{\Phi_\theta}{r} - \sin\alpha \sin\theta \right)^2 + 2\Phi_{xr} \left(\Phi_x + \cos\alpha \right) \left(\Phi_r + \sin\alpha \cos\theta \right)$$

$$+ 2 \frac{\Phi_{x\theta}}{r} \left(\Phi_x + \cos\alpha \right) \left(\frac{\Phi_\theta}{r} - \sin\alpha \sin\theta \right) + 2 \frac{\Phi_{r\theta}}{r} \left(\Phi_r + \sin\alpha \cos\theta \right)$$

$$\times \left(\frac{\Phi_\theta}{r} - \sin\alpha \sin\theta \right) - 2 \sin\alpha \left(\frac{\Phi_\theta}{r} - \sin\alpha \sin\theta \right) \left(\frac{\Phi_r}{r} \sin\theta + \frac{\Phi_\theta}{r^2} \cos\theta \right) \right\}$$

$$\tag{2-2}$$

The solution of Eq. 2-2 must satisfy the following upstream and boundary conditions:

1. All flow perturbations vanish everywhere upstream of the body, i.e.,

$$\Phi \left(0, r, \theta \right) = \Phi_x \left(0, r, \theta \right) = 0 \tag{2-3}$$

2. The flow is everywhere tangent to the body surface, i.e.,

$$\Phi_r \left(x, R, \theta \right) + \sin\alpha \cos\theta = \frac{dR}{dx} \left[\cos\alpha + \Phi_x \left(x, R, \theta \right) \right] \tag{2-4}$$

where

$R = R(x)$ defines the body surface.

Although the differential equation (Eq. 2-2) taken together with the above boundary conditions can be shown to have a unique solution, its determination in any specific case presents considerable difficulty. In practice, therefore, approximate solutions must be accepted.

2.2   First-Order Theory

Because the body is slender and at a small angle of attack, the perturbation potential, Φ, is small. A reasonable approximation can then be obtained by discarding all second-order and higher-order terms in Eq. 2-2, so that

$$\Phi_{rr} + \frac{\Phi_r}{r} + \frac{\Phi_{\theta\theta}}{r^2} - \beta^2 \Phi_{xx} = 0 \qquad (2-5)$$

where

$$\beta = \sqrt{M^2 - 1}$$

For the special case of axially symmetric bodies, a solution in the following form is sought.

$$\Phi(x,r,\theta) = \phi_0(x,r) \cos\alpha + \phi_1(x,r) \sin\alpha \cos\theta \qquad (2-6)$$

where ϕ_0 and ϕ_1 are also solutions of Eq. 2-5 corresponding respectively to the axial and cross-flow components of the perturbation velocity.

The axial-flow potential, ϕ_0, may be obtained from

$$\phi_{orr} + \frac{\phi_{or}}{r} - \beta^2 \phi_{oxx} = 0 \qquad (2-7)$$

and the cross-flow, ϕ_1, from

$$\phi_{1rr} + \frac{\phi_{1r}}{r} - \frac{\phi_{1\theta\theta}}{r^2} - \beta^2 \phi_{1xx} = 0 \qquad (2-8)$$

The tangential boundary condition given in Eq. 2-4 may also be separated into conditions for the axial and cross-flow components, i.e.,

$$\phi_{or} = \frac{dR}{dx}(1 + \phi_{ox}) \qquad (2-9)$$

and

$$\phi_{1r} + 1 = \frac{dR}{dx}\phi_{1x} \qquad (2-10)$$

A further restriction is introduced by assuming that the body is slender enough to allow ϕ_{ox} and $\phi_{1x} \to 0$; hence the boundary conditions may be replaced by

$$\phi_{or} = \frac{dR}{dx} \qquad (2\text{-}11)$$

and

$$\phi_{1r} + 1 = 0 \qquad (2\text{-}12)$$

2.2.1   Evaluation of First-Order Potentials

The general solutions (Ref. 3) of Eqs. 2-7 and 2-8 which also satisfy the free-stream conditions are, for the axial case,

$$\phi_o(x, r) = - \int_0^{x-\beta r} \frac{f(\xi) \, d\xi}{\sqrt{(x - \xi)^2 - \beta^2 r^2}} \qquad (2\text{-}13)$$

and, for the transverse case,

$$\phi_1(x, r) = \frac{1}{\beta r} \int_0^{x-\beta r} \frac{(x - \xi) \, g(\xi) \, d\xi}{\sqrt{(x - \xi)^2 - \beta^2 r^2}} \qquad (2\text{-}14)$$

The functions f and g are determined from the boundary conditions. Details of the methods required for the solution of these equations are presented in Refs. 3 to 6.

2.2.2   Application to Open-Nosed Bodies

The methods just described can be applied to open-nosed bodies provided that there is no "spill-over" at the lip, i.e., when all of the air in the free stream within the diameter of the inlet passes into the body (see Ref. 7).

2.3   Linearized Theory

The first-order solutions discussed in the preceding subsection are frequently, but incorrectly, referred to as linearized solutions. Lighthill (Ref. 1), the first to consider the strictly linearized solutions to the flow equations, has pointed out that the characteristic surfaces associated with the first-order equations (which are conical in form) remain aligned with the axis of the body as the body is moved

to an angle of attack. On the other hand, those associated with the
linearized equations remain aligned with the free-stream direction.
The former is in better accord with the actual flow conditions in the
immediate neighborhood of the body, and it is this region which is
usually of interest. Thus, in the evaluation of pressure distributions,
the first-order solution would be expected to yield the greater accuracy.
This is confirmed by the first-order and linearized approximations to
$(dC_N/d\alpha)_{\alpha=0}$ for a cone of 10-deg semi-apex angle. These approximations
are compared with the values obtained by use of exact theory in Fig. 2-1
(derived from data in Ref. 2). Since, as demonstrated by this figure,
the linear theory gives such a poor approximation of the exact values,
it remains of academic interest only.

2.4   Van Dyke's Hybrid Theory

        Though the use of the first-order approximation yields a solu-
tion of adequate accuracy in many applications, there are times when
higher accuracy is required. The possibility of deriving second-order
solutions by a process of iteration has been investigated by Van Dyke.
By means of the second-order solution obtained for axial flow the aero-
dynamic characteristics of cone flow are shown to be much nearer the
values obtained from the exact theory than those obtained by the first-
order solution. This is shown in Fig. 2-3, where the pressure coef-
ficients for two cones are determined by the three methods. Van Dyke
then derived the second-order cross-flow equations and found that solu-
tions were only possible for the simple case of conical flow. Re-exam-
ination of the usual approximations made in first-order theory led
Van Dyke to a refinement of these approximations and consequently to
much improved agreement with exact calculations. A comparison of
$(dC_N/d\alpha)_{\alpha=0}$ obtained by these different methods is given in Fig. 2-2
for a 10-deg cone.

        Encouraged by this improvement in first-order solutions,
Van Dyke proposed a "hybrid" solution for the body at an angle of at-
tack. This theory combines the first-order cross flow with the second-
order axial flow. The result of one such calculation is also shown in
Fig. 2-2. The good agreement with the exact solution may be noted over
a wide range of Mach numbers. This method has the advantage that it may
be used for discontinuous contours.

        The full development of these theories, as well as many more
examples, is given in Refs. 2 and 8. In Ref. 9 Van Dyke reduces the
second-order method for axial flow to a routine computation. He also
presents tables of basic functions and standard computing forms as well
as a sample calculation. The procedure is summarized so explicitly that
the computations may be carried out even though all the details of the
underlying theory have not been mastered.

2.5   Slender-Body Theories

        The first-order approximations, which depend on the solution
of Volterra-type integral equations, cannot in general be obtained in
closed form. Realizing this, Von Karman (Ref. 10) suggested that the
asymptotic solutions of the equations for the case of very slender bodies
would yield results of sufficient accuracy to serve most needs. Such
asymptotic solutions to the first-order differential equations are termed

"first-order slender-body approximations." Lighthill (Ref. 11),
Laitone (Ref. 12), and others have gone further and declared that the
replacement of Eq. 2-2 by Eq. 2-5 introduces errors of a magnitude com-
parable to the disparity which exists between the exact and asymptotic
solutions of the first-order equations. In other words, considering
the simplifications that have been intrvuuced in setting up the first-
order equations, the slender-body theory represents as accurate a solu-
tion as can be hoped for. However, even though this statement may be
true for a mathematically slender body, the actual practical type of
body cannot, as Van Dyke points out, generally be considered a slender
body and therefore may not validly be included in this comparison of
accuracies. To expand these conclusions, Van Dyke classifies super-
sonic-body flow problems as follows:

   1. Slender bodies at moderate Mach numbers.

$$\left.\begin{array}{l} \epsilon << 1 \\ \beta\epsilon << 1 \end{array}\right\} \beta = 0(1)$$
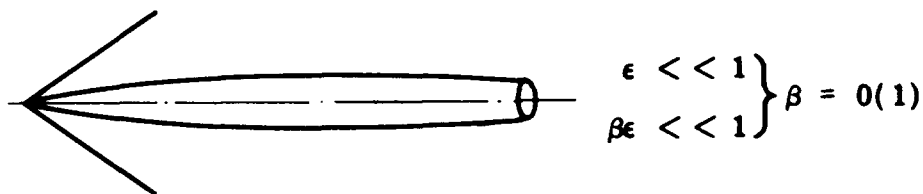
   2. Slender bodies at hypersonic Mach numbers.

$$\left.\begin{array}{l} \epsilon << 1 \\ \beta\epsilon = 0(1) \end{array}\right\} \beta = 0(1/\epsilon)$$
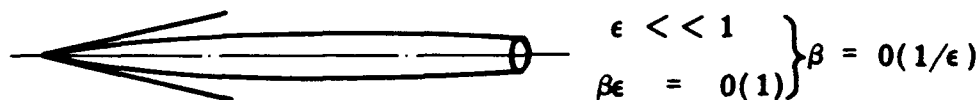
   3. Bodies of moderate fineness ratio at moderate Mach numbers.

$$\left.\begin{array}{l} \epsilon = 0(1) \\ \beta\epsilon = 0(1) \end{array}\right\} \beta = 0(1)$$
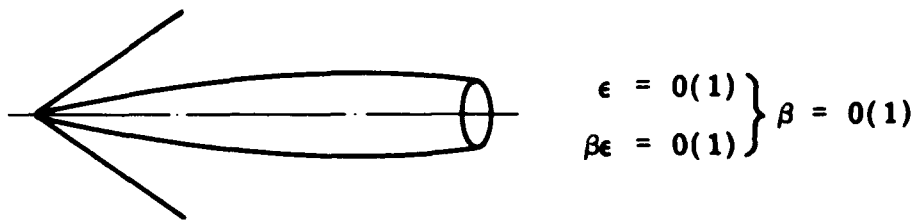
where

   ϵ = maximum slope of meridian contour

   $\beta = \sqrt{M^2 - 1}$

For a logically complete classification, bodies of moderate thickness
at hypersonic Mach numbers should also be included. However, since
this case involves detachment of the nose shock, it is not embraced by
the perturbation theory and is therefore excluded from consideration in
this subsection.

     Slender-body theory, since it is based on the order estimates
of Class 1, is restricted in its application to problems falling within
this class. But cases of practical import frequently fall into Class 3,
and it is here that the first-order solutions represent a marked improve-
ment over the slender-body solutions.

The preceding remarks are equally applicable to the higher-order slender-body theories of Broderick (Ref. 13) and others since, in all of these analyses, both ϵ and $\beta\epsilon$ are assumed to be small quantities.

Although the slender-body approximation has been introduced in the preceding discussion as the asymptotic solution to the first-order differential equations, it can be shown that it is completely equivalent to the supersonic counterpart of the slender-body cross-flow theory developed by Munk in Ref. 14. The merit in Munk's presentation is that it emphasizes the physical implications of the theory.

Despite its limitations, in those cases in which it is applicable, slender-body theory possesses the distinctive virtue of being easy to apply.

2.5.1 Munk's Slender-Body Theory

By assuming that the body is slender, the angle of attack small, and the gradient of the velocity potential in the flow direction negligible, Munk obtained the following expression for the normal force coefficient.

$$C_N = (K_2 - K_1) \sin 2\alpha \qquad (2\text{-}15)$$

where

$\qquad K_1$ and K_2 = virtual mass coefficient in longitudinal and lateral motions

On the basis of a more detailed examination of the slender-body hypothesis, Ward in Ref. 15 concluded that it is more exact to assume that the resultant force is inclined at an angle $\alpha/2$ to the vertical in a downstream direction. Hence, in this instance, Eq. 2-15 becomes

$$C_N = (K_2 - K_1) \sin 2\alpha \cos \alpha/2 \qquad (2\text{-}16)$$

Lamb (Ref. 16) gives an expression for deriving K_1 and K_2 for various ellipsoids. The values of K_1, K_2, and $K_2 - K_1$ for ellipsoids of revolution with various length-to-diameter ratios are tabulated on the following page.

Although the coefficients are evaluated specifically for ellipsoids of revolution, they give a good approximation to any axisymmetric body with comparable fineness ratio. For slender bodies the value of $K_2 - K_1 = 1$ gives results of sufficient accuracy for most practical purposes.

Table 2-1

Virtual Mass Coefficients

ℓ/d	K_1	K_2	$K_2 - K_1$
1.0	0.500	0.500	0
1.5	0.305	0.621	0.316
2.0	0.209	0.702	0.493
2.5	0.156	0.763	0.607
3.0	0.122	0.804	0.682
4.0	0.082	0.860	0.778
5.0	0.059	0.894	0.835
6.0	0.045	0.917	0.872
7.0	0.036	0.933	0.897
8.0	0.029	0.945	0.916
9.0	0.024	0.954	0.930
10.0	0.021	0.960	0.939
∞	0.000	1.000	1.000

2.6   Method of Characteristics

By means of simplifying assumptions some solutions have been found in special cases for the general differential equation of potential flow. Several methods of arriving at a solution of the general equation have been devised, utilizing numerical integration or a combination of numerical integration and graphical construction.

One of the most useful is the method of characteristics, which has been applied to many basic types of flow field. The determination of the flow characteristics in the region between an attached shock wave and the pointed axially-symmetric body which creates the shock wave has been treated by Tollmein and Schafer in Ref. 17. A detailed description of the step-by-step procedure as well as a fully worked example which extends the calculations into the region of a curved shock-wave (assuming isentropic flow between shocks) is given by Cronvich in Ref. 18. Although this method requires much tedious work, it has been used with success for determining the pressure distribution over arbitrary nose shapes and for determining the contour of the inner body of a ram-jet engine for a given compression ratio. In supersonic diffuser studies the characteristics method has been used successfully to find the additive drag (due to spill over) by analyzing the field over the specified contour at Mach numbers below the design Mach number.

A procedure by which the method of characteristics may be used to design axially symmetric supersonic nozzles is presented in Ref. 19.

By assuming a distribution pattern of the vorticity downstream of a shock wave, Ferri in Ref. 20 has extended the application of the method of characteristics to supersonic rotational flow.

The accuracy of a characteristics calculation is dependent upon the fineness of the "mesh" employed and the number of iterations to which the calculations are taken. The optimum spacing of the initial points should be a function of the rate of change of the parameters in the flow field being investigated and of the desired accuracy in the end results.

2.7   Conical Flow Solutions

Solutions of potential flow fields about conical bodies have been found by several independent methods. The solutions are more easily obtained for conical flow because the pressure, velocity, and density are constant in irrotational flow over conical surfaces having the same vertex as the conical body.

2.7.1   Taylor-Maccoll and Kopal Methods

Taylor and Maccoll (Ref. 21), using the equation for potential flow (Eq. 2-2), calculated the flow parameters along conical rays from the vertex by means of a numerical integration which starts from known flow along the cone surface and progresses through angular increments. At the same time they calculated the pressure change that would occur across an oblique shock of the same inclination as each ray. The point of agreement between the values of pressure ratio from each set of calculations determined the location of the shock wave for the particular cone angle and surface velocity ratio chosen. The scope of these calculations was very much extended under the direction of Kopal. Reference 22 presents tabulated data for the characteristics of the flow fields about cones whose semi-vertex angle ranges from 5 deg to 50 deg for Mach numbers up to infinity.

2.7.2   Tangent-Cone Method

The pressures on arbitrarily shaped bodies of revolution may be estimated by means of the flow parameters for cones whose shapes correspond to those of the body surface from point to point. In the simplest application of this method the slope of the body is averaged over segments of any desired length and the pressure is taken to be that of the equivalent cone. This assumes a different total head pressure for each segment, i.e., a pressure loss due to the bow shock associated with the corresponding cone at the free-stream Mach number. Thus the nose segment is the only one which has the pressure referred to the correct stagnation pressure.

A second method of applying the cone-tangent method is to correct the local total head pressure for each segment by comparing the assumed conical shock with the actual bow shock of the curved body.

The relative accuracy of the two methods is dependent on the Mach number and the fineness ratio of the nose and the distance from the vertex. This is shown in Fig. 2-4, where the pressure distribution (taken from Ref. 31) for tangent-ogives of fineness ratios of 1.5, 2, and 3 calculated by both methods at Mach numbers of 1.5, 2, 3, and 6 is compared with that obtained by the method of characteristics.

All the necessary conical flow information for both methods of application is given in Ref. 22.

2.8   Shock-Expansion Method

The generalized shock-expansion method proposed by Eggers and Savin (Refs. 23 and 24) is an extremely simple and versatile method for determining the flow field about bodies in supersonic flow. This method is somewhat limited in the range of Mach numbers and fineness ratios which can be treated; however, the inherent simplicity of the method merits special attention. It is assumed that the flow field in the vicinity of the vertex of the ogive can be obtained from conical flow theory. Therefore, the flow properties at the surface immediately behind the bow shock wave are considered as known quantities and provide initial conditions for the Prandtl-Meyer type flow which follows. Thus, the flow field about an ogive-cylinder can be determined in two steps:

1. The flow conditions at the vertex can be obtained from existing solutions for conical flow (e.g., Ref. 22);

2. The flow downstream of the vertex can be computed by means of the Prandtl-Meyer equations or tables (e.g., Ref. 28 or 29).

Comparison of solutions obtained by the generalized shock-expansion method with exact solutions indicates that the method yields accurate pressure distributions over ogival noses only if the hypersonic similarity parameter (Subsec. 2.10.3) is greater than approximately 1.2 or 1.3 (Ref. 25). A weakness of this method is that it cannot take into account the known pressure drop at the shoulder (see Fig. 4-1) of an ogive cylinder. If a cylindrical afterbody is long, then the constant pressure predicted by the shock-expansion method will yield moment and normal-force derivatives that are considerably in error even though the hypersonic similarity parameter is much greater than 1.2. The simplicity and accuracy of the method for the ogive portion of the body at large values of the hypersonic similarity parameter make it extremely valuable and useful.

2.8.1   Second-Order Shock-Expansion Method

The generalized shock-expansion method is so convenient and simple that any attempt to extend its range of applicability is likely to be worthwhile. Syvertson and Dennis (Ref. 26) offer a second-order shock-expansion method which successfully extends the range of usefulness of the shock-expansion method to include values of the hypersonic similarity parameter less than unity. It should be mentioned, however, that the second-order shock-expansion method is tedious to apply because the numerical computations are relatively complex.

2.8.2   Modified Second-Order Shock-Expansion Method for Use with Ogives

An accurate and simple scheme for obtaining pressure distributions and lift and moment curve slopes for ogival nose-cylinder combinations by simplifying the second-order shock expansion method has been developed by Fenter (Ref. 27). Assuming that the exponent in the relation for the pressure over any segment of such a shape varies inversely with the hypersonic similarity parameter, the following relation for the pressure distribution may be obtained.

$$\frac{p_n}{p_\infty} = \frac{p_{cn}}{p_\infty} + \left(\frac{p_n'}{p_\infty} - \frac{p_{cn}}{p_\infty}\right) e^{-\frac{s}{K\ell_N}} \qquad (2\text{-}17)$$

where

> s = distance along the meridian line from the origin of each segment (see sketch below)
>
> ℓ_N = length of the nose section
>
> K = hypersonic similarity parameter, Md/ℓ
>
> d = body diameter
>
> ℓ = length of body
>
> ' = condition at the most forward point of a segment of the equivalent tangent body (s = 0)

and subscripts

> n = specific segment of equivalent tangent body
>
> d = condition on the equivalent tangent cone

The values of p' and M' are found by means of a Prandtl-Meyer expansion through $(\delta_n - \delta_{n+1})$ deg (see tables in Ref. 28)
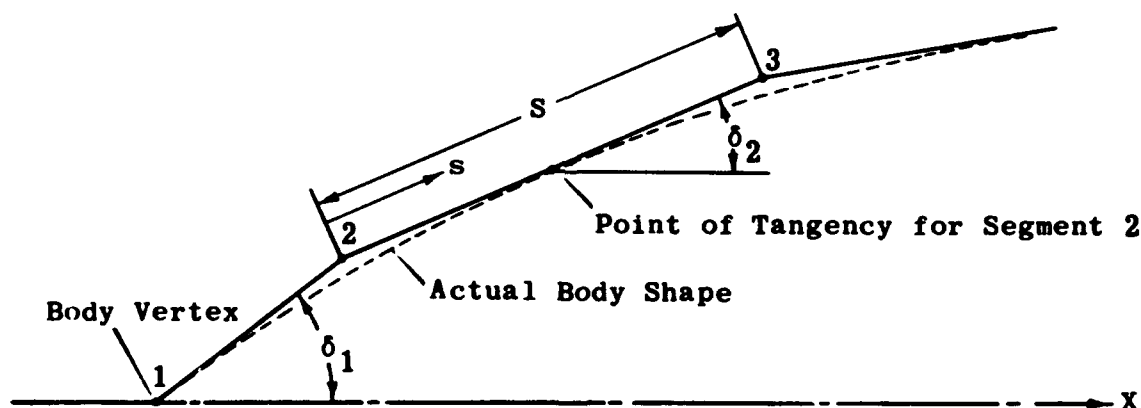
This method has been shown by experiment to give good results over a wide range of the hypersonic similarity parameter and for Mach numbers as low as 2. Its agreement with the method of characteristics for various conditions of the similarity parameter, specific Mach number, and nose length is given in Figs. 2-5 to 2-7 (derived from Refs. 25 and 27).

2.9   Relative Merits of the Various Methods

The selection of any one of the several methods (described in preceding subsections) for evaluating the flow about bodies will be determined primarily by the accuracy required and the time available for calculations. Most of the methods are compared in Fig. 2-8 (from

Ref. 31) which shows their general limitations and optimum areas of application. In this figure, errors in pressure drag associated with the application of these various theories have been plotted against the similarity parameter, K or $\frac{M}{\ell_N/d}$ (see Subsec. 2.10.3). The "standard" pressure drag, i.e., the zero error drag, is calculated by means of characteristics. It may be seen that the second-order theory gives the most accurate results for $K < 1.2$ and the conical-shock-expansion theory is best for $K > 1.2$. Linearized theory is poor for $K > 0.5$.

The value of such a curve is limited because it is based on integrated pressures rather than a pressure distribution. Instead of being indicative of a close approximation to the actual pressure distribution, the smallest drag error may possibly be due to compensating errors. This may be exemplified by a comparison of the pressure and drag curves for the tangent-cone method in Figs. 2-4 and 2-5.

The Fenter method (published more recently than Ref. 31 and therefore not included in Fig. 2-8) has been shown to have a pressure distribution very close to that obtained by the characteristics method for values of $K > 1$.

The generalized shock expansion, the Newtonian flow, and the tangent-cone methods are perhaps the simplest and quickest to use, but they are more accurate in the hypersonic range than at lower supersonic Mach numbers (see Subsec. 2.10). The Fenter method is rapid and only slightly more involved than the above-mentioned methods and has the added advantage of a larger range of usefulness (as low as $M = 2$).

2.10   Hypersonic Flow

The hypersonic regime may in general be considered as an extension of the supersonic continuum, and the theories developed for supersonic flow should be valid for the hypersonic case as long as the fluid retains the properties of an ideal gas with a constant value of the ratio of the specific heats. Even in the case of an ideal gas there are limiting values of the combination of flow properties and model geometry within which the supersonic theories may be used. These, discussed in Subsec. 2.10.3, are shown in Fig. 2-12. In the limit the density becomes so low that the boundary layer is of the same order of magnitude as the mean free path, and the gas may no longer be regarded as a continuum but must be considered as made up of discrete particles. The Newtonian impact theory provides the solution for most problems in this regime, which is fully treated in Section 16 of this Handbook (Ref. 170).

One of the first requirements then is to define (usually in terms of temperature) the conditions under which the gas imperfections may no longer be neglected. For the most common medium, air, the thermal imperfections are no longer negligible at temperatures greater than $1200°R$. Up to $5000°R$, corrections for these imperfections may be applied to the isentropic flow equations to give results of adequate accuracy for most purposes. Equations, graphs, and excellent tables for this purpose are given in Ref. 29. At temperatures greater than $5000°R$ the effects of oxygen dissociation make it necessary to re-formulate the basic equations.

The definition of the hypersonic slender body given in Sub-
sec. 2.5 limits the value of $\beta\theta$ (or $\beta\epsilon$) to the order of 1. By so doing
it confines the combinations of flow speed and shock-wave angle to
values which preclude excessive temperatures behind the bow shock wave.
Subsequent subsections present the actual values of the parameter $\beta\theta$,
for which the various supersonic theories may be extended into the hy-
personic regime.

Aerodynamic characteristics have been determined experimen-
tally at very high Mach numbers in wind tunnels which have limited
stagnation temperatures and which avoid dissociation effects by the
use of monatomic gases. Consequently, care should be used in applying
such data to similar bodies in free flight, where the minimum ambient
temperature is 390°R and the temperature behind the bow shock may
rapidly produce non-ideal gas conditions.

2.10.1   Hypersonic Boundary Layer

At high Mach numbers the shock waves and expansion fans sub-
tend shallow angles with the body surface, and the regions of flow dis-
turbance are limited to relatively thin layers, often termed the "hyper-
sonic shock layers." The sketch below illustrates this for a slender
body in hypersonic flow.
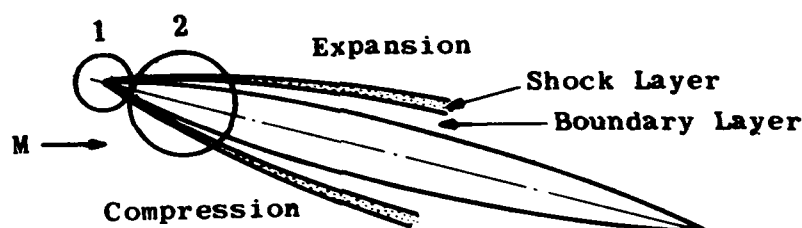
At the vertex, region 1 of the sketch, the shock lies so close
to the surface that the boundary layer equations are no longer valid.
In region 2, although the shock and boundary layer interaction is still
very strong, the Prandtl boundary-layer equations give a reasonably ac-
curate description of the flow conditions. As the flow progresses along
the body the interaction becomes weaker. In this thin region of the
shock and boundary layers the normal components of the pressure and ve-
locity gradients are steep. Furthermore, since even for slender bodies
the shocks are strong, the entropy gradients are also significant.

In many respects the hypersonic shock layer resembles the con-
ventional type of viscous boundary layer. Lees (Ref. 43) found solu-
tions for the viscous flow over a flat plate and a wedge at hypersonic
velocities by applying approximations that were similar to those which
Prandtl introduced in his treatment of the viscous boundary layer. In
his work, Lees also includes skin-friction and heat-transfer calculations.

2.10.2   Method of Characteristics

The method of characteristics may be applied to hypersonic
flow since it represents an exact solution of the non-viscous equations.
However, the rapid changes in flow variables make a fine mesh imperative
and add to the labor of the calculations. Moreover, the entropy gra-
dients imply significant rotational flow which may not be neglected.

Rossow in Ref. 25 has developed a method whereby the effects of rotation may be superimposed on an irrotational solution. The effect of such an addition is shown in Figs. 2-10 and 2-11.

2.10.3 Hypersonic Similarity Rule

For slender bodies (where θ is small) the shock wave angle, β, is small and the quantity $(\beta - \theta)$ is also small. Under these assumptions and those of a perfect gas with constant γ, the shock wave equation

$$M^2 \sin \beta - 1 = \frac{\gamma + 1}{2} M^2 \frac{\sin \beta \sin \theta}{\cos (\beta - \theta)} \tag{2-18}$$

may be reduced to

$$\frac{\beta}{\theta} = \frac{\gamma + 1}{4} + \sqrt{\left(\frac{\gamma + 1}{4}\right)^2 + \frac{1}{(M\theta)^2}} \tag{2-19}$$

Similarly, the Prandtl-Meyer relation for an expansion becomes

$$\frac{M_\infty}{M} = 1 + \frac{\gamma - 1}{2} (M_\infty \theta) \tag{2-20}$$

It may be seen that both compression and expansion may be expressed solely in terms of $(M_\infty \theta)$. This quantity, known as the hypersonic similarity parameter and often designated by K, is expressed in several slightly different forms, i.e.,

$$M_\infty \theta \sim M_\infty \tan \theta \sim M_\infty \frac{d}{\ell_N} \tag{2-21}$$

The pressure coefficient may be expressed as

$$C_p = \frac{p - p_\infty}{q} = \frac{p - p_\infty}{\frac{1}{2} \gamma p_\infty M_\infty^2}$$

$$= \frac{2}{\gamma M_\infty^2} \left\{ \left[\frac{2 + (\gamma - 1) M_\infty^2}{2 + (\gamma - 1) M^2} \right]^{\frac{\gamma}{\gamma - 1}} - 1 \right\} \tag{2-22}$$

By the use of Eqs. 2-19 and 2-20, when M_∞ and M are large, Eq. 2-22 reduces to

$$C_p = \frac{2}{\gamma M_\infty^2} \left[\left(1 + \frac{\gamma - 1}{2} M_\infty \theta \right)^{\frac{2\gamma}{\gamma - 1}} - 1 \right] \tag{2-23}$$

i.e.,

$$C_p = \theta^2 \ f \ (M_\infty \ \theta) \qquad\qquad (2\text{-}24)$$

or

$$C_p = \left(\frac{d}{\ell_N}\right)^2 f_1 \ (K) \qquad\qquad (2\text{-}25)$$

This hypersonic similarity rule was first enunciated by Tsien (Ref. 32) and is based upon the equations of irrotational flow. Hayes (Ref. 33) has shown that the rule is equally applicable to rotational flows.

Ehret, Rossow, and Stevens (Ref. 30) examined the applicability of the rule to non-rotational flows, and Rossow in Ref. 25 did the same for the rotational case. The usefulness of the rule for the purpose of correlating pressure data at particular values of K is shown in Figs. 2-9 to 2-11.

The range of M, ℓ_N/d, and K within which the hypersonic similarity rule will predict pressure to within 5% of the exact value is shown in Fig. 2-12 (taken from Ref. 30).

Van Dyke in Ref. 34 has shown that the hypersonic rule may be extended into the supersonic regime by substituting $\beta = \sqrt{M^2 - 1}$ for M in the similarity parameter. The effect of this transformation is shown in Fig. 2-13 where the pressures on three cones are reduced to a single curve when the flow is supersonic.

2.10.4   Hypersonic Small-Disturbance Theory

Van Dyke in Ref. 35 has shown that by use of the similarity parameter, hypersonic small-disturbance equations may be derived. However, their solution cannot be obtained without further simplification and therefore their practicality is limited to providing pilot solutions to new problems.

2.10.5   Shock-Expansion Method

As the domain of disturbance surrounding a slender body in hypersonic flow becomes thinner, the flow perturbations assume a two-dimensional character. Thus, if the flow at the vertex of a slender body may be assumed conical, the ensuing flow on any streamline may be approximated by means of Prandtl-Meyer expansions (tables of which are presented in Refs. 28 and 29). The method for non-lifting bodies is given by Eggers and Savin in Ref. 23. A comparison of the pressures on ogival noses calculated by the shock-expansion method and by the method of characteristics is given in Fig. 2-14 (taken from Ref. 23) for K = 0.5 to 2.0. As K increases, the agreement becomes very close.

Savin, in Ref. 24, extends the method to bodies at angles of attack up to 15 deg. The method of calculation is fully detailed and

substantiated by comparison with experimental data for ogives whose ℓ_N/d is 3 and 5 at Mach numbers of 3 to 5. The agreement is good for

$$K \geq 1 \quad \text{and} \quad \alpha/\theta \leq 1/2$$

where

α = angle of attack

θ = semi-vertex angle

Beyond these values the agreement is only fair. The use of this method is also discussed in Refs. 27 and 37.

Zienkiewicz and Bolton-Shaw (Refs. 38 and 39) extended the range of applicability of this simple shock-expansion theory by the use of an empirical factor with the Prandtl-Meyer relations.

2.10.6   Newtonian Impact Theory

The Newtonian concept of flow assumes that the shock wave lies on the body surface and that the component of momentum normal to the surface is fully transferred to the body. This condition is attained when $M_\infty \to \infty$ and $\gamma \to 1$.

The pressure coefficient through an oblique shock is given by

$$C_p = \frac{p - p_\infty}{q_\infty} = \frac{2 \sin \beta \sin \theta}{\cos (\beta - \theta)} \tag{2-26}$$

where

β = shock wave angle

θ = angle through which the flow is turned

i.e., θ = local slope of body surface

In hypersonic flow $\beta \sim \theta$, and hence Eq. 2-26 reduces to

$$C_p = 2 \sin^2\beta \; 2 \sin^2\theta \tag{2-27}$$

Ivey, Klunker, and Bowen in Ref. 40 have modified the Newtonian theory to include the pressure relief due to centrifugal force when the meridian line of the slender body is curved, e.g., in ogives and parabolic

shapes. They give the pressure coefficient as

$$C_p = \frac{2f'^2}{1 + f'^2} + \frac{ff''}{(1 + f'^2)^{3/2}}$$ (2-28)

which may be reduced to

$$C_p = 2f'^2 + ff''$$ (2-29)

since f'^2 is small compared to 1. The body shape is defined by
$r = f(x)$ and f' and f'' are the first and second derivatives with
respect to x. This method is only valid in the region of positive
pressures, which is roughly the portion forward of the maximum diam-
eter. The method is often applied successfully to the nose section
of blunt bodies as well as to slender bodies (see Subsec. 4.6).

From Fig. 2-8 it may be seen that the accuracy of the New-
tonian method is satisfactory for values of $K > 2$. The accuracy of
the method is discussed further in Subsec. 6.8 and illustrated in
Fig. 6-42 where two curves show, for a typical example, that the un-
modified Newtonian equations are closer to the exact solution than is
the case when the centrifugal forces are included (see also Ref. 41).
Eggers, Resnikoff, and Dennis in Ref. 42 calculated the effect of the
centrifugal forces on minimum drag bodies (see Subsec. 6.7). They
showed that the modified Newtonian theory gives slightly better pre-
dictions of pressure distribution than the simple impact theory for
those bodies which have blunter noses than tangent ogives.

2.10.6.1   Assumption of $\gamma = 1$

The assumption of $\gamma = 1$ in the Newtonian method may be justi-
fied because the pressure coefficient through both a compression shock
and an expansion fan is independent of γ. This suggests that the sim-
plification may be applied throughout the hypersonic range. Van Dyke in
Ref. 100 compares the pressure coefficient on several cones for a wide
range of similarity parameters and shows that when $\gamma = 1$ the values are
about 3% less than those for the same cones when $\gamma = 1.4$.

The physical implications of using $\gamma = 1$ are beyond the scope
of this section of the Handbook. The assumption that all entropy and
temperature changes take place in the shock itself simplifies the mathe-
matical model and enables results to be predicted that are accurate
enough for design studies.

2.10.7   Tangent-Cone Approximation

The tangent-cone method described in Subsec. 2.7.2 may also
be used in the hypersonic regime. It may be seen in Fig. 2-8 that when
the total head pressure ratio is corrected for each segment the accuracy
remains good for increasing values of the hypersonic similarity parameter.

2.10.8   Comparison of Methods for Hypersonic Flow

The pressure coefficient for a tangent ogive with $\ell_N/d = 3$ at M = 6, i.e., for K = 2, has been calculated by several methods and the results shown in Fig. 2-15 (taken from Ref. 31). It may be seen that the tangent-cone method (with local total head pressure), the Newtonian impact method, and the application of shock-expansion theory all give a pressure distribution in very good agreement with the exact (characteristics) solution.

Fig. 2-2. Comparison of solution obtained by several theories for normal-force slope on a 10-deg half-angle cone. (Source: Ref. 2)

Fig. 2-1. Comparison of first-order theory and linearized theory with the exact solution for normal-force slope on a 10-deg half-angle cone. (Source: Ref. 2)

21

Fig. 2-3   NAVWEPS Report 1488 (Vol. 3, Sec. 8)
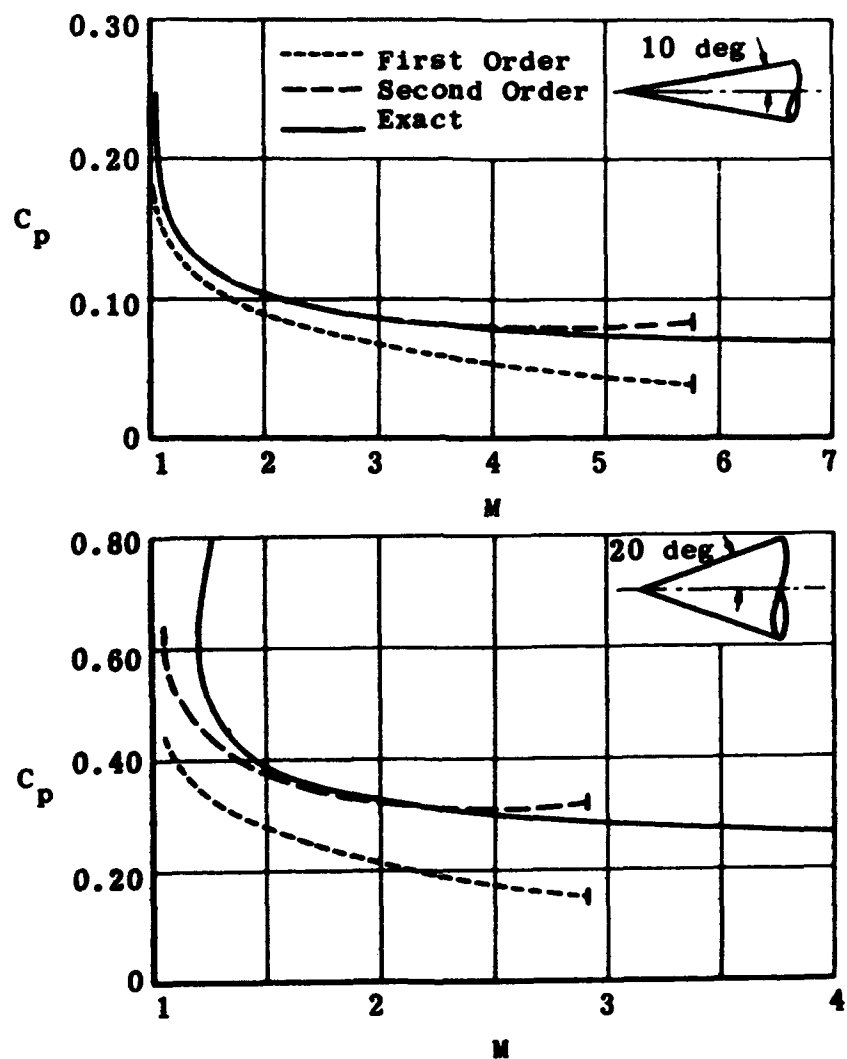
Fig. 2-3. Comparison of first-order and second-order solutions
          with the exact solution for the pressure coefficients for
          10-deg and 20-deg half-angle cones. (Source: Ref. 2)
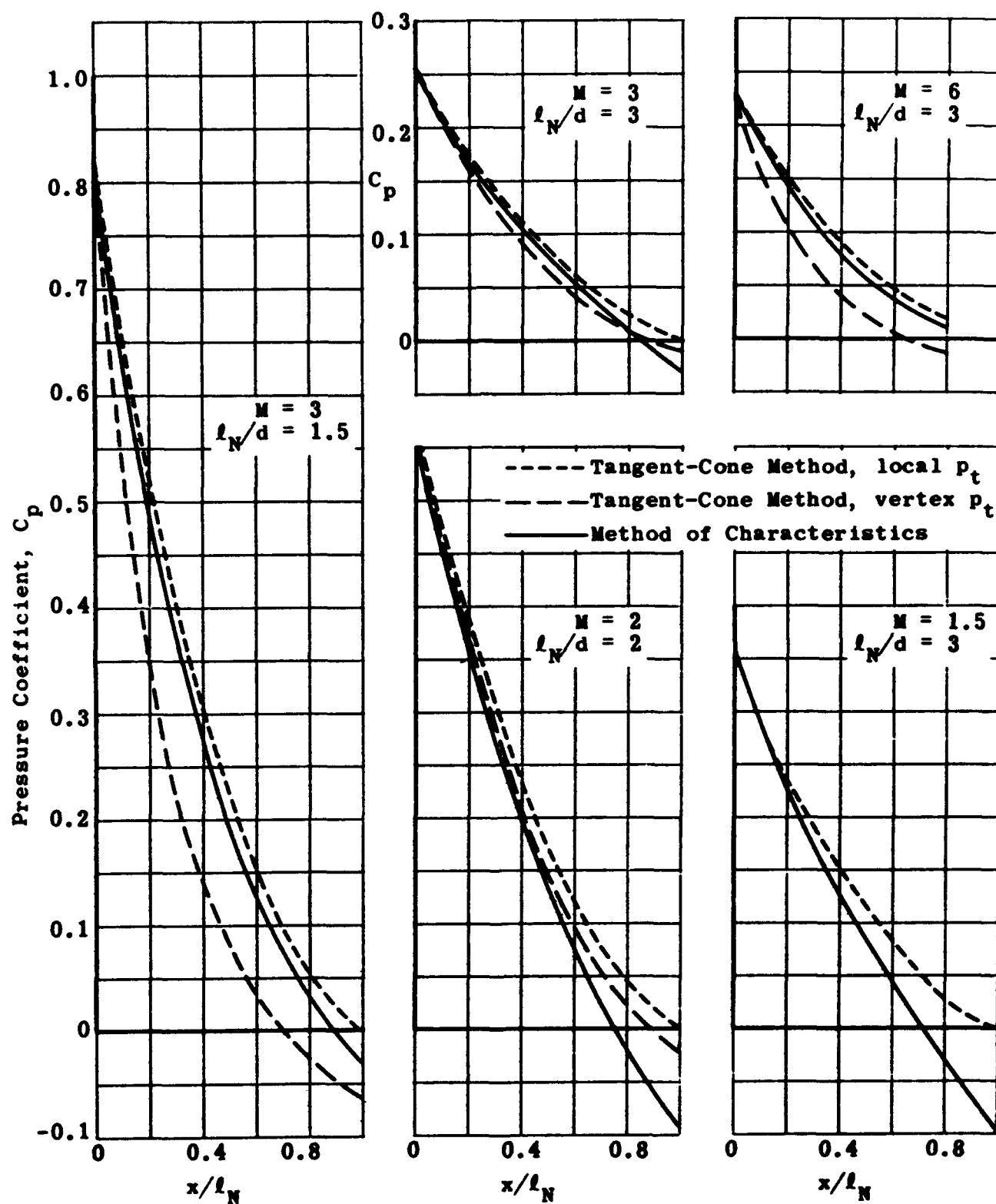
Fig. 2-4. Comparison of pressure distributions on tangent
ogives derived by tangent-cone and characteristics
methods. (Source: Ref. 31)

Fig. 2-5   NAVWEPS Report 1488 (Vol. 3, Sec. 8)
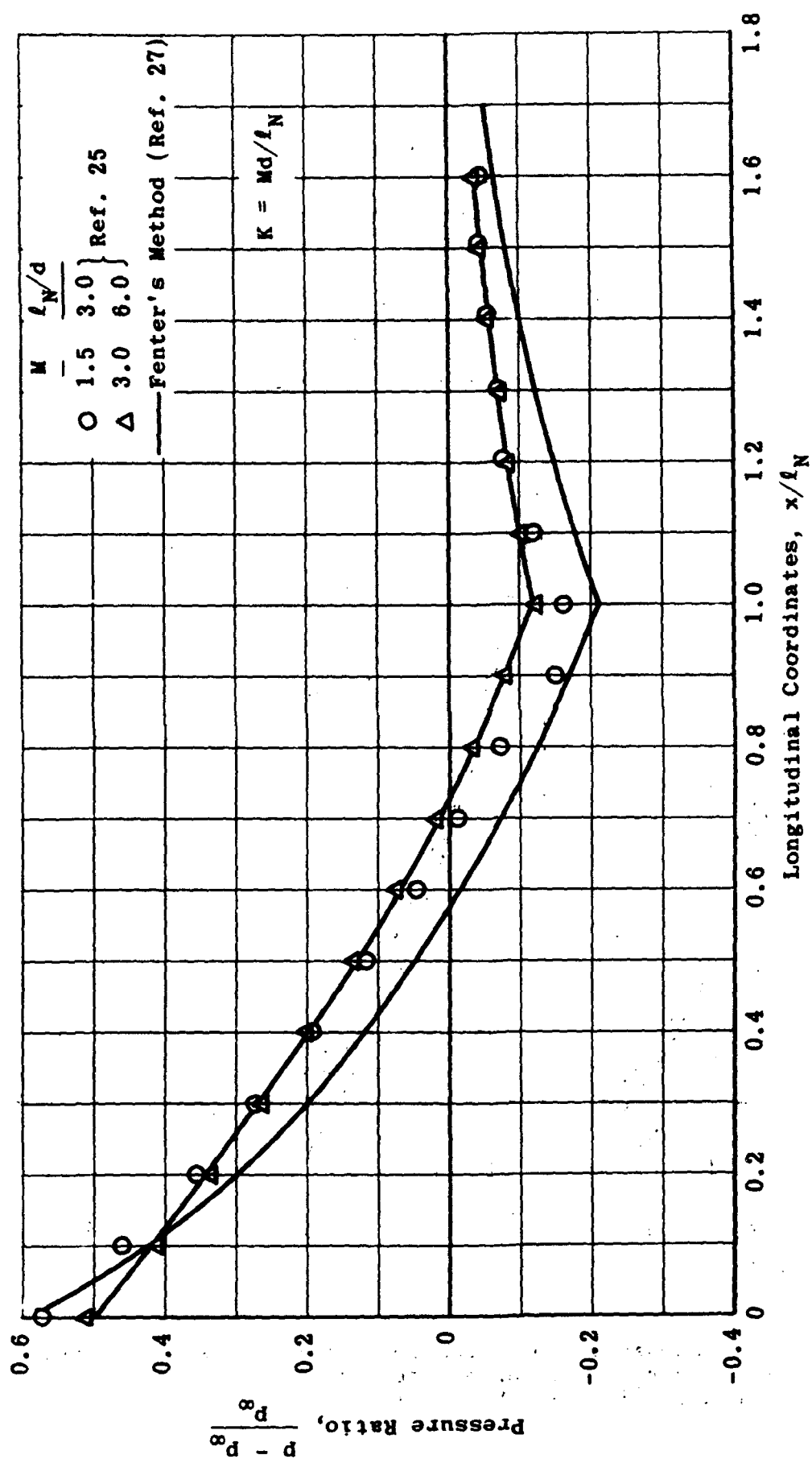
Fig. 2-5. Comparison of pressure ratios for tangent ogives derived by Fenter's method and the method of characteristics; K = 0.5.
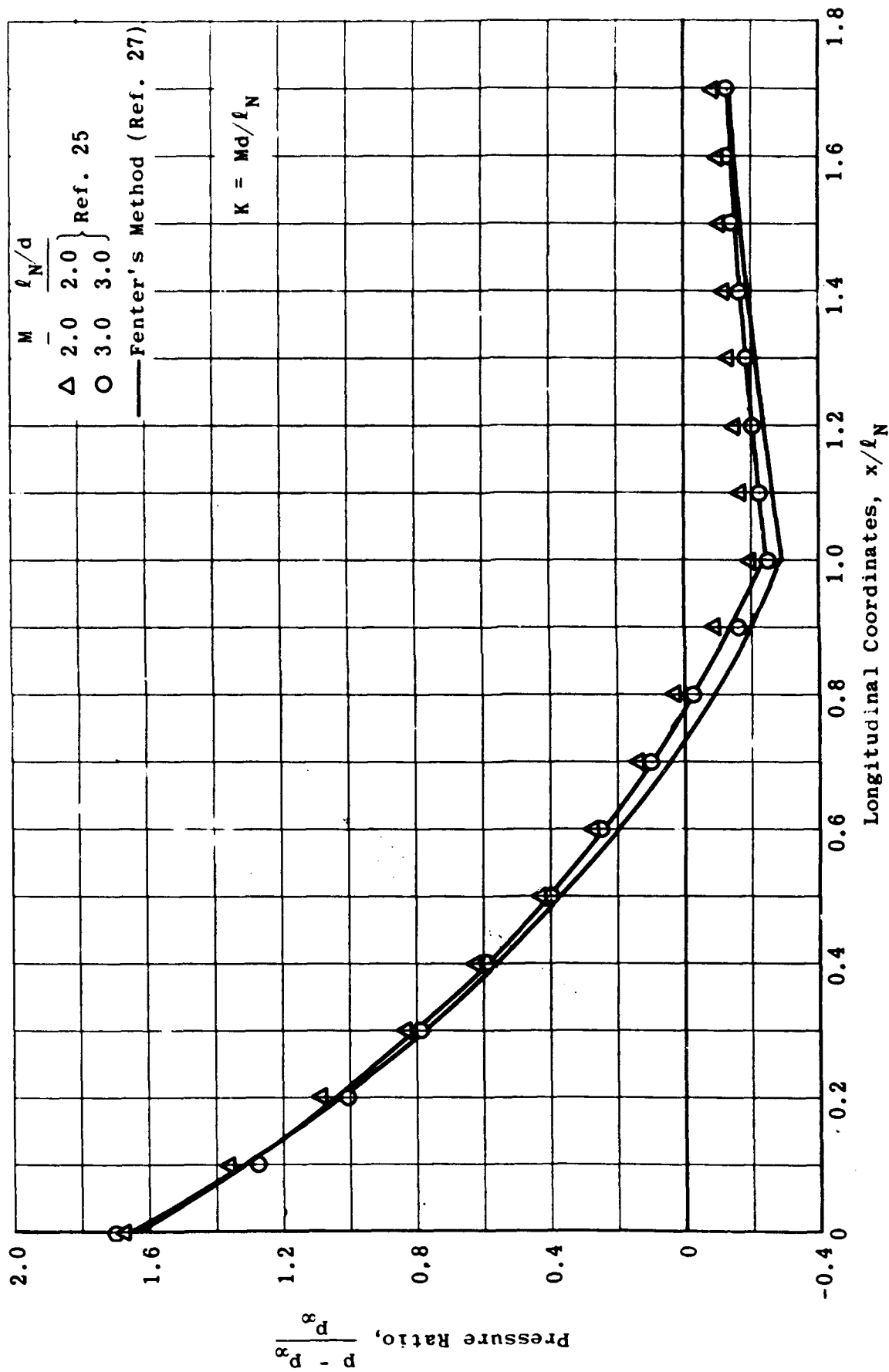
Fig. 2-6. Comparison of pressure ratios for tangent ogives derived by Fenter's method and the method of characteristics; K = 1.0.

Fig. 2-7   NAVWEPS Report 1488 (Vol. 3, Sec. 8)
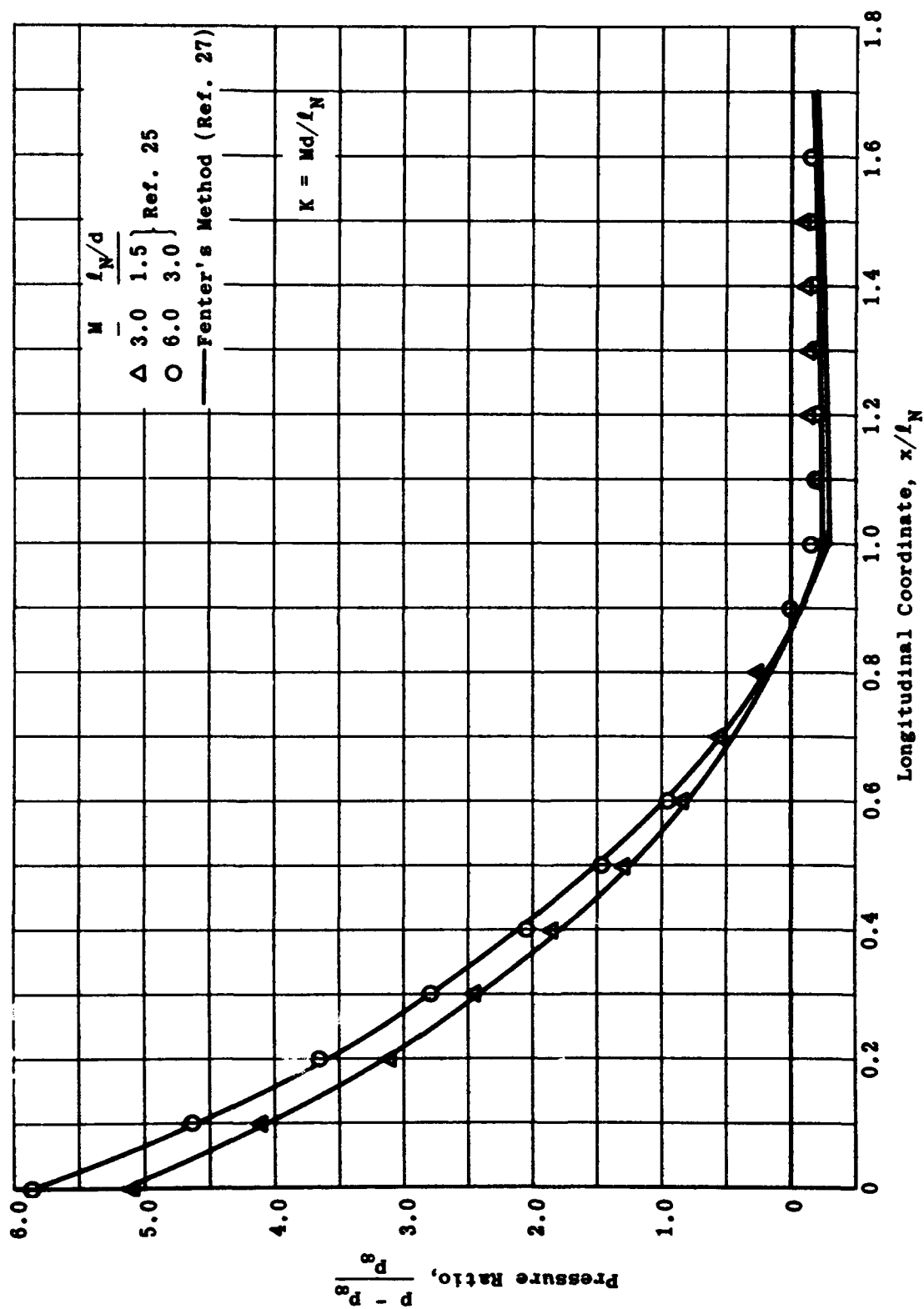
Fig. 2-7. Comparison of pressure ratios for tangent ogives derived by Fenter's method and the method of characteristics; K = 2.0.
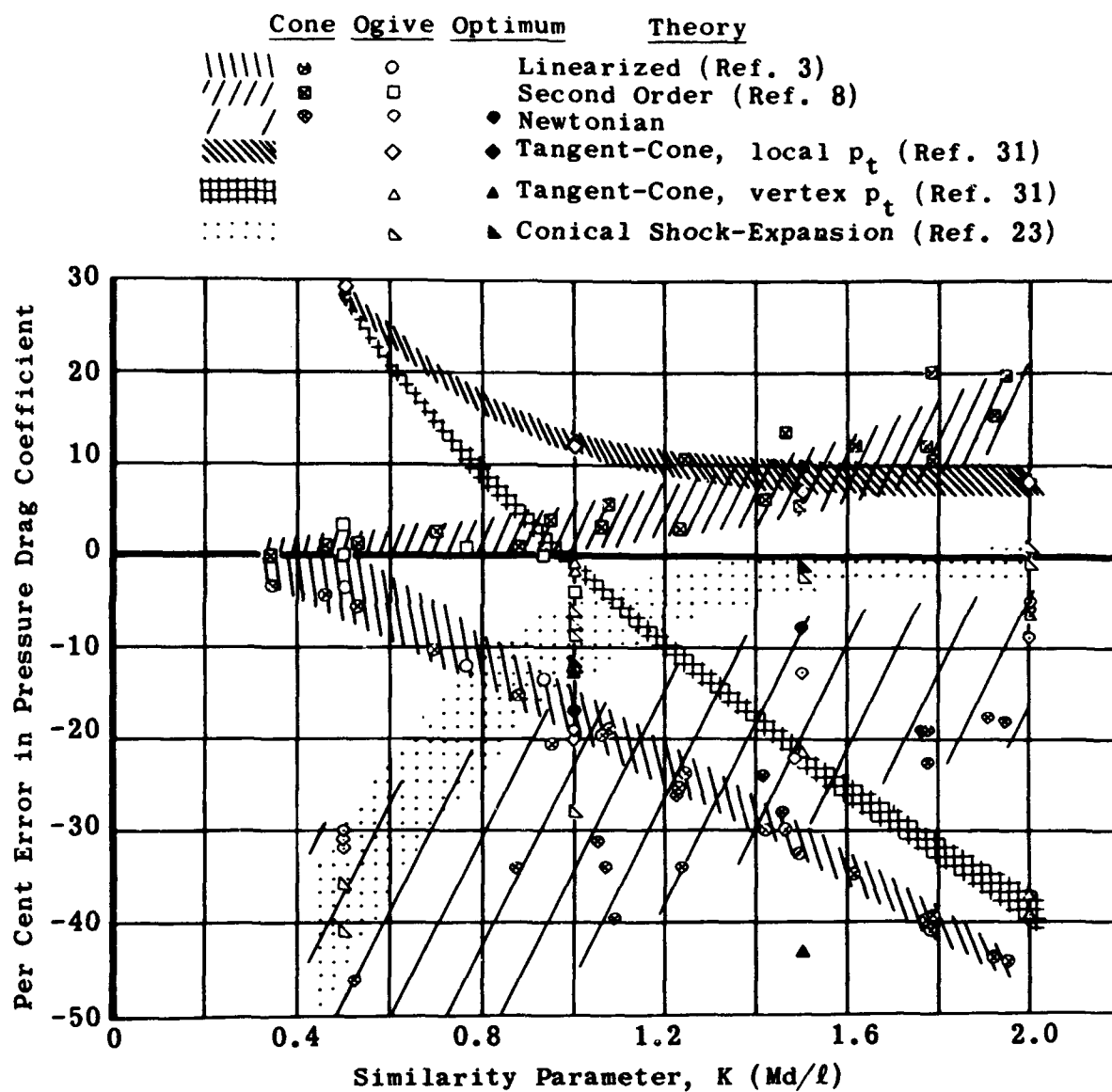
Fig. 2-8. Comparison of the accuracy of drag derived by several
    methods of computation for cones and ogives. (Source: Ref. 31)

Fig. 2-9   NAVWEPS Report 1488 (Vol. 3, Sec. 8)
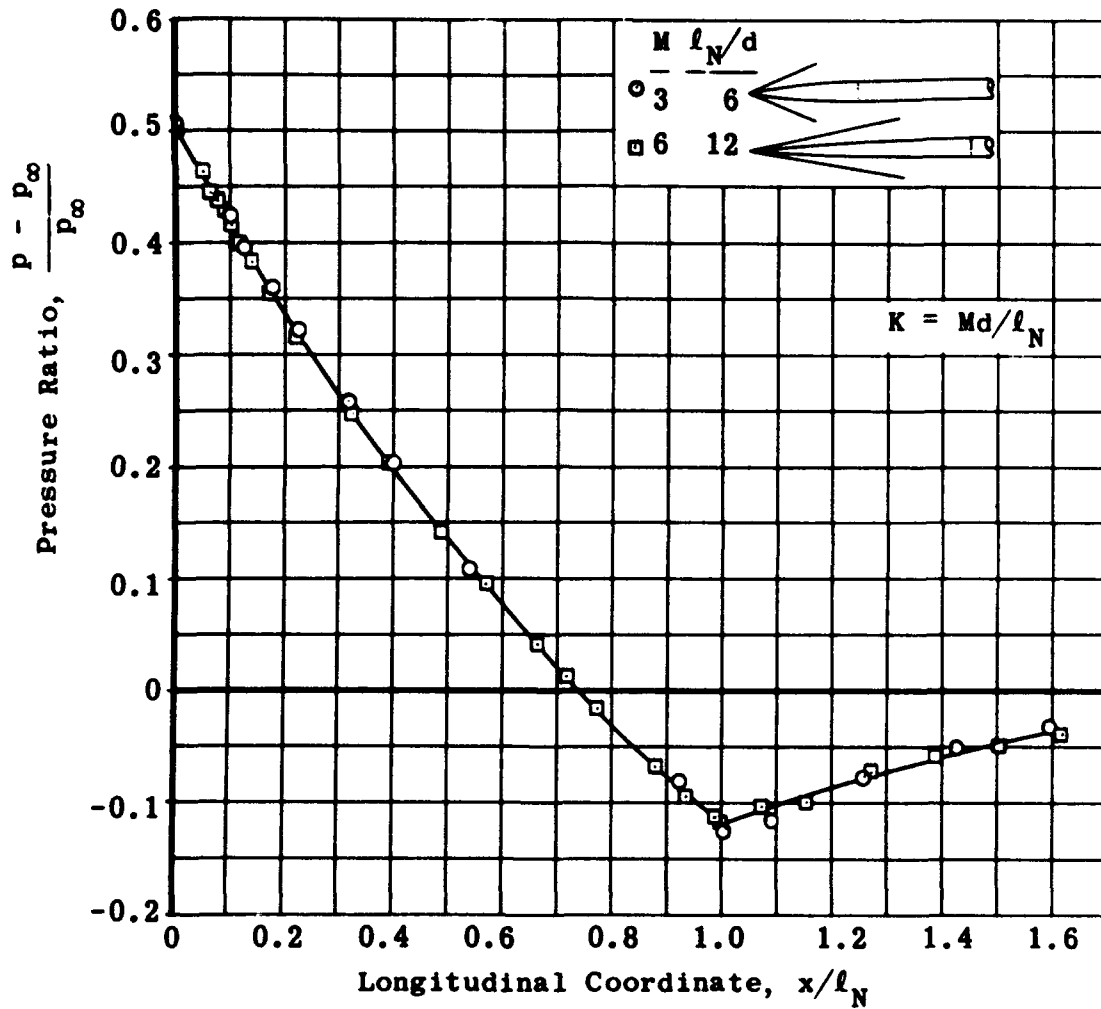
Fig. 2-9. Correlation of pressure distribution over tangent
    ogives as determined by the method of characteristics;
    K = 0.5. (Source: Ref. 25)
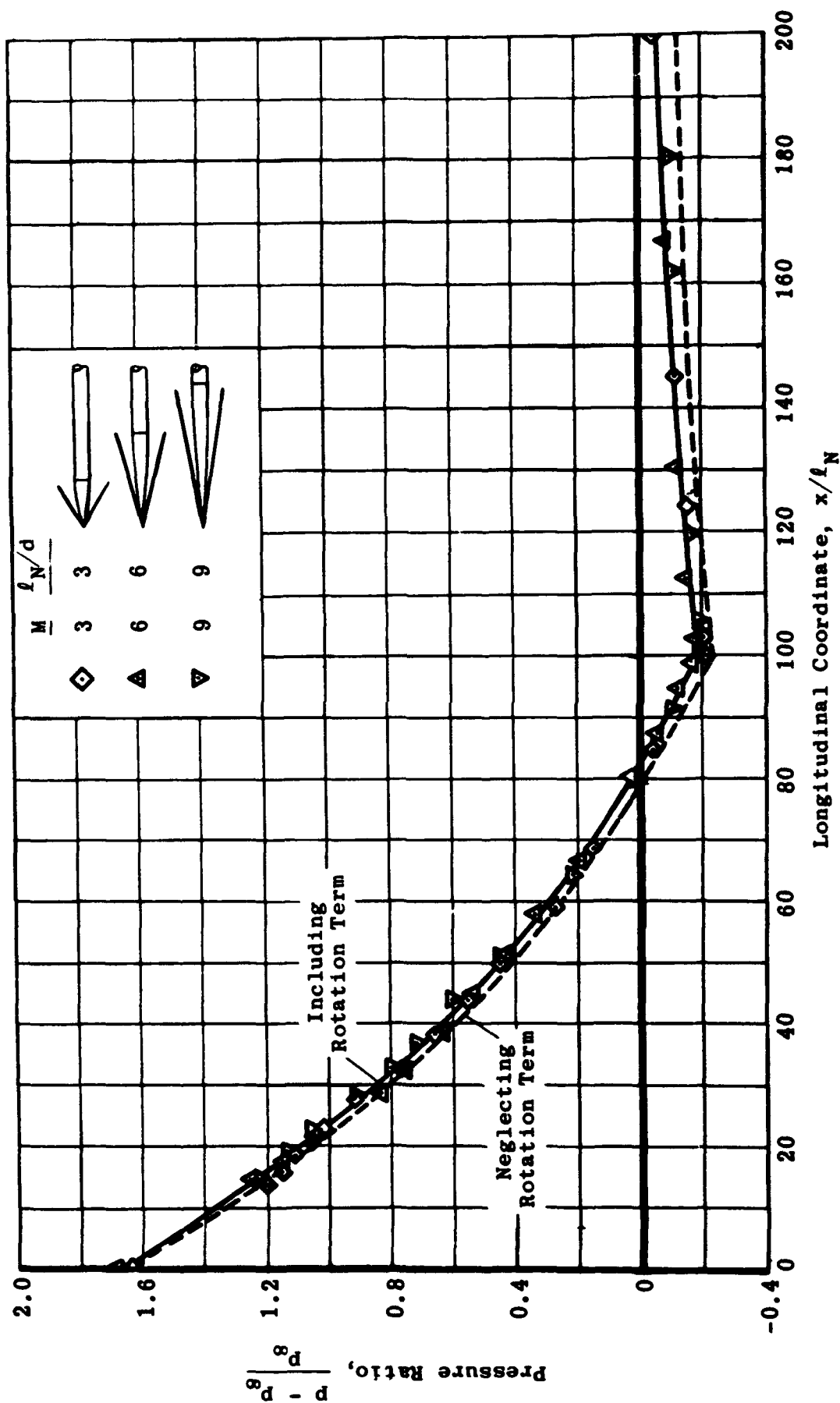
Fig. 2-10. Correlation of pressure distribution over tangent ogives as determined by the method of characteristics; K = 1.0. (Source: Ref. 25)

Fig. 2-11   NAVWEPS Report 1488 (Vol. 3, Sec. 8)
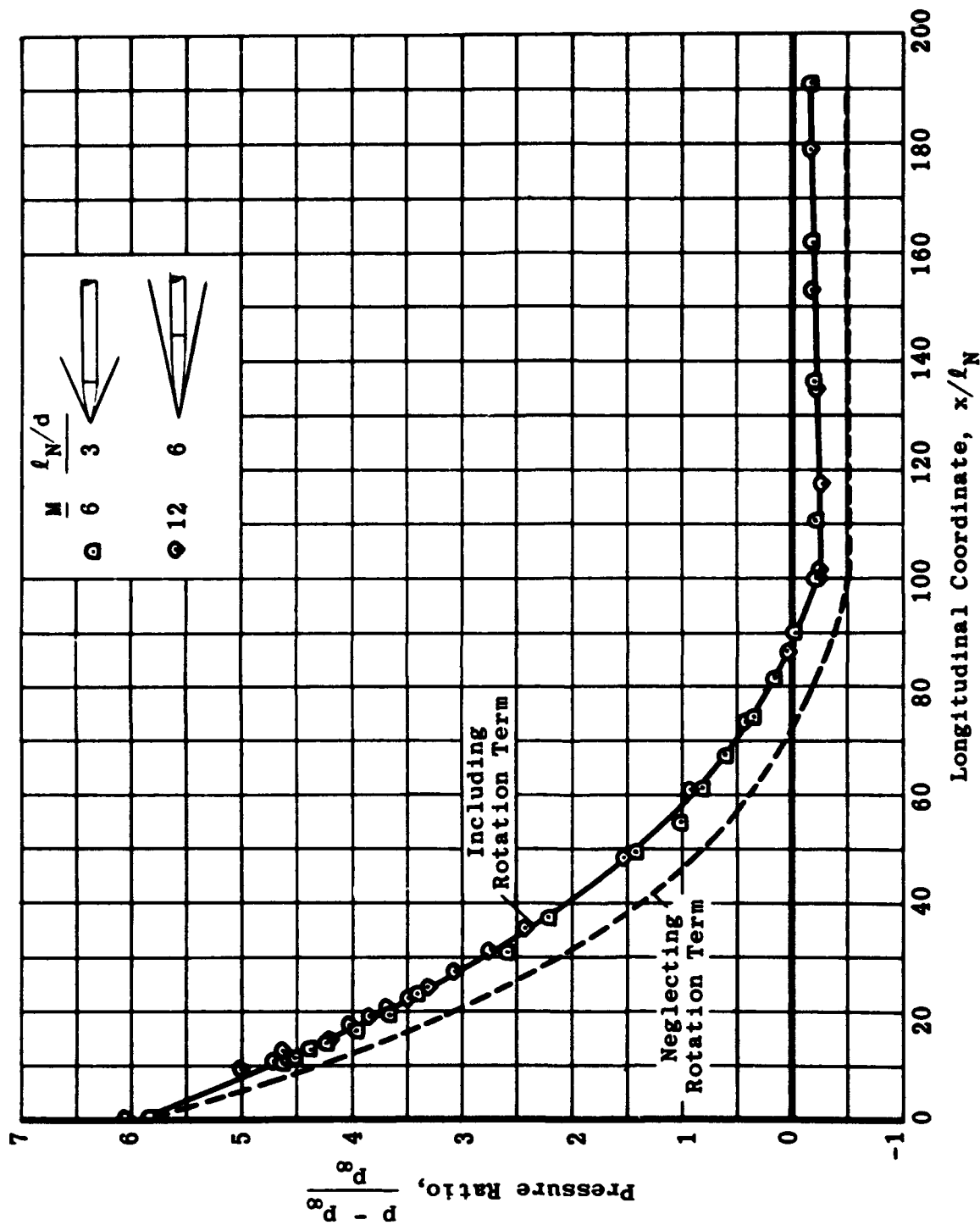
Fig. 2-11. Correlation of pressure distribution over tangent ogives as determined by the method of characteristics; K = 2.0. (Source: Ref. 25)
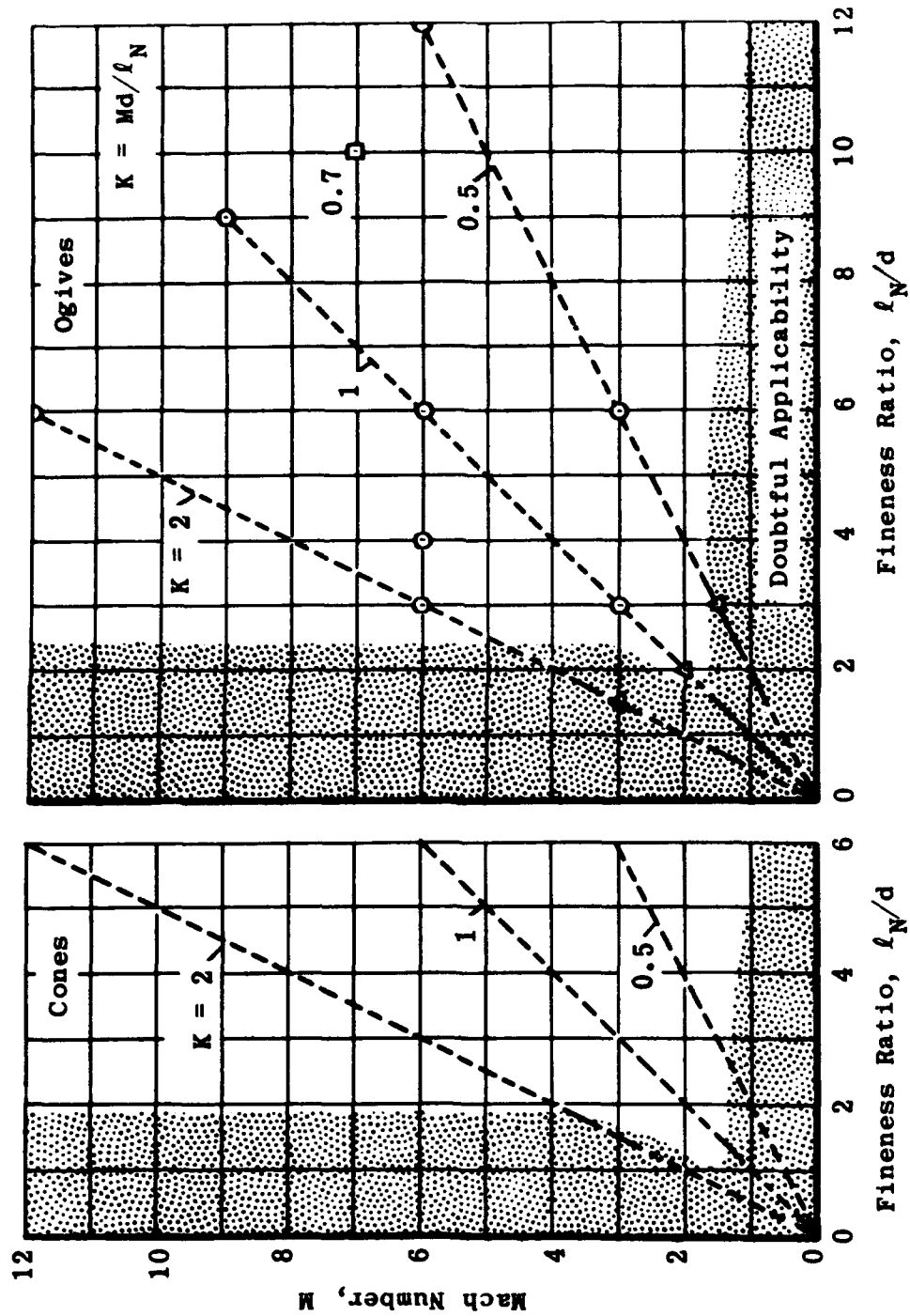
Fig. 2-12. Range of usefulness of the hypersonic similarity parameter for cones and ogives at several values of K. (Source: Ref. 30)

Fig. 2-13   NAVWEPS Report 1488 (Vol. 3, Sec. 8)
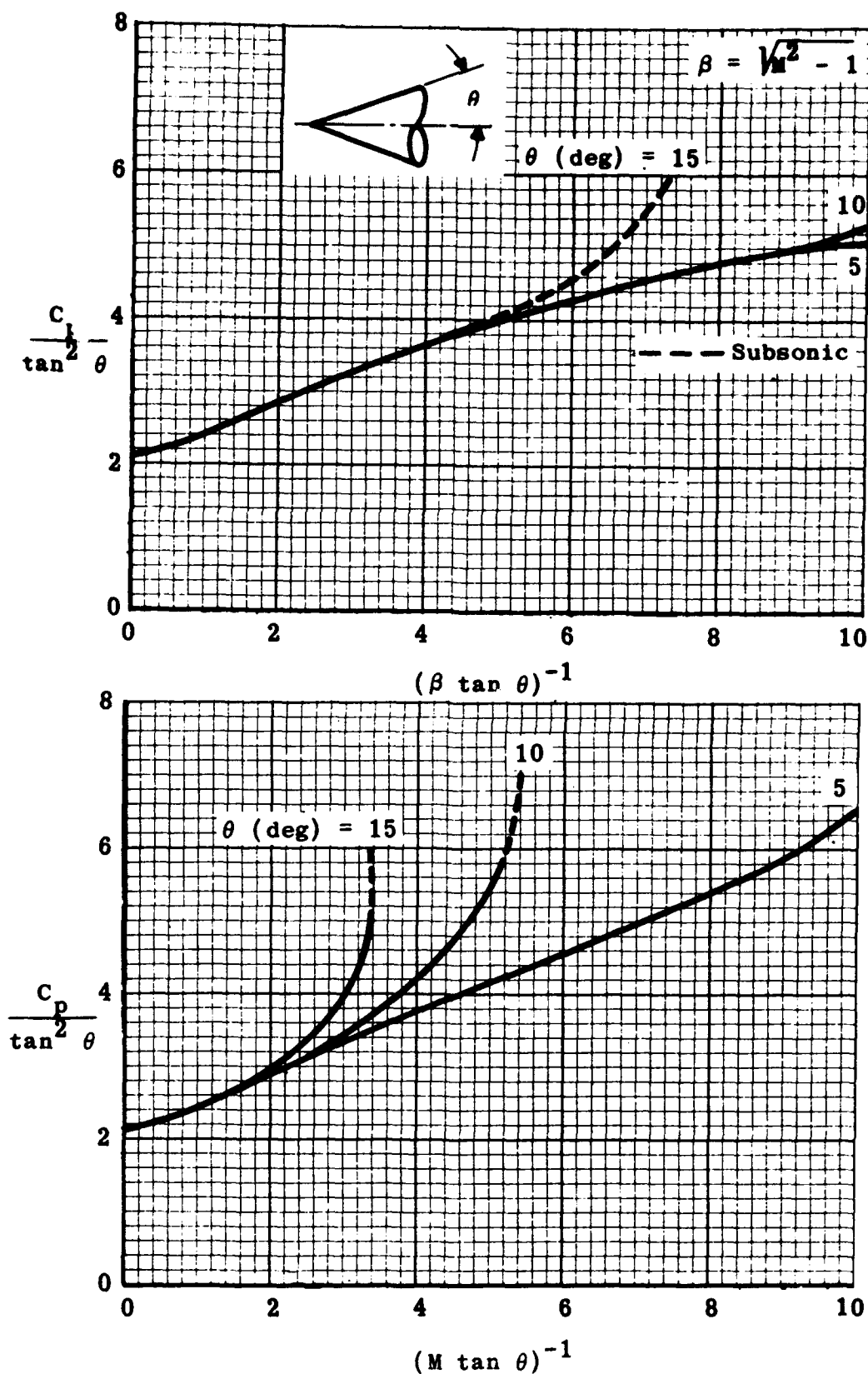
Fig. 2-13. Comparison of correlation of the pressure coefficients
on cones by means of the hypersonic similarity parameter and
the modified hypersonic similarity parameter. (Source: Ref. 35)
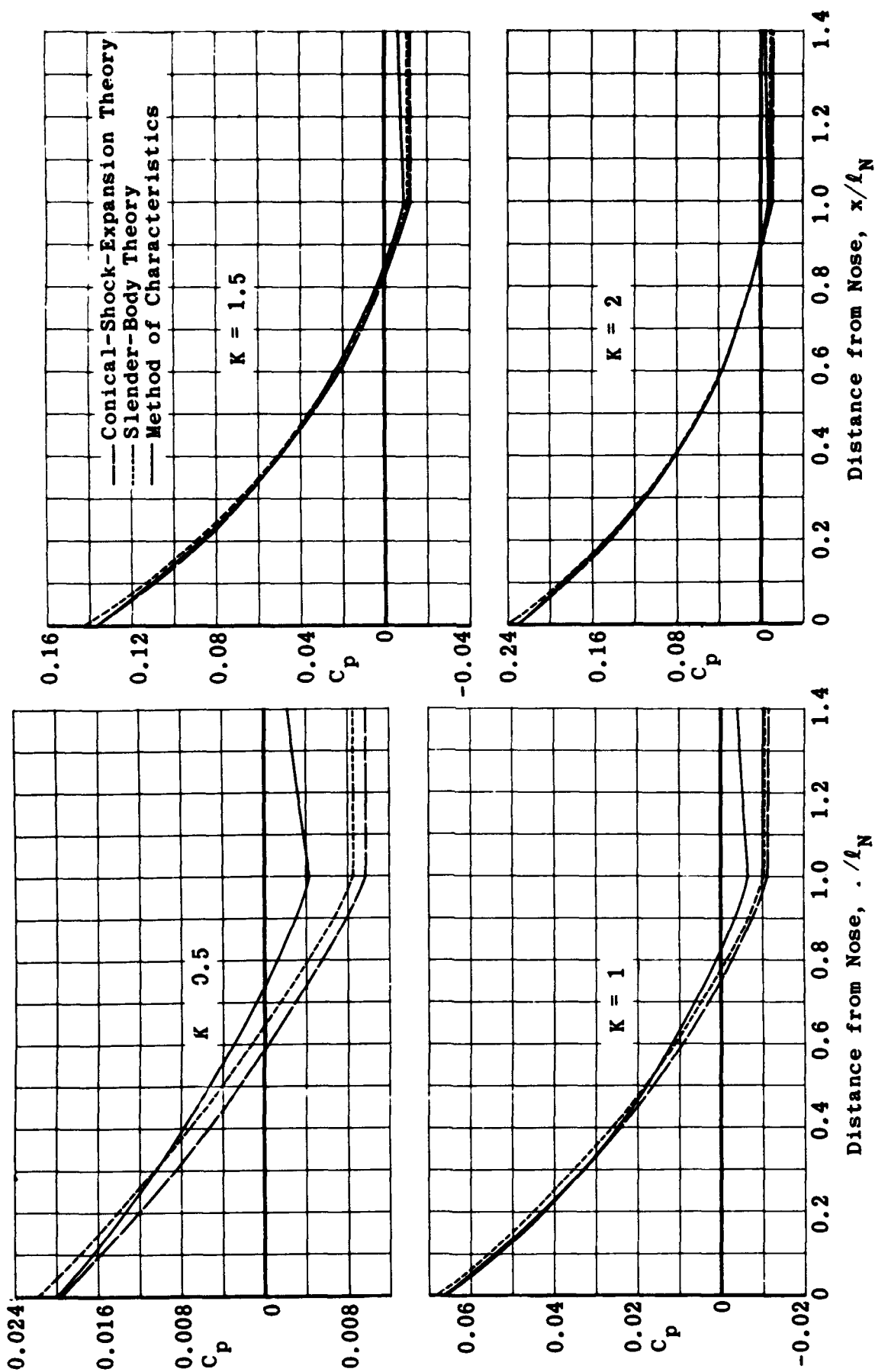
Fig. 2-14. Comparison of the pressure distribution on ogival noses derived by three methods; M = 6. (Source: Ref. 23)

Fig. 2-15   NAVWEPS Report 1488 (Vol. 3, Sec. 8)
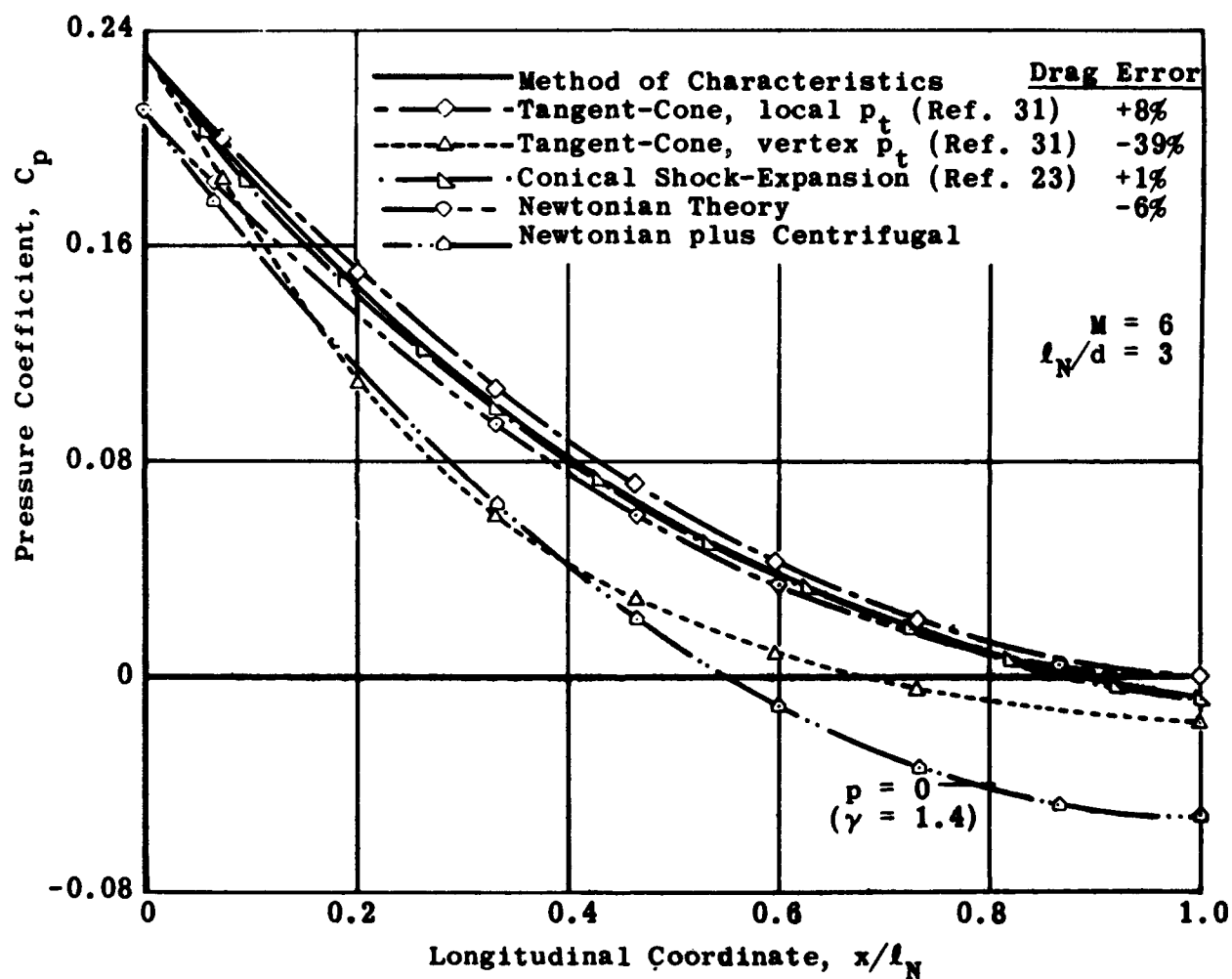
Fig. 2-15. Comparison of the pressure distribution over tangent
ogives obtained by various methods. (Source: Ref. 31)

3.   Flow Characteristics at Low to High Angles of Attack

        The application of potential flow theory must necessarily be
restricted to those cases wherein separation effects are small. The
observed separation of flow on the leeward side of bodies of revolution
at all but the smallest angles of attack severely limits the applica-
bility of strictly potential theory to the body case. This is indicated
by a comparison of experimental data obtained on bodies of revolution
with estimates based on potential theory; the divergence in certain in-
stances may appear at angles of attack as low as 4 deg. Allen and
Perkins (Refs. 44 and 45) were the first to attempt to make due allow-
ance for such viscous effects. Subsequently, Hill (Ref. 46) and Kelly
(Ref. 47) introduced refinements into the Allen method, thus extending
its useful range. The first part of this subsection is devoted to a
description of the Allen-Perkins method, and following parts deal with
the refinements proposed by Hill and Kelly.

3.1   Allen-Perkins Viscous Cross-Flow Theory

        Munk (Ref. 14) was the first to draw attention to the simi-
larity of cross flow around slender bodies of revolution and the flow
developed about two-dimensional cylinders started impulsively into
motion from rest. Jones (Ref. 48) examined in some detail the laminar
flow about infinite two-dimensional yawed cylinders and showed that the
flow in planes perpendicular to its axis is uninfluenced by the axial
flow. In other words, the cross flow is solely dependent on the com-
ponent of flow perpendicular to the axis. A similar result was obtained
by Young and Booth (Ref. 49) for the case of turbulent boundary-layer
flow. These results encouraged Allen and Perkins to extend and apply
Munk's hypothesis to the case of viscous fluids.

        In predicting the characteristics of inclined bodies of revo-
lution, Allen assumed that the total cross-force exerted on a body's
transverse segment is made up of two parts: (1) a contribution from
potential cross-flow and (2) a contribution from viscous cross-flow.

        The relation for C_N arising from potential cross-flow has
been derived in Subsec. 2.5.1 for pointed afterbodies. For blunt-based
bodies, Allen gives

$$C_N = (K_2 - K_1) \frac{S_b}{S} \sin 2\alpha \cos \frac{\alpha}{2} \qquad (3\text{-}1)$$

and

$$C_m = (K_2 - K_1) \left[\frac{v - S_b (\ell - x_m)}{SL} \right] \sin 2\alpha \cos \frac{\alpha}{2} \qquad (3\text{-}2)$$

where

K_1 = virtual mass associated with the axial motion of the body

K_2 = virtual mass associated with the transverse motion of the
      body

S_b = base area

ℓ = length of body

x_m = distance of moment center aft of nose

S = reference area for coefficient definition

L = reference length used in definition of moment coefficient

v = volume of the body

The contributions of the viscous cross-forces must now be evaluated.
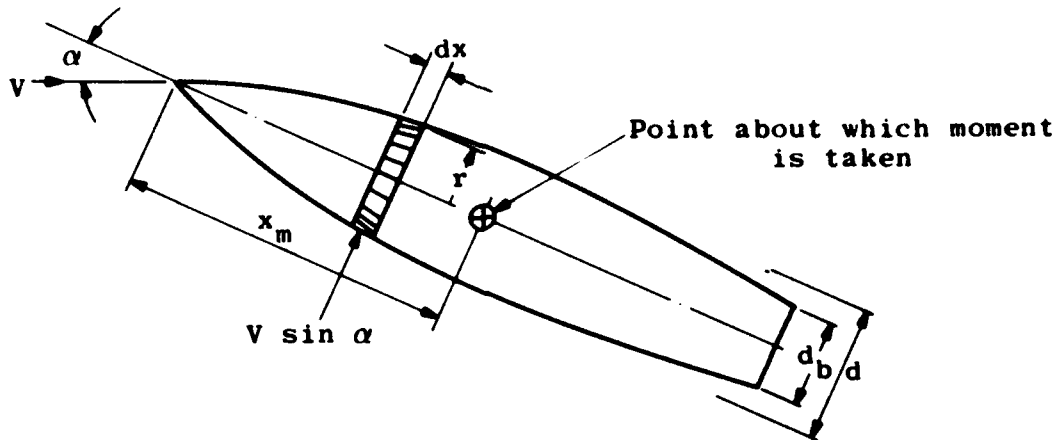
The viscous force (vis) acting on the shaded segment of the body (above) may be expressed by

$$dN_{vis} = C_{D_c} \; 2r \; \tfrac{1}{2}\rho V^2 \; \sin^2 \alpha \; dx \qquad (3\text{-}3)$$

The section drag coefficient, C_{D_c}, is a function of both the cross-flow Reynolds number,

$$Re_c = \frac{2r \; V \; \sin \alpha}{\nu} \qquad (3\text{-}4)$$

where

ν = kinematic viscosity in the free stream

and the cross-flow Mach number,

$$M_c = \frac{V \; \sin \alpha}{a} \qquad (3\text{-}5)$$

where

a = velocity of sound in the free stream

A summary of the available data on the drag coefficients, C_{D_c}, of infinite two-dimensional circular cylinders is presented in Figs. 3-1

and 3-2. Figure 3-1 gives the drag, C_{D_c}, as a function of Reynolds number based on cylinder diameter. Within the range of most practical applications, i.e., Re from 10^4 to 10^5, the cross-flow drag coefficient is relatively insensitive to Re and approximately equal to 1.2. It may drop to 0.35 for a critical Reynolds number region. Figure 3-2, which is derived from the combined data of Refs. 45 and 54, shows the effect of the cross-flow Mach number on the cross-flow drag coefficient. The coefficient values in both these figures are for infinite cylinders in steady-state flow.

The normal force resulting from viscous cross-flow is obtained directly by integrating Eq. 3-3, with due regard to the assumed constancy of C_{D_c}, i.e.,

$$N_{vis} = \frac{1}{2} \rho V^2 \sin^2 \alpha \ C_{D_c} \ A_p \qquad (3-6)$$

where

A_p = planform area of the body

i.e.,

$$C_{N\ vis} = C_{D_c} \frac{A_p}{S} \sin^2 \alpha \qquad (3-7)$$

and

$$C_{m\ vis} = C_{D_c} \frac{A_p}{S} \left(\frac{x_m - x_p}{L} \right) \sin^2 \alpha \qquad (3-8)$$

where

x_p = distance from the nose to the centroid of the planform area

In the case of strictly potential flow, Munk made due allowance for the effects of the forward and aft parts of the body in his expressions for normal force and pitching moment by introducing into both the factor $(K_2 - K_1)$. A corresponding reduction factor for the viscous terms has been evaluated by Goldstein (Ref. 50). The ratio (η) of the force on a finite cylinder (transverse to the flow) to the force exerted on the same length of an infinite two-dimensional cylinder (transverse to the flow) in terms of fineness ratio is plotted in Fig. 3-3 (from Ref. 45).

Equations 3-7 and 3-8 thus become

$$C_{N\ vis} = \eta \ C_{D_c} \frac{A_p}{S} \sin^2 \alpha \qquad (3-9)$$

and

$$C_{m \text{ vis}} = \eta \, C_{D_c} \, \frac{A_p}{S} \left(\frac{x_m - x_p}{L} \right) \sin^2 \alpha \qquad (3\text{-}10)$$

The expressions for total normal force and pitching moment are thus

$$C_N = (K_2 - K_1) \, \frac{S_b}{S} \, \sin 2\alpha \, \cos \frac{\alpha}{2} + \eta \, C_{D_c} \, \frac{A_p}{S} \sin^2 \alpha \qquad (3\text{-}11)$$

and

$$C_m = (K_2 - K_1) \, \frac{[v - S_b \, (\ell - x_m)]}{SL} \, \sin 2\alpha \, \cos \frac{\alpha}{2}$$

$$+ \eta \, C_{D_c} \, \frac{A_p}{S} \, \frac{(x_m - x_p)}{L} \sin^2 \alpha \qquad (3\text{-}12)$$

It is within the error of the simplifying assumptions on which this method is based to replace $\sin \alpha$ by α, and $\cos \alpha/2$ by 1. Moreover, the fineness ratios of most practical bodies is sufficiently large to justify the use of $(K_2 - K_1) = 1$.

With these simplifications Eqs. 3-11 and 3-12 become

$$C_N = 2 \left(\frac{S_b}{S} \right) \alpha + \eta \, C_{D_c} \left(\frac{A_p}{S} \right) \alpha^2 \qquad (3\text{-}13)$$

$$C_m = 2 \, \frac{[v - S_b \, (\ell - x_m)]}{SL} \, \alpha + \eta \, C_{D_c} \, \frac{A_p}{S} \left(\frac{x_m - x_p}{L} \right) \alpha^2 \qquad (3\text{-}14)$$

Equations 3-13 and 3-14 represent a significant improvement over the potential flow method for the prediction of body characteristics at moderate and high angles of attack.

3.2   Modifications to the Viscous Cross-Flow Theory

In general it may be stated that the cross-flow theory is most accurate for moderate supersonic speeds (around $M \geq 1.5$) and is progressively impaired in the higher supersonic speed range. At low subsonic speeds the Allen theory overestimates C_N and at high supersonic speeds it underestimates C_N. With a view to improving its accuracy at low and high speeds, certain refinements have been introduced in the method. These are described in the following subsections.

3.2.1   Hill's Refinements

Hill (Ref. 46) pointed out that only the flow external to the boundary layer is potential in nature. To make more accurate evaluation of the potential-flow contributions to the normal force and pitching moments he suggests that one should employ a hypothetical body whose surface is defined by the exterior of the boundary layer on the actual body.

This correction is significant only where the viscous layer is thick enough to produce an appreciable change in the body diameter. It is usually negligible where the boundary layer is laminar and no extensive regions of separation are present.

3.2.2   Kelly's Refinements

In addition to incorporating the modifications proposed by Hill, Kelly (Ref. 47) made two further amendments to Allen's method. The first improvement concerns the use of a constant cross-flow drag coefficient along the entire length of the body. In the case of infinite two-dimensional circular cylinders started impulsively from rest, the experiments of Schwabe (Ref. 51) have shown that the drag coefficient grows from zero to a peak value which is twice the steady-state value (see Fig. 3-4).

On the basis of the "cross-flow" hypothesis a similar distribution along the axis of a body of revolution at angle of attack should be used. Both Allen and Hill were aware of this, but apparently believed that the errors resulting from the assumption of uniform steady-drag value along the entire length of the body would in most practical applications be small.

Kelly approximated the Schwabe curve of drag growth by the formula

$$C_{D_c} = C_{D_s} \left(0.49 \frac{x}{r} \tan \alpha - 0.0056 \frac{x^3}{r^3} \tan^3 \alpha + 0.00003 \frac{x^5}{r^5} \tan^5 \alpha \right)$$

$$(3-15)$$

where

C_{D_s} = steady-state cross-flow drag value (assumed as unity in this expression)

Equation 3-15 is plotted in Fig. 3-4 (from Ref. 47).

It is implicit in the Kelly approach that variations in Reynolds number and Mach number change only the value of C_{D_s}, i.e., growth of the drag coefficient is essentially independent of both Re and M.

When Eq. 3-15 is substituted in Eq. 3-3 and α substituted for tan α and sin α (for angles of attack less than 10 deg), one then obtains, after integration,

$$C_{N \ vis} = \frac{2C_{D_s}}{S} (A_N \ \alpha^3 + B_N \ \alpha^5 + C_N \ \alpha^7) \qquad (3-16)$$

When the factor $\dfrac{x - x_m}{L}$ is introduced into Eq. 3-3 one may obtain

$$C_{m \ vis} = \frac{2C_{D_s}}{S} (A_m \ \alpha^3 + B_m \ \alpha^5 + C_m \ \alpha^7) \qquad (3-17)$$

where A, B, C are functions of x/r, i.e., of body shape (see Ref. 47), and are usually normalized for $C_{D_s} = 1.20$ rather than for 1.0 as in Eq. 3-15. When $2\ell/d$ tan $\alpha < 3$, only cubic terms must be retained; for $3 \leqq 2\ell/d$ tan $\alpha \leqq 6$, both cubic and fifth power terms must be retained; for $2\ell/d$ tan $\alpha \geqq 6$, all terms must be retained. A further refinement to this technique has been developed which makes the use of these coefficients unnecessary (see Subsec. 3.2.3).

Kelly also proposed the use of $\eta = 1$ in Eqs. 3-9 to 3-14 for the case of blunt-based bodies. He justifies this on the grounds that marked departures from the cross-flow hypothesis are likely to occur only over the nose portion of the body, where the viscous effects are known to be small. Deviations from the cross-flow hypothesis would also occur over the boattailed afterbody, where the viscous effects are maximized and hence, in this case, $\eta = 1$.

The refinements introduced above justify the use of the best available theories in evaluating the potential terms. Thus, in the supersonic regime, it is suggested that Van Dyke's second-order theory be used in place of the simpler Munk theory. (Values of $(dC_N/d\alpha)_{\alpha=0}$ and $(dC_m/d\alpha)_{\alpha=0}$ predicted by the Van Dyke theory for a wide range of body shapes have been computed and presented in Ref. 30.)

3.2.3   Use of Cross-Flow Drag Coefficient

Perkins and Jorgenson (Ref. 52) and Mello (Ref. 53) carried out extensive studies of the pressure and normal force distributions over bodies of revolution and placed special emphasis on the development of a reliable method for applying the cross-flow drag correction discussed in the previous subsection. In measurements of cross-flow drag as a function of distance from the vertex, they found that the drag rose steadily for a distance along the body and then declined slowly to a steady-state value. The peak value occurred in the region along the body at which second-order theory predicted the lowest local normal-force coefficient.

They also found that the ratio C_{D_c}/C_{D_s} could in general be expressed as a function of distance from the vertex, independently of

angle of attack within a close range of Reynolds numbers. Such a curve is shown in Fig. 3-5. Since the maximum value of C_{D_c}/C_{D_s} and the lowest value of the potential cross-flow occur at approximately the same position, the use as a norm of the position at which the latter occurs would improve the correlation of the data.

It must be noted that Refs. 52 and 53 present results for two Mach numbers (1.5 and 2.0) and most particularly for angles of attack from 8 to 23 deg. At low angles of attack the viscous contribution is relatively small and insensitive to the method used. Figures 3-6 to 3-8 compare the measured normal-force coefficient and center of pressure with values computed by the methods of Refs. 52 and 53. In all cases it is assumed that laminar flow existed over the entire body. It can be seen that the agreement is very good in this limited Reynolds number and Mach number range. Within the limits of present knowledge, a simple procedure by which aerodynamic characteristics may be computed may be summarized as follows:

1. Compute the local normal-force coefficient, c_N, versus x from the potential flow distribution, using one of the basic methods described in Subsec. 2, i.e., Eqs. 2-15 or 2-16. This computation determines ℓ_m, the value of x at which c_N is a minimum.

2. From Fig. 3-5 and ℓ_m find C_{D_c}/C_{D_s} versus x.

3. From Figs. 3-1 and 3-2 determine the appropriate values of C_{D_s}.

4. Then compute

$$C_{N \text{ vis}} = 2 \, C_{D_s} \frac{\sin^2 \alpha}{S} \int_0^\ell r \left(\frac{C_{D_c}}{C_{D_s}} \right) dx$$

and   (3-18)

$$C_{m \text{ vis}} = \frac{2 \, C_{D_s}}{SL} \sin^2 \alpha \int_0^\ell r \left(\frac{C_{D_c}}{C_{D_s}} \right) (x_m - x) \, dx$$

5. The total normal-force and pitching-moment coefficients are then given by

$$C_N = \int_0^\ell c_N \, dx + C_{N \text{ vis}}$$

and   (3-19)

$$C_m = \frac{\ell}{L} \int_0^\ell c_N (x_m - x) \, dx + C_{m \text{ vis}}$$

3.3   Flow Conditions on Leeward Side of Body

The success achieved by the viscous theory in predicting the aerodynamic characteristics of bodies up to high angles of attack in itself demonstrates to some degree the validity of the basic hypothesis, i.e., that even in the case of viscous fluids there exists a close similarity between the perturbed motions of the fluid particles in planes transverse to the flow direction and the motion of fluid particles in the corresponding unsteady two-dimensional problem.

Additional verification of the hypothesis is provided by comparison of the cross-flow patterns developed on the leeward sides of bodies with those developed in the wakes of cylinders started impulsively from rest (Ref. 51). In the case of a cylinder started from rest shortly after the initiation of the motion, two vortices begin to form at the rear stagnation point. In the case of a circular cylinder the time interval which elapses between the start of forward movement and the onset of separation is given by

$$t = 0.351 \ r/V \sin \alpha \qquad\qquad (3\text{-}20)$$

As the vortices increase in strength, they move outwards symmetrically along well defined loci as indicated by the broken line in the left-hand sketch below.

Path of Symmetrical
Vortex Pair
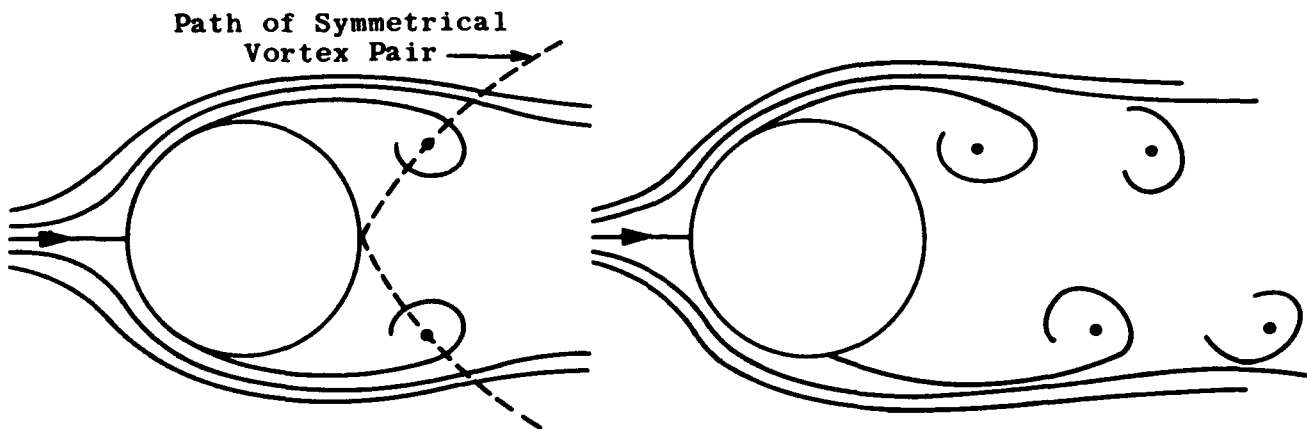
Eventually they reach a point at which they become unstable with respect to asymmetric flow disturbances. This marks the transition to a Bernard-von Karman vortex street as depicted in the right-hand sketch. These stages of evolution are indicated in the vapor screen photographs shown in Fig. 3-9 (from Ref. 56).

Attempts have been made to define the point at which symmetric vortices begin to form on bodies of revolution aft of which the pressure distribution becomes appreciably modified by the separation. Some results are presented in Fig. 3-11, where the theoretical curve (Eq. 3-20) is added for comparison. The large scatter is attributed to the fact that the separation points were estimated from examination of schlieren photographs, wher separation may have occurred to some degree before it became recogniza e as such.

The cross-flow analogy should be applied with caution. In many cases, shortly after the appearance of asymmetric vortex patterns on bodies of revolution, unsteadiness of flow sets in and manifests itself as a switchover of vortex patterns from one side of the body to the other (see Fig. 3-10). Such unsteadiness, though having negligible effect on the body characteristics as such, assumes importance when control surfaces are attached to the body since it then gives rise to appreciable fluctuations in rolling moment and imposes additional and perhaps intolerable demands on the roll control system. Tests have recently been made (Ref. 56) to correlate the onset of unsteadiness with body nose geometry and other relevant parameters. Some of the results are summarized in Fig. 3-12. The scatter is large in this figure, and neither of the parameters used is entirely satisfactory as a basis of correlation. Though the phenomenon of instability is far from understood and definitive criteria for predicting its onset cannot be made at present, the following general statements are appropriate.

1. For the case of conical-nosed bodies, the smaller the vertex angle the lower the angle of attack at which instability sets in.

2. Noses other than conical are compared with a cone of the same fineness ratio in order to determine their stability phenomena. If the apex angle is larger than that of the equivalent cone the flow will be more stable than that of the cone. If it is smaller, the flow will be less stable.

3. The actual shape of the afterbody, unlike that of the forebody, appears to have little influence on the nature of the separated flow. Its length, however, is definitely significant. Even though assymetry (hence instability) is not present for a given nose shape and afterbody, it may be produced by lengthening the afterbody provided always that the cross-flow Reynolds number is such that instability would occur on an infinitely long circular cylinder.

4. Increase in Mach number decreases the amplitude of the unsteady fluctuations and probably delays the onset of instability.

According to the results reported by Gowen in Ref. 58, the vortex configuration may prove to be sensitive to the slightest rotational asymmetries of the body in the immediate neighborhood of the apex where the boundary layer is extremely thin. If this sensitivity is verified, it offers significant possibilities.

It is evident that the development of asymmetric vortex patterns on the leeward side of bodies at high angles of attack are undesirable because they give rise to large induced rolling moments as a result of their interaction with aerodynamic surfaces mounted on the body. Even worse is the situation in which the rolling moments vary erratically. Means have therefore been sought to alleviate this situation by enforcing the formation of symmetric vortex patterns. Mounting separation strips along the side of the body in order to fix the separation points proved inadequate.
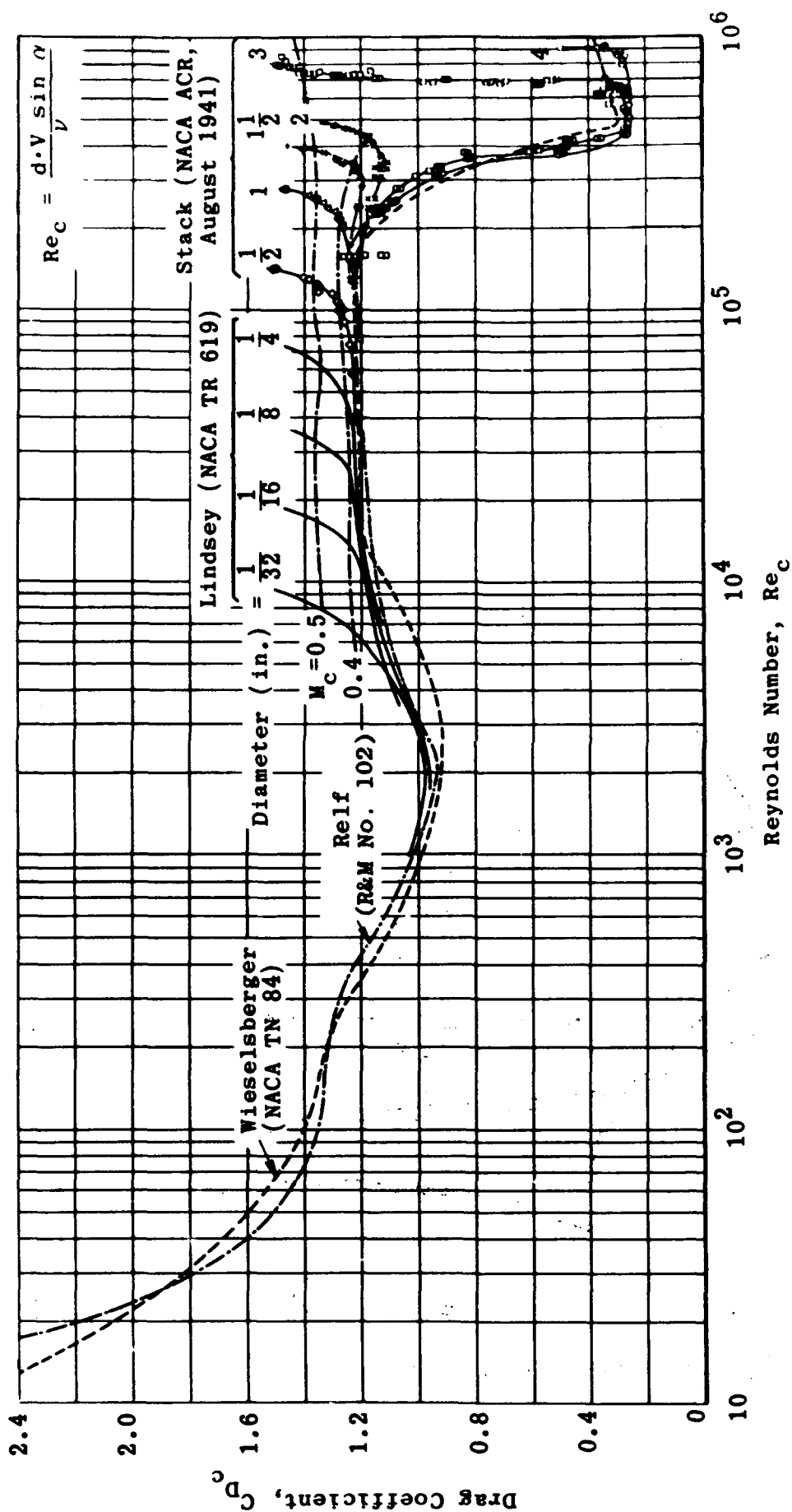
Fig. 3-1. Cross-drag coefficient for a circular cylinder as a function of the cross-flow Reynolds number. (Source: Ref. 45)

Fig. 3-2   NAVWEPS Report 1488 (Vol. 3, Sec. 8)
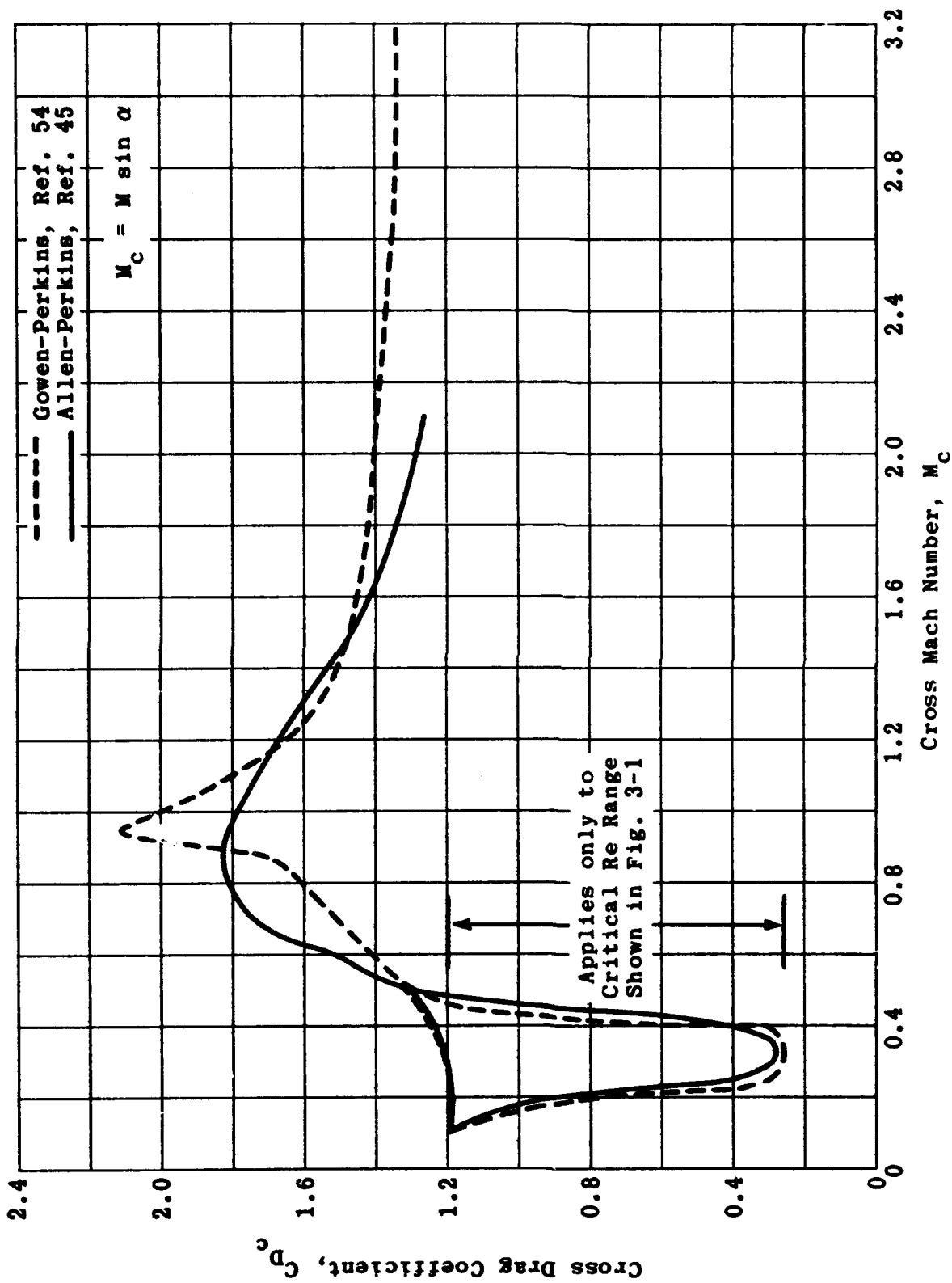
Fig. 3-2. Cross-drag coefficient for a circular cylinder as a function of cross Mach number. (Source: Refs. 45 and 54)
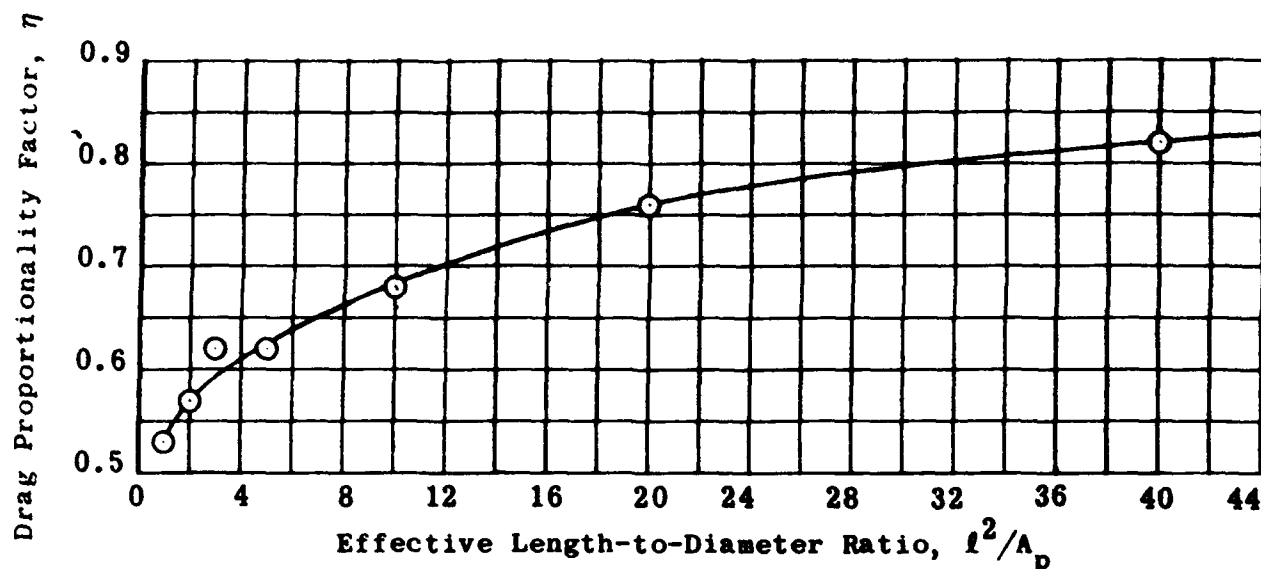
Fig. 3-3. Ratio of the drag of a finite cylinder to that of an
infinite cylinder as a function of the fineness ratio of
the finite cylinder. (Source: Ref. 45)
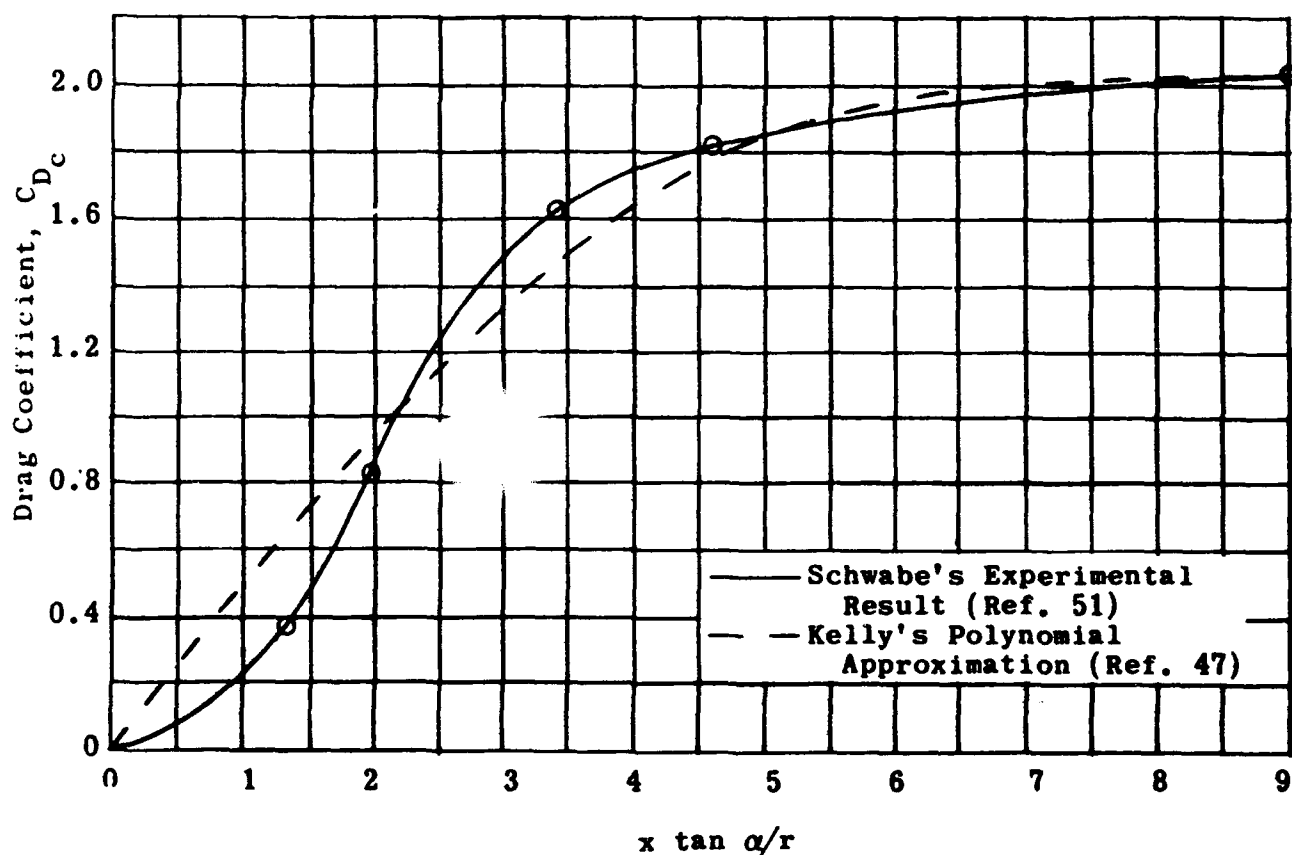
Fig. 3-4. Correlation of the Kelly and Schwabe values of the
cross drag coefficient of a cylinder as a function of the
distance along the cylinder. (Source: Ref. 47)

47

Fig. 3-5   NAVWEPS Report 1488 (Vol. 3, Sec. 8)
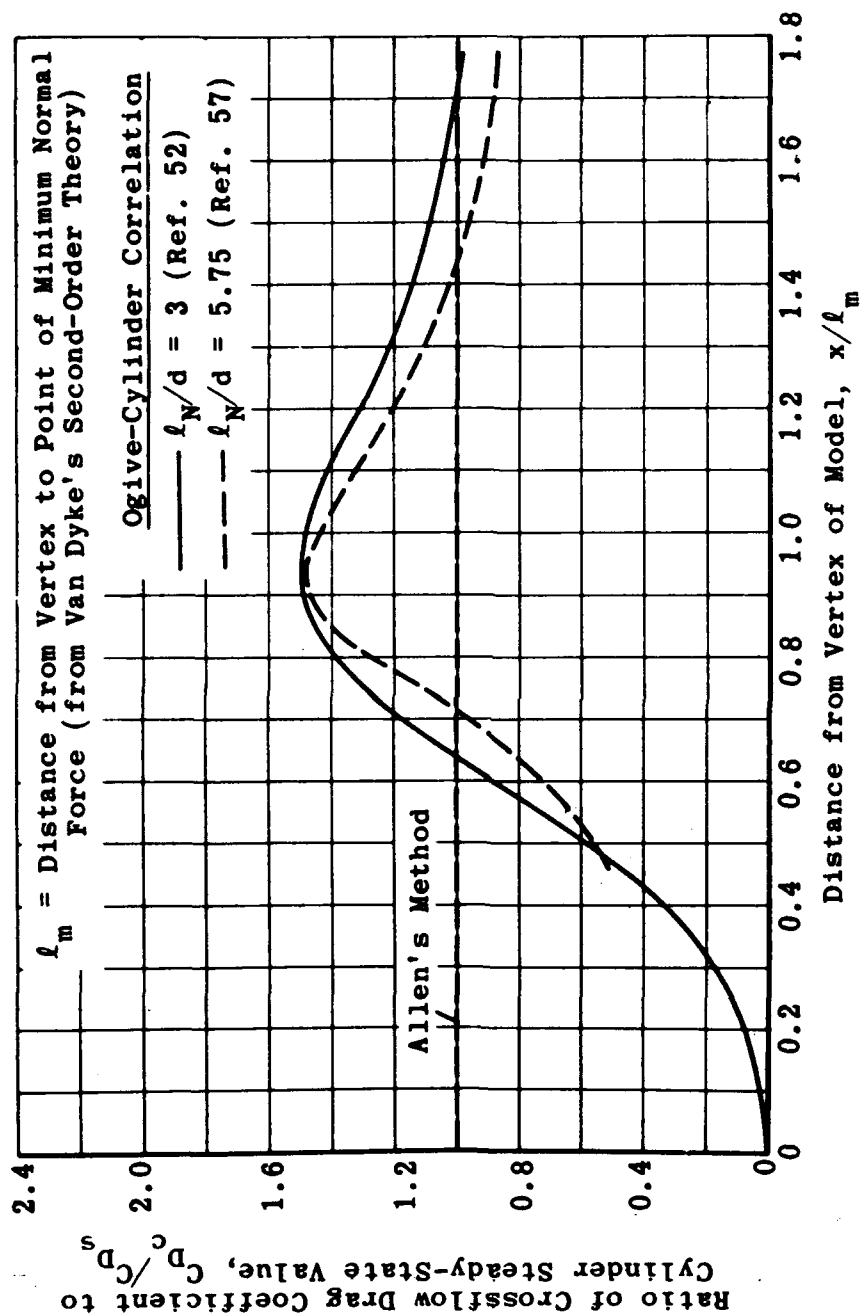
Fig. 3-5. Correlation of cross drag coefficient as a function of distance along the
cylinder; M = 2. (Source: Ref. 52)
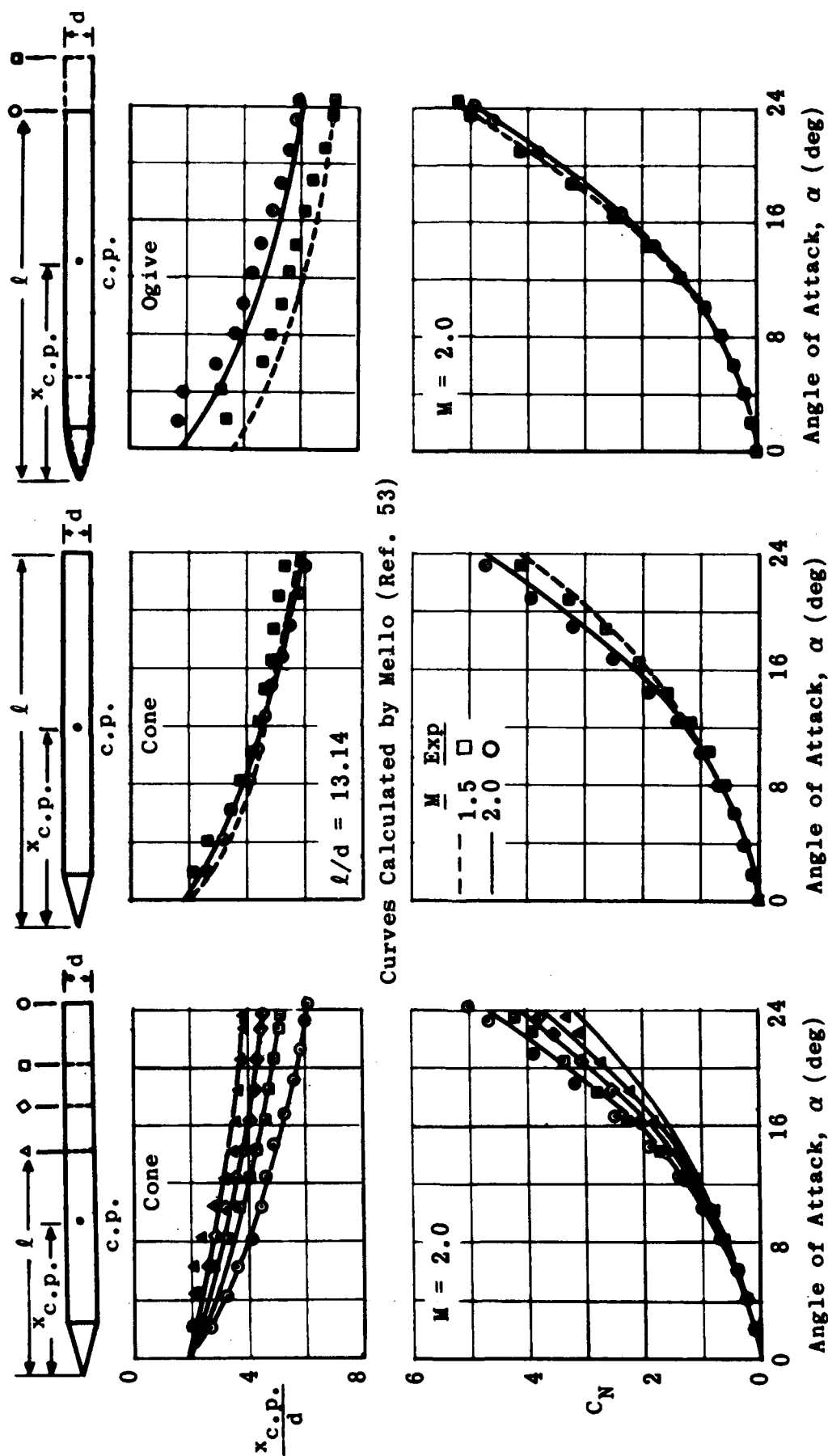
Fig. 3-6. Normal-force and center-of-pressure characteristics as a function of angle of attack for cones and ogives, with Mach number and fineness ratio as parameters. (Source: Ref. 53)

Fig. 3-7   NAVWEPS Report 1488 (Vol. 3, Sec. 8)
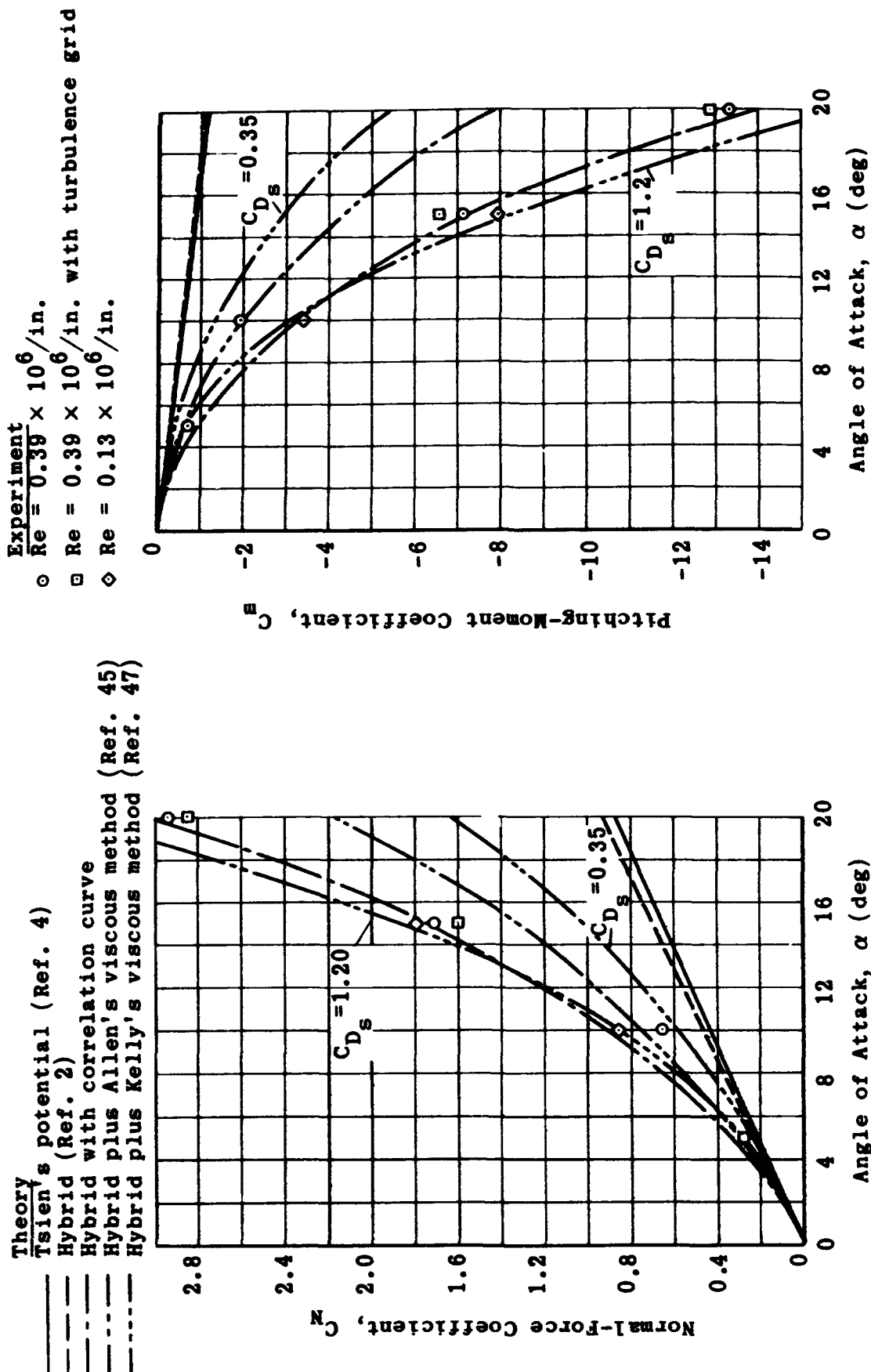
Fig. 3-7. Comparison of theoretical and experimental normal-force and pitching-moment (about the nose) coefficients for tangent-ogive cylinders; M = 2. (Source: Ref. 52)
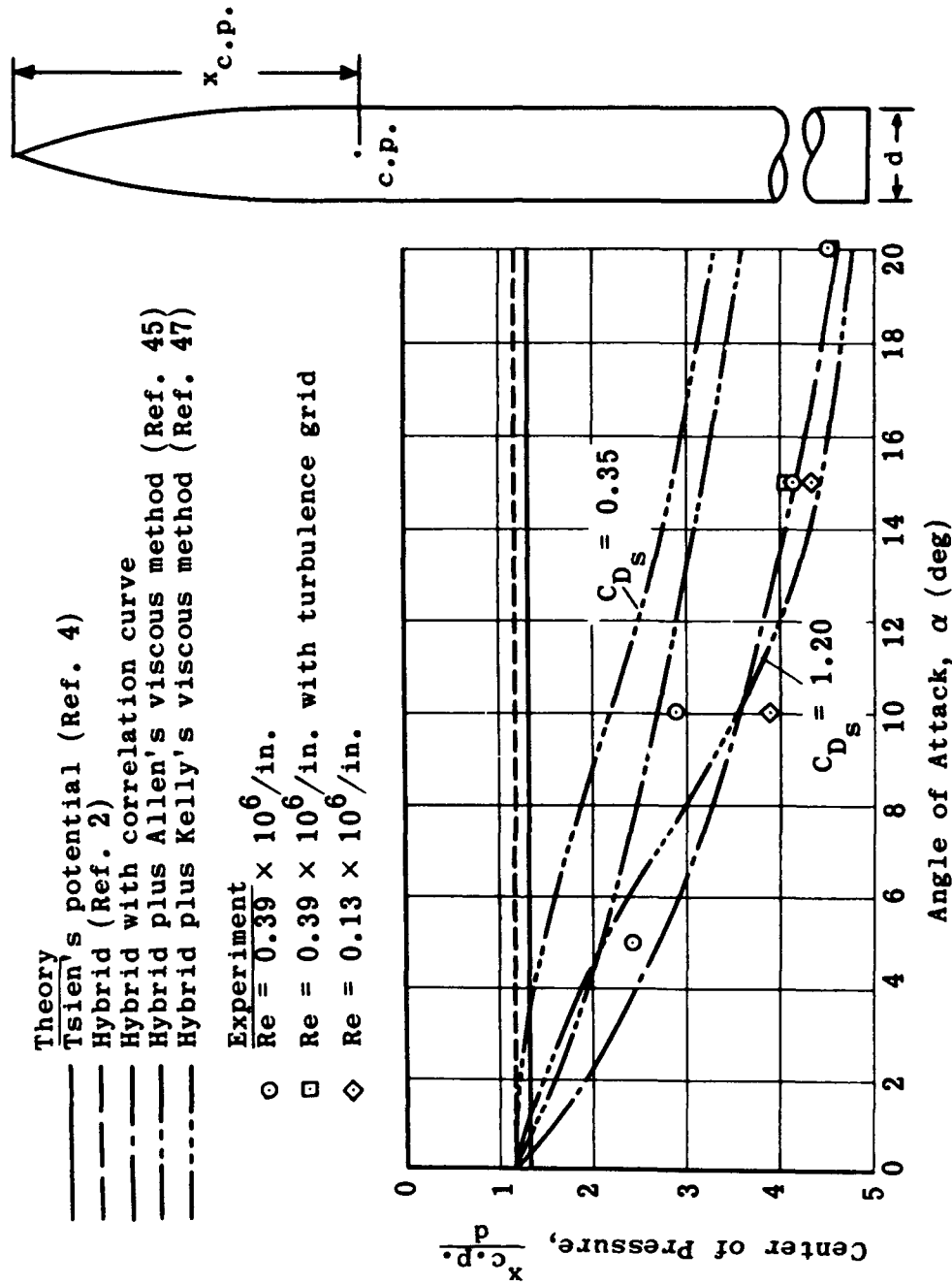
Fig. 3-8.   Comparison of theoretical and experimental center-of-pressure locations for tangent-ogive cylinders; $M = 2$, $\ell_N/d = 3$.   (Source: Ref. 52)

Fig. 3-9   NAVWEPS Report 1488 (Vol. 3, Sec. 8)
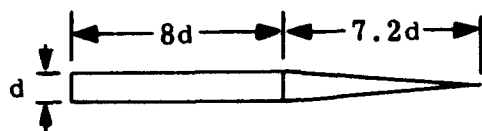
α = 10 deg

α = 20 deg
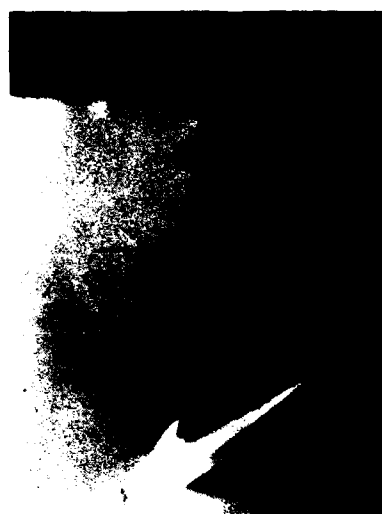
α = 30 deg

Fig. 3-9. Vapor-screen photographs of the wake on the leeward side of a cone-cylinder model for various angles of attack; M = 2, Re = 0.1×10^6. (Source: Ref. 56)
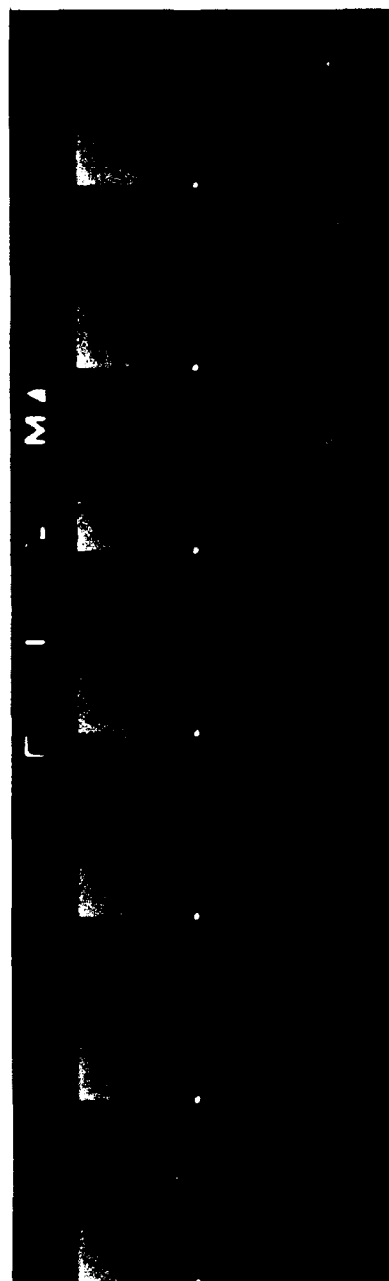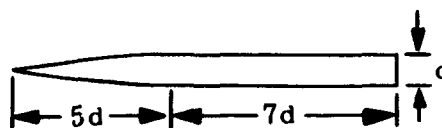
Fig. 3-10. Vapor-screen sequence showing fluctuation of vortices on the cross-flow wake of an inclined body with an ogival nose; α = 36, M = 2, Re = 0.5×10^6. (Source: Ref. 58)
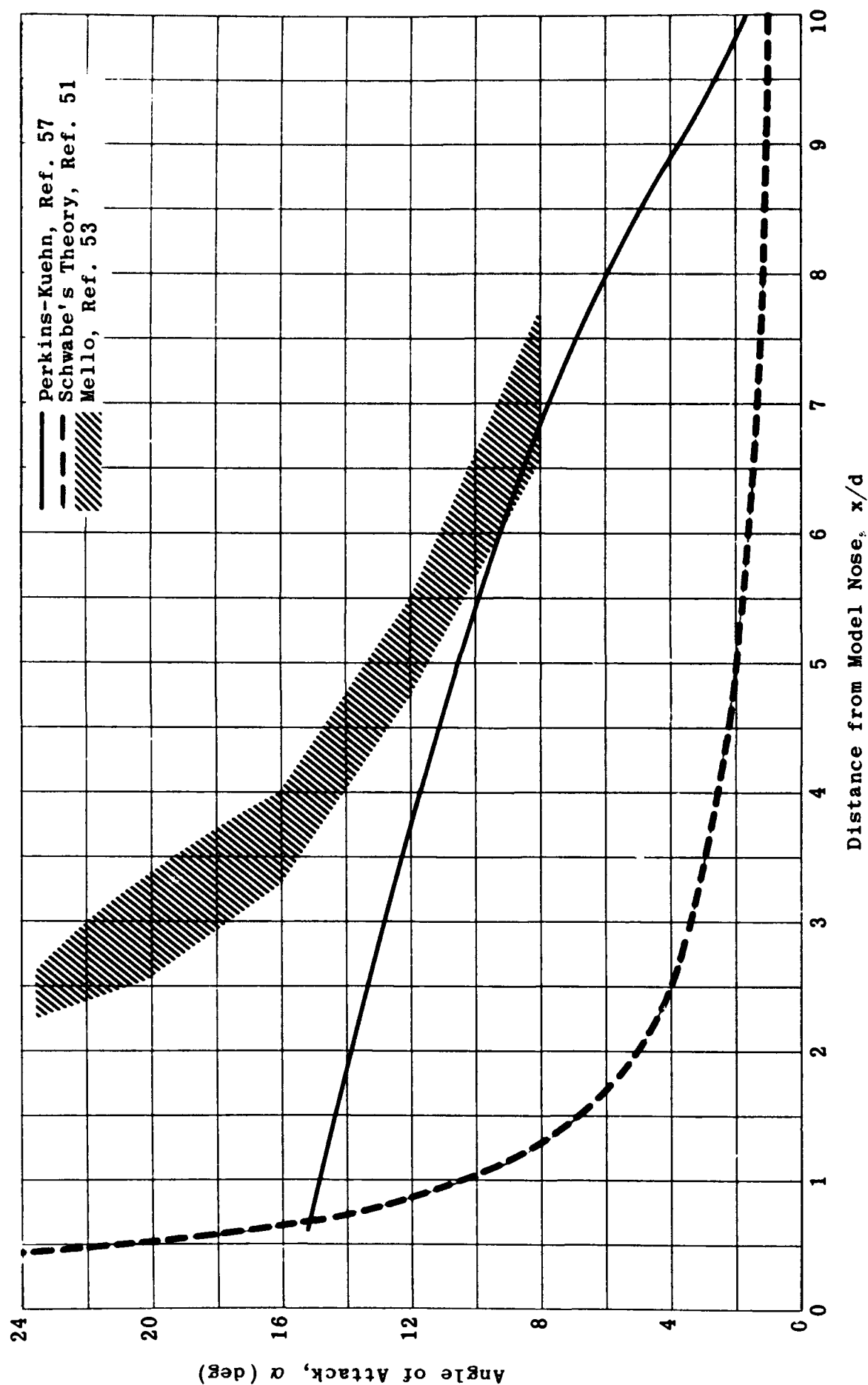
Fig. 3-11. Onset of vortex separation on the leeward side of a cylinder as a function of angle of attack.

Fig. 3-12   NAVWEPS Report 1488 (Vol. 3, Sec. 8)
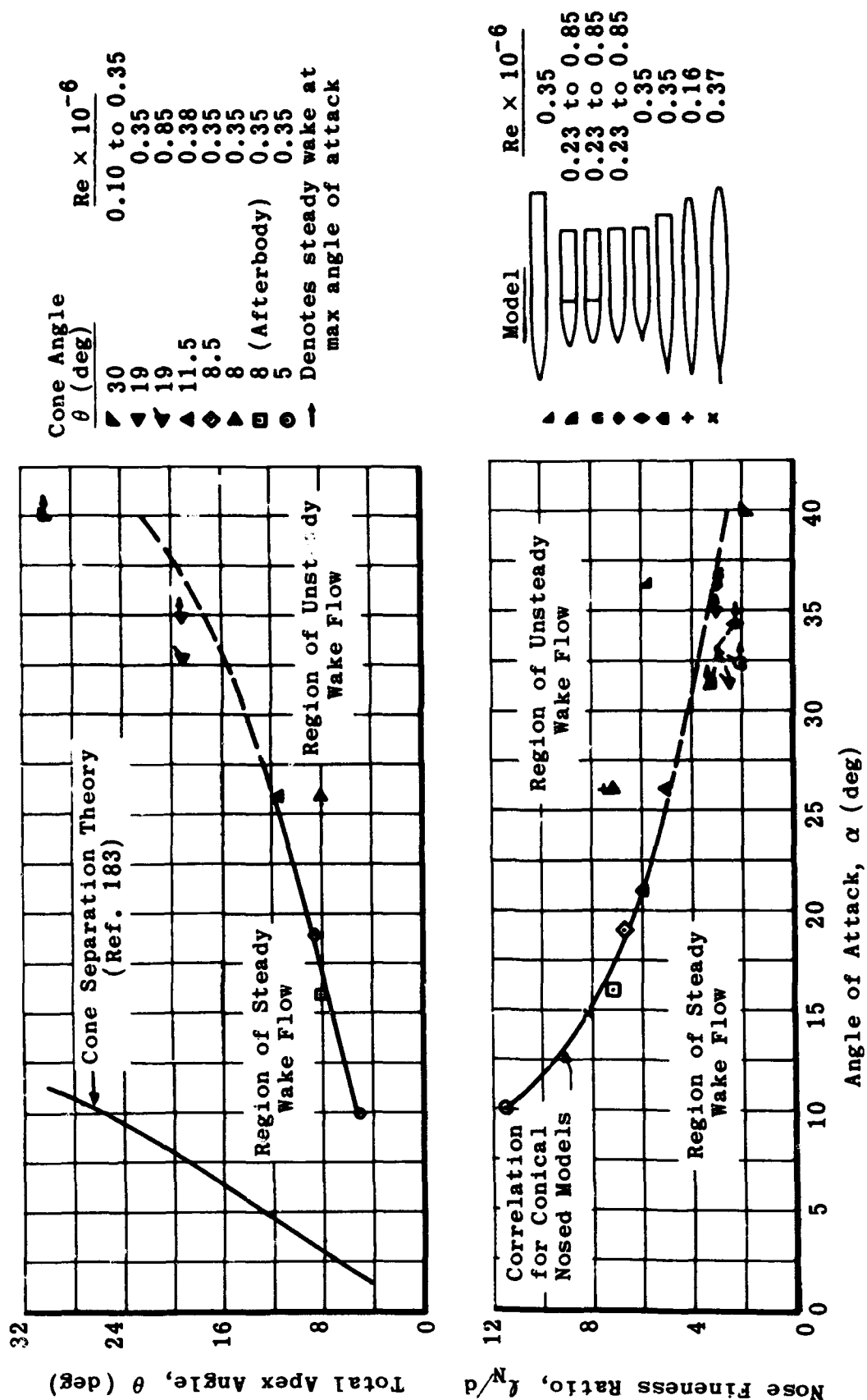
Fig. 3-12. Critical angle of attack for steady cross flow as a function of the apex angle and the fineness ratio. (Source: Ref. 56)

4.   Pressure Distribution

Detailed information on the manner in which pressure is distributed over various types of aerodynamic configurations moving at supersonic speeds is needed for many reasons. Among the more significant, it is necessary for an understanding of the contribution of various parts of the body (i.e., nose, mid-body, or boattail) to the over-all characteristics of aerodynamic forces and moments and to establish the strength requirements of both the skin and the load-carrying structure within the body. The design of joints, auxiliary structures such as radomes, and special equipment which must be mounted on or in the surface of the body is critically dependent on expected pressure distributions.

Practical body designs violate many of the underlying assumptions of the theories given in Subsecs. 2 and 3. In this subsection the theories are compared with test data for many bodies other than slender ones, and the effects of detached shocks, blunt noses, and flow separation are discussed. Modifications to the basic theories are suggested and where possible empirical relations are derived in order to extend the range within which realistic pressure distributions may be predicted.

The qualitative characteristics of the longitudinal pressure distributions at zero angle of attack of some of the bodies of revolution to be discussed in this subsection are shown in Fig. 4-1.

4.1   Cones and Cone-Cylinders

When the nose shock is conical in form and attached to the apex, the fluid properties and the velocity components remain constant along each ray emanating from the apex of the cone. Such a feature renders this type of flow particularly amenable to theoretical evaluation. Figure 4-2 shows the free-stream Mach number at which the shock detaches as a function of the semi-angle of the cone.

Basing their work on the Taylor-Maccoll method of calculating the properties of the flow field around cones at zero angle of attack (Ref. 21), personnel at MIT have made numerical computations of the flow fields around cones for the 5- to 50-deg range of cone semi-apex angles over the entire Mach number range, from that at which the shock attaches to infinity. Their results are presented in tabular and graphical form in Ref. 22. References 55 and 66 extend this work to include small angles of attack and high angles of attack, respectively (see Subsec. 4.1.2). The tables of Ref. 22 give exact solutions to the non-viscous, ideal gas equations and will therefore need modification where viscous forces and gas imperfections are no longer negligible. Some representative pressure coefficients, taken from the extensive tables in Ref. 22, are plotted in Fig. 4-3 for Mach numbers at which the bow shock is attached.

4.1.1   Cone-Cylinder Combinations at Zero Angle of Attack

Characteristic solutions of the flows about an extensive family of cone-cylinders (all at zero angle of attack) have been obtained by Clippinger, Giese, and Carter and the results tabulated in

Ref. 63. From these tables the pressure distribution along the surface of a cylindrical afterbody was plotted for cone semi-apex angles of 10, 20, 30, 40, and 50 deg at various Mach numbers. These curves appear in Figs. 4-4 to 4-6. (Pressures on the conical surfaces may be obtained from Ref. 22.) The typical below-ambient pressure immediately aft of the shoulder returns gradually to the free-stream value. With the smaller cone angles, as the Mach number increases the flow must traverse a greater length of afterbody before the pressure finally returns to the free-stream value. At higher cone angles, the calculations were not carried far enough along the body to show the trends. It may be noted that many of them exceed the ambient value even at the shoulder.

4.1.2   Cone-Cylinder at Angle of Attack

When a cone is no longer aligned with the free-stream flow the circumferential pressure distribution will be a strong function of angle of attack and Mach number. Van Dyke (Ref. 2) calculated the longitudinal pressure distribution for the meridian rays along the top, bottom, and side of a cone-cylinder having a 10-deg conical nose and mounted at a 12-deg angle of attack in a free-stream flow of Mach number 2.0. The results are shown in Fig. 4-7 together with experimentally determined pressure coefficients for the same conditions. It may be seen that the Van Dyke hybrid theory (Subsec. 2.4) predicts the pressure with good accuracy for about 2 diameters downstream of the shoulder.

Exact solutions for the pressure distribution in non-viscous, ideal gas flow have not yet been obtained for the general case of cones at an angle of attack. Among the several approximations to the flow about yawed cones, Stone's first-order theory (Ref. 64) and second-order theory (Ref. 65) represent the most determined attack on the problem. In effect, Stone resolved the perturbation in the flow properties (resulting from the yawing of the cone) into its Fourier components and reformulated equations for the flow properties. Utilizing Stone's equations, Kopal and his associates tabulated the first and second-order perturbations. Their tables appear in Refs. 55 and 66. Young and Siska in Ref. 68 made improvements in the method of Stone's calculations, and Ferri in Ref. 59 corrected an error that occurred near the cone surface in the Stone solution. However, Roberts and Riley in Ref. 60 showed that though these corrections were logically necessary, they may be neglected in practice as is demonstrated in Figs. 4-8 and 4-9, which compare measured and predicted pressure distributions at widely differing Mach numbers around yawed cones. It should be noted that the MIT Tables (Refs. 55 and 66) are given in terms of the wind axes rather than the more usual body axes. Equations for transformation of the axes are given in Ref. 62 by Van Dyke, Young, and Siska.

The results of a systematic experimental study by Holt and Blackie (Ref. 67) of the pressure distribution around 15- and 20-deg cones at M = 3.53 and angles of attack from zero to 25 deg are presented in Figs. 4-10 and 4-11. It may be noted that the pressure on the underside (ϕ = 0) of the 15-deg cone is smaller than that for the 20-deg cone at corresponding values of $\alpha + \theta$. The pressure on the sides (ϕ = 90 deg) decreases slightly as the angle of attack is increased, while the pressure at $\phi \sim$ 80 deg is virtually independent of α.

Similar data obtained by Young and Siska for 10- and 15-deg cones at a Mach number of 2.0 are presented in Ref. 68 and plotted in Fig. 4-12.

The distribution around nearly any cone at moderate angles
of attack can be approximated with reasonable accuracy for a wide range
of Mach numbers. Values for the pressure coefficient for cones at zero
angle of attack can be obtained from Ref. 22 or a similar source and
the character of the circumferential pressure distribution for an angle
of attack determined by cross plots of Figs. 4-8 to 4-12. Experimental
data on cones at angles of attack are given by Cronvich in Ref. 61.

4.1.3   Cones of Elliptical Cross-Section

Under certain design conditions, it may be desirable to use
conical shapes of other than circular cross-section. The pressure dis-
tribution, force and moment characteristics, and drag of cones of ellip-
tical cross-section are discussed by Ward in Ref. 15, Kahane and Solarski
in Ref. 69, Ferri, Ness, and Kaplita in Ref. 70, and Ferri in Ref. 71.
The pressure distribution calculated by three different methods is shown
in Figs. 4-13 to 4-16 and in one case is substantiated by measured
values. Reference 70 also includes the pressure distribution over a
drop-shape cone and a faired triangular prism at Mach numbers of 1.6
to 9.1. These are shown for the zero angle of attack case in Fig. 4-17.
The normal-force characteristics of elliptical cones are presented in
Subsec. 5.2.1 and the pressure drag in Subsec. 6.6.

4.1.4   Double Cones

The primary advantage of using a double cone in a body of
revolution is that the pressure losses which accompany a given loss in
velocity are considerably less for two successive compressions than
they are for a single compression. One of the principal uses for such
a configuration is for the supersonic diffusion of the inlet air of a
turbo-jet, ram-jet, or other type of engine whose efficiency depends
on a high-pressure recovery of the incoming air. In Ref. 185, Kennedy
has calculated the flow field surrounding biconic noses having angles
of 25/40, 20/40, and 25/35 deg for Mach numbers between 2 and 4.

The double-cone nose is subject to a distinctive real-fluid
effect which is illustrated by the sketch and pressure distribution of
Fig. 4-18 (from Ref. 88). The pressure rise caused by the second cone
inhibits boundary-layer stabilization so that the flow tends to separ-
ate, thus making the effective angle of the first cone to be consider-
ably larger than its actual angle. The change in effective angle will
depend on the geometry (length and angle of both cones), the Mach num-
ber and Reynolds number, as well as the condition of back pressure at
the base of the second cone in the presence of an air inlet. Under the
conditions of Fig. 4-18, the effective cone angle due to separation was
more than double the initial cone angle. Much of the advantage to be
gained by the use of a double cone is lost under such circumstances.
In the case illustrated, an extreme combination of angles was chosen
in order to indicate the importance of checking this condition under
realistic environmental conditions for any given configuration.

This "bridging" phenomenon has a critical effect on the per-
formance of high-altitude ram-jet vehicles since it affects both pres-
sure recovery and air capture. Experimental investigations by Konrad
(Ref. 72) of a 15-deg isentropic spike at a Mach number of 4.8 and
simulated high altitude have shown that the separation always occurs
in the laminar boundary layer and that its effect may be reduced by

tripping the boundary layer. (Early boundary-layer transition may pro-
duce other unwanted effects.) Figure 4-19 shows the large separation
at Re/ft = 3.2×10^5 (a simulated free-flight altitude of 109,000 ft).
Figure 4-20 shows the decreased separation region at Re/ft = 6.7×10^5
(95,000 ft), and Fig. 4-21 shows the very much decreased separation
with the addition of a trip ring at Re/ft = 7.8×10^5 (91,000 ft).

4.2   Ogives and Ogive-Cylinders

The planform shape of an ogival nose is defined by the arcs
of a circle as shown in the sketch below.
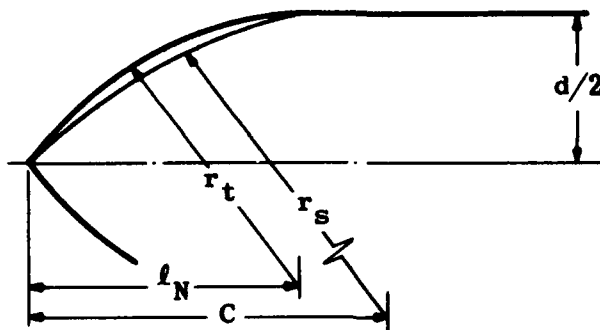
Secant ogives, the name applied to any general ogival shape, are com-
pletely defined by two criteria:

1. The radius of the ogival contour or arc in terms of the body
   diameter, r_s/d;

2. The distance of the center of curvature of the ogive aft of
   a line normal to the centerline of the ogive at its base,
   again expressed in terms of the body diameter, $(C - \ell_N)/d$.

When $C > \ell_N$, the intersection of the nose with a cylindrical
afterbody will form a corner. When $C = \ell_N$ the nose will form a continu-
ous line with a cylindrical afterbody at the junction and is referred
to as a tangent ogive.

An ogive has the advantage of providing without increased
drag a larger apex angle and greater nose volume than a cone of the
same length-to-diameter ratio. The drag of a tangent ogive is slightly
larger than that of the inscribed cone, while secant ogives have less
than either (see Fig. 6-2).

Theoretical techniques for calculating the pressure distribu-
tion over ogives are discussed in Subsec. 2, and the pressure distribu-
tions for a family of tangent-ogive-cylinder bodies at zero angle of
attack are presented by Ehret, Rossow, and Stevens in Ref. 30. (These
pressure distributions were obtained by use of the method of character-
istics and in terms of the hypersonic similarity parameter.) Later,
Rossow presented corrected data (Ref. 25) for the effect of flow rota-
tion which he found could be calculated separately and added to the
non-rotational solution. The corrected data are presented in Figs. 4-22
and 4-23 in the form of plots of the pressure ratio, p/p_∞, against the

hypersonic similarity parameter, K (where $K = Md/\ell_N$), for various per-
centages of the nose length aft of the apex. On the basis of these
curves, the following empirical expression has been developed (Ref. 30)
for surface pressure on a tangent ogive:

$$\frac{p}{p_\infty} = \left(\frac{p}{p_\infty}\right)_{apex} \cdot 10^{\,m\,\frac{x}{\ell_N}} \qquad\qquad (4\text{-}1)$$

where

$\left(\dfrac{p}{p_\infty}\right)_{apex}$ = ratio of surface pressure to free-stream pressure at
the apex

= ratio of cone pressure to free-stream pressure on a
cone whose vertex angle is equal to the apex angle
(values may be read from top curve of Fig. 4-22)

ℓ_N = nose length

d = body diameter

m = a parameter given by the empirical relation,

$$m = -\,0.62\,(K - 0.113) \qquad\qquad (4\text{-}2)$$

As Eqs. 4-1 and 4-2 are empirically derived, their validity is limited
to the range of the test data, i.e., $0.5 < K < 2$.

Fenter in Ref. 27 points out that although the hypersonic
similarity rule is taken in general to apply only to high Mach numbers
and very high fineness ratios, it may be applied with reasonable ac-
curacy down to Mach numbers of two.

The pressure distribution over a tangent-ogive-cylinder with
an over-all length of 10 diameters and a nose length of 3 diameters has
been obtained experimentally by Perkins and Jorgensen and compared with
theory for a Mach number of 2.0 at various angles of attack from zero
to 20 deg (Ref. 52). The data are plotted both longitudinally and cir-
cumferentially for all conditions. The longitudinal data for various
radial positions and angles of attack are plotted in Figs. 4-24 to 4-31,
and the circumferential distributions are plotted against radial angle
for various stations and angles of attack in Figs. 4-32 to 4-34.

Figure 4-24 shows that the experimental data agree well with
the theories at ze.o angle of attack, with the exception that the first-
order theory is poor near the apex. In subsequent figures only the
first-order theory and the Van Dyke hybrid theory are compared with
the experimental results. For all angles of attack and for most cir-
cumferential angles, the hybrid theory predicts too large a value of
the pressure coefficient at the vertex. Good agreement between theory
and experiment over most of the body is obtained only up to a 5-deg
angle of attack, the differences between theory and experiment becoming
progressively greater as the angle of attack increases. Because of the
good agreement between second-order theory and experiment at zero angle

of attack, the failure of the hybrid theory even for moderate angles
of attack is probably attributable to inaccuracies inherent in the
first-order cross-flow contribution. Flow separation which occurs at
all but the lowest angle of attack is the principal cause of the poor
agreement between theory and experiment for the flow over the top, or
leeward, side of the cylindrical afterbody.

At all angles of attack above 5 deg, effects of cross-flow
separation are indicated in the circumferential data plots (Figs. 4-32
to 4-34). As the angle of attack increases from 5 to 10 deg, a region
of separated flow is formed on the leeward side of the body at the aft
section. With further increase in the angle of attack, the separated
flow region moves forward and also progresses toward the windward side
of the body until at 20-deg angle of attack it encompasses almost the
entire leeward side. In this separated flow region, secondary flow ef-
fects associated with the body vortices are also observed. A slight
flow asymmetry on the leeward side of the body is indicated by a com-
parison of the flagged and unflagged symbols in Figs. 4-32 to 4-34.

Changes in the pressure distribution at any angle of attack
result principally from changes in the characteristics of the boundary-
layer separation, i.e., whether separation takes place under laminar or
turbulent conditions. Hence the boundary-layer transition is an index
of the Reynolds number effect. Since an increase in the turbulence
level of an air stream is known to induce effects which are qualitatively
similar to those resulting from an increase in Reynolds number, an ef-
fectively high Reynolds number may be achieved in a wind tunnel by in-
creasing the free-stream turbulence. This result has been obtained by
using a special grid mounted in the tunnel's stilling section in com-
bination with a maximum pressure. The pressure distributions obtained
under these conditions together with the data collected at low tunnel
pressures without the turbulence grid provide a fairly wide range of
effective Reynolds numbers. It may be noted from Figs. 4-35 to 4-37
that large Reynolds number effects are evidenced only by the data for
10-deg angle of attack. For angles of attack of 15 and 20 deg, Reynolds
number effects are present but much less pronounced. The changes in
the pressure distributions on a cylindrical afterbody which accompany
the increase in Reynolds number at 10-deg angle of attack are qualita-
tively the same as those which result from boundary-layer transition
on a circular cylinder. When boundary-layer transition occurs ahead
of the point at which laminar separation would usually occur, the sepa-
ration point moves toward the leeward side of the cylinder and the pres-
sure recovery on that side increases. On the cylindrical afterbody of
the same model, the increase in Re/in. from 0.13×10^6 to 0.39×10^6
is accompanied by a movement of the flow separation point toward the
leeward side of the body and an increase in the pressure recovery on
that side. From these data, for Re/in. of 0.39×10^6 at $\alpha = 10$ deg,
it is inferred that boundary-layer transition occurred on the inclined
body near the junction of the nose and the cylindrical afterbody.

The results of a theoretical study of the pressure distribu-
tions over tangent-ogive-cylinder bodies at 0 to 9-deg angles of attack
are presented by Dunn in Ref. 73. This study includes nose lengths of
1.5 to 4.0 diam in the Mach number range of 1.25 to 4.0 for all cases
where the value of Md/ℓ_N was less than 1.0. In all the figures pre-
sented herein, the pressure coefficient is plotted as a function of the

distance from the nose. The parameters, however, are varied from one group of figures to another in order to demonstrate their effects on the pressure distribution and to facilitate interpolation where required. The parameters and constants for these figures are listed below.

Variable Parameter	Constants	Figures
α, ϕ	M, ℓ_N/d	4-38 to 4-45
M	α, ϕ, ℓ_N/d	4-46 to 4-49
ℓ_N/d	M, α, ϕ	4-50 to 4-53
α	M, ℓ_N/d, ϕ	4-54 to 4-56

These IBM calculations covering a wide range of Mach numbers and nose lengths, are based on Van Dyke's second-order theory. It should be remembered that this theory does not include viscous effects and is invalid in the presence of any flow separation.

Although experimental confirmation of the results of this study are not included in Rϵf. 73, appropriate experimental data has been taken from Ref. 52 and compared with Dunn's calculations in Figs. 4-57 and 4-58. The agreement is good.

Theoretical and experimental determinations of the pressure near the vertex of an ogive-nosed body of revolution were also made by Dye (Ref. 74). The equation for the ogive is $r = 0.2x - 0.1x^2$, where r is the radius at a distance x from the vertex. This is roughly a 25-caliber tangent ogive with $\ell_N/d = 5$. The Mach number is 2 and the angle of attack range is ± 12 deg, and ten values of ϕ were taken around the nose.

4.3 Pressure Distribution on Ducted Bodies

Ducted or open-nosed bodies of revolution are required for air-breathing engines either in the body of the vehicle or in special pods mounted apart from the main body. Several methods are available for calculating the pressure distribution, lift, drag, and moment characteristics over the nose of such a body.

4.3.1 Methods for Calculating Pressure Distributions

The techniques listed below offer satisfactory agreement with experimentally determined pressure distributions on unity mass-flow-ratio cowls for combinations of contours and flow parameters that lie within certain boundary conditions.

Linearized-Source Distribution Method (Refs. 7 and 75).--This method (see Subsec. 2.2.2) gives satisfactory results for slender bodies at moderate supersonic speeds but increases in error as either the Mach number or the surface slope becomes too large.

Characteristics of Rotational Flow (Ref. 20).--Although accurate, this method of characteristics is tedious and time-consuming and requires modification in the presence of detached shocks. The method is discussed in Subsec. 2.6.

Van Dyke's Second-Order Method (Ref. 8).--Van Dyke's method (Subsec. 2.4) is limited to contours whose slope is everywhere less than $0.94 \ (M^2 - 1)^{-1/2}$. This condition corresponds to maximum surface angles of 28, 18, and 13 deg at Mach numbers of 2, 3, and 4, respectively.

Two-Dimensional Shock-Expansion Method (Refs. 23, 26, and 76).--With this technique, treated in Subsec. 2.8, the three-dimensional shock effects are neglected as are also the reflection of small disturbances originating at the surfaces. These effects introduce only small errors, however, so long as the lip angle is small and the lip shock is attached.

Linearized Characteristics Method (Refs. 5 and 77).--The results obtained by this method (see Subsecs. 2.2 and 2.6) approach those of the source-distribution method, but for results of the same degree of accuracy the characteristics method requires much more time.

Heaviside Operational Method (Ref. 78).--The Heaviside operator is applied to the linear perturbation theory for supersonic flow past a cylindrical tube of nearly constant radius. Solutions are derived for the cases of zero and non-zero angle of attack.

4.3.2   Comparison of Calculated and Experimental Pressures

The linear theory was used by Kennedy in Ref. 79 to calculate the external pressure distributions and wave drags of several families of ogive-cone noses at various Mach numbers. For the basic configuration illustrated in Fig. 4-59 the pressure distribution is given in terms of inlet radius, r_i; Mach number; inlet-to-maximum-area ratio, A_i/S; ogive caliber, R; and cone angle, θ. The ogive is tangent to the cone at the point of junction. A typical set of results for zero angle of attack is shown in Fig. 4-59.

The source-distribution method was used by Jack in Ref. 75 to calculate the surface pressure on conical and curved cowlings both with and without spill-over and having an innerbody cone half-angle of 25 deg in all cases but one, the exception being 20 deg. The pressure distributions for the conical cowls are shown in Fig. 4-60, normalized to be independent of Mach number by use of the factor $\beta = \sqrt{M^2 - 1}$. For the range of tip angles studied (0.5 to 3.0 deg) the pressure has two-dimensional values near the lip and decreases rapidly toward the expected conical flow value. Close to the lip the modified pressure coefficient, $\beta^2 C_p$, was found to vary linearly with ($\beta \tan \theta$). Further from the lip the variation was proportional to $(\beta \tan \theta)^2 \log_e (\beta \tan \theta)$. The variation of $\beta^2 C_p$ with $x/\beta r_i$ can be expressed as

$$\beta^2 C_p = f_1 \cdot (\beta \tan \theta) - f_2 \cdot \left[(\beta \tan \theta)^2 \log_e (\beta \tan \theta) \right] \qquad (4\text{-}3)$$

where θ is expressed in radians, and f_1 and f_2 are functions of $x/\beta r_i$ (Fig. 4-61). This technique for calculating the pressure distribution along conical cowlings will provide reasonably accurate results over the range of ($\beta \tan \theta$) for which the linearized theory is valid. Figure 4-62 gives the value of the pressure coefficient close to the lip for three Mach numbers and lip angles up t 15 deg and shows the magnitude of the error incurred by using the .earized characteristics method rather than the more accurate shock expansion technique.

Bodies for which the shock wave from a central body passes upstream of the cowl lip (spill-over) were also considered in order to obtain the effect of additive drag for a free-stream Mach number of 2.0. (Additive drag, as defined by Ferri and Nucci, is the integral of the pressure coefficient along the bounding streamline between the conical shock and the cowl lip.) The coordinates and contours of the inlets used to investigate these effects are given in Fig. 4-64. Although the curves were chosen arbitrarily, the lip of each body was faired into a streamline of the conical field produced by the central body. The design parameters selected for the body were

$$\text{Free-stream Mach number, } M = 2.0$$

$$\text{Area ratio, } A_i/S = 0.539$$

$$\text{Fineness ratio, } \ell_N/d = 4.0$$

$$\text{Cone half-angle, } \theta = 25 \text{ deg}$$

The linearized pressure distributions for the three inlets having cowl positioning angles, θ, of 32, 36, and 40 deg are shown in Fig. 4-65.

Illustrated in Fig. 4-63 are the variations of pressure distribution with Mach number for a conical cowling (1.9-deg angle) designed for the conditions noted above, with the lip at $x/r_i = 0.159$.

At $M = 2.0$, this configuration produces a shock that intersects the lip. At Mach numbers below 2.0, the pressure distribution upstream of the lip produces an additive drag because the conical shock is upstream of the cowl lip. As the Mach number increases, the pressure ratios of the cowl become higher.

The coordinates and contours for a series of non-conical inlets are shown in Fig. 4-66. The design parameters are the same as those noted above for the conical case. The initial lip angle for three of the four contours is the same as the flow-deflection angle behind the conical shock emanating from the central body. The results may be somewhat in error because of the large slopes of the lips; however, the linearized theory should predict the drag trends of these bodies. Pressure distributions for the curved contours of Fig. 4-66 are given in Fig. 4-67.

Comparisons of pressure distributions obtained with linearized characteristics and with the more accurate source distribution methods for various cowl configurations are given in Figs. 4-68 and 4-69.

Pressure coefficients were determined experimentally by Samanich (Ref. 80) for a family of nine cowls in a Mach-number range

of 1.98 to 4.90. Details of the configuration are presented in
Fig. 4-70, and the experimentally determined pressure coefficients are
given in Table 4-1. The pressures were also calculated by means of
the two-dimensional shock-expansion theory. Agreement between the mea-
sured and calculated values was good at the lower cowl projected areas,
but the difference increased as the cowl area ratio increased or as
the shock detachment at the cowl lip was approached. Figure 4-71 is a
typical plot of the results for three of the cowls at one Mach number.

Because many more boundary conditions and parameters are in-
volved in ducted body pressure calculations than in those for a solid
body, no attempt has been made to interrelate the three studies
(Refs. 75, 79, and 80) on the ducted bodies that have been described.
The over-all aerodynamic characteristics have also been calculated in
these references. Normal forces and moments will be discussed in Sub-
sec. 5, and drag characteristics in Subsec. 6.

Theoretical techniques for determining the external contours
of ducted bodies of minimum drag will be found in Refs. 81, 82, and 83.

4.4   Pressure Distribution over Boattails

Detailed experimental studies of the pressure distribution
over conical and ogival boattails at test velocities of M = 1.5, 2.0,
and 2.5 are reported by Maxwell and Shutts in Ref. 165. The configura-
tions tested in this investigation are illustrated in Fig. 4-72. For
the case of conical boattails the results show that the pressure de-
creases at the beginning of the ogive by an amount corresponding to a
two-dimensional expansion for the given angular change and initial Mach
number ahead of the corner. Immediately after the corner, however, the
three-dimensional effect is sensed and the pressure tends to return to
a higher value. For the case of a faired or ogival boattail with a
gradual change in direction of body contour, the combination of these
two effects results in a completely different pressure distribution, as
would be expected. The pressure distribution curves in Figs. 4-73 to
4-75 illustrate these effects.

Another study of the pressure distribution over boattails in
a free stream at M = 1.91 and angles of attack up to 6 deg is reported
by Cortright and Schroeder in Ref. 150. Figures 4-76 and 4-77 present
experimental pressure distributions over and slightly ahead of the boat-
tail configuration. The mean distributions for all of the configura-
tions for the case of zero angle of attack are compared with both lin-
earized theory (Ref. 7) and the method of characteristics (Ref. 20) in
Fig. 4-78. In this figure the variation of pressure coefficient with
axial distance is given for both sides of the boattail break (i.e., the
start of the boattail) to facilitate comparison of the pressure distri-
butions of other configurations. The agreement between the experimental
measurements obtained with different boattails of equal angle is gen-
erally quite good. The mean distributions obtained with boundary-layer
transition at the tip of the body (i.e., by use of a wire) show small
departures from the natural transition case. Figure 4-78 also shows
that the pressure distribution predicted by the method of characteris-
tics is parallel to the experimental value and slightly more negative,
which would be expected qualitatively in the presence of the body bound-
ary layer. Figure 4-78 also indicates that the linearized theory of
Ref. 7 was less satisfactory for predicting the pressure distributions,

particularly for the larger boattail angles, than the method of char-
acteristics. In connection with the linearized theory, however, it
should be pointed out that the use of an approximate form of the pres-
sure coefficient,

$$C_p = - \frac{2v_x}{V} \qquad (4-4)$$

resulted in an improved prediction of the average pressure level on
the boattail.

The distribution of calculated pressure coefficients along
boattails of 2.5 to 17.5 deg for M = 3.24 are shown in Fig. 4-79 (from
Ref. 140).

4.5   Bodies of Continually Varying Diameter

The longitudinal pressure distribution over bodies of revolu-
tion of continually varying diameter was measured at test Mach numbers
of 1.62, 1.93, and 2.41 by Bromm and Goodwin (Ref. 84) in connection
with investigations of body shapes for minimum wave drag (discussed in
Subsec. 6.7). The configurations employed during this study are shown
in Fig. 4-80 and the pressure distributions over the various bodies
are presented in Figs. 4-81 and 4-82. As indicated in the figures,
the variation of pressure distribution with Reynolds number is very
slight. Conclusions concerning the drag characteristics appear in Sub-
sec. 6.7. These data provide additional experimental information for
ogival noses and boattails in the supersonic speed range.

The pressure distribution for a parabolic-arc body whose
cross-section is elliptical has been derived by Kahane and Solarski and
reported in Ref. 69. The method is based on the Ward slender-body
theory of Ref. 15. The results of the calculations for M = 2 are shown
in Fig. 4-83 for both circular and elliptical eccentricity (ϵ = 1/3)
cross sections.

4.6   Blunt-Nosed Bodies

Although a pointed-nose configuration is generally accepted
as the optimum one for supersonic flight, it is nevertheless often
necessary to use blunt-nosed bodies to accommodate radomes and to re-
duce heat-transfer effects at very high speeds, e.g., for re-entry
bodies. The detached shock wave associated with such noses creates a
condition of mixed flow over the forward portion of the nose. At the
foremost point the flow is subsonic and the pressure is equal to the
stagnation value behind a normal shock wave for the given free-stream
Mach number and ambient pressure conditions. The local velocity then
increases and passes through the sonic value as the air flows around
the curved surface of the body, and the pressure and density decrease
accordingly.

Much information, both theoretical and experimental, is avail-
able for simple blunt-nosed shapes such as spheres, flat faces, spherical-
nosed cones, truncated cones, and general oval shapes. Such information
can be found in Refs. 85 to 91.

4.6.1   Spheres

The distance between the detached shock and the nose of the body is a function of the free-stream Mach number and the nose shape. The methods used to calculate this "stand-off" distance are reviewed by Van Dyke in Ref. 85, which also shows that existing theories are inadequate for rigorous calculations. However, a numerical method outlined therein, may be used to survey the field between the shock wave and the body. Van Dyke's application of this method compares well with experimental measurements as is shown in Fig. 4-84. Corresponding experimental results obtained by Kendall (Ref. 87) for flat-faced three-dimensional bodies are presented in Fig. 4-85.

The pressure distributions for a hemisphere in the Mach number range of 2.0 to 18.8 have been collected from Refs. 54, 88, 187, and 191 to 194 by Julius (Ref. 86) and are plotted in Fig. 4-86. As indicated by these data, the ratio of local surface pressure to stagnation pressure behind the shock wave is independent of Mach number and is approximated very closely by the following simple expression, derived from the Newtonian impact concept.

$$\frac{C_p}{C_{p\ max}} = \cos^2 \theta \tag{4-5}$$

where θ is the angle between the surface and the normal to the free stream. The agreement becomes poor at low Mach numbers when θ approaches 90 deg. Virtually identical pressure distributions were obtained when the Reynolds number was varied by a factor of 3 or 4. When the simple Newtonian equation, Eq. 4-5, is modified to account for the surface curvature, the agreement with experimental data (Kendall, Ref. 87) is not as good as in the case of the unmodified equation.

The Mach number distribution is shown in Fig. 4-87. In the lower Mach-number range, it may be noted that the local Mach number at the 90-deg station exceeds the free-stream value. The angular location of the sonic line on the body may be approximated by the following empirical expression.

$$\theta_s(\text{rad}) = 0.690 + \frac{0.263}{M^2 - 1} \tag{4-6}$$

The experimentally determined shape of the sonic lines for various Mach numbers is shown in Fig. 4-89, where it is compared with Van Dyke's calculated sonic lines for M = 2 and 6 (Ref. 184). The general shape is in better agreement at M = 6 than it is at M = 2. The slope of the shock wave and radius of curvature at the vertex are shown in Figs. 4-88 and 4-90, and the estimated velocity distribution along the axial streamline is shown in Fig. 4-91 (all from Ref. 87).

4.6.2   Flat-Faced Cylinders and Disks

Information similar to that given for spheres is presented in Figs. 4-92 to 4-100 (from Ref. 87 except where noted) for flat-faced cylinders and disks placed in supersonic streams with their flat faces normal to the flow direction. It may be seen in Fig. 4-92 (from Ref. 86)

that the pressure on such a face is not constant but begins to decrease
at a radial distance about half-way between the stagnation point (disk
center) and the outer edge until near the outer edge it is about 80% of
stagnation value. The Mach number distribution over the face of a disk
is virtually independent of the free-stream Mach number (Fig. 4-93).
The pressure distribution along the sides of a cylinder with a flat
face headed into the stream is shown in Fig. 4-94. The flow around the
edge of a disk (Fig. 4-94) like the flow over the face (Fig. 4-95) is
nearly independent of the free-stream Mach number. The pressure aft of
the corner is governed strongly by viscous effects. Along the cylindri-
cal body the flow becomes Mach-number dependent and rapidly approaches
the free-stream static pressure.

        Figure 4-95 shows the slope of the shock wave and indicates
that the shock wave is parabolic for $M < 2$ and non-parabolic for $M > 2$.
It may also be seen from Fig. 4-95 that the slope of the shock wave is
almost independent of M (for $M > 2$) in the region of the front face.
In like manner the shock-wave curvature near the vertex is almost in-
dependent of Mach number at Mach numbers greater than about 2.5
(Fig. 4-96). The velocity distribution near the vertex and the sonic
lines at the shoulder are shown in Figs. 4-97 and 4-98.

        Pressure distributions on a flat-faced cylinder at an angle
of attack of 4 deg and at Mach numbers of 1.88 and 2.86 were obtained
experimentally by Potter, Shapiro, and Murphy (Ref. 92). The circum-
ferential distribution at 3 stations along the cylindrical surface are
plotted in Figs. 4-99 and 4-100. It may be noted that at the higher
Mach number (2.86) the pressure on the windward side has almost returned
to the static pressure at $1/2$ d from the shoulder.

4.6.3   Spherical-Nosed and Truncated Cones

        Flat or rounded axisymmetric truncated-cone configurations
have the advantages of aerodynamic stability and good heat-transfer
characteristics on both the front face and afterbody. The low velocity
on the front face and low density on the conical afterbody are both
conducive to minimizing the over-all heat transfer. Such configura-
tions were studied extensively (Refs. 87 and 89) in the Mach number
range of 1.75 to 8, with several variations in the basic configuration.
The resulting pressure distributions are presented in Figs. 4-101 to
4-107. Shadowgraph tracings of the flow and shock-wave pattern over a
44-deg truncated cone are shown for $M = 1.82$ and 2.81 in Fig. 4-102 to
illustrate the condition of over-expansion just aft of the shoulder
and to show the effect of shock stand-off and conical shock-wave char-
acteristics on the shock-wave pattern and flow conditions at different
Mach numbers.

        In general, for all of the configurations investigated, the
data indicated a slight increase in velocity along the front face as
the contour length from the stagnation point increases. Similar tests
with a spherical-nosed cone are described in Ref. 88 and the results
are shown in Fig. 4-108. Along the circular arc connecting the front
face and the conical portion, a rapid acceleration occurs which may or
may not result in a localized over-expansion at the start of the conical
portion, depending on the Mach number, cone angle, and angle of attack.
The strongest over-expansion occurs at the lowest Mach numbers, gener-
ally less than Mach 3. Examination of the shadowgraphs shows the shock
waves which result from the over-expansion and induce boundary-layer

separation. Plots of the ratio of static pressure on the surface to
stagnation pressure after the shock wave show that the pressure distri-
bution over the face and corner is relatively unaffected by Mach number.
However, Mach number effects are evident on the conical portion at the
lower Mach numbers. In no case was the conical section long enough to
achieve the limiting pressure, i.e., that which would exist on a sharp-
nosed cone of the same apex angle. It has been shown that increasing
the shoulder radius results in an alleviated pressure gradient in the
corner region and in a smaller over-expansion.

The pressure distribution over the rounded blunt shapes of a
limited family were measured at M = 4.95 by Cooper and Mayo (Ref. 90).
The model dimensions and resulting pressure distributions are shown in
Fig. 4-109.

4.6.4   Noses with Elliptical Planform

Holder and Chinneck (Ref. 93) have measured the pressure dis-
tribution, drag, and shock-wave geometry of noses which are elliptical
in planform (the centerline of the body is the major axis of the half-
ellipse). The length-to-diameter ratio of the nose ranged from zero
(blunt) to 4.0. The pressure distributions in terms of the axial posi-
tion are shown in Fig. 4-110. The curves in this figure show clearly
that the pressure coefficient not only becomes more negative at the
shoulder as the nose becomes more blunt, but that the negative region
extends farther down the body. Figure 4-111 gives a more detailed
pressure distribution over the nose in terms of the radial rather than
the axial dimension. Figures 4-112 and 4-113 give the shape of the
shock wave for the various noses and also the stand-off distance of the
shock waves from the nose.

4.6.5   Blunt Bodies at Very High Mach Numbers

During preliminary evaluation of the design of a re-entry
vehicle the ability to predict the pressure distribution under a wide
range of ambient conditions acquires prime importance. The extent of
heat-transfer effects are not fully known. Henderson in Ref. 91 shows
that existing aerodynamic and blast-wave theories are adequate for cal-
culating the direct and induced inviscid pressures on simple axisymmet-
ric bodies at zero angle of attack. The extent to which viscous effects
can change the pressures is also indicated. Measured and calculated
pressures are compared quite favorably in Fig. 114 for three blunt-body
shapes at Mach numbers of 15.6 and 19.0. The tests were conducted in
hypersonic tunnels under perfect-gas conditions and thus are not com-
pletely representative of free flight in the atmosphere at these high
Mach numbers.

4.7   Cylinders Alone at 90-Deg Angle of Attack

The pressure distribution around cylinders placed at 90 deg
to a supersonic stream have been measured experimentally at relatively
high and at very low Reynolds numbers (Refs. 88 and 94). Measurements
at M ~ 5.7 have been taken from both references and compared in
Fig. 4-115 in order to show the slight effect of a large change in
Reynolds number.

Pressure coefficients for Mach numbers of 1.32 to 5.73 (from Ref. 94) are presented in Table 4-2. Although the Reynolds numbers are very low (from 37 to 4100), the relative pressures as a function of both M and ϕ may prove useful. They show that the zero pressure coefficient moves from the 72-deg position at M = 1.32 to 126 deg at M = 5.73 and that the pressure coefficient drops to -0.77 at M = 1.32, whereas the lowest value at M = 5.73 is -0.020.

Table 4-1

Experimental Pressure Coefficients (Source: Ref. 80)

Cowl 1

x (in.)	Mach Number				
	1.98	2.47	2.94	3.88	4.90
0.07	0.510	0.400	0.345	0.312	0.276
0.11	0.468	0.366	0.315	0.276	0.246
0.16	0.401	0.320	0.267	0.242	0.244
0.21	0.368	0.290	0.232	0.229	0.205
0.28	0.364	0.285	0.224	0.196	0.187
0.36	0.315	0.248	0.208	0.172	0.169
0.44	0.276	0.223	0.180	0.162	0.157
0.54	0.258	0.203	0.157	0.155	0.145
0.64	0.256	0.208	0.166	0.140	0.133
0.76	0.224	0.180	0.153	0.127	0.121
0.90	0.197	0.162	0.126	0.114	0.109
1.05	0.167	0.134	0.103	0.103	0.097
1.20	0.152	0.127	0.103	0.088	0.085
1.36	0.118	0.097	0.084	0.071	0.073
1.55	0.090	0.071	0.052	0.060	0.055
1.90	0.034	0.030	0.023	0.032	0.025
2.40	-0.008	-0.003	0.002	0.006	0.014

Cowl 2

x (in.)	Mach Number				
	1.98	2.47	2.94	3.88	4.90
0.07	0.506	0.413	0.350	0.323	0.294
0.11	0.456	0.351	0.292	0.271	0.246
0.16	0.425	0.337	0.298	0.249	0.235
0.20	0.421	0.335	0.291	0.247	0.223
0.30	0.387	0.318	0.261	0.229	0.217
0.38	0.370	0.296	0.257	0.215	0.205
0.48	0.340	0.287	0.253	0.200	0.191
0.60	0.337	0.277	0.231	0.197	0.181
0.74	0.312	0.250	0.203	0.181	0.169
0.89	0.280	0.233	0.195	0.165	0.157
1.08	0.257	0.215	0.188	0.152	0.145
1.30	0.233	0.197	0.165	0.136	0.127
1.55	0.187	0.156	0.125	0.114	0.109
1.90	0.145	0.124	0.101	0.090	0.091
2.25	0.104	0.089	0.082	0.069	0.067
2.60	0.087	0.076	0.070	0.058	0.055
2.95	0.071	0.056	0.050	0.045	0.049
3.30	0.037	0.030	0.028	0.029	0.055
3.70	0.008	0.013	0.008	0.016	0.025
4.50	-0.032	-0.015	-0.011	-0.004	0.007

Cowl 3

x (in.)	Mach Number				
	1.98	2.47	2.94	3.88	4.90
0.08	0.576	0.459	0.398	0.325	0.304
0.12	0.503	0.380	0.328	0.289	0.262
0.16	0.468	0.358	3.309	0.274	0.244
0.22	0.436	0.337	0.295	0.251	0.226
0.30	0.435	0.340	0.309	0.247	0.238
0.40	0.410	0.326	0.279	0.238	0.226
0.52	0.381	0.310	0.267	0.228	0.214
0.66	0.362	0.283	0.247	0.208	0.196
0.80	0.342	0.277	0.241	0.198	0.191
0.98	0.315	0.251	0.217	0.185	0.173
1.18	0.271	0.221	0.193	0.164	0.155
1.40	0.236	0.189	0.168	0.139	0.131
1.65	0.210	0.173	0.155	0.126	0.119
1.90	0.184	0.157	0.133	0.113	0.107
2.20	0.163	0.140	0.120	0.100	0.098
2.50	0.154	0.131	0.117	0.093	0.095
2.75	0.144	0.126	0.112	0.088	0.089
3.25	0.111	0.097	0.079	0.072	0.071
3.75	0.064	0.056	0.044	0.047	0.065
4.25	0.065	0.042	0.036	0.037	0.042
4.75	0.034	0.036	0.028	0.027	0.035
5.25	0.022	0.018	0.012	0.021	0.030
6.00	-0.014	-0.013	-0.010	0.004	0.012
6.75	-0.035	-0.030	-0.024	-0.011	0.000

x = Axial distance aft of cowl lip

Cowl design shown in Fig. 4-70

Table 4-1   NAVWEPS Report 1488 (Vol. 3, Sec. 8)

Table 4-1 (cont'd)

Experimental Pressure Coefficients (Source: Ref. 80)

Cowl 4

x (in.)	Mach Number				
	1.98	2.47	2.94	3.88	4.90
0.08	0.861	0.685	0.605	0.522	0.485
0.11	0.755	0.610	0.529	0.446	0.413
0.15	0.675	0.537	0.459	0.412	0.377
0.21	0.622	0.503	0.408	0.381	0.342
0.28	0.594	0.481	0.427	0.361	0.330
0.35	0.532	0.449	0.397	0.328	0.306
0.43	0.471	0.399	0.338	0.299	0.282
0.53	0.387	0.324	0.262	0.247	0.223
0.64	0.320	0.279	0.244	0.203	0.193
0.76	0.236	0.195	0.176	0.154	0.139
0.90	0.191	0.163	0.133	0.128	0.115
1.05	0.135	0.115	0.090	0.095	0.082
1.20	0.082	0.078	0.063	0.062	0.062
1.35	0.013	0.024	0.023	0.029	0.032
1.50	-0.003	0.006	0.004	0.019	0.026

Cowl 5

x (in.)	Mach Number				
	1.98	2.47	2.94	3.88	4.90
0.08	0.914	0.756	0.693	0.563	0.534
0.12	0.810	0.645	0.621	0.499	0.474
0.16	0.751	0.595	0.551	0.462	0.438
0.22	0.723	0.582	0.508	0.448	0.420
0.28	0.716	0.592	0.557	0.440	0.418
0.36	0.675	0.563	0.534	0.418	0.408
0.44	0.619	0.529	0.490	0.405	0.391
0.54	0.568	0.485	0.443	0.377	0.355
0.64	0.504	0.437	0.418	0.333	0.319
0.76	0.414	0.362	0.349	0.277	0.271
0.90	0.310	0.273	0.256	0.224	0.211
1.04	0.251	0.220	0.207	0.183	0.176
1.20	0.216	0.201	0.193	0.152	0.146
1.36	0.178	0.160	0.164	0.129	0.128
1.54	0.146	0.135	0.124	0.107	0.104
1.90	0.094	0.090	0.089	0.076	0.080
2.35	0.021	0.034	0.046	0.037	0.044
2.80	-0.034	-0.014	-0.001	0.007	0.020

Cowl 6

x (in.)	Mach Number				
	1.90	2.47	2.94	3.88	4.90
0.08	0.953	0.743	0.645	0.564	0.523
0.12	0.924	0.711	0.606	0.538	0.505
0.16	0.845	0.680	0.584	0.508	0.482
0.22	0.773	0.642	0.554	0.492	0.458
0.30	0.732	0.629	0.559	0.475	0.452
0.38	0.661	0.588	0.515	0.453	0.434
0.50	0.585	0.530	0.461	0.407	0.392
0.74	0.464	0.436	0.391	0.336	0.390
0.90	0.394	0.382	0.325	0.293	0.314
					0.278
1.08	0.336	0.331	0.284	0.255	0.242
1.30	0.288	0.290	0.257	0.227	0.212
1.55	0.238	0.246	0.221	0.194	0.182
1.90	0.172	0.189	0.160	0.151	0.146
2.25	0.102	0.138	0.118	0.111	0.110
2.60	0.064	0.103	0.089	0.087	0.086
2.95	0.031	0.068	0.058	0.065	0.068
3.30	-0.012	0.037	0.036	0.041	0.059
3.70	-0.053	0.008	0.009	0.025	0.032
4.30	-0.079	-0.014	-0.011	0.008	0.015

x = Axial distance aft of cowl lip

Cowl design shown in Fig. 4-70

Table 4-1 (cont'd)

Experimental Pressure Coefficients (Source: Ref. 80)

Cowl 7

x (in.)	Mach Number				
	1.98	2.47	2.94	3.88	4.90
0.08	1.116	1.009	0.909	0.773	0.726
0.12	0.968	0.877	0.783	0.649	0.625
0.16	0.875	0.782	0.685	0.582	0.548
0.22	0.713	0.633	0.539	0.499	0.459
0.28	0.596	0.535	0.480	0.400	0.388
0.36	0.486	0.438	0.390	0.334	0.316
0.44	0.424	0.384	0.325	0.288	0.269
0.54	0.343	0.299	0.249	0.241	0.221
0.64	0.276	0.251	0.224	0.187	0.180
0.76	0.194	0.172	0.160	0.143	0.138
0.88	0.128	0.125	0.101	0.107	0.102
1.00	0.080	0.081	0.067	0.073	0.078
1.12	0.035	0.043	0.063	0.056	0.055
1.26	0.011	0.027	0.028	0.035	0.043
1.40	-0.009	0.008	0.014	0.026	0.031

Cowl 8

x (in.)	Mach Number				
	1.98	2.47	2.94	3.88	4.90
0.08	1.230	1.103	0.995	0.832	0.793
0.12	1.126	1.011	0.922	0.771	0.739
0.16	1.013	0.897	0.804	0.711	0.680
0.22	0.902	0.802	0.698	0.640	0.596
0.28	0.823	0.738	0.690	0.576	0.549
0.36	0.737	0.659	0.613	0.511	0.495
0.44	0.620	0.564	0.509	0.446	0.430
0.54	0.534	0.478	0.422	0.390	0.361
0.64	0.482	0.440	0.411	0.339	0.323
0.76	0.410	0.357	0.343	0.285	0.275
0.90	0.324	0.297	0.263	0.236	0.227
1.08	0.254	0.233	0.203	0.192	0.180
1.24	0.203	0.196	0.181	0.148	0.144
1.42	0.145	0.142	0.138	0.114	0.120
1.62	0.090	0.092	0.083	0.084	0.085
1.92	0.038	0.050	0.050	0.055	0.055
2.42	-0.031	-0.007	0.009	0.010	0.025

Cowl 9

x (in.)	Mach Number				
	1.90	2.47	2.94	3.88	4.90
0.08	1.226	1.074	0.939	0.799	0.766
0.11	1.116	0.973	0.871	0.733	0.706
0.16	1.051	0.897	0.789	0.691	0.664
0.22	0.973	0.846	0.734	0.668	0.634
0.30	0.903	0.836	0.748	0.639	0.622
0.38	0.819	0.783	0.712	0.606	0.610
0.48	0.723	0.707	0.635	0.553	0.539
0.60	0.552	0.567	0.498	0.467	0.443
0.74	0.485	0.497	0.460	0.397	0.384
0.90	0.400	0.425	0.391	0.334	0.324
1.08	0.327	0.349	0.309	0.282	0.270
1.30	0.252	0.279	0.241	0.231	0.216
1.55	0.202	0.238	0.213	0.186	0.181
1.90	0.128	0.168	0.154	0.135	0.139
2.25	0.050	0.095	0.087	0.092	0.097
2.60	-0.001	0.094	0.052	0.063	0.067
2.95	-0.039	0.024	0.031	0.033	0.049
3.25	-0.057	-0.003	-0.001	0.017	0.038
3.60	-0.081	-0.016	-0.006	0.012	0.025

x = Axial distance aft of cowl lip

Cowl design shown in Fig. 4-70

Table 4-2　　　　　　　　NAVWEPS Report 1488 (Vol. 3, Sec. 8)

Table 4-2

Distribution of Pressure Coefficient, C_p, around a Cylinder (Source: Ref. 94)

M_∞	1.32	1.65	1.82	1.90	3.55	3.83	4.02	4.19	4.38	4.45	4.88	5.29	5.73
Re_∞	37	56	100	210	330	610	1030	1870	3360	460	840	1230	4100
$C_{p\,max}$	1.44	1.604	1.615	1.649	1.779	1.783	1.803	1.815	1.810	1.763	1.797	1.87	1.838
$\phi(deg)$													
0	1.46	1.58	1.62	1.64	1.77	1.79	1.79	1.78	1.80	1.77	1.795	1.82	1.82
9	1.43	1.56	1.60	1.62	1.74	1.75	1.76	1.78	1.765	1.735	1.77	1.79	1.79
18	1.33	1.48	1.50	1.545	1.65	1.65	1.68	1.69	1.665	1.615	1.675	1.685	1.70
27	1.16	1.35	1.37	1.60	1.50	1.50	1.52	1.52	1.52	1.445	1.49	1.530	1.525
36	0.98	1.21	1.19	1.225	1.30	1.30	1.32	1.32	1.325	1.240	1.30	1.325	1.325
45	0.75	1.03	0.99	1.025	1.08	1.08	1.09	1.08	1.09	1.00	1.08	1.10	1.10
54	0.50	0.82	0.75	0.80	0.85	0.85	0.87	0.85	0.84	0.77	0.855	0.85	0.86
63	0.25	0.60	0.54	0.57	0.64	0.63	0.65	0.62	0.60	0.545	0.640	0.635	0.635
72	0	0.36	0.34	0.35	0.44	0.45	0.45	0.44	0.415	0.370	0.465	0.445	0.445
81	-0.21	0.16	0.15	0.16	0.29	0.30	0.30	0.29	0.280	0.230	0.315	0.295	0.300
90	-0.39	-0.02	-0.01	0.02	0.17	0.18	0.18	0.18	0.170	0.130	0.205	0.190	0.195
99	-0.53	-0.165	-0.13	-0.10	0.08	0.085	0.09	0.09	0.080	0.050	0.120	0.110	0.115
108	-0.64	-0.295	-0.23	-0.18	0.015	0.015	0.03	0.03	0.025	0	0.055	0.060	0.06
117	-0.70	-0.38	-0.30	-0.23	-0.025	-0.03	-0.01	-0.01	-0.01	-0.03	0.015	0.020	0.025
126	-0.74	-0.42	-0.33	-0.23	-0.045	-0.06	-0.045	-0.035	-0.04	-0.045	-0.005	-0.01	0
135	-0.76	-0.44	-0.33	-0.23	-0.065	-0.07	-0.05	-0.05	-0.045	-0.050	-0.02	-0.02	-0.010
144	-0.77	-0.64	-0.32	-0.20	-0.08	-0.07	-0.06	-0.05	-0.04	-0.05	-0.025	-0.025	-0.020
153	-0.77	-0.43	-0.28	-0.17	-0.08	-0.07	-0.06	-0.45	-0.03	-0.05	-0.025	-0.025	-0.015
162	-0.76	-0.41	-0.26	-0.10	-0.08	-0.07	-0.06	-0.04	-0.025	-0.05	-0.025	-0.020	-0.005
171	-0.75	-0.40	-0.24	-0.16	-0.08	-0.07	-0.05	-0.04	-0.02	-0.05	-0.025	-0.015	0
180	-0.75	-0.40	-0.24	-0.16	-0.08	-0.07	-0.05	-0.04	-0.02	-0.05	-0.025	-0.010	0

Cone Cylinder

Low M and θ

Cone Cylinder

High M and θ

Ogive Cylinder

Ducted Cone-Cylinder

Conical Boattail

Ogival Boattail
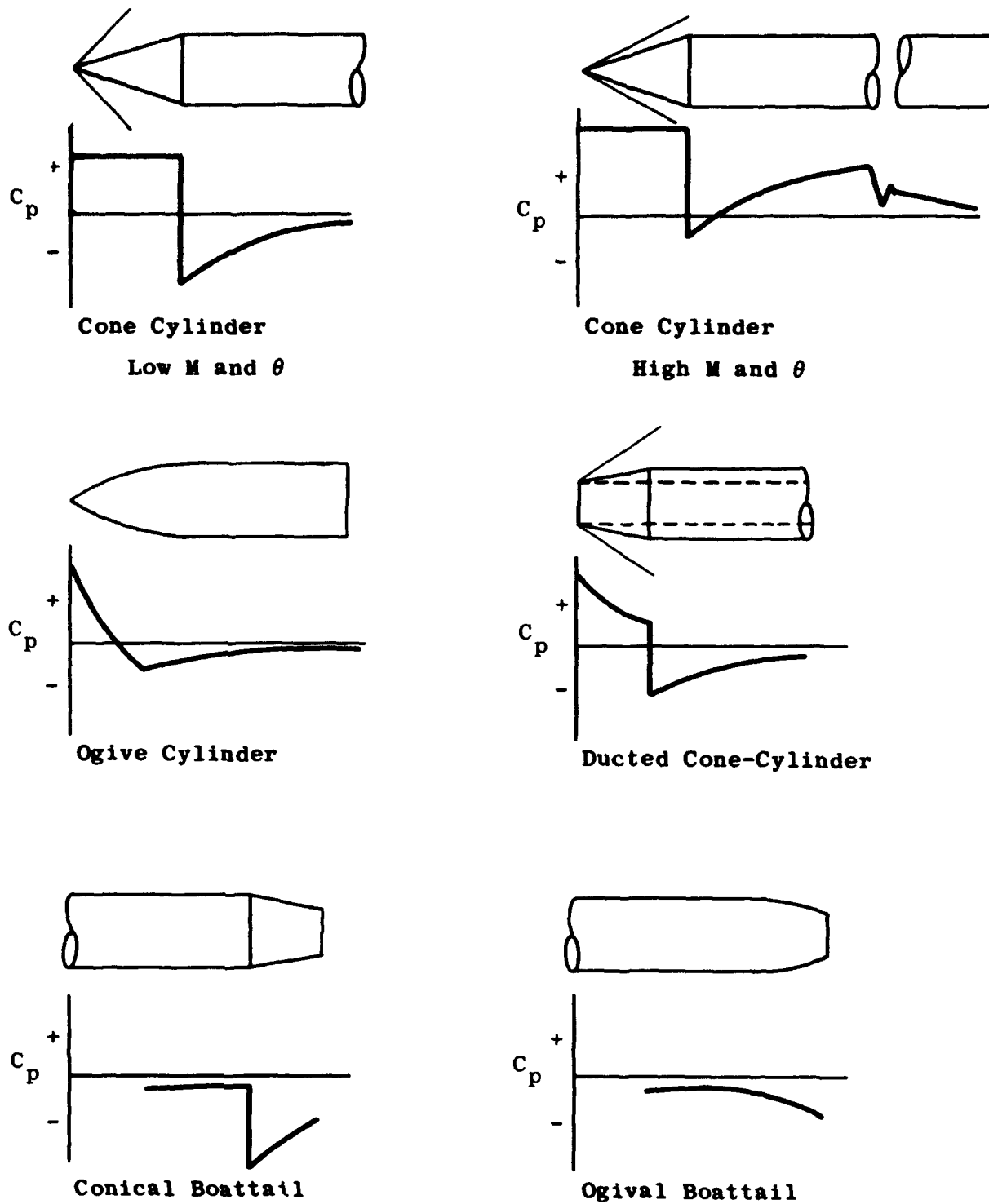
Fig. 4-1. Qualitative characteristics of the longitudinal pressure distribution on various bodies of revolution.

Fig. 4-2   NAVWEPS Report 1488 (Vol. 3, Sec. 8)
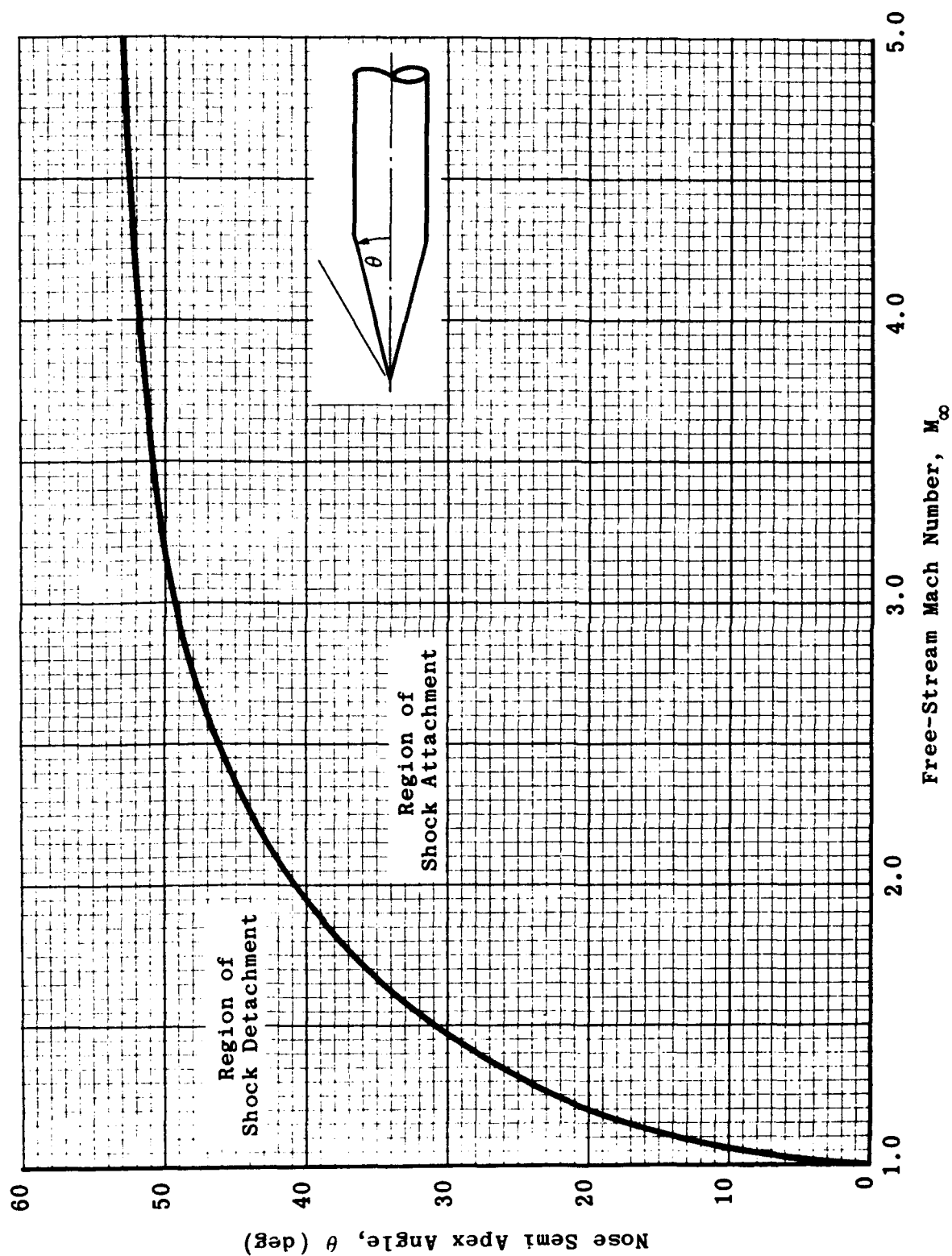
Fig. 4-2.   Shock detachment Mach number for conical noses.
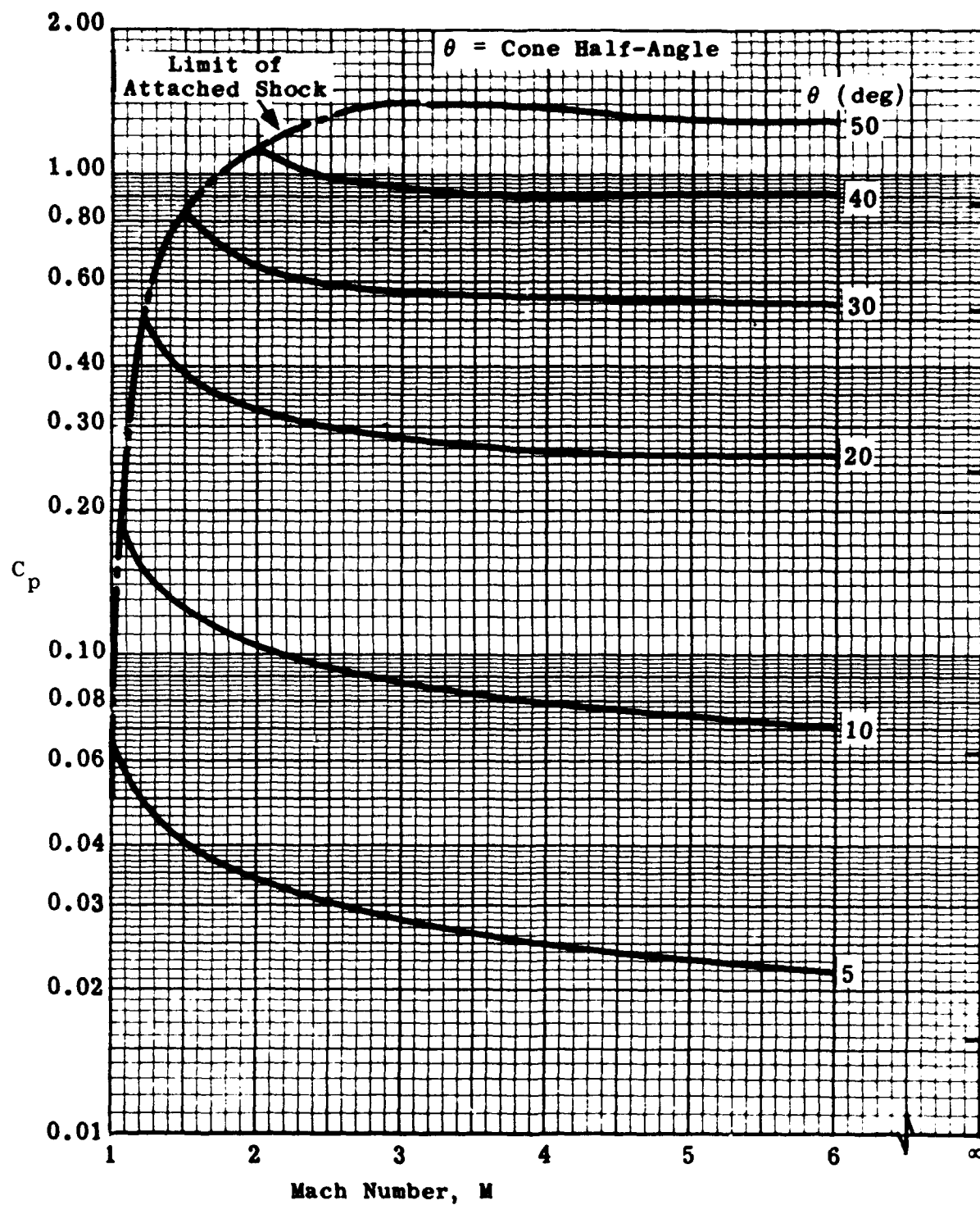
Fig. 4-3.   Pressure coefficient as a function of Mach number and
conical nose angle.   (Source: Ref. 22)

Fig. 4-4   NAVWEPS Report 1488 (Vol. 3, Sec. 8)
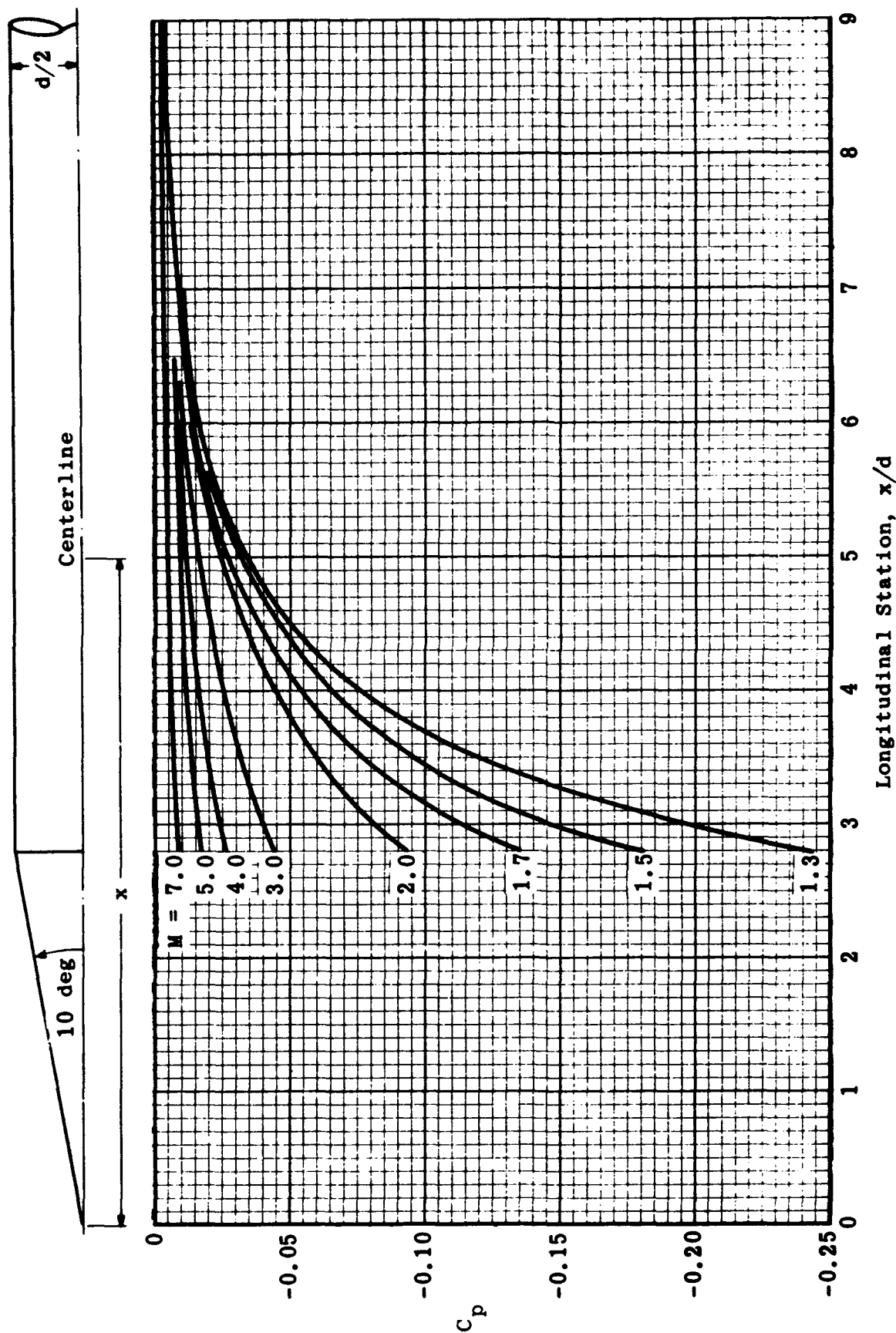
Fig. 4-4. Pressure distribution along the afterbody of a cone cylinder for various Mach numbers; $\theta = 10$ deg. (Source: Ref. 63)
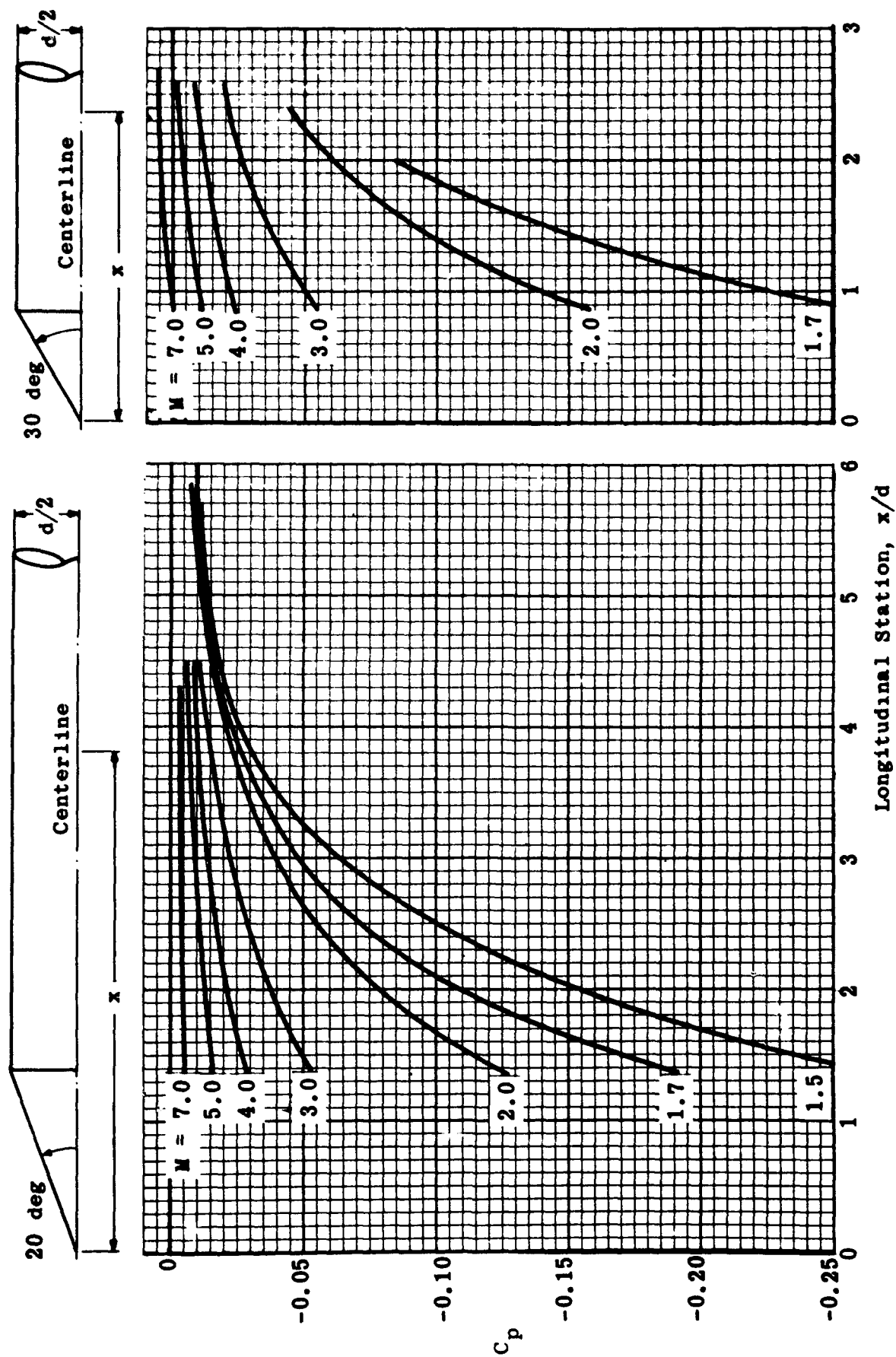
Fig. 4-5. Pressure distribution along the afterbody of a cone cylinder for various Mach numbers; $\theta = 20$ deg and 30 deg. (Source: Ref. 63)

Fig. 4-6   NAVWEPS Report 1488 (Vol. 3, Sec. 8)
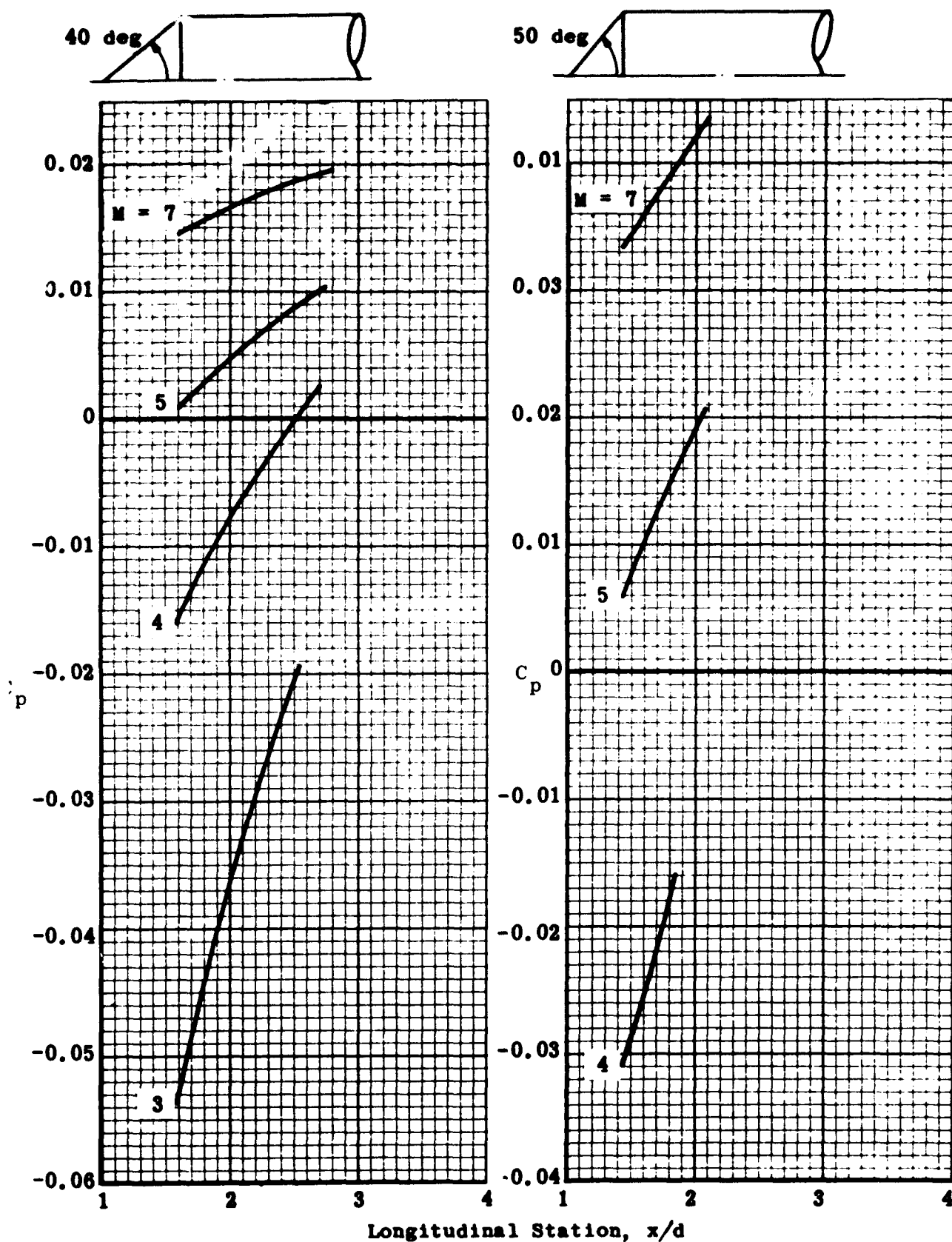
Fig. 4-6. Pressure distribution along the afterbody of a cone
cylinder for various Mach numbers; θ = 40 and 50 deg.
(Source: Ref. 63)
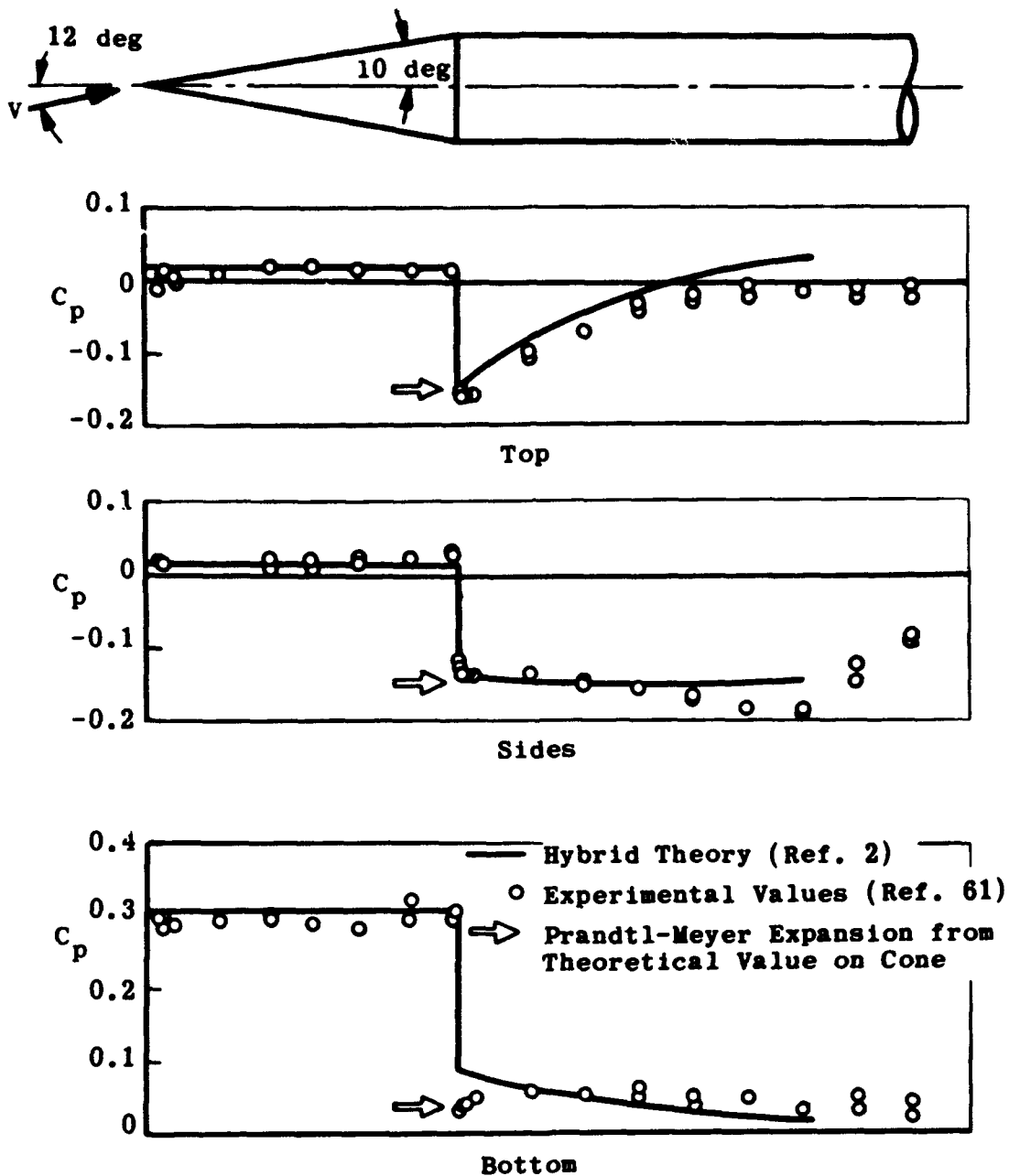
Fig. 4-7. Comparison of hybrid theory and experiment for a 10-deg cone cylinder; M = 2, α = 12 deg. (Source: Ref. 2)

Fig. 4-8   NAVWEPS Report 1488 (Vol. 3, Sec. 8)
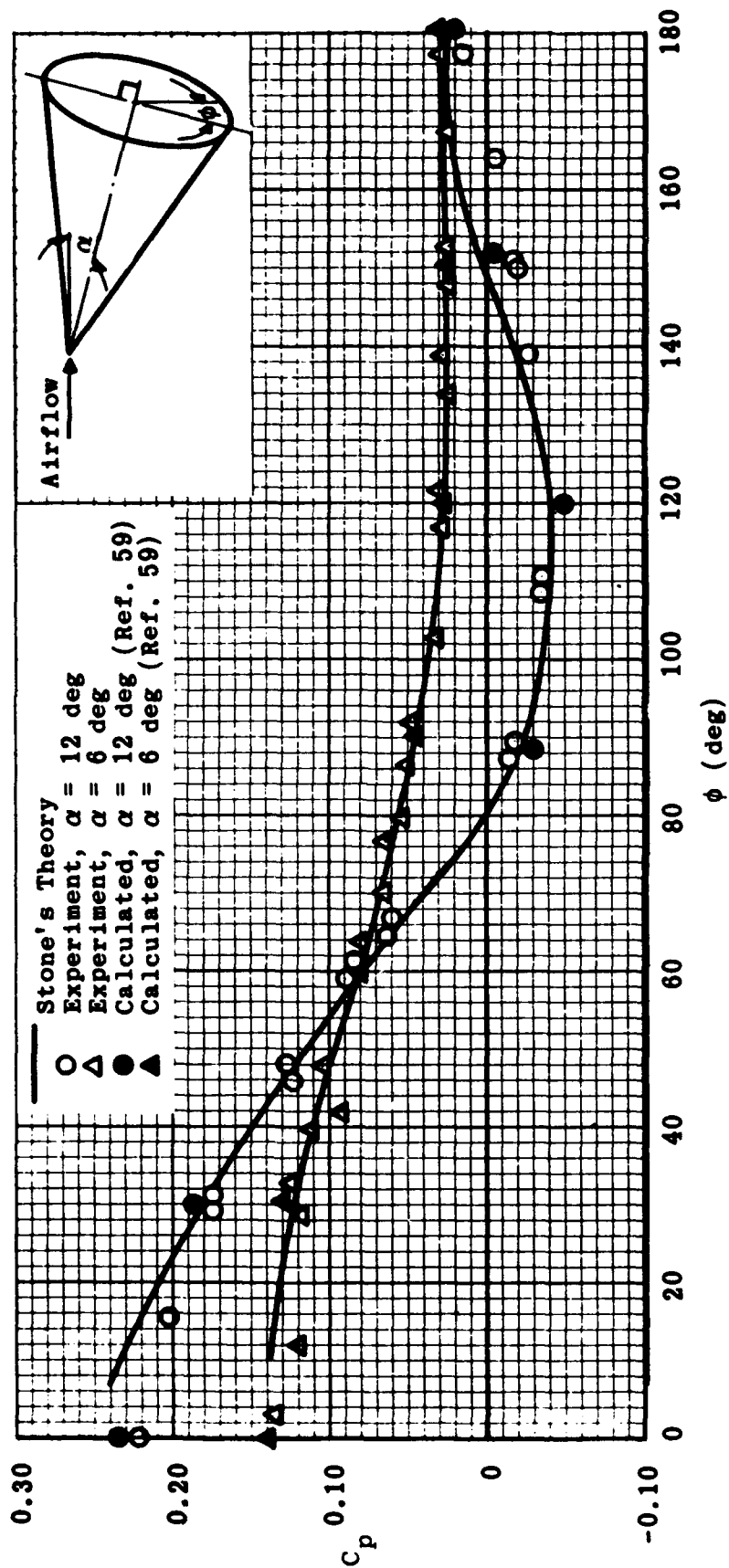
Fig. 4-8. Comparison of pressure distributions obtained by theory and experiment for cones at angle of attack; M = 1.6. (Source: Ref. 60)
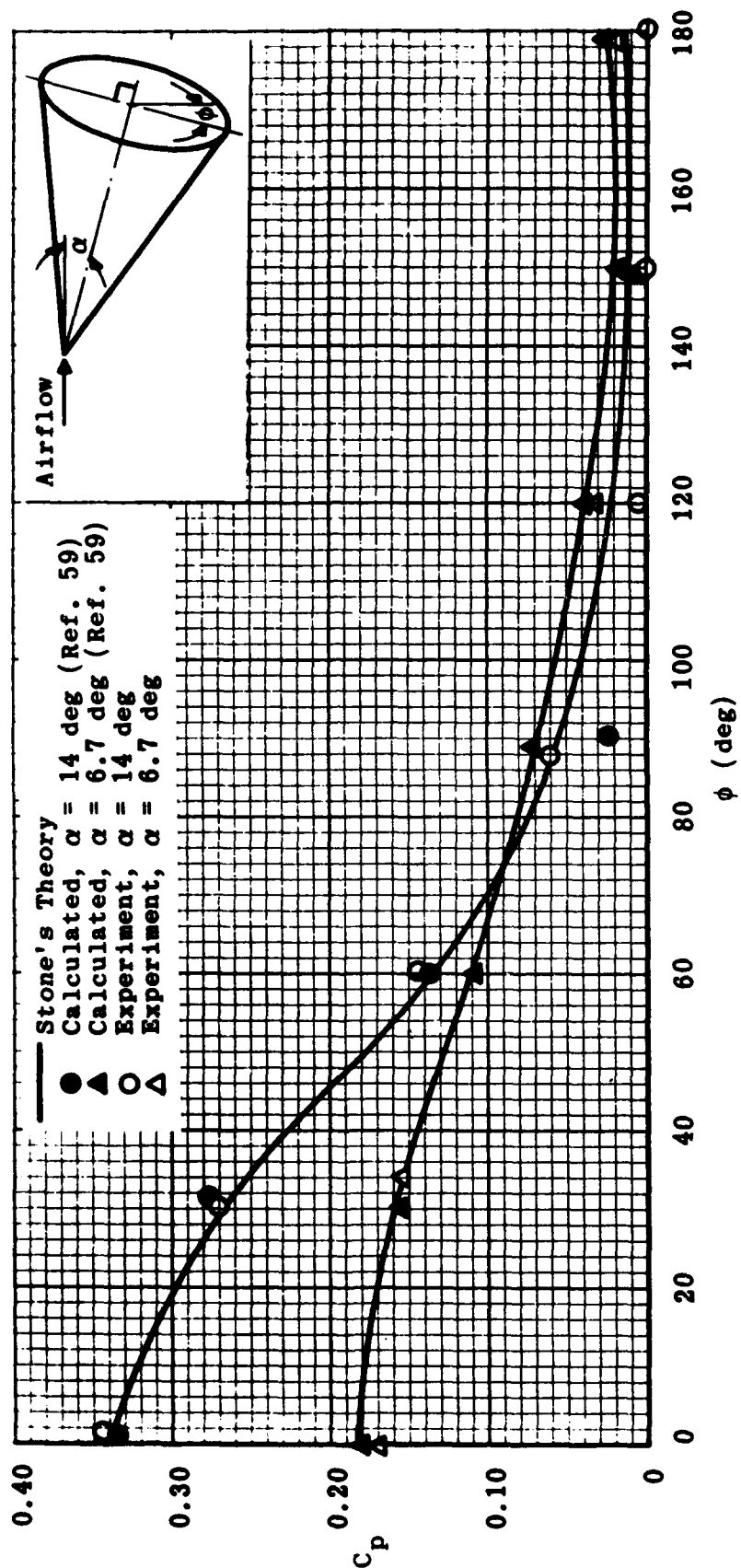
Fig. 4-9. Comparison of pressure distributions obtained by theory and experiment for cones at angle of attack; M = 6.86. (Source: Ref. 60)

Fig. 4-10   NAVWEPS Report 1488 (Vol. 3, Sec. 8)
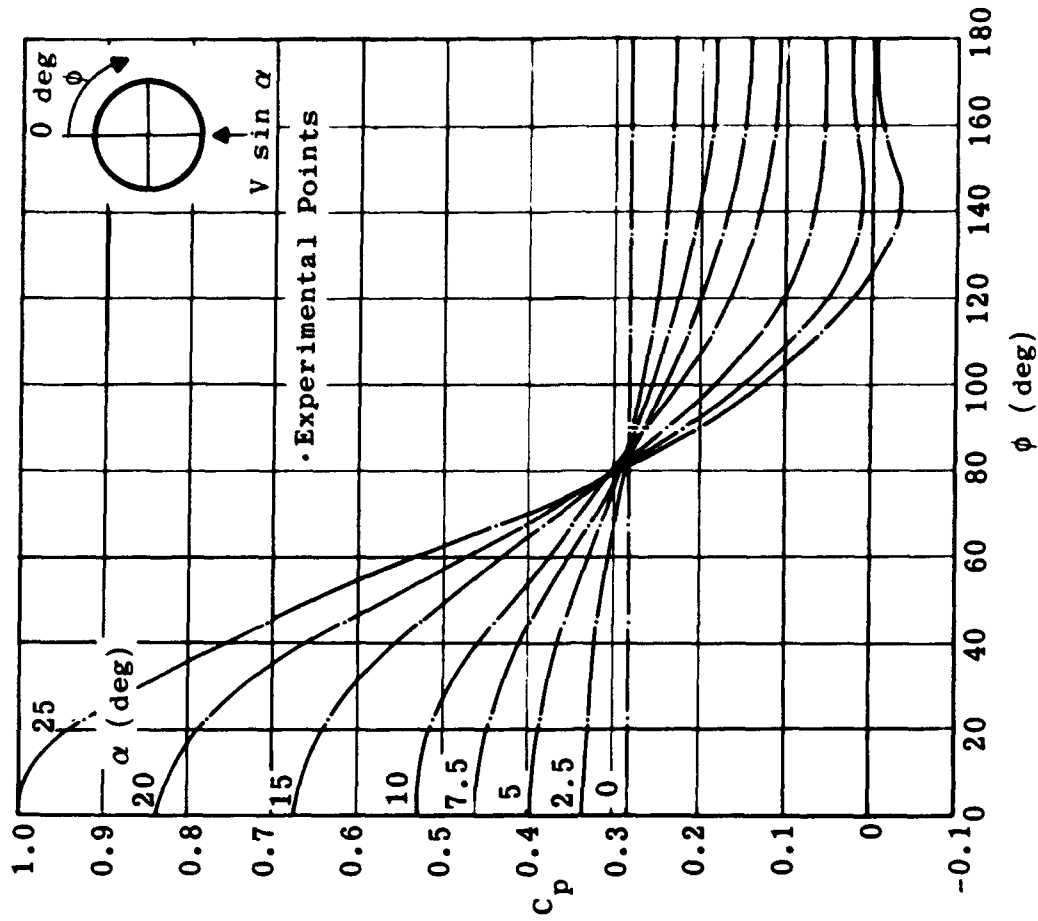
Fig. 4-11. Experimental pressure distribution on a 20-deg cone at angle of attack; M = 3.53. (Source: Ref. 67)
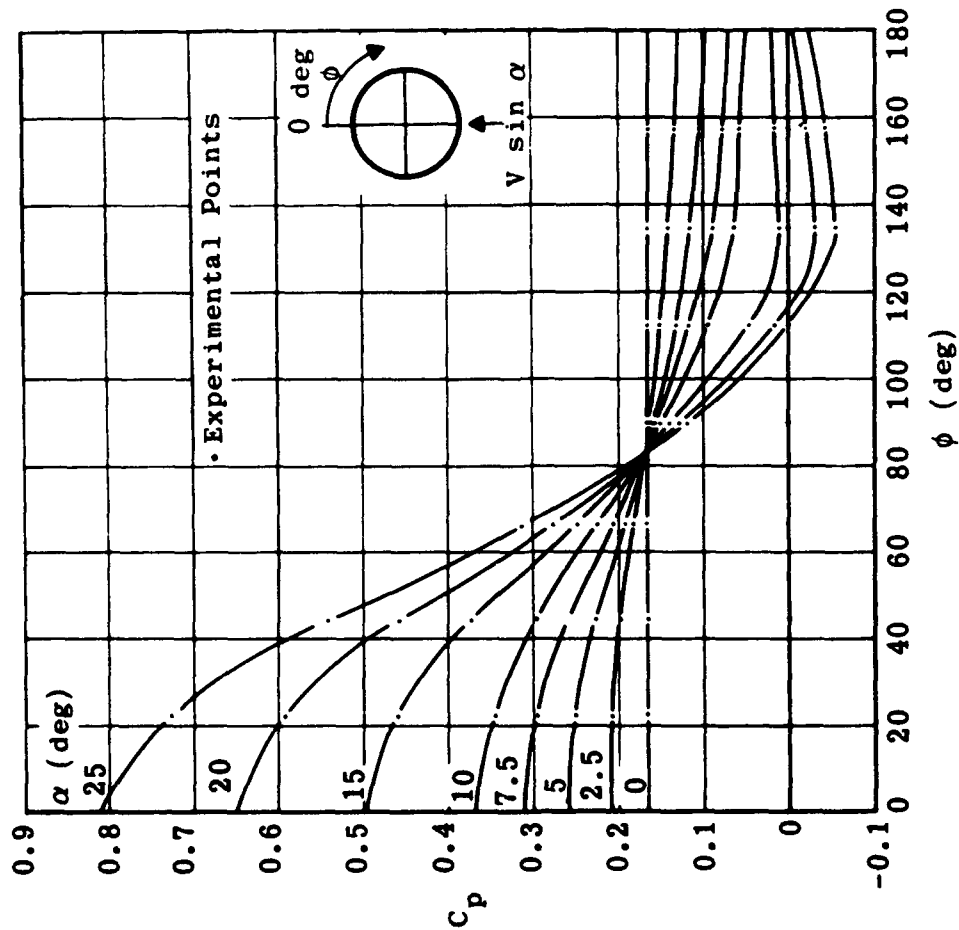
Fig. 4-10. Experimental pressure distribution on a 15-deg cone at angle of attack; M = 3.53. (Source: Ref. 67)
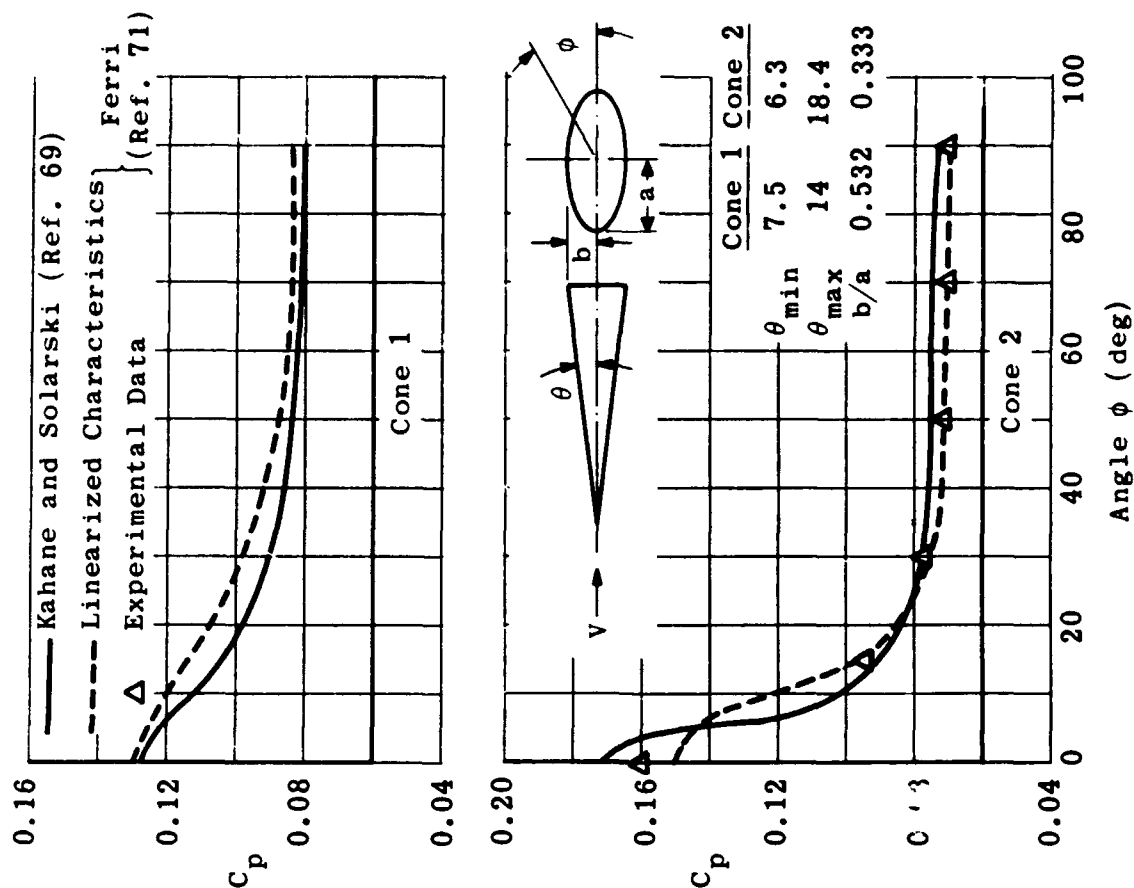
Fig. 4-13. Comparison of calculated and experimental pressure distributions for elliptical cones; $M = 1.81, \alpha = 0$ deg. (Source: Ref. 69)
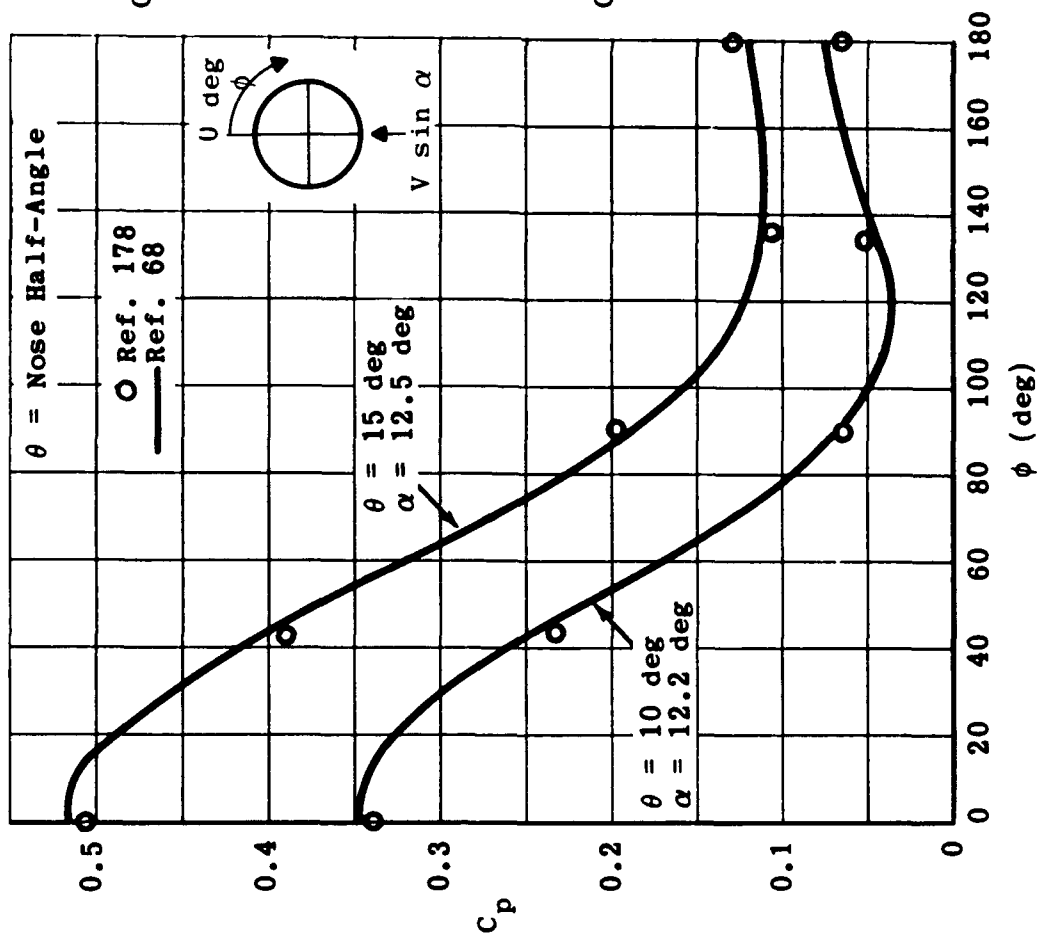
Fig. 4-12. Comparison of theoretical and experimental pressure coefficients on 10 and 15-deg cones at angle of attack; $M = 2$. (Source: Ref. 68)

Fig. 4-14   NAVWEPS Report 1488 (Vol. 3, Sec. 8)

Fig. 4-15. Variation of pressure coefficient around elliptic cones of varying eccentricity; M = ν = 0 deg. (Source: Ref

Fig. 4-14. Comparison of calculated pressure distributions for elliptical cones at various Mach numbers; α = 0 deg. (Source: Ref. 70)

Fig. 4-16. Variation of pressure coefficient around elliptical
cones of varying eccentricity; M = 2.78, α = 6 deg.
(Source: Ref. 70)

Fig. 4-17   NAVWEPS Report 1488 (Vol. 3, Sec. 8)
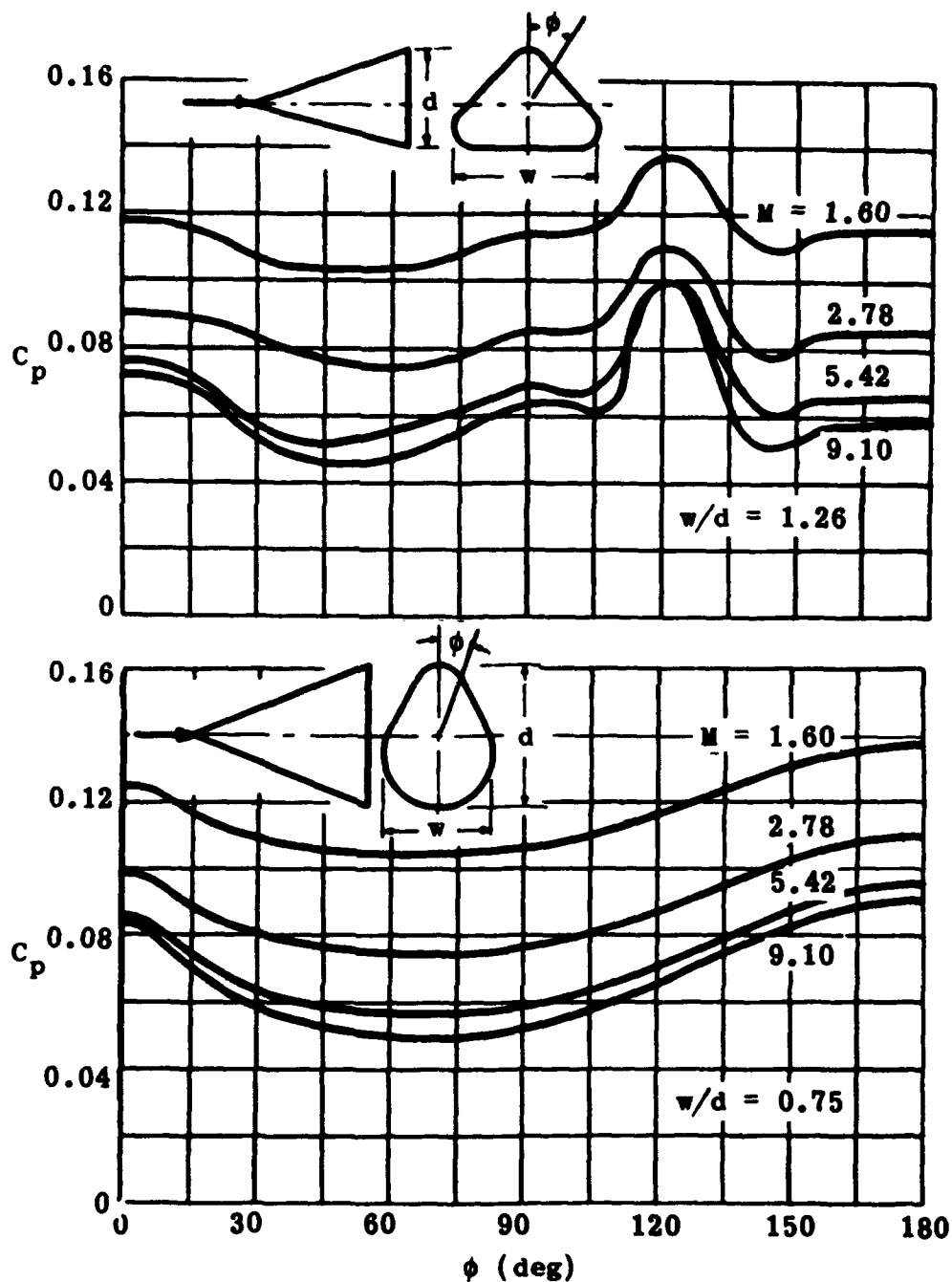
Fig. 4-17. Variation of pressure coefficient around triangular
   and drop-shaped cones at varying Mach numbers; α = 0 deg.
   (Source: Ref. 70)
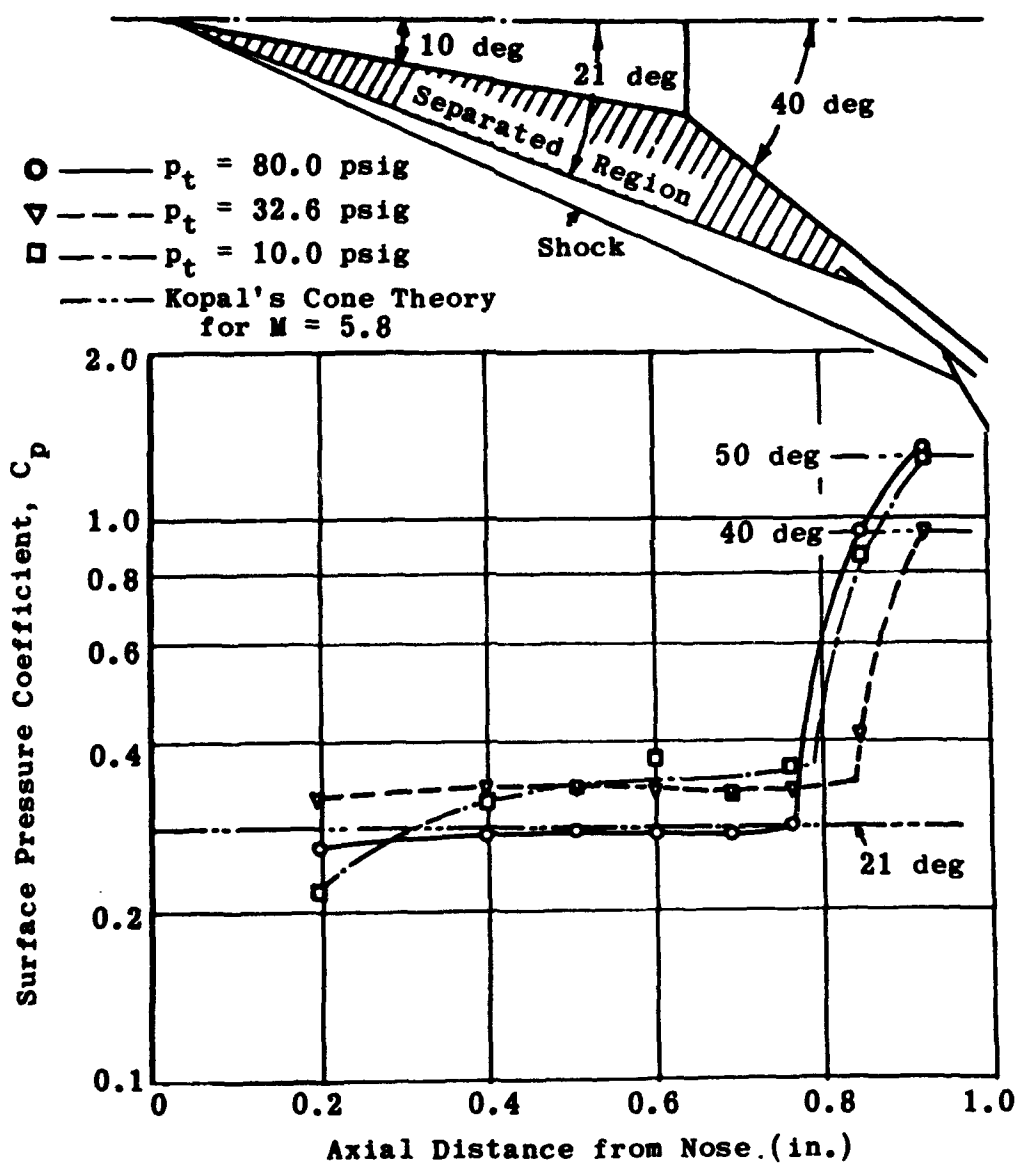
Fig. 4-18. Pressure distribution on a double cone with varying
            stagnation pressure; M = 5.8. (Source: Ref. 88)

Fig. 4-19   NAVWEPS Report 1488 (Vol. 3, Sec. 8)
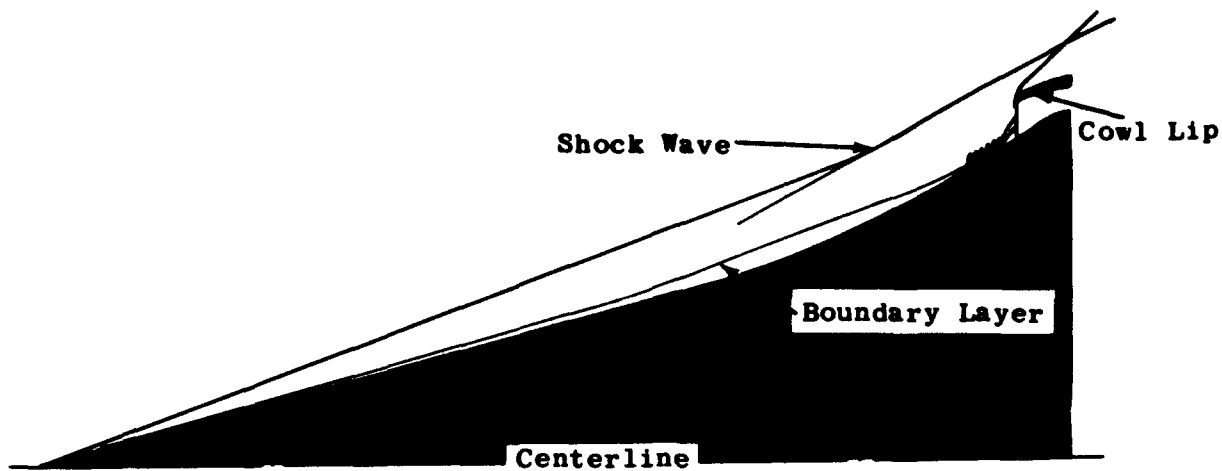
Fig. 4-19.   Isentropic spike in flow at M = 4.8; simulated
altitude = 109,000 ft, Re/ft = 3.2 × 10^5.
(Source: Shadowgraphs from Ref. 72)
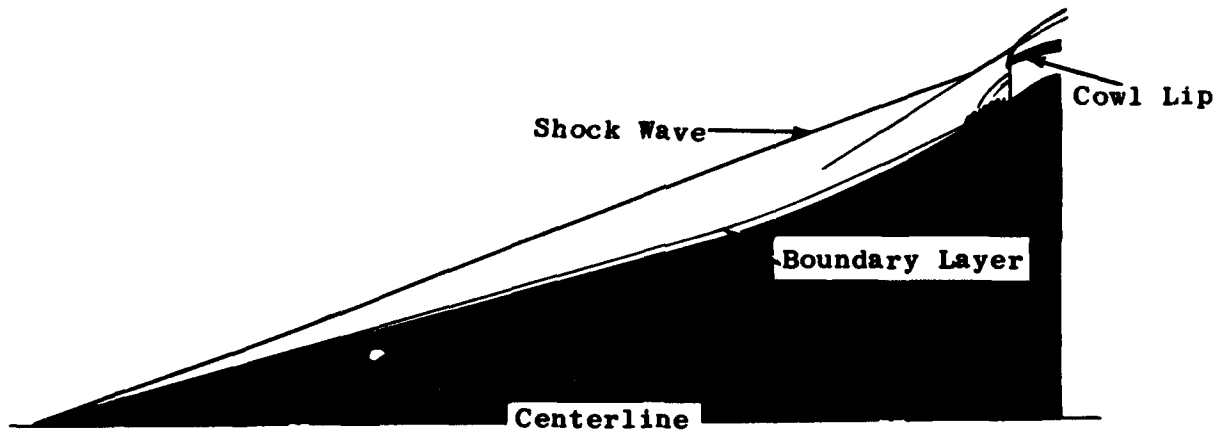
Fig. 4-20.   Isentropic spike in flow at M = 4.8; simulated
altitude = 95,000 ft, Re/ft = 6.7 × 10^5.
(Source: Shadowgraphs from Ref. 72)
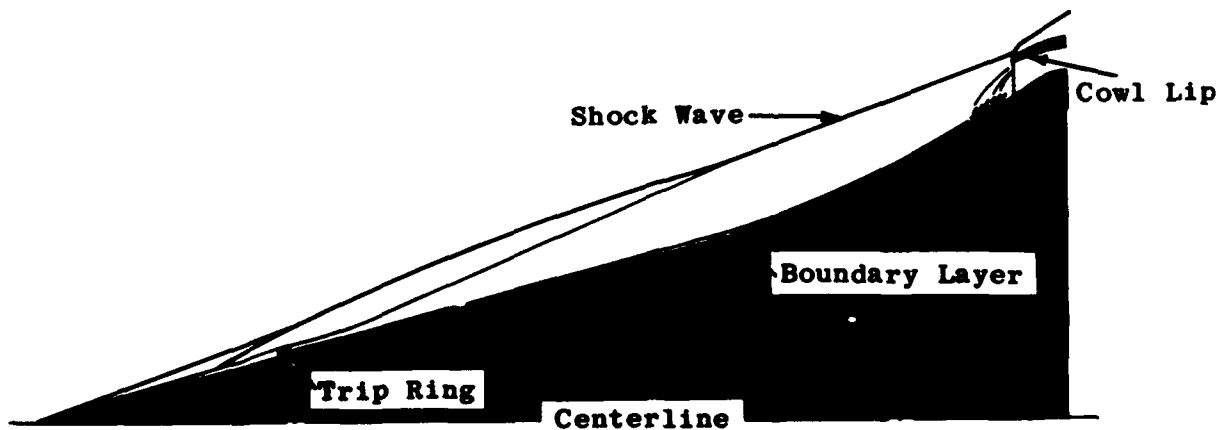
Fig. 4-21.   Isentropic spike in flow at M = 4.8 with trip ring
added; simulated altitude = 91,000 ft, Re/ft = 7.8 × 10^5.
(Source: Shadowgraph from Ref. 72)
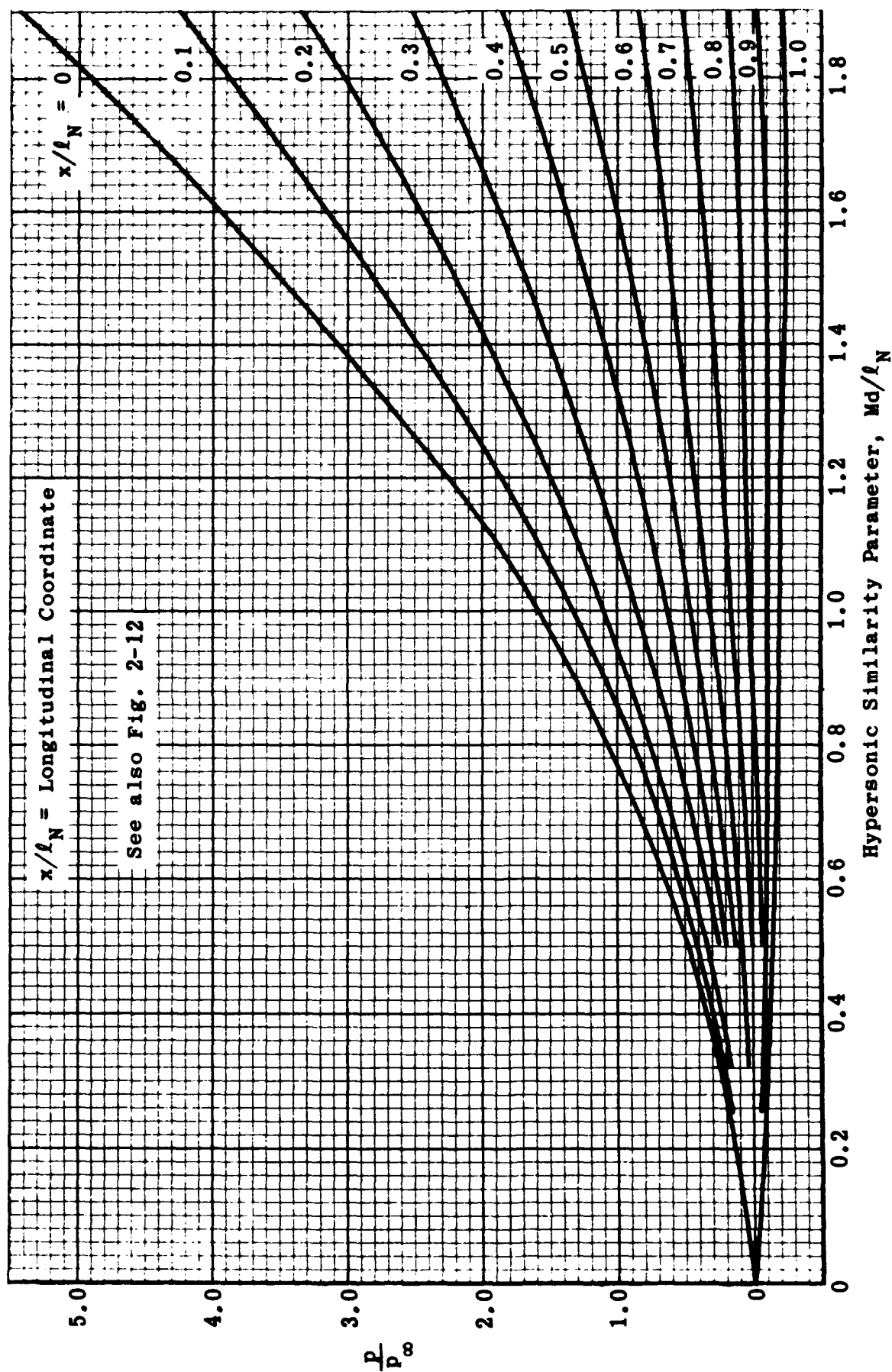
Fig. 4-22.   Pressure ratio for tangent ogives as a function of the hypersonic
             similarity parameter. (Source: Ref. 30)

Fig. 4-23   NAVWEPS Report 1488 (Vol. 3, Sec. 8)
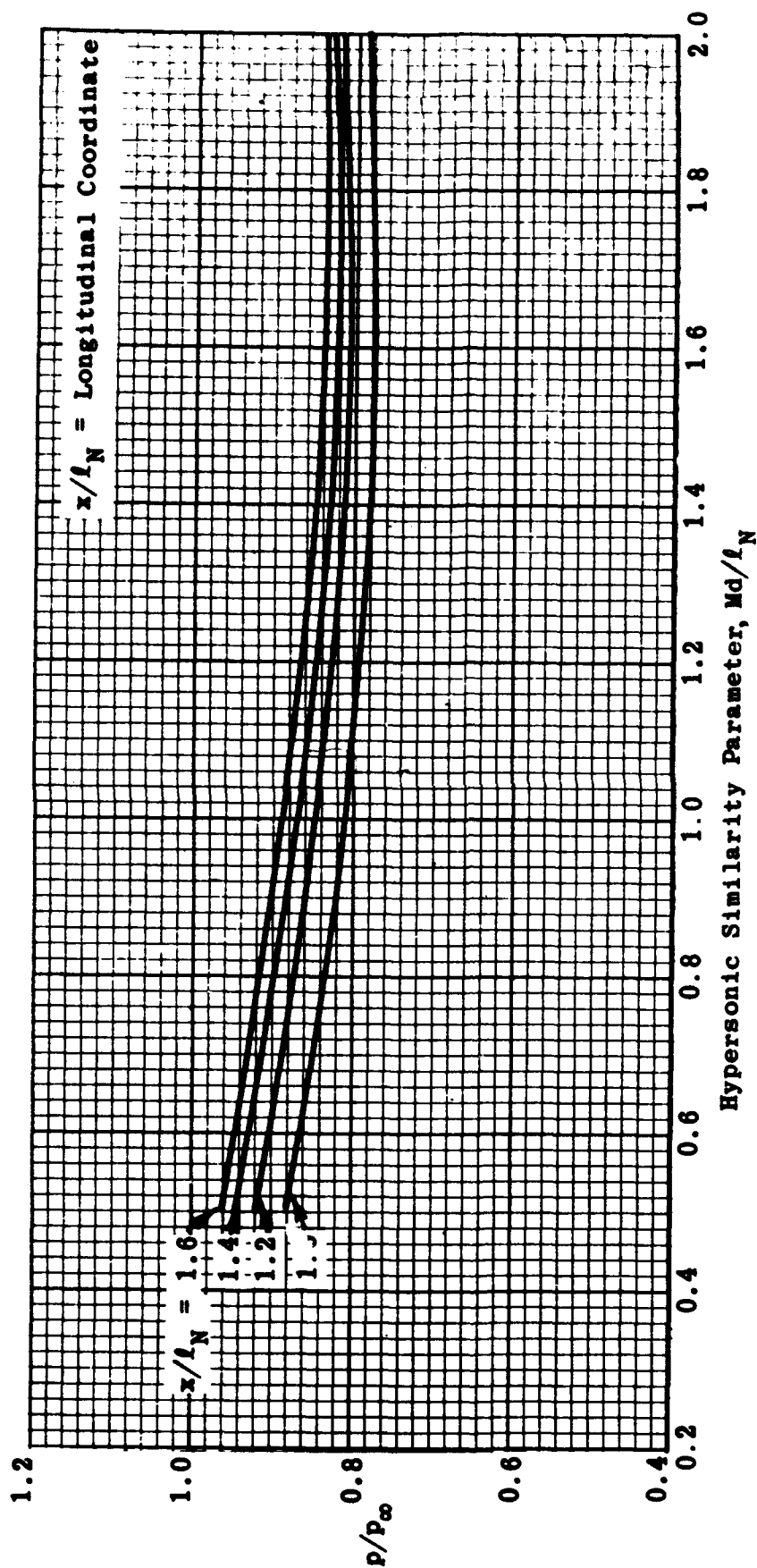
Fig. 4-23. Pressure ratio for afterbodies of tangent-ogive cylinders as a function of the hypersonic similarity parameter. (Source: Ref. 30)
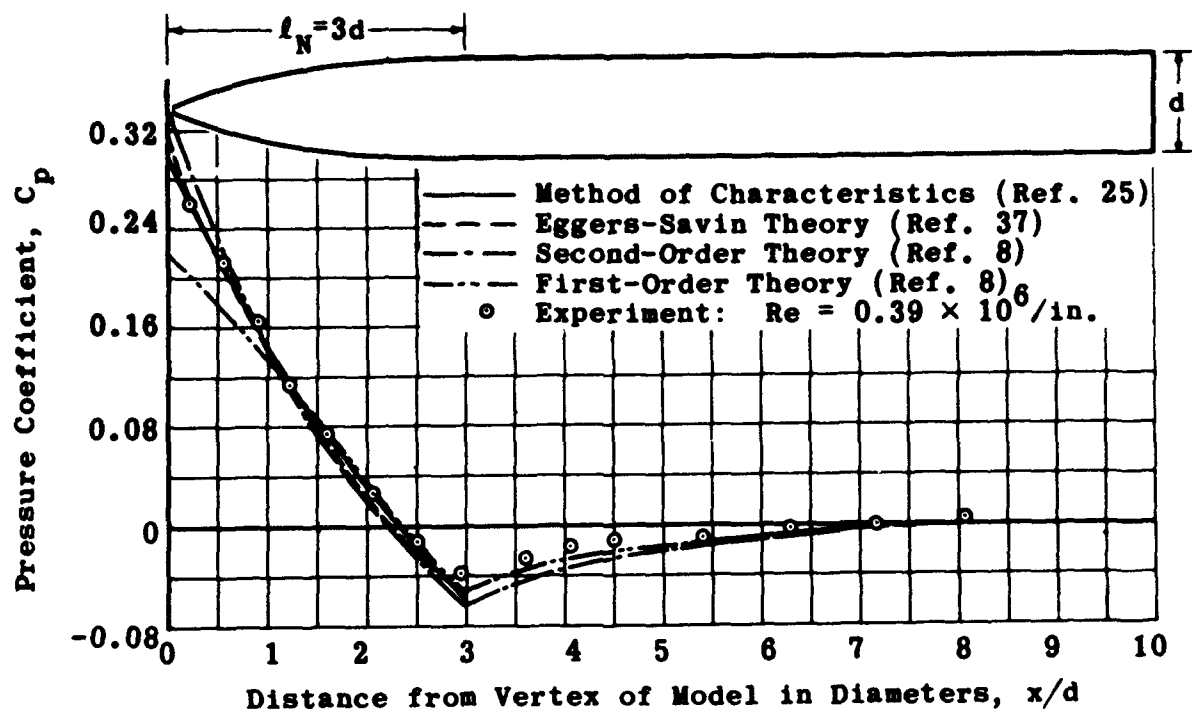
Fig. 4-24. Comparison of theoretical and experimental pressure
distribution on a tangent-ogive cylinder at zero angle of
attack; M = 2. (Source: Ref. 52)
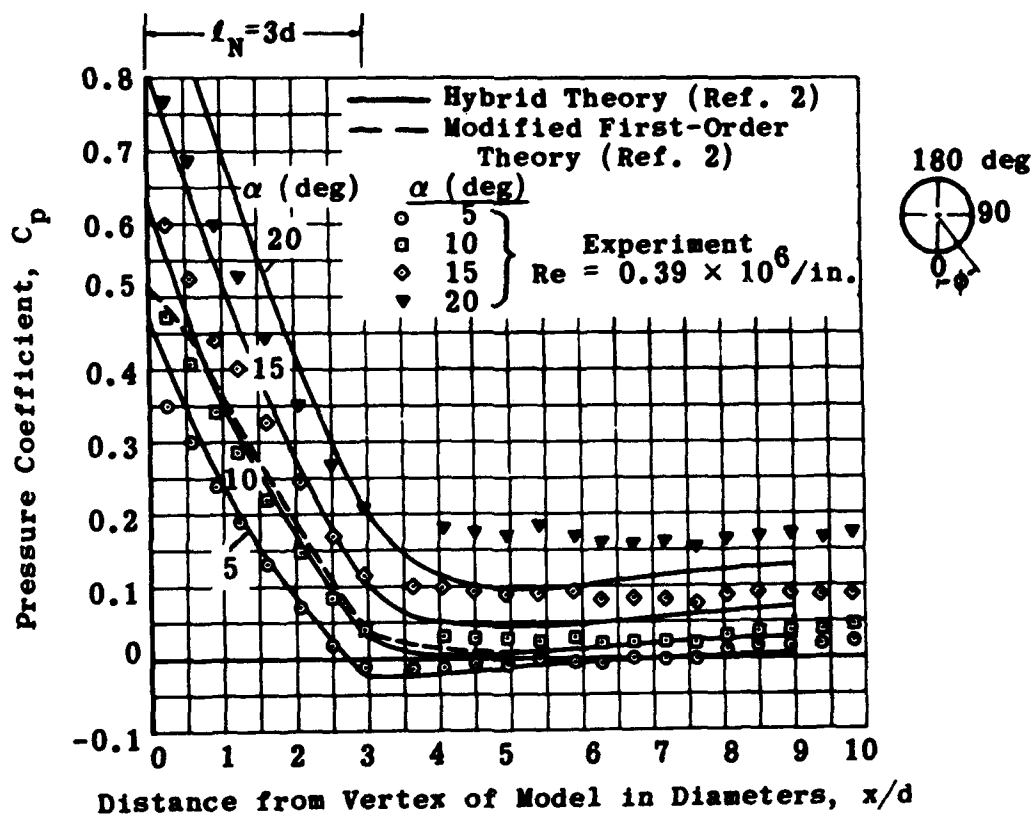
Fig. 4-25. Comparison of theoretical and experimental pressure
distribution on a tangent-ogive cylinder at various angles
of attack; M = 2, ϕ = 0 deg. (Source: Ref. 52)

Fig. 4-26   NAVWEPS Report 1488 (Vol. 3, Sec. 8)

Fig. 4-27. Comparison of theoretical and experimental pressure distribution on a tangent-ogive cylinder at various angles of attack; M = 2, φ = 60 deg. (Source: Ref. 52)
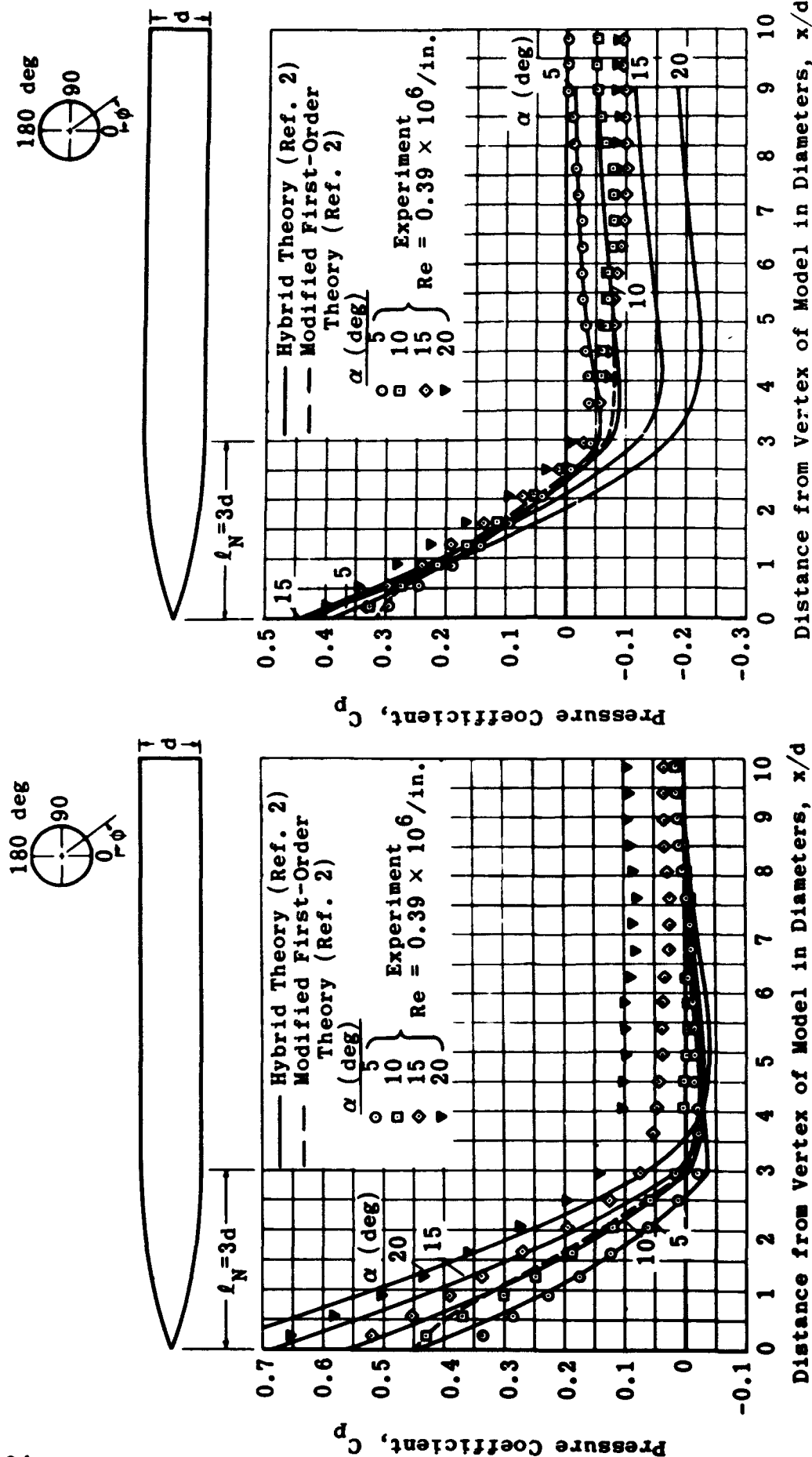
Fig. 4-26. Comparison of theoretical and experimental pressure distribution on a tangent-ogive cylinder at various angles of attack; M = 2, φ = 30 deg. (Source: Ref. 52)
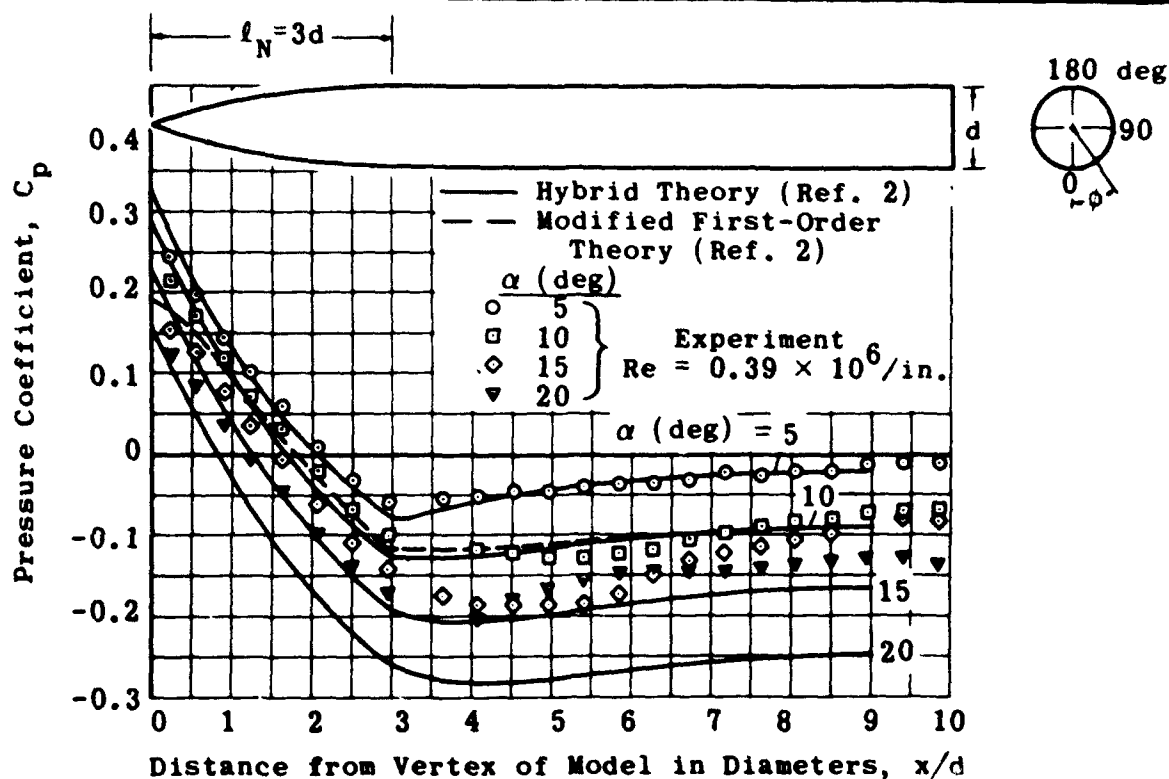
Fig. 4-28. Comparison of theoretical and experimental pressure distribution on a tangent-ogive cylinder at various angles of attack; $M = 2$, $\phi = 90$ deg. (Source: Ref. 52)
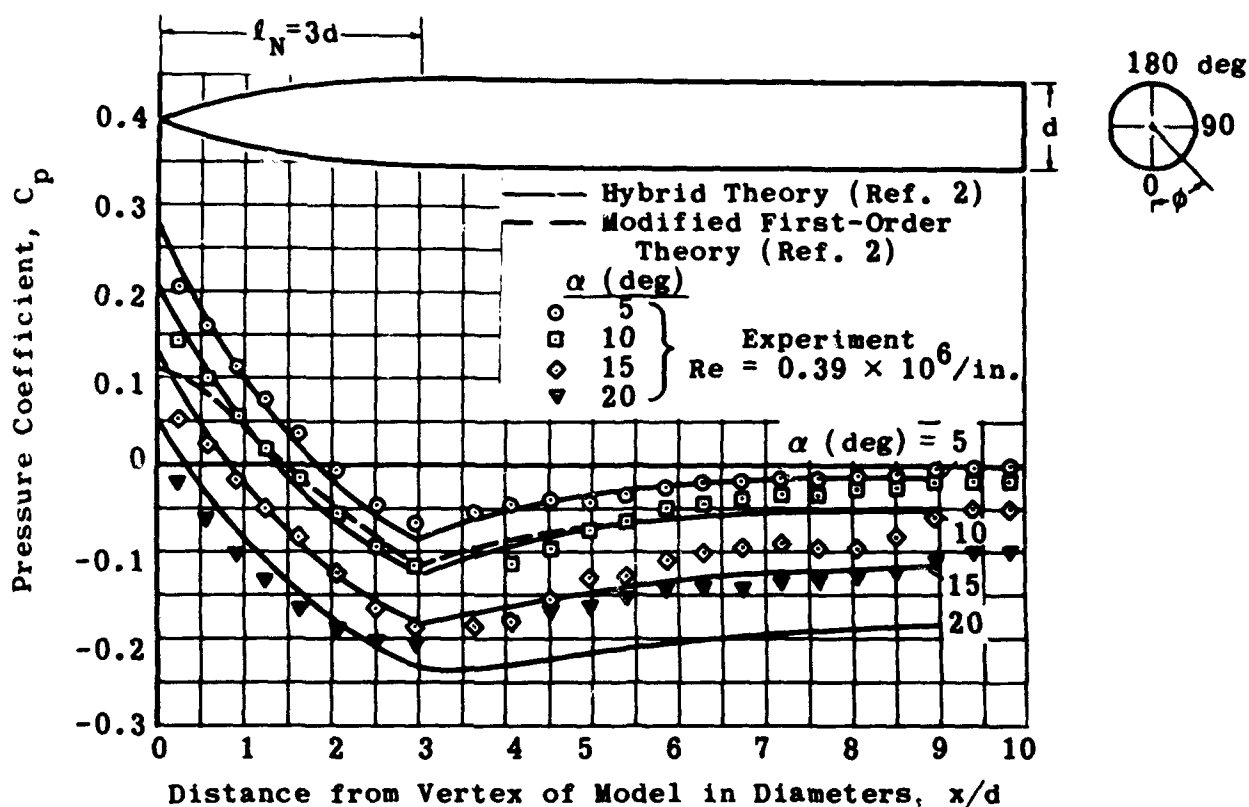
Fig. 4-29. Comparison of theoretical and experimental pressure distribution on a tangent-ogive cylinder at various angles of attack; $M = 2$, $\phi = 120$ deg. (Source: Ref. 52)

Fig. 4-30   NAVWEPS Report 1488 (Vol. 3, Sec. 8)
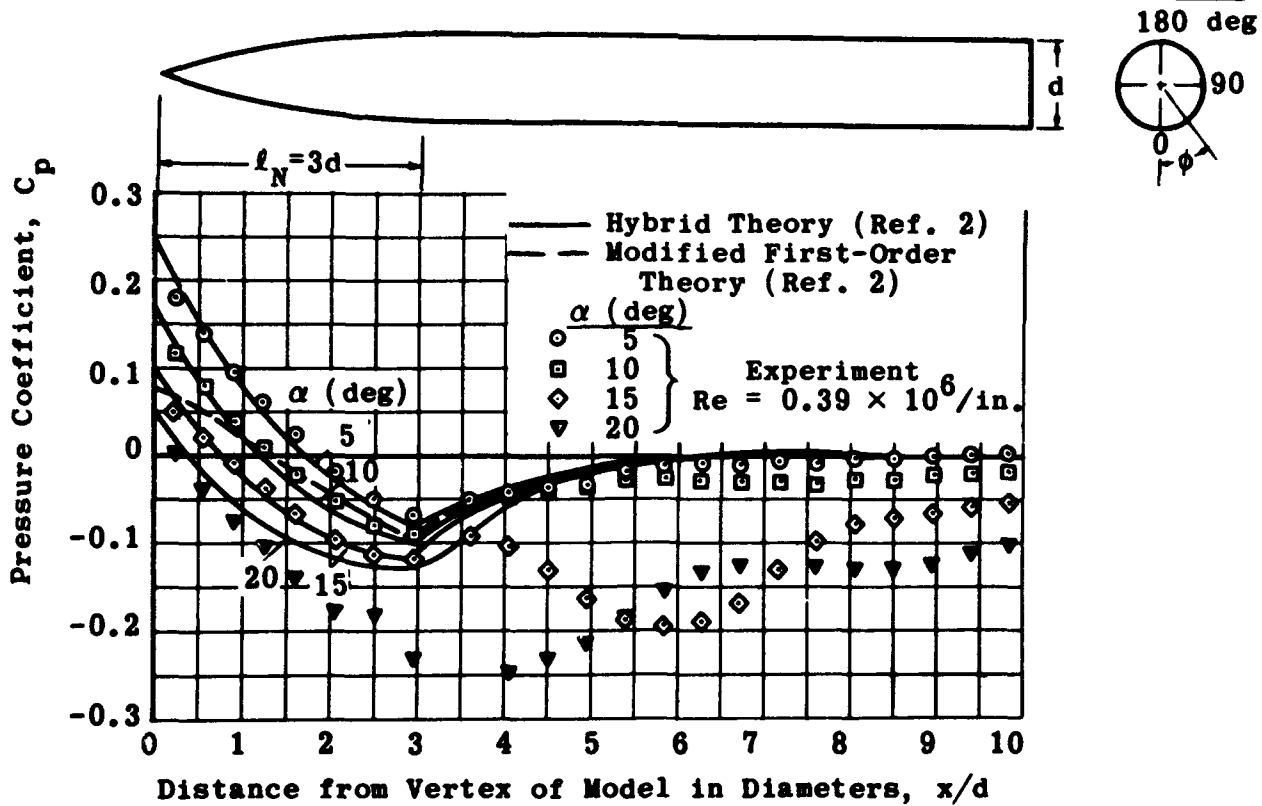
Fig. 4-30. Comparison of theoretical and experimental pressure
distribution on a tangent-ogive cylinder at various angles
of attack; M = 2, ϕ = 150 deg. (Source: Ref. 52)
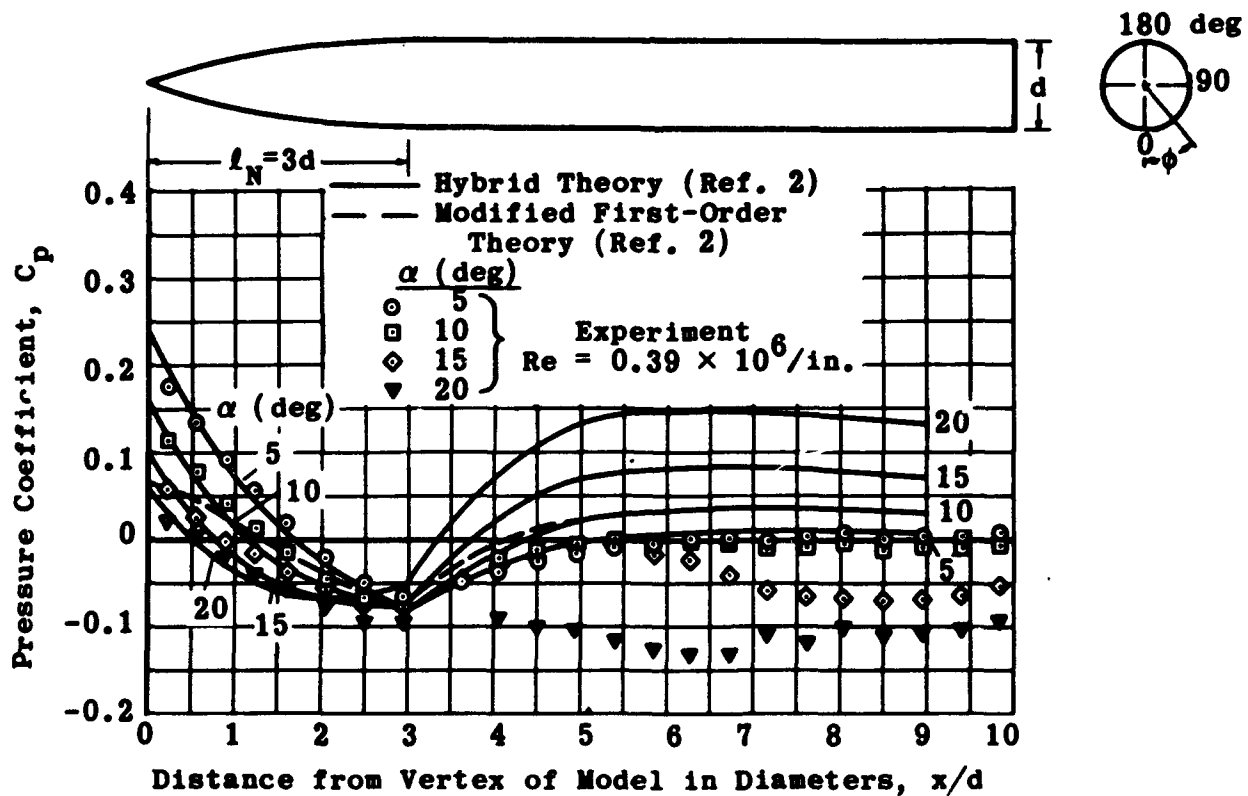
Fig. 4-31. Comparison of theoretical and experimental pressure
distribution on a tangent-ogive cylinder at various ngles
of attack; M = 2, ϕ = 180 deg. (Source: Ref. 52)
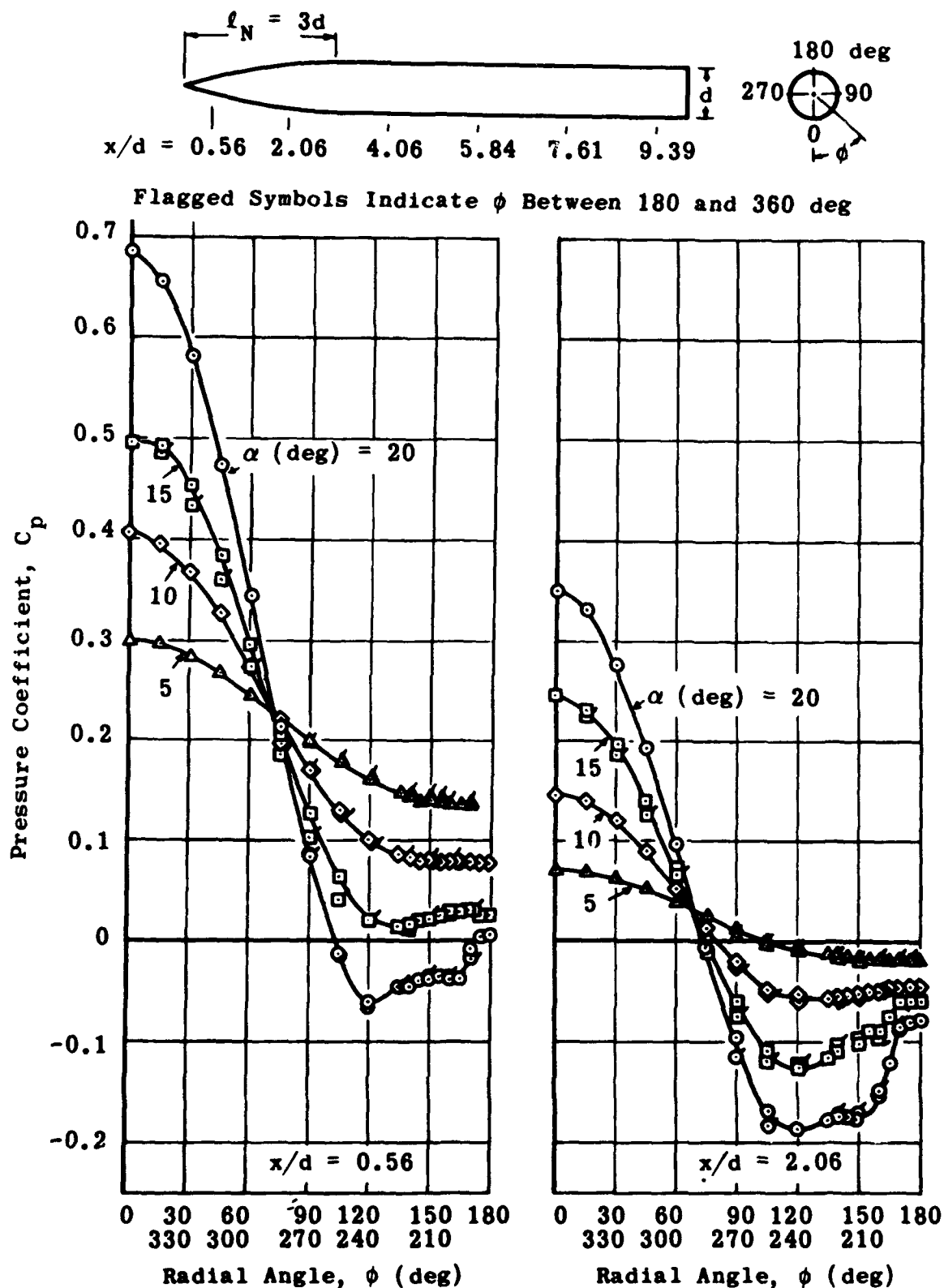
Fig. 4-32. Circumferential pressure distributions on a tangent-ogive cylinder at various angles of attack at x/d = 0.56 and 2.06; M = 2, Re/in. = 0.39 × 10^6. (Source: Ref. 52)

Fig. 4-33   NAVWEPS Report 1488 (Vol. 3, Sec. 8)
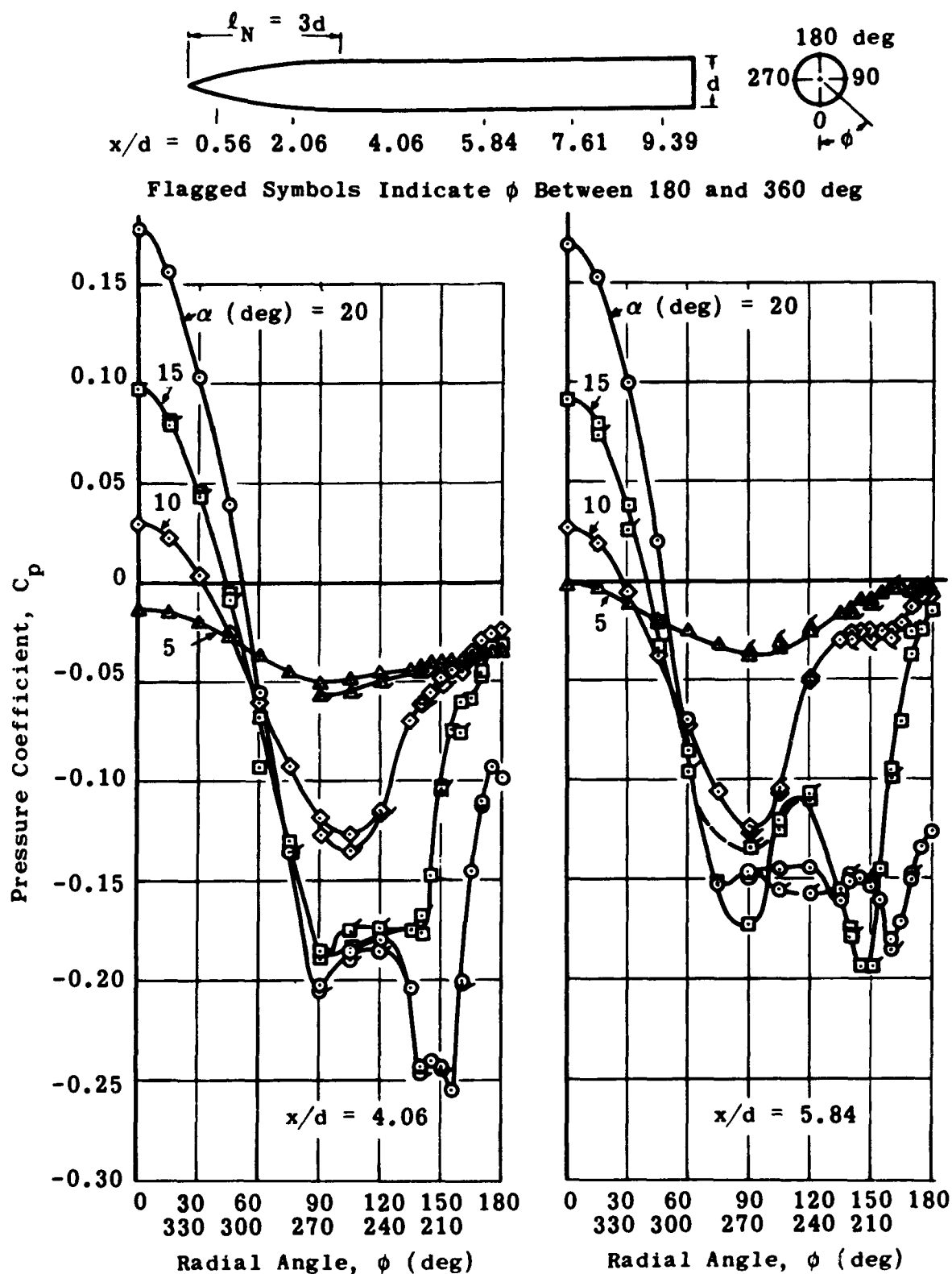
Fig. 4-33. Circumferential pressure distributions on a tangent-ogive cylinder at various angles of attack at x/d = 4.06 and 5.84; M = 2, Re/in. = 0.39 × 10^6. (Source: Ref. 52)
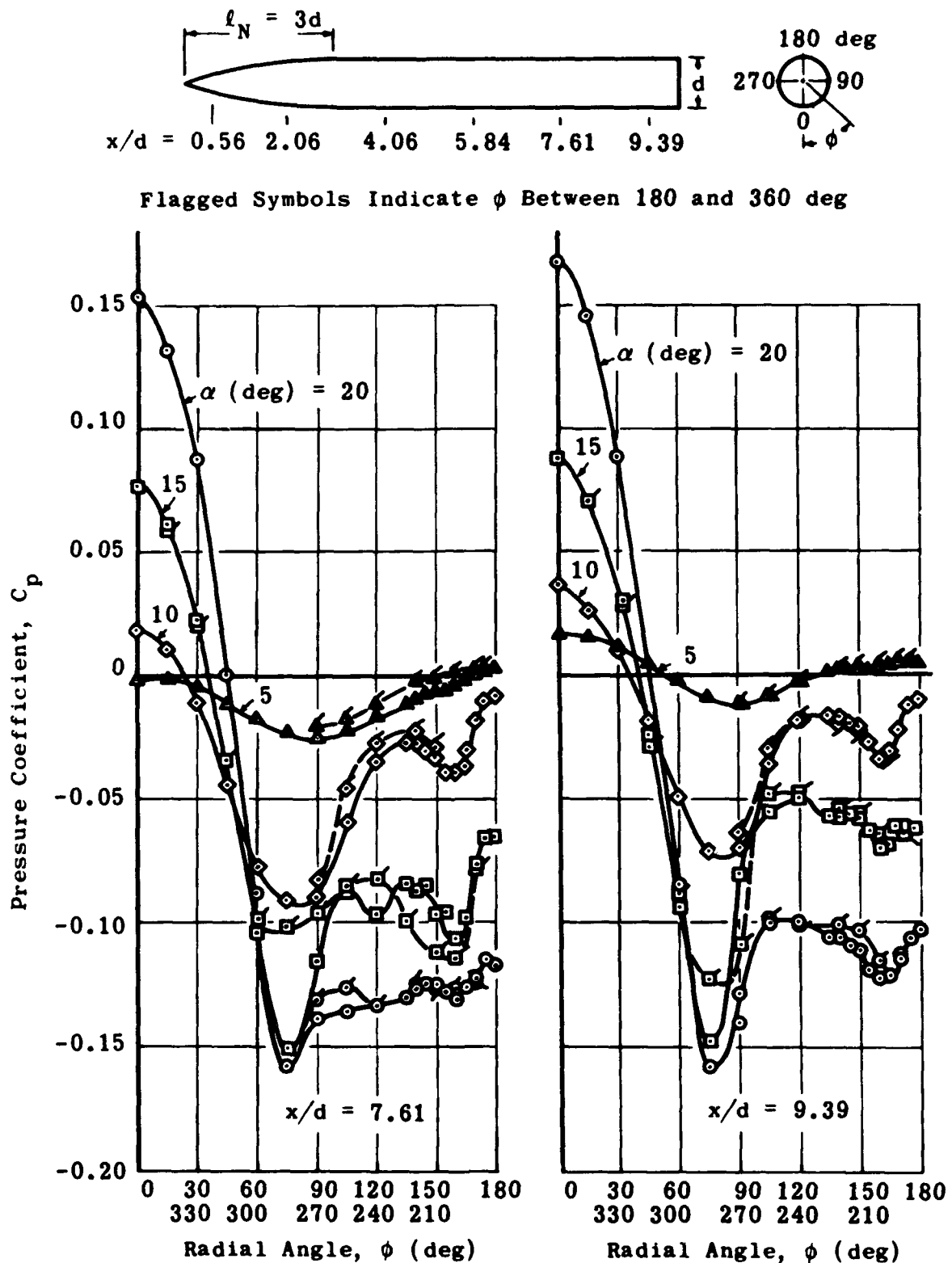
Fig. 4-34. Circumferential pressure distributions on a tangent-
ogive cylinder at various angles of attack at x/d = 7.61
and 9.39; M = 2, Re/in. = 0.39 × 10^6. (Source: Ref. 52)

Fig. 4-35   NAVWEPS Report 1488 (Vol. 3, Sec. 8)
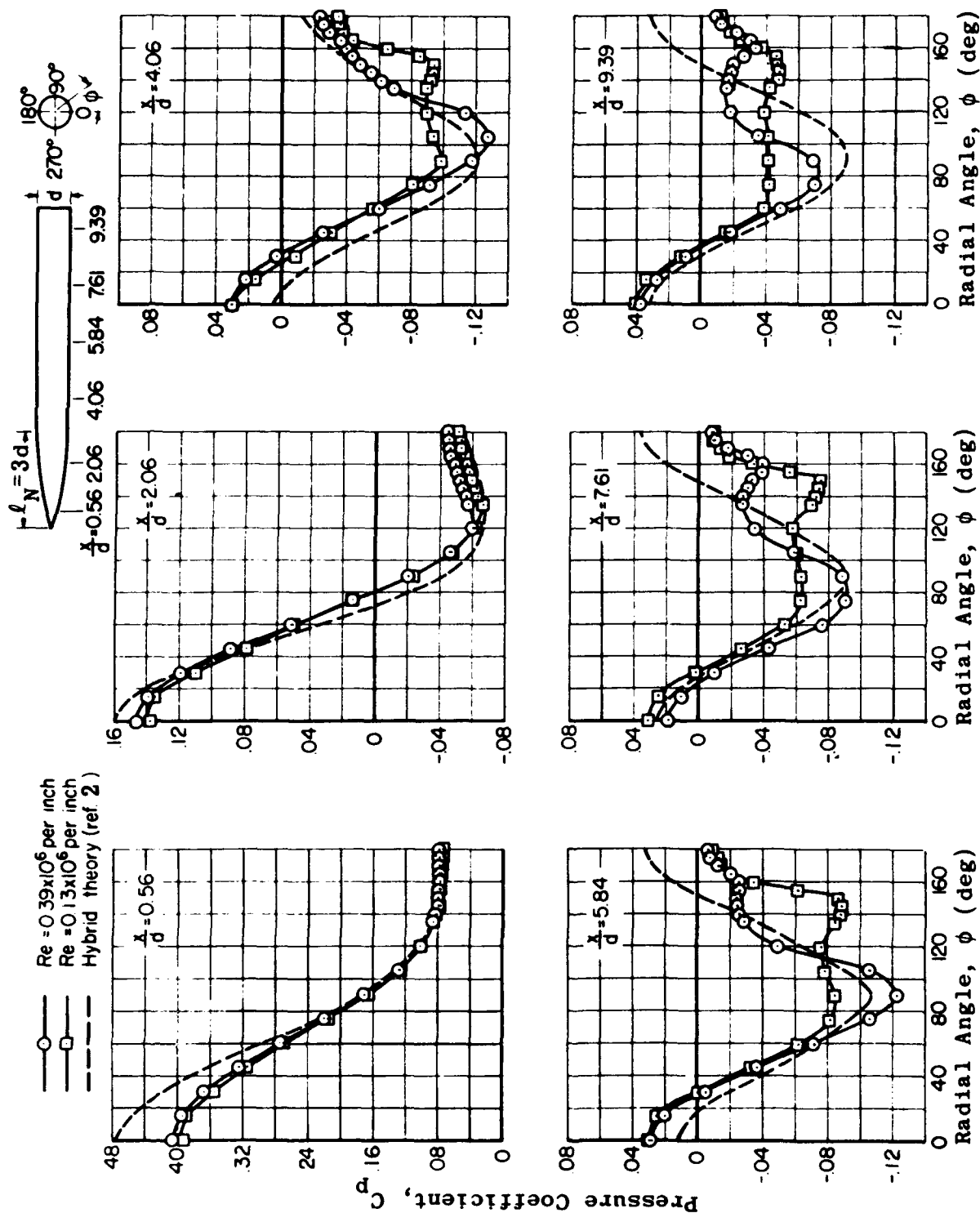
Fig. 4-35. Effect of Reynolds number on the circumferential pressure distribution on a tangent-ogive cylinder at M = 2; α = 10 deg. (Source: Ref. 52)
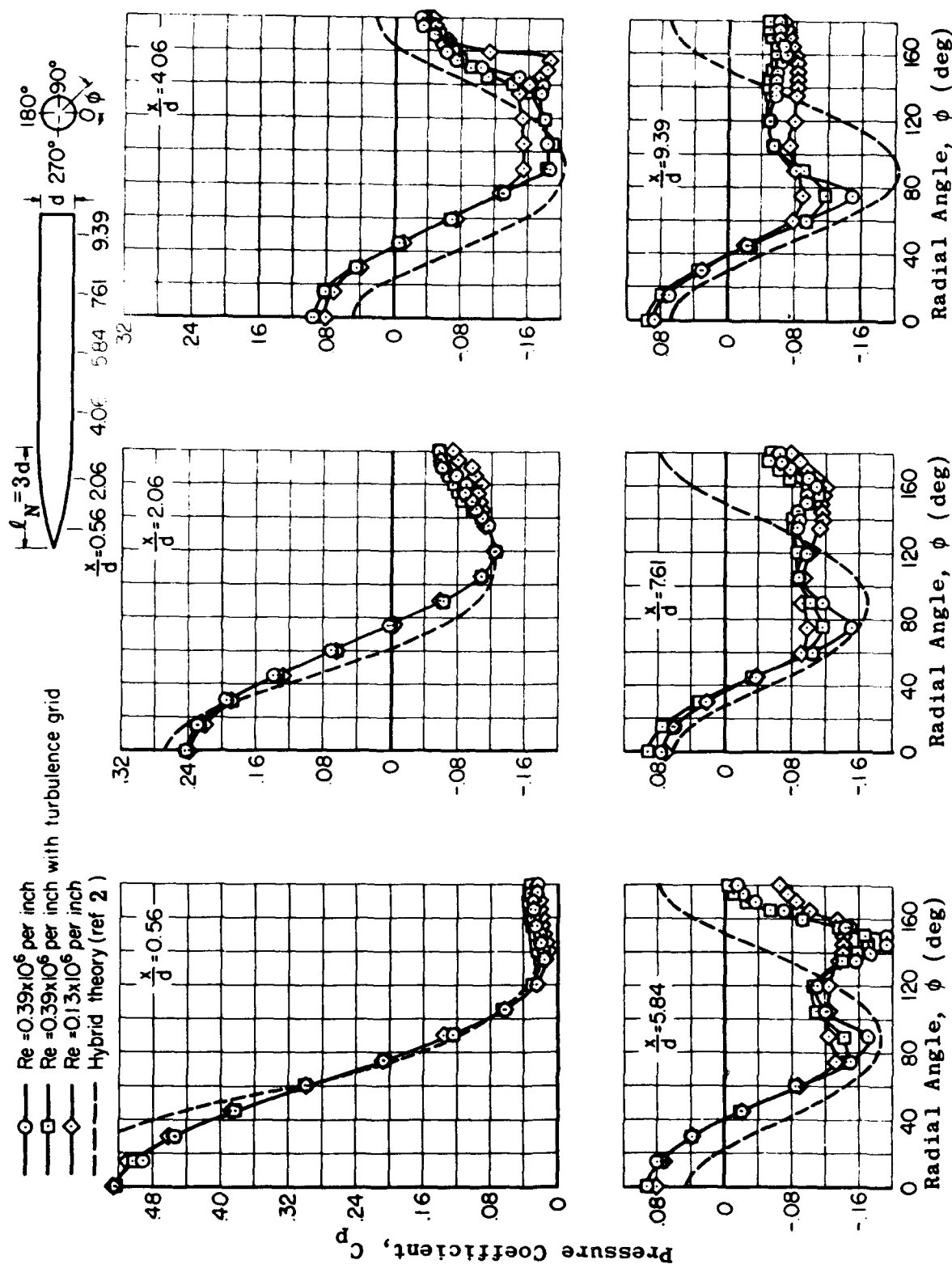
Fig. 4-36. Effect of Reynolds number on the circumferential pressure distribution on a tangent-ogive cylinder at M = 2, α = 15 deg. (Source: Ref. 52)

Fig. 4-37   NAVWEPS Report 1488 (Vol. 3, Sec. 8)
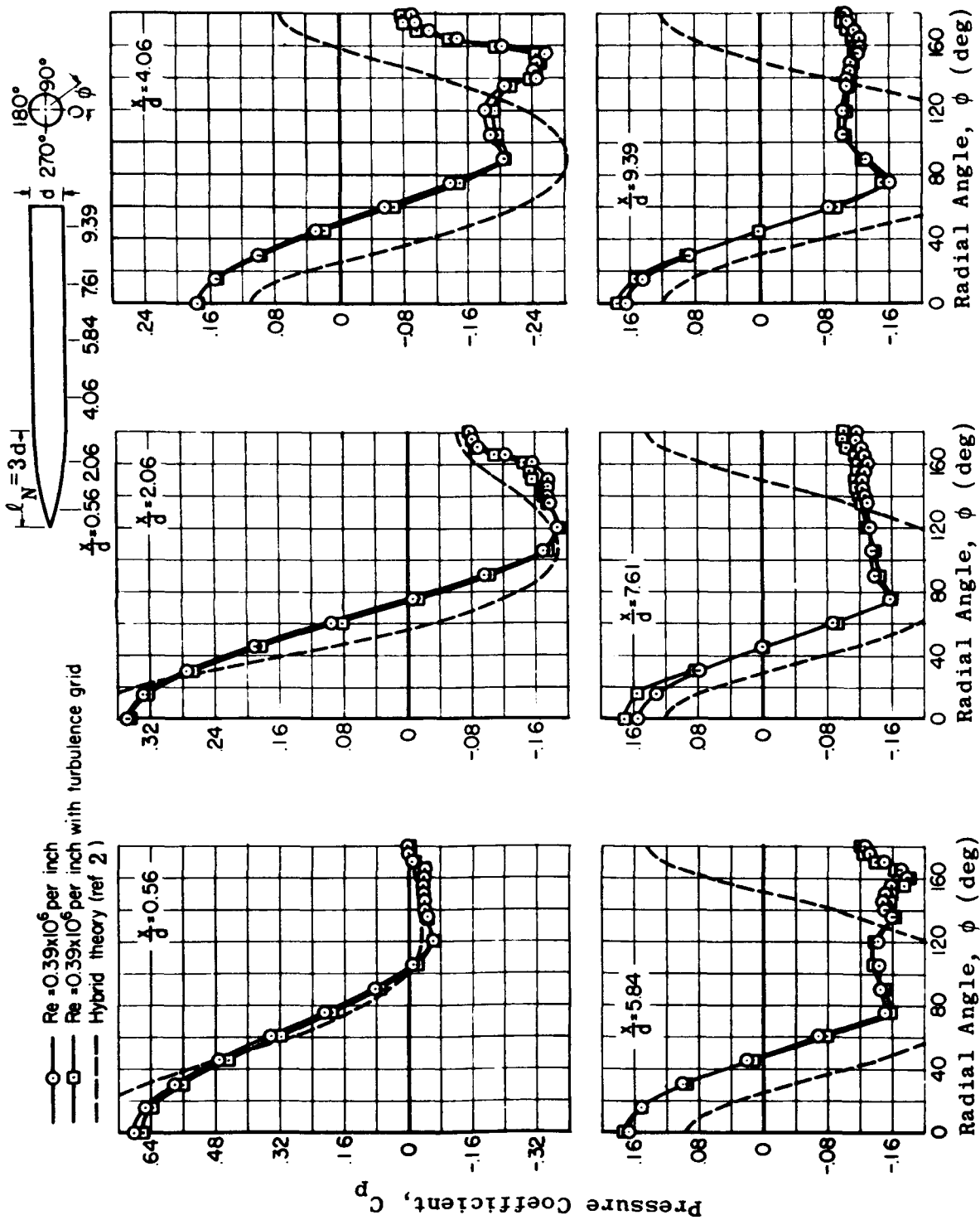
Fig. 4-37.   Effect of Reynolds number on the circumferential pressure distribution on a tangent-ogive cylinder at M = 2, α = 20 deg.   (Source: Ref. 52)
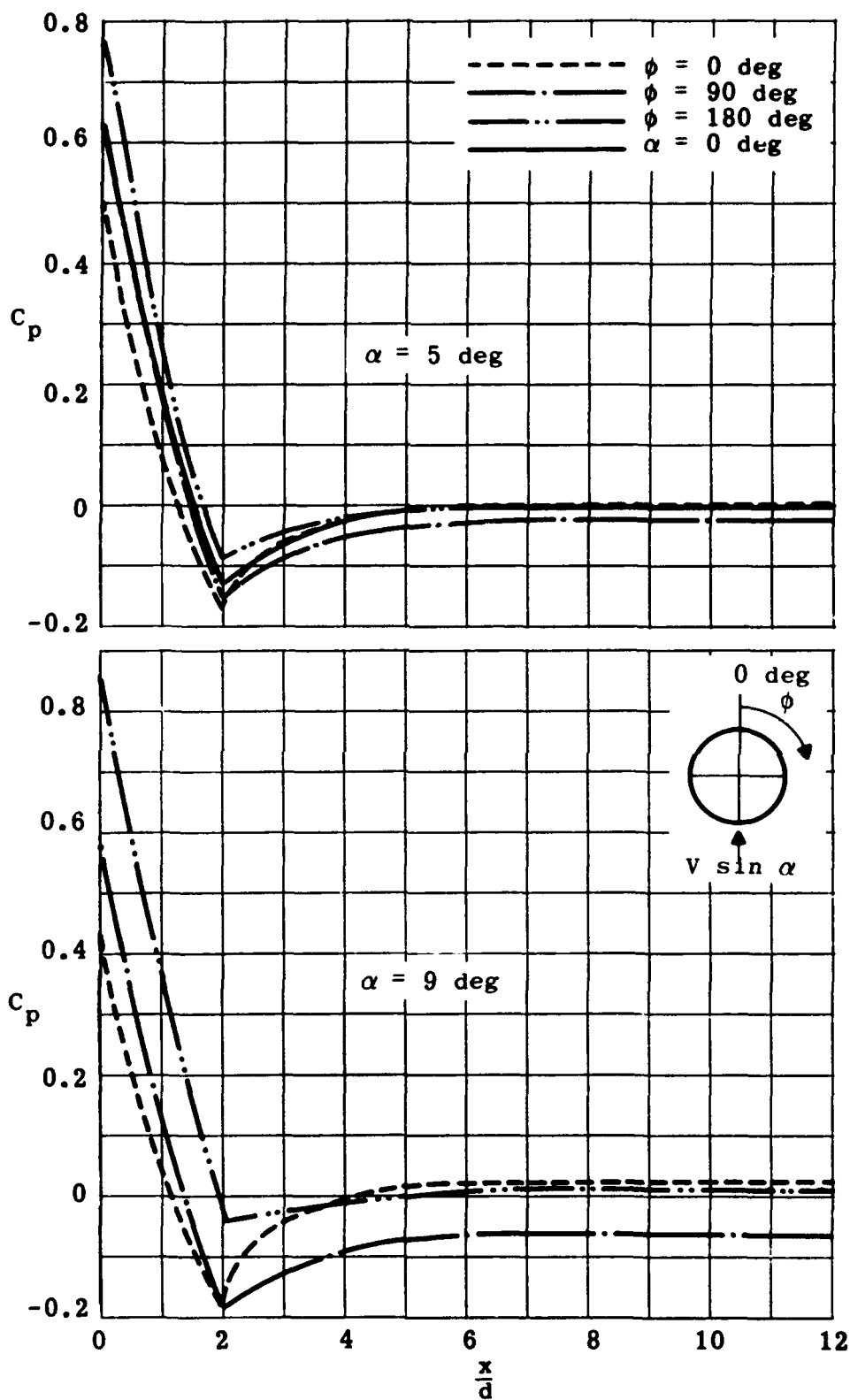
Fig. 4-38. Calculated pressure distributions on tangent-ogive
cylinders at α = 0, 5, and 9 deg; M = 1.5, ℓ_N/d = 2.
(Source: Ref. 73)

Fig. 4-39   NAVWEPS Report 1488 (Vol. 3, Sec. 8)
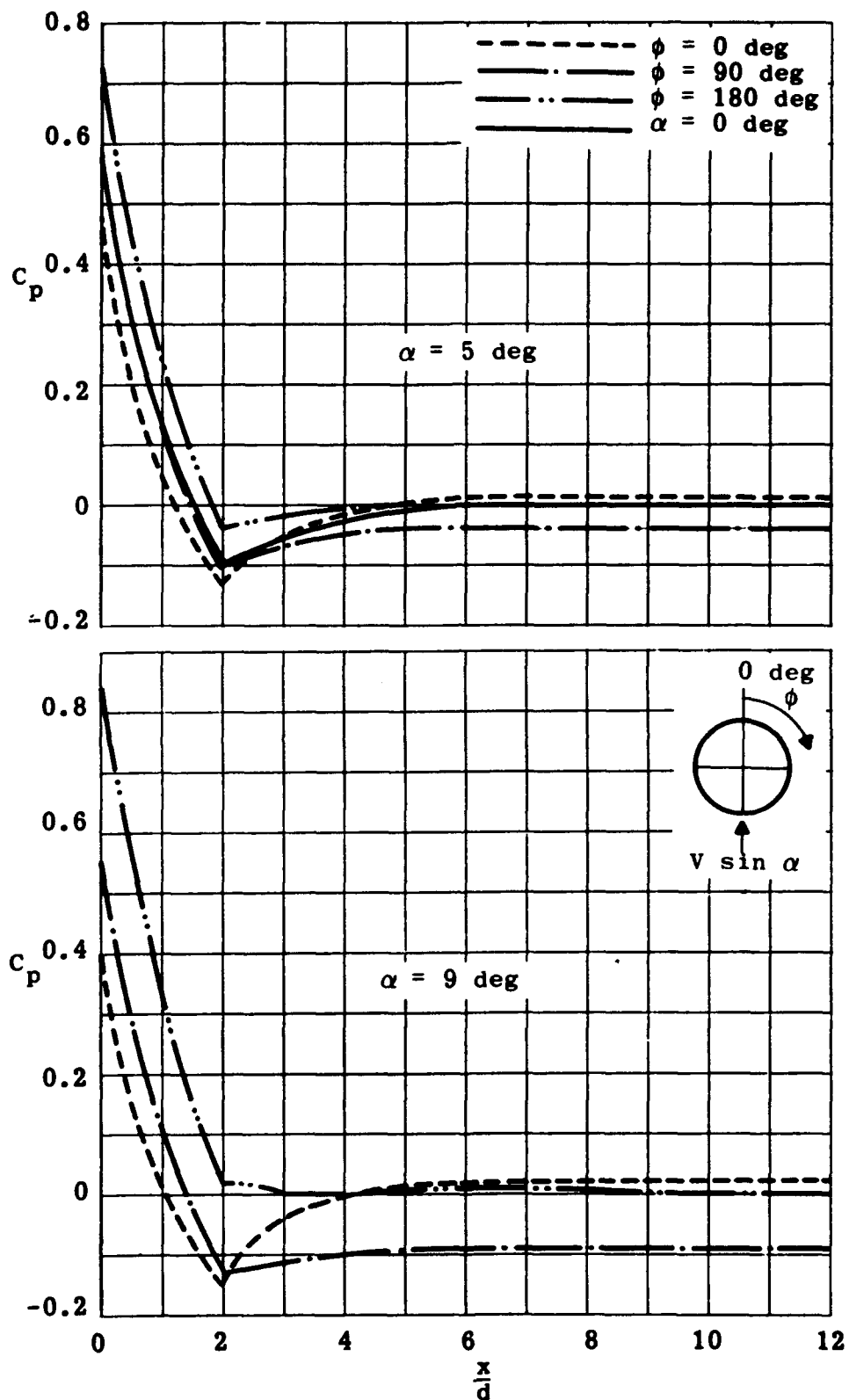
Fig. 4-39. Calculated pressure distributions on tangent-ogive cylinders at α = 0, 5, and 9 deg; M = 2, ℓ_N/d = 2. (Source: Ref. 73)
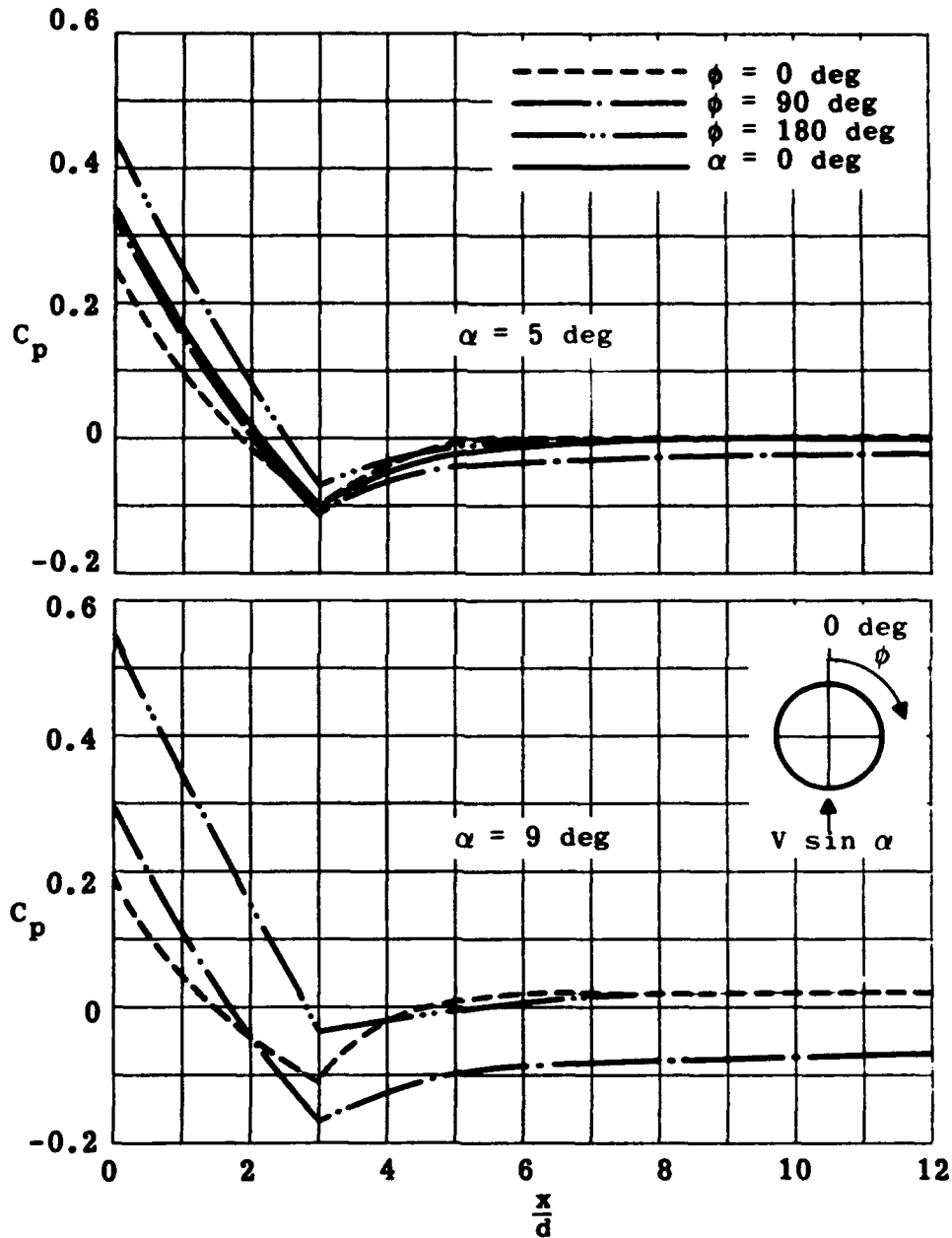
Fig. 4-40. Calculated pressure distributions on tangent-ogive cylinders at $\alpha = 0$, 5, and 9 deg; $M = 1.5$, $\ell_N/d = 3$. (Source: Ref. 73)

Fig. 4-41   NAVWEPS Report 1488 (Vol. 3, Sec. 8)
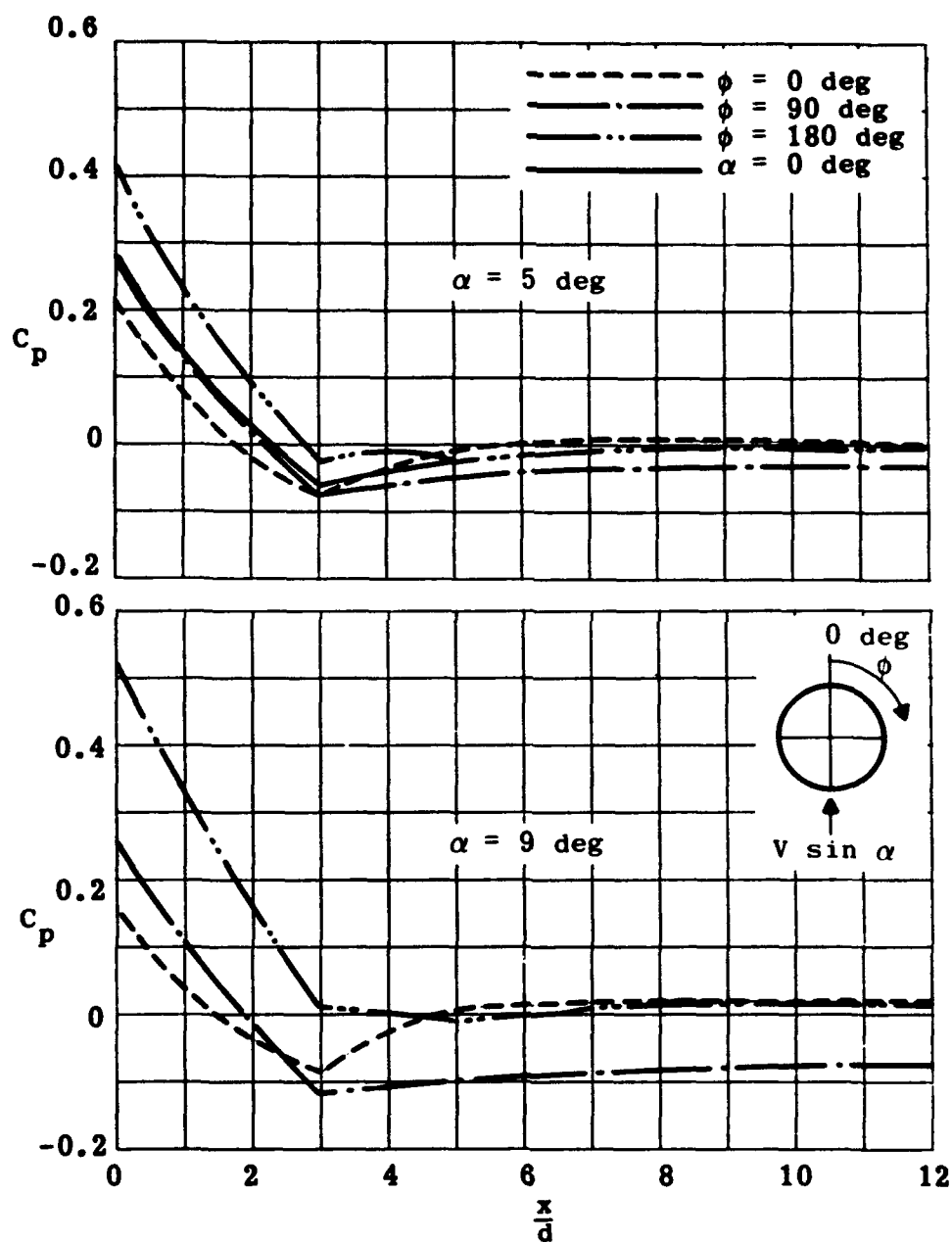
Fig. 4-41. Calculated pressure distributions on tangent-ogive cylinders at α = 0, 5, and 9 deg; M = 2, ℓ_N/d = 3. (Source: Ref. 73)

Fig. 4-43. Calculated pressure distributions on tangent-ogive cylinders at α = 0, 5, and 9 deg; M = 1.5, ℓ_N/d = 4. (Source: Ref. 73)
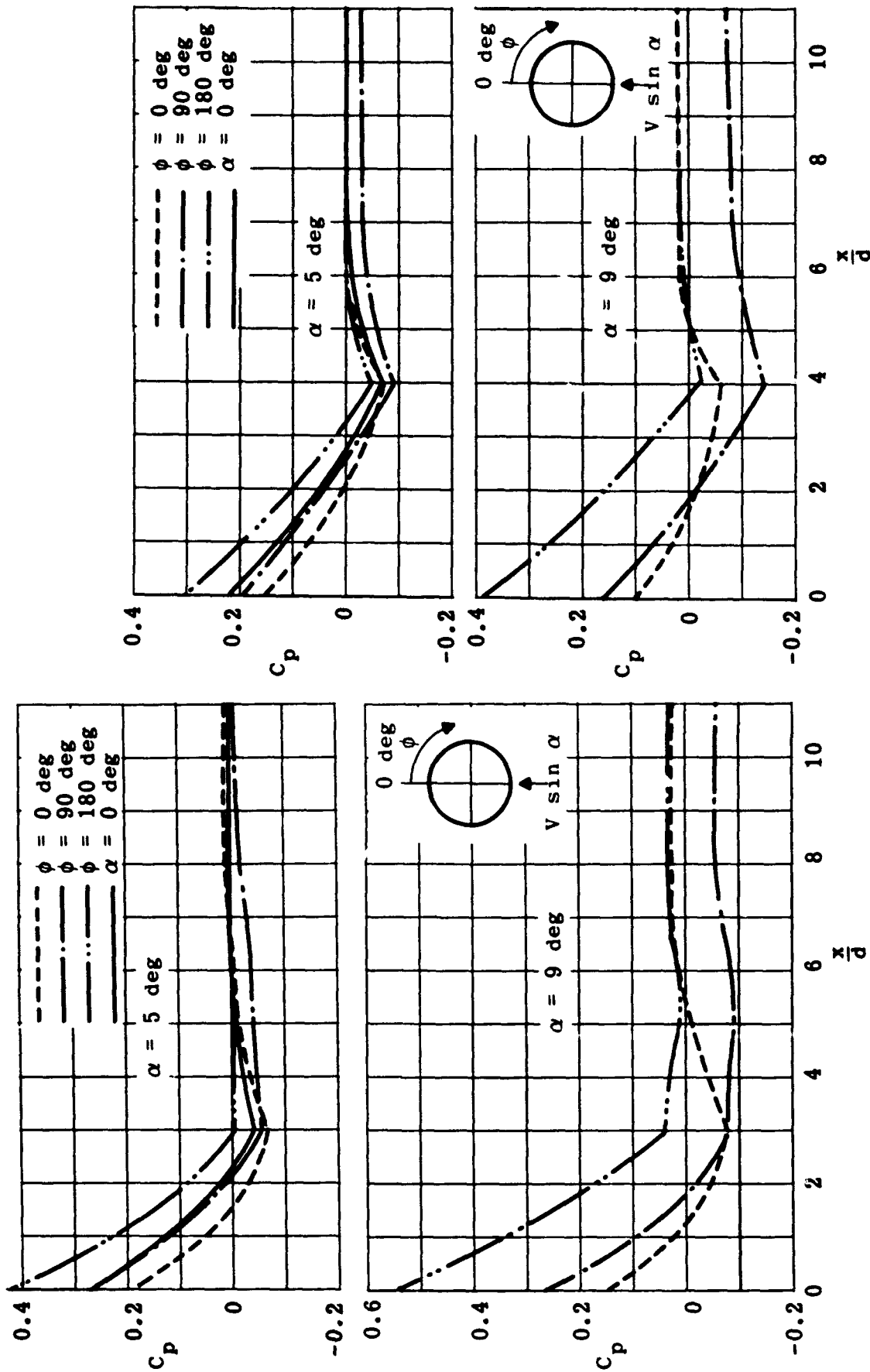
Fig. 4-42. Calculated pressure distributions on tangent-ogive cylinders at α = 0, 5, and 9 deg; M = 3, ℓ_N/d = 3. (Source: Ref. 73)

Fig. 4-44   NAVWEPS Report 1488 (Vol. 3, Sec. 8)
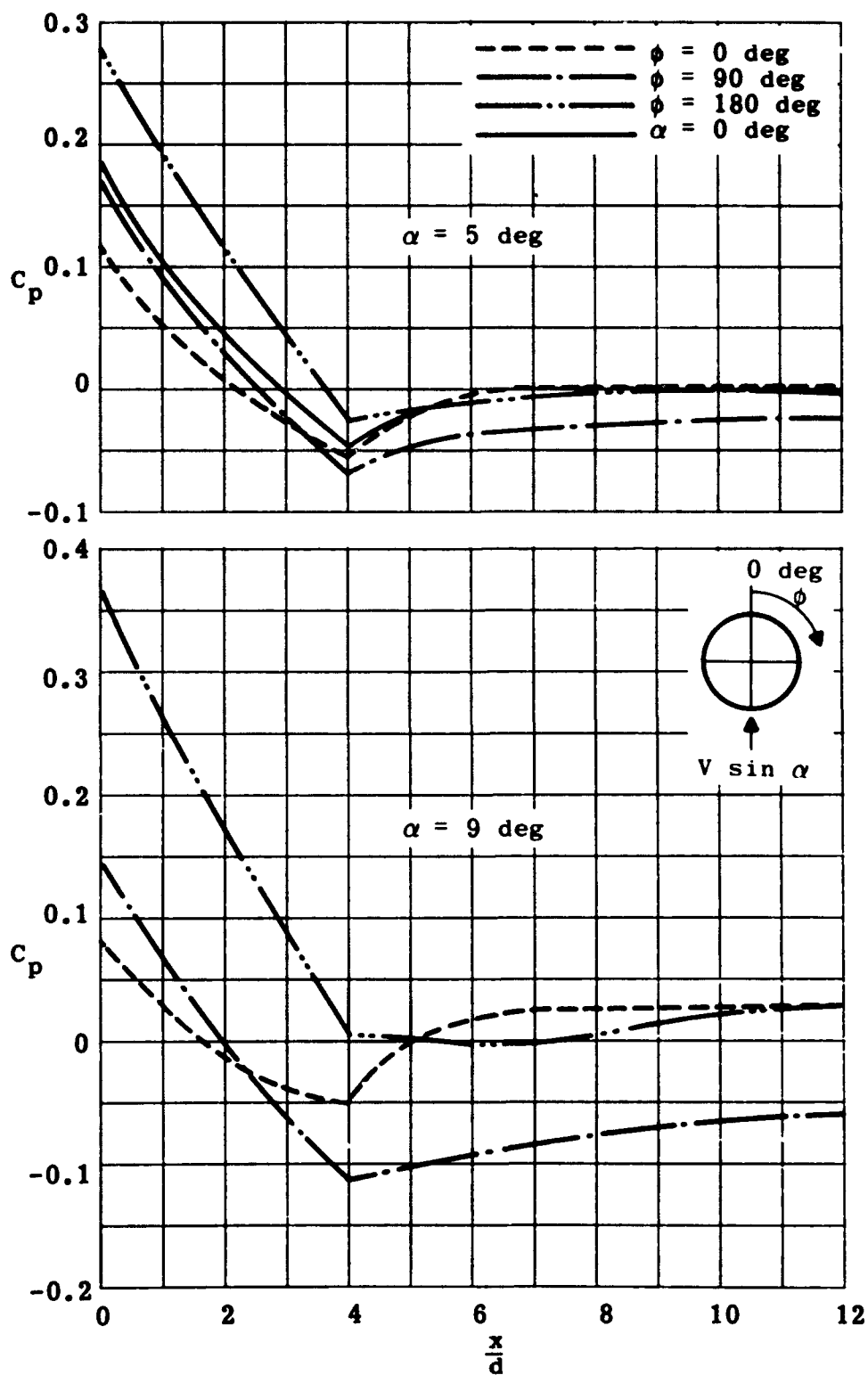
Fig. 4-44. Calculated pressure distributions on tangent-ogive
cylinders at α = 0, 5, and 9 deg; M = 2, ℓ_N/d = 4.
(Source: Ref. 73)
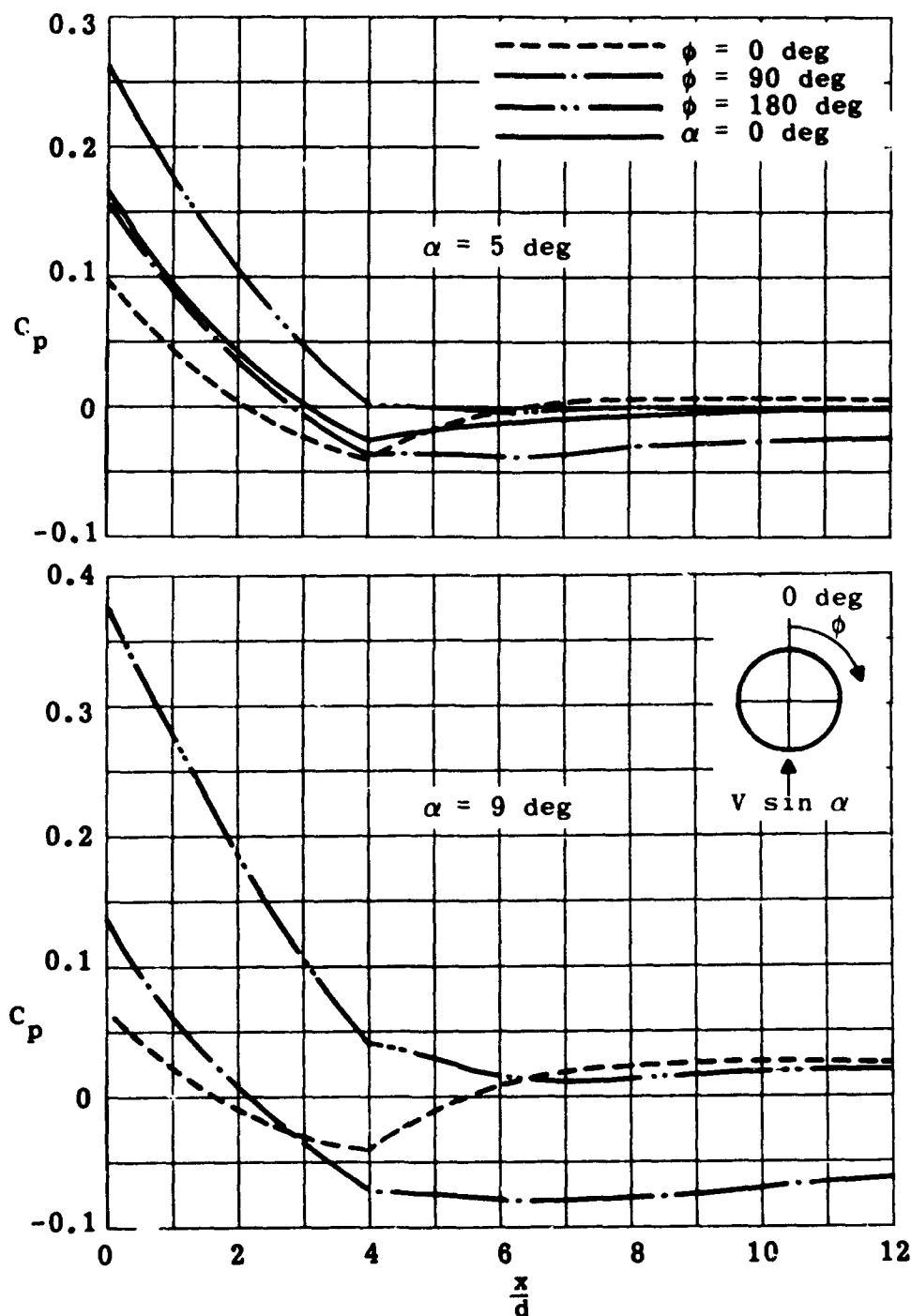
Fig. 4-45. Calculated pressure distributions on tangent-ogive cylinders at α = 0, 5, and 9 deg; M = 3, ℓ_N/d = 4. (Source: Ref. 73)

Fig. 4-46   NAVWEPS Report 1488 (Vol. 3, Sec. 8)

Fig. 4-47. Mach number effect on pressure distribution along a tangent-ogive cylinder; $\ell_N/d = 3$, $\alpha = 5$ deg, $\phi = 0$ deg. (Source: Ref. 73)
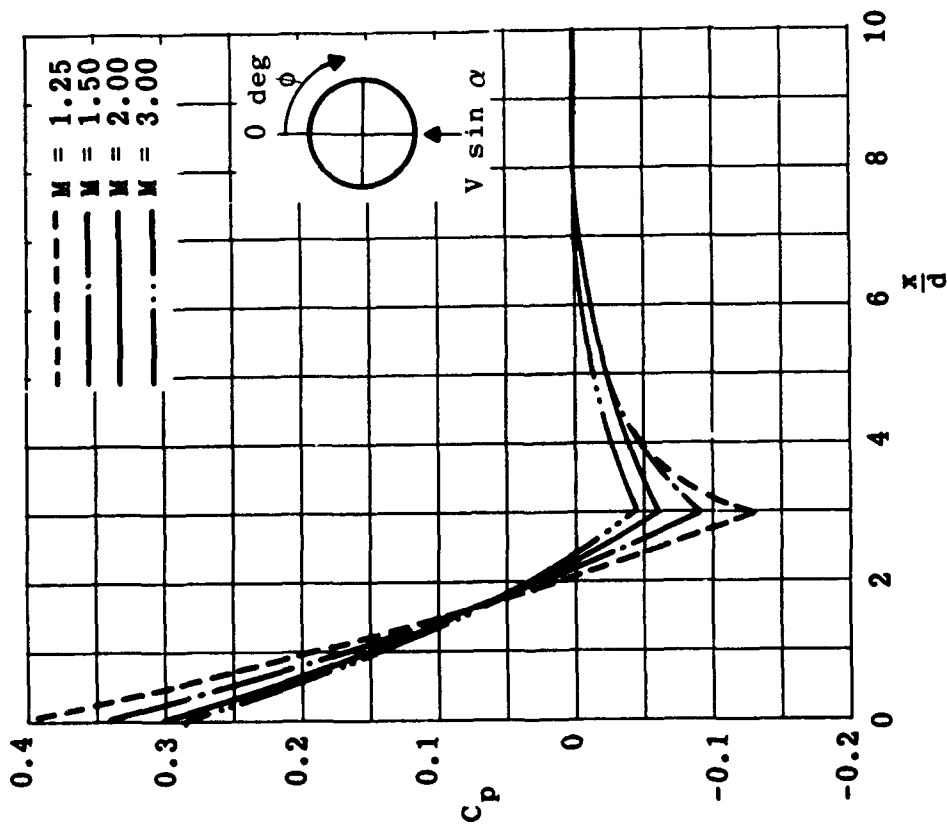
Fig. 4-46. Mach number effect on pressure distribution along a tangent-ogive cylinder; $\ell_N/d = 3$, $\alpha = 0$ deg. (Source: Ref. 73)
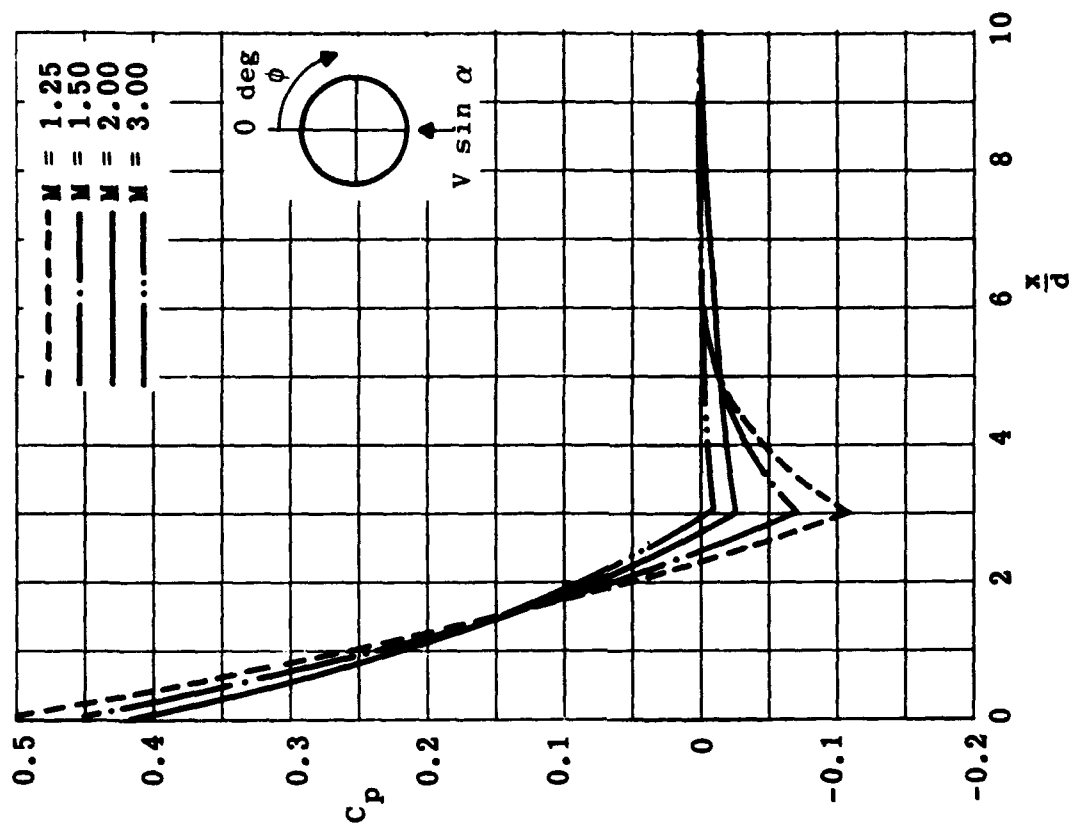
Fig. 4-49. Mach number effect on pressure distribution along a tangent-ogive cylinder; $\ell_N/d = 3$, $\alpha = 5$ deg, $\phi = 180$ deg. (Source: Ref. 73)
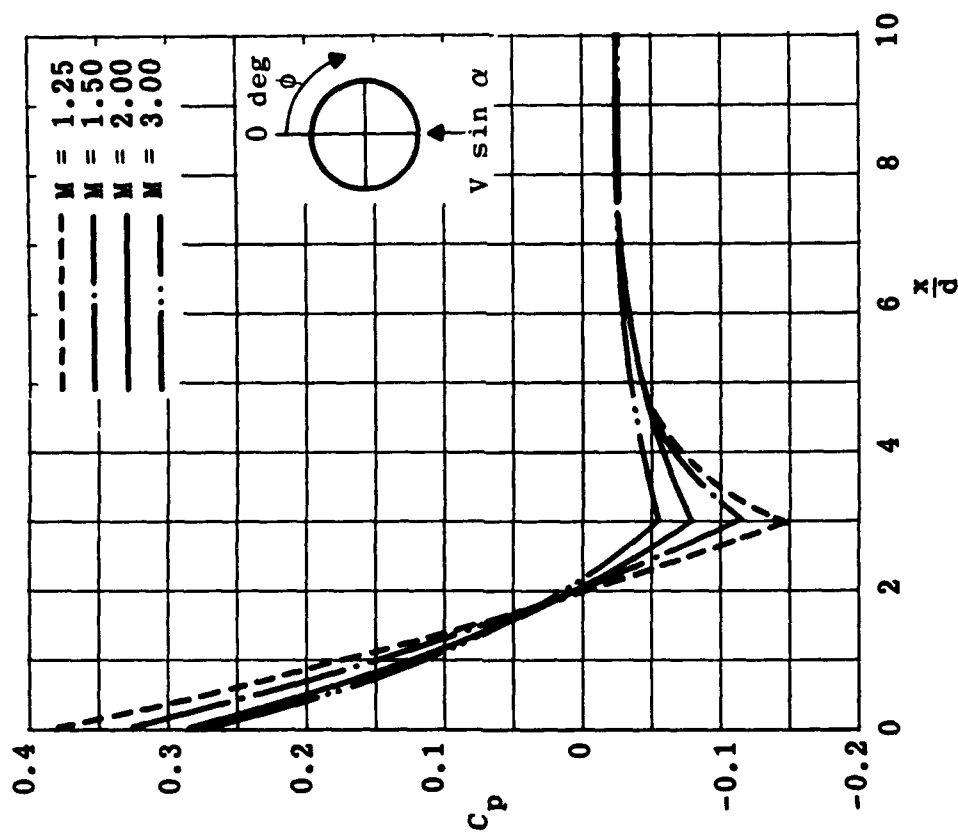
Fig. 4-48. Mach number effect on pressure distribution along a tangent-ogive cylinder; $\ell_N/d = 3$, $\alpha = 5$ deg, $\phi = 90$ deg. (Source: Ref. 73)

111

Fig. 4-50   NAVWEPS Report 1488 (Vol. 3, Sec. 8)
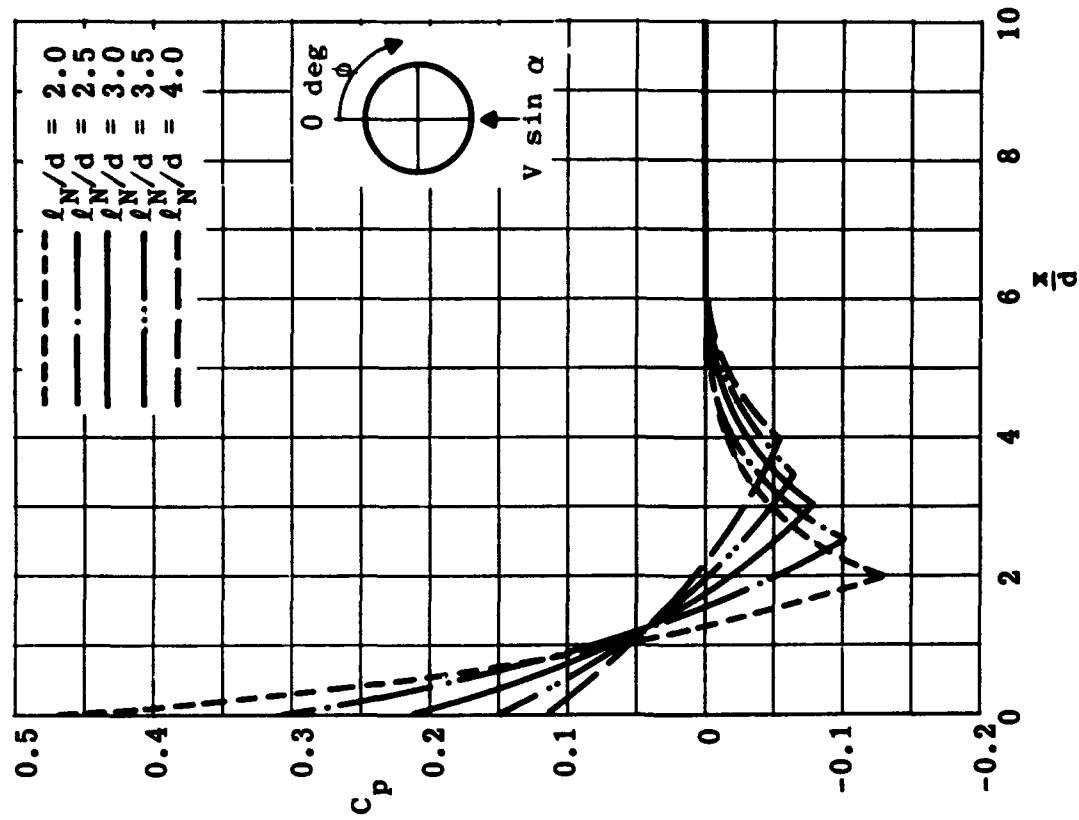
Fig. 4-51. Fineness ratio effect on pressure distribution along a tangent-ogive cylinder; $M = 2$, $\alpha = 5$ deg, $\phi = 0$ deg. (Source: Ref. 73)
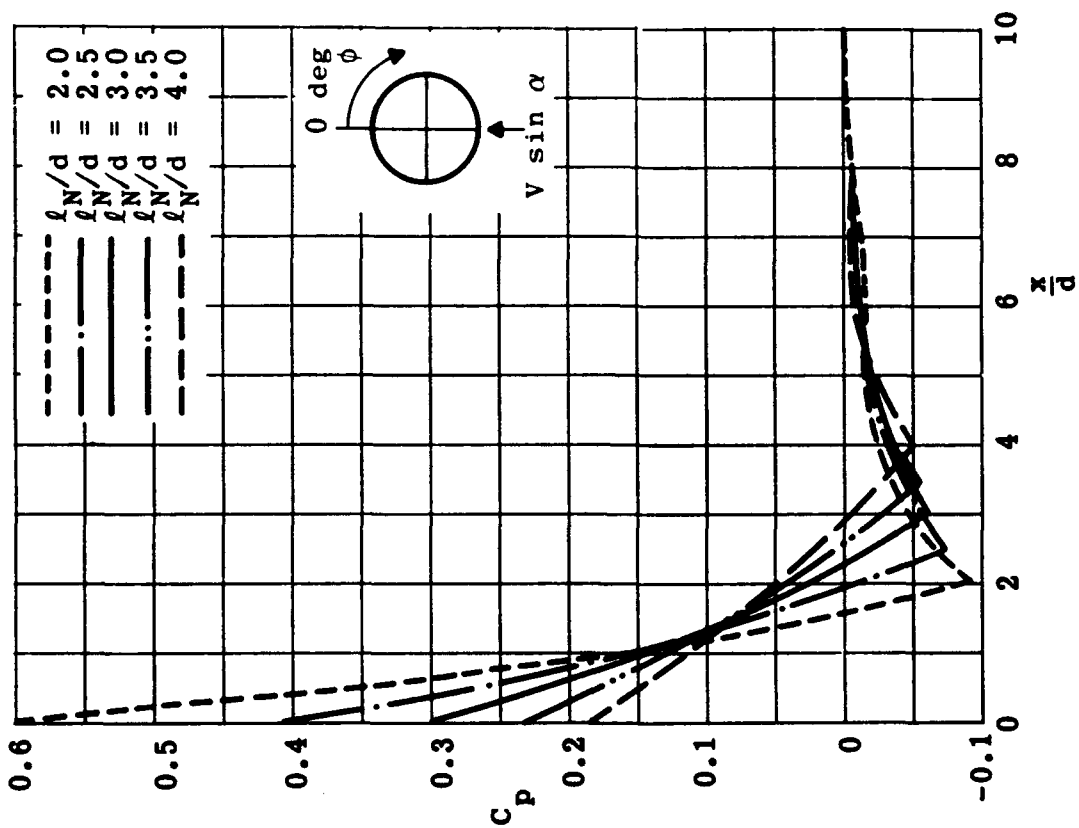
Fig. 4-50. Fineness ratio effect on pressure distribution along a tangent-ogive cylinder; $M = 2$, $\alpha = 0$ deg. (Source: Ref. 73)
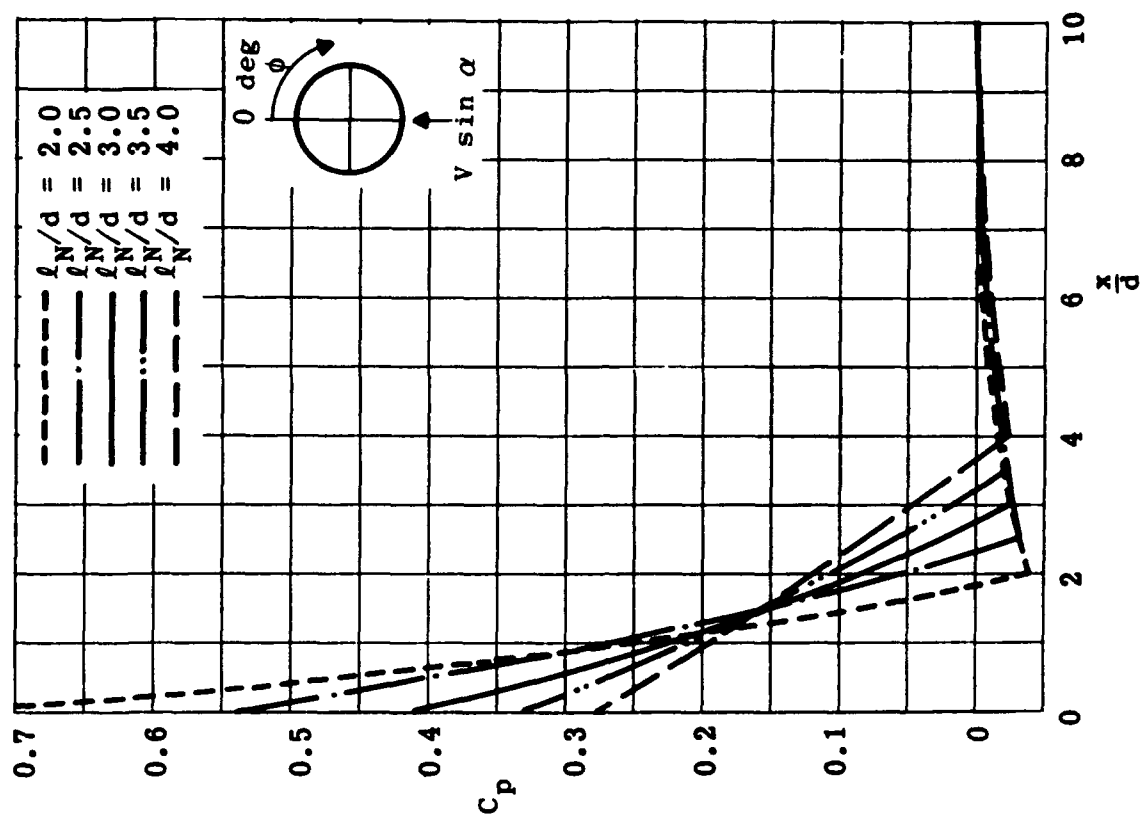
Fig. 4-53. Fineness ratio effect on pressure distribution along a tangent-ogive cylinder; M = 2, α = 5 deg, ϕ = 180 deg. (Source: Ref. 73)
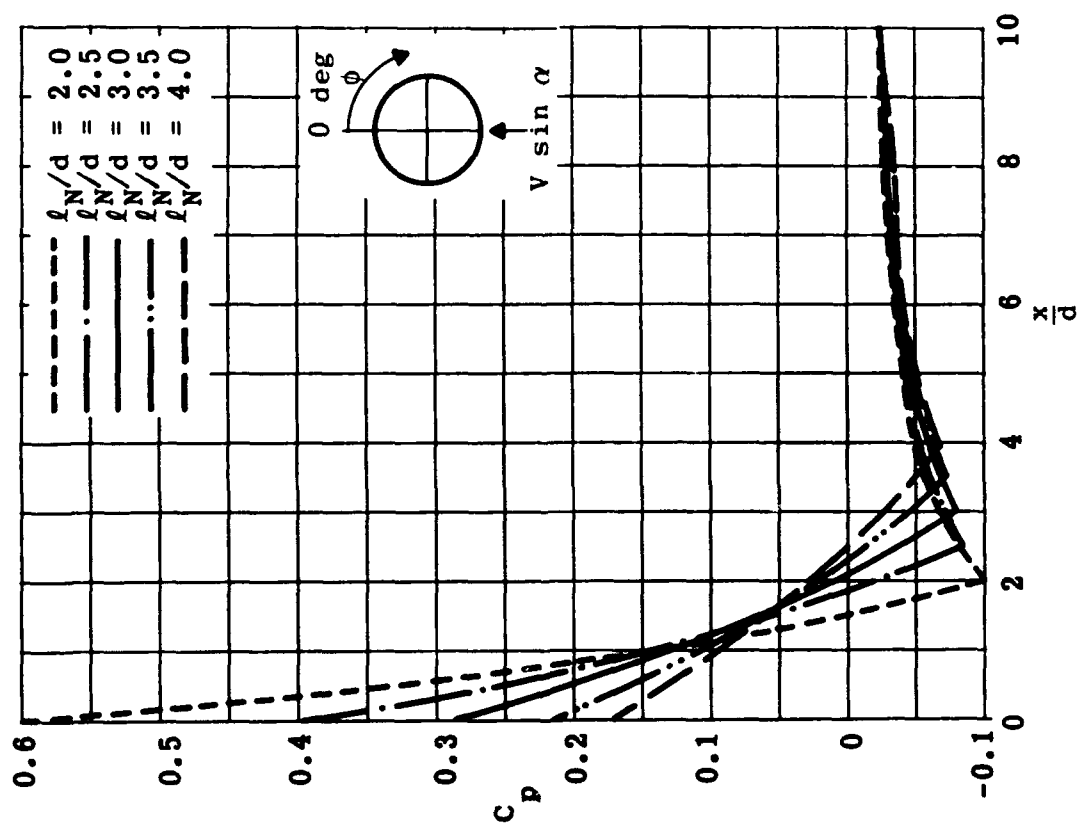
Fig. 4-52. Fineness ratio effect on pressure distribution along a tangent-ogive cylinder; M = 2, α = 5 deg, ϕ = 90 deg. (Source: Ref. 73)

Fig. 4-54   NAVWEPS Report 1488 (Vol. 3, Sec. 8)
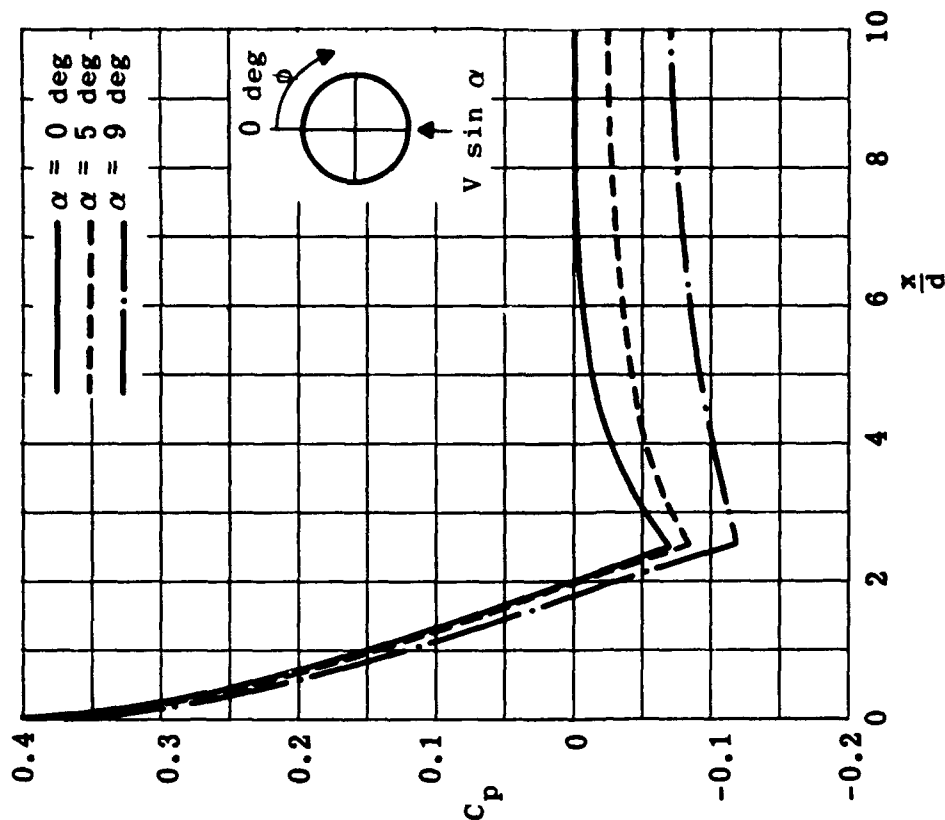
Fig. 4-55. Angle-of-attack effect on pressure distribution along a tangent-ogive cylinder; $\ell_N/d = 2.5$, $M = 2$, $\phi = 90$ deg. (Source: Ref. 73)
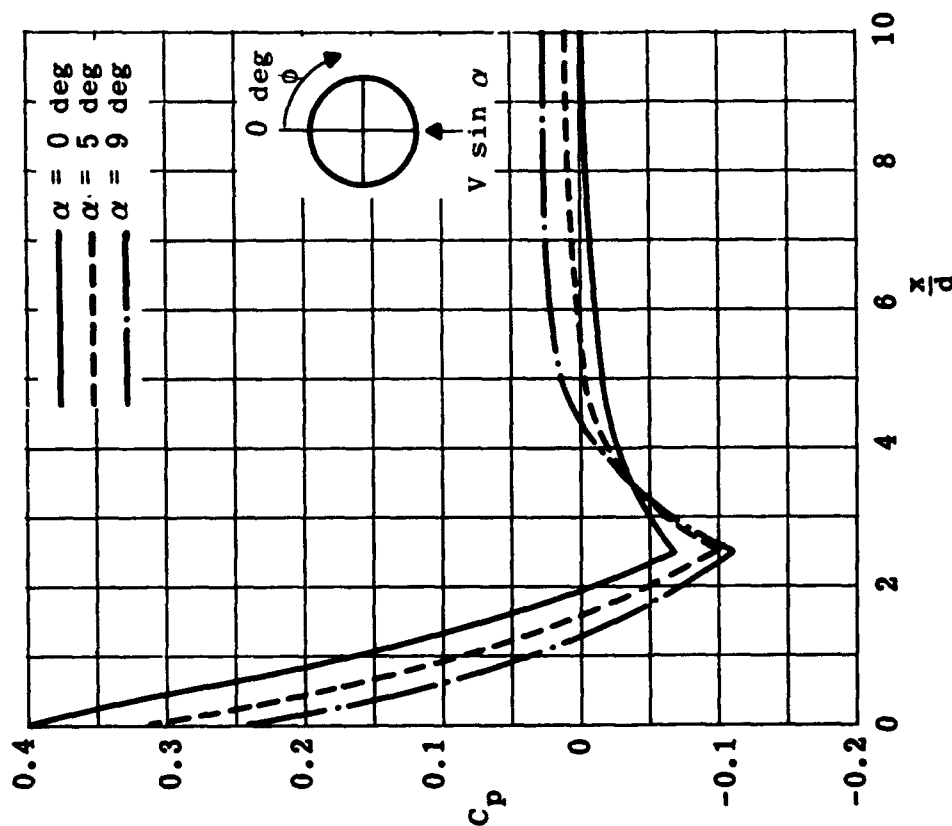
Fig. 4-54. Angle-of-attack effect on pressure distribution along a tangent-ogive cylinder; $\ell_N/d = 2.5$, $M = 2$, $\phi = 0$ deg. (Source: Ref. 73)
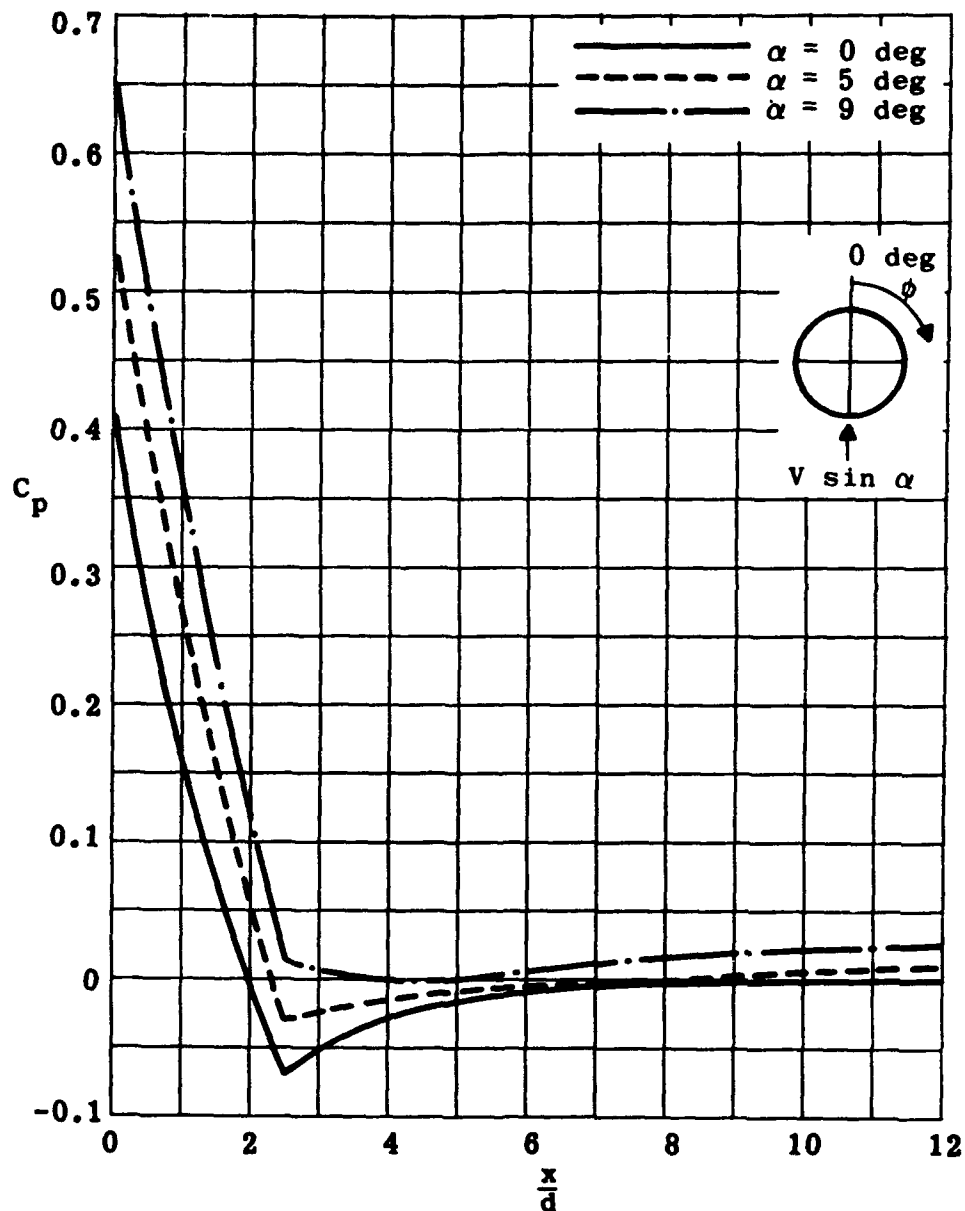
Fig. 4-56. Angle-of-attack effect on pressure distribution along a tangent-ogive cylinder; $\ell_N/d = 2.5$, $M = 2$, $\phi = 180$ deg. (Source: Ref. 73)

Fig. 4-57   NAVWEPS Report 1488 (Vol. 3, Sec. 8)
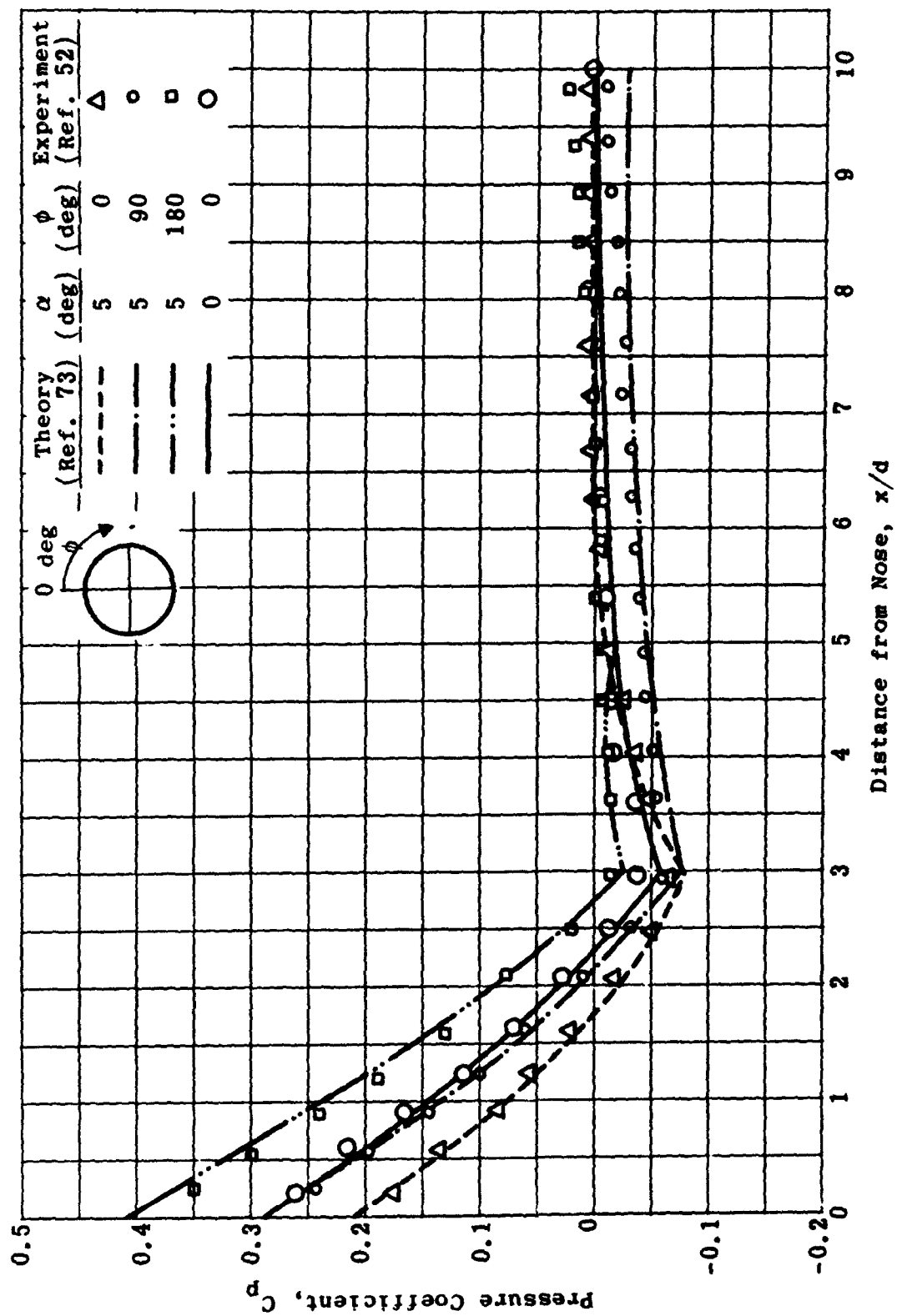
Fig. 4-57. Comparison of theoretical and experimental pressure distributions along tangent-ogive cylinders; $M = 2$, $\alpha = 0$ and 5 deg, $\phi = 0$ to 180 deg.
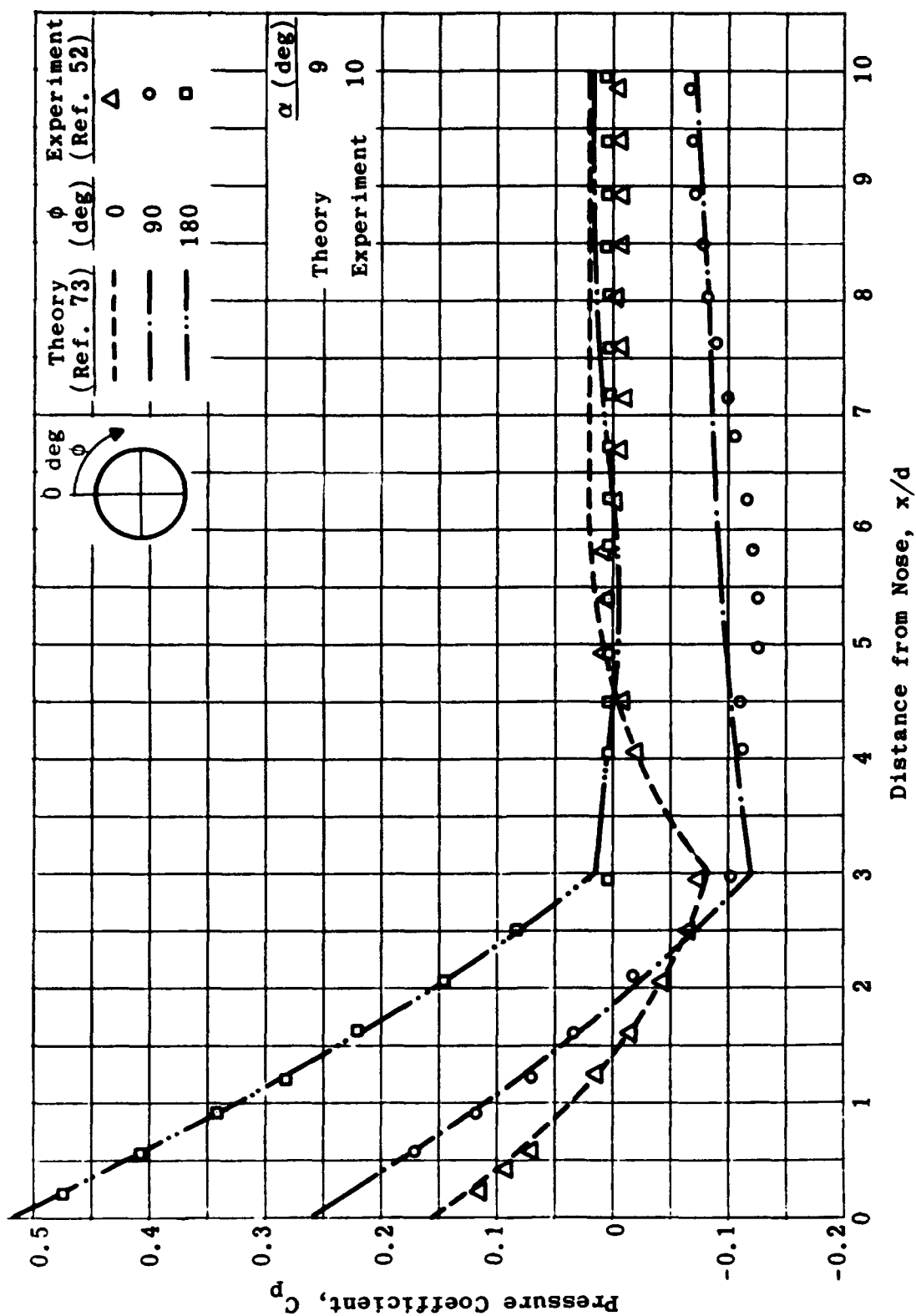
Fig. 4-58.   Comparison of theoretical and experimental pressure distributions along tangent-ogive cylinders; M = 2, α = 9 and 10 deg, ϕ = 0 to 180 deg.

Fig. 4-59   NAVWEPS Report 1488 (Vol. 3, Sec. 8)
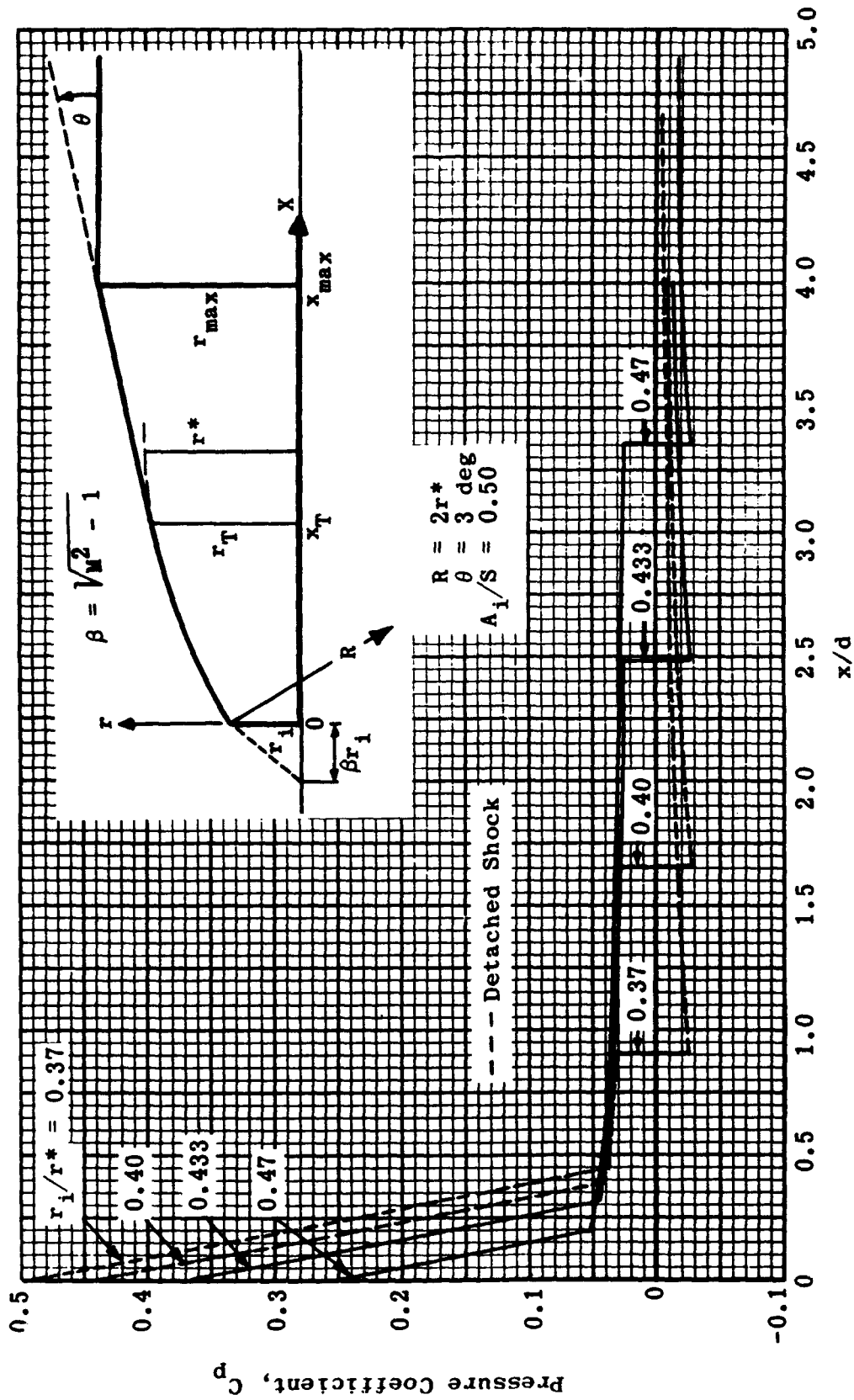
Fig. 4-59.   Pressure distribution on a ducted ogive cone; $\alpha = 0$, M = 2.   (Source: Ref. 79)

Fig. 4-61

Fig. 4-61. Variation of functions f_1 and f_2 for use with Eq. 4-3. (Source: Ref. 75)

Fig. 4-60. Normalized pressure distribution for a family of conical cowlings. (Source: Ref. 75)

Fig. 4-62   NAVWEPS Report 1488 (Vol. 3, Sec. 8)

Linearized Characteristics (Ref. 77)
Shock-Expansion (Ref. 76)
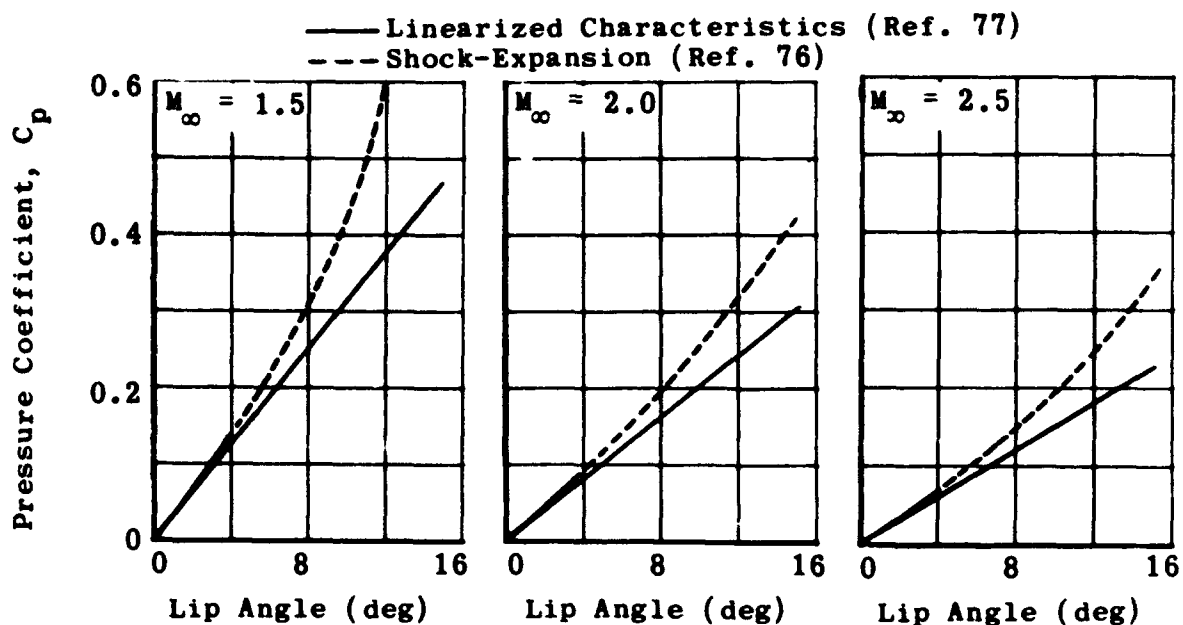
Fig. 4-62. Comparison of lip pressure coefficient as a function of lip angle as calculated by two methods. (Source: Ref. 75)
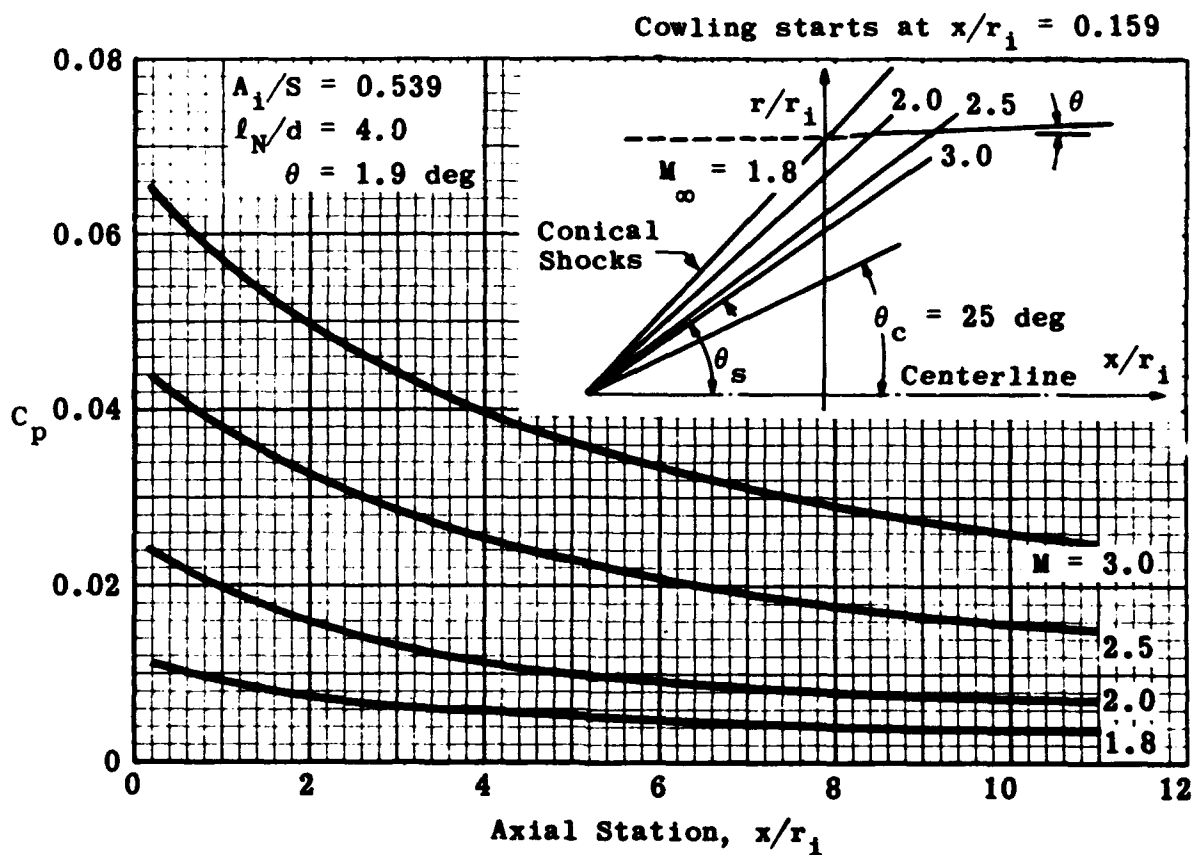
Fig. 4-63. Mach-number effect on pressure distribution over a cowling designed for M = 2. (Source: Ref. 75)

x/r_o	r_1/r_o	r_2/r_o	r_3/r_o
0.136	--	--	1.026
0.240	--	--	1.048
0.345	--	--	1.060
0.428	--	1.100	1.066
0.553	--	1.130	1.076
0.658	--	1.150	1.083
0.762	--	1.170	1.085
0.936	1.260	1.190	1.090
1.176	1.310	1.210	1.096
1.596	1.350	1.230	1.106
2.226	1.360	1.240	1.123
5.246	1.360	1.280	1.202
8.236	1.360	1.310	1.280
11.04	1.360	1.358	1.360
11.34	1.360	1.360	--
11.84	1.360	--	--

$$M = 2$$
$$\ell_N/d = 4$$
$$A_i/S = 0.539$$

$\theta_s = 42.6$ deg
$\theta_c = 25$ deg
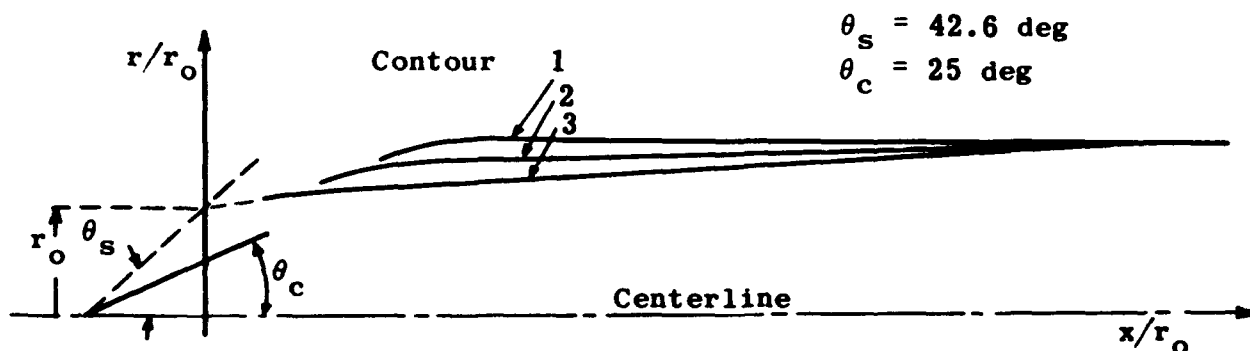
Fig. 4-64. Details of cowling inlets used to investigate additive
drag. (Source: Ref. 75)

Fig. 4-65   NAVWEPS Report 1488 (Vol. 3, Sec. 8)
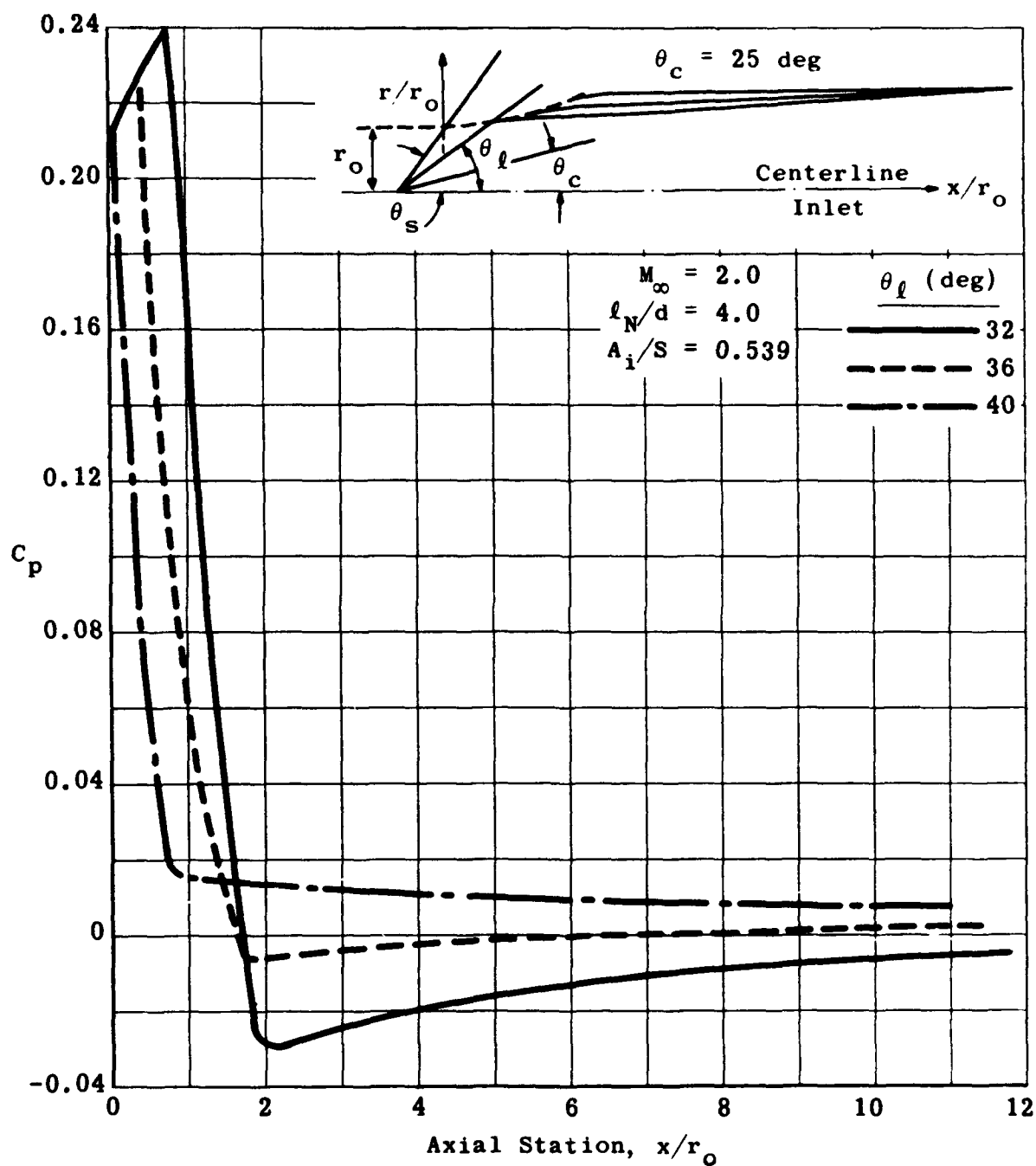
Fig. 4-65. Pressure distribution over streamline and body contour,
with additive drag. (Source: Ref. 75)

x/r_i	r_1/r_i	r_2/r_i	r_3/r_i
0	1.00	1.00	1.00
0.313	1.07	1.07	1.05
0.626	1.13	1.13	1.09
0.939	1.18	1.18	1.12
1.25	1.23	1.20	1.15
1.56	1.26	1.217	1.17
1.88	1.30	1.221	1.19
2.19	1.32	1.225	1.20
2.51	1.33	1.23	1.22
2.82	1.34	1.234	1.23
4.12	1.36	1.25	1.25
5.43	1.36	1.27	1.27
6.74	1.36	1.29	1.29
8.04	1.36	1.32	1.32
9.34	1.36	1.34	1.34
10.9	1.36	1.36	1.36

$$M = 2$$
$$\ell_N/d = 4$$
$$A_i/S = 0.539$$
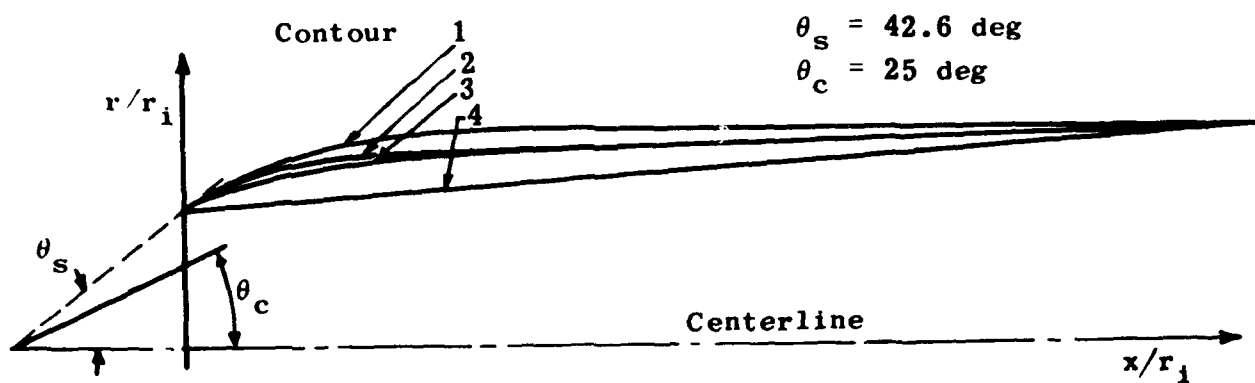
Fig. 4-66. Design details for non-conical inlets. (Source: Ref. 75)

Fig. 4-67   NAVWEPS Report 1488 (Vol. 3, Sec. 8)
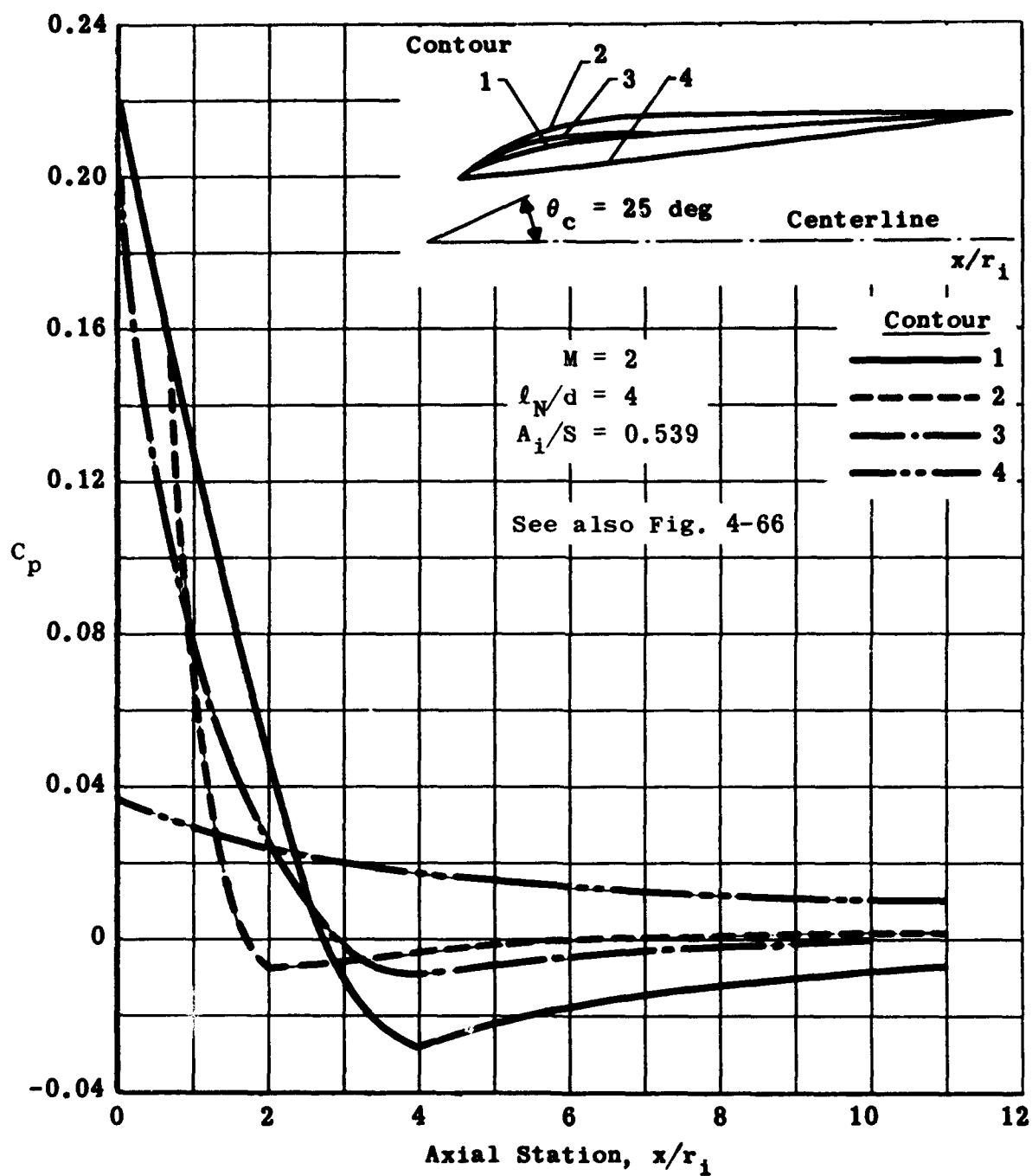
Fig. 4-67. Pressure distributions over non-conical cowlings.
(Source: Ref. 75)
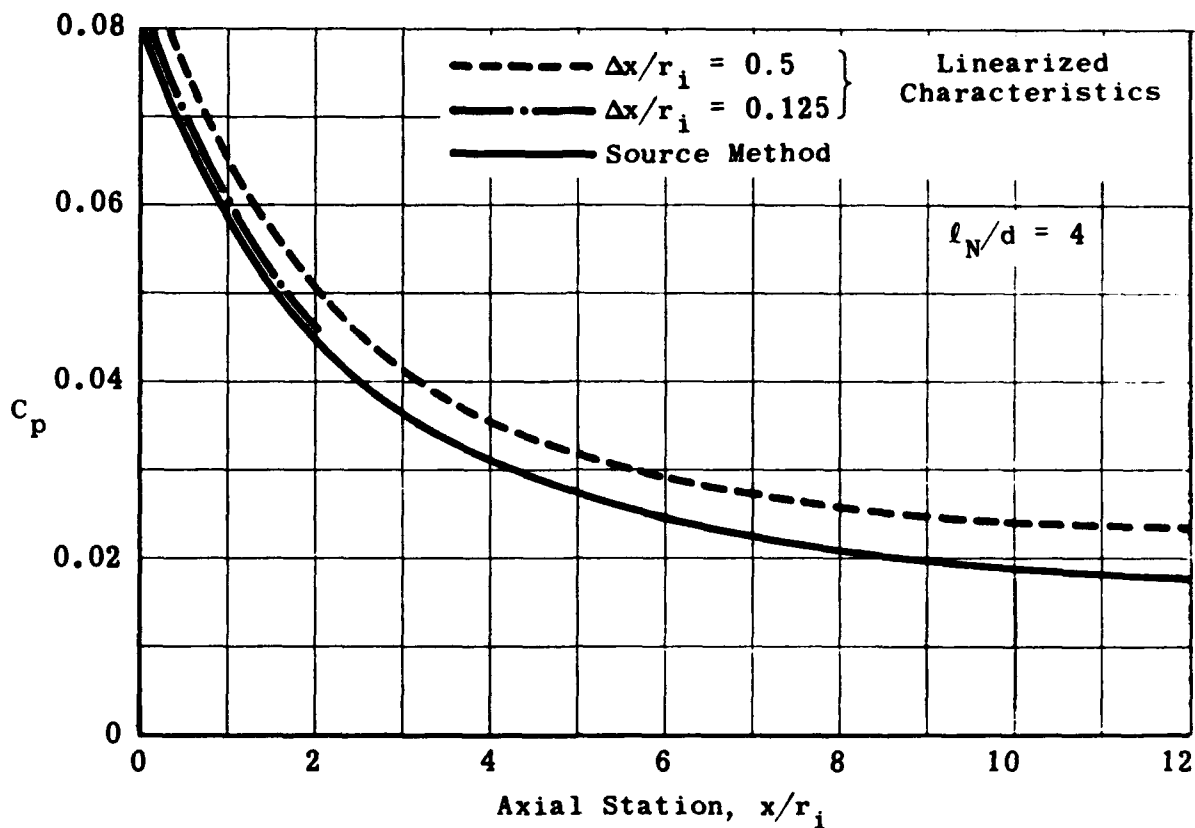
Fig. 4-68. Cowling pressure distributions calculated by the characteristics method and source distribution method; $M = 1.5$, $A_i/S = 0.393$. (Source: Ref. 75)
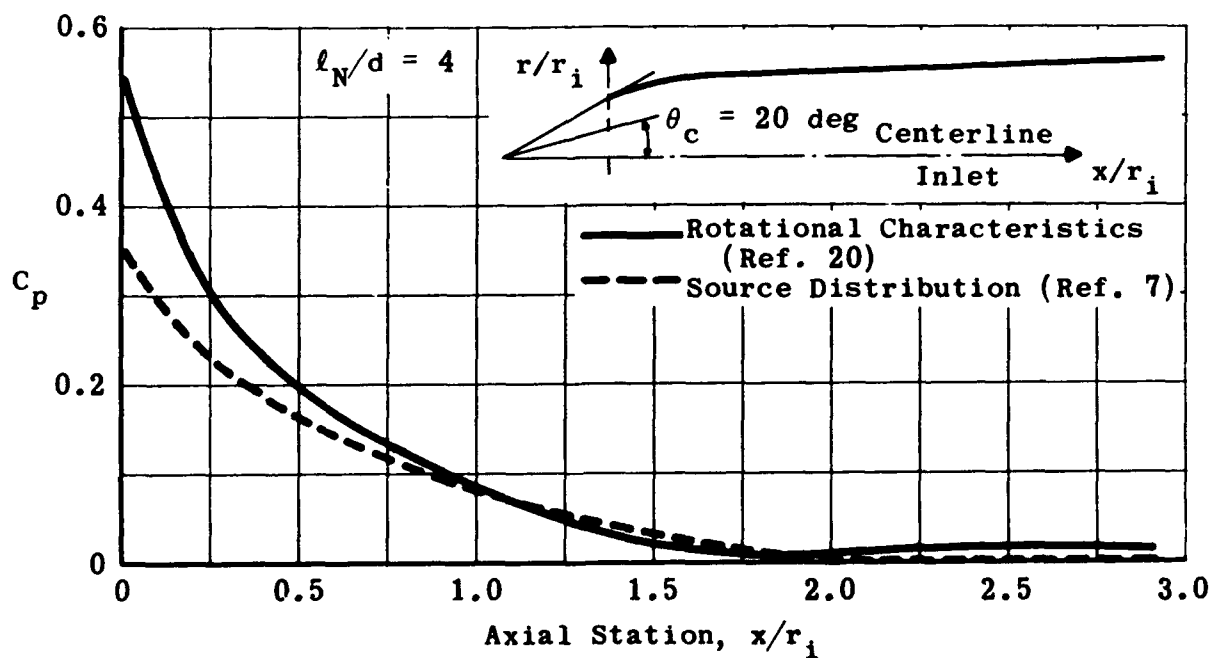
Fig. 4-69. Cowling pressure distributions calculated by the characteristics method and source distribution method; $M = 1.8$, $A_i/S = 0.490$. (Source: Ref. 75)

Fig. 4-70   NAVWEPS Report 1488 (Vol. 3, Sec. 8)
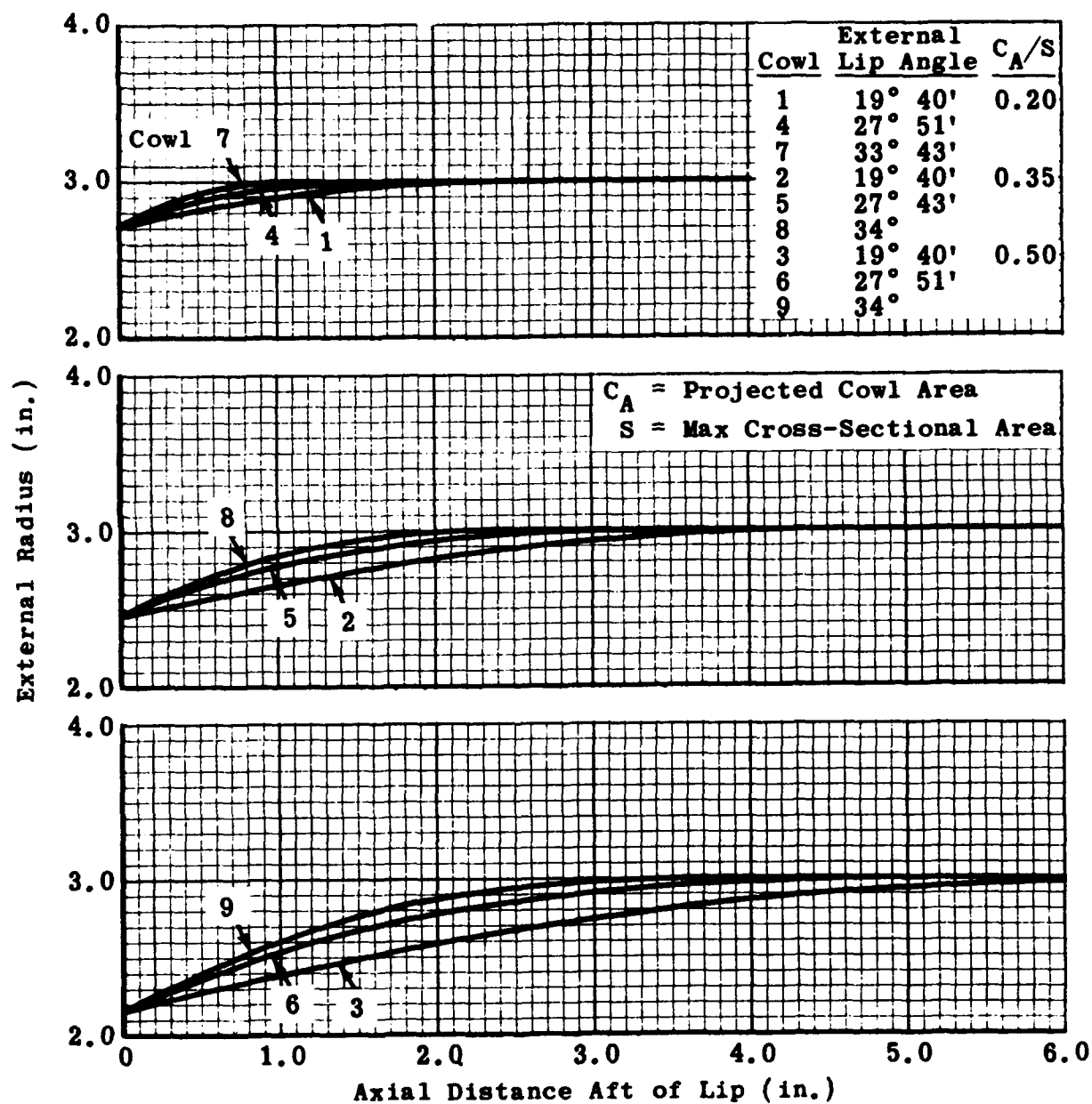
Fig. 4-70. Geometric details of nine cowls. (Source: Ref. 80)
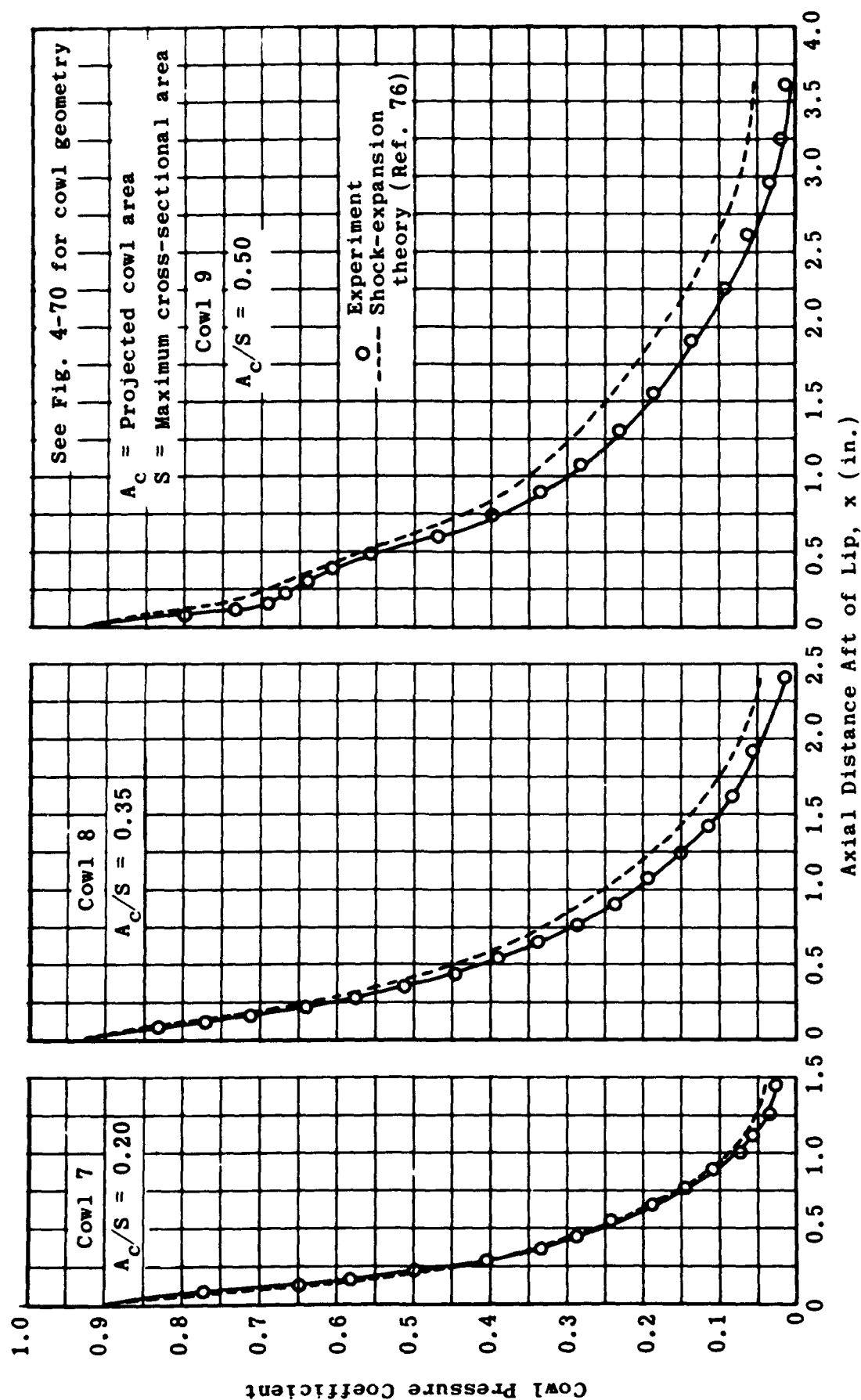
Fig. 4-71. Comparison of typical experimental and theoretical cowl pressure distributions;
M = 3.88. (Source: Ref. 80)

Fig. 4-72   NAVWEPS Report 1488 (Vol. 3, Sec. 8)
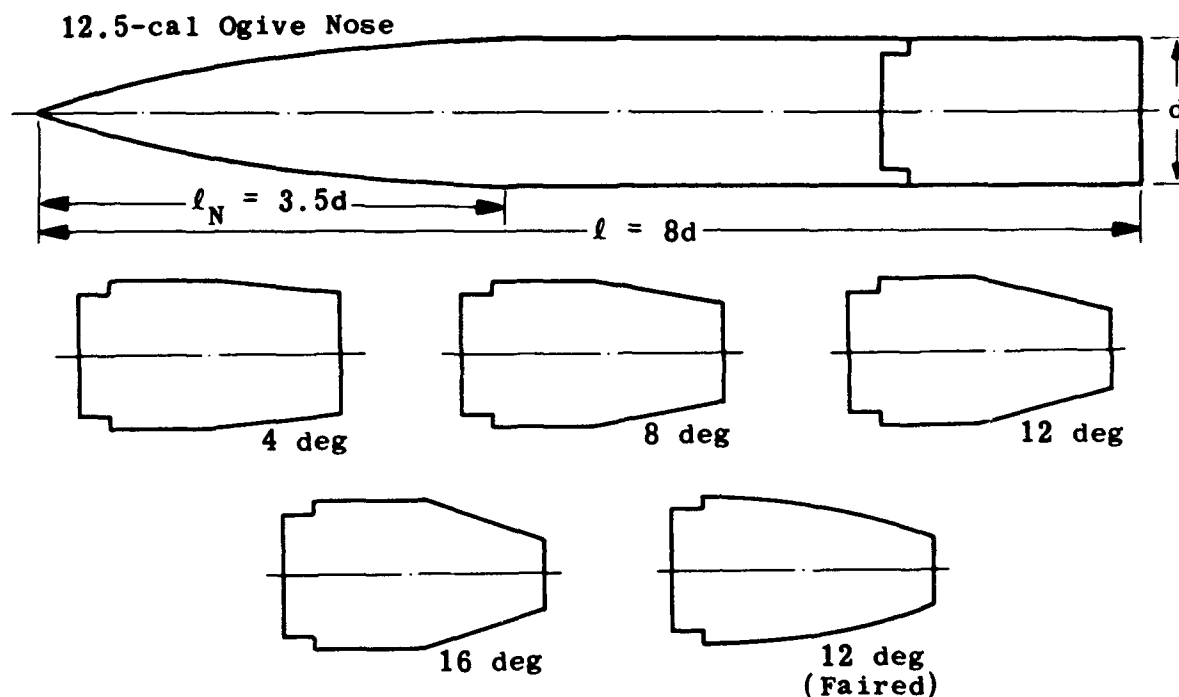
Fig. 4-72. Boattail configurations employed in pressure distribution investigations. (Source: Ref. 165)
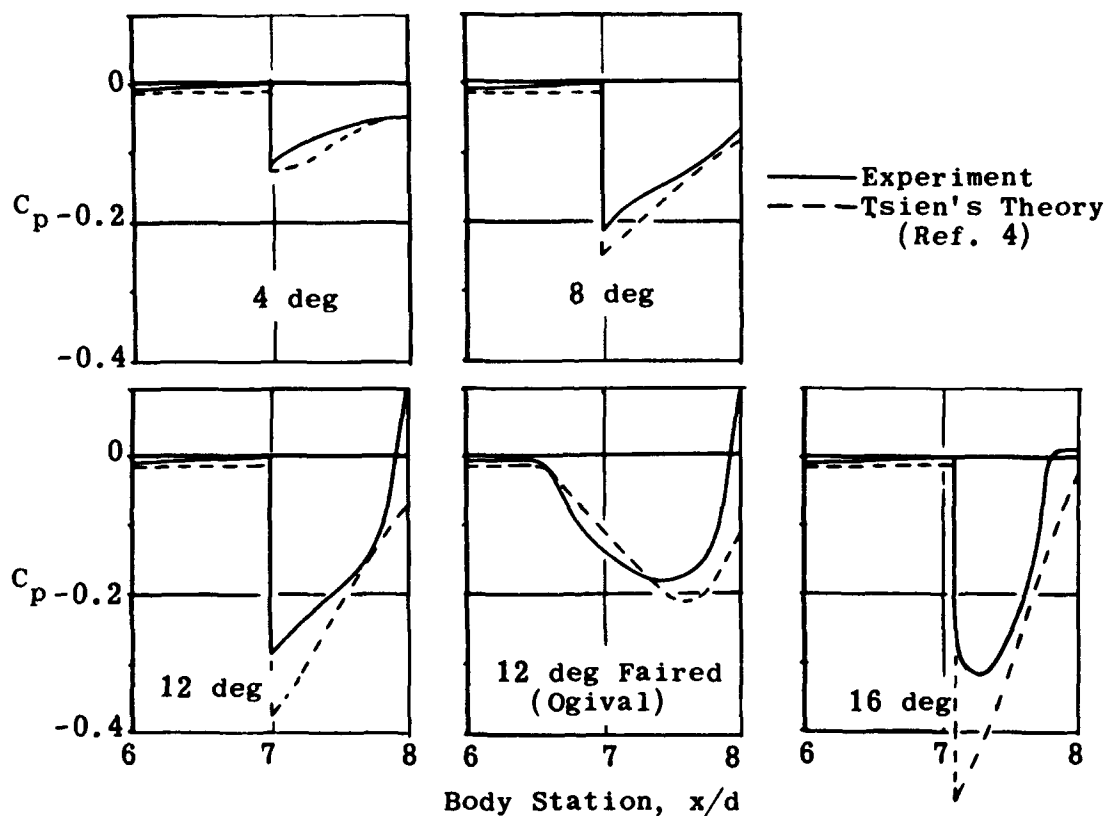
Fig. 4-73. Comparison of theoretical and experimental pressure distributions over a family of boattails; M = 1.5, α = 0 deg. (Source: Ref. 165)
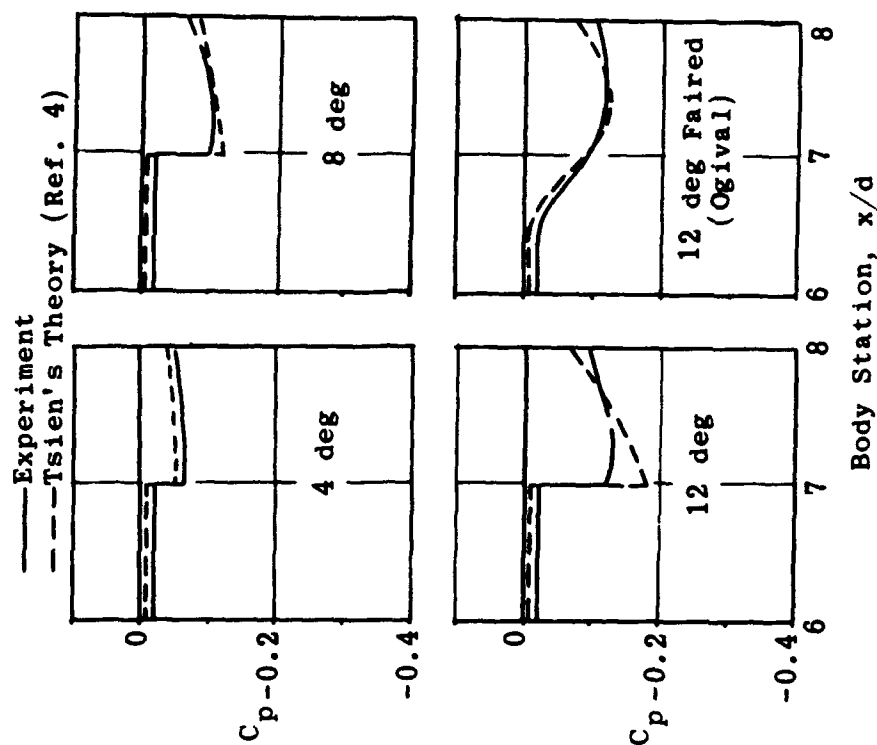
Fig. 4-75. Comparison of theoretical and experimental pressure distributions over a family of boattails; M = 2.5, α = 0 deg. (Source: Ref. 165)
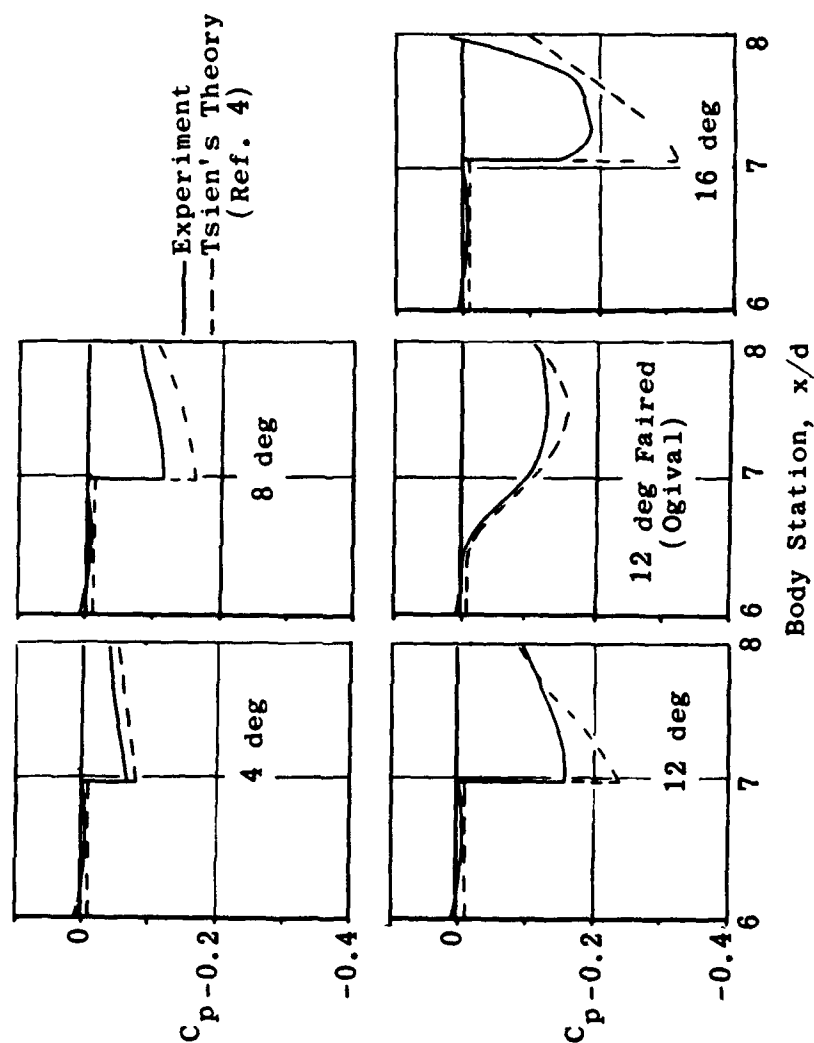
Fig. 4-74. Comparison of theoretical and experimental pressure distributions over a family of boattails; M = 2.0, α = 0 deg. (Source: Ref. 165)

Fig. 4-76   NAVWEPS Report 1488 (Vol. 3, Sec. 8)

θ = Boattail Angle
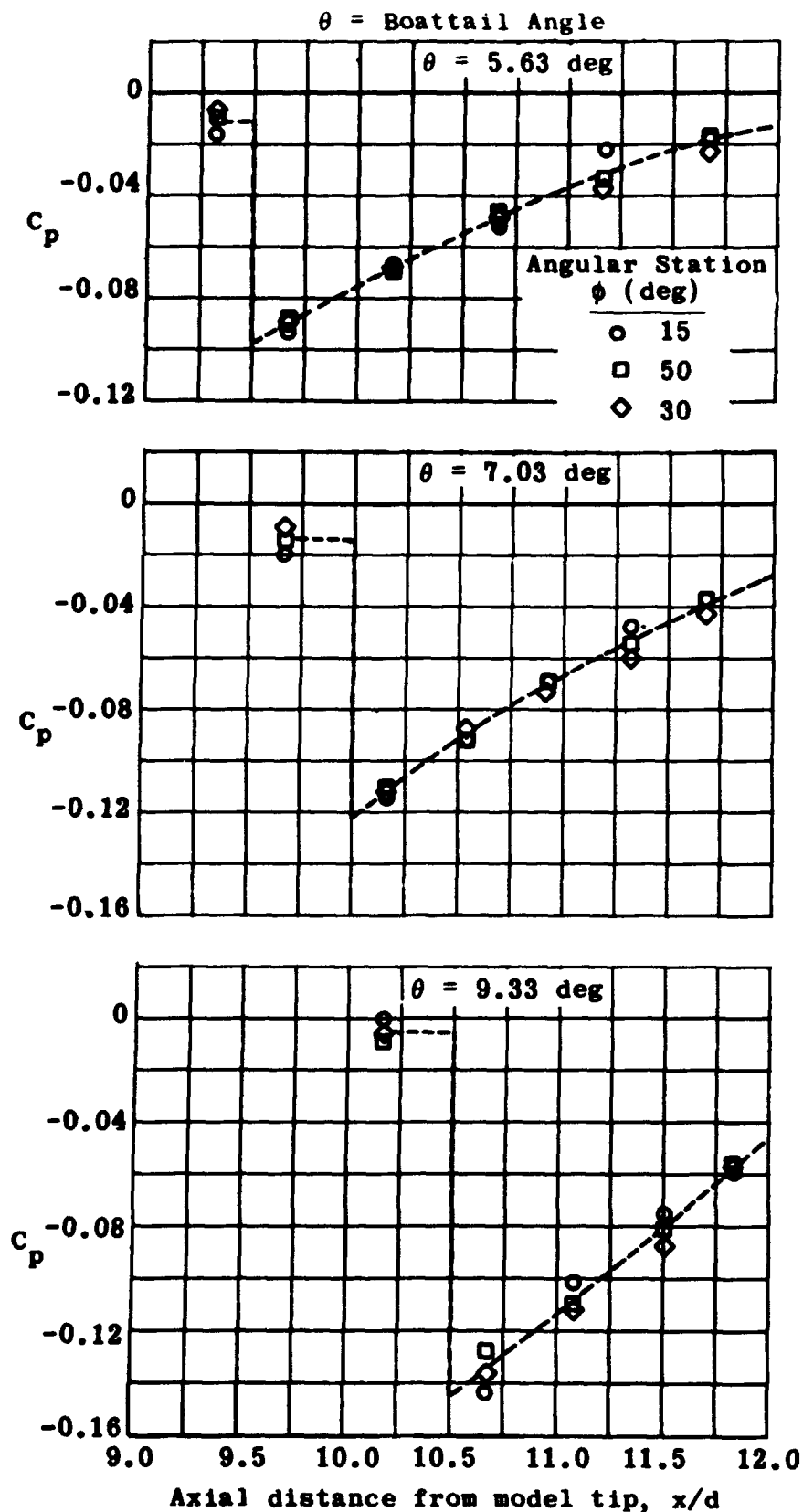
Fig. 4-76. Pressure distributions over three complete boattails;
M = 1.91, α = 0 deg, d_b/d = 0.506. (Source: Ref. 150)
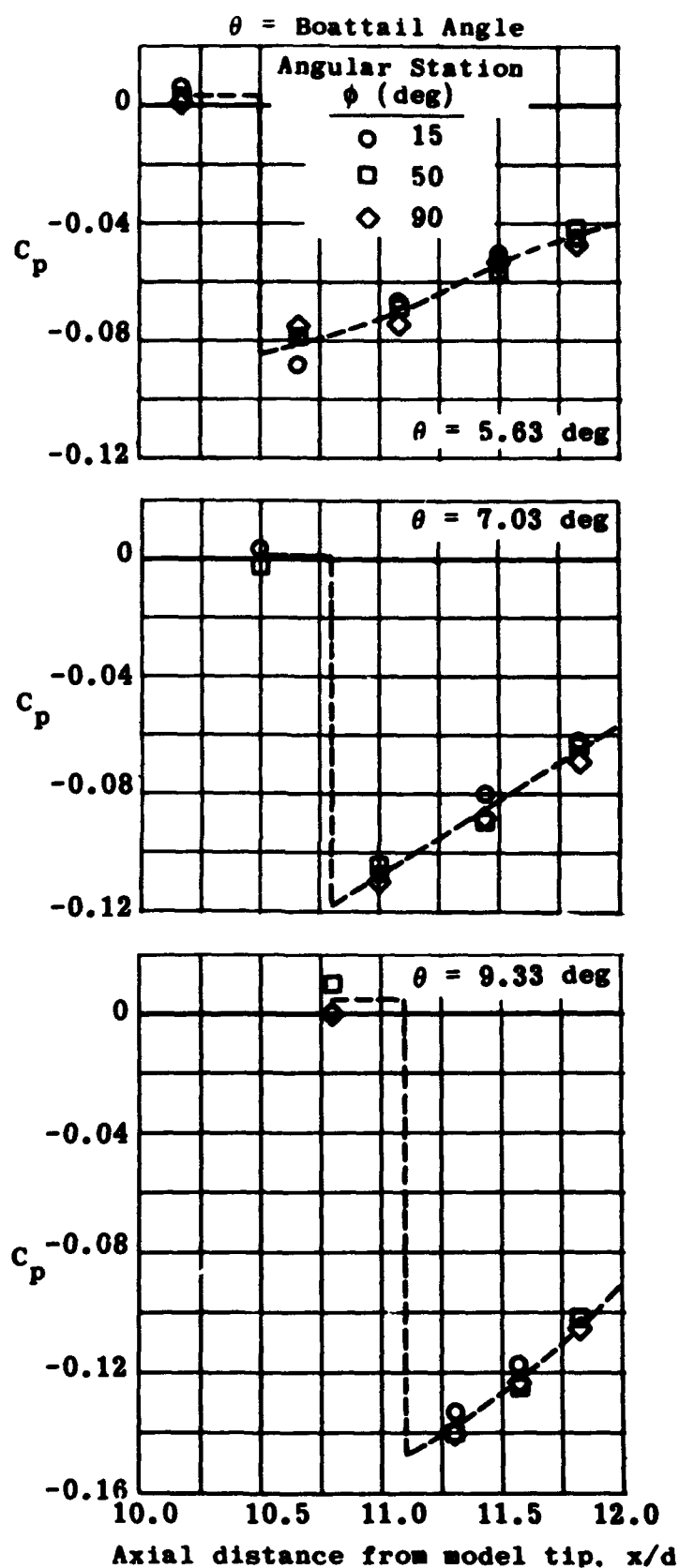
Fig. 4-77. Pressure distributions over three partial boattails;
M = 1.91, α = 0 deg, d_b/d = 0.704. (Source: Ref. 150)

Fig. 4-78   NAVWEPS Report 1488 (Vol. 3, Sec. 8)
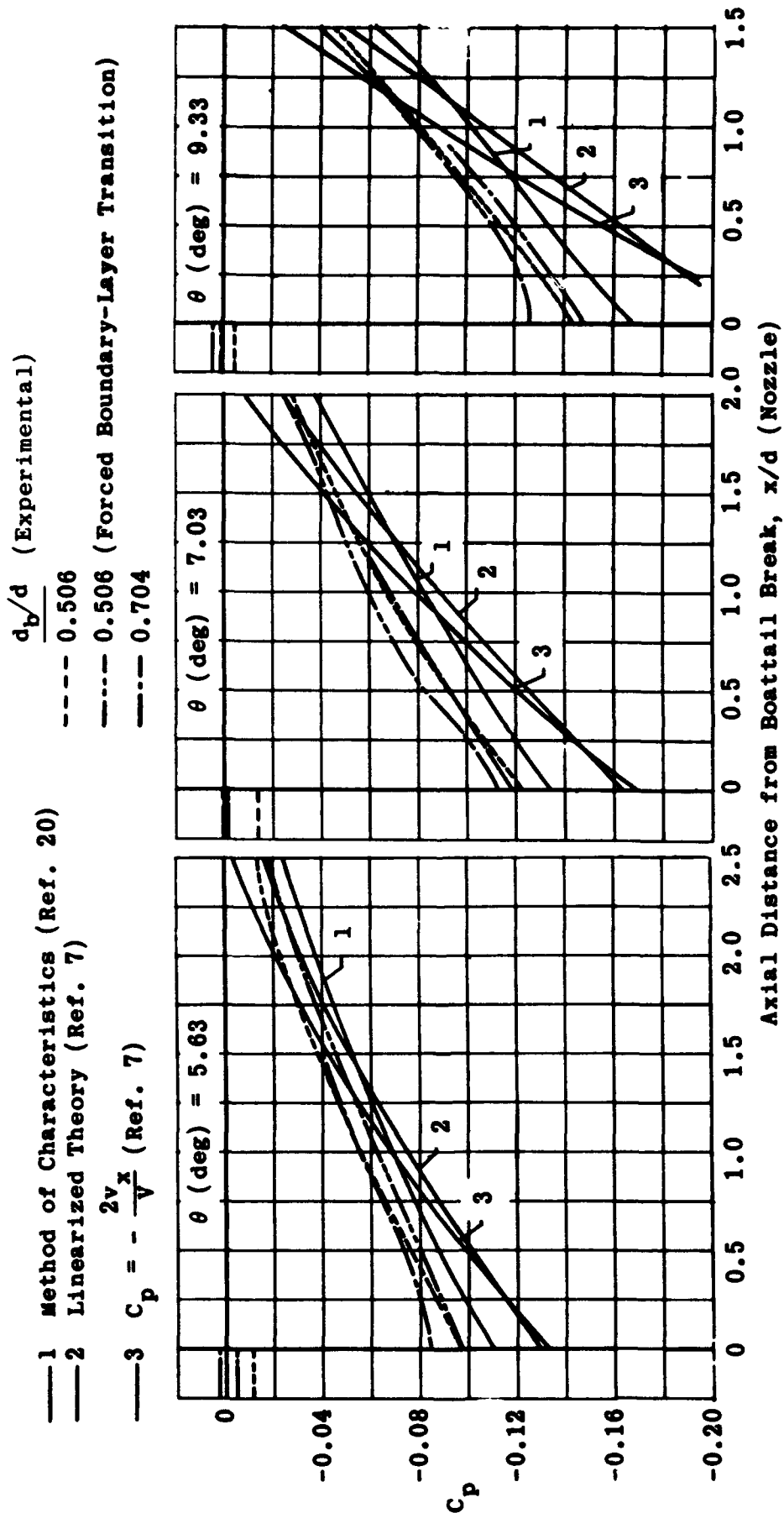
Fig. 4-78. Comparison of theoretical calculations for various boattails; M = 1.91, α = 0 deg. (Source: Ref. 150)
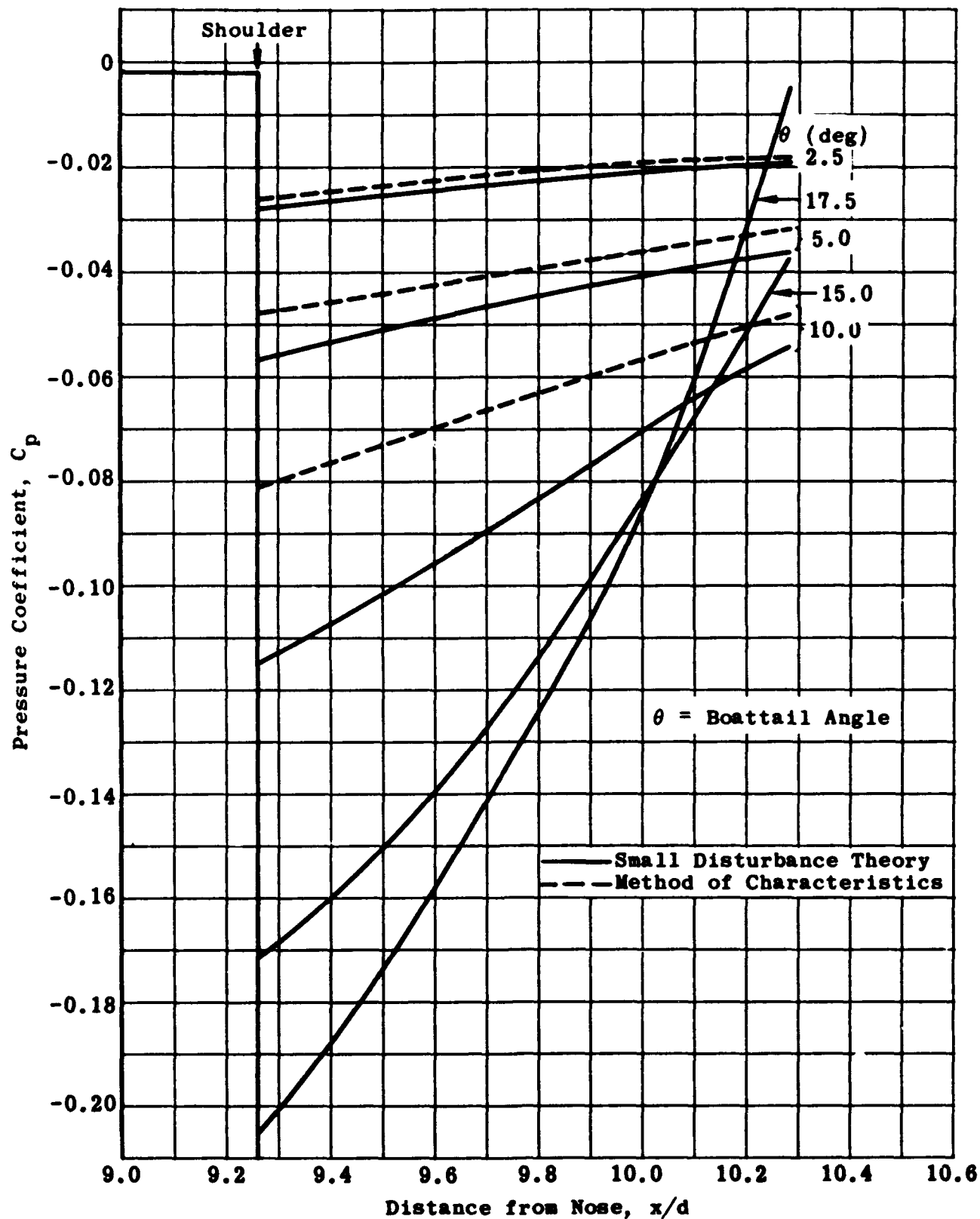
Fig. 4-79. Boattail pressures in terms of boattail angle calculated
by small disturbance method and characteristics method; M = 3.24,
α = 0 deg. (Source: Ref. 140)

Fig. 4-80   NAVWEPS Report 1488 (Vol. 3, Sec. 8)
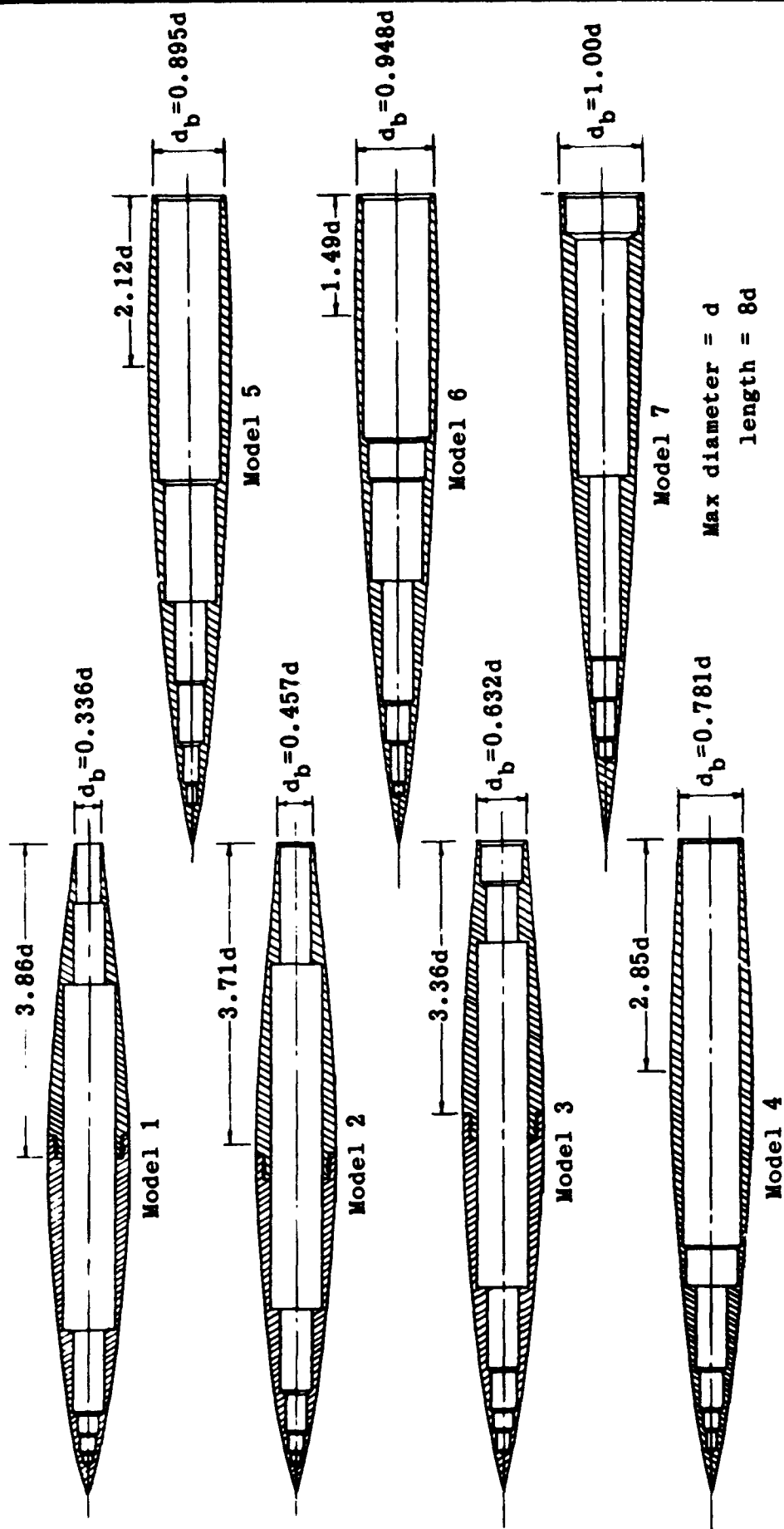
Fig. 4-80. Body shapes used for minimum drag studies. (Source: Ref. 84)

Model 1   Model 2   Model 3   Model 4

M = 1.62

M = 1.93

M = 2.41

Distance from Model Nose, x/ℓ
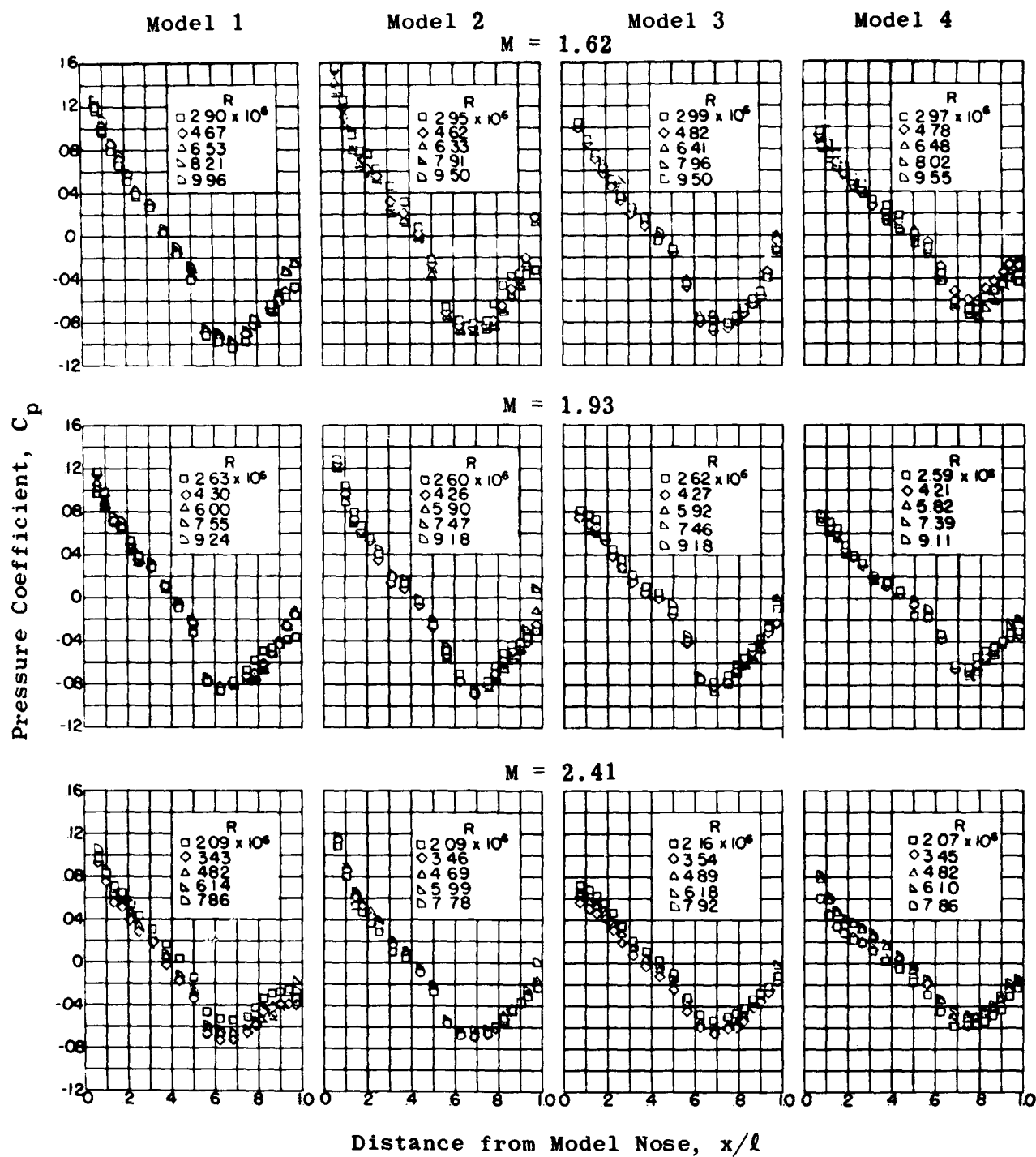
Fig. 4-81. Pressure distributions for varying Mach numbers and
Reynolds numbers for minimum drag bodies, models 1 to 4.
(Source: Ref. 84)

Fig. 4-82   NAVWEPS Report 1488 (Vol. 3, Sec. 8)
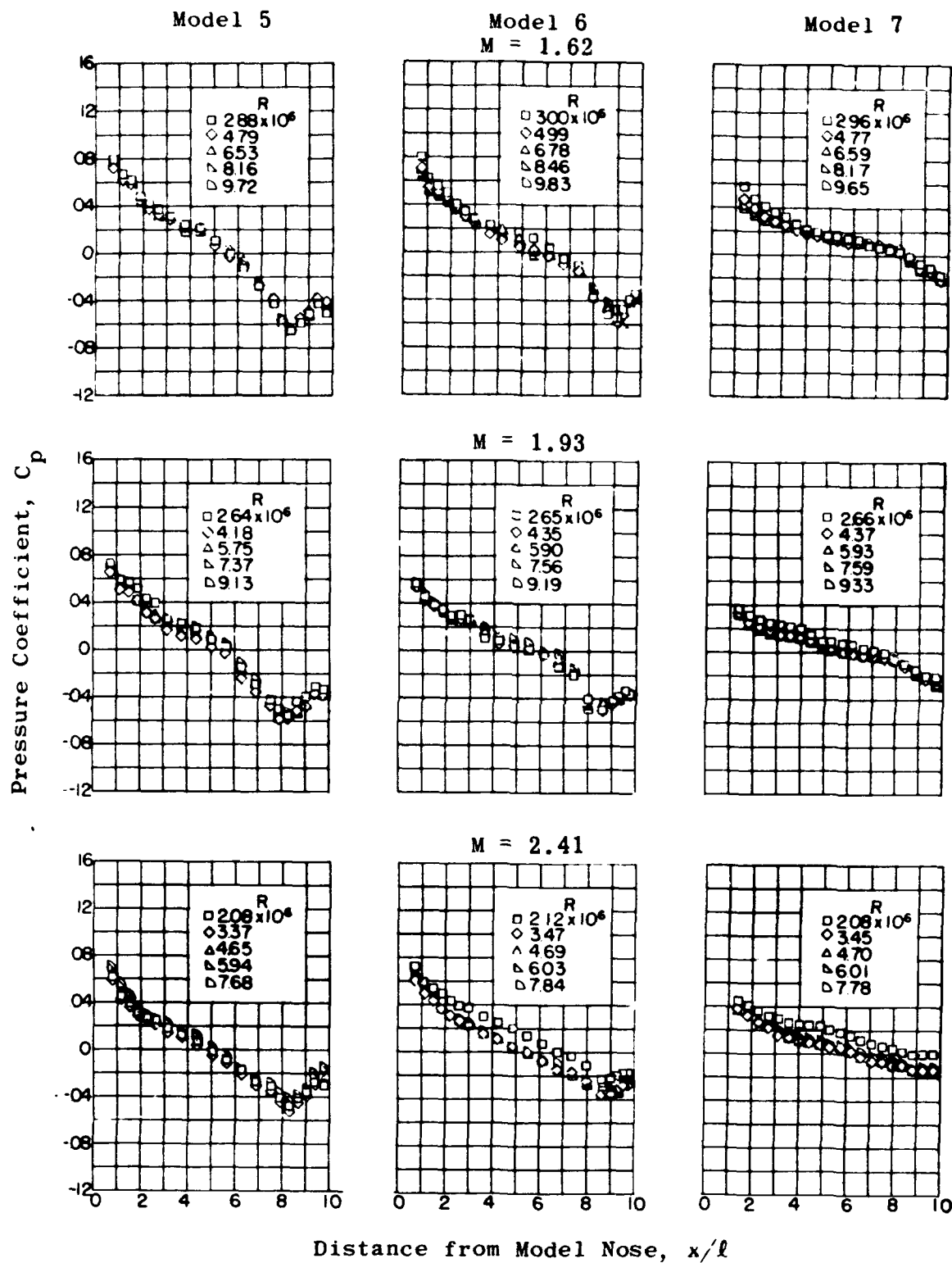
Fig. 4-82. Pressure distributions for varying Mach numbers and Reynolds numbers for minimum drag bodies, models 5 to 7. (Source: Ref. 84)

Numerical Solution (Ref. 85)
o Heberle, Wood, and Gooderum (Ref. 186)
□ Oliver (Ref. 88)
◇ Crawford and McCauley (Ref. 187)
▲ Charters (Unpublished BRL Photos)
▲ Sugimoto (Ref. 188)
⬚ Ladenburg, Winckler, and
    Van Voorhis (Ref. 189)
◌ Rainey (NACA TN 4170)
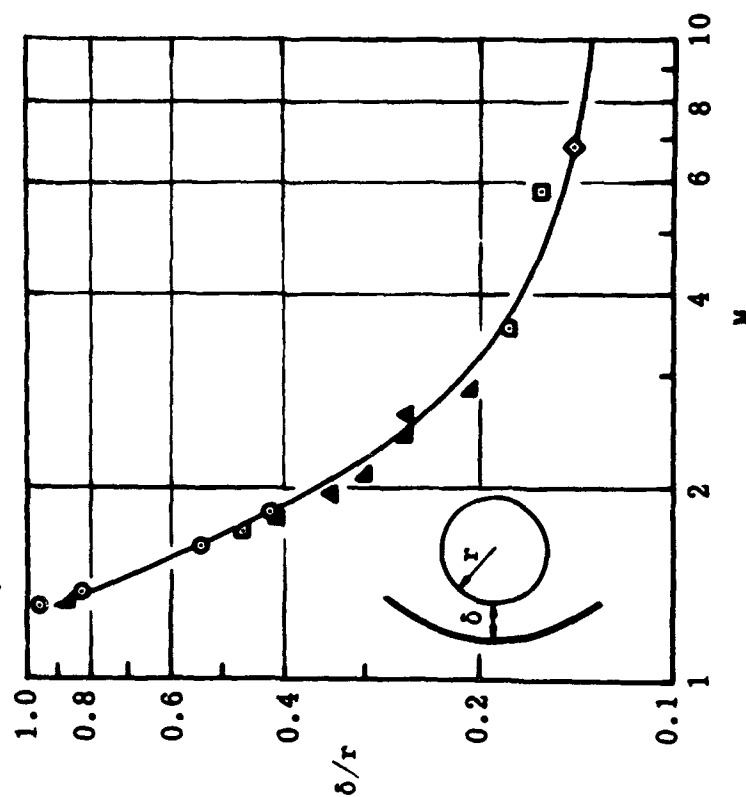
Fig. 4-84. Shock-wave stand-off distance for
spheres in air. (Source: Ref. 85)
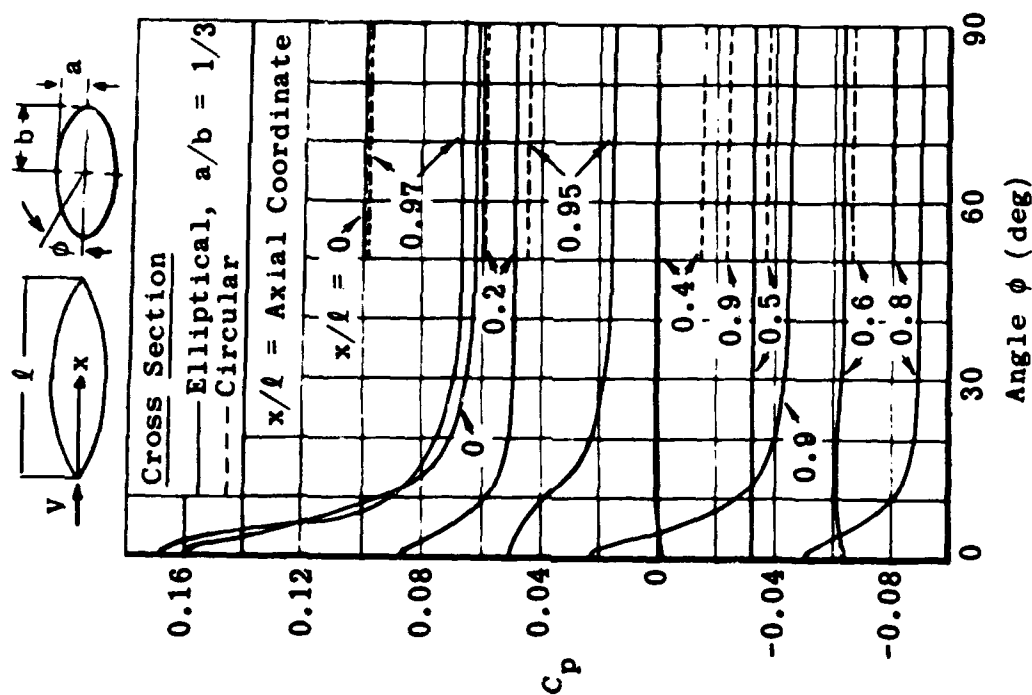
Fig. 4-83. Pressure distributions on parabolic-
arc bodies of elliptical and circular cross
section; effective $\ell/d = 10$, $M = 2$.
(Source: Ref. 69)

Fig. 4-85   NAVWEPS Report 1488 (Vol. 3, Sec. 8)
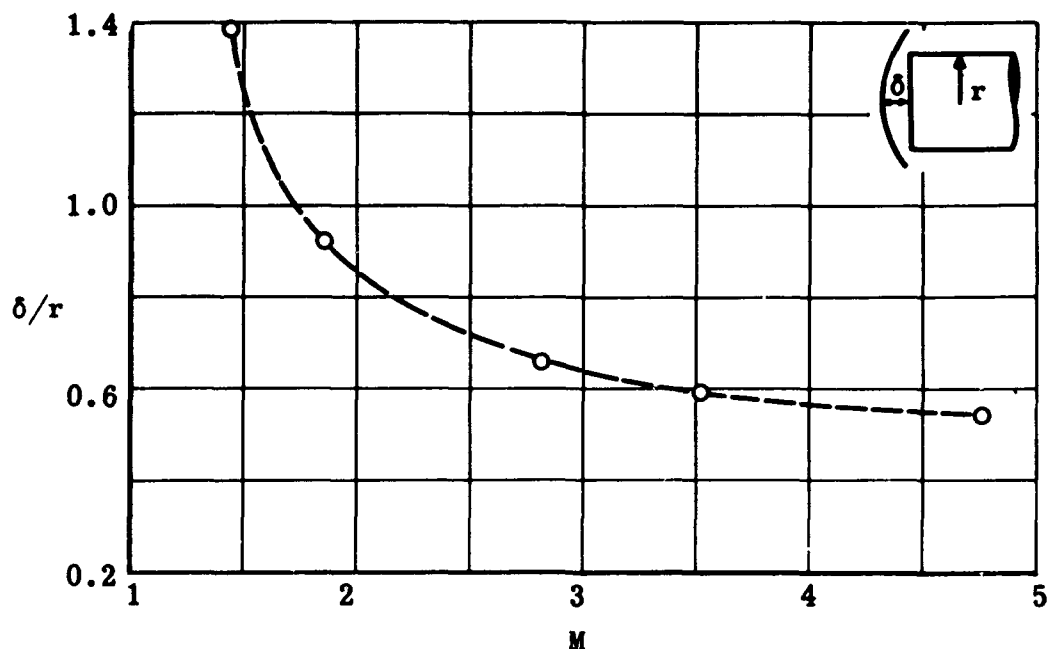
Fig. 4-85.   Shock-wave stand-off distance for a flat-faced cylinder.
(Source: Ref. 87)
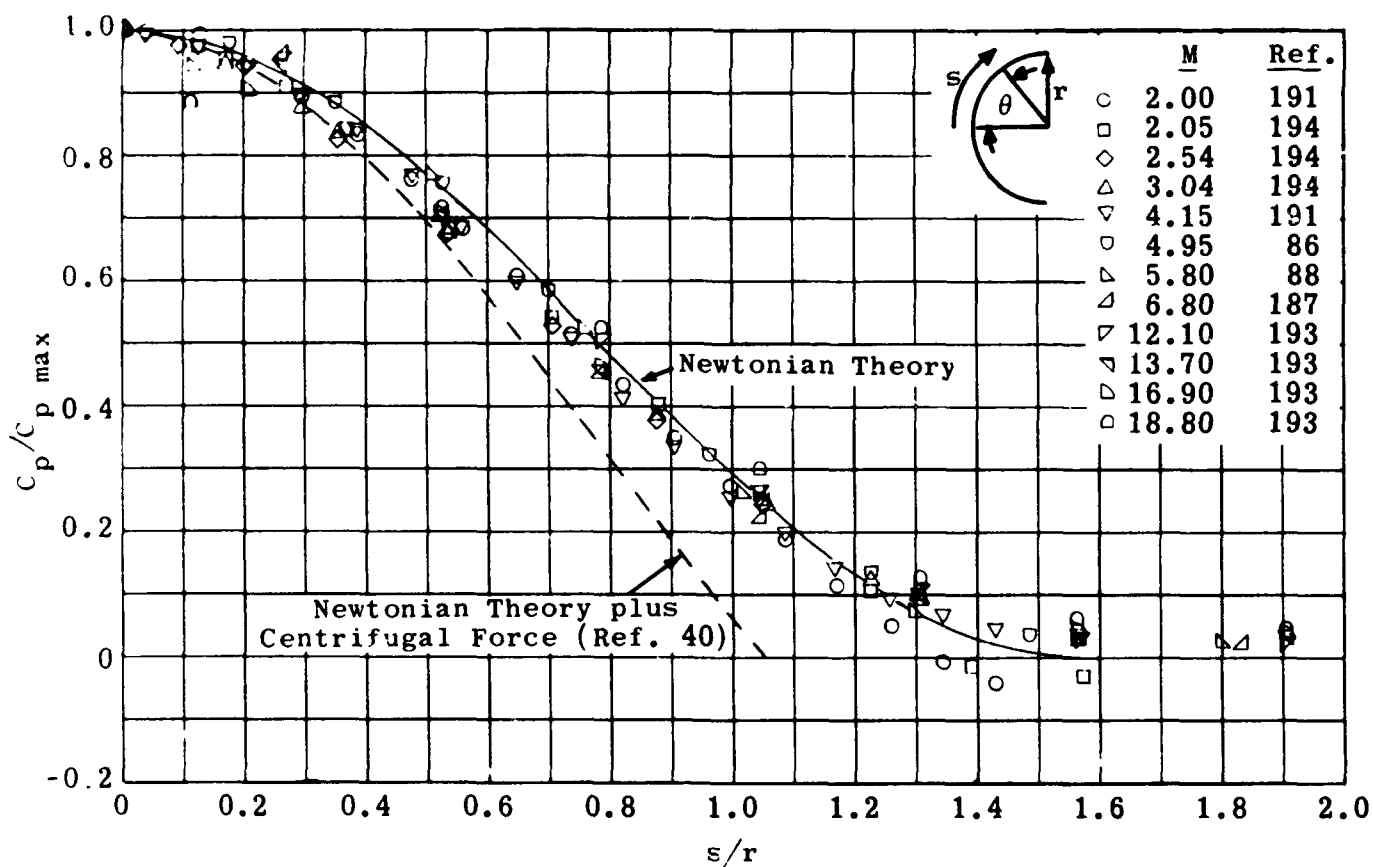
Fig. 4-86.   Compilation of pressure distributions around a hemi-
sphere for varying Mach numbers.   (Source: Ref. 86)
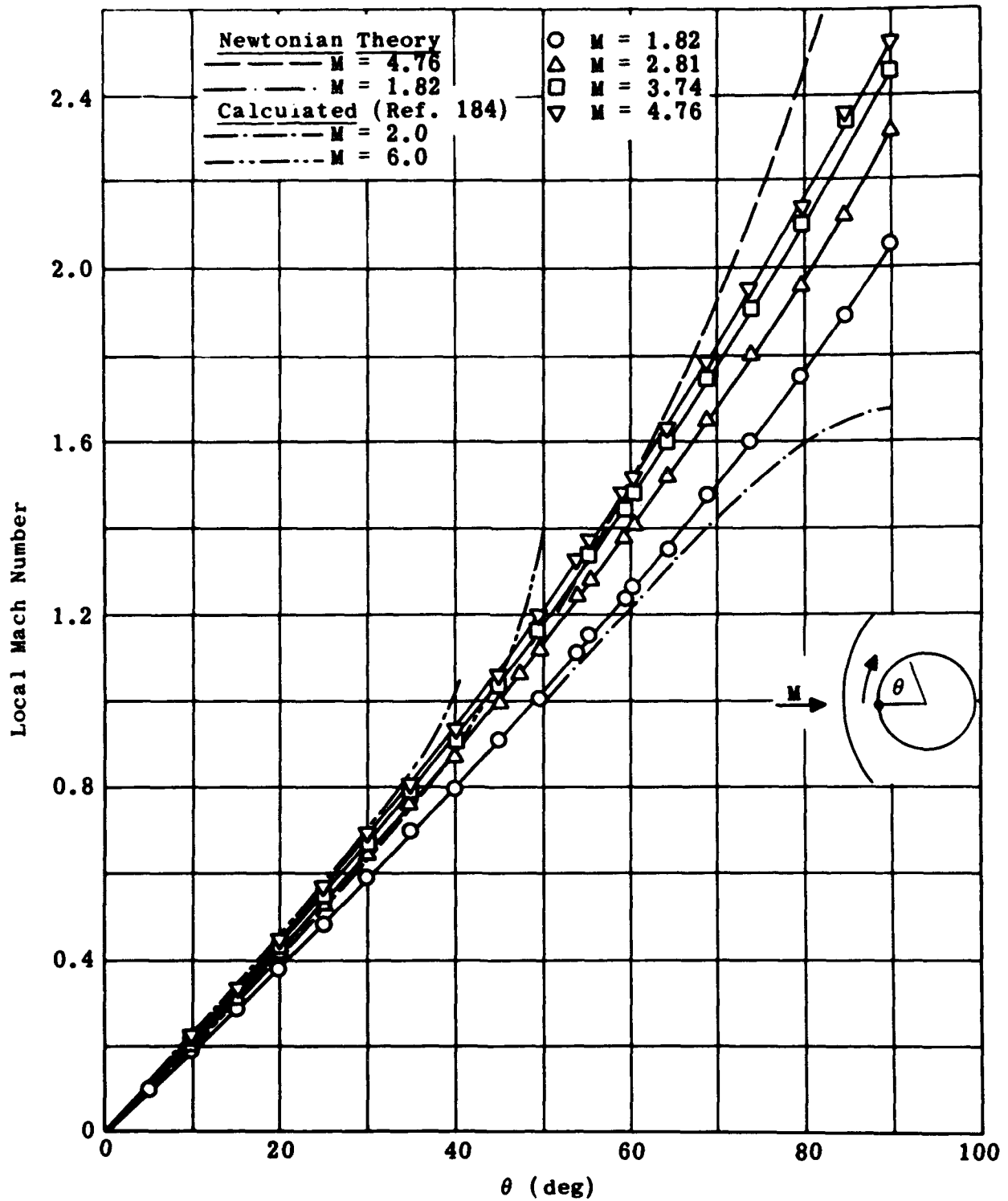
Fig. 4-87.   Mach-number distributions over a sphere for various
           free-stream Mach numbers. (Source: Ref. 87)

Fig. 4-88   NAVWEPS Report 1488 (Vol. 3, Sec. 8)
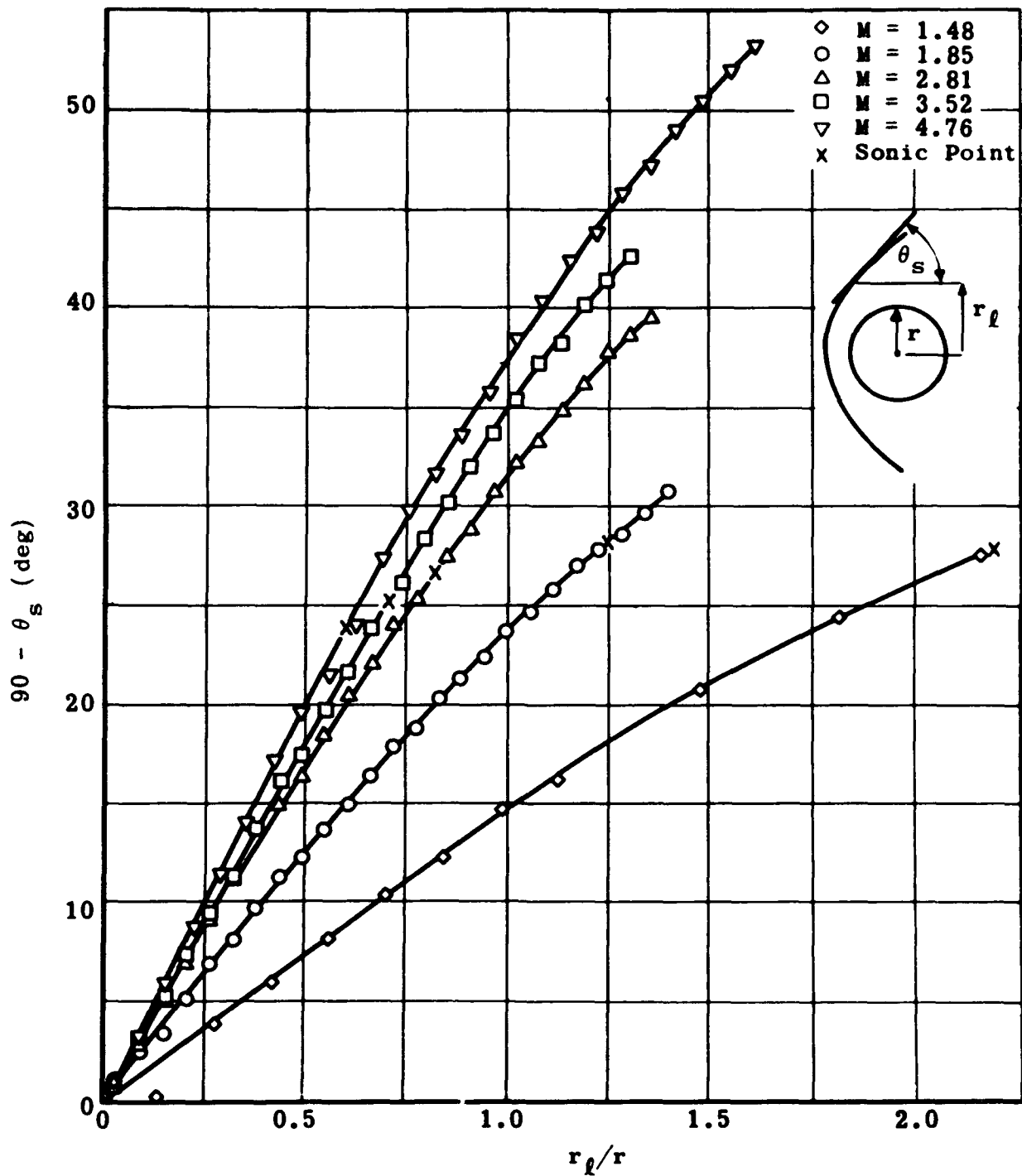
Fig. 4-88.   Local shock-wave angle for a sphere at various free-
stream Mach numbers. (Source: Ref. 87)

Fig. 4-90. Radius of curvature at the vertex of the shock wave due to a sphere at various Mach numbers. (Source: Ref. 87)

Fig. 4-89. Location of the sonic line between a sphere surface and the shock wave for various free-stream Mach numbers. (Source: Ref. 87)

Fig. 4-91   NAVWEPS Report 1488 (Vol. 3, Sec. 8)
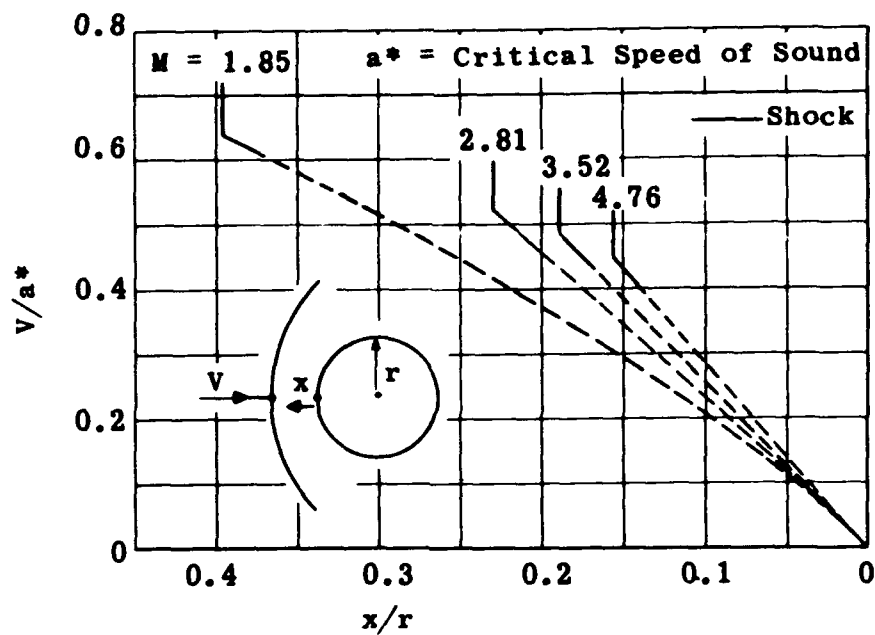
Fig. 4-91. Estimated velocity distributions along an axial stream-
line between a sphere and its shock wave. (Source: Ref. 87)
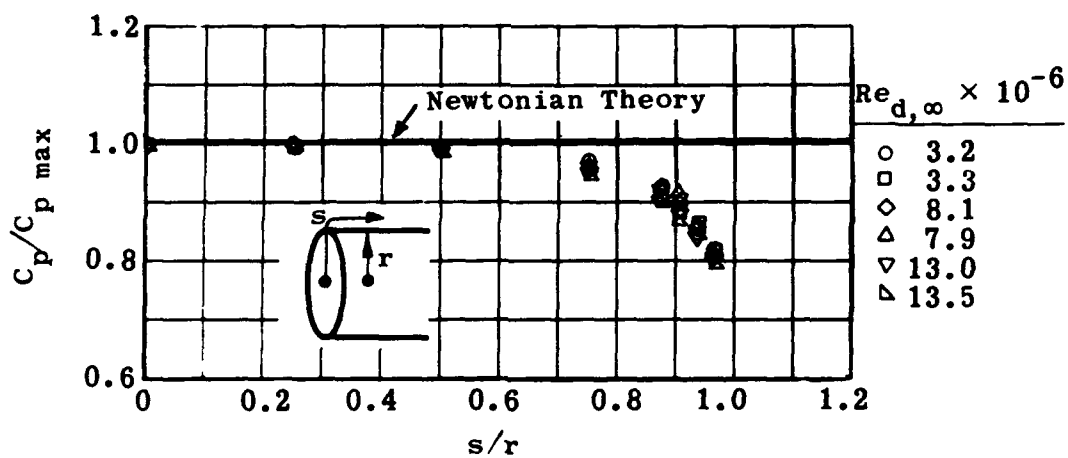
Fig. 4-92. Comparison of experimental and theoretical pressure
distributions on a flat-faced cylinder at M = 4.95.
(Source: Ref. 86)
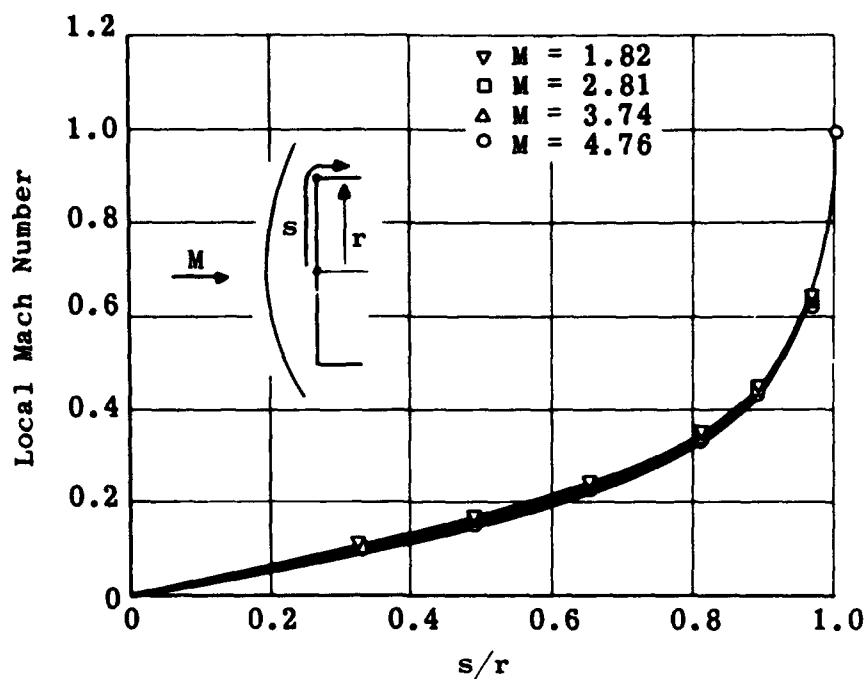
Fig. 4-93. Local Mach-number distribution over the face of a disk
for various free-stream Mach numbers. (Source: Ref. 87)
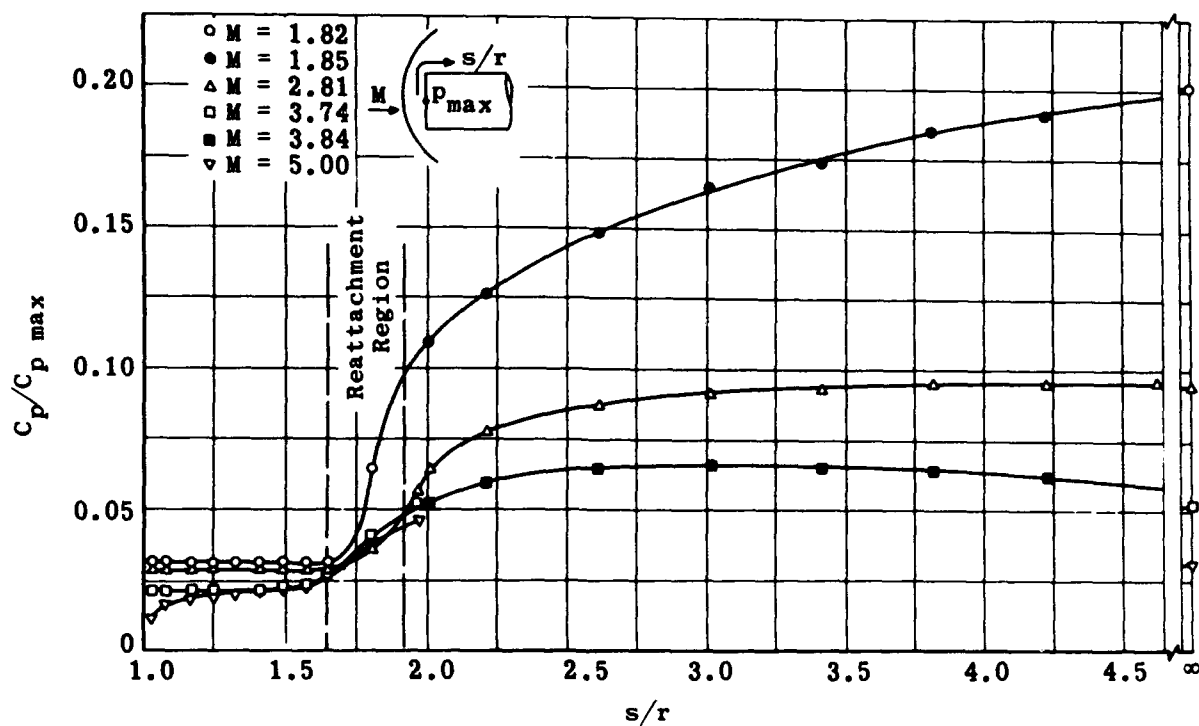
Fig. 4-94. Pressure distribution over a flat-faced cylinder for
various Mach numbers. (Source: Ref. 87)

143

Fig. 4-95   NAVWEPS Report 1488 (Vol. 3, Sec. 8)
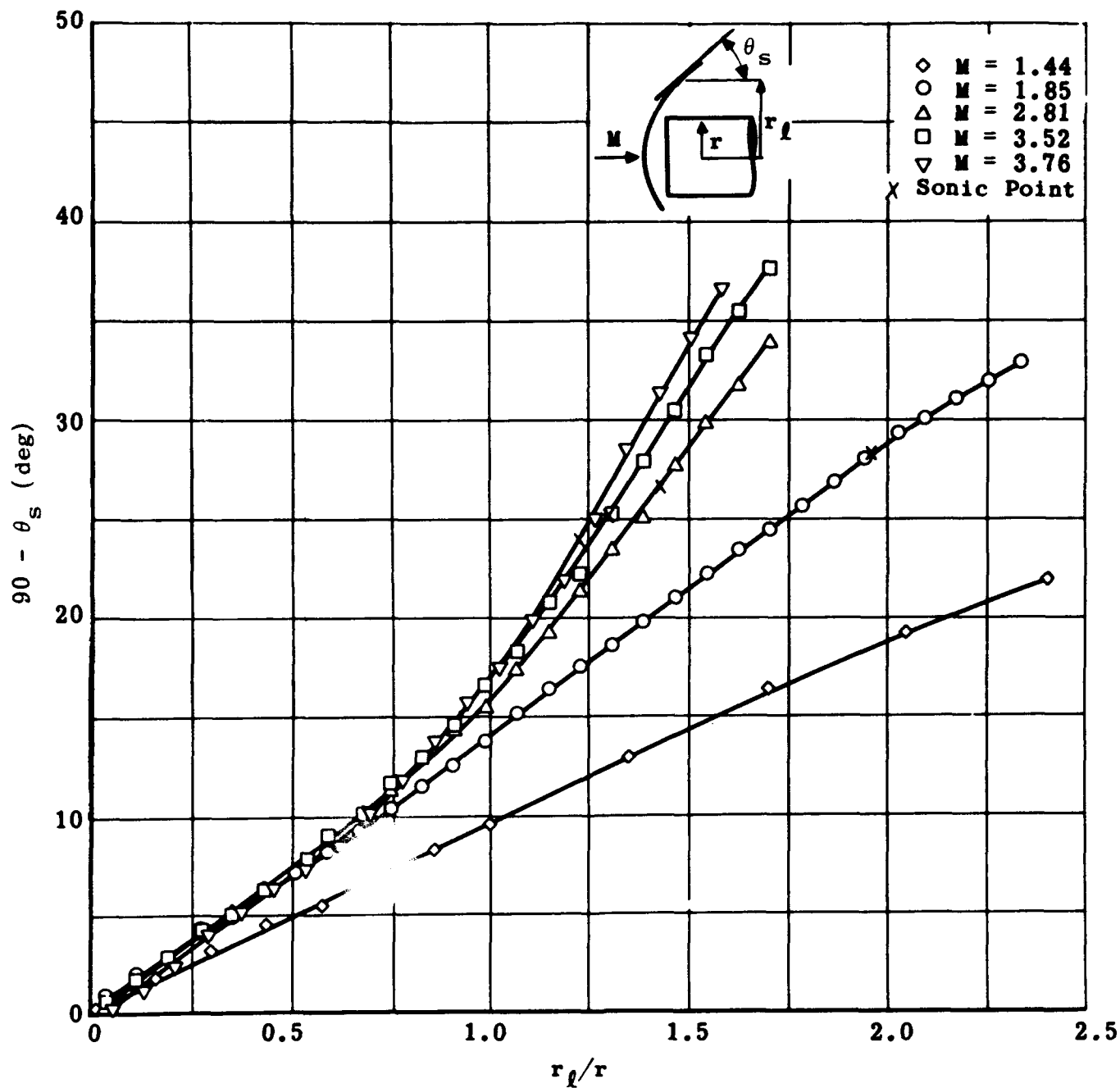
Fig. 4-95.   Shock-wave angle for a flat-faced cylinder at various
Mach numbers. (Source: Ref. 87)
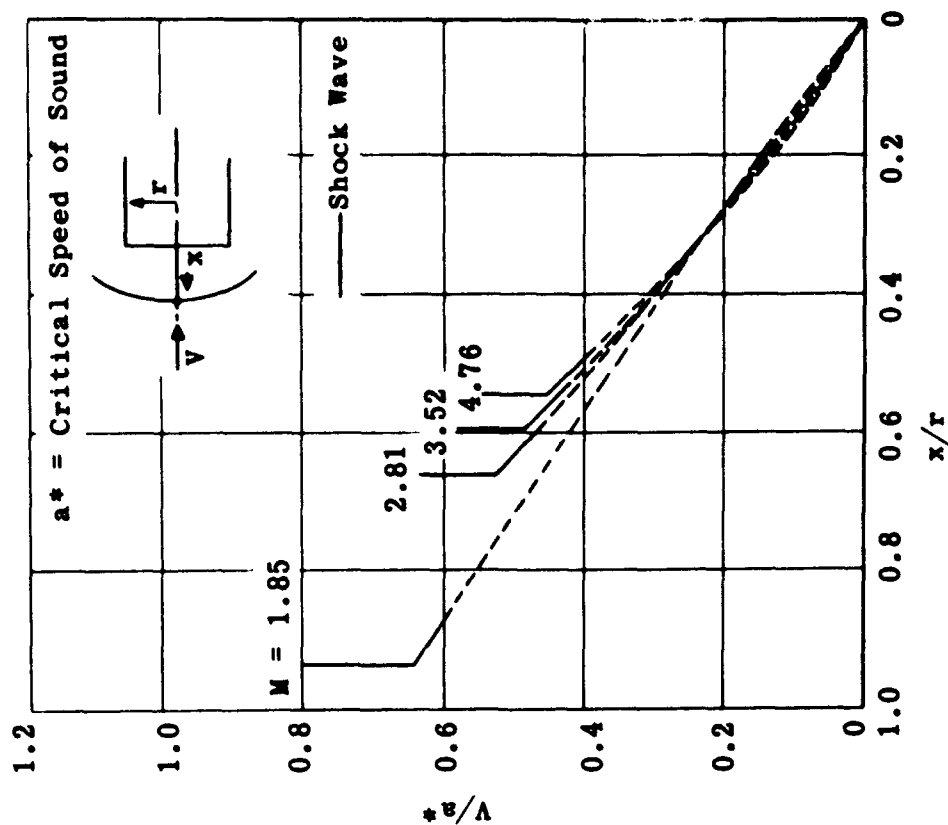
Fig. 4-97. Axial velocity distribution between a flat-faced cylinder and its shock wave. (Source: Ref. 87)
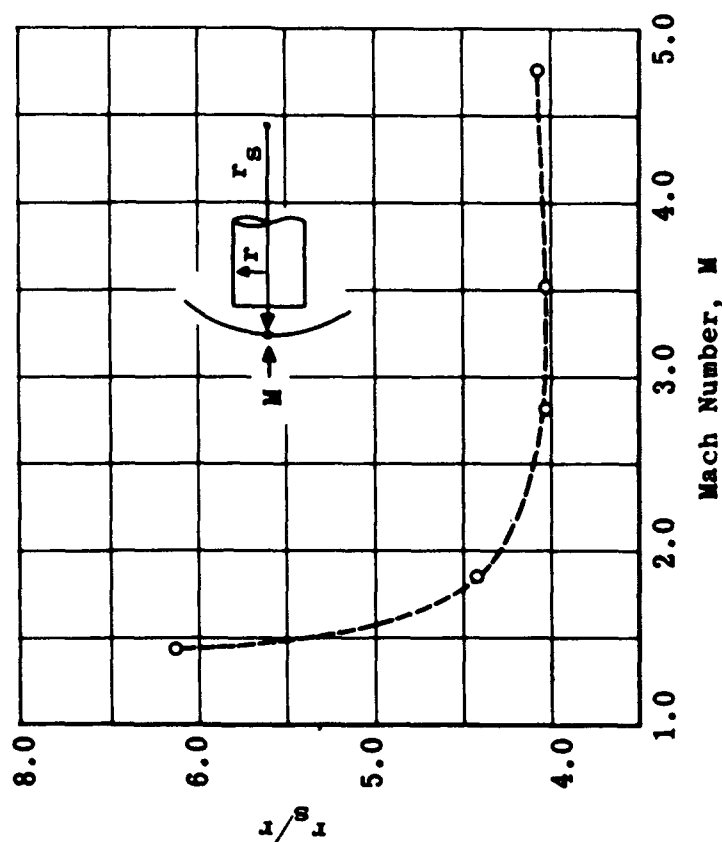
Fig. 4-96. Radius of curvature at the shock-wave vertex of a flat-faced cylinder at various Mach numbers. (Source: Ref. 87)

Fig. 4-98   NAVWEPS Report 1488 (Vol. 3, Sec. 8)
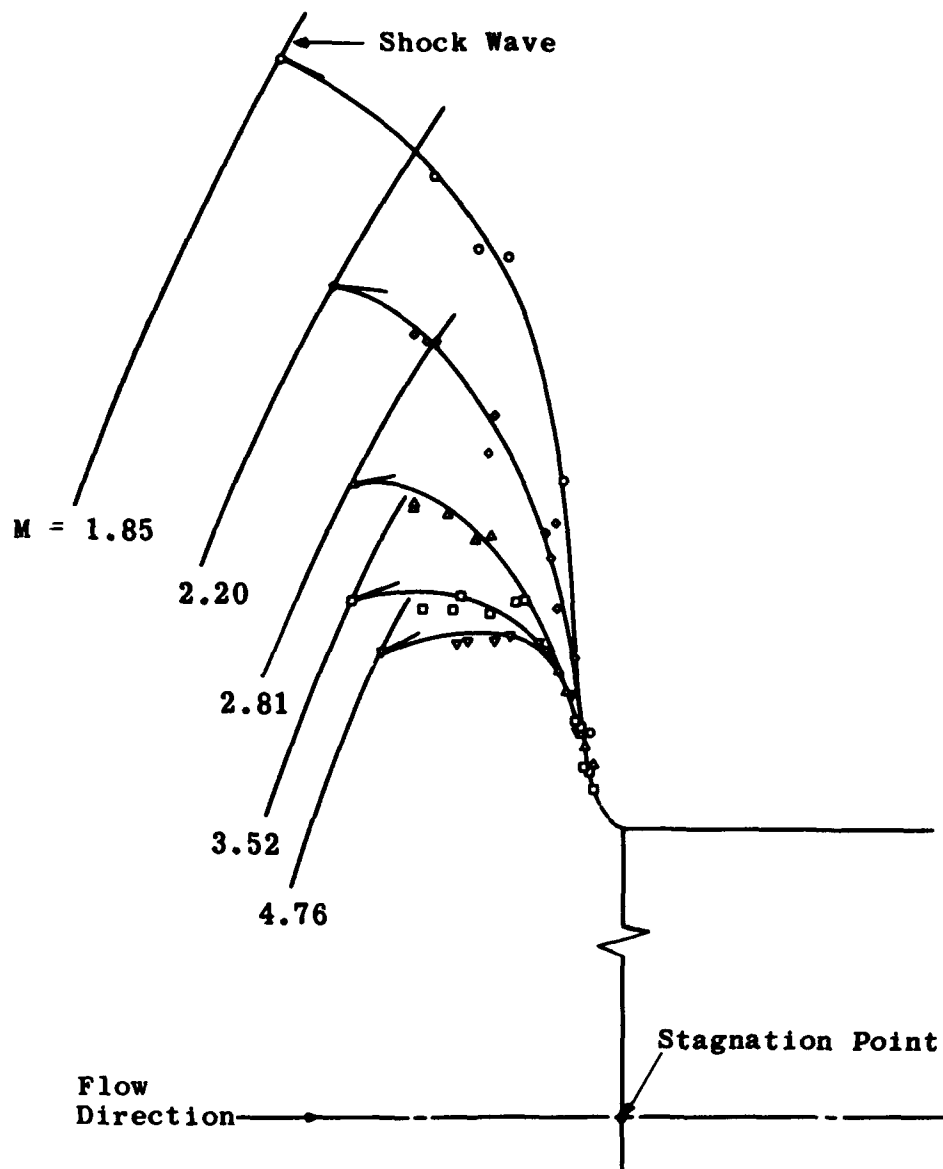
Fig. 4-98. Location of the sonic line between a flat-faced
cylinder and the shock wave for various free-stream
Mach numbers. (Source: Ref. 87)
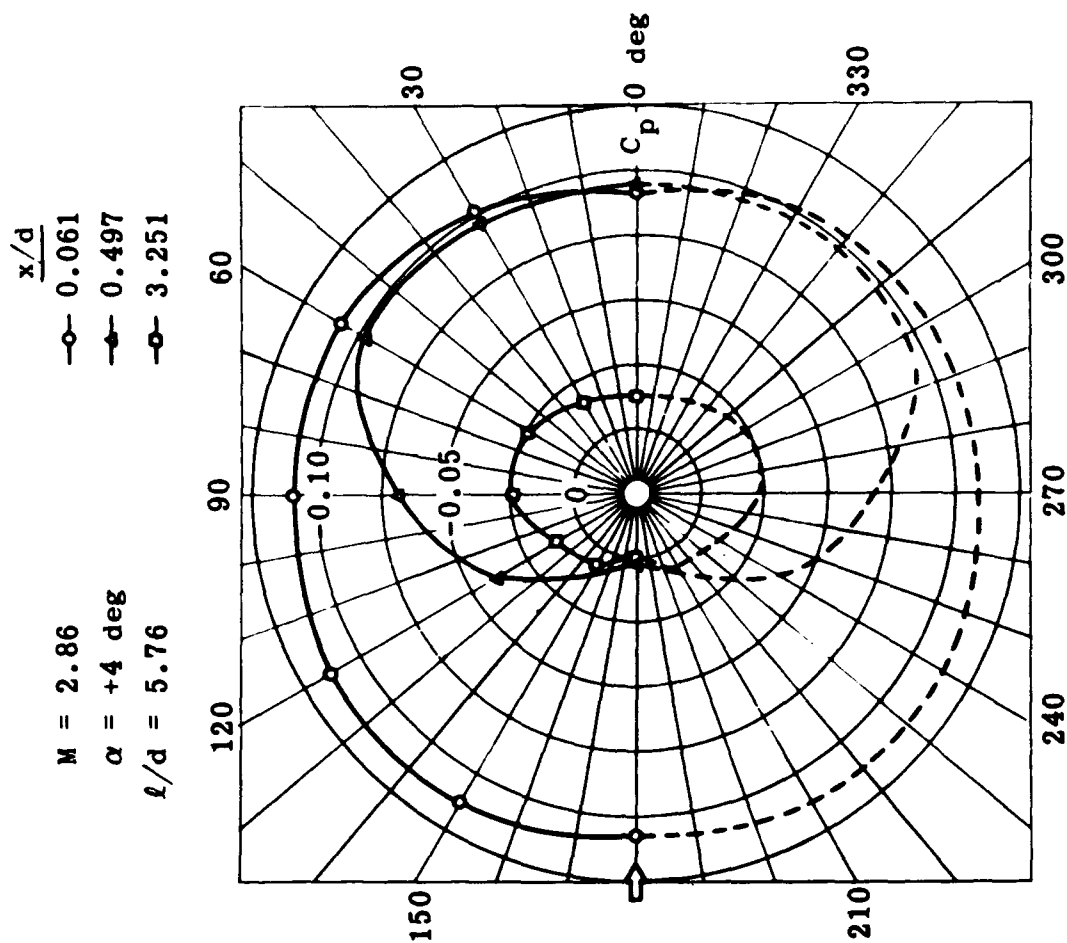
Fig. 4-100. Circumferential pressure distribu-
tions at three stations on a cylinder at
M = 2.86. (Source: Ref. 92)
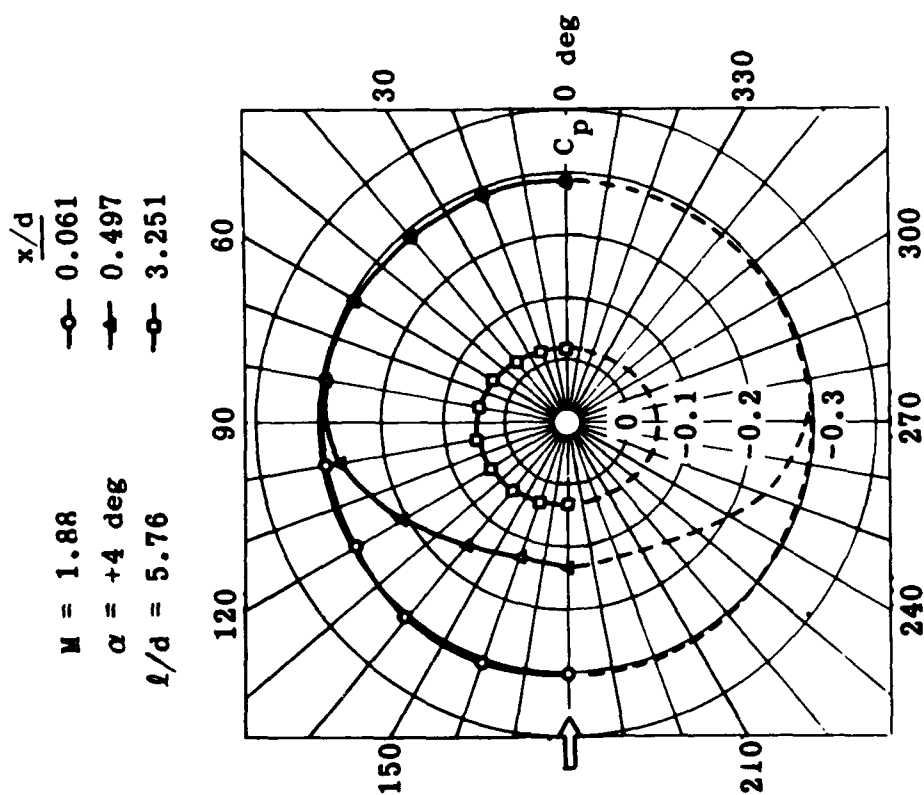
Fig. 4-99. Circumferential pressure distribu-
tions at three stations on a cylinder at
M = 1.88. (Source: Ref. 92)

147

Fig. 4-101   NAVWEPS Report 1488 (Vol. 3, Sec. 8)
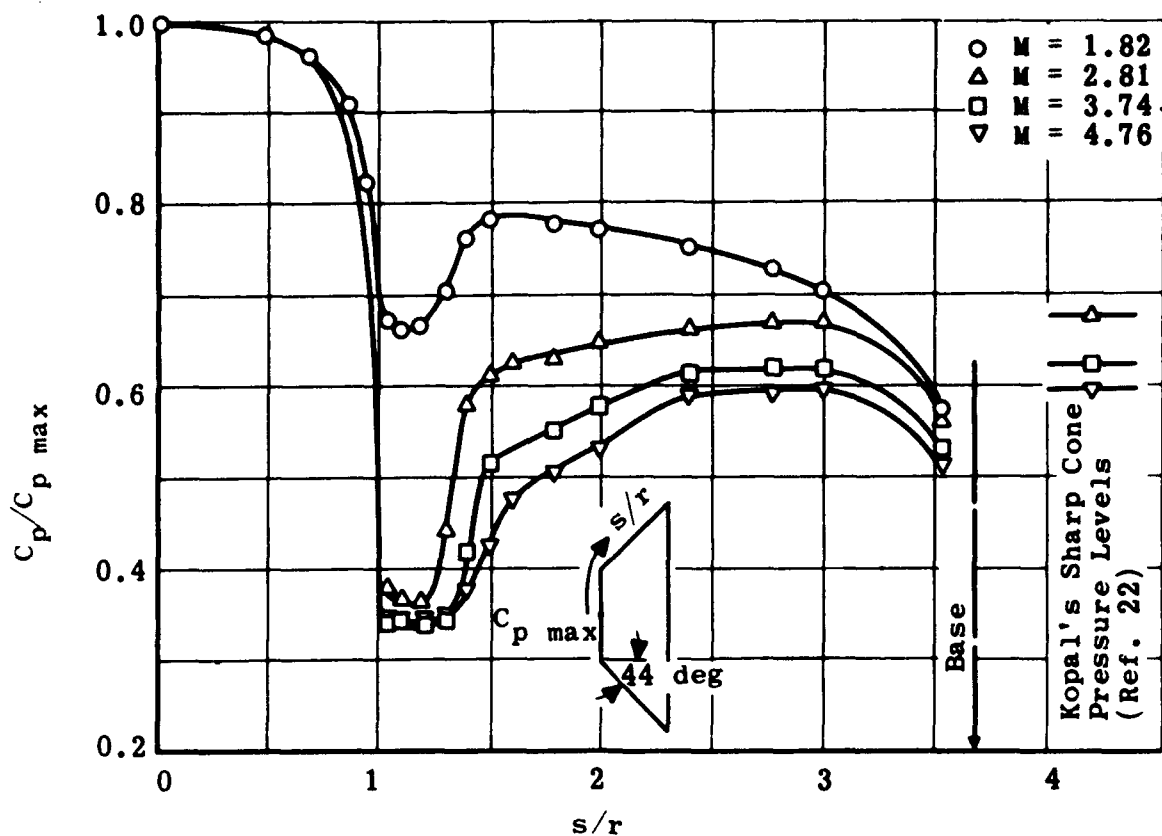
Fig. 4-101.   Pressure distribution over a truncated cone at
several Mach numbers. (Source: Ref. 87)
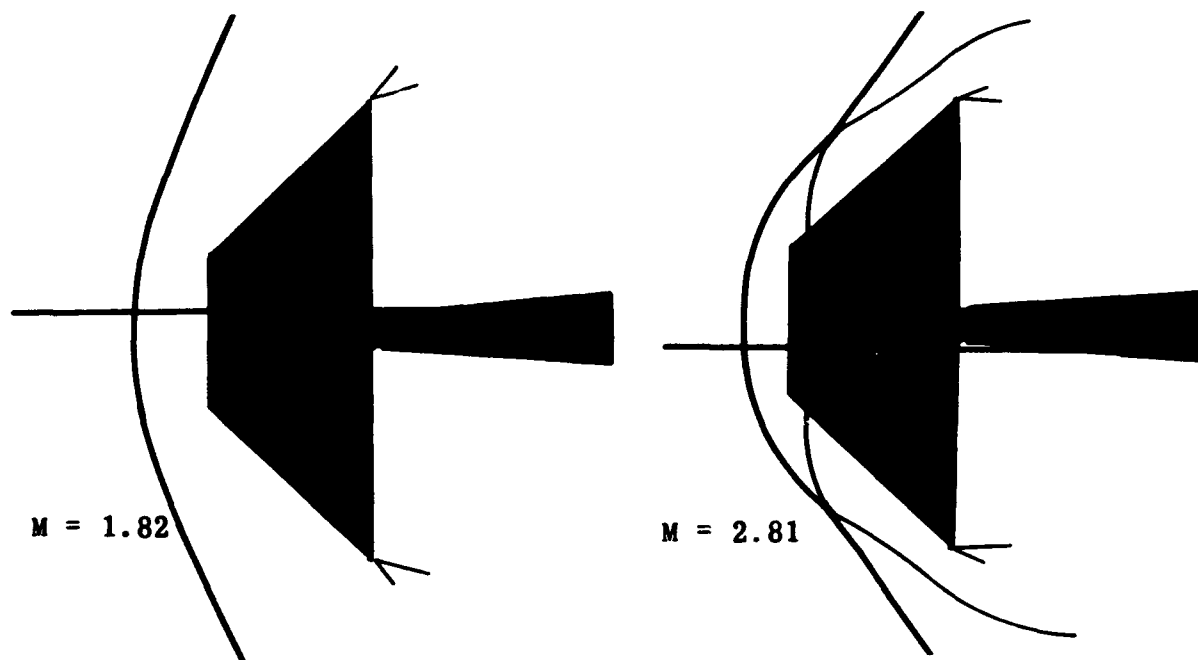
Fig. 4-102.   Shock-wave pattern of a truncated cone at M = 1.82
and 2.81. (From schlieren shadowgraphs, Ref. 87)
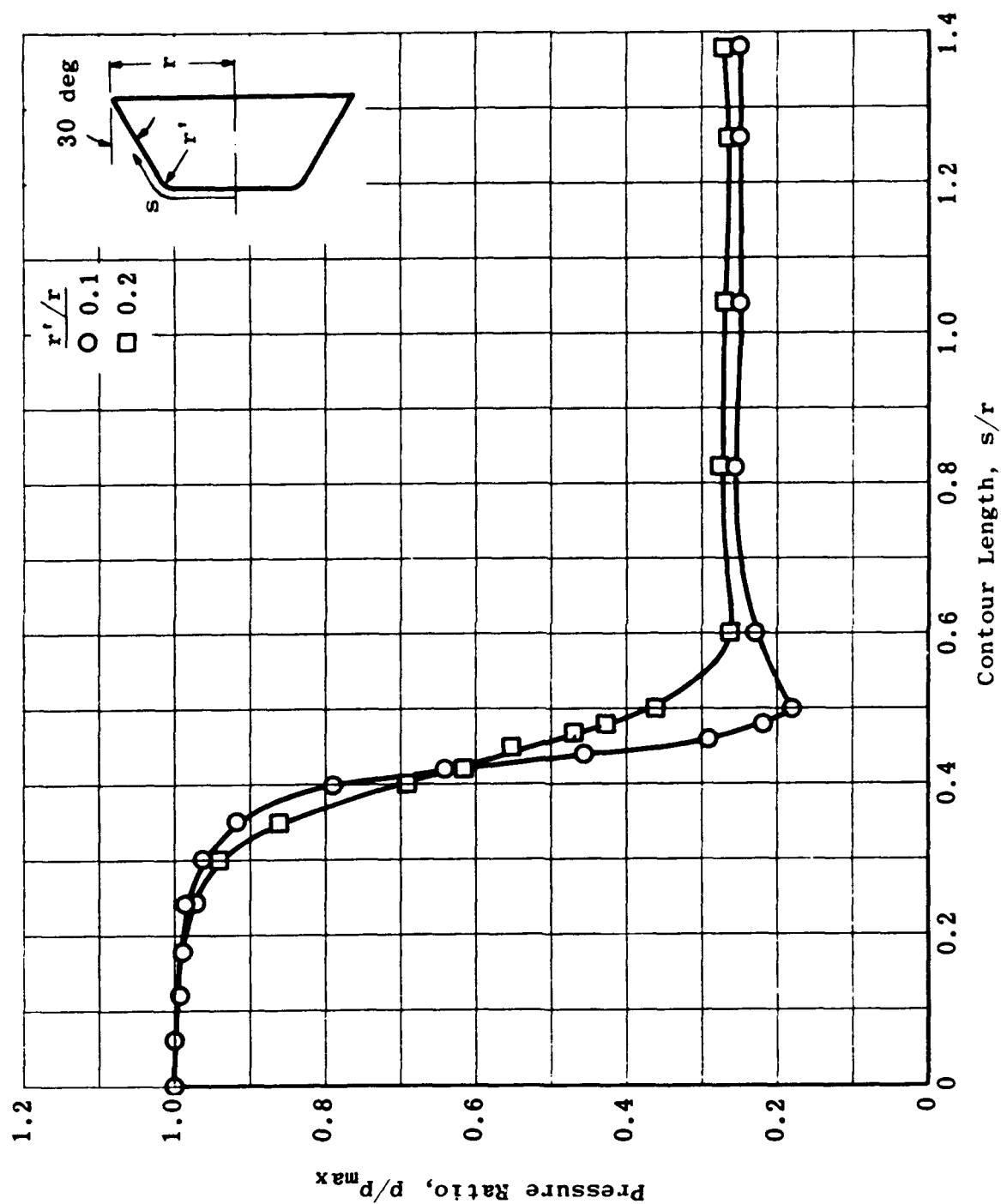
Fig. 4-103. Effect of corner radius on pressure distribution over a truncated cone at M = 4.84; r'/r = 0.1 and 0.2. (Source: Ref. 89)

Fig. 4-104   NAVWEPS Report 1488 (Vol. 3, Sec. 8)
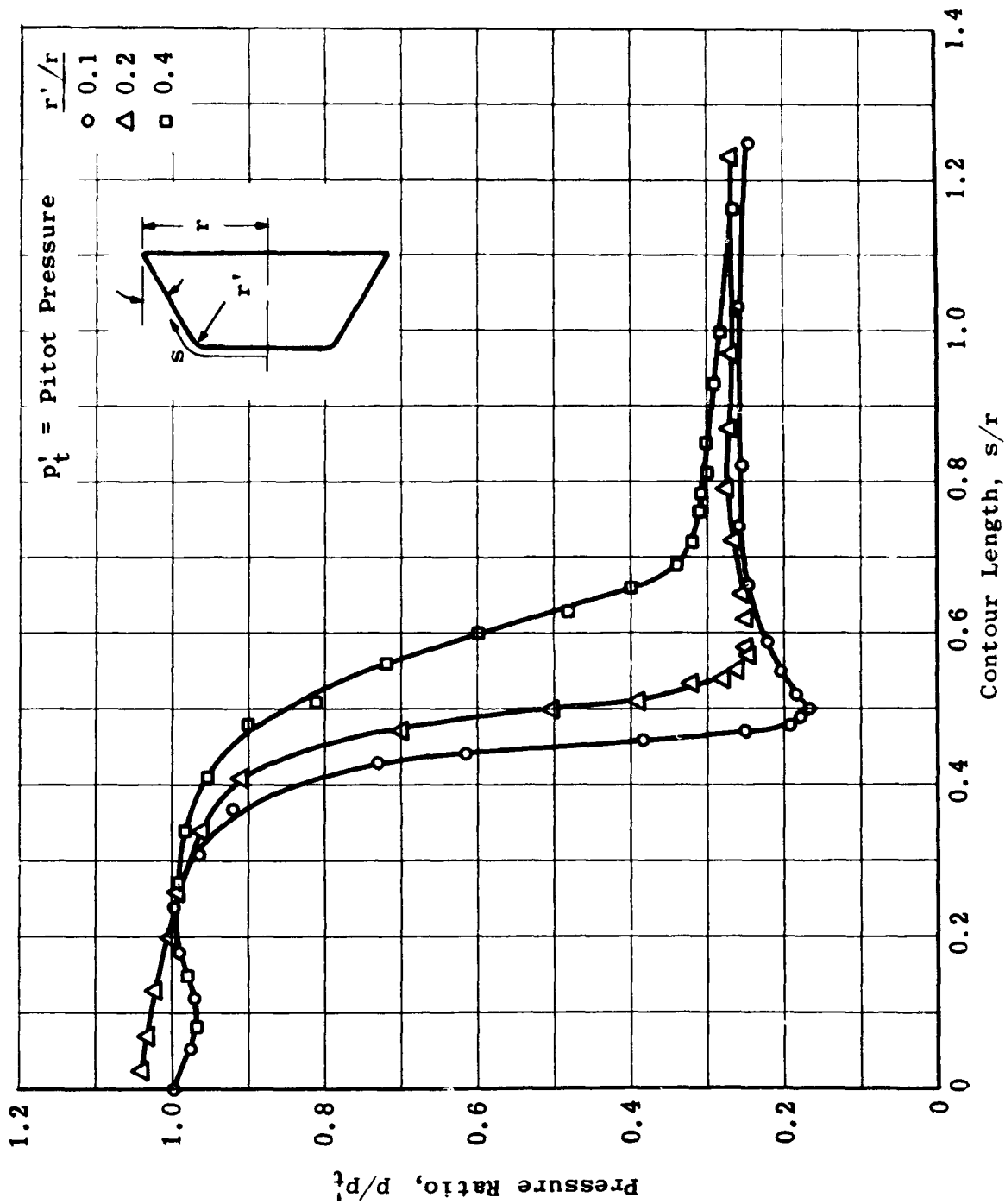
Fig. 4-104. Effect of corner radius on pressure distribution over a faired truncated cone at M = 4.84; r'/r = 0.1, 0.2, and 0.4. (Source: Ref. 89)
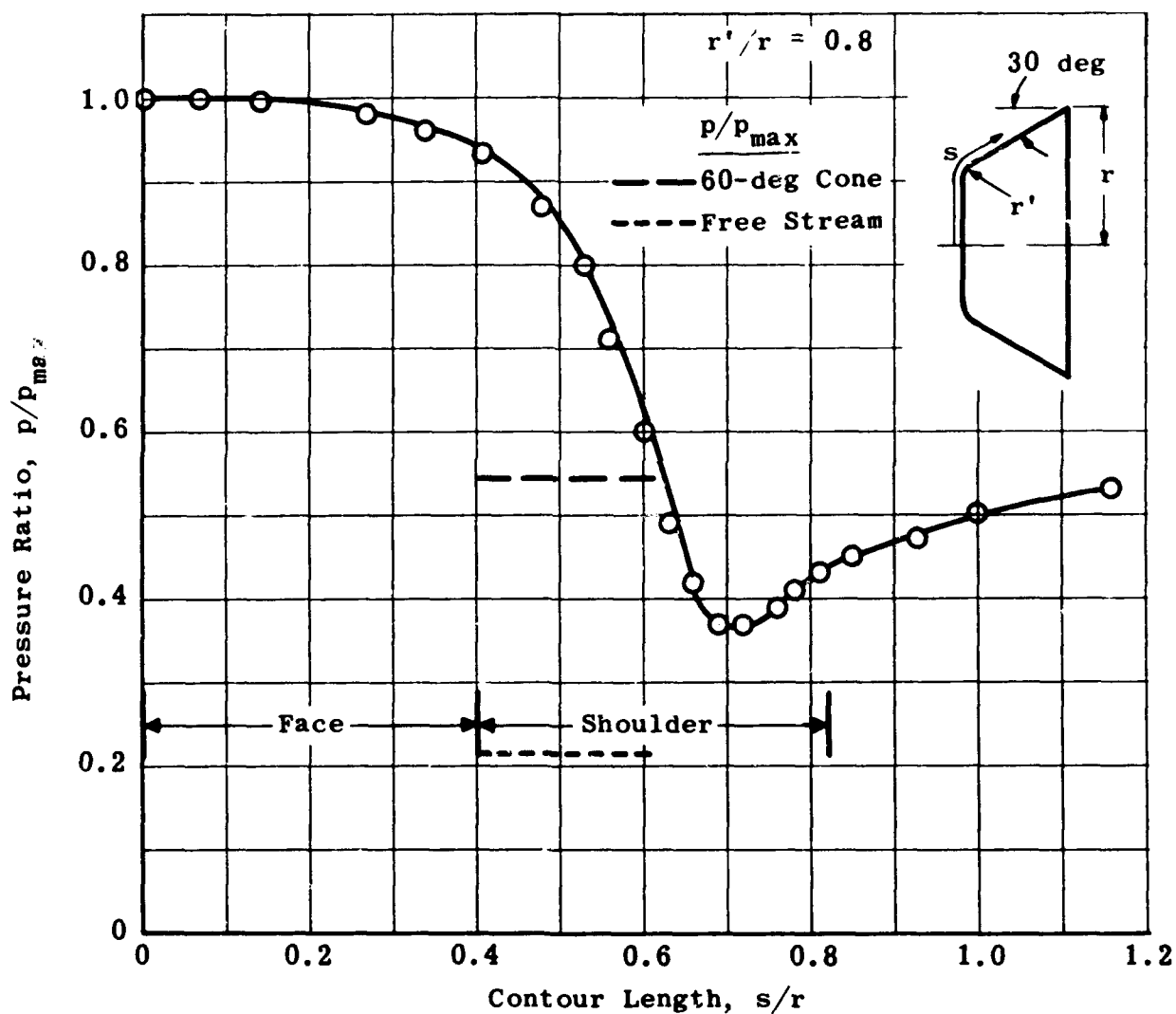
Fig. 4-105. Effect of corner radius on pressure distribution over a faired truncated cone at M = 1.79; r'/r = 0.8. (Source: Ref. 89)

Fig. 4-106   NAVWEPS Report 1488 (Vol. 3, Sec. 8)
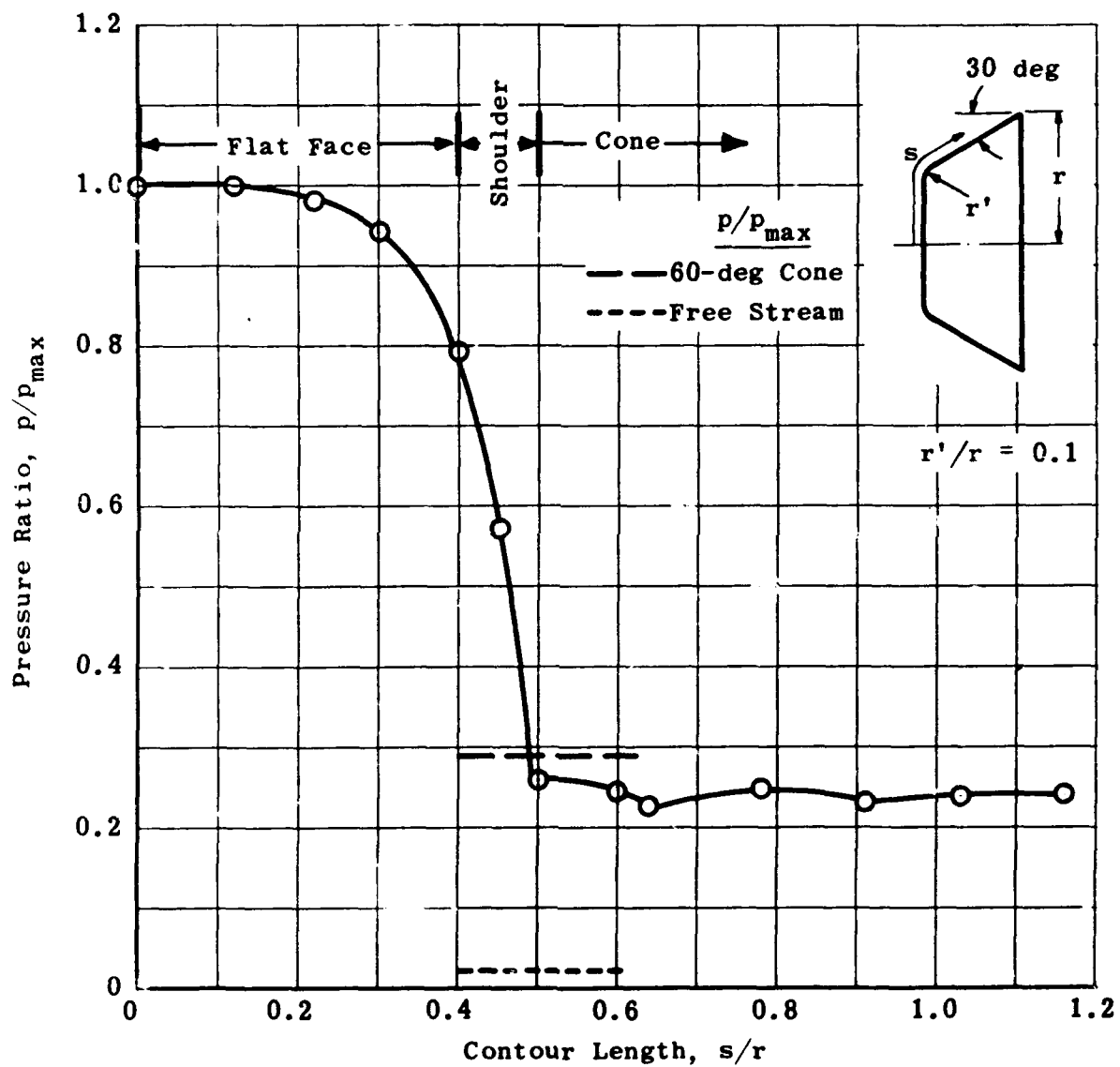
Fig. 4-106. Effect of corner radius on pressure distributions over a truncated cone at M = 7.2; r'/r = 0.1. (Source: Ref. 89)
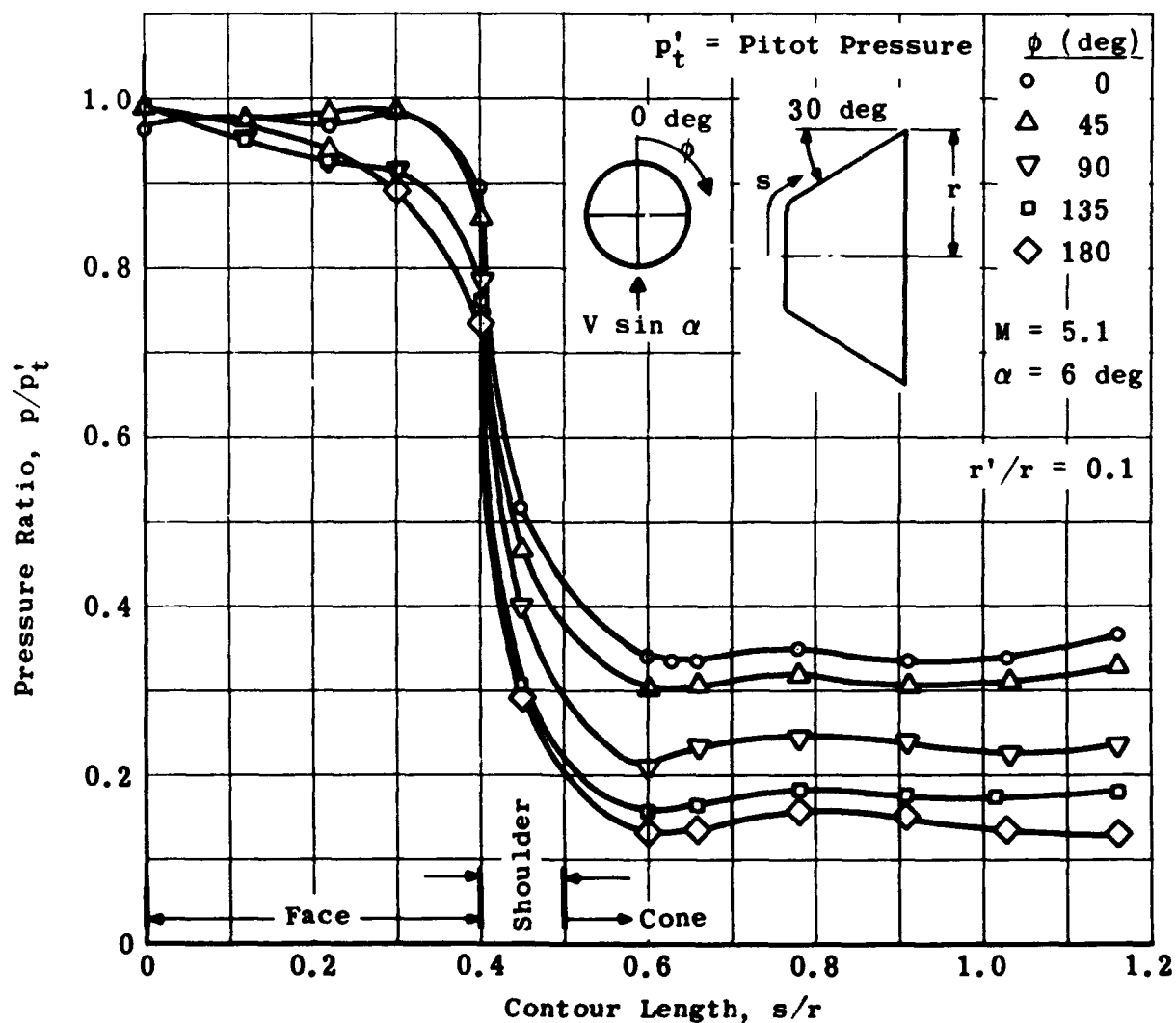
Fig. 4-107.   Pressure distribution on a truncated cone; α = 6 deg,
M = 5.1.   (Source: Ref. 89)

Fig. 4-108   NAVWEPS Report 1488 (Vol. 3, Sec. 8)
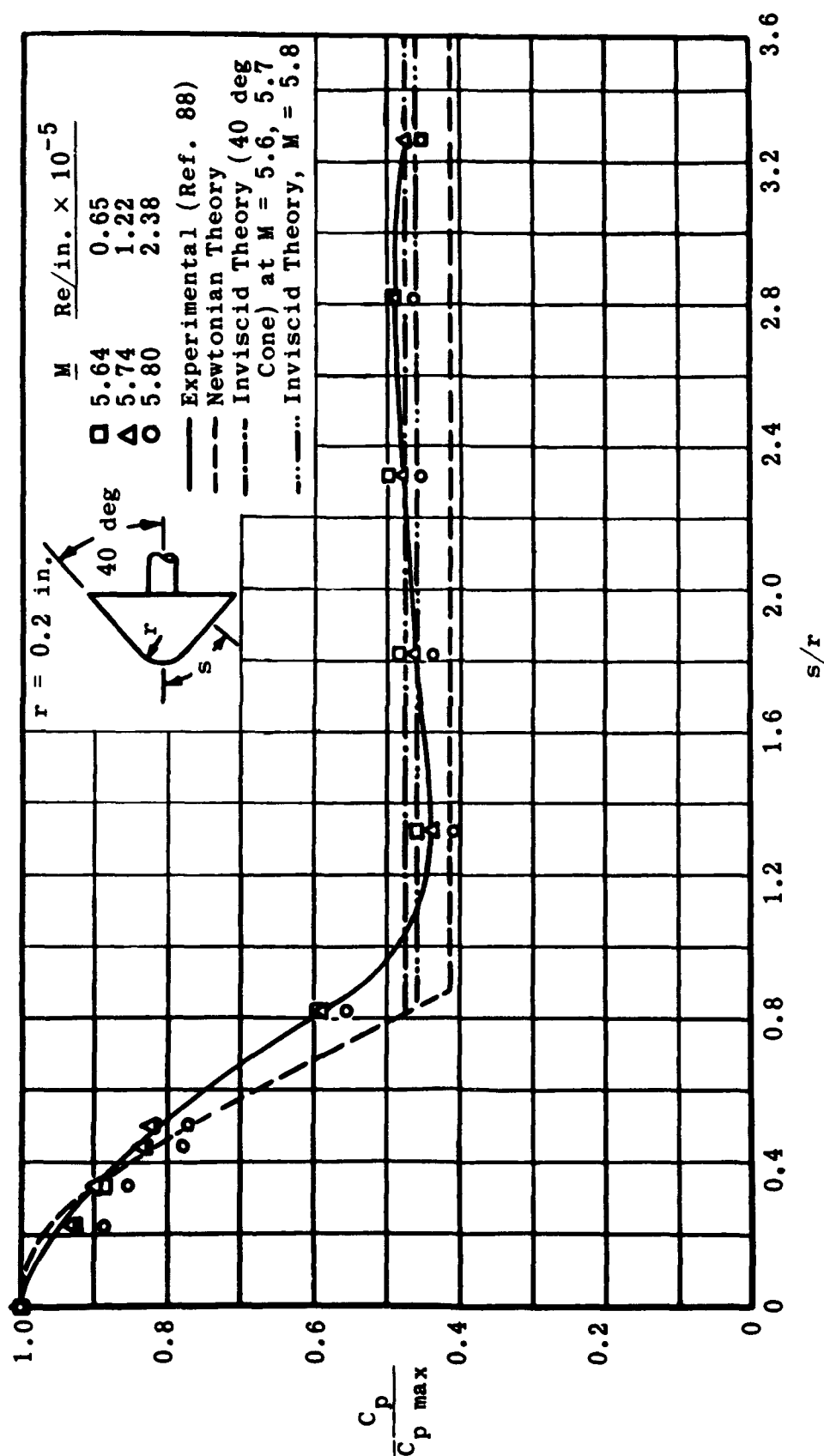
Fig. 4-108. Comparison of theoretical and experimental pressure distribution on a spherical-nosed cone at M = 5.64, 5.74, and 5.80. (Source: Ref. 88)

Nose No. 1

x	y
0.024	0.353
0.047	0.464
0.071	0.543
0.094	0.606
0.118	0.659
0.141	0.704
0.165	0.744
0.188	0.779
0.212	0.810
0.235	0.839
0.259	0.864
0.282	0.887
0.306	0.908
0.329	0.926
0.353	0.943
0.376	0.958
0.400	0.971
0.423	0.982
0.447	0.992
0.470	1.000

Nose No. 2

x	y
0.019	0.417
0.038	0.524
0.057	0.598
0.076	0.656
0.095	0.703
0.113	0.744
0.132	0.779
0.151	0.810
0.170	0.838
0.189	0.863
0.208	0.885
0.227	0.905
0.246	0.922
0.265	0.938
0.284	0.952
0.303	0.965
0.321	0.976
0.340	0.985
0.359	0.993
0.378	1.000

Nose No. 3

x	y
0.014	0.320
0.028	0.422
0.042	0.495
0.056	0.554
0.071	0.604
0.085	0.648
0.099	0.687
0.113	0.723
0.127	0.755
0.141	0.786
0.155	0.813
0.169	0.840
0.183	0.864
0.197	0.887
0.212	0.908
0.226	0.929
0.240	0.948
0.254	0.966
0.268	0.984
0.282	1.000

Nose No. 4

x	y
0.011	0.386
0.023	0.486
0.034	0.555
0.046	0.610
0.057	0.656
0.069	0.696
0.080	0.731
0.092	0.763
0.103	0.791
0.115	0.818
0.126	0.842
0.138	0.864
0.149	0.885
0.161	0.905
0.172	0.923
0.184	0.940
0.195	0.957
0.207	0.971
0.218	0.986
0.230	1.000

Fig. 4-109. Comparison of theoretical and experimental pressure distributions over various rounded noses; M = 4.95. (Source: Ref. 90)

155

Fig. 4-110   NAVWEPS Report 1488 (Vol. 3, Sec. 8)
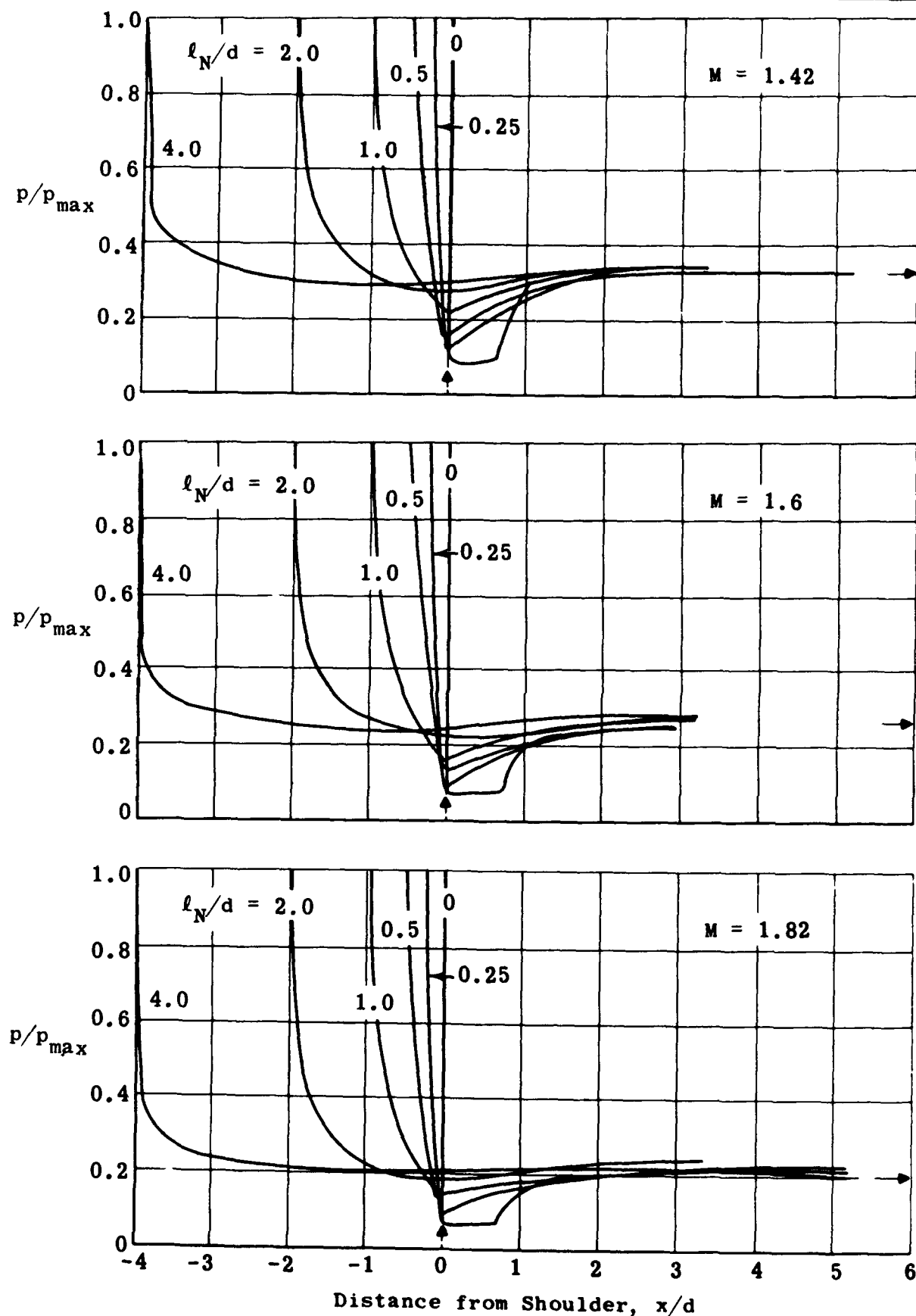
Fig. 4-110. Experimental pressure distributions on elliptical
planform noses of various fineness ratios; M = 1.42, 1.6,
and 1.82. (Source: Ref. 93)
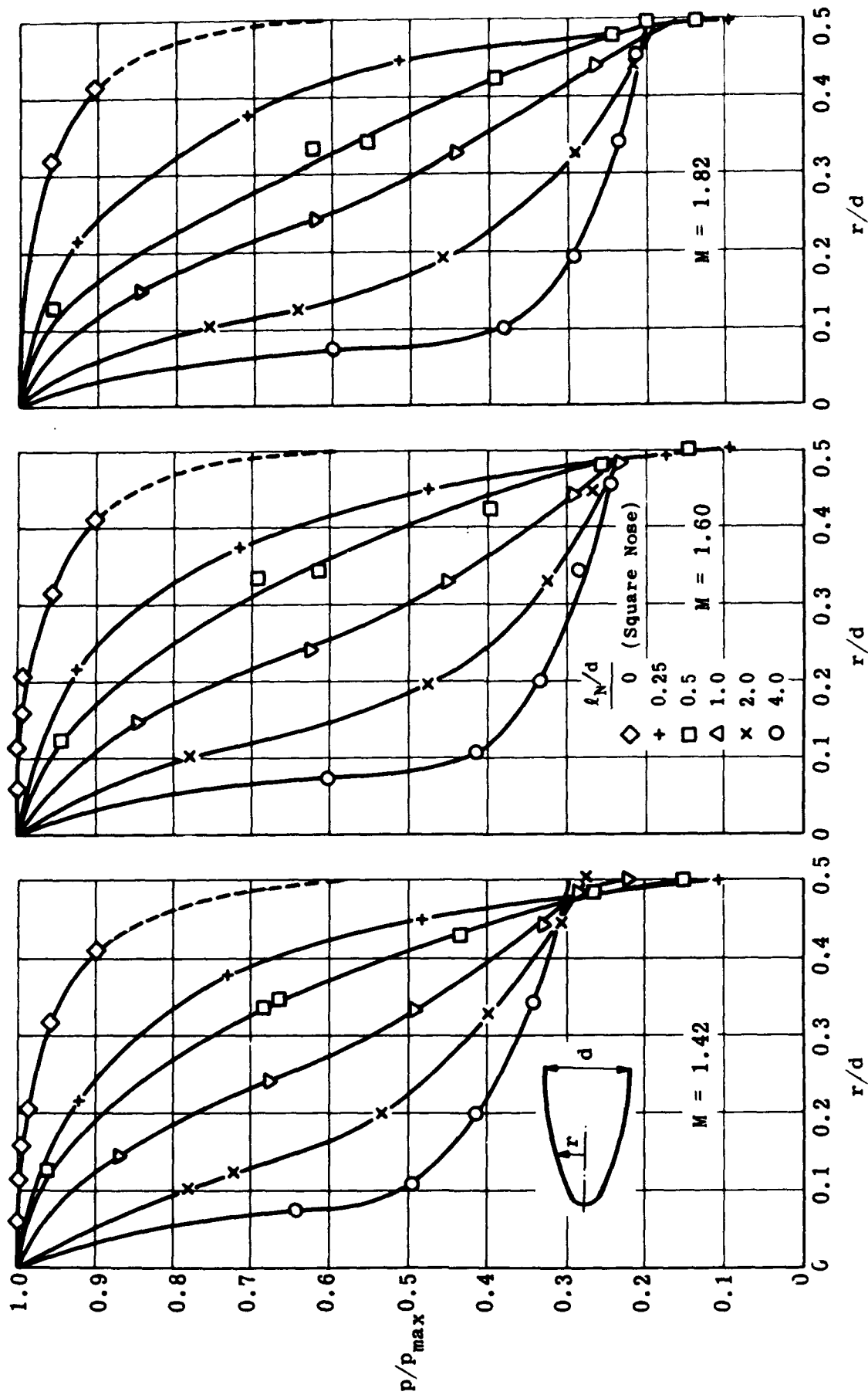
Fig. 4-111. Experimental pressure distributions over an elliptical nose given in terms of the local radius; M = 1.42, 1.6, and 1.82. (Source: Ref. 93)

Fig. 4-112   NAVWEPS Report 1488 (Vol. 3, Sec. 8)
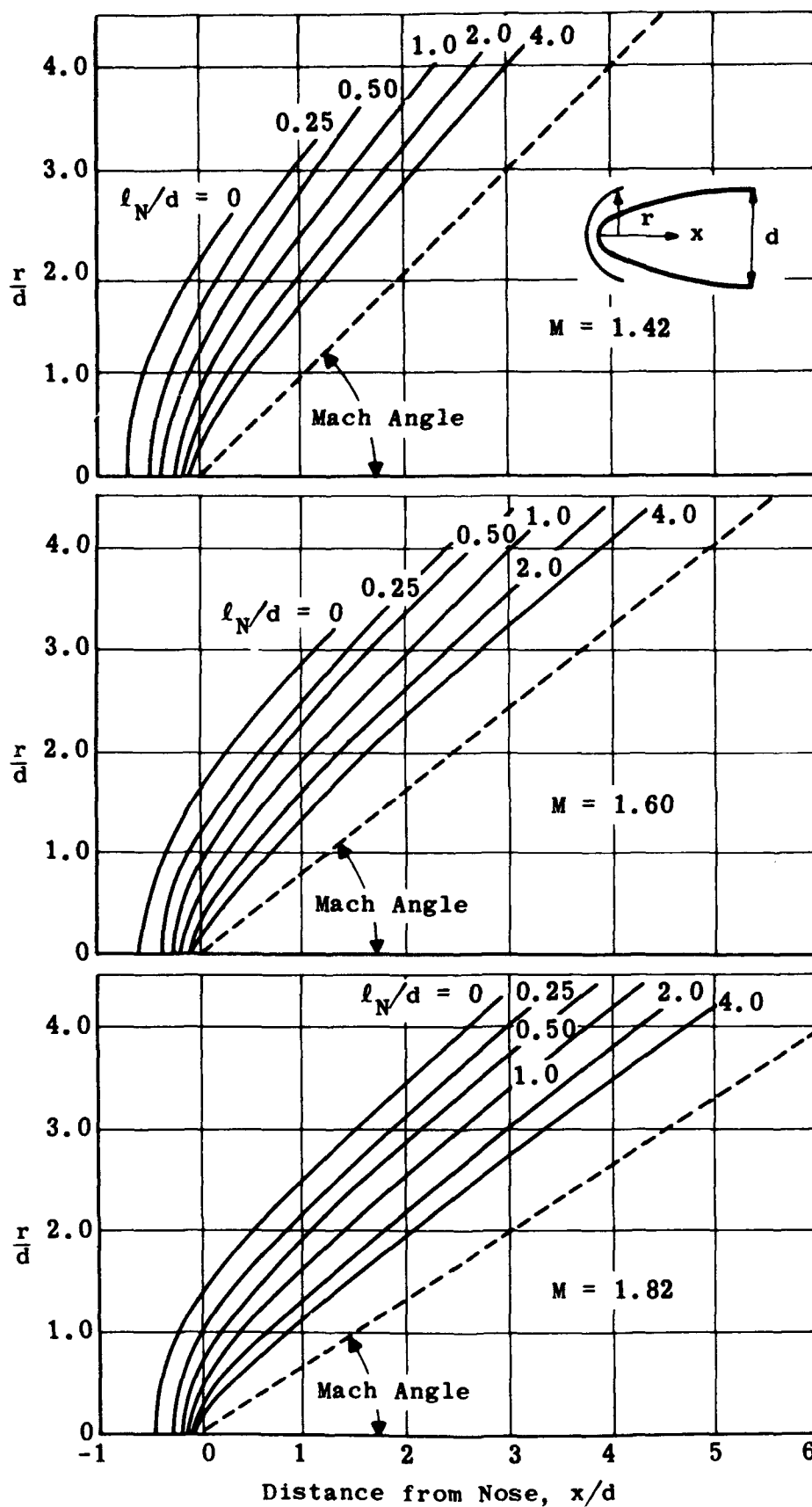
Fig. 4-112.   Observed bow waves for elliptical noses; M = 1.42,
1.6, and 1.82. (Source: Ref. 93)
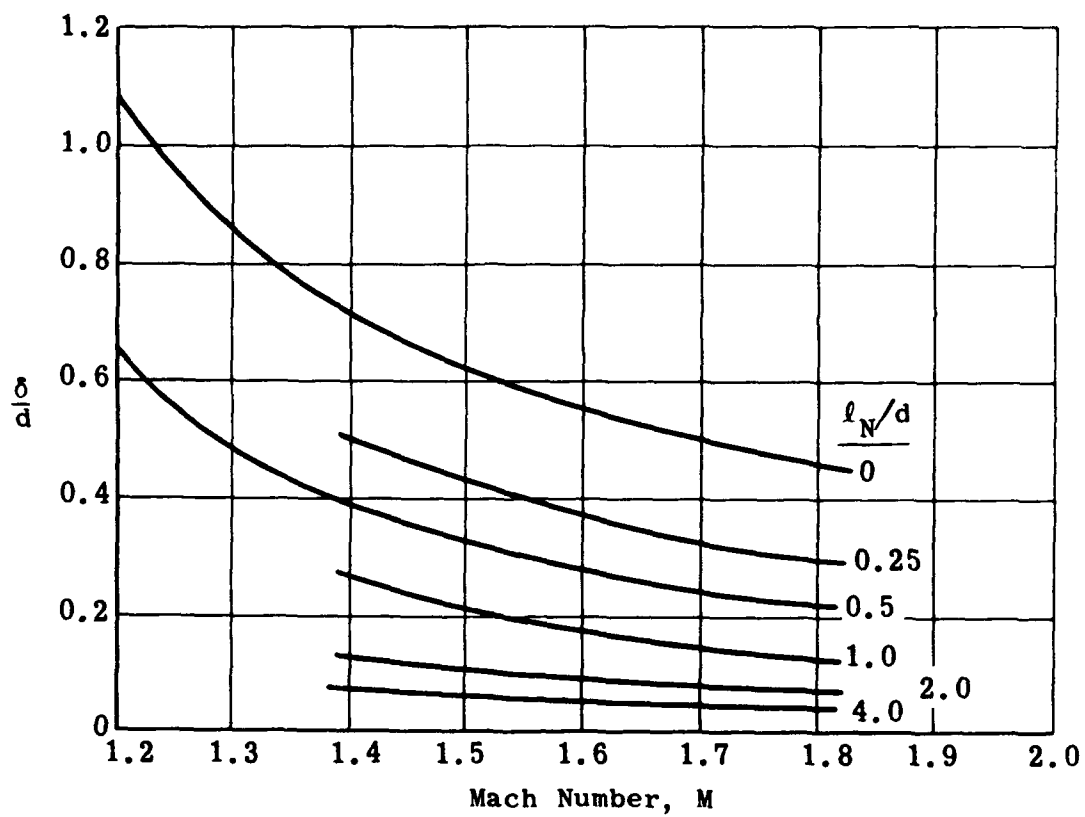
Fig. 4-113.   Shock-wave stand-off distance for elliptical noses
of various fineness ratios in terms of free-stream Mach
number.   (Source: Ref. 93)

Fig. 4-114   NAVWEPS Report 1488 (Vol. 3, Sec. 8)
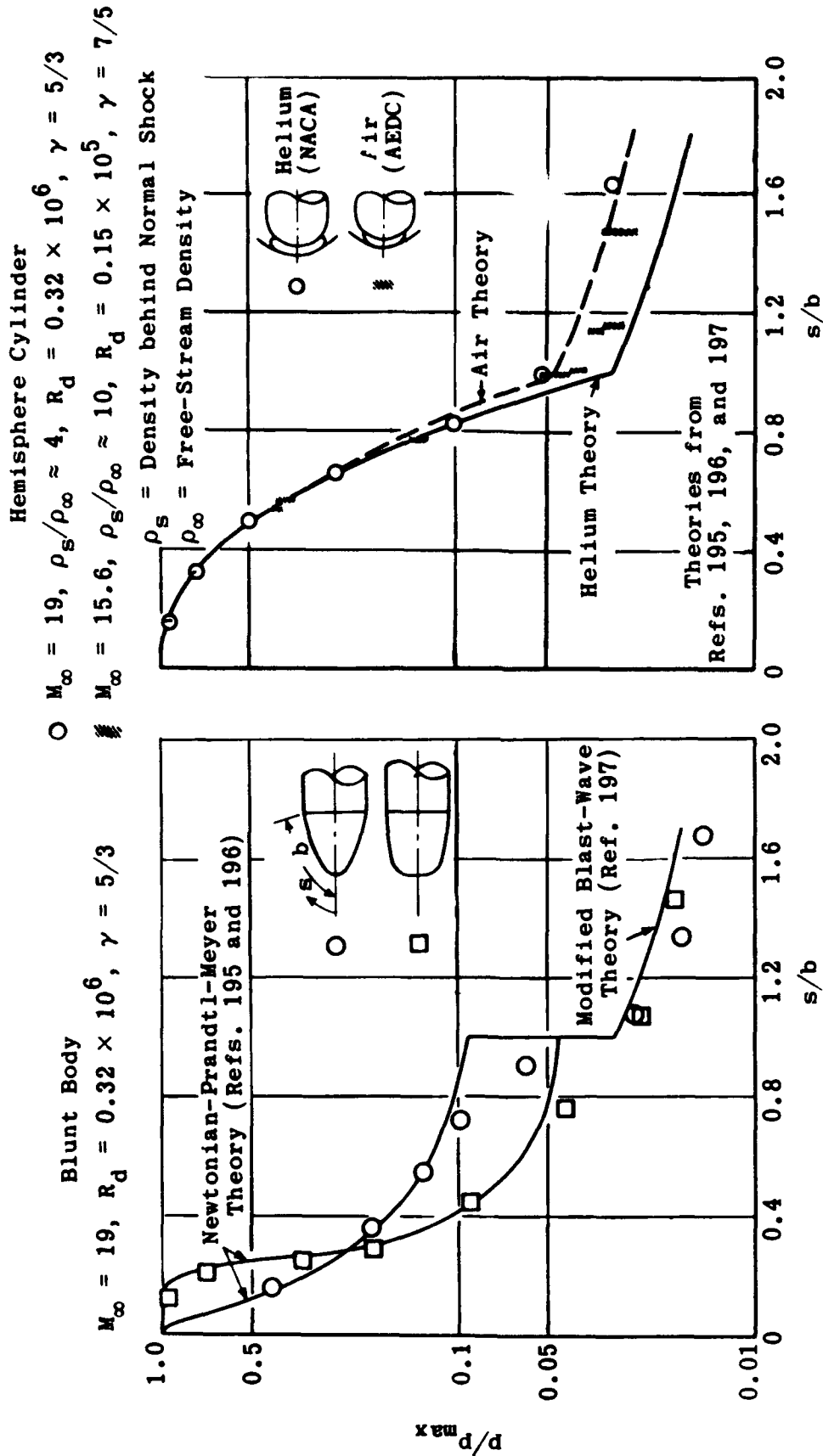
Fig. 4-114. Pressure distributions on blunt-nosed bodies at hypersonic Mach numbers.
(Source: Ref. 91)
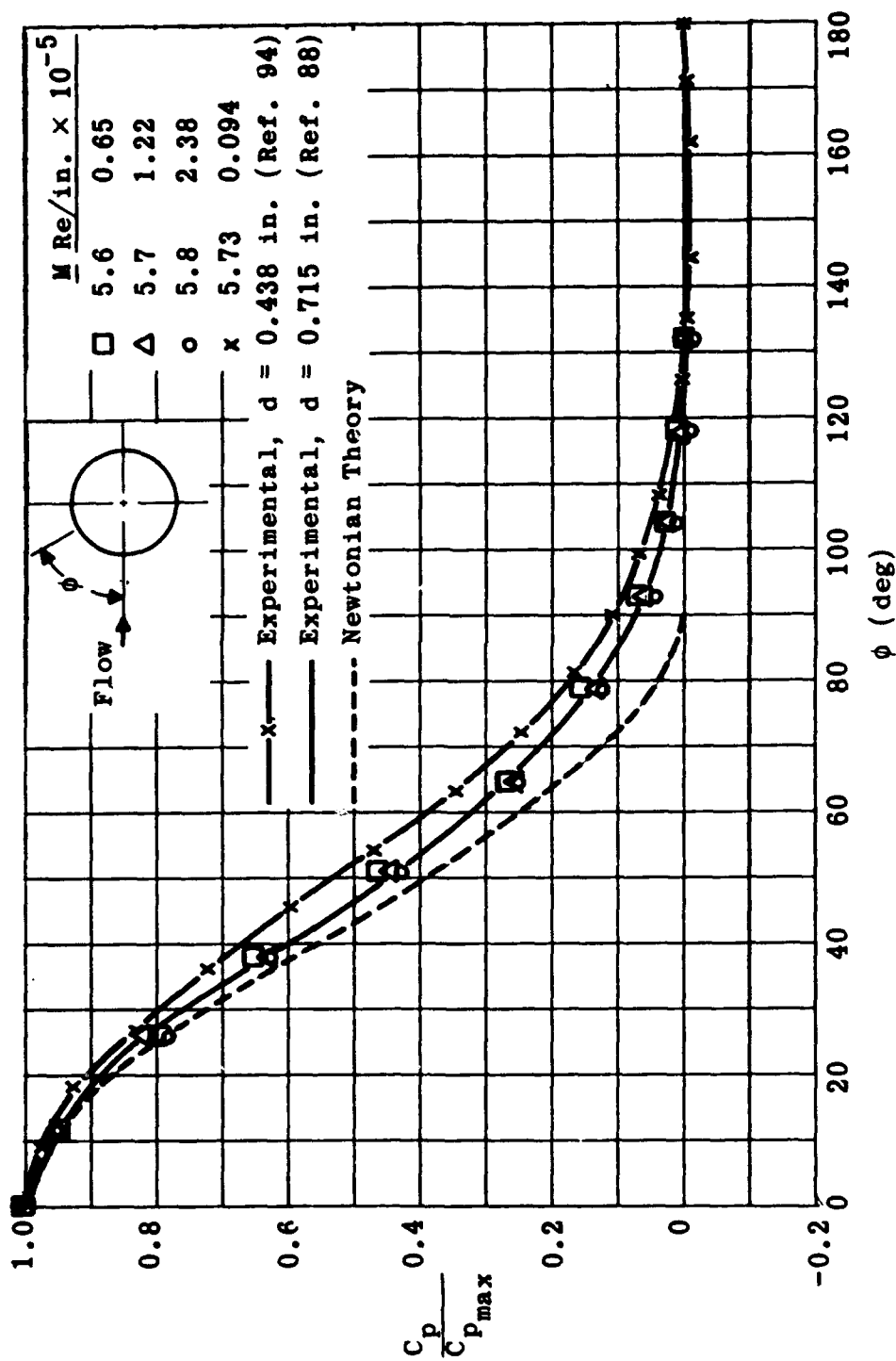
Fig. 4-115.   Pressure distributions around transverse cylinders at M = 5.7.

5.   Force and Moment Characteristics of Simple Bodies

It is possible to integrate the pressures obtained by means of the theories or methods outlined in Subsecs. 2, 3, and 4 and thus calculate the forces over any body for which a pressure distribution can be established. Such a task, however, is tedious and gives increasingly questionable results as the angle of attack increases beyond the limit allowed by the simplifying assumptions of the various methods. The calculation of total forces on bodies is also hampered by the lack of any completely realistic theory for the pressures at or near the body base or anywhere in the presence of separated flow.

Since it is therefore necessary to rely on experimentally determined force and moment characteristics, this subsection will be devoted for the most part to a presentation of experimental studies of various configurations. Very little correlation between sets of data is possible since configurations vary considerably, depending on the purpose and particular interests of the study as well as the Mach number and Reynolds number ranges available at the facility at which the tests were made. General trends will be noted and wherever possible test results will be compared with theoretically derived values supported by empirical relationships. The range of flow parameters and geometric configurations is wide enough to allow interpolation and application to most required body designs. The measured values of the normal-force coefficient and the position of the center of pressure at high angles of attack are of particular interest since this is the region in which the theories are least reliable. Operation at high angles of attack in the case of tactical missiles is very necessary in order to develop high maneuverability without recourse to large aerodynamic surfaces. Knowledge of high angle-of-attack performance characteristics is also required for estimating the effects of lateral or aft launching of a missile from an aircraft in flight.

5.1   Normal-Force Characteristics of Slender Bodies

The distribution of the local normal-force coefficient (per inch per unit angle) for a tangent-ogive-cylindrical body at angles of attack of 5, 10, 15, and 20 deg is given in Fig. 5-1. The experimental data at M = 2 collected by Perkins and Jorgensen (Ref. 52) are compared in this figure with three different theoretically derived potential flow values. It may be seen that even as far forward as the aft part of the nose section the divergence between experiment and theory is greater than that between the different theories. Over the cylindrical section the inadequacy of the potential flow theories at all but very low angles of attack is clearly demonstrated by these comparisons. Although both the Tsien and Van Dyke methods predict the general shape of the load distribution curve, it is evident that the lift carried on the cylindrical afterbody even at a 5-deg angle of attack is considerably greater than that predicted by potential flow theories. At high angles of attack, the largest part of the difference between theory and experiment is attributed to separation effects. In Figs. 5-2 and 5-3 the experimental data is compared with three different cross-flow calculations: (1) the Allen-Perkins cross-flow theory (Subsec. 3.1) with Van Dyke's hybrid potential flow (Subsec. 2.4); (2) the Allen-Perkins theory with Tsien's potential flow theory; and (3) the Kelly cross-flow theory (Subsec. 3.2.2) with Van Dyke's hybrid theory. Although none of these methods give very good agreement with the distribution of the normal-force coefficient, except at low angles of attack, they have been shown

to give reasonably good prediction of the total normal force. To check
the influence of the Reynolds number on these separation effects, tests
were re-run with an extra turbulence grid in the stagnation chamber.
The addition of this grid moved the transition point from about 7.5
diameters to 6 diameters from the nose but produced little change in
the normal-force coefficient except at $\alpha = 15$ deg. When the Reynolds
number was reduced from 0.39×10^6 to 0.13×10^6/in. there was a sig-
nificant increase in normal force over the cylinder at a 10-deg angle
of attack but much less at 15 deg. Even though they cover a very limi-
ted range of test parameters, these results indicate the importance of
experimental data at high angles of attack and point out the need for
improved theoretical treatment of the subject.

The total normal-force coefficient, C_N, for families of cone-
cylinders and tangent-ogive-cylinders is given in Figs. 3-9, 5-4, and
5-5 (from Refs. 47 and 95) for a wide range of all flow parameters and
body configurations. The early departure from linearity of C_N with α
is clearly exhibited in these figures. In fact, it may be seen that
the linear range of C_N does not extend much beyond $\alpha = 4$ deg, whereas
in the case of two-dimensional shapes such as wings, the linear char-
acteristic is retained to much higher angles of attack. The marked
departure from linearity of C_N versus α is due principally to the oc-
currence of the cross-flow drag discussed in Subsec. 3. The fact that
these forces vary in proportion to the square of the cross-flow ve-
locity (i.e., to α^2) explains the almost parabolic variation of C_N with
α. The most significant trend that may be observed in these figures is
the increase in C_N with increase in body length for angles of attack
greater than about 4 deg. This is to be expected since the additional
length is subjected to additional cross-flow drag. The nose fineness
ratio has only a minor influence on C_N except in the case of very slender
noses at high Mach numbers.

The normal-force coefficient slope for a tangent-ogive-cylinder
and a cone-cylinder with the same nose length and at zero angle of attack
is shown as a function of fineness ratio in Fig. 5-6 for a range of Mach
numbers (Buford, Ref. 98). The experimental data for the ogive are com-
pared with the first-order theory of Van Dyke (Ref. 2) to which the
cross-flow correction has been added. The agreement is reasonably good
for short bodies but very poor as the length is increased. Figure 5-7
(also from Ref. 98) compares experimental values of $dC_N/d\alpha$ at $\alpha = 0$ for
a 10-deg half-angle cone with the exact theory. Here the agreement is
relatively good over the test range of $1.2 < M < 4$. The measured value
of $dC_N/d\alpha$ at the shoulder of the 10-deg cone (approximately 0.31) taken
from Fig. 5-6 agrees well with the nearly constant value predicted by
the Stone-Kopal theory as shown in Fig. 5-8. The initial slope of the
normal-force curve is shown as a function of nose length and over-all
fineness ratio for several Mach numbers in Fig. 5-9. The curves in
Fig. 5-9 show clearly the increase in $dC_N/d\alpha$ with Mach number for all
body lengths greater than the nose length. It may also be seen that
the maximum value of $dC_N/d\alpha$ is associated with slightly longer bodies
as the Mach number increases. These values (from Ref. 96) are calcu-
lated by means of the linearized theory and should be compared with ex-
perimental data such as that shown in Fig. 5-6, which indicates that
once the peak value of $dC_N/d\alpha$ has been reached the values do not drop

off. Measured values for cone-cylinders are shown in Fig. 5-10 (from Ref. 95).

5.1.1   Center of Pressure of Slender Bodies

The experimentally determined distance of the center of pressure from the nose vertex as a function of the free-stream characteristics and the body geometry is given in Figs. 5-11 to 5-14 (from Refs. 95 to 99). Experimental values for a tangent-ogive-cylinder are compared with first-order theory in Fig. 5-13. For low angles of attack and short bodies the flow is predominantly potential and the center of pressure remains constant. As the angle of attack is increased above approximately 4 deg the transverse forces arising from cross flow and separation on the leeward side of the body become increasingly effective, and the center of pressure moves aft. In the case of cones for which the flow over the surface is everywhere supersonic, the pressure is constant along each ray emanating from the apex of the cone; hence the center of pressure of a cone alone is theoretically located at a point approximately two-thirds of the cone length aft of the apex. Actually, second-order effects cause the center of pressure to be somewhat aft of this position by an amount which increases as the cone angle increases.

Figure 5-14 (from Ref. 99) shows that for Reynolds numbers of 2×10^6 to 15×10^6 there is no significant change (at this Mach number, 3.12) in the position of the center of pressure with respect to Reynolds number. The general trends that may be noted are that an increase in Mach number or in body length results in an aft movement of the center of pressure and that nose fineness ratio and Reynolds numbers have only slight effects on the center of pressure of slender bodies.

5.1.2   Pitching Moment

Calculated values of the pitching-moment slope, $dC_m/d\alpha$ at $\alpha = 0$, are shown in Fig. 5-15 for tangent-ogive cylinders of various configurations and Mach numbers of 1.4 to 3.5. The values of $dC_m/d\alpha$ at $\alpha = 0$ corresponding to the data from Refs. 47, 95, and 96 may be easily obtained from the equation

$$\left(\frac{dC_m}{d\alpha}\right)_{\alpha=0} = \left(\frac{dC_N}{d\alpha}\right)_{\alpha=0} \frac{x_{cg} - x_{c.p.}}{d} \qquad (5-1)$$

where the terms are illustrated below.
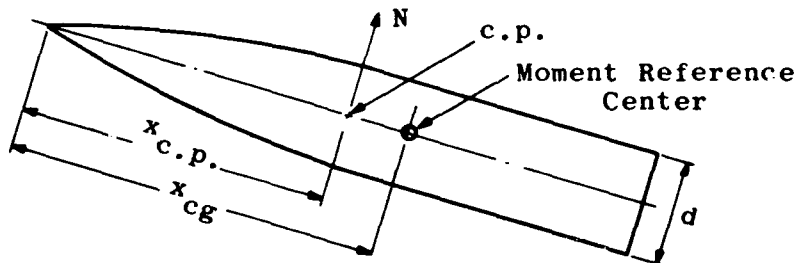
Usually, x_{cg} is taken as the centroid of the planform. The pitching moment is often a complex function of the angle of attack and generally must be determined experimentally. For an estimation of the stability characteristics of a simple axially symmetric body, the value of $dC_m/d\alpha$ at $\alpha = 0$ is a useful tool. Figure 5-16 (from Ref. 99 by Jack and Burgess) indicates that the effect of Reynolds number on the pitching moment is very slight.

5.1.3   Force Characteristics of Pure Cylinders

The aerodynamic characteristics of a geometrically complex missile are usually approximated by the simple process of adding the contribution of component parts. Hence, despite its seemingly impractical shape, it is often desirable to know the aerodynamic characteristics of a pure cylinder moving with its longitudinal axis inclined at small angles of attack to the air stream. Such a configuration with an ℓ/d ratio of 5.76 was tested at Mach numbers of 1.88 and 2.86. The results are reported by Potter, Shapiro, and Murphree in Ref. 92 and plotted in Figs. 5-17 to 5-19.

5.1.4   Force Characteristics of Skirted Bodies

A theoretical technique for determining the lift, pitching moment, and drag of cone-cylinder bodies whose aft section is a cone frustum has been developed by Deep and Henderson (Ref. 101). This study was based entirely on linearized theory (but since the experimental data currently available is classified, it is not possible to discuss the accuracy of the results). No allowance was made for effects of flow detachment at the beginning of the skirt or for any real-fluid effects. The configurations and stream properties for which the calculations were made are shown in Fig. 5-20, while representative results appear in Figs. 5-21 to 5-24. The normal-force characteristics were obtained by numerical integrations of the basic pressure data. The center-of-pressure positions were determined from both the pitching moment due to normal force and the effective pitching moment which includes the moment due to axial force. For large contour slopes the latter effect cannot be neglected. The effect of frustum geometry appears to have greater influence on $dC_N/d\alpha$ than does the cylinder length. The effect of Mach number depends greatly on the geometric parameters. As would be anticipated, the center of pressure is strongly affected by the separation distance between the nose and the cone frustrum. Although the absolute value of the characteristics has not been verified, these figures indicate the extent and nature of the variations that will occur due to changes in the geometry and flow parameters.

5.1.5   Correlation of Normal Forces by Means of the Hypersonic
           Similarity Parameter

The hypersonic similarity rule states that the normal force and pitching moment on two bodies are related and their flow fields are similar provided that the bodies have the same thickness distribution and the same similarity parameter, i.e., two bodies, A and B, with

$$\left(\frac{Md}{\ell_N}\right)_A = \left(\frac{Md}{\ell_N}\right)_B$$

will have similar characteristics when

$$(\ell_a/\ell_N)_A = (\ell_a/\ell_N)_B \qquad (5-2)$$

where

ℓ_a = length of the afterbody

ℓ_N = length of the nose

Van Dyke has shown (Ref. 34) that by replacing M in the hypersonic simi-larity parameter by $\beta = \sqrt{M^2 - 1}$, the range of application is much ex-tended (see Subsec. 2.10.2).

Dorrance and Norell (Ref. 102) have correlated experimental results from many tests in a Mach number range of 1.57 to 4.24 by means of the hypersonic similarity parameter. The correlations are shown in readily usable forms in Figs. 5-25 to 5-41. The variables, parameters, and constants for each graph are tabulated below.

Variable	Parameter	Constant	Figure
βC_N and βC_m vs $\beta \alpha$	M	$\ell_a/\ell_N = 0$ $K = 0.6$	5-25*
βC_N and βC_m vs $\beta \alpha$	M	$\ell_a/\ell_N = 0.62$ $K = 0.6$	5-26
$\dfrac{dC_N}{d\alpha}$ vs K	ℓ_a/ℓ_N	$\alpha = 0$	5-27
$\dfrac{dC_m}{d\alpha}$ vs K	ℓ_a/ℓ_N	$\alpha = 0$	5-28
$\dfrac{x_{c.p.}}{\ell_a/\ell_N}$ vs K	ℓ_a/ℓ_N	$\alpha = 0$	5-29
βC_N vs ℓ_a/ℓ_N	$\beta \alpha$	$K = 0.25,$ $0.5, 1.0, 2.0$	5-30 to 5-33
βC_m vs ℓ_a/ℓ_N	$\beta \alpha$	$K = 0.25,$ $0.5, 1.0, 2.0$	5-34 to 5-37
$\dfrac{\beta^2 dC_N}{d(x/d)}$ vs ℓ_a/ℓ_N	$\beta \alpha$	$K = 0.25,$ $0.5, 1.0, 2.0$	5-38 to 5-41

where

$K = \beta d/\ell_N$ rather than the more usual Md/ℓ_N

*Figure 5-25 presents data for a cone, and Figs. 5-26 to 5-41 deal with cone-cylinder configurations.

After the values of ℓ_a/ℓ_N and K have been determined for any particular
configuration and Mach number it is possible by use of a single cross
plot to determine the normal-force coefficient or the pitching-moment
coefficient as a function of the angle of attack. The longitudinal
distribution of the normal force on the body may be found by a similar
procedure. The accuracy of the charts was tested by comparing them
with coefficients obtained from experimental data. Figure 5-42 shows
one such comparison with satisfactory agreement. Figure 5-43 shows the
range of parameters which were used to compile the charts and beyond
which the reliability has not been established.

5.2   Lift and Drag

Up to this point the forces acting on a body have been con-
sidered in terms of the body axes, with C_A the force coefficient in the
axial direction and C_N that in the direction normal to the body axis.
It is sometimes more useful to relate the forces to the wind axis (see
below), in which case the drag force is in the direction of the free
stream and the lift force is normal to it in the plane of the body
symmetry.
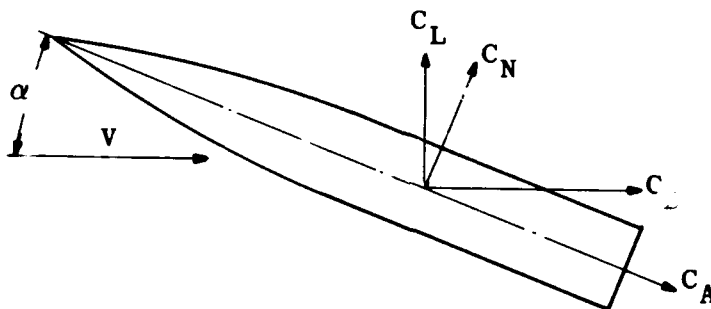
These forces are related as follows:

$$C_L = C_N \cos \alpha - C_A \sin \alpha$$

$$C_D = C_N \sin \alpha + C_A \cos \alpha$$

$$(5-3)$$

The axial part of the drag force (usually known as wave drag,
pressure drag, or zero-lift drag) will be discussed in Subsec. 6. The
normal-force contribution to the drag (often known as drag due to lift
or drag due to normal force) is proportional to sin α or, since α is
usually small, to α. However, second-order effects, non-symmetrical
configurations, and open inlets will modify this conclusion slightly.
In cases where these characteristics must be known within accuracies
of 10 to 15%, actual measurements should be obtained.

5.2.1   Lift and Drag of Cones of Elliptical Cross Section

Pressure distribution and the pressure drag of cones of el-
liptical cross-section are given general treatment in Subsecs. 4.1.3
and 6.5, respectively. However, one graph is included here since it
compares (at one Mach number and angle of attack) the lift, drag,
normal-force and axial-force coefficients for a limited family of

elliptical cones. The values are calculated by Ferri, Ness, and Kaplita by means of the superposition of linearized conical-flow solutions upon the solution of the nonlinear flow around a circular cone. The work is reported in Ref. 70 from which Fig. 5-44 is taken.

5.2.2   Lift, Pitching Moment, and Center of Pressure of Ducted Bodies

The theoretical pressure distribution of a specific family of ogival cone-cylinder ducted bodies was given in Subsec. 4.3 together with a diagram (Fig. 4-59) showing the details of the configurations that were considered. In Figs. 5-45 to 5-47 (from Ref. 79) typical plots are given for the lift coefficient slope, the pitching-moment slope, and the ratio C_m/C_L for the family of curves at $M = 2$ and $\alpha = 0$. From the last figure the position of the center of pressure may be calculated by using

$$C_m/C_L = \frac{x_{cg} - x_{c.p.}}{d_{max}} \qquad (5\text{-}4)$$

Usually x_{cg} is taken as the centroid of the planform. The wave-drag characteristics of these configurations are treated in Subsec. 6.3.

5.2.3   Lift-Drag Ratio

Since the lift-to-drag ratio of a body may be regarded as a measure of its aerodynamic efficiency, it is necessary to obtain the ratio as frequently as the force measurements themselves. The maximum lift-to-drag ratio to be expected from a pointed body of revolution of practical shape inclined at an angle of attack to a supersonic stream will be between 2.5 and 4.0, depending on Mach number, angle of attack, nose and boattail shapes, and the distribution of the body cross-sectional area. The maximum L/D usually occurs when the angle of attack is between 6 and 10 deg. At this attitude the potential flow still predominates; hence the nose and boattail shapes are important factors in determining L/D. Cross-flow lift is present and becomes increasingly important as the body length is increased. At a given Mach number any fore and aft body shape will have an optimum length for maximization of L/D. Radical departures from the usual circular cross-sectional shape will also affect the lift-to-drag ratio.

Figure 5-49 (from Ridyard, Ref. 103) shows how an increase in the fineness ratio of a cylindrical body aft of 10 and 20-deg half-angle conical noses affects L/D at $M = 6.86$. At this Mach number the peak value of L/D is achieved with an afterbody fineness ratio of about 6. However, as can be seen, the variation about this maximum is not very great and the body length is not very critical.

Sanger and Bredt (Ref. 104) predicted that the use of flat-bottomed bodies, in addition to improving lifting characteristics, would result in an increased value of peak lift-drag ratios. The data shown in Fig. 5-48 (from Ref. 103) confirms this prediction at one Mach number (6.86) and one fineness ratio (6). It may be noted that in this case the cross section of the body is almost square. Dennis and Cunningham (Ref. 95) measured lift and drag and computed the lift-drag ratio for a family of flat-bottomed cone-cylinder models for Mach numbers

of 3, 4.25 and 6.28. The maximum lift-drag ratio of these models is
compared with that of cones of the same over-all fineness ratio
($\ell/d = 10$) in Fig. 5-50. From this rather sparse data one may see
that the improvement in lift-drag ratio by means of a flat bottom is
dependent on Mach number and the fineness ratio of the cylindrical
afterbody. The technique seems most successful at high Mach numbers.

5.3 Non-Steady Normal-Force and Pitching-Moment Derivatives

The effects of oscillatory movement in finless missiles trav-
elling at supersonic speeds assume increased importance when the prob-
lems of dynamic stability are considered. Dorrance in Ref. 105 treated
the effects of four types of unsteady motion on a slender pointed body
and derived expressions for the normal-force and pitching-moment sta-
bility derivatives in each case. The body for which the calculations
were made was generated by a parabolic arc about the longitudinal axis.
The equation for the arc is

$$r = 0.02 \ (10x - x^2) \quad \text{for} \quad 0 \leqq x \leqq 8 \tag{5-5}$$

This corresponds roughly to a 25-caliber tangent ogival nose with a
fineness ratio of 5 and over-all fineness ratio of 8. The four cases
which were considered for this body are given below.

5.3.1 Periodic Pitching about a Fixed Point

The center of rotation of the pitching moment was chosen at
$x = 4.78 \ d_{max}$, which is typical of certain rocket-propelled missiles.
The values of the unsteady derivatives $C_{N_{\dot{\alpha}}}$ and $C_{m_{\dot{\alpha}}}$ are shown as a func-
tion of the Mach number in Fig. 5-51. These derivatives are dimension-
less forms given by

$$C_{N_{\dot{\alpha}}} = \frac{\partial C_N}{\partial \dot{\alpha}(\ell/V)} \quad \text{and} \quad C_{m_{\dot{\alpha}}} = \frac{\partial C_m}{\partial \dot{\alpha}(\ell/V)}$$

where

ℓ = missile length

V = free-stream velocity

It may be seen from Fig. 5-51 that the inclusion of the first-order
frequency terms in the oscillating velocity potential gives values that
are higher than those from slender-body theory. In the Mach number
range presented, the normal-force derivative is 5 to 11% greater than
slender-body values, and the pitching-moment derivative is 40 to 150%
greater.

5.3.2 Periodic Normal Oscillation

The values given by Dorrance for $C_{N_{\dot{w}}}$ and $C_{m_{\dot{w}}}$, where w is the
periodically varying upwash velocity, and the values derived by slender-
body theory are also given in Fig. 5-51. The difference between the

steady and unsteady pitching-moment derivatives is very large.

$$C_{N_{\dot{w}}} \text{ is defined as } \frac{\partial C_N}{\partial \dot{w}(\ell/v^2)} \text{ and } C_{m_{\dot{w}}} \text{ as } \frac{\partial C_m}{\partial \dot{w}(\ell/v^2)} .$$

5.3.3   Steady Pitching about a Fixed Point

As before, the fixed center of rotation is $x = 4.78 \, d_{max}$. The pitching velocity about this point is q. The values of C_{N_q} and C_{m_q} versus Mach number are shown in Fig. 5-52.

$$C_{N_q} \text{ is defined as } \frac{\partial C_N}{\partial q(\ell/v)} \text{ and } C_{m_q} \text{ as } \frac{\partial C_m}{\partial q(\ell/v)} .$$

In dynamic stability analyses the steady pitching derivatives, C_{N_q} and C_{m_q}, are usually employed in place of the unsteady derivatives, $C_{N_{\dot{\alpha}}}$ and $C_{m_{\dot{\alpha}}}$. A comparison of Figs. 5-51 and 5-52 shows that when this procedure is followed, not only the magnitude of the derivatives but also the Mach number trend will be in error. In both cases, however, the sign of the pitching-moment derivative is such as to indicate a damping moment due to pitching angular velocity.

5.3.4   Steady Angle of Attack

This case was treated in Subsec. 5.1.2 but is included here so that it may be readily compared with steady pitching and harmonic pitching. As indicated in Fig. 5-52 the pitching moment coefficient, $C_{m_{\alpha}}$, is not greatly different from that predicted by the slender-body theory, but the normal-force coefficient, $C_{N_{\alpha}}$, differs widely, especially as the Mach number is increased.

5.3.5   Effect of Boattail Flaring on Stability Derivatives

The effect of a flared aft section in place of the boattail was also considered by Dorrance. The relation between the two bodies is shown in the sketch below and the stability derivatives are presented in the table that follows.

4-deg Flare
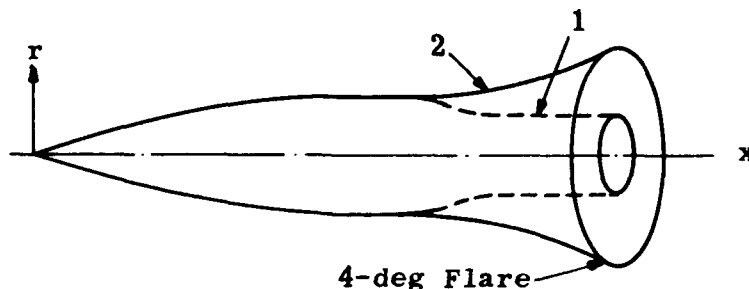
Body	C_{N_α}	C_{m_α}	C_{N_q}	C_{m_q}	$C_{N_{\dot\alpha}}$	$C_{m_{\dot\alpha}}$	$C_{N_{\dot w}}$	$C_{m_{\dot w}}$
1	0.82	0.93	0.33	-0.13	1.58	-0.13	1.25	-0.002
2	3.63	0.15	1.47	-0.48	3.08	-0.59	1.61	-0.114

The values in the table are those derived from slender-body theory only and serve to provide a qualitative comparison of the stability of the two configurations. The addition of the flared skirt has (1) increased the lift, (2) moved the static center of pressure rearward and thus improved the margin of static stability, and (3) increased the damping in pitch. In general, it appears that increasing the base area of a body of revolution improves its steady and non-steady lift and pitching-moment characteristics in the Mach number range of 1.3 to 2.3.

5.4   Magnus Moments

Magnus moments (named after Wilhelm Magnus) result from the combination of the incremental normal forces which occur on a body of revolution due to its spinning motion and those due to the cross flow caused by the inclination of the body centerline to the oncoming airstream. The circulation created by the rotational motion of the body in a real fluid when resolved with the normal component of the forces due to the forward velocity creates forces distributed along the body at right angles to the mean flow. When the rotational rate is high, as in the case of shells or certain types of guided or ballistic missiles, the forces and resulting moments thus created may be quite large (but still considerably less than the usual normal force and moment due to angle of attack alone). Such forces can also be created by surfaces placed well forward on a body which could be deflected to produce a swirl on the body aft of the surfaces, assuming that the body is subject to angles of attack at the same time as the surfaces. Within the range of realistic spin ratios, the Magnus forces and moments of a configuration will generally be about 1/15 or 1/10 the usual normal force and pitching moment due to angle of attack. However, such small effects may seriously alter the flight path of a projectile, particularly when it is launched in the presence of high side winds.

In Ref. 107, Greene has summarized the experimental Magnus force and moment characteristics of 7 and 5-caliber bodies of revolution at speeds ranging from subsonic to M = 2.87.

It was found that within the test range of the spin parameter, pd/2V, the Magnus forces acting on these bodies were linearly related to the spin rate, p. The variation of the Magnus slope coefficient, C_{y_p}, with angle of attack and supersonic Mach number is shown in Figs. 5-53 and 5-54 for the 5-caliber and 7-caliber missiles, respectively. Figure 5-55 gives the Magnus slope coefficient for a wide range of Mach numbers at several angles of attack. From these three graphs it may be noted that C_{y_p} (see Figs. 5-53 and 5-54) increases with angle of attack, α, up to about 12 to 16 deg, where it then either decreases or remains relatively constant. The effects of both angle of attack and Mach number are less critical as the Mach number increases. Reference 107 presents no data on the effect of Reynolds number at the higher Mach numbers. The effect in the low Mach number range as shown in Fig. 5-57 indicates that the Reynolds number is a very important parameter and that the data given in Figs. 5-53 and 5-54 must be regarded as

giving qualitative rather than quantitative results since the Reynolds number varies throughout.

The effect of nose shape and spin parameter are both shown in Fig. 5-56 for M = 1.75 and the 5-caliber body. There is a progressive increase in the Magnus force as the bluntness of the nose is increased, this effect being most marked above 8-deg angle of attack. The absence of a discontinuous shoulder in the Haack-Sears configuration appears to increase the Magnus force.

Figures 5-58 and 5-59 indicate the center-of-pressure positions of the Magnus force of both the 5 and 7-caliber bodies to be between 1 and 2 calibers forward of the base at almost all test Mach numbers. For the 7-caliber body, the center of pressure remains essentially at 2 calibers from the base in the Mach number range noted. As pointed out previously for the case of the cone, the Magnus moment may be influenced by the type (or types) of flow over the body and by the location of the transition point between laminar and turbulent flow. Although the Reynolds number effect is likely to be greater than that of the Mach number, a quantitative value has not yet been established.

The marked decrease in Magnus force for the 5-caliber length relative to the 7-caliber length and the more aft location of its center of pressure also should be noted. As indicated in Figs. 5-60 and 5-61, the reduction in Magnus force is much greater between the two lengths than would be expected from a comparison of the relative planform areas of the two configurations. It should be noted that the center of pressure in both cases, although nearer the base for the 5-caliber body, is actually located at about the same point when the measurement is made in terms of the total length of each body.

Figure 5-62 shows the effect of various test nose shapes on the Magnus center of pressure for the 5-caliber body at varying angles of attack. It may be seen that there is little or no change in the center of pressure above approximately 8 deg. Even though the data at small angles is relatively uncertain, it can be seen that the center of pressure below 8 deg is moved rearward rather abruptly when the nose shape is changed from the cone or typical projectile nose to the tangent or Haack-Sears shapes. The addition of No. 100 grit to a portion of the cone nose produces a fairly large shift in the center of pressure at angles of attack below 6 deg. While this shift is similar to that observed for some of the blunter nose shapes, the Magnus force coefficient is little changed. It thus appears that a fairly strong viscous effect is changing the force distribution over the body at the smaller angles of attack.

Since varying Reynolds number may have a significant effect on the Magnus moments and complete information is not available, particular configurations should be tested for this characteristic in the applicable range of Reynolds numbers.

In their attempts to develop a rotational fluid theory that could be applied without many simplifying assumptions to the prediction of various rotation effects, Nicolaides and Brady (Ref. 106) investigated Magnus moments on pure cones in supersonic flight. Their studies demonstrated that the size and the sign of the Magnus moments may be critically dependent on the nature of the boundary layer, i.e., whether it is laminar, turbulent, or mixed. For the 20-deg cone used in these tests,

the value of the Magnus moment slope was found to be a function of the mean transition distance and could be expressed, with a probable error of 0.080, as

$$C_{m_{p\alpha}} = 0.38 - 0.18 \, \ell_t \qquad (5\text{-}6)$$

where

$$C_{m_{p\alpha}} = \text{slope of Magnus moment coefficient} = \frac{m_{p\alpha} \, p\alpha}{\frac{pd}{2V} \, qS \, d\alpha}$$

ℓ_t = mean transition distance, in diameters, from the nose

and the subscripts

p = rate of roll

α = angle of attack

A comparison of the probable error with the constants in the above equation shows that this expression is not very accurate. This inaccuracy is attributed to (1) the difficulty of determining the mean transition point from the photographic data (vertical spark shadowgraph), (2) the distribution and nature of the range data, and (3) the chaotic nature (alternating turbulent and laminar flow, probable unsteady conditions, etc.) of the boundary layer on many of the rounds.
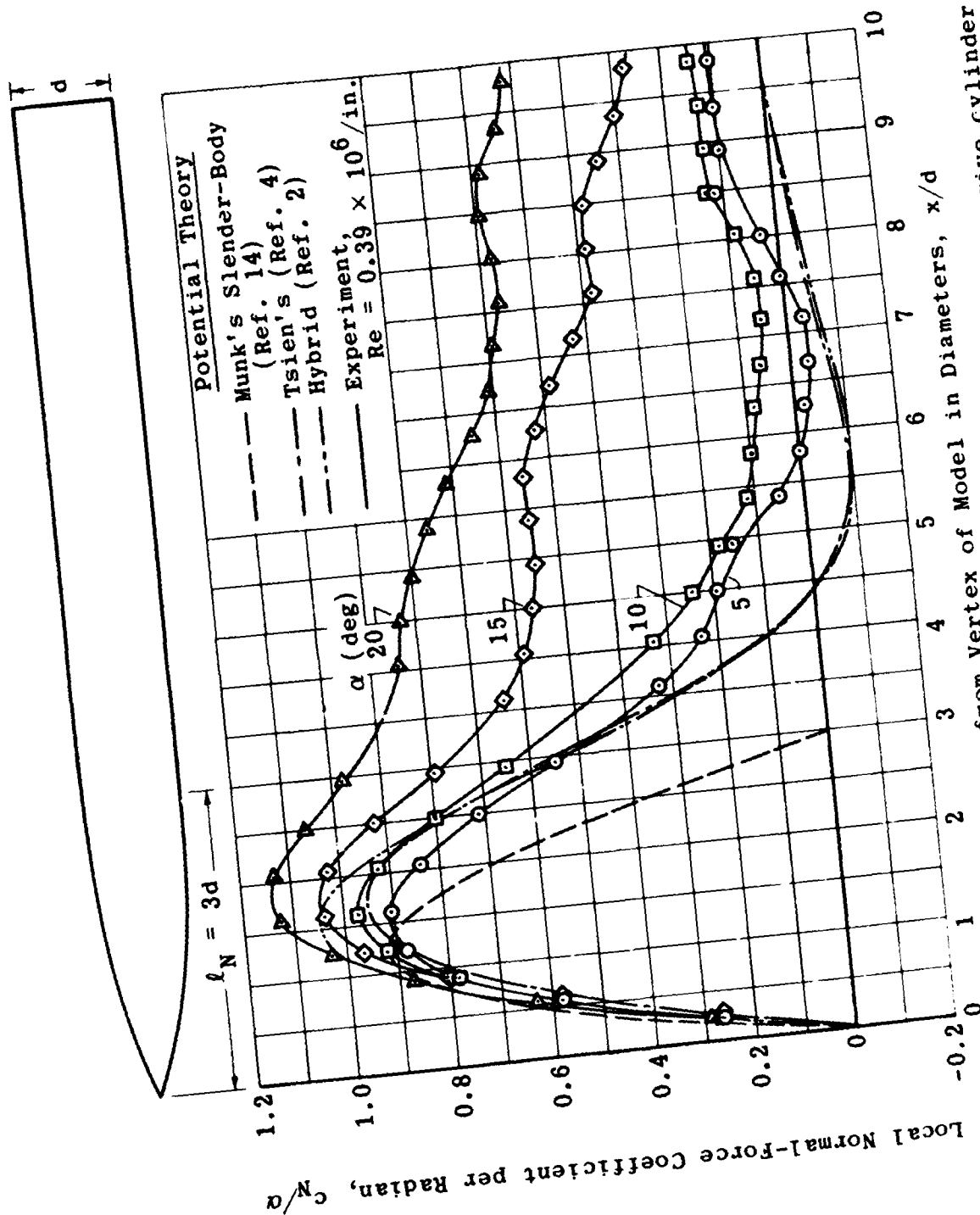
Fig. 5-1

Fig. 5-1. Local normal-force coefficient distribution for a tangent-ogive cylinder; M = 2.

$\ell_N = 3d$

Hybrid Theory (Ref. 2) plus
Allen's Viscous Method (Ref. 45)
Tsien's Potential (Ref. 4) plus
Allen's Viscous Method
Hybrid Theory plus Kelly's Viscous
Method (Ref. 47)

Experiment, $Re = 0.39 \times 10^6$/in.

$\alpha = 5$ deg

Local Normal-Force Coefficient, c_N

Experiment
$Re = 0.39 \times 10^6$/in.
$Re = 0.39 \times 10^6$/in. (re-run)
$Re = 0.13 \times 10^6$/in.

$\alpha = 10$ deg

Local Normal-Force Coefficient, c_N

Distance from Vertex of Model in Diameters, x/d
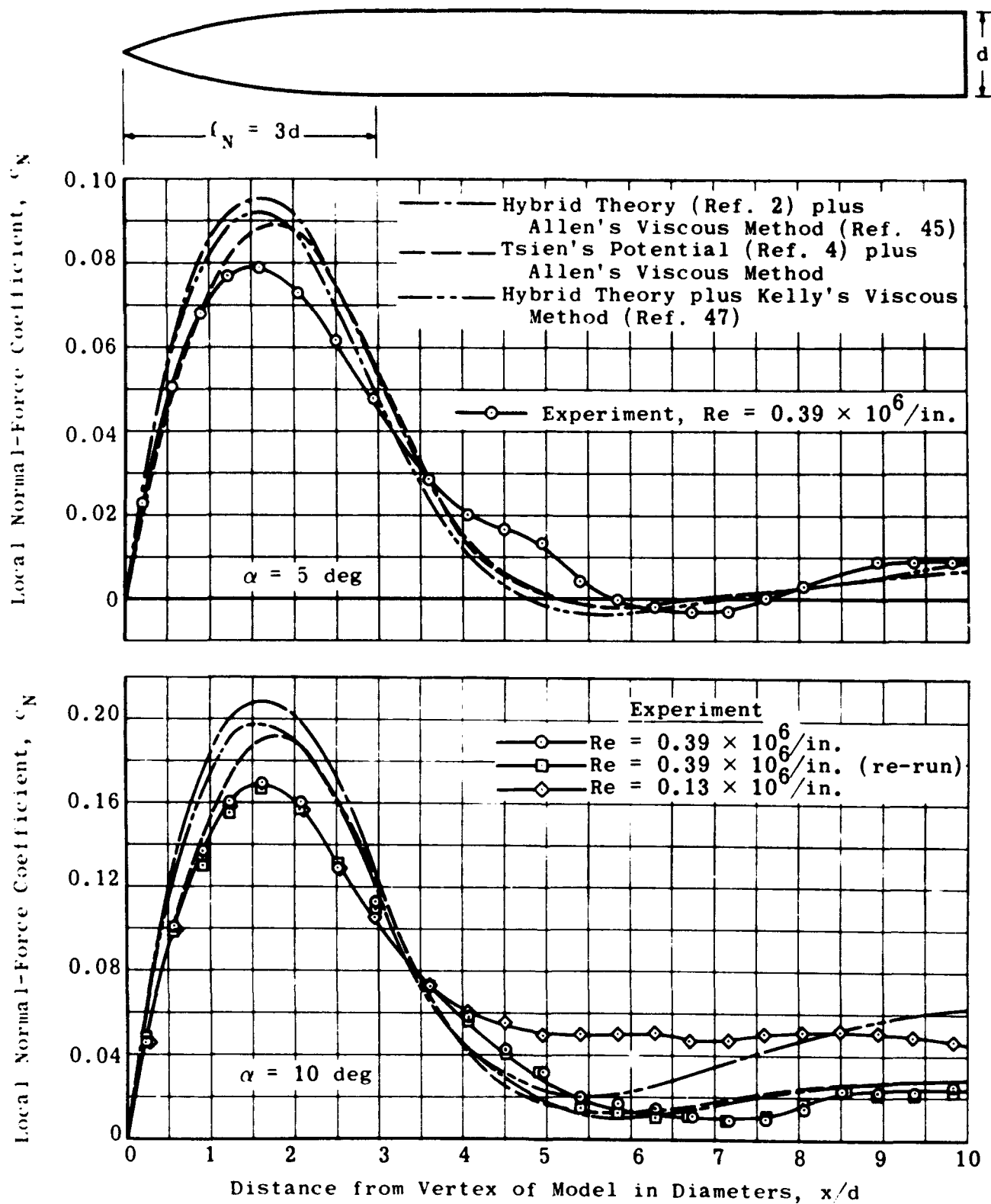
Fig. 5-2. Comparison of experimental and theoretical normal-force
distributions for a tangent-ogive cylinder; $M = 2$, $\alpha = 5$ and
10 deg. (Source: Ref. 52)
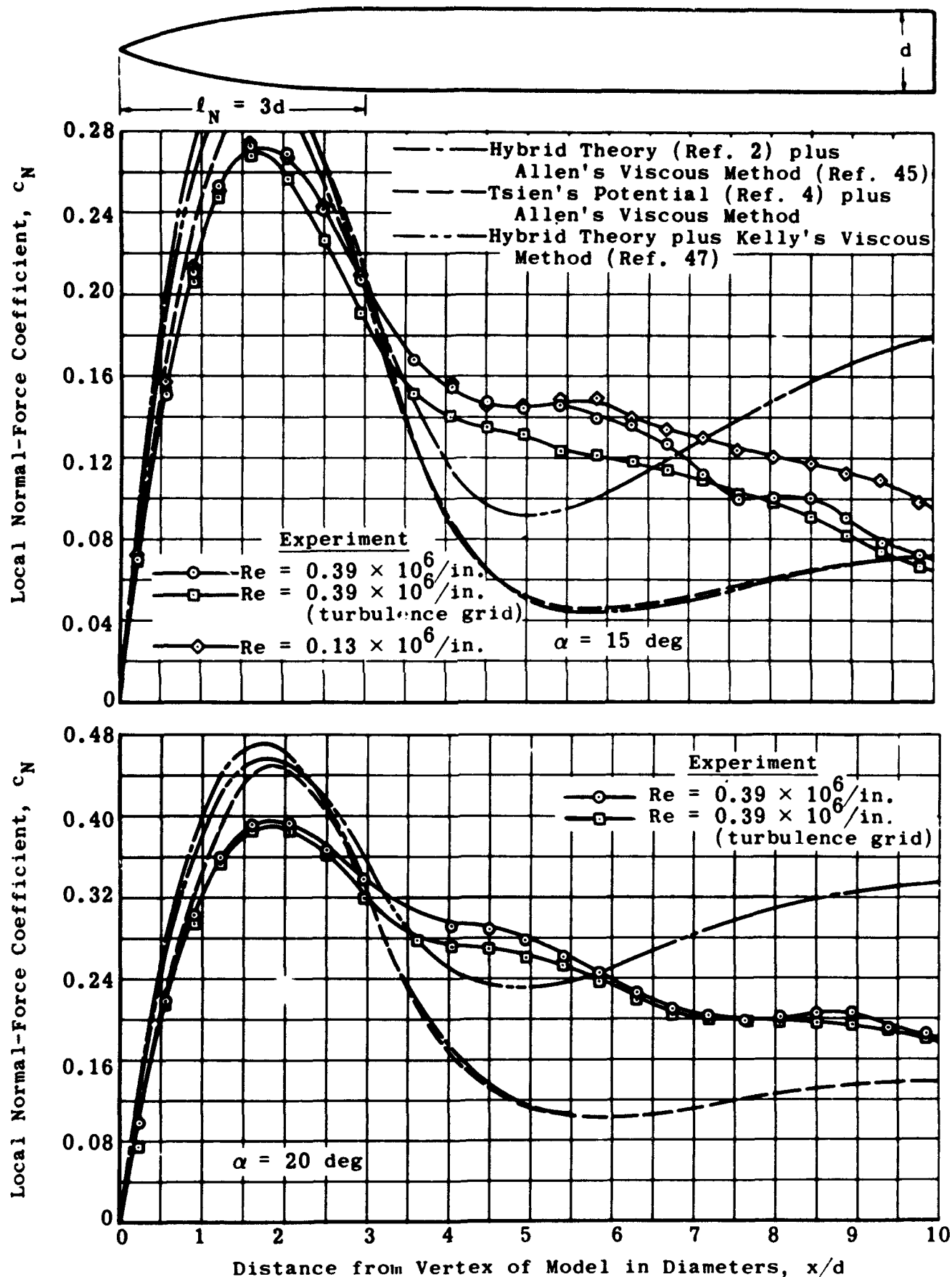
Fig. 5-3. Comparison of experimental and theoretical normal-force
distributions for a tangent-ogive cylinder; M = 2, α = 15 and
20 deg. (Source: Ref. 52)

177

Fig. 5-4   NAVWEPS Report 1488 (Vol. 3, Sec. 8)
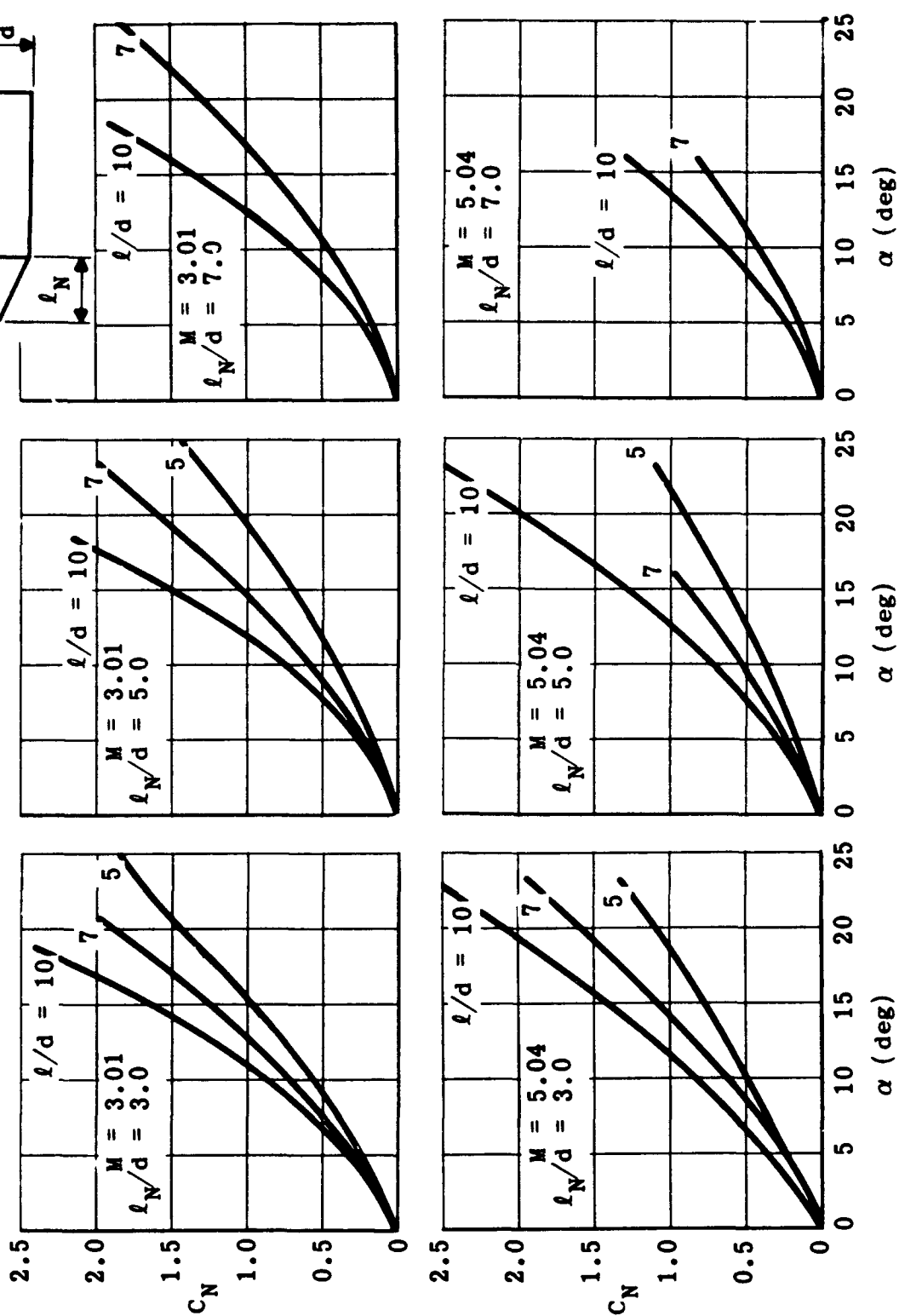
Fig. 5-4.   Measured normal-force coefficient versus angle of attack for cone-cylinder
            combinations; M = 3.01 and 5.04.   (Source: Ref. 95)
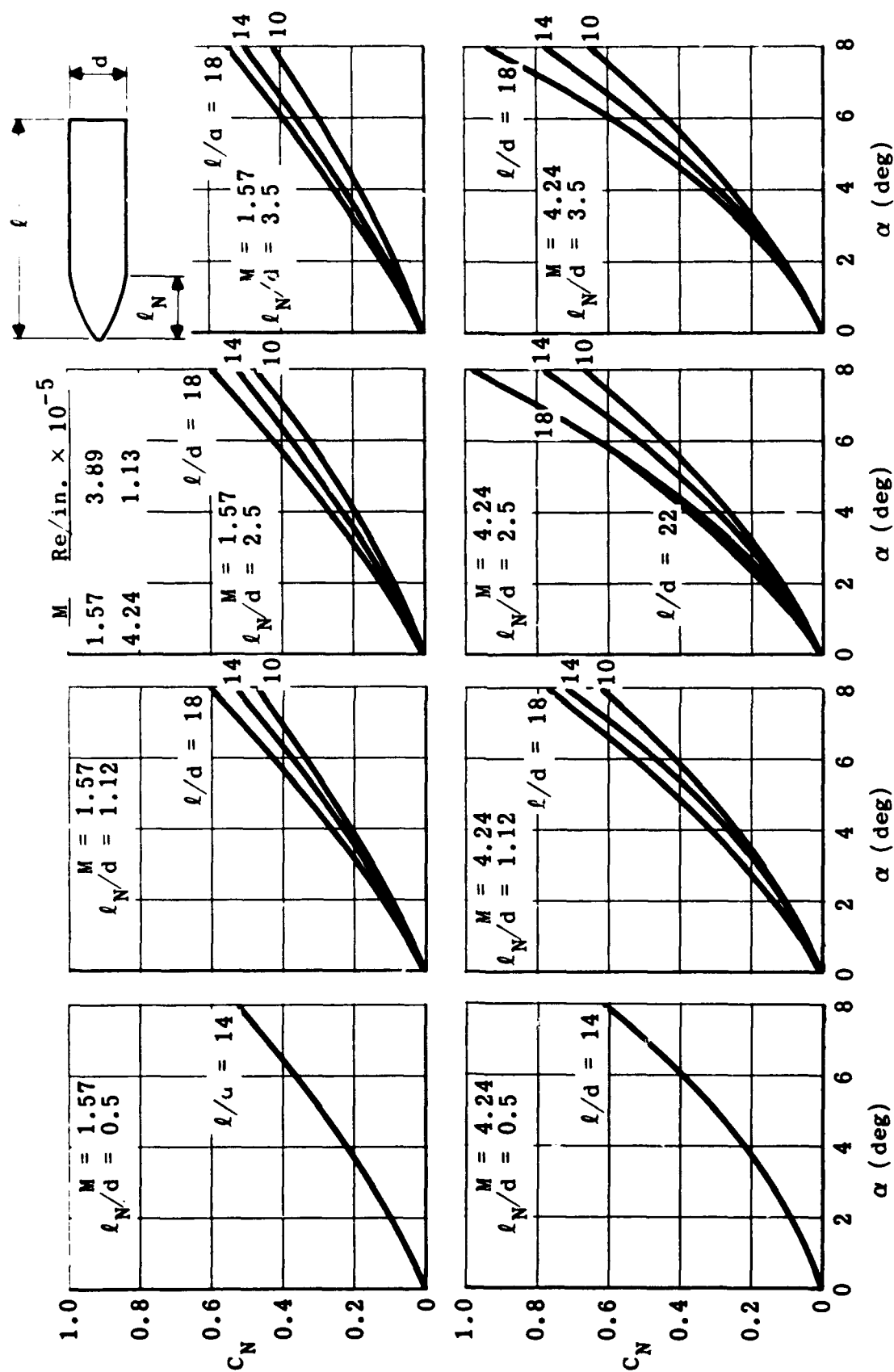
Fig. 5-5. Measured normal-force coefficient versus angle of attack for tangent-ogive-cylinder combinations; M = 1.57 and 4.24. (Source: Ref. 97)

Fig. 5-6   NAVWEPS Report 1488 (Vol. 3, Sec. 8)
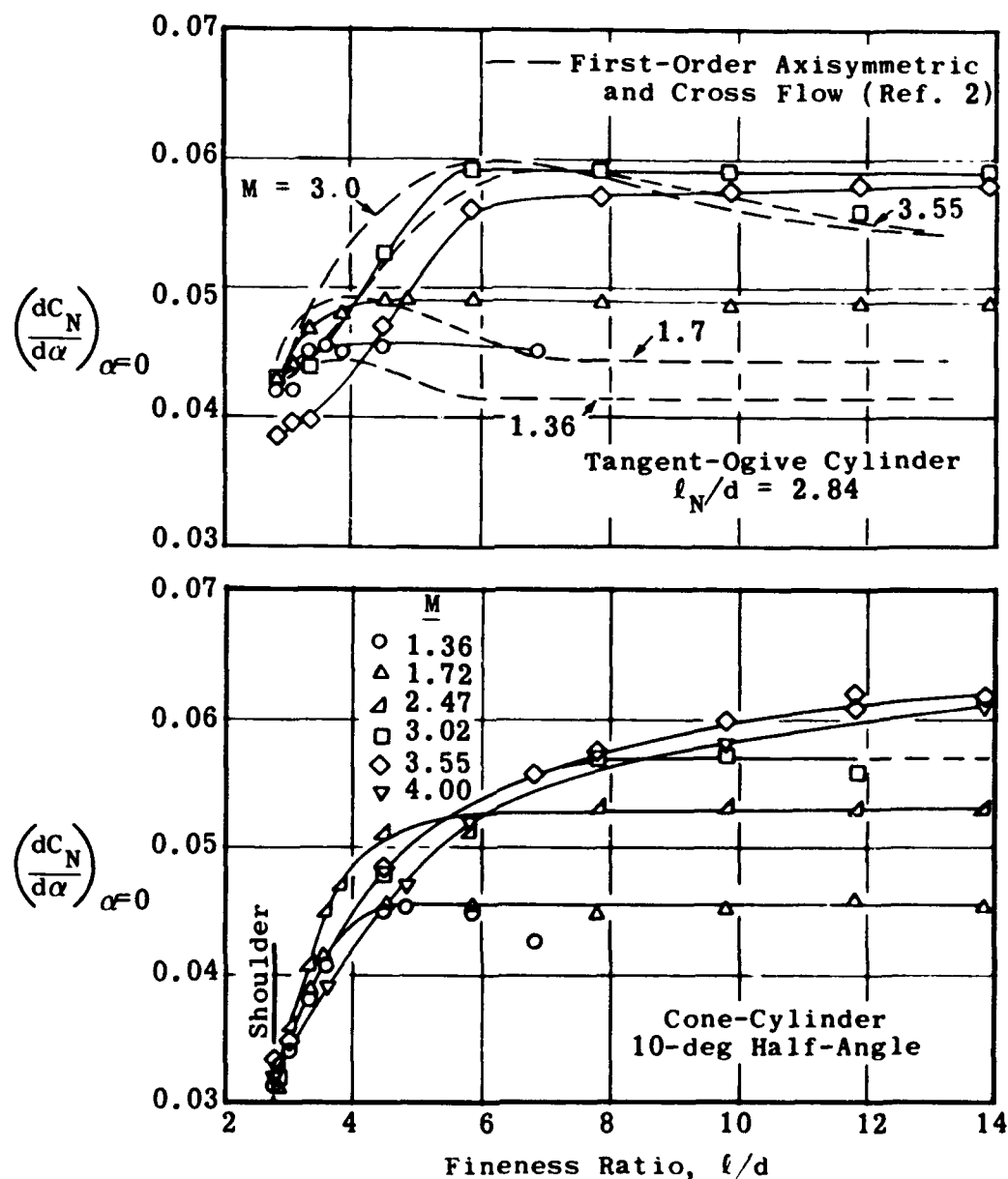
Fig. 5-6. Comparison of theoretical and experimental values of
initial normal-force slope versus fineness ratio for ogival-
nosed and conical-nosed cylinders at various Mach numbers.
(Source: Ref. 98)
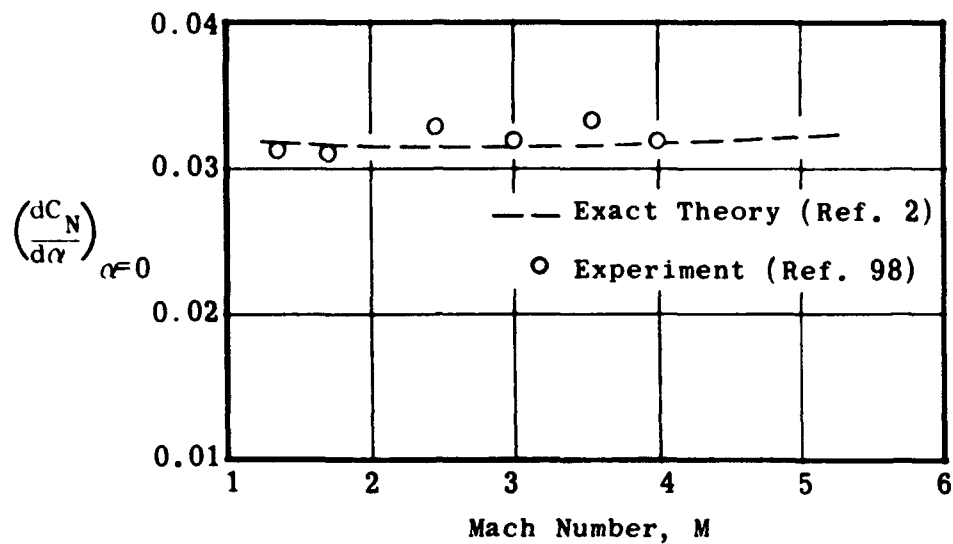
Fig. 5-7. Comparison of experimental values with exact theory for initial normal-force slope as a function of Mach number for a 10-deg half-angle cone. (Source: Ref. 98)
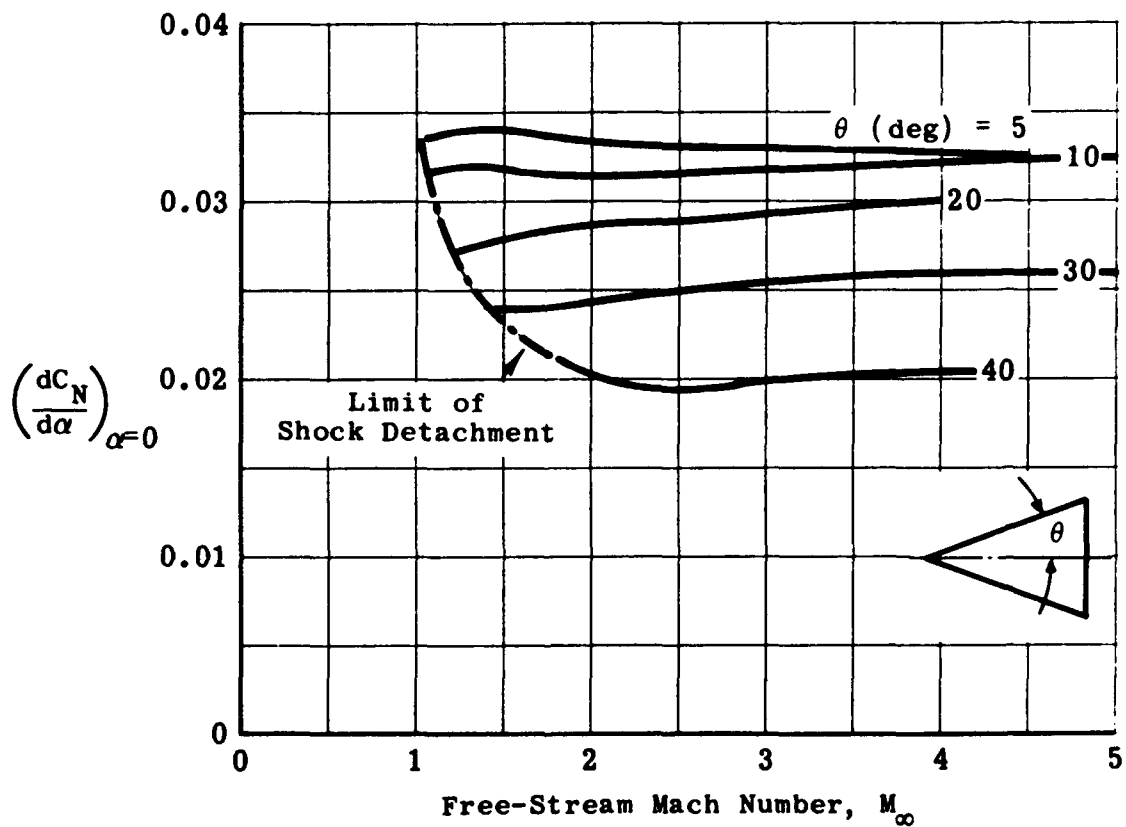
Fig. 5-8. Initial slope of normal-force versus Mach number for cones predicted by Stone-Kopal first-order theory. (Source: Ref. 96)

Fig. 5-9   NAVWEPS Report 1488 (Vol. 3, Sec. 8)
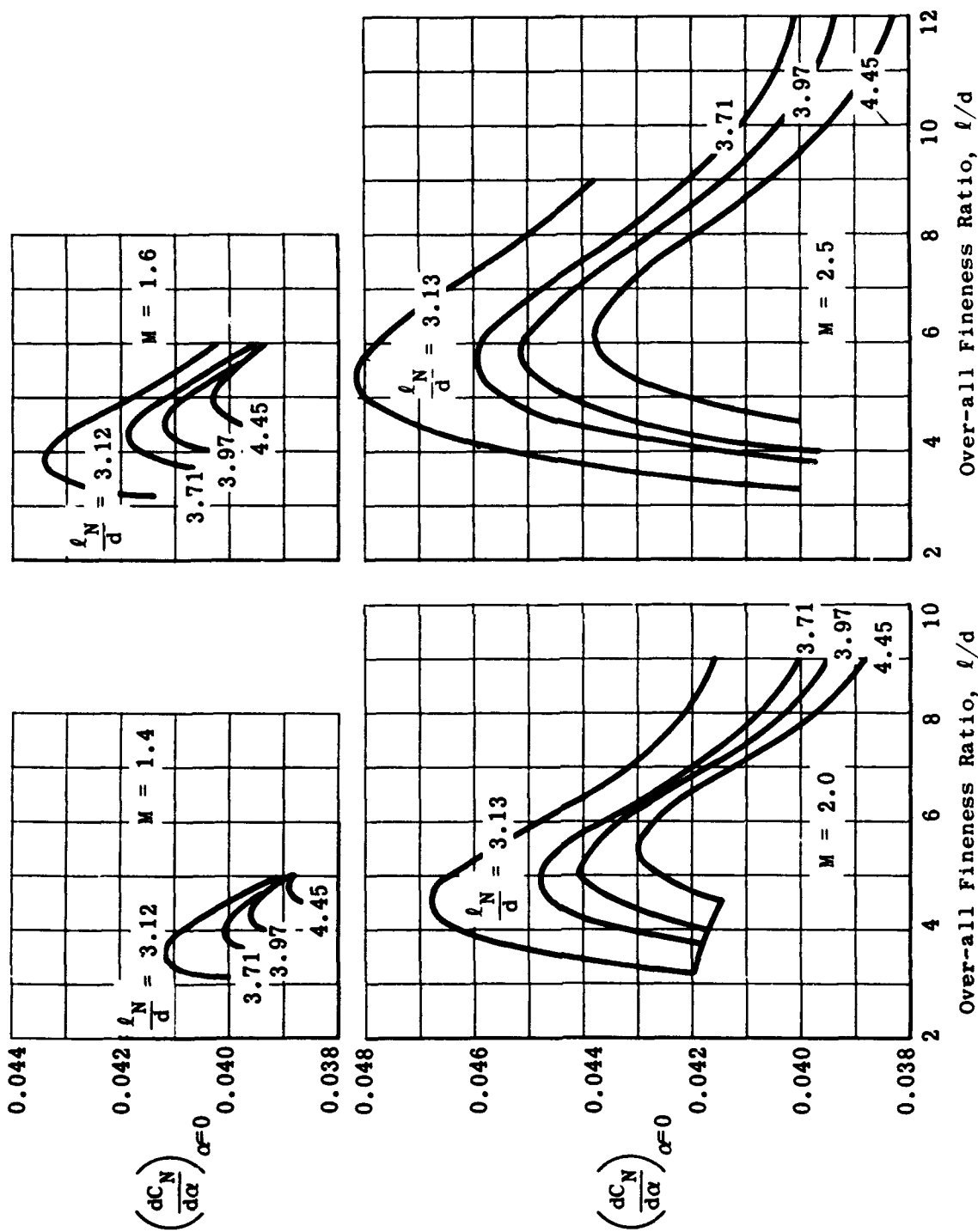
Fig. 5-9. Calculated initial slope of normal-force curves versus fineness ratio for tangent-ogive cylinders; M = 1.4 to 3.5 (Source: Ref. 96)
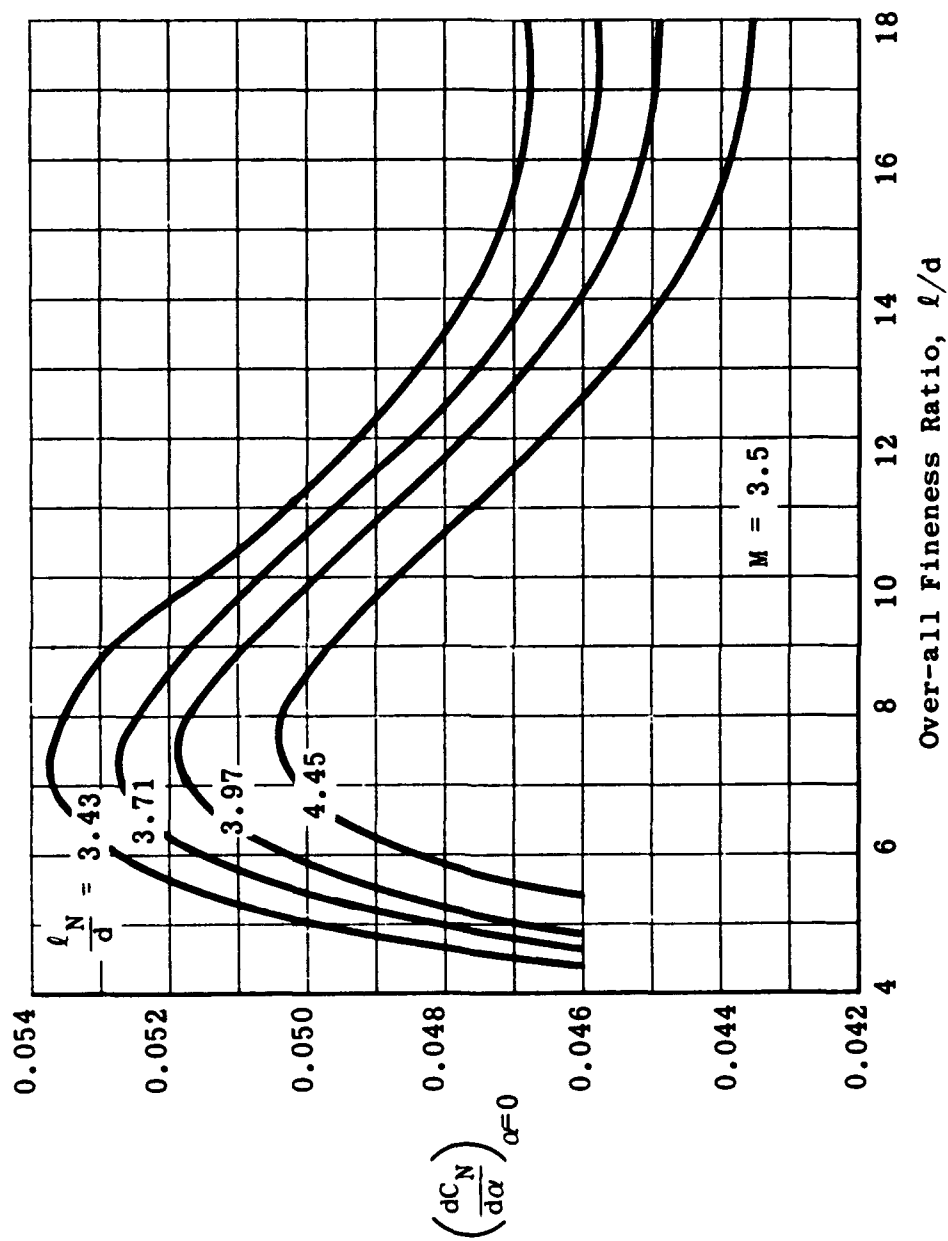
Fig. 5-9 (Cont'd). Calculated initial slope of normal-force curves versus fineness ratio for tangent-ogive cylinders; M = 1.4 to 3.5. (Source: Ref. 96)

Fig. 5-10   NAVWEPS Report 1488 (Vol. 3, Sec. 8)
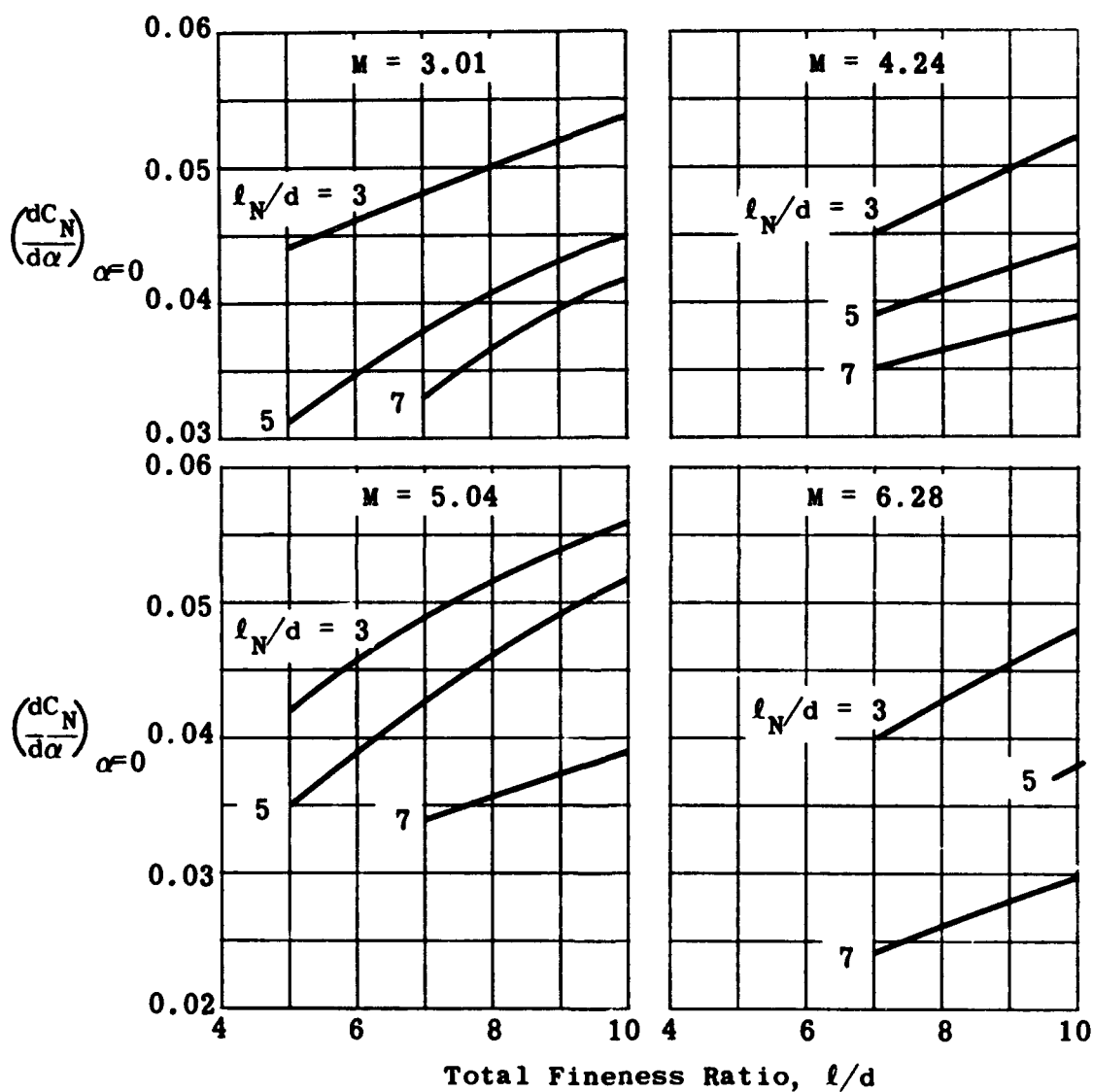
Fig. 5-10. Measured initial normal-force slope versus fineness
    ratio for cone-cylinders at several nose fineness ratios and
    Mach numbers. (Source: Ref. 95)
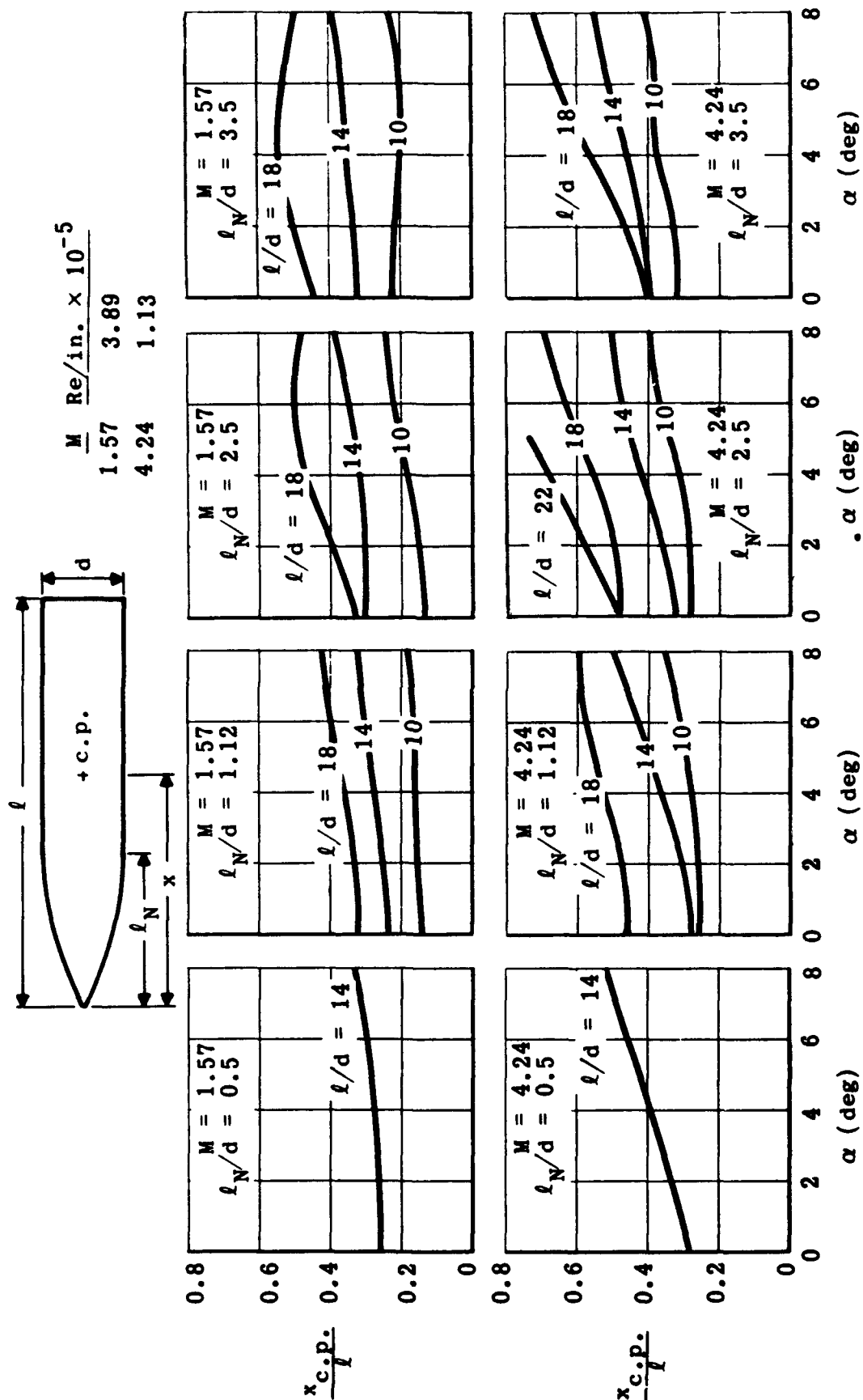
Fig. 5-11. Measured center-of-pressure location versus angle of attack for tangent-ogive cylinders with varying nose and body fineness ratios; M = 1.57 and 4.24. (Source: Ref. 97)

Fig. 5-12   NAVWEPS Report 1488 (Vol. 3, Sec. 8)
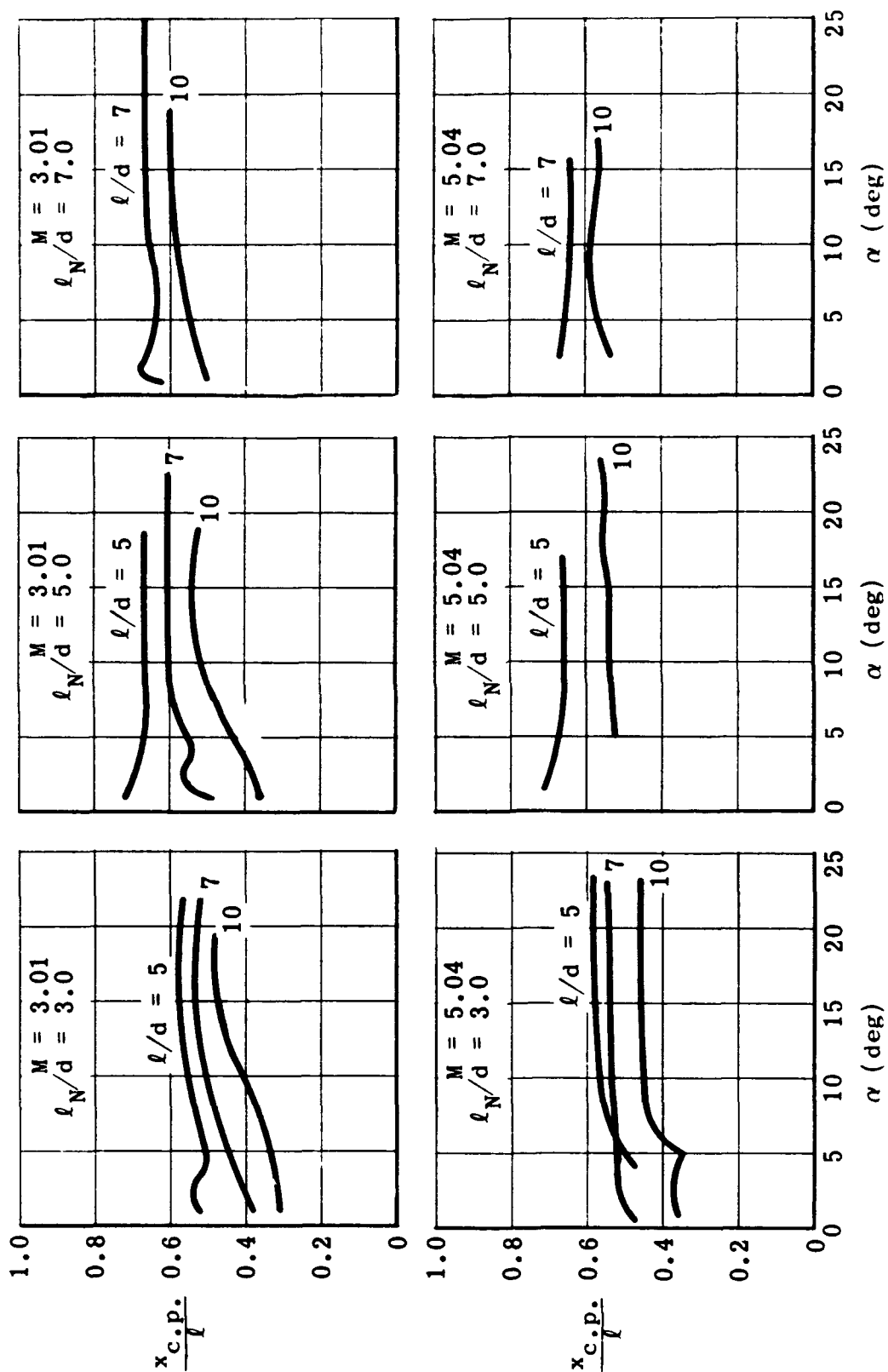
Fig. 5-12. Measured center-of-pressure location versus angle of attack for tangent-ogive cylinders with varying nose and body fineness ratios; M = 3.01 and 5.04. (Source: Ref. 95)
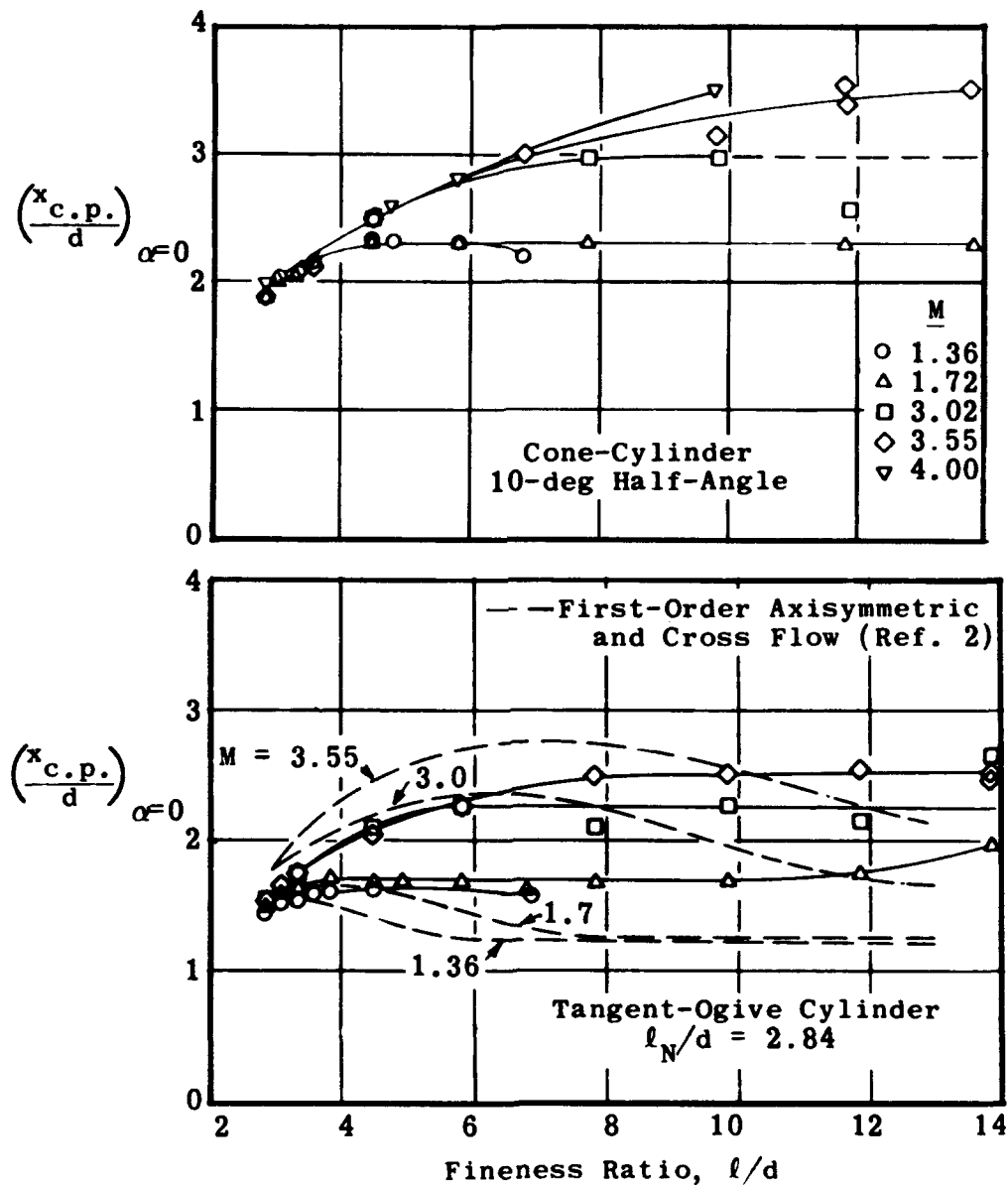
Fig. 5-13. Comparison of theoretical and experimental center-of-pressure locations versus fineness ratio for ogival-nosed and conical-nosed cylinders at various Mach numbers. (Source: Ref. 98)

Fig. 5-14   NAVWEPS Report 1488 (Vol. 3, Sec. 8)
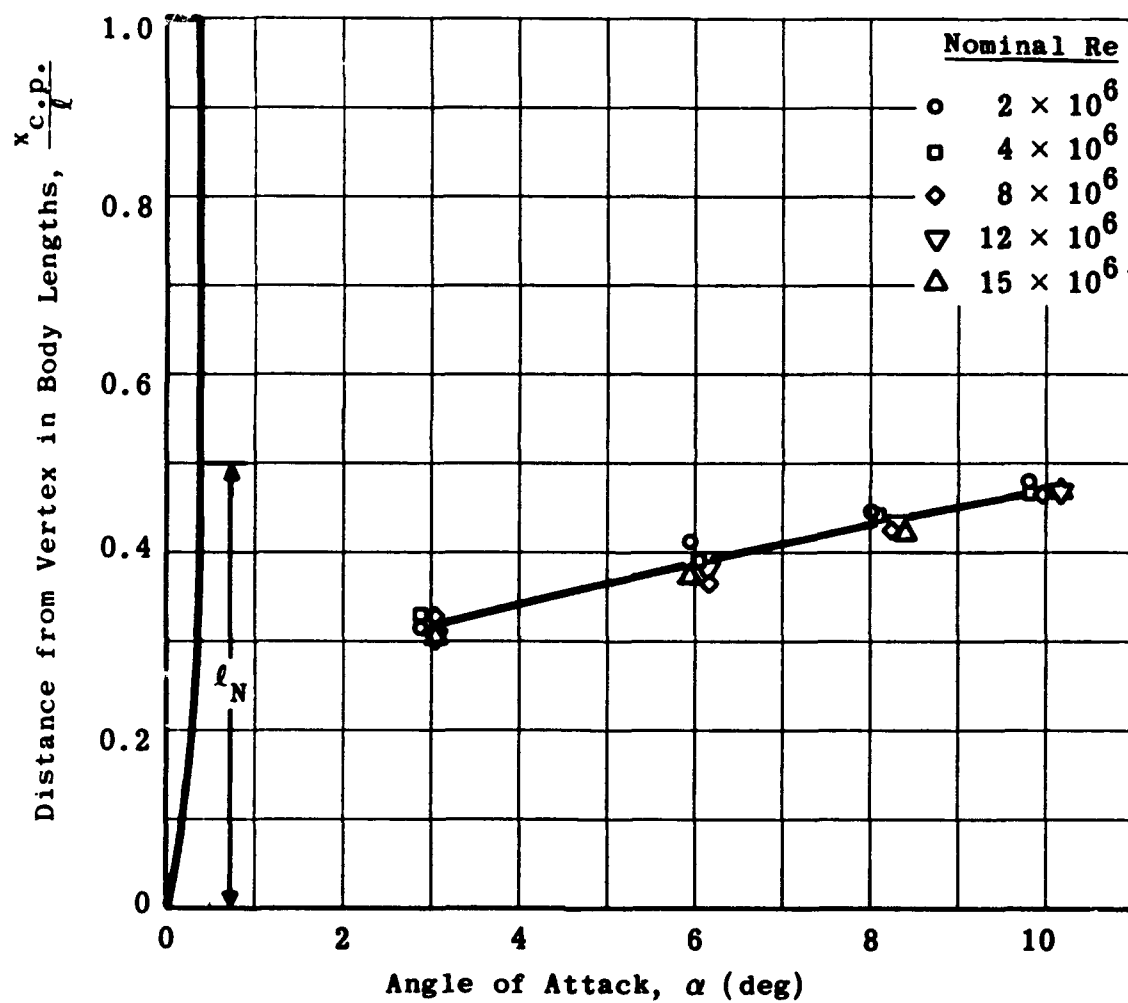
Fig. 5-14. Effect of Reynolds number on center-of-pressure
            location versus angle of attack for a cylindrical body
            with near-parabolic nose; M = 3.12. (Source: Ref. 99)
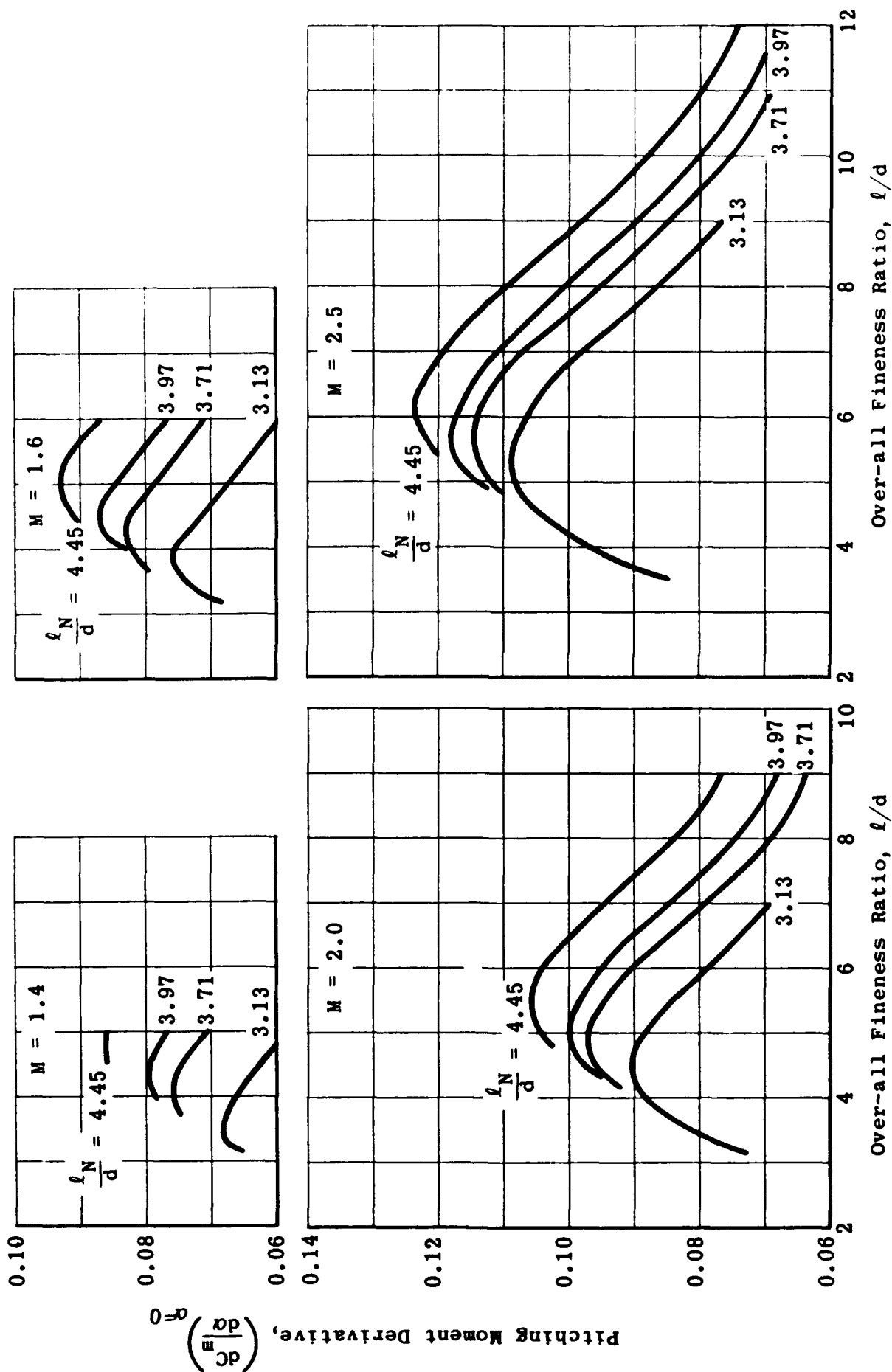
Fig. 5-15. Calculated initial slope of pitching moment about the base versus fineness ratio of tangent-ogive cylinders for several nose fineness ratios and Mach numbers. (Source: Ref. 96)

Fig. 5-15   NAVWEPS Report 1488 (Vol. 3, Sec. 8)
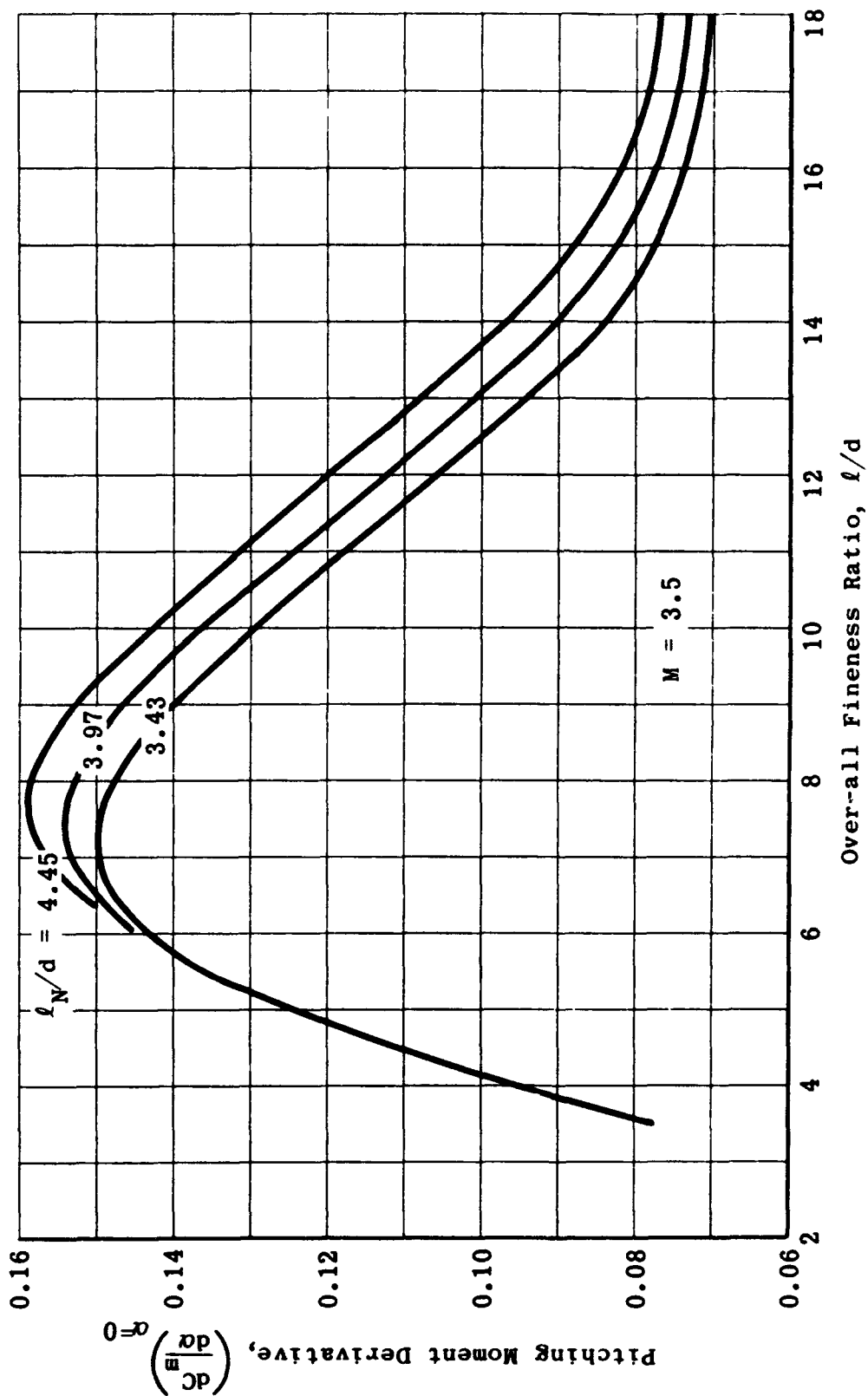
Fig. 5-15 (Cont'd). Calculated initial slope of pitching moment about the base versus fineness ratio of tangent-ogive cylinders for several nose fineness ratios and Mach numbers. (Source: Ref. 96)
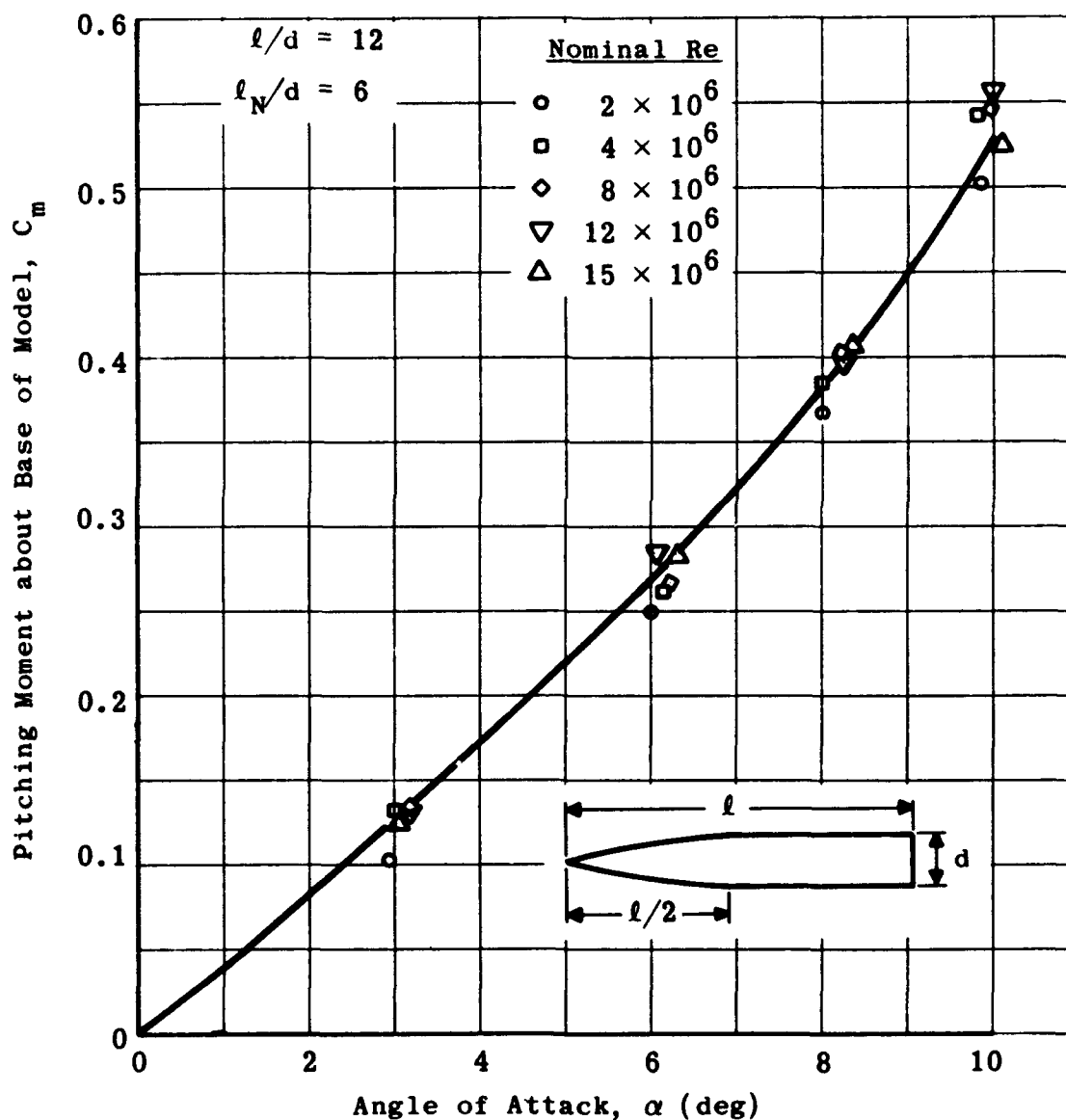
Fig. 5-16. Effect of Reynolds number on pitching moment versus angle of attack for a cylindrical body with near-parabolic nose; M = 3.12. (Source: Ref. 99)

Fig. 5-17   NAVWEPS Report 1488 (Vol. 3, Sec. 8)
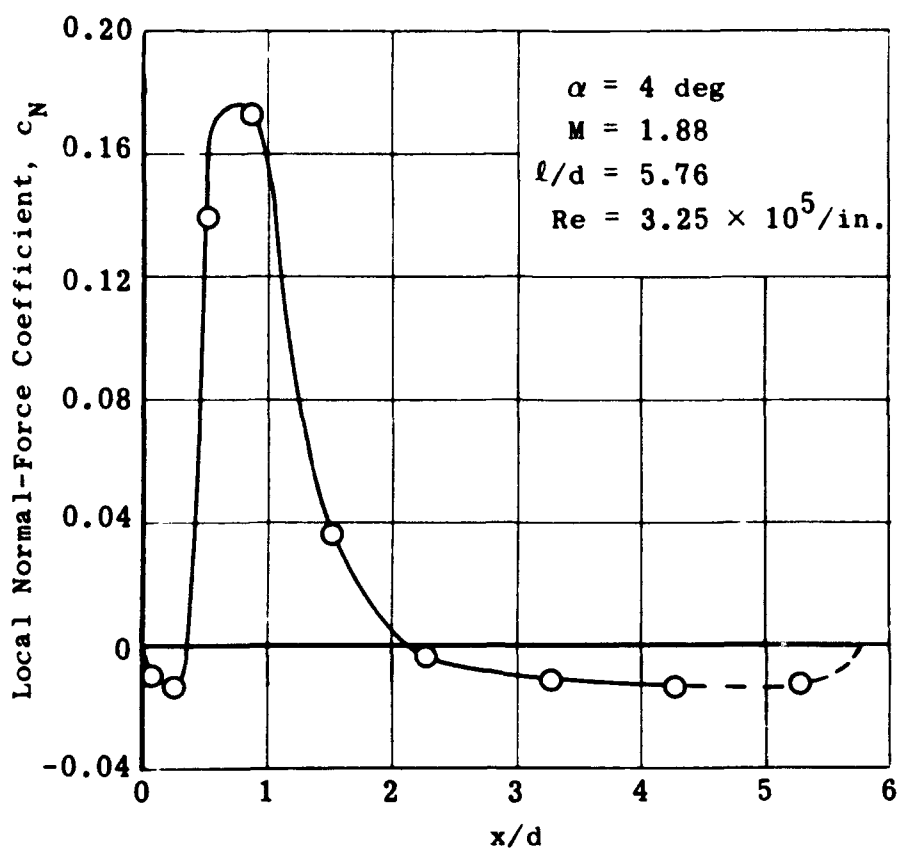
Fig. 5-17. Distribution of experimental local normal-force
coefficient along a cylinder; M = 1.88, α = 4 deg.
(Source: Ref. 92)
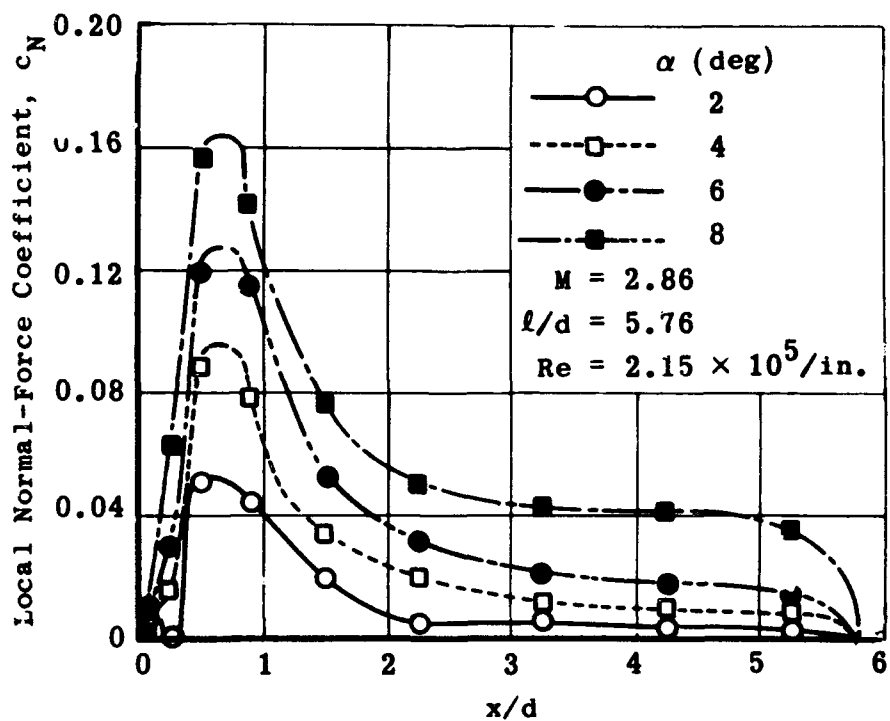
Fig. 5-18. Distribution of experimental local normal-force
coefficient along a cylinder; M = 2.86, α = 2 to 8 deg.
(Source: Ref. 92)
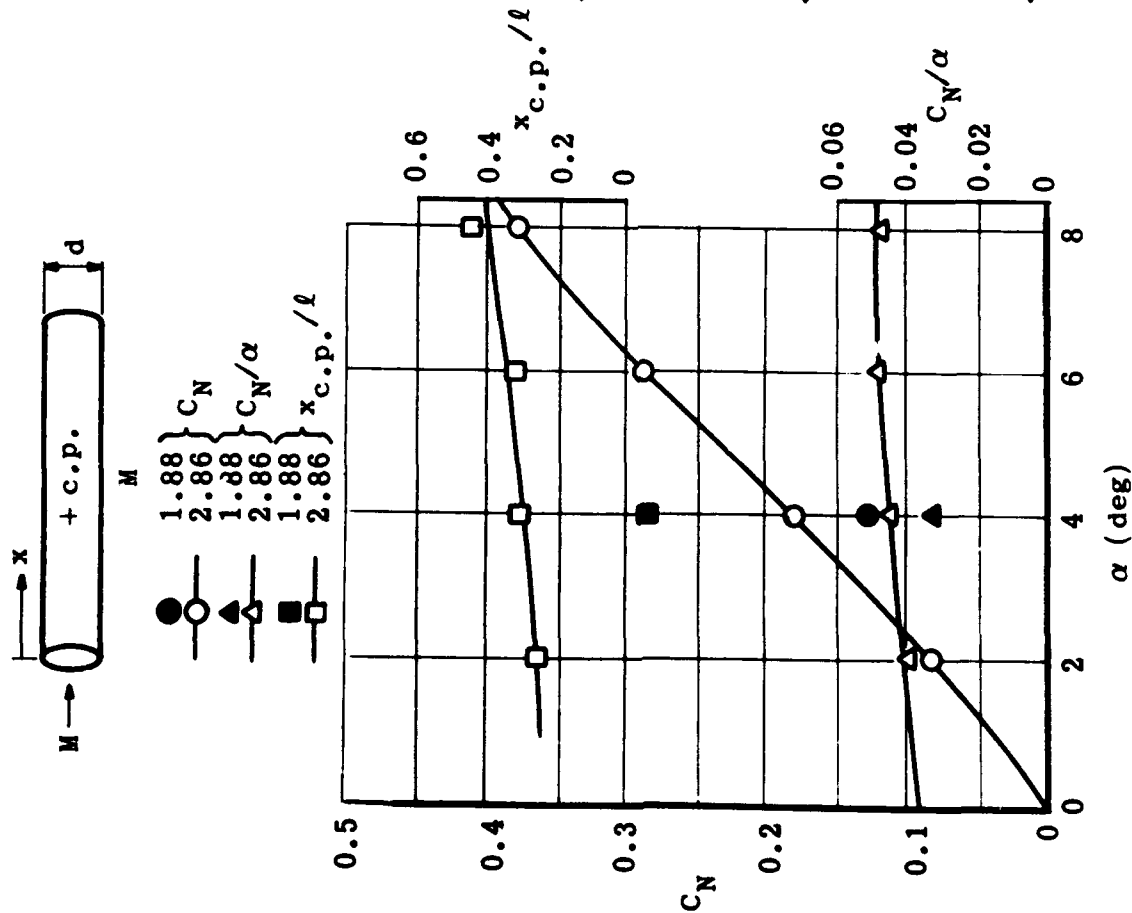
Fig. 5-19. Total normal-force coefficient and
center-of-pressure location versus angle
of attack for cylinders; M = 1.88 and 2.86.
(Source: Ref. 92)

Fig. 5-20. Configurations for skirted-body
study. (Source: Ref. 101)

Body	Cylinder ℓ_c/d_c	Frustum Half-Angle, θ (deg)
A-1	1	6
A-2	3	6
A-3	5	6
B-1	1	14
B-2	3	14
B-3	5	14
C-1	1	22
C-2	3	22
C-3	5	22

193

Fig. 5-21   NAVWEPS Report 1488 (Vol. 3, Sec. 8)
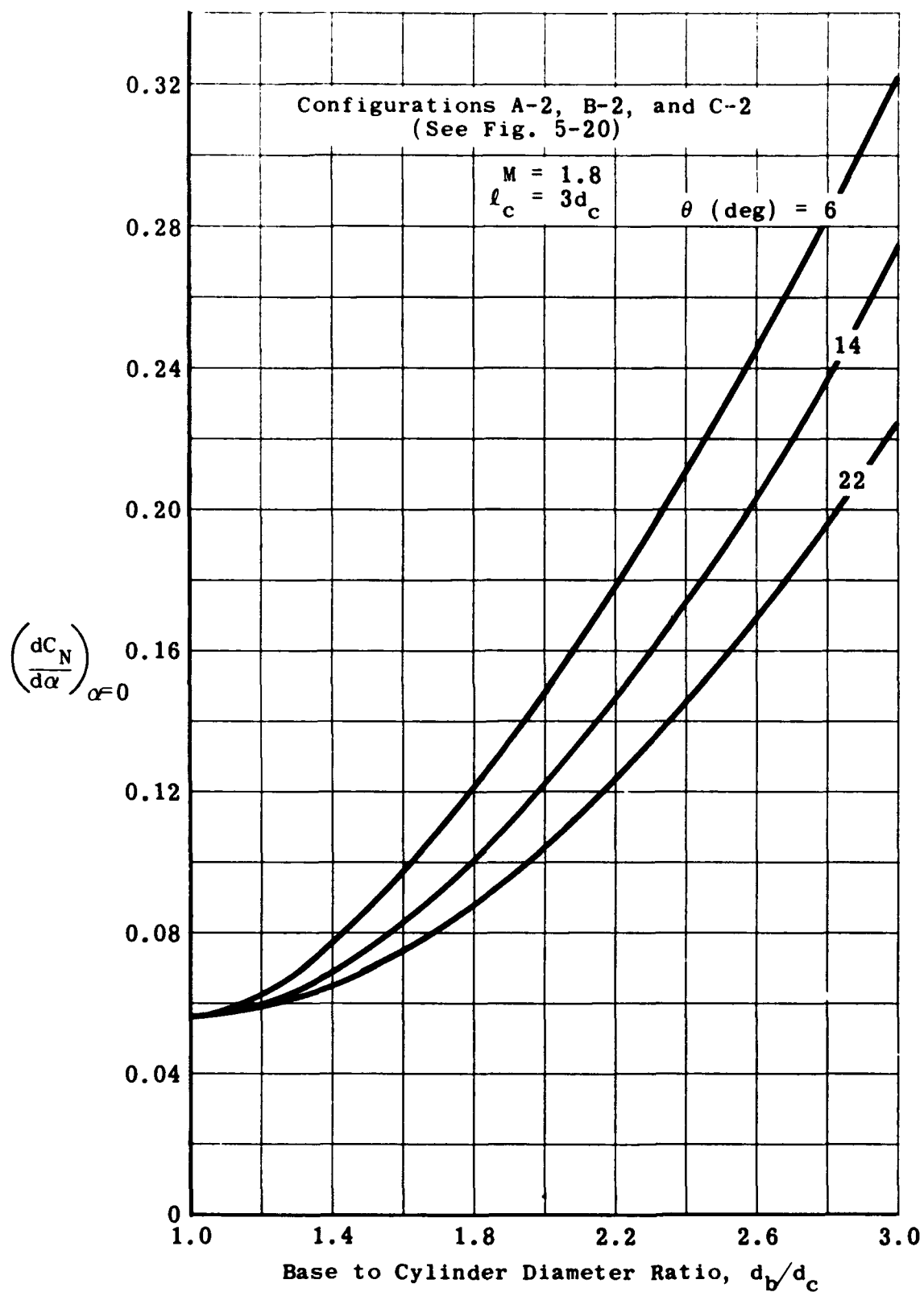
Fig. 5-21. Calculated initial normal-force slope versus base-to-
body diameter ratio; M = 1.8. (Source: Ref. 101)
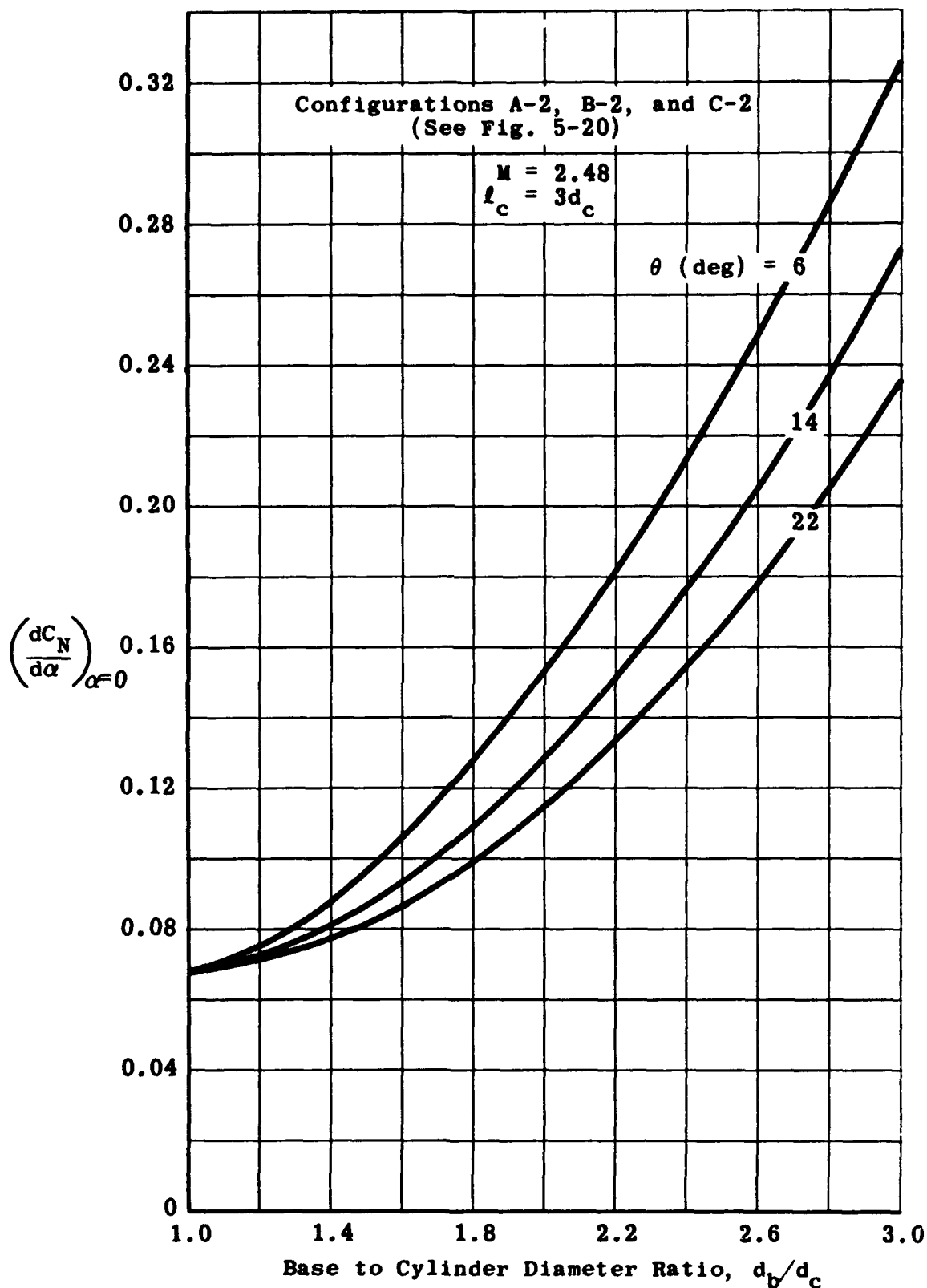
Fig. 5-22. Calculated initial normal-force slope versus base-to-body diameter ratio; M = 2.48. (Source: Ref. 101)

Fig. 5-23   NAVWEPS Report 1488 (Vol. 3, Sec. 8)
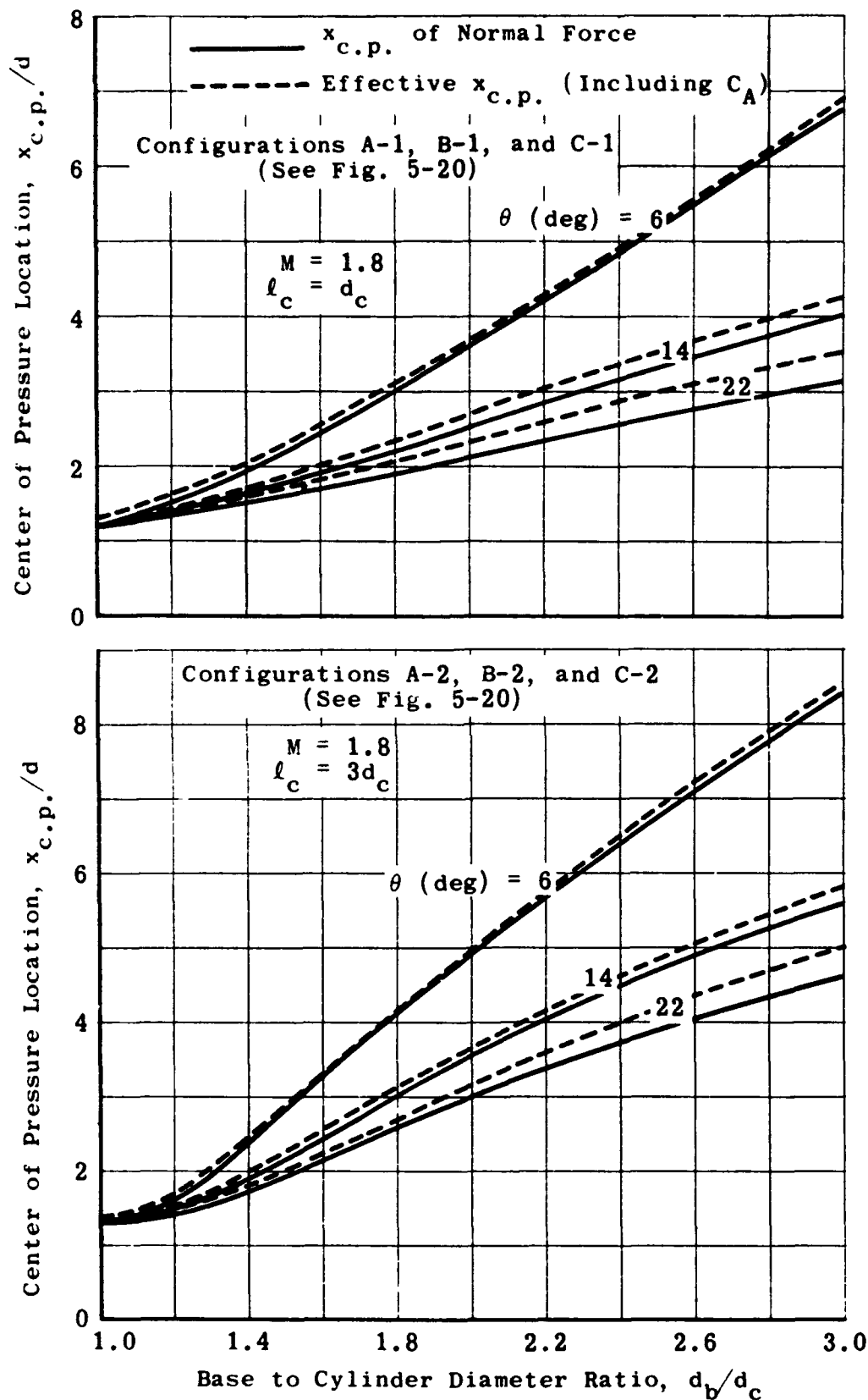
Fig. 5-23. Calculated center-of-pressure location versus base-to-body diameter ratio; M = 1.8. (Source: Ref. 101)
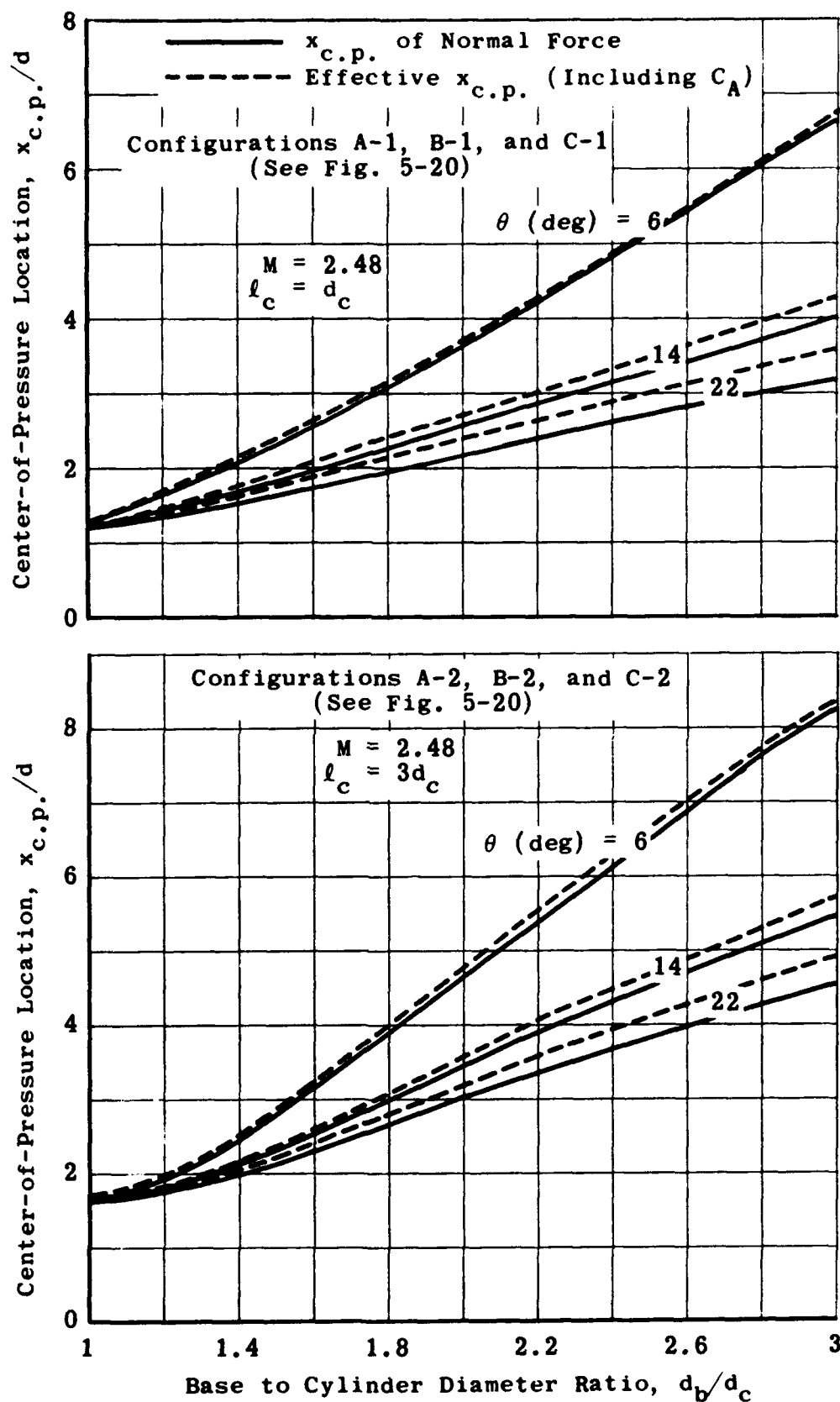
Fig. 5-24. Calculated center-of-pressure location versus base-to-body diameter ratio; M = 2.48. (Source: Ref. 101)

Fig. 5-25   NAVWEPS Report 1488 (Vol. 3, Sec. 8)
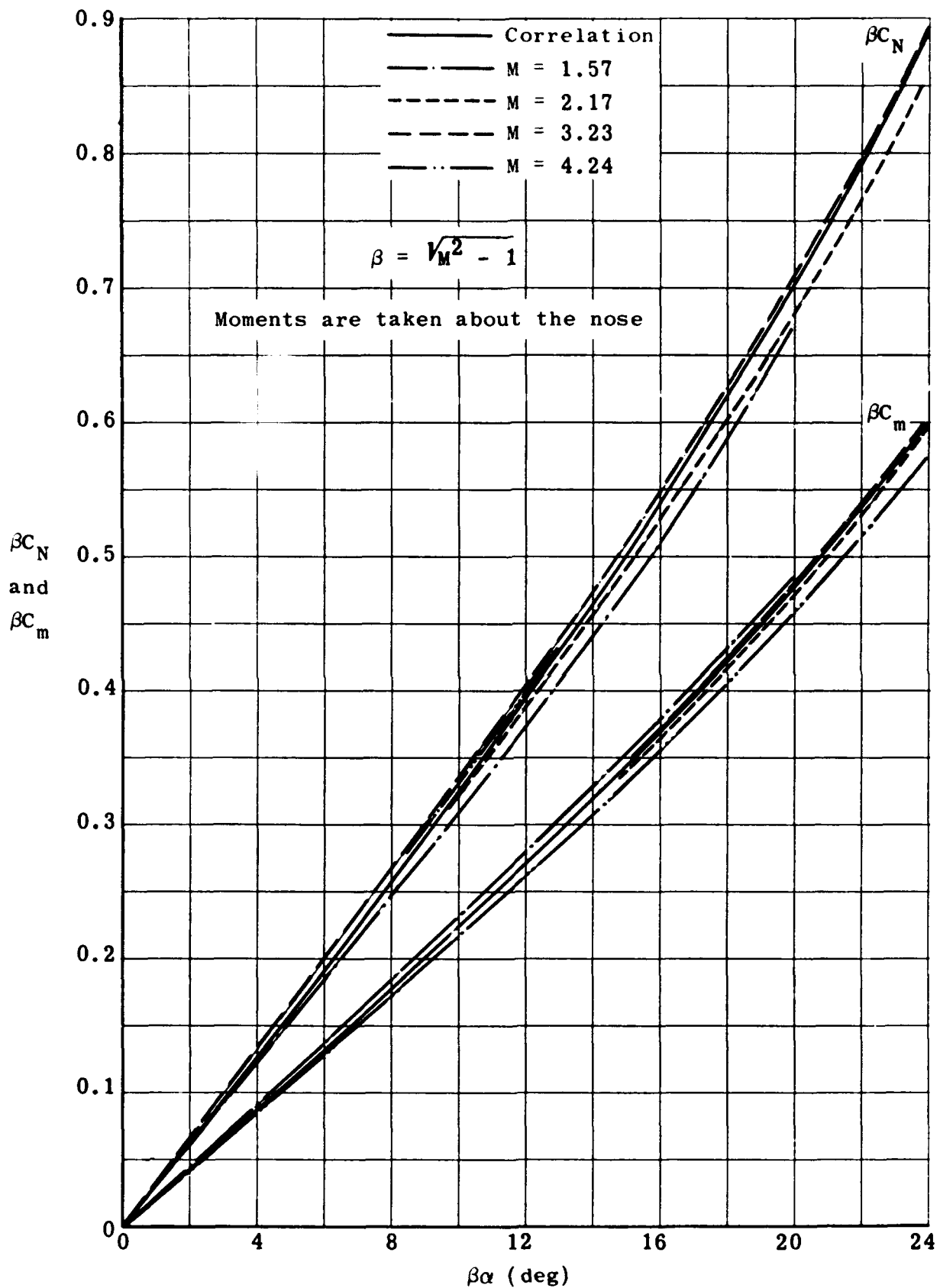
Fig. 5-25. Correlation of βC_N and βC_m versus $\beta\alpha$ for cones at various Mach numbers; $K = 0.6$. (Source: Ref. 102)
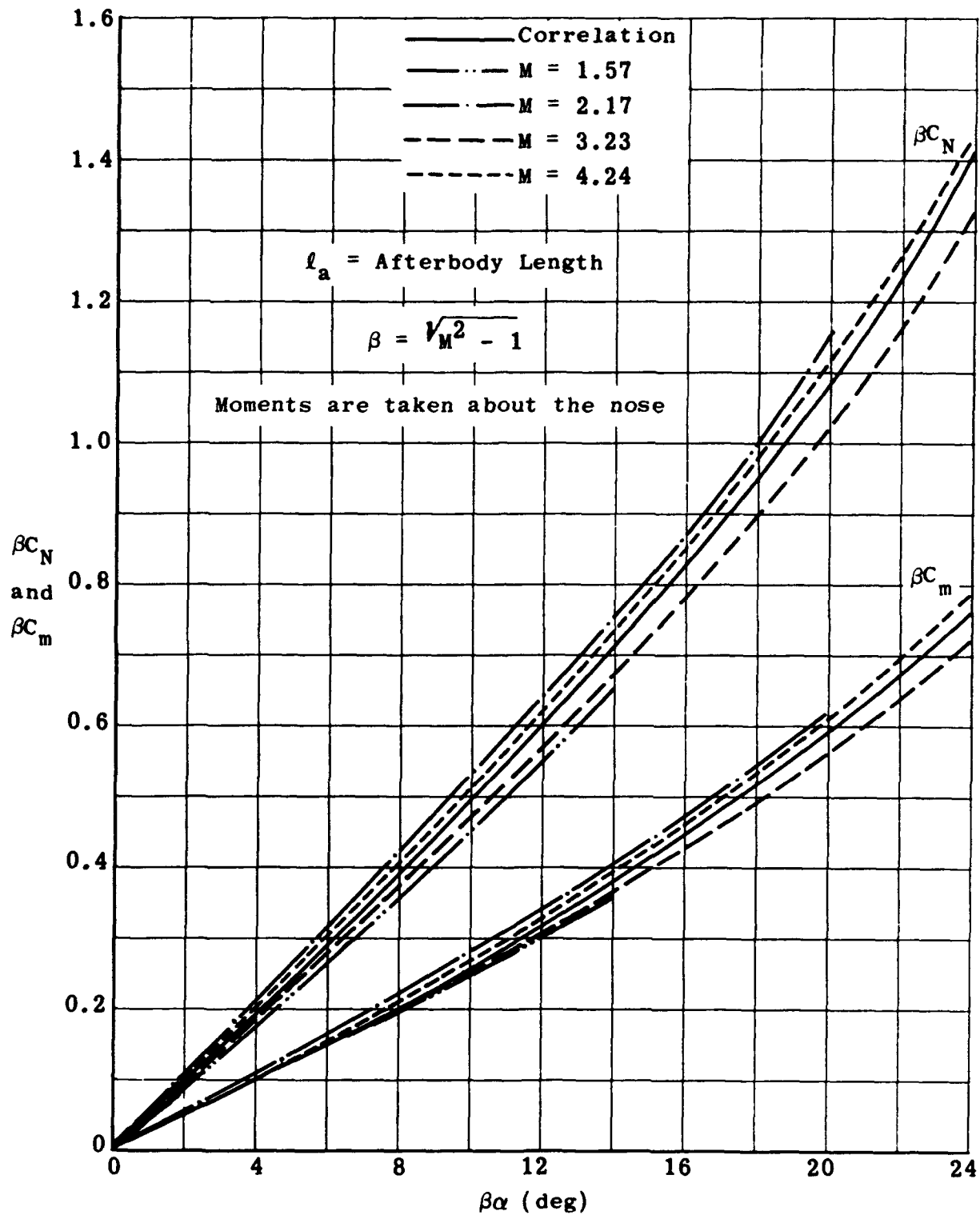
Fig. 5-26.   Correlation of βC_N and βC_m versus $\beta\alpha$ for cone-cylinders; K = 0.6, ℓ_a = 0.62 ℓ_N. (Source: Ref. 102)

Fig. 5-27   NAVWEPS Report 1488 (Vol. 3, Sec. 8)
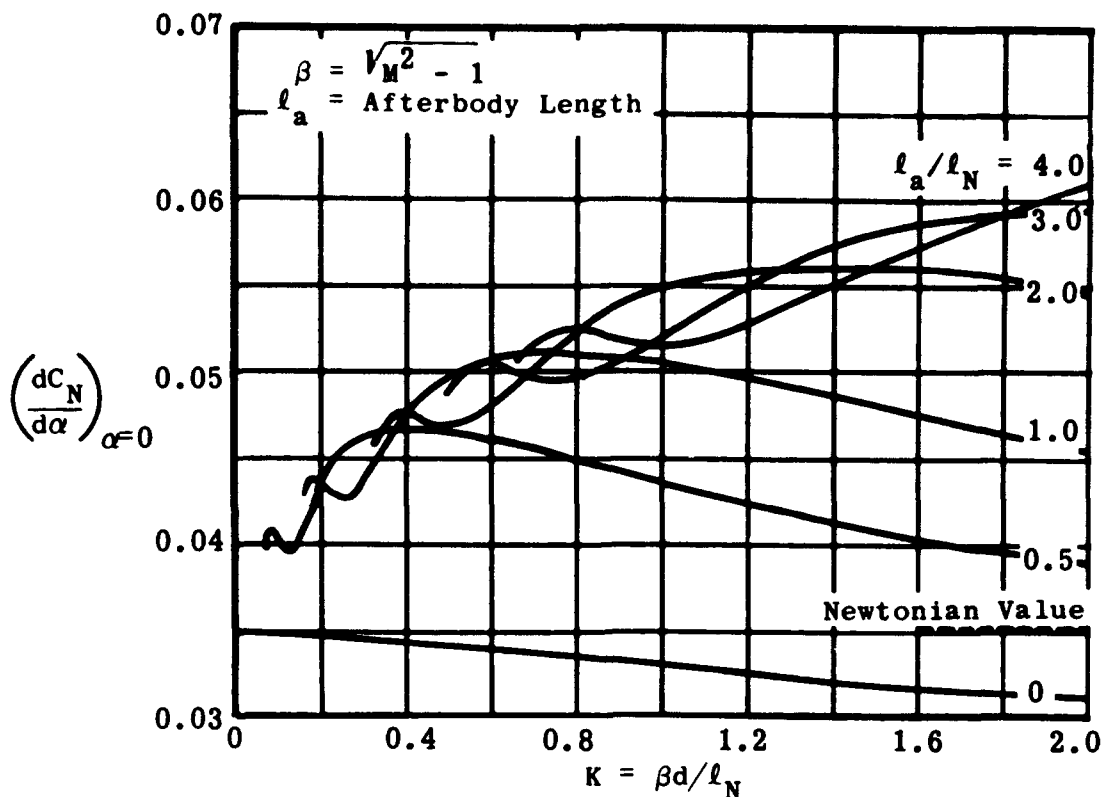
Fig. 5-27. Calculated initial normal-force slope versus K for
various cone-cylinders at zero angle of attack.
(Source: Ref. 102)
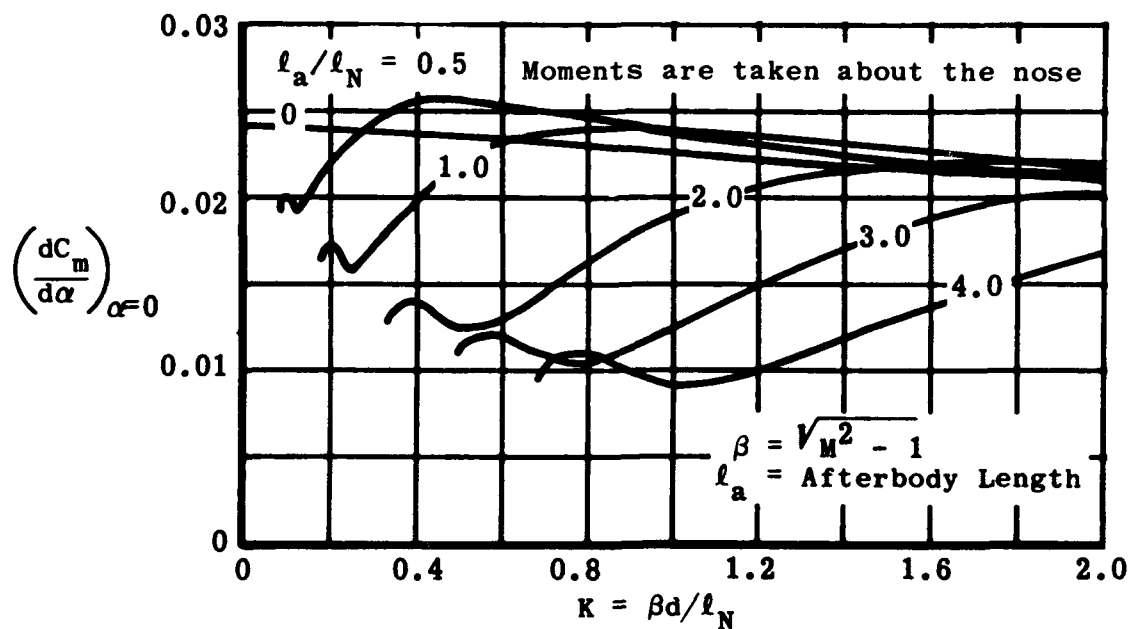
Fig. 5-28. Calculated initial pitching-moment slope versus K
for various cone-cylinders at zero angle of attack.
(Source: Ref. 102)

$$\beta = \sqrt{M^2 - 1}$$

ℓ_a = Afterbody Length

$\left(\dfrac{x_{c.p.}}{\ell}\right)_{\alpha=0}$

$K = \beta d/\ell_N$
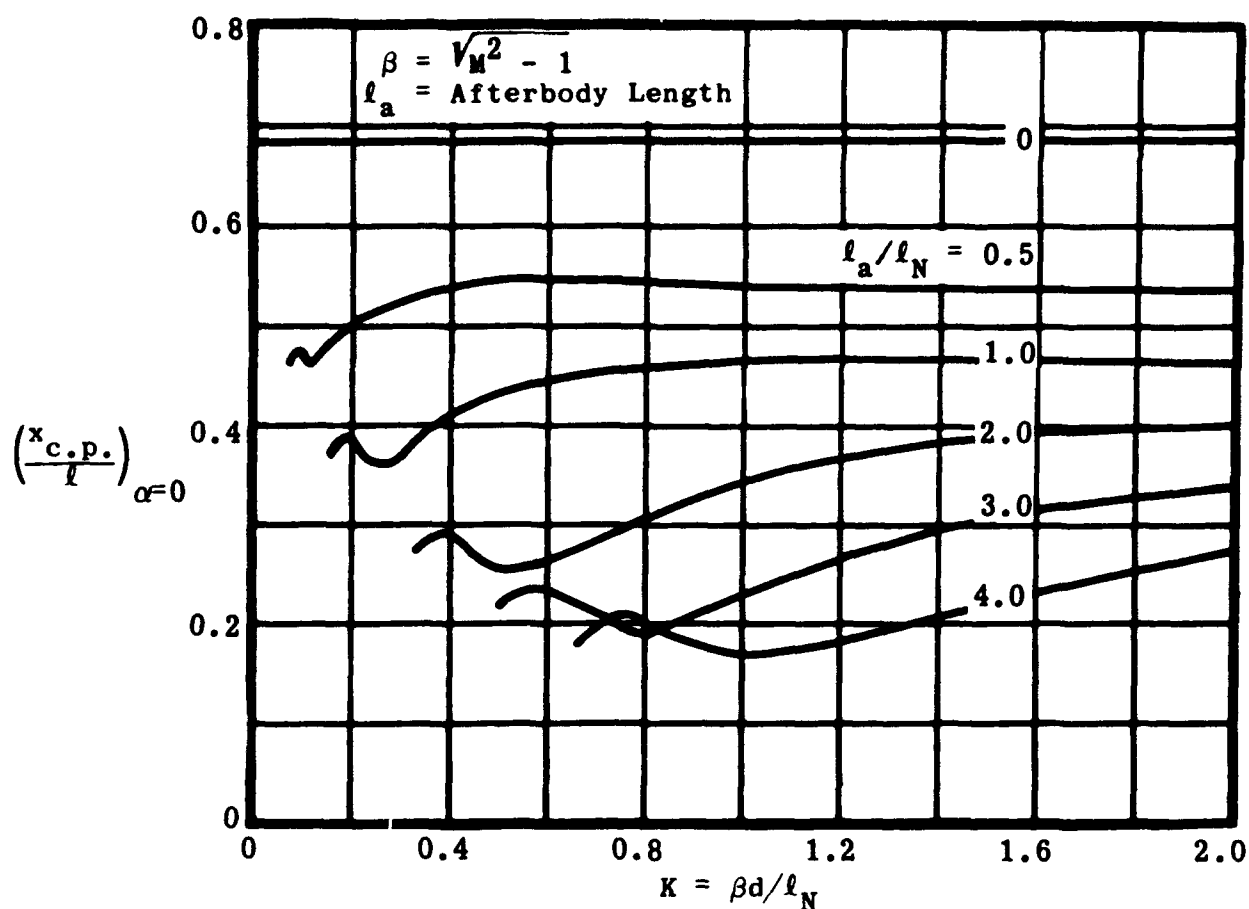
Fig. 5-29. Calculated center-of-pressure location versus K
for various cone-cylinders at zero angle of attack.
(Source: Ref. 102)

$K = 0.25$ $\beta\alpha$ (deg) = 20

βC_N

ℓ_a/ℓ_N

Fig. 5-30. βC_N versus ℓ_a/ℓ_N for cone-cylinders at various angles
of attack; K = 0.25. (Source: Ref. 102)

Fig. 5-31   NAVWEPS Report 1488 (Vol. 3, Sec. 8)

Fig. 5-32. βC_N versus ℓ_a/ℓ_N for cone-cylinders at various angles of attack; K = 1.0. (Source: Ref. 102)

Fig. 5-31. βC_N versus ℓ_a/ℓ_N for cone-cylinders at various angles of attack; K = 0.50. (Source: Ref. 102)

Fig. 5-33. βC_N versus ℓ_a/ℓ_N for cone-cylinders at various angles of attack; K = 2.0. (Source: Ref. 102)

Fig. 5-34. βC_m versus ℓ_a/ℓ_N for cone-cylinders at various angles of attack; K = 0.25. (Source: Ref. 102)

Fig. 5-35   NAVWEPS Report 1488 (Vol. 3, Sec. 8)
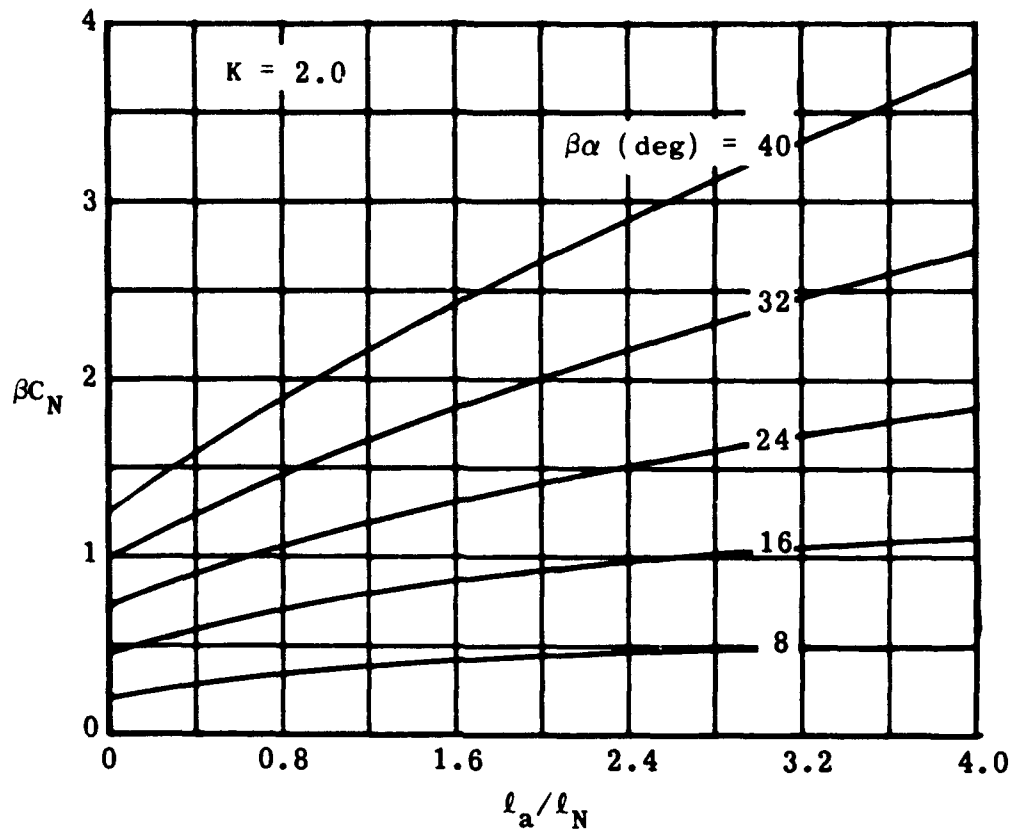
Fig. 5-36. βC_m versus ℓ_a/ℓ_N for cone-cylinders at various angles of attack; K = 1.0. (Source: Ref. 102)

Fig. 5-35. βC_m versus ℓ_a/ℓ_N for cone-cylinders at various angles of attack; K = 0.50. (Source: Ref. 102)

Fig. 5-37. βC_m versus ℓ_a/ℓ_N for cone-cylinders at various angles of attack; K = 2.0. (Source: Ref. 102)

Fig. 5-38. Normal-force distribution coefficient versus ℓ_a/ℓ_N for cone-cylinders at various angles of attack; K = 0.25. (Source: Ref. 102)

Fig. 5-39   NAVWEPS Report 1488 (Vol. 3, Sec. 8)
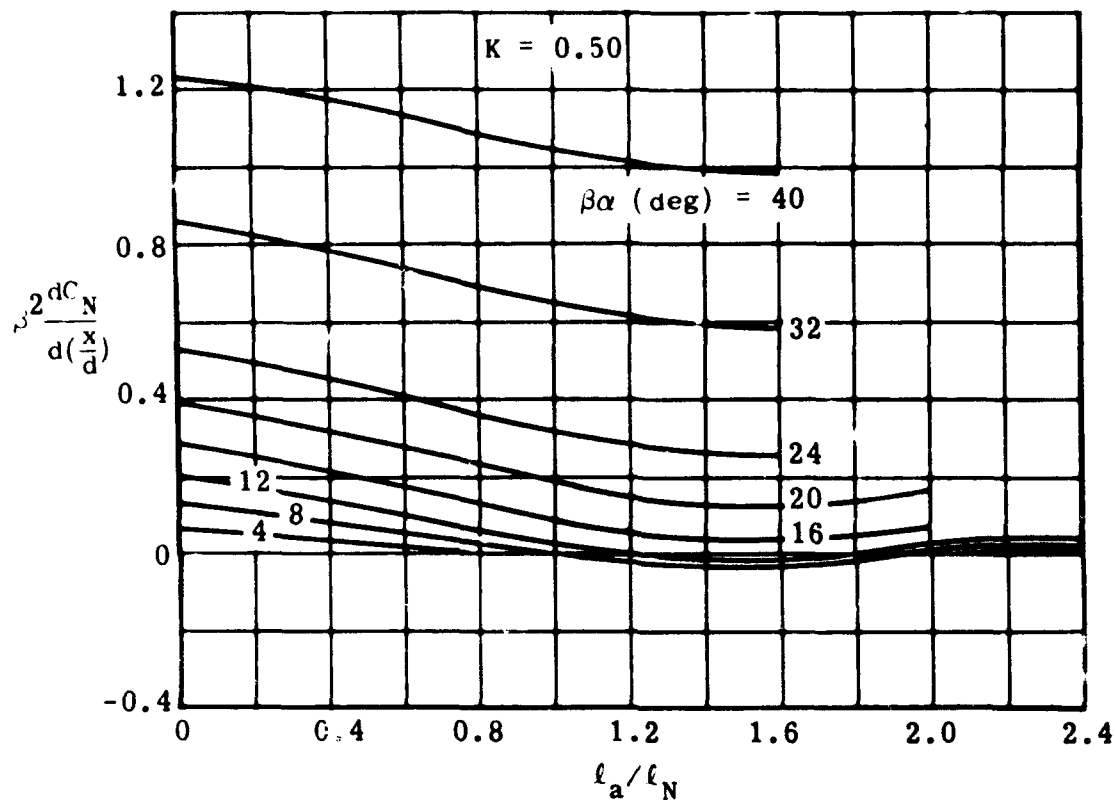
Fig. 5-39. Normal-force distribution coefficient versus ℓ_a/ℓ_N for cone-cylinders at various angles of attack; K = 0.50. (Source: Ref. 102)
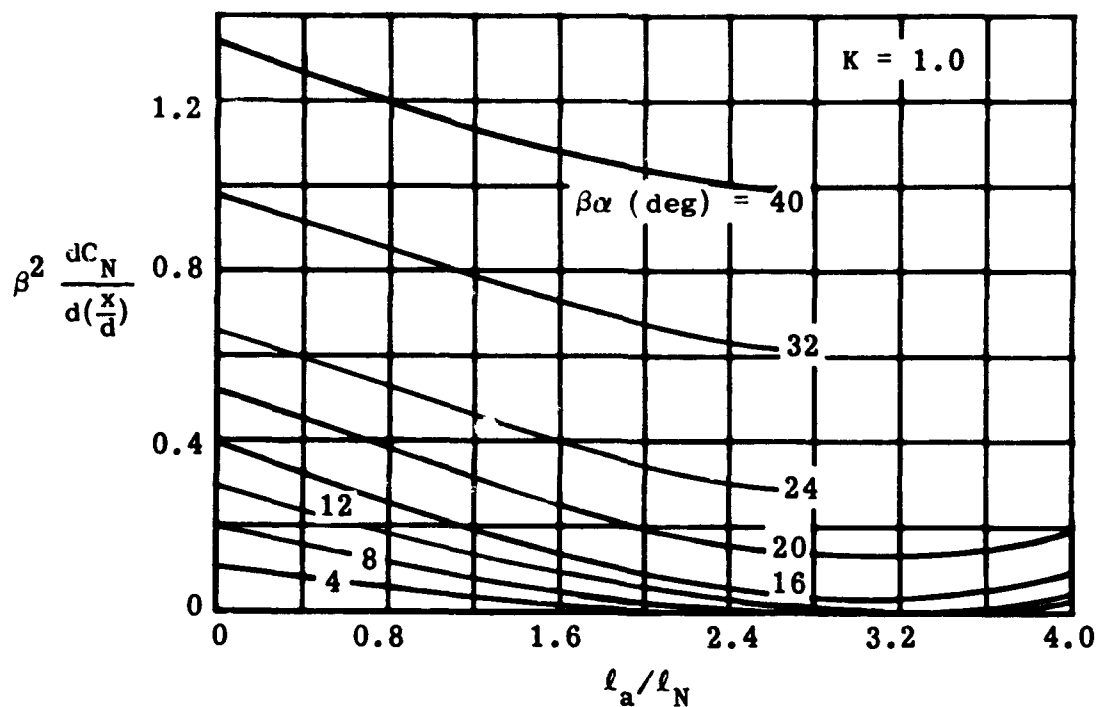
Fig. 5-40. Normal-force distribution coefficient versus ℓ_a/ℓ_N for cone-cylinders at various angles of attack; K = 1.0. (Source: Ref. 102)
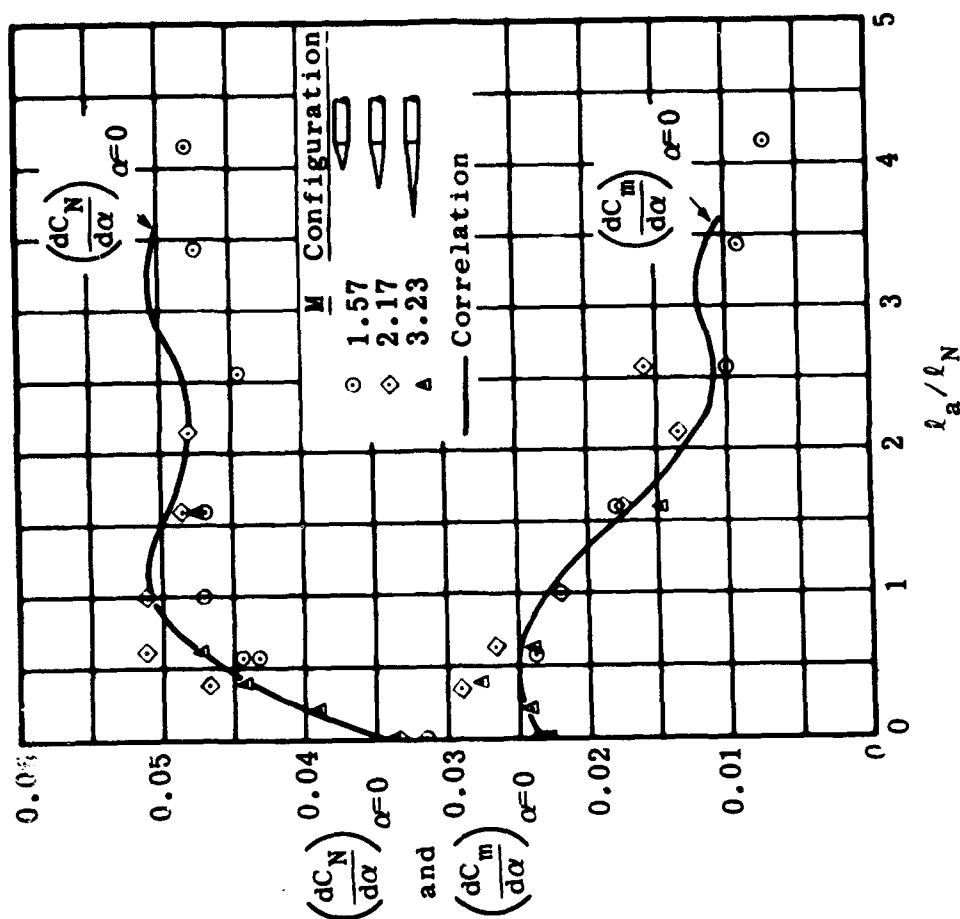
Fig. 5-42. Comparison of experimental normal-force and pitching-moment slopes with values obtained from hypersonic correlation charts; K = 0.6. (Source: Ref. 102)
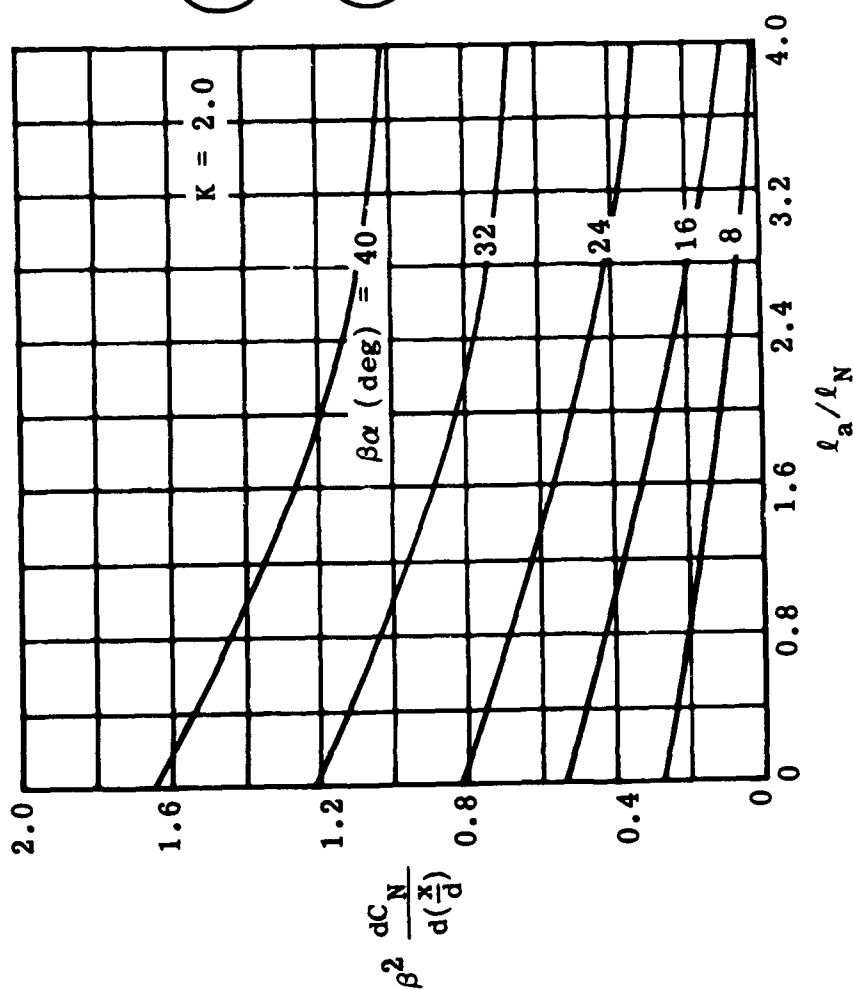
Fig. 5-41. Normal-force distribution coefficient versus ℓ_a/ℓ_N for cone-cylinders at various angles of attack; K = 2.0. (Source: Ref. 102)

Fig. 5-43   NAVWEPS Report 1488 (Vol. 3, Sec. 8)
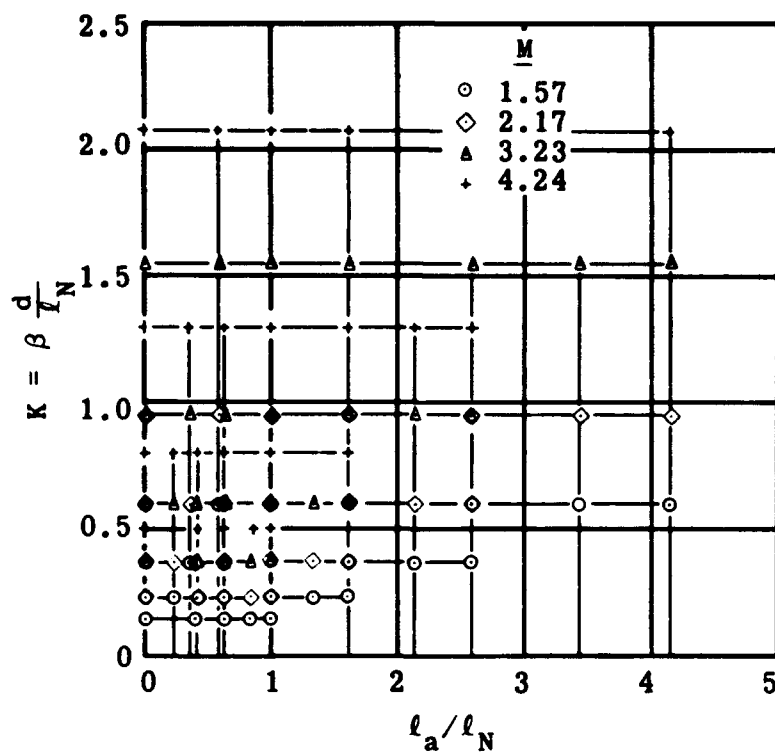
Fig. 5-43. Range of parameters K and ℓ_a/ℓ_N for NOL tests of cone-cylinders. (Source: Ref. 102)
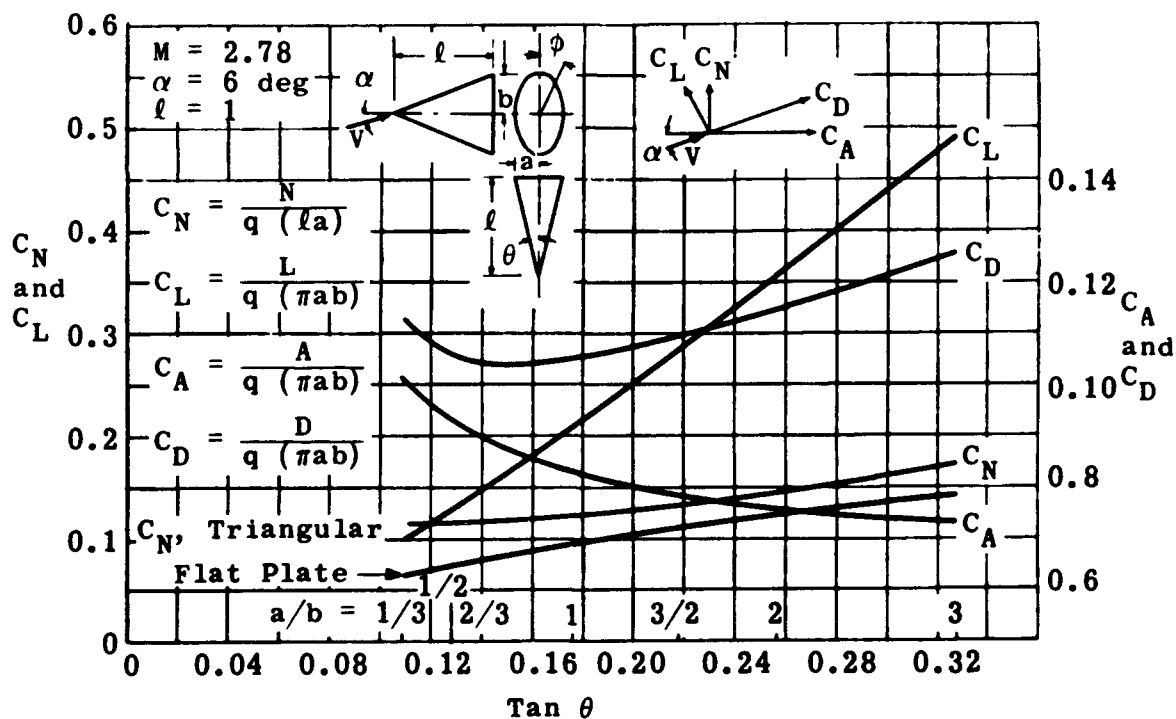
Fig. 5-44. Lift, drag, normal-force, and axial-force coefficients versus tan θ for various elliptical cones; M = 2.78, α = 6 deg. (Source: Ref. 70)

Fig. 5-45. Lift coefficient slope of a ducted ogive cone as a function of inlet radius and distance from the lip. (Source: Ref. 79)

Fig. 5-46   NAVWEPS Report 1488 (Vol. 3, Sec. 8)
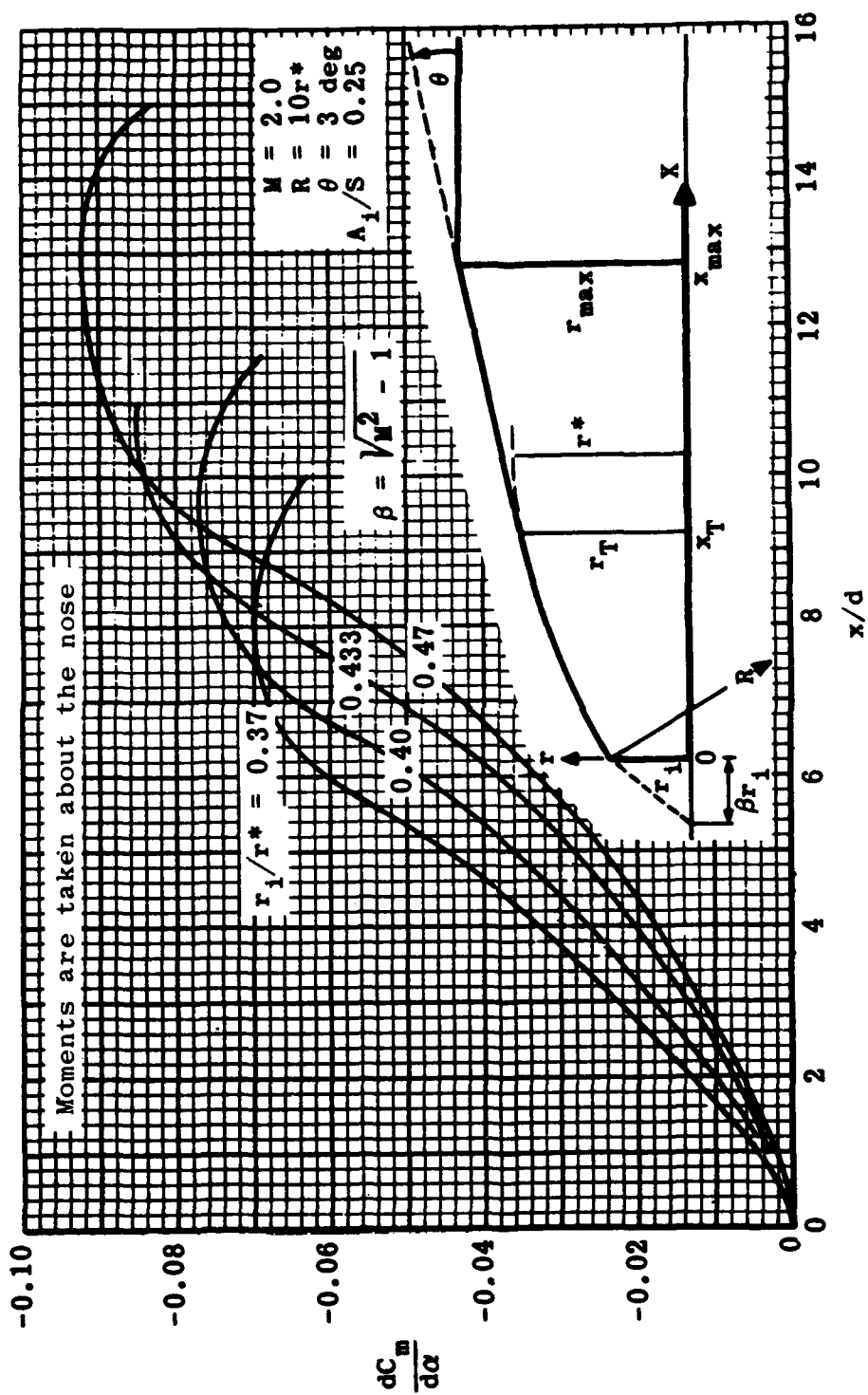
Fig. 5-46. Pitching-moment coefficient slope of a ducted ogive cone as a function of inlet
radius and distance from the lip. (Source: Ref. 79)
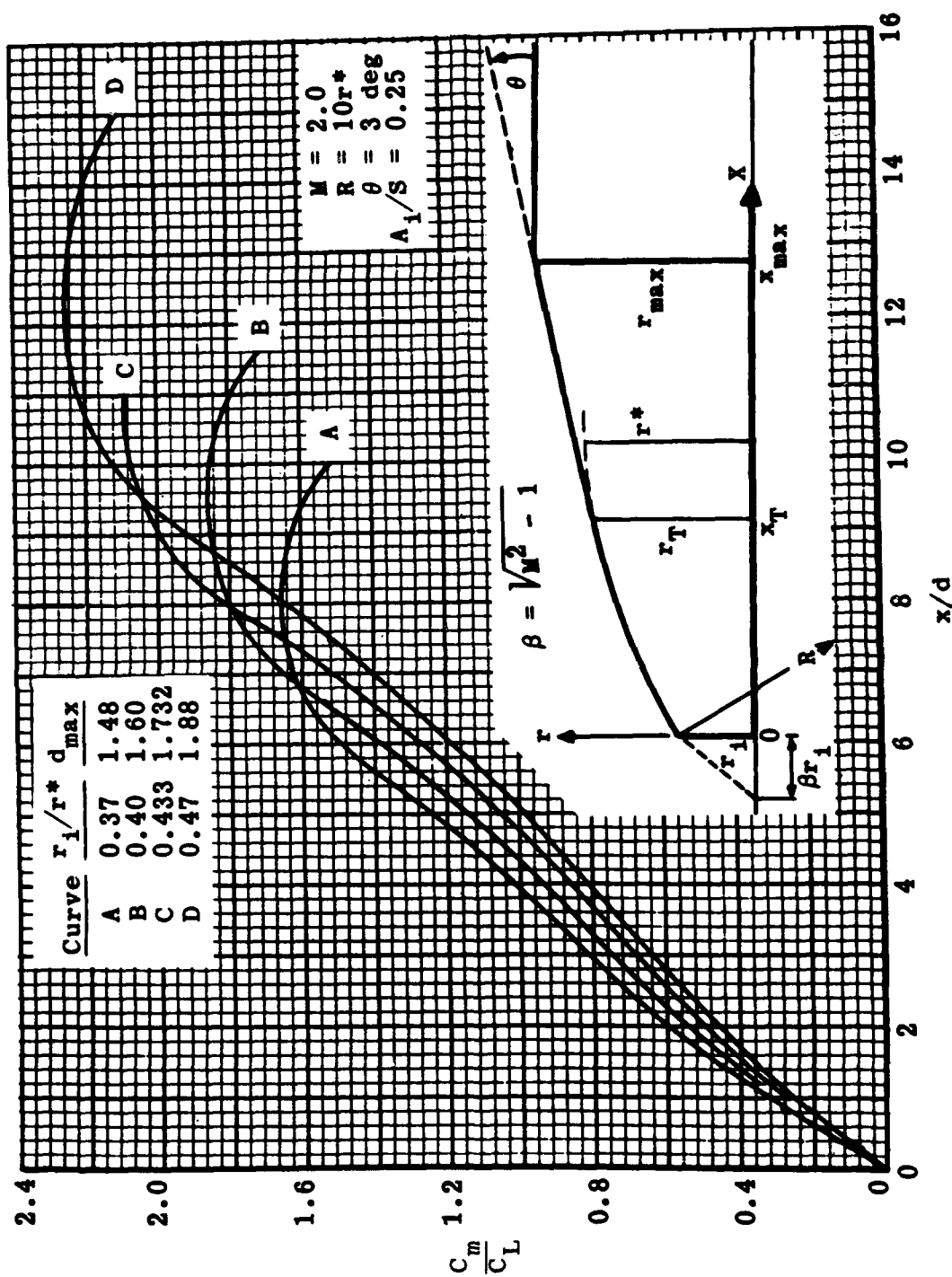
Fig. 5-47. Center-of-pressure location of a ducted ogive cone as a function of inlet radius and distance from the lip. (Source: Ref. 79)

Fig. 5-48   NAVWEPS Report 1488 (Vol. 3, Sec. 8)
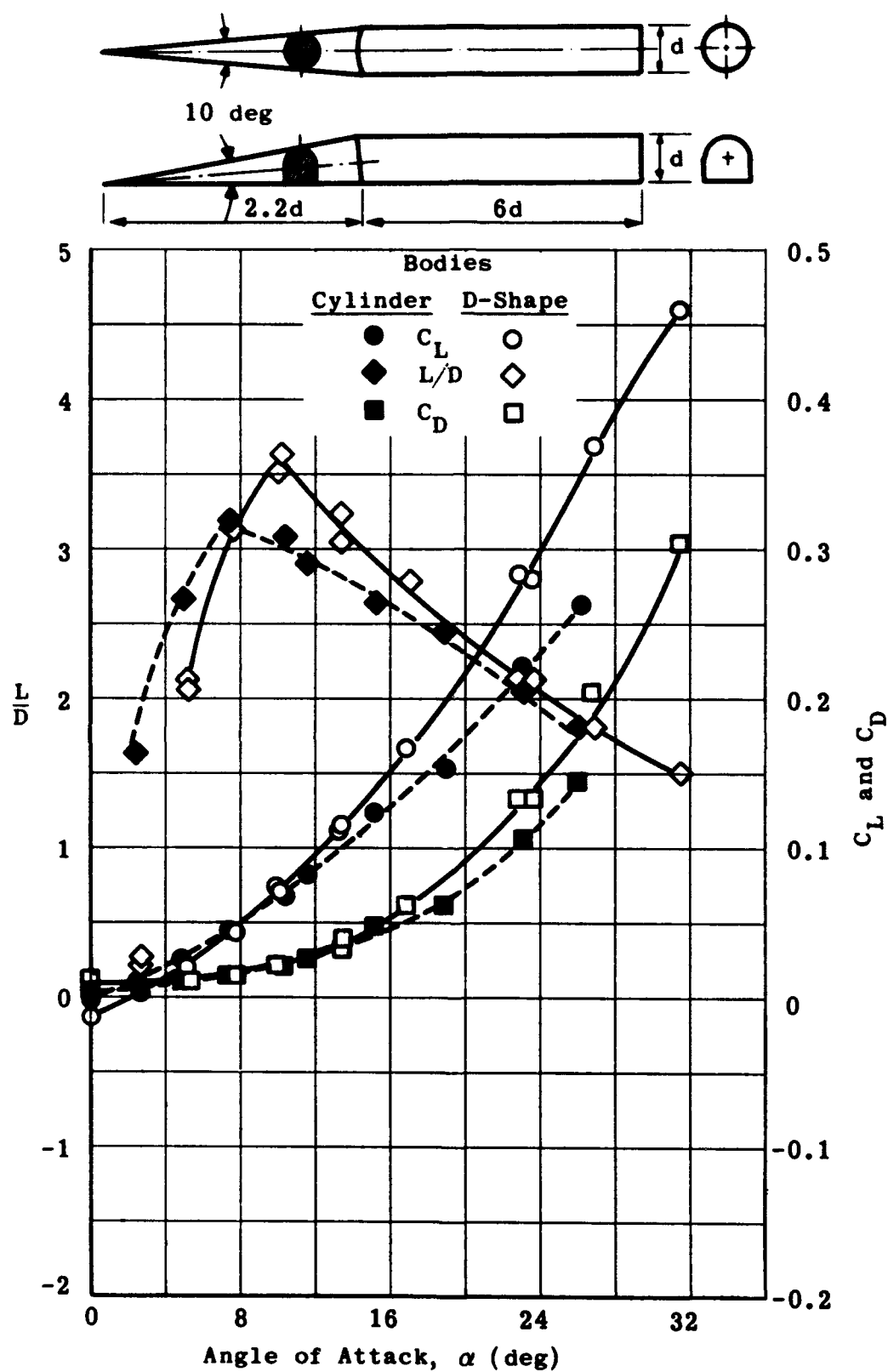
Fig. 5-48.   Variation of C_L, C_D, and L/D with angle of attack for cone-cylinder and flat-bottom bodies; l/d = 6, M = 6.86. (Source: Ref. 103)
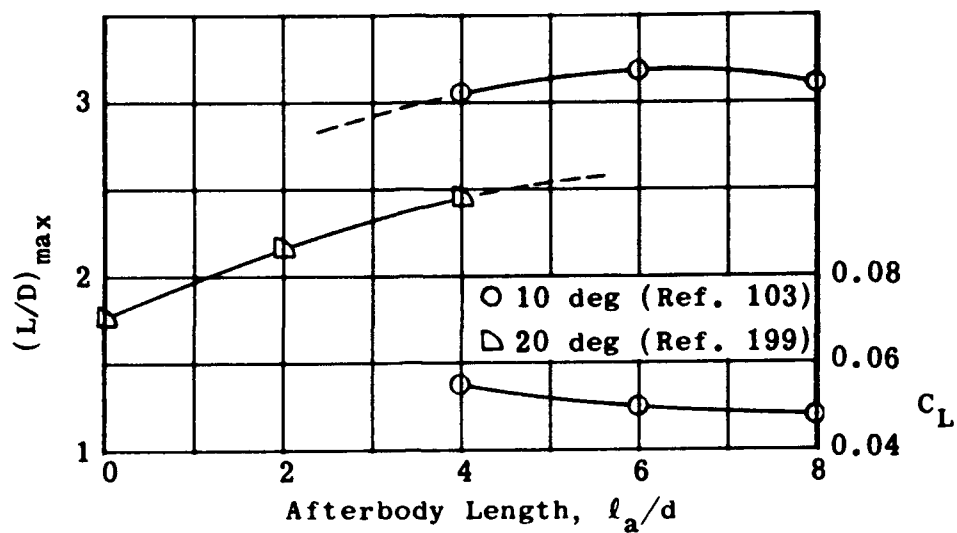
Fig. 5-49. Variation of maximum lift-to-drag ratio and lift
coefficient for body fineness ratio; M = 6.86.
(Source: Ref. 103)
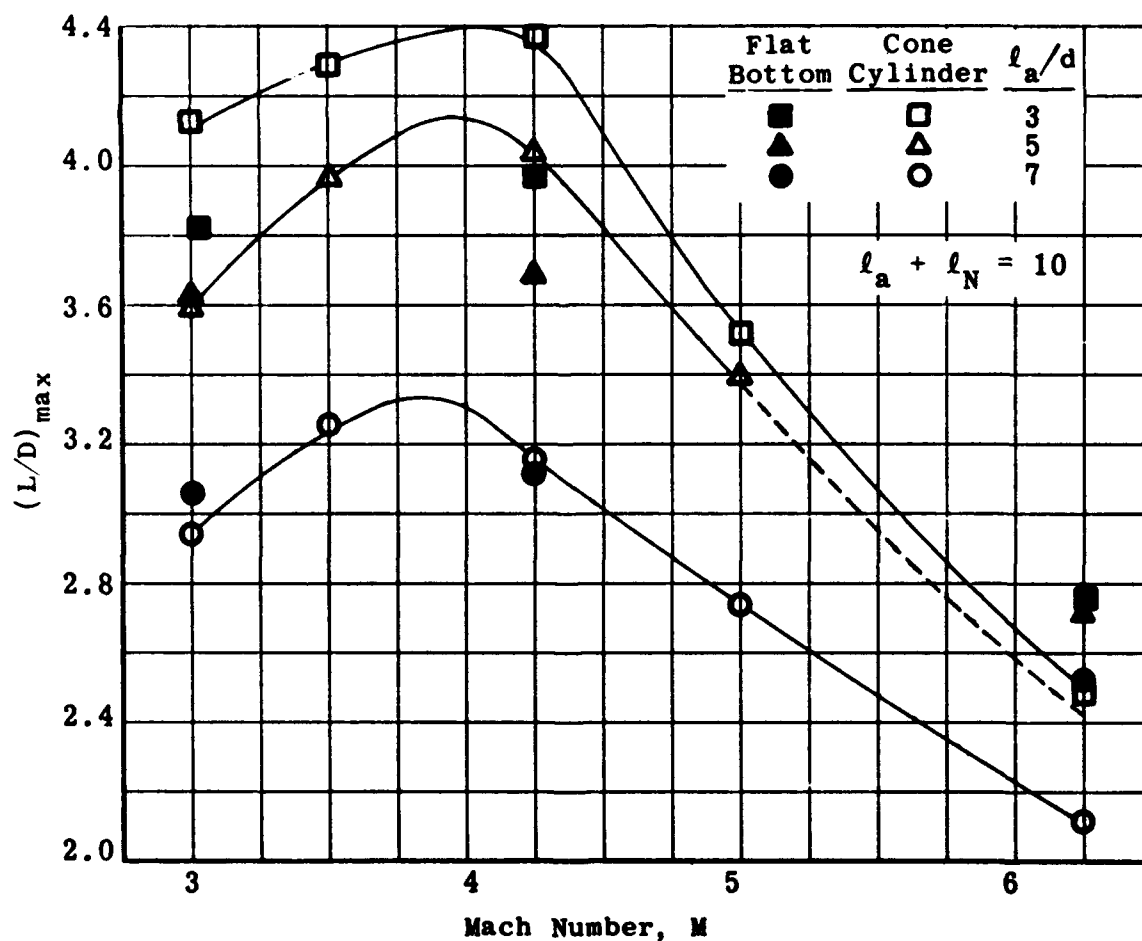
Fig. 5-50. Maximum lift-to-drag ratio versus Mach number for
flat-bottomed and cylindrical bodies. (Source: Ref. 95)

213

Fig. 5-51   NAVWEPS Report 1488 (Vol. 3, Sec. 8)
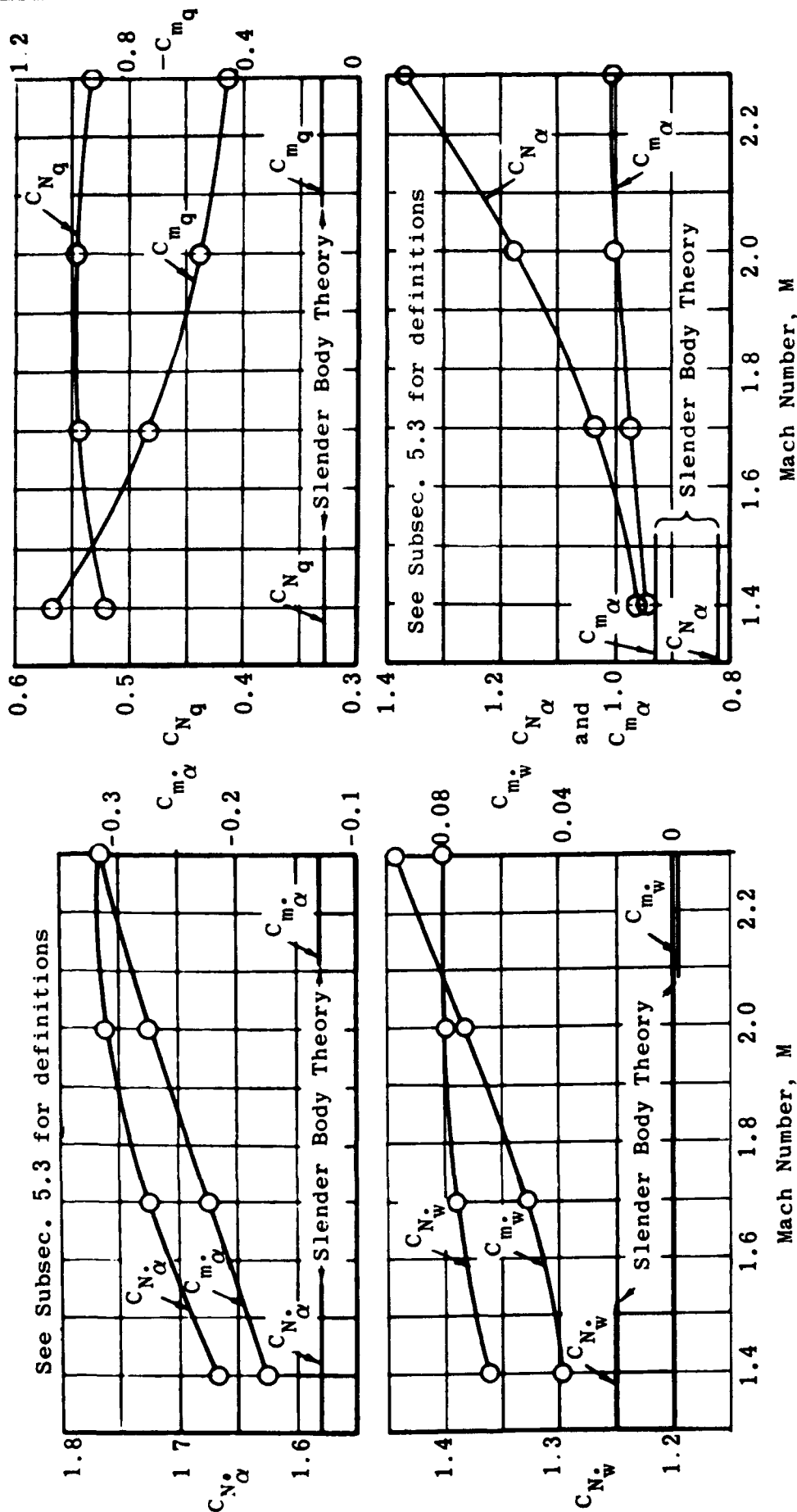
Fig. 5-51. Non-steady-state stability derivatives of $\dot{\alpha}$ and $\dot{w}$ for a boattailed body. (Source: Ref. 105)

Fig. 5-52. Steady-state stability derivatives of q and α for a boattailed body. (Source: Ref. 105)
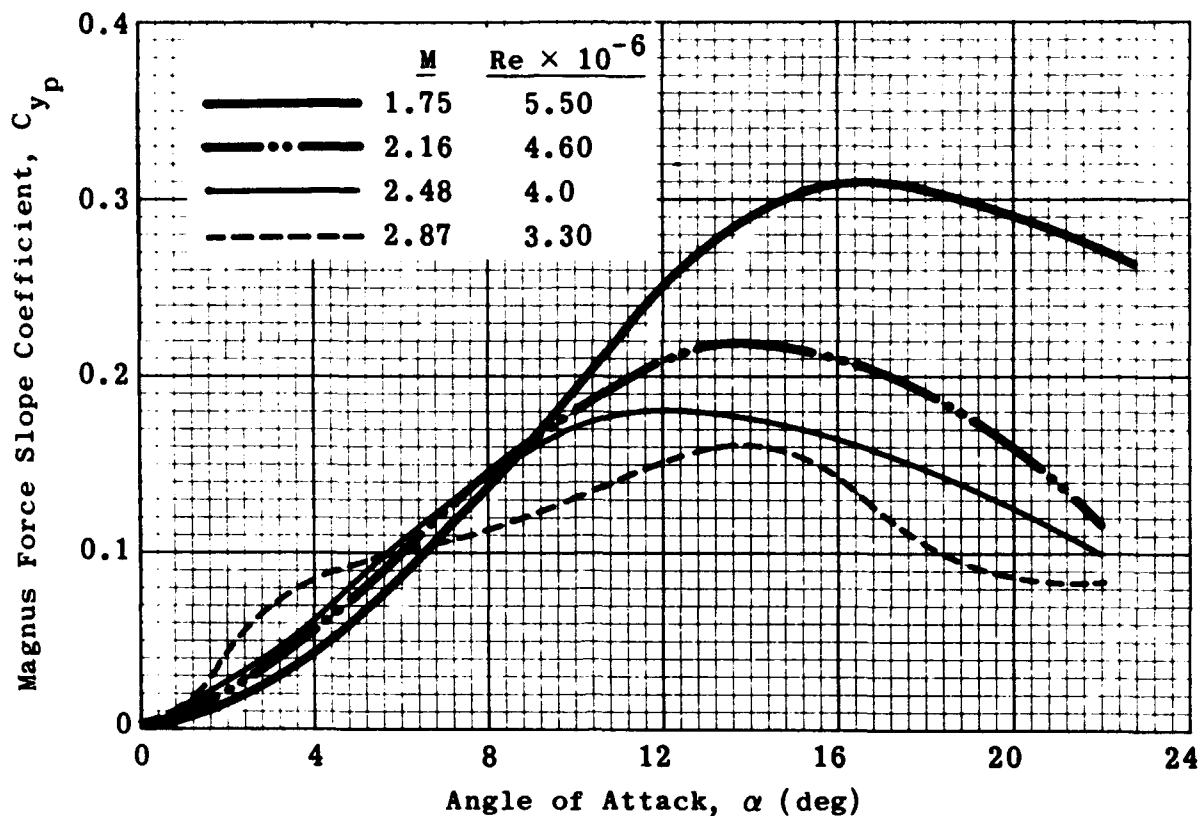
Fig. 5-53. Magnus force slope coefficient versus angle of attack
for a 5-caliber body of revolution at various Mach numbers.
(Source: Ref. 107)
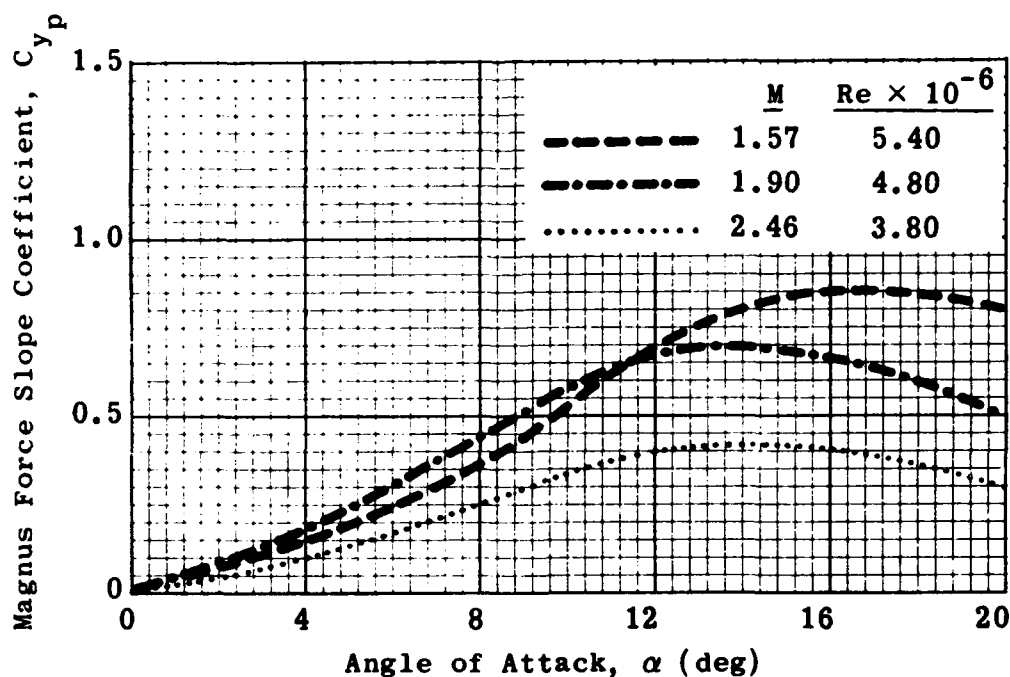
Fig. 5-54. Magnus force slope coefficient versus angle of attack
for a 7-caliber body of revolution at various Mach numbers.
(Source: Ref. 107)

215

Fig. 5-55   NAVWEPS Report 1488 (Vol. 3, Sec. 8)
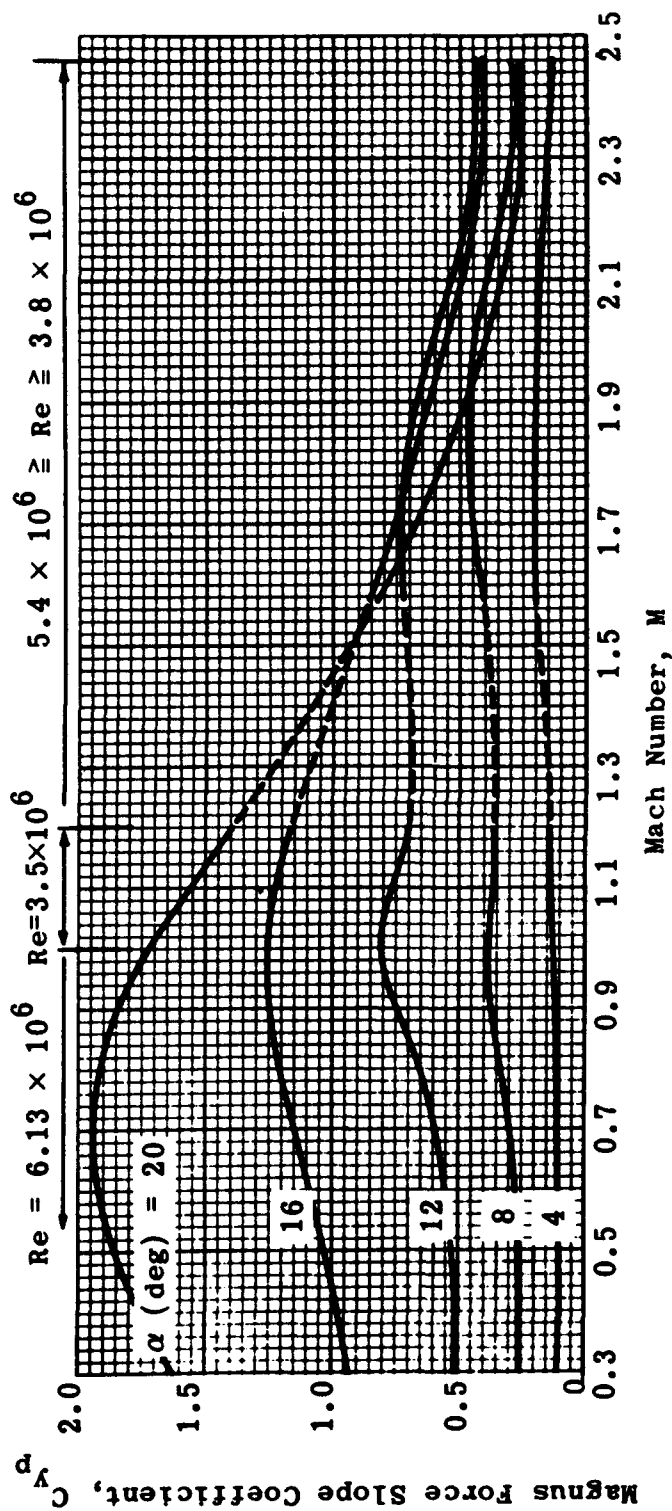
Fig. 5-55. Magnus force slope coefficient versus Mach number for a 7-caliber body of revolution at various angles of attack. (Source: Ref. 107)
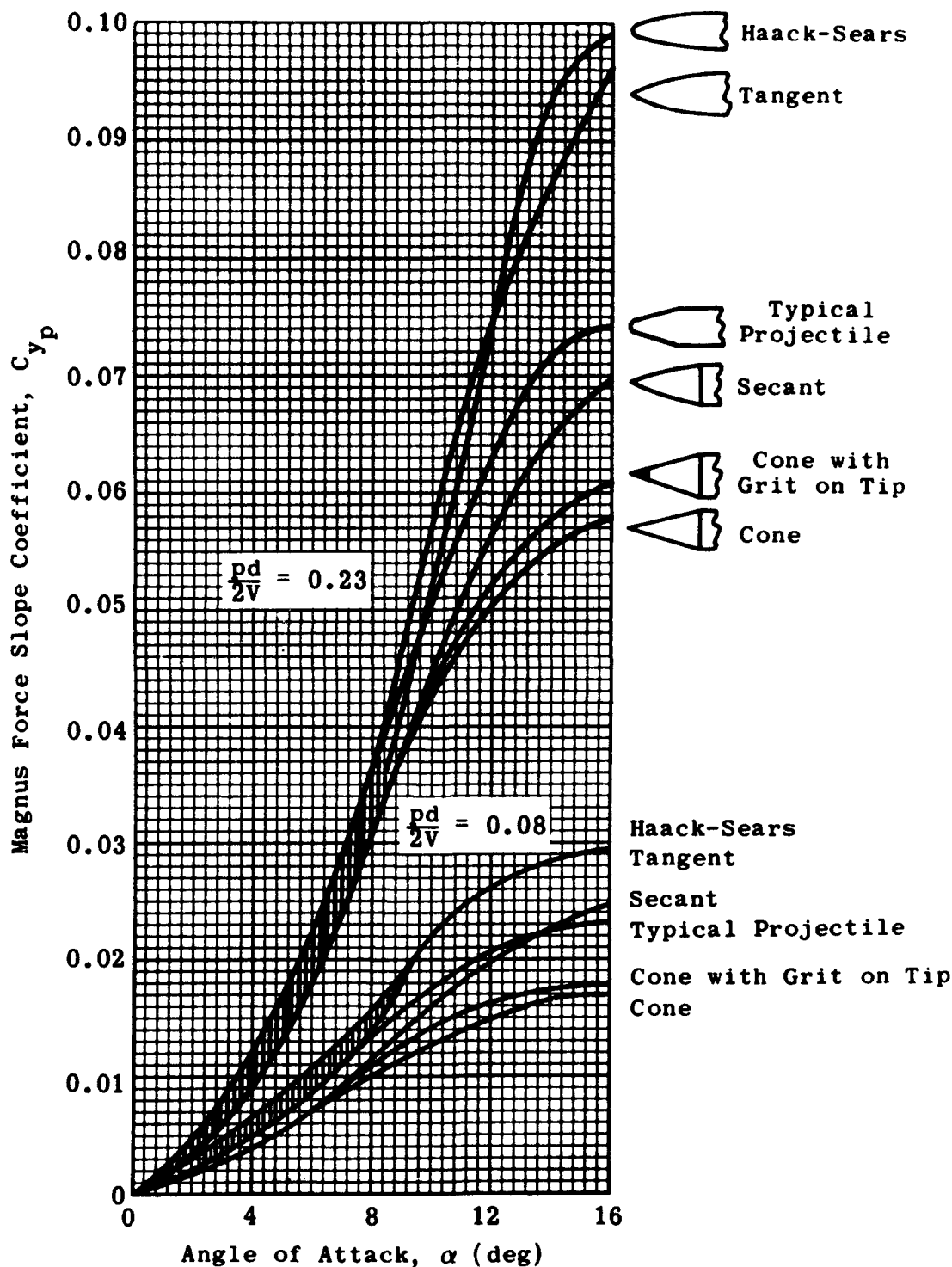
Fig. 5-56. Effect of nose shape on the Magnus force slope coefficient versus angle of attack for a 5-caliber body of revolution; M = 1.75. (Source: Ref. 107)

Fig. 5-57   NAVWEPS Report 1488 (Vol. 3, Sec. 8)
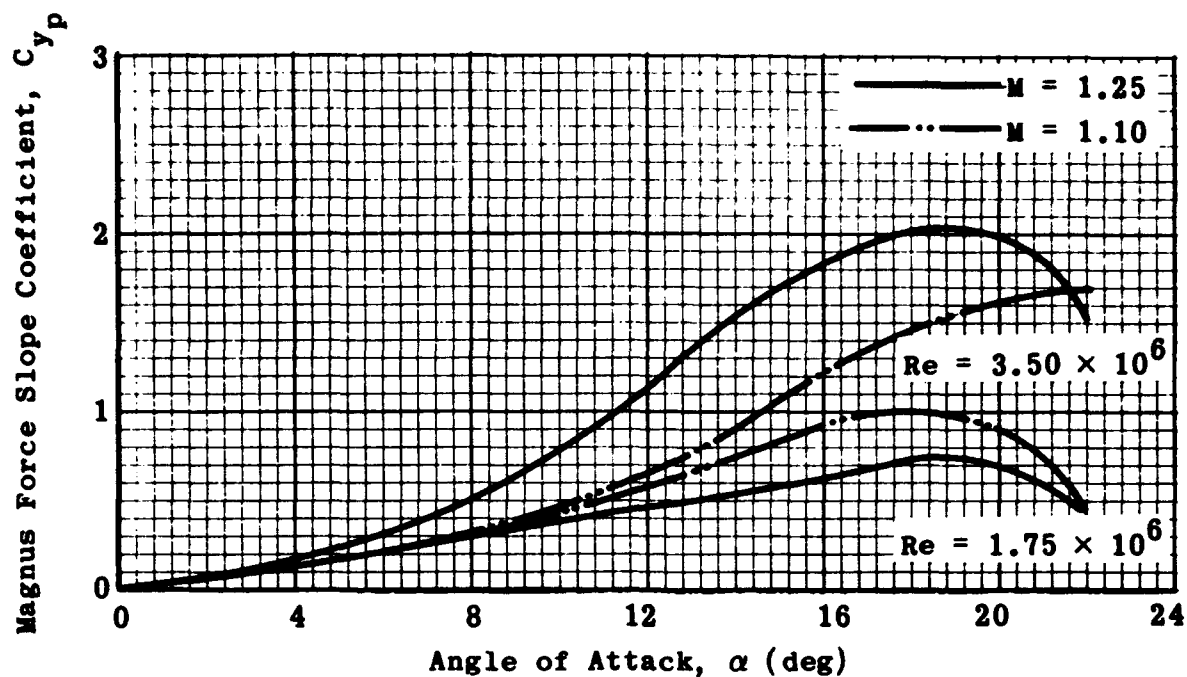
Fig. 5-57. Magnus force slope coefficient versus angle of attack
for a 7-caliber body of revolution; M = 1.10 and 1.25.
(Source: Ref. 107)
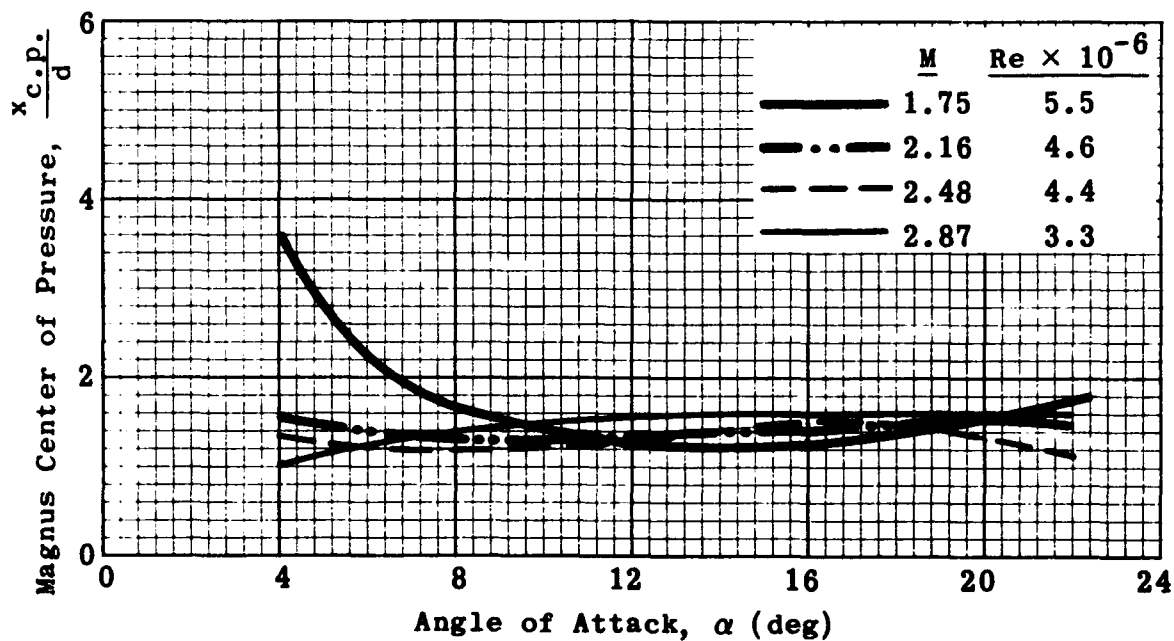
Fig. 5-58. Distance of Magnus center of pressure from base of
5-caliber body versus angle of attack for four Mach num-
bers. (Source: Ref. 107)
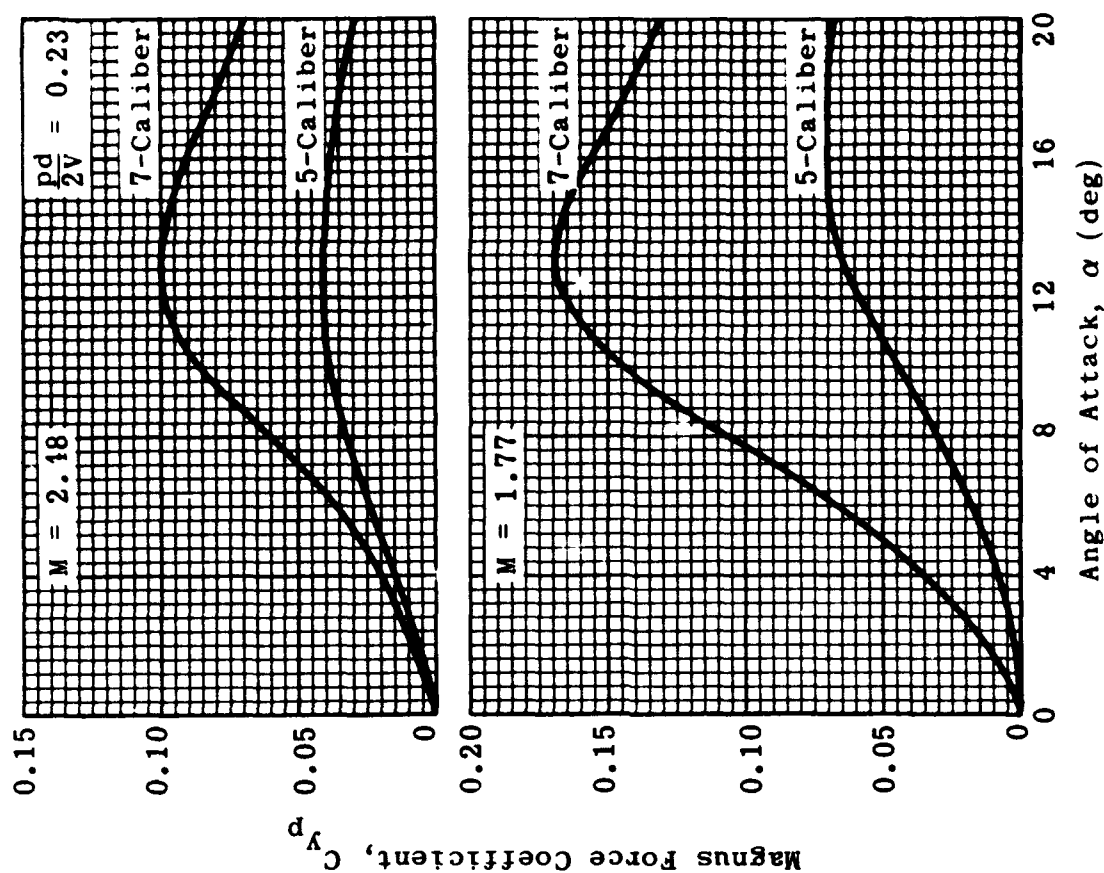
Fig. 5-60. Effect of length on Magnus force coefficient versus angle of attack for 5- and 7-caliber bodies; M = 1.77 and 2.48. (Source: Ref. 107)
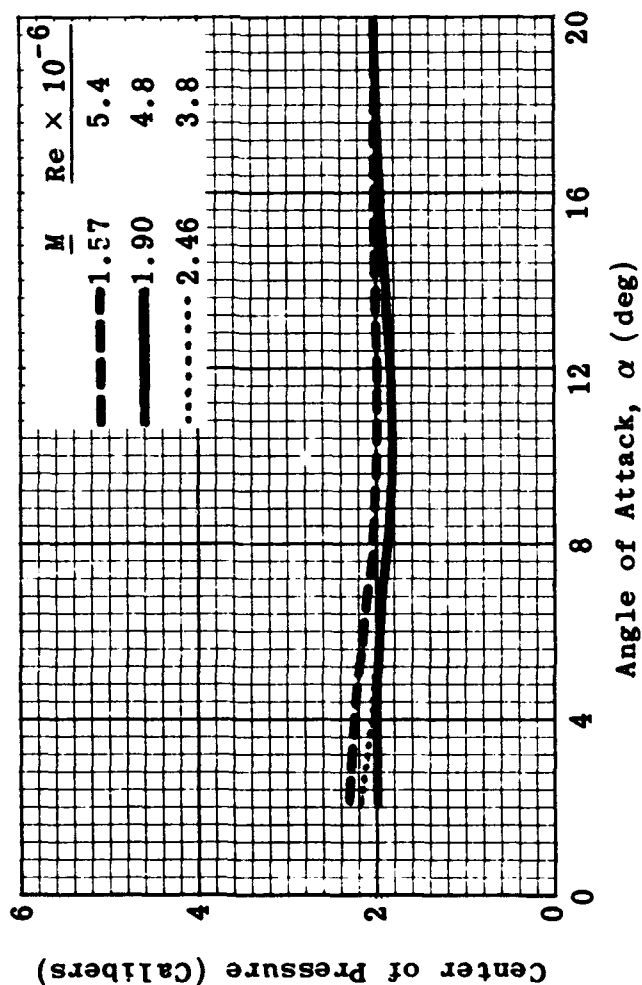
Fig. 5-59. Distance of Magnus center of pressure from base of 7-caliber body versus angle of attack for three Mach numbers. (Source: Ref. 107)

Fig. 5-61   NAVWEPS Report 1488 (Vol. 3, Sec. 8)

Fig. 5-62. Effect of nose shape on Magnus center of pressure versus angle of attack for a 5-caliber body; M = 1.75. (Source: Ref. 107)

Fig. 5-61. Effect of length on Magnus center of pressure versus angle of attack for 5- and 7-caliber bodies; M = 1.77 and 2.48. (Source: Ref. 107)

6.   Pressure Drag and Skin Friction

         The drag force, as defined in Subsec. 5.2, is the total force
acting in an aft direction parallel to the free-stream direction. The
relationship between lift, drag, normal force, and axial force has also
been stated (Eq. 5-3). Where the angle of attack is small the drag due
to lift is negligible; hence the axial force is an approximate represen-
tation of the drag, and the terms are often used interchangeably. The
over-all drag force may be considered as made up of three components:
(1) pressure, wave, or form drag; (2) skin-friction drag; and (3) base
drag. The first two components will be discussed in this subsection and
the third, base drag, in Subsec. 7.

         For bodies with pointed noses, moderate boattailing, and over-
all fineness ratios of 8 to 12 in the range $1 < M < 3$, the pressure drag
will constitute one-tenth to one-fourth of the total drag. The skin
friction and the base drag may each contribute about one-third to two-
thirds of the remainder, their proportions depending on the configura-
tion, flight speed, and Reynolds number. As the Mach number is increased
the pressure and skin-friction drag also increase, and the base drag de-
creases until, at about Mach number 5, it becomes negligible in compari-
son with nose drag.

         There are two general approaches to the study of the pressure
or wave drag of bodies operating at supersonic speeds. In the first
and simplest approach, the drag may be considered as the integrated
axial component of the pressure over the body. It may then be calcu-
lated in all cases for which a theoretical pressure distribution may be
obtained. The theories, outlined in Subsecs. 2 and 3, are in general
limited to slender bodies at moderate Mach numbers. They give reliable
drag forces over the forward portion of a body but may not be applied
where there is separated flow. A second approach to the drag problem
considers the conservation of energy in the fluid itself. The contri-
bution of the body drag may be equated to the change in energy across
the shock waves, giving rise to the term wave drag. As subsequent dis-
cussion will show, this method may be used for the case of blunt bodies,
where the assumption of small perturbations cannot be made. The disad-
vantages of this method will also be discussed.

6.1   Pressure Drag of Cones

         The zero-lift pressure-drag coefficient for right-circular
cones will be equal to the value of the constant pressure coefficient,
$C_p = (p - p_\infty)/q_\infty$, over the cone when the drag coefficient is referenced
to the base area of the cone. The pressure coefficient is tabulated in
Ref. 22 for a wide range of Mach numbers and cone angles; representative
values are shown in Fig. 4-3, which also clearly indicates the points
of shock detachment. A plot of the cone semi-apex angle corresponding
to shock detachment as a function of M (assuming $\alpha = 0$) appears in
Fig. 4-2. The shock wave is detached for any combination of nose angle
and Mach number above the curve shown in this figure. Figure 4-3 may
also be used with reasonable accuracy for ogives or any other pointed
bodies if the apex angle is substituted for the cone angle. In Sub-
sec. 5.2 it was shown that the increase in drag due to angle of attack
may be expressed as $C_N \sin \alpha$ or $C_N \alpha$, and as such has been discussed in
Subsec. 5. The axial force on pure cones decreases as the angle of at-
tack increases, as illustrated for two Mach numbers in Fig. 6-1, which
compares the experimental data of Cronvich and Bird (Ref. 178) with the

theory of Young and Siska (Ref. 68). Both data and theory are in reasonable agreement.

6.2   Pressure Drag of Ogives

The parameters which define ogive geometry are shown in a sketch in Subsec. 4.2. The geometric variations may be expressed in terms of

$$\frac{\ell_N}{d} \quad \text{and} \quad \frac{r_t}{r}$$

where

ℓ_N = nose length

r_t = radius of tangent ogive

r = radius of given ogive

Use of these parameters permits a particularly compact and informative presentation of zero-lift pressure drag data. Such data, presented in Fig. 6-2, indicates the following conclusions.

1. The drag coefficient for a tangent ogive (r_t/r = 1) is only slightly larger than that of the inscribed cone (r_t/r = 0), and the difference decreases as ℓ_N/d increases.

2. The radius of a secant ogive of minimum drag is approximately twice that of the corresponding tangent ogive for a given ℓ_N/d ratio, i.e., $r_t/r \sim 0.5$.

3. The minimum pressure drag of a secant ogive is about 83% of the drag of a cone having the same ℓ_N/d, i.e., an inscribed cone.

Zienkewicz in Ref. 108 has suggested the use of an empirical expression for estimating the zero-lift pressure drag of an ogive in terms of the drag, C_{D_c}, for a cone whose semi-vertex angle is equal to that of the ogive, i.e.,

$$\frac{C_D}{C_{D_c}} = 0.326 + 0.674 \left(1 - \frac{\ell_N}{C}\right)^{1.8} \tag{6-1}$$

where ℓ_N, C, and d are defined in a sketch in Subsec. 4.2. This expression may be used in the ranges of

$$C/d \geqq 2, \quad M \geqq 1.6, \quad \text{and} \quad \frac{Md}{C} \leqq 1$$

Figure 6-3 (from Ref. 93) shows the zero-lift pressure drag as a function of ℓ_N/d for bodies whose noses are ellipsoids of revolution. This drag was obtained by the integration of measured pressures at Mach numbers of 1.42, 1.60, and 1.82. The pressure distribution for these bodies is presented in Figs. 4-110 and 4-111.

6.3   Pressure Drag of Ducted Cones

Methods of calculating the pressure distribution of ducted bodies of revolution and the typical distributions over such bodies are presented in Subsec. 4.3. In the case of conical ducted bodies, the pressure at the leading edge of the lip is virtually a two-dimensional or wedge pressure which decreases with distance along the cowl until it approximates the three-dimensional or cone value. As the inlet-to-base-diameter ratio increases, the projected area of the cowl decreases. However, the effective area over which the two-dimensional pressure acts is increased. Because of this, the drag does not decrease in proportion to the frontal area, but instead remains nearly constant with increasing inlet size until the inlet-to-base-diameter ratio is greater than about 0.6. This is illustrated in Fig. 6-4 (from Ref. 110) which gives the calculated drag coefficient as a function of the inlet-to-base-diameter ratio.

The wave drag of a series of ducted bodies with ogive-cone cowls was determined by Kennedy (Ref. 79). The study was carried out for the following combinations of parameters. (See Fig. 6-5 for nomenclature and basic geometry.)

r_i/r^*	$R/2r^*$	A_i/S	M	θ (deg)
0.37	1	0.25	1.50	2
0.40	2	0.50	2.00	3
0.47	3		2.25	4
	5		2.50	
	7.5			

However, the method was not applicable for the 18 combinations listed below.

r_i/r^*	$R/2r^*$	A_i/S	M	θ (deg)
0.37	1	0.25	2.25	2
		0.50	2.50	3
				4
0.40	1	0.25	2.50	2
		0.50		3
				4

Representative results of the calculations are given in Figs. 6-5 to 6-10. Though they do not cover all the cases given in Ref. 79, they will permit interpolation for similar shapes.

The wave drag of a family of conical cowls calculated by Jack in Ref. 75 is shown in Figs. 6-11 to 6-13. The cowl angles may be derived from

$$\tan \theta = \frac{1 - \sqrt{A_1/S}}{2\ell_N/d} \tag{6-2}$$

It may be noted that the coefficient of wave drag decreases as fineness ratio, Mach number, or area ratio increases. The dependence of the wave drag on Mach number is relatively small compared with its dependence on fineness ratio or area ratio. Although the wave drag decreases with an increase in fineness ratio, the friction drag (discussed in Subsec. 6.8) increases. For large fineness ratios, the friction drag becomes the predominant part of the total drag; hence, this fact must be considered when designing an optimum cowling.

The wave drag for one of the cowlings is shown as a function of Mach number in Fig. 6-14 (from Ref. 75). At Mach numbers below 2 the shock from the inner body passes outside the cowl lip and creates additive drag. The additive drag obtained from this figure is quantitatively doubtful but sufficiently accurate to indicate the rapid rise in drag at below-design Mach numbers.

The experimental pressure drag of several cowls having large lip angles were obtained at Mach numbers of 1.90 to 4.90 by Samanich (Ref. 80). The cowls are shown in Fig. 4-70, and a typical pressure distribution is noted in Table 4-1. The wave drag of several of these cowls is shown in Figs. 6-15 and 6-16.

The empirical chart in Fig. 6-17 may be used to estimate the pressure-drag coefficient of cowls of approximate or actual elliptical contour. A combination of data from Ref. 80 was utilized for this figure. (Its use is illustrated by the arrows.) The pressure-drag coefficient at Mach 3.4 of an elliptically contoured cowl having a projected area that is 20% of the total frontal area $(A_1/S = 0.80)$ and an initial angle of 34 deg is found by following the arrows. The coefficient so obtained is approximately 0.096.

6.4   Pressure Drag of Boattails

Since the flow conditions and pressures over a boattail interact intimately with the base pressure and drag, it is highly advantageous to combine these phenomena for treatment under one general heading. Drag and lift characteristics of conical and ogival boattails are therefore brought together for discussion in Subsec. 7, which is devoted to base drag. A discussion of pressure distribution appears in Subsec. 4.4.

6.5   Pressure Drag of Skirted Bodies

Calculations of the wave drag on a series of skirted bodies shown in Fig. 5-20 was made by Deep and Henderson (Ref. 101). Representative values of the drag coefficient for M = 1.8 and 2.48 are given in Fig. 6-18 for one of the geometric families (see Subsec. 5.14).

6.6   Cones of Elliptical and Other Cross-Sections

        As indicated in Subsecs. 4.1.3 and 5.2.1, the cross-sectional
shape has only a secondary influence on the drag of slender bodies.
However, since shapes other than circular may be desired (e.g., to meet
packing requirements or system specifications), it is necessary to know
the aerodynamic characteristics of cones of elliptical cross-section.
These characteristics are treated in Refs. 15, 69, 70, and 71. The drag
coefficients shown in Figs. 6-19 to 6-21 are taken from Ref. 70. The
effect of variations in effective fineness ratio (defined by the param-
eter $\ell/\sqrt{\pi ab}$) on the resulting drag coefficient of such cones is shown
in Fig. 6-19, and the reduction in drag to be accomplished as a function
of Mach number with various values of eccentricity as compared with the
drag of a corresponding circular cone (same length and cross-sectional
area) is shown in Figs. 6-20 and 6-21.

        Reference 70 also treats cones whose cross section is a drop
shape and also a triangle with rounded corners. A comparison of the
drag coefficients for all the cones of different cross section is given
in Fig. 6-22 for Mach numbers of 1 to 9.

6.7   Minimization of Pressure Drag

        Much effort has been directed towards the design of nose and
body shapes that have a minimum drag coefficient. In his early studies,
von Karman found that the optimum nose shape very closely resembled that
of a secant ogive having a radius of twice that of the corresponding
tangent ogive (see Subsec. 6.2) and a rounded nose with a diameter one-
tenth that of the body. By the use of an approximate equation for the
wave drag of slender bodies of revolution, Adams in Ref. 111 determined
the optimum shapes for the minimum wave drag of three specific families
of boattailed bodies. The first family consists of bodies having a
given length and base area and a body contour passing through a pre-
scribed point between the nose and base. The second has a fixed length,
base area, and maximum area. The third has a given length, volume, and
base area. The method presented is easily generalized to determine
minimum wave-drag profiles which pass through any prescribed number of
points. According to linearized theory, the optimum profiles are found
to have pointed noses, a zero slope at the body base, and no variation
of the wave-drag coefficient with Mach number. For the bodies whose
contours pass through a specified point, the maximum body diameter is
usually larger than the diameter at the specified point. The location
of a specified maximum diameter is not arbitrary but is determined from
the ratio of base diameter to maximum diameter. As long as the wetted
area of the body and the Reynolds number do not vary widely, the skin
friction will generally be independent of the over-all shape and hence
need not be considered for an optimum body design. The family of shapes
considered is given in Fig. 6-23 and the drag results obtained in
Ref. 111 are shown in Figs. 6-24 to 6-36.

        Haack (Ref. 112) obtained the same minimum drag bodies as
Adams but based his work on Ward's equations (Ref. 15) instead of
von Karman's drag equations.

        Harder and Renneman in Ref. 113 applied higher-order terms to
the determination of drag and optimum body shape and established shapes
which have slightly less drag than the "Haack-Adams" bodies. The drag

results are compared in Fig. 6-25. (Since the equations from which
these curves were obtained are lengthy, the reader is directed to the
reference for further details.) The optimum body shapes obtained by
Harder and Renneman are compared with those obtained by Haack and Adams
in Fig. 6-26 for two values of the volume parameter and a fixed value
of the base area parameter. It may be seen that there is little dif-
ference between the optimum shapes derived by the different methods.
There is a small but definite effect of Mach number on the Harder-
Renneman optimum shape as is shown in Fig. 6-27.

Bromm and Goodwin (Ref. 114) conducted an experimental in-
vestigation into the effect of varying Reynolds number and Mach number
on the wave drag at zero lift for seven boattailed bodies of revolution
that were designed for minimum wave drag in accordance with the Haack-
Adams methods. Their tests covered a Reynolds number range of approxi-
mately 2×10^6 to 10^7 at Mach numbers of 1.62, 1.93, and 2.41. These
tests indicated that there was little variation in the pressure distri-
bution with Reynolds number in the range tested (see Figs. 4-81 to 4-83).
The experimental wave-drag coefficients obtained by integration of the
pressures and shown in Fig. 6-28 were less than the values predicted by
the Adams theory. The discrepancy increased with Mach number to a value
as great as 45% of the theoretical drag for low ratios of base area to
maximum area. This is a further contradiction of the Adams theory which
implies that the drag is independent of Mach number.

Both Lighthill's method (Ref. 11) and the method of charac-
teristics predict lower drag for some boattailed bodies than does the
method given by Haack and Adams. A comparison of the drag obtained by
the several theories is given in Fig. 6-29, but even here the Mach num-
ber effect is small compared to that shown in Fig. 6-28. It would ap-
pear that there are real flow effects on boattails that are not taken
into account by the theories.

In Ref. 115 Parker develops a technique for determining the
minimum external wave drag of ducted as well as pointed bodies of revo-
lution without boattailing, assuming attached shock waves at the lip.
The expressions for the drag of various sections of the body are some-
what complex but have been solved for several cases.

In Ref. 42, Eggers, Resnikoff, and Dennis also determined the
approximate shapes of non-lifting, non-boattailed bodies for minimum
pressure drag in the Mach number range between 2.73 to 6.28. With the
aid of Newton's laws of resistance, the investigations were carried out
for various combinations of body length, base diameter, surface area,
and volume. In general, it was found that when the body length is fixed,
the body for least drag has a blunt nose; but when the length is not
fixed, the body has a sharp nose. The additional effect on minimum drag
shape of curvature of the flow over the surface is shown to increase the
bluntness of the shapes in the region of the nose and the curvature of
the body in the region downstream of the nose. According to calculations,
these shape modifications have only a slight tendency to reduce drag.
Several bodies of revolution of fineness ratio 3 and 5, including the
calculated shapes for minimum drag for a given length and base diameter
and for a given base diameter and surface area, were tested at Mach num-
bers of 2.73 to 6.28. The comparison of theoretical and experimental
fore-drag coefficients indicates that the calculations for minimum-drag
bodies produced reasonably good results. The body for a given length
and base diameter has as much as 20% less fore drag than a cone of the
same fineness ratio.

Somewhat complex analytical expressions are given in parametric form in Ref. 42 for the minimum-drag body under the assumptions of a given length and diameter, length and volume, length and surface area, base diameter and volume, and base diameter and surface area. Figure 6-30 shows the shape of several minimum-drag bodies of fineness ratio 5 calculated from these formulae. The bluntest nose is obtained when the drag is minimized for a given length and surface area. For a given diameter and volume the nose is a cusp. The expression for the minimum-drag shape for a given length and diameter may be closely approximated by

$$\frac{2r}{d} = \left(\frac{x}{\ell}\right)^n \quad \text{for} \quad n \leqq 1 \tag{6-3}$$

where, in the usual terminology,

r = radius of any cross section

x = distance from apex

d = maximum diameter

ℓ = total length

When $n = 1$, the body is a cone, i.e., the minimum-drag body for a given base diameter and surface area. A series of bodies based on this relation with various values of n were tested throughout the Mach range of 2.73 to 6.28 and for fineness ratios of 3 and 5; the results are shown in Fig. 6-31. It can be seen that the nose defined by the exponent $n = 3/4$ provides the least drag of any of these shapes at both length-to-diameter ratios, and this has been found to be generally true throughout a wide range of Mach numbers and fineness ratios.

Bodies of revolution having fineness ratios of 6.04 and 12.5 were investigated by Hart and Katz for the purpose of determining how drag is affected when the location of the maximum body diameter is varied. Results taken from Ref. 116 (by Hart and Katz) and shown in Fig. 6-32 indicate that the least drag will be encountered when the point of maximum diameter is located about 60% aft of the nose. It should be noted, however, that only relatively low Mach numbers are considered in this study and that the effect of tail fins is also included.

6.8   Pressure Drag of Blunt Bodies

Perturbation theories cannot be used for estimating the drag of round-nosed bodies because the assumption of small perturbations on which such theories are based is violated. It is therefore necessary to rely on other methods.

When the shape of the head shock is known, the drag can be obtained in theory by computing the momentum loss through the shock. But in practice, even though a photograph of the head shock is available, the field of view is usually so limited that a considerable portion of the associated shock loss cannot be computed. The recent work of Whitman in Ref. 117 on the asymptotic behavior of shocks associated with axially symmetric bodies may prove useful in extrapolating the form of

the head shock beyond the limits imposed by the photograph. The com-
putation of drag by means of losses through associated shocks must take
into account all shocks arising from the configuration. A consideration
of the bow shock alone will provide only a lower limit for the pressure
drag.

If the shape of the shock is unknown the situation is even
more discouraging. Some expressions for the general shape of the bow
shock at large distances from the body are presented in Ref. 117. In
addition, Busemann in Ref. 118 offers criteria for determining at which
points on the body, shocks (either attached or detached) will occur.

Statements of such nature, however, do not provide an accur-
ate basis for developing theoretical methods for the computation of
flows with detached shocks. Semi-empirical methods have been developed,
one of the best known being that of Moeckel (Ref. 119). When applied
to the location of detached shocks, Moeckel's method yields results of
"engineering" accuracy; when used to estimate drag, however, its results
are much less certain and it should be used only as a last resort.

Sometimes a rough, though adequate, estimate of the nose drag
of round-nosed bodies can be made by superimposing the wave drags of
certain basic shapes, i.e., by combining the form drag of the hemis-
pherical nose with the pressure drag on the afterbody, assuming that
the pressure distribution on the afterbody is uninfluenced by nose
bluntness.

Actually, however, the rapidly accumulating mass of experi-
mental data on this subject is making the use of such techniques less
necessary, and such data should be utilized wherever possible. Some
of these data are presented in the following subsections.

6.8.1   Pressure Drag of Spheres

The drag of spheres, while of notable academic interest, is
also of practical interest. Spherical or near-spherical shapes are em-
ployed in certain phases of ordnance, and hemispherical noses are of
growing importance in high-speed or recovery missiles because of their
favorable heat-transfer properties. The drag coefficient of steel and
aluminum spheres at supersonic speeds has been measured by several in-
vestigators (Refs. 121 to 124) and many of the results are plotted in
Fig. 6-33. The drag contribution of the forward half of the sphere was
obtained from integration of pressures measured in wind tunnels, but
most of the other measurements were made in free-flight ranges on spheres
whose diameters ranged from 0.25 in. to 1.5 in. Skin-friction effects
which may be included in the flight-test data are negligible in compari-
son with the pressure drag. In the studies of Ref. 121, the effects of
extreme roughness were found to produce only a slight increase ($< 3\%$)
in drag.

It should be noted that the curves of Fig. 6-33 are applicable
for Reynolds numbers above approximately 10^4 based on sphere diameter.
Below this value, the drag coefficient steadily increases as the Reynolds
number is decreased. While exact information concerning the value of
drag for a wide range of Mach numbers in this Reynolds number range is
not available, some idea of the trend and values at particular conditions

can be obtained from Figs. 6-34 and 6-36 (from Refs. 122 and 124, respectively).

Charters and Thomas in Ref. 121 developed the following empirical expressions for the shape of the mean drag coefficient curve of Fig. 6-36 in the various speed regimes.

Subsonic $(0 \leqq M \leqq 0.5)$

$$C_D = 0.489$$

(6-4)

Transonic $(0.5 \leqq M \leqq 1.6)$

$$C_D = 0.807 + 0.764 (M - 1) - 0.206 (M - 1)^2 - 0.918 (M - 1)^3$$

(6-5)

Supersonic $(1.6 \leqq M \leqq 4.0)$

$$C_D = 0.970 + 0.306 \left(\frac{1}{M} - \frac{1}{2.75}\right) - 0.605 \left(\frac{1}{M} - \frac{1}{2.75}\right)^2$$

(6-6)

Hypersonic $(4.0 \leqq M \leqq 10)$

$$C_D = 0.91$$

(6-7)

6.8.2   Pressure Drag of Rotating Cubes

The drag of 1/4-in. and 3/8-in. rotating cubes was measured by Hansche and Rinehart (Ref. 120) in the speed range between M = 0.5 to 3.5, and the results are shown in Fig. 6-35. Since the cubes were rotating, the frontal area varied. A value of 1.5 d^2 (where d is the cube edge) was arbitrarily taken as the reference area in computing the drag coefficient presented in Fig. 6-35.

6.8.3   Alleviating Pressure Drag of Blunt Bodies

In many applications where it is necessary to maintain low drag, the use of blunt noses imposes an almost intolerable aerodynamic penalty. Means have therefore been sought to alleviate the drag of blunt bodies without impairing the functioning of the guidance system housed in the blunt nose. One method of accomplishing this purpose is by the use of a spike projecting ahead of the nose as illustrated in Fig. 6-37. With no projection of the spike there is a detached bow shock with its associated high drag. As the spike is pushed forward, the shock pattern and pressure distribution does not change markedly until the spike is long enough to reach the shock wave. As it is pushed farther forward the boundary layer on the rod is unable to sustain the pressure rise through the normal shock, and a violent instability is encountered. This phenomenon is described by Crawford in Ref. 132 and Jones in Ref. 133. Additional forward movement of the rod results in eventual transition to a stable shock configuration consisting of a

conical shock attached to the spike and having in its wake a "dead-air" region that is conical in form and embracing most of the blunt nose, as shown below.
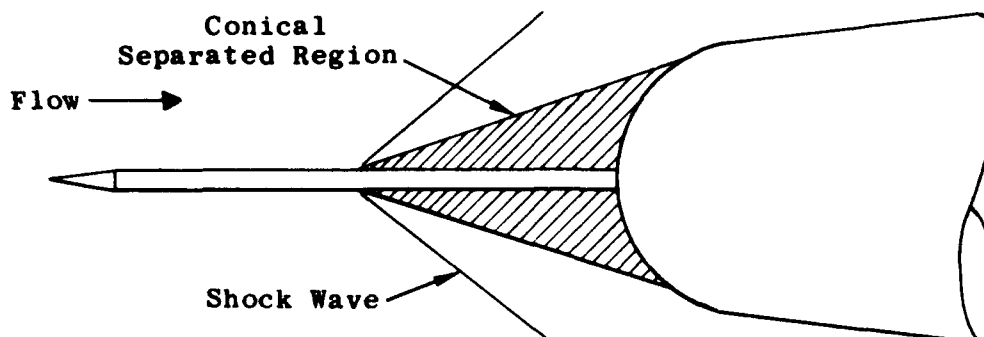
          At the junction of the dead-air region and the body nose, a secondary shock is invariably formed. Apart from the losses associated with this secondary shock and with those of the viscous dissipation in the dead-air region, the drag may be regarded as that of the equivalent cone cylinder. As the spike is projected still farther, a point will be reached at which the boundary layer formed on the rod immediately upstream of the separation point becomes turbulent. The boundary layer is then capable of sustaining a much larger pressure rise, and there is consequently a rapid movement of the separation point in a downstream direction. Such a downstream movement of the separation point results in an increase in the apex angle of the equivalent cone and an increase in drag coefficient.

          These changes in flow regime are reflected in Fig. 6-37 (from Ref. 133), in which the nose drag (including skin friction) is plotted against rod projection for two different degrees of nose bluntness. The drag is appreciably reduced as the length of the rod increases until an optimum rod length equal to about 3.5 or 4.0 times the nose radius is reached, after which the drag increases again. (It should be noted that the use of spikes results in an increase in heat transfer to the nose of the body. It is not difficult to envisage circumstances where the heating penalty might completely outweigh any advantages to be gained through drag reduction.) Crawford's detailed study in Ref. 132 presents the pressure distribution and integrates it to give the drag of a hemspherical nose with varying rod lengths and Reynolds numbers.

          The effect of the spike length upon the pressure drag of the hemisphere is shown in Fig. 6-38 (from Ref. 132). In this case the drag coefficient was determined by graphically integrating the areas under curves of the pressure coefficients plotted against $(r/R)^2$, where r is the local radius and R is the radius of the hemisphere. It is apparent that the pressure drag of the hemisphere is reduced as the spike length is increased to 3 diameters. There is little change in the drag coefficient as the spike length is further increased to 4 diameters except in the case of Reynolds numbers above approximately 0.8×10^6. In this case the drag coefficient is associated with the sharp increase in the angle between the separated flow and the body, and the rapid upstream movement of the boundary-layer transition and consequent flow separation.

          The drag coefficients are plotted as a function of Reynolds number in Fig. 6-39 (from Ref. 132), showing again the drag reduction

caused by the increasing spike length and indicating the manner in which the drag coefficient increases as the Reynolds number is increased. This drag increase is caused by the expected increase in pressure under the separated boundary layer in the region of transition.

6.9   Skin-Friction Drag

Inasmuch as skin-friction, heat-transfer, and other boundary-layer phenomena are given detailed treatment in Sections 13 and 14 of this Handbook, only sufficient information will be presented herein to permit computation of the skin-friction drag for any given configuration under a wide range of flight parameters. It should be noted also that since the skin friction may account for as much as half of the zero-lift drag of a body, the estimates must be as accurate as present information will allow.

6.9.1   Laminar Skin-Friction on a Flat Plate

Although the behavior of laminar boundary layers is amenable to theoretical treatment, the mathematical complexities of existing theories are such that investigations have been restricted essentially to the two-dimensional or the flat-plate case. Values of the mean skin-friction coefficient, C_f, for a flat plate as a function of free-stream Mach number and the Reynolds number (based on distance from the plate leading edge and the free-stream velocity and viscosity) are presented in Fig. 6-41 (from Ref. 135). The value of the local laminar skin-friction, c_f, may be obtained from

$$c_f = \frac{1}{2} C_f \qquad (6-8)$$

The flat-plate values of skin-friction coefficients may be used along a cylindrical body without an appreciable loss of accuracy. There are, however, three effects which may significantly alter the flow pattern and boundary-layer structure.

1. Where the longitudinal or meridian curvature is large, centrifugal forces may become significant. These forces are negligible if both δ, the boundary-layer thickness, and $\delta^2 \, dK/dx$, where K is the curvature of the meridian, are small. These conditions are usually satisfied in practice except in the immediate neighborhood of discontinuities in the slope of body contour.

2. Skin friction is affected by the lateral curvature to a limited degree as shown in Fig. 6-40 (from Ref. 126, which treats this effect in detail). From this figure it can be seen that in the case of bodies of extremely high fineness ratio, when the local body radius becomes comparable with the boundary-layer thickness, this effect can become significant.

3. In regions of increasing diameter the boundary layer tends to thin out. This causes an increase in the slope of the velocity profile and hence in skin friction. In regions of diminishing diameter, the reverse holds true.

Mangler (Ref. 127) derived a transformation which, when the local boundary-layer thickness is small compared with local section radius, makes it possible to translate the problem of the compressible laminar boundary-layer on an axially symmetric body into that of a two-dimensional boundary-layer flow along a curved wall. Reference 128 compares the results of computations which utilized flat-plate formulae with those of a more exact but time-consuming analysis involving this Mangler transformation in order to determine the over-all drag of an RM-10 body (parabolic in form and having a fineness ratio of 12.2). The two estimates thus derived differed by only 6%. Though the errors associated with the use of flat-plate formulae are much larger for the case of blunt-nosed bodies, their use is justified on the grounds that skin-friction drag makes up a small proportion of the total drag of such a configuration so that larger errors in its estimation can there-fore be tolerated.

6.9.1.1   Laminar Skin-Friction on Nose Sections

Three-dimensional effects on nose sections preclude the ap-plication of the flat-plate formula. It has been shown that a good approximation for the mean skin friction on all conical and near-conical noses may be obtained by multiplying the flat-plate values of Fig. 6-41 by the factor $2/\sqrt{3}$. The local value is found by multiplying by $\sqrt{3}/2$ (Ref. 136).

6.9.2   Turbulent Skin-Friction on a Flat Plate

Even though considerable effort has been expended on theory and experiment, the mechanism of turbulence is not yet well understood. The derived relationships are consequently of a semi-empirical nature.

One of the most reliable formulae available for the estimation of mean turbulent skin-friction on a flat plate is that of Van Driest, given in Refs. 131 and 135. This formula was used to obtain the turbu-lent skin-friction curves shown in Fig. 6-42.

Another formula which is rather more compact though somewhat less accurate is recommended by Monaghan in Ref. 174. This formula is expressed as

$$C_f = 0.074 \; Re^{-1/5} \left(1 + 0.9 \; \frac{\gamma - 1}{2} \; M^2 \right)^{-\frac{2.2}{5}} \qquad (6-9)$$

Axially symmetric cases which have thus far been treated in the literature are cones by Van Dyke (Ref. 129) and axial cylinders by Eckert (Ref. 130). When the results of Eckert's analysis of the turbu-lent flow along an axially aligned cylinder, presented in Fig. 6-43, are compared with the analogous results for the laminar boundary layer already given in Fig. 6-40, the turbulent boundary layer in correspond-ing cases is shown to be less sensitive to lateral curvature than the laminar. Hence the application of flat-plate formulae to curved sur-faces is even more justified in turbulent applications. For turbulent flow the relation between local skin-friction coefficient and the mean value is

$$c_f = \frac{4}{5} \; C_f \qquad (6-10)$$

6.9.2.1 Turbulent Skin-Friction on a Cone

The flat-plate mean turbulent skin-friction coefficient may be multiplied by $2/\sqrt{3}$ to give the mean skin-friction value for any cone. The local conical skin-friction coefficient is $4\sqrt{3}/5$ times the mean flat-plate value.

6.9.3 Boundary-Layer Transition

Since the mean turbulent skin-friction values for the flat plate in the Re range of 10^5 to 10^7 may be two to six times as great as those in the laminar boundary layer, the location of the transition from laminar to turbulent boundary layer is a very important factor in the estimation of the total skin-friction coefficient for a missile. The accurate prediction of the point or even the region of transition is extremely difficult since it is sensitive to many influences, among which are stream turbulence, Mach number, nose shape, pressure gradient along a meridian, surface temperature, and finish. Even when some of these factors are well defined the transition region cannot be located with certainty. A good review of these factors is given by Gazely in Ref. 125.

6.10 Evaluation of Skin Friction in the Presence of Heat Transfer

Since heat transfer is treated fully in Section 14 of the Handbook, this subsection will present only the equations and charts necessary to find the surface temperature of supersonic vehicles. The skin-friction coefficient is markedly influenced by the temperature of the surface over which the air is flowing, and this temperature is influenced not only by the ambient temperature but by the previous flight history of the missile.

To obtain a complete evaluation of the skin friction during any flight, calculations must be made step by step. For each interval the skin friction and the trajectory would be determined by iteration. Since the wall temperature depends on the heat capacity of the skin, any variation in skin materials or thickness must be accounted for. Such a calculation would be long and complex. A simplified technique for obtaining an accurate calculation of skin-friction coefficient in supersonic flight in the presence of heat transfer has been developed by McIntosh, Hebert, and Dershin in Ref. 175. This method employs an estimated flight trajectory and computes the skin temperature and skin friction step by step along it. The method is based on standard techniques for calculating temperatures on a surface in a supersonic stream and on an approximate average heat-transfer coefficient. From these the temperature of the wall at any location at any particular time may be calculated. The method is described fully and treated with illustrative examples in Ref. 175. Only the outline is presented here.

6.10.1 Computation of a Preliminary Trajectory

An estimated trajectory is calculated by any of the usual methods under the assumption of an insulated body surface. The skin-friction value at each step is dependent on the Reynolds number corresponding to calculated altitude, velocity, and missile length as the characteristic dimension. For the given Re and M, C_f is found from

the curve of $T_r = T_w$ in Fig. 6-44, and C_f from the Karman-Schoenherr curve in Fig. 6-41.

6.10.2   Computation of Temperature during Boost

The skin temperature, T_{w1}, at the end of boost is determined from the following equation.

$$T_{w1} = T_{r1} + (T_{wo} - T_{ro}) \left(1 + \frac{h\ell}{2k}\right)^{-1} e^{-\frac{ht_1}{G}}$$

$$- \left(1 + \frac{h\ell}{2k}\right)^{-1} \left(\frac{T_{r1} - T_{ro}}{t_1}\right) \frac{G}{h} \left(1 - e^{-\frac{ht_1}{G}}\right)$$

(6-11)

where

T_{wo} = known wall temperature

T_{r1} = recovery temperature

h = heat-transfer coefficient

k = thermal conductivity of skin material

ℓ = thickness of skin

G = heat capacity of skin

t = time

and subscript

o refers to zero time

1 refers to time at the end of boost.

T_{wo} and T_{ro} are assumed to be known. Theoretically they would be equal and the second term of Eq. 6-11 would disappear. In practice it is found that the missile skin before launching is hotter than the ambient air, i.e., $T_{wo} > T_{ro}$. The value of T_{r1} can be taken from Fig. 6-45 and from the known parameters of the estimated trajectory; h_1 can be taken from Fig. 6-46 and from the equation

$$h_1 = h_o \frac{M_1^{0.8}}{x^{0.2}}$$

(6-12)

where

x is the distance from the vertex to the point in question

h is taken as 3/4 h_1

G, ℓ, k are inherent in the skin specifications (as follows).

Airframe Material Characteristics

Material	$\left(\dfrac{G}{BTU/ft^2}\right)$	$\left(\dfrac{k}{BTU/ft\ sec\,°F}\right)$
Steel	5.0ℓ (in.)	7×10^{-3}
Aluminum	3.25ℓ (in.)	2.5×10^{-2}
Magnesium	2.37ℓ (in.)	1.2×10^{-2}

6.10.3 Computation of Temperature during Cruise

For times of powered flight, i.e., from t_1 to t_2 seconds, the wall temperature at any time, t, is given by

$$T_{wt} = T_{rt} - \left(\frac{h\ell}{2k} + 1\right)^{-1} \cdot \frac{G}{h}\left[\left(\frac{T_{r1} - T_{ro}}{t_1}\right)e^{-\frac{ht}{G}}\left(e^{\frac{ht_1}{G}} - 1\right)\right.$$

$$\left. + \left(\frac{T_{r1} - T_{r2}}{t_2 - t_1}\right)\left(e^{-\frac{h}{G}(t - t_1)} - 1\right)\right] \tag{6-13}$$

To find T_{rt}, T_{r1} and T_{r2} are plotted as a function of time (as shown below) and a linear variation of T_r is assumed between the two points.
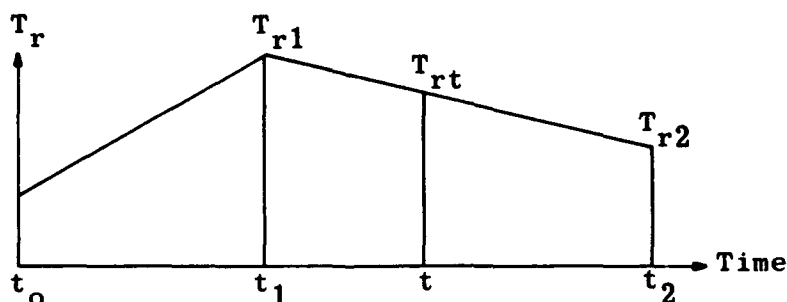
T_r may then be read off for any value of $t_1 < t < t_2$. A similar plot is made for h as a function of t.

6.10.4 Computation of Maximum Temperature during Cruise

The maximum temperature attained during sustained flight is obtained from

$$T_{w\ max} = -\frac{G}{k}\log_e \frac{\left(\dfrac{T_{r1} - T_{r2}}{t_2 - t_1}\right)\left(1 + \dfrac{h\ell}{2k}\right)}{\left(\dfrac{T_{r1} - T_{ro}}{t_1}\right)\left(e^{\frac{ht_1}{G}} - 1\right) + \left(\dfrac{T_{r1} - T_{r2}}{t_2 - t_1}\right)e^{\frac{ht_1}{G}}} \tag{6-14}$$

235

Values of G and k are those tabulated previously for typical airframe materials.

6.10.5   Computation of Skin Friction

Using the computed values of T_w/T_1 for the required point on the trajectory, the value of C_f/C_{f_i} may then be read from Fig. 6-44 or computed from the equation,

$$C_f/C_{f_i} = \left(0.5 + 0.5\,\frac{T_w}{T_1} + 0.03916 M_1^2\right)^{-2/3} \tag{6-15}$$

The value of C_{f_i} is given in Fig. 6-41 (Karman-Schoenherr line) or may be computed directly from

$$\frac{0.242}{\sqrt{C_{f_i}}} = \log_{10}\left(Re_x \cdot C_{f_i}\right) \tag{6-16}$$

6.11   Influence of Surface Roughness on Transition and Skin Friction

Up to this point, attention has been directed toward the drag of smooth surfaces. However, no surface is smooth in a strictly geometrical sense. The surface of a typical missile or aircraft contains many small protrusions such as rivet heads, lap joints, etc. Even the surface itself is generally full of pits and ridges, the size and nature of which would be dependent on the fabrication technique. These irregularities affect the drag in two ways. In the first place, they give rise to disturbances in the laminar boundary layer which tend to promote an early transition to turbulent flow. In the second place, each protrusion, if it is sufficiently large, has a "form drag" of its own and thus contributes directly to the total drag. (Sometimes in order to avoid an addition to the over-all drag force, it is desirable to hold the roughness to a level low enough to prevent individual roughness elements from having any form drag. This imposes a more exacting finish specification than is required to avoid a marked change in transition location.)

Schlichting in Ref. 171 presents a summary of the qualitative and quantitative aspects of the influence of surface roughness on skin-friction drag for the low-speed case. But comparable data which can be applied to the supersonic case is meager. Certain available data (Refs. 172 and 173), however, suggest that the influence of roughness is qualitatively (and in certain respects, quantitatively) much the same in supersonic flow as in subsonic or transonic. Czarnecki, Robinson, and Hilton (Ref. 173) derived the skin-friction coefficient from drag measurements made on four ogive-cylinder models having surface roughnesses of 23, 85, 240, and 480 μ in. rms. The effects of surface roughness at the test Mach number of 1.6 were found to be similar to those at subsonic speeds. Smoothed curves of the skin-friction coefficient, C_{f_w} (based on wetted area) as a function of Reynolds number are shown in Fig. 6-47 together with the theoretical curves for laminar and turbulent boundary layers. The difference between the experimental

data and the theoretical curve in the laminar-flow region is believed to be due to the low accuracy inherent in measuring low pressures and small forces. The variation of ΔC_f with Reynolds number is given in Fig. 6-48 for various values of k'/ℓ, where k' is admissible maximum roughness height, ℓ is body length, and $\Delta C_f = C_f$ rough $- C_f$ smooth.

Figure 6-49 shows the critical roughness height, k'/ℓ beyond which the drag will be increased due to the roughness. The straight line represents incompressible data obtained by Nikuradse for turbulent flow over a flat plate with varying roughness. The two largest test roughnesses (from Ref. 173) agree well with Nikuradse's values, but the remaining two were tested at a Reynolds number much lower than the critical one. The admissible roughness, k', may be found from

$$k' \text{ (in.)} = 198 \, (\text{Re/ft})^{-0.9} \qquad (6\text{-}17)$$

6.12   Influence of Large Protrusions on Skin Friction

The influence at supersonic speeds of large protuberances such as rivet heads, lap joints, or other surface irregularities has not been studied extensively. Hopko (Ref. 172) made some such measurements by free-flight tests. The configurations he studied are shown with the resulting drag curves in Fig. 6-50. In the latter figure the drag has been broken down into its constituent parts in order to show clearly the added drag due to the protrusions. It may be as large as 15% of the total drag.

In the case of larger protrusions such as antennae, housings, booster shoes, etc., the lift and moment characteristics of the configuration may also be affected. Hence, such features should be included in the over-all experimental studies of the aerodynamic characteristics of a given configuration.

6.13   Simplified Computer Methods of Determining Drag for Design Studies

A simplified method has been established by Bowers in Ref. 198 for making and programming engineering approximations of drag coefficient curves which are used in making preliminary design studies and calculating missile trajectories. The method consists of programming a series of drag curves, each a function of Mach number, determining a multiplying constant for each curve, and then summing the product of the curves and their respective constants.

A practical set of curves comprises the following essentials.

1. Cone drag curve, $f_1(M)$, of a 15-deg half-angle cone (Fig. 6-51). Variations of cone angle from this basic curve causes the drag to vary approximately as the square of the sine of the angle. Thus, C_1, the first constant, is given by

$$C_1 = \frac{\sin^2 \theta}{\sin^2 15} \cdot \frac{S_c}{S} \qquad (6\text{-}18)$$

where

θ = cone semi-angle

S_c = frontal area of cone

S = reference area

2. <u>Hemisphere</u> <u>drag</u> <u>curve</u>, $f_2(M)$, which may be taken from Fig. 6-33 and its associated constant,

$$C_2 = \frac{S_{nose}}{S} \tag{6-19}$$

When the blunt nose may not be approximated by a hemisphere,

$$C_2 = k \frac{S_{nose}}{S} \tag{6-20}$$

where

k = ratio of Newtonian drag on the blunt nose to the Newtonian drag of a hemisphere (i.e., $0.8 < k < 2$)

3. <u>Base</u> <u>drag</u> <u>coefficient</u>, $f_3(M)$, which must be chosen according to the type of base under consideration, with or without boat-tailing; closed or annular, with or without an issuing jet. Examples of such drag curves are presented in Subsec. 7. The constant is

$$C_3 = \frac{S_b}{S} \tag{6-21}$$

4. <u>Skin-friction</u> <u>drag</u> <u>curve</u>, $f_4(M)$, which will also be dependent on the anticipated altitude and Reynolds number. It is usual to assume all turbulent flow and either an average altitude (weighted with respect to time) or the similarly derived average Reynolds number. A curve of C_f vs M may then be constructed from Fig. 6-42. The constant is

$$C_4 = \frac{\text{Wetted Area}}{S} \tag{6-22}$$

The over-all drag coefficient as a function of Mach number is then

$$C_D = C_1 f_1 + C_2 f_2 + C_3 f_3 + C_4 f_4 \tag{6-23}$$

The technique may be expanded as desired. It may be necessary to consider a hemispherical cap followed successively by several conical segments rather than just one, or a curve may be added for an ogival boat-tail portion.
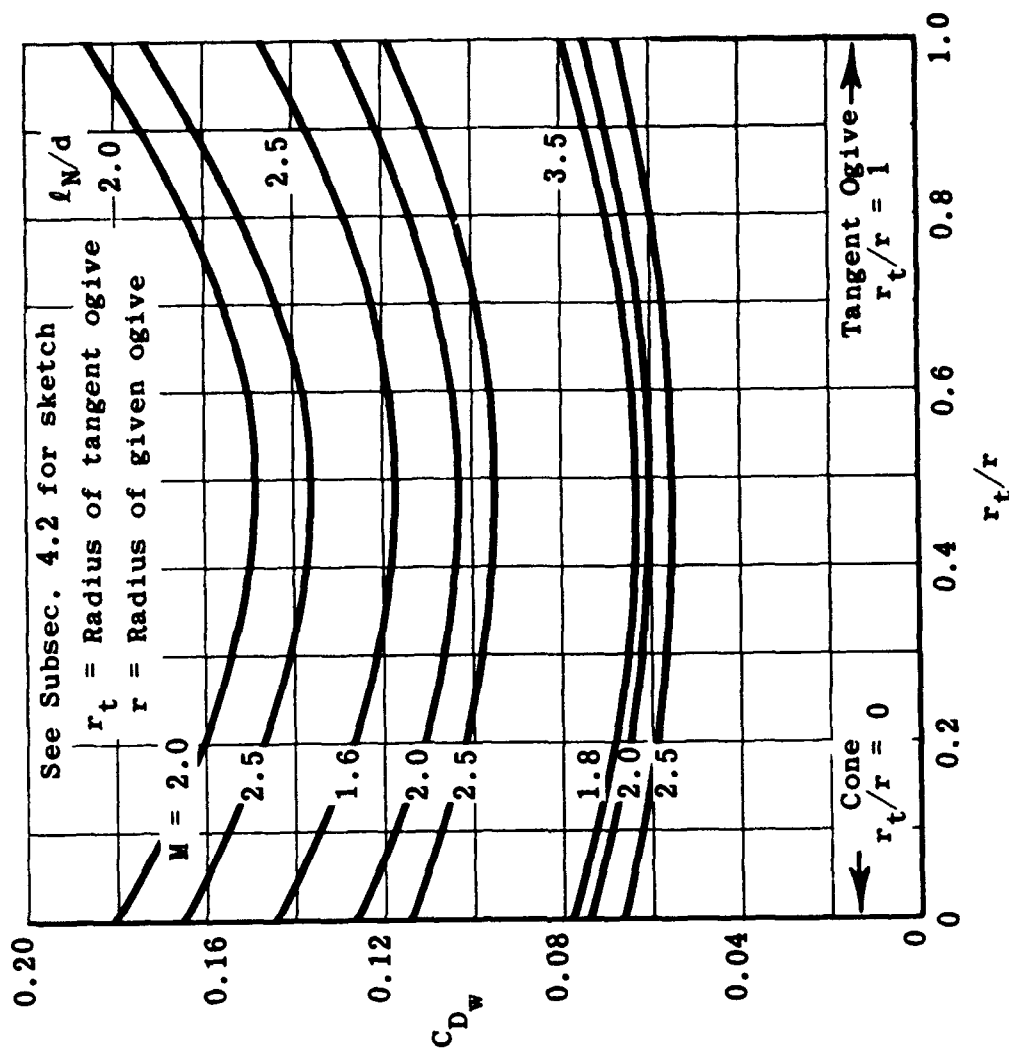
Fig. 6-2. Wave drag of secant ogives in terms of ogive radius for several Mach numbers and nose fineness ratios.
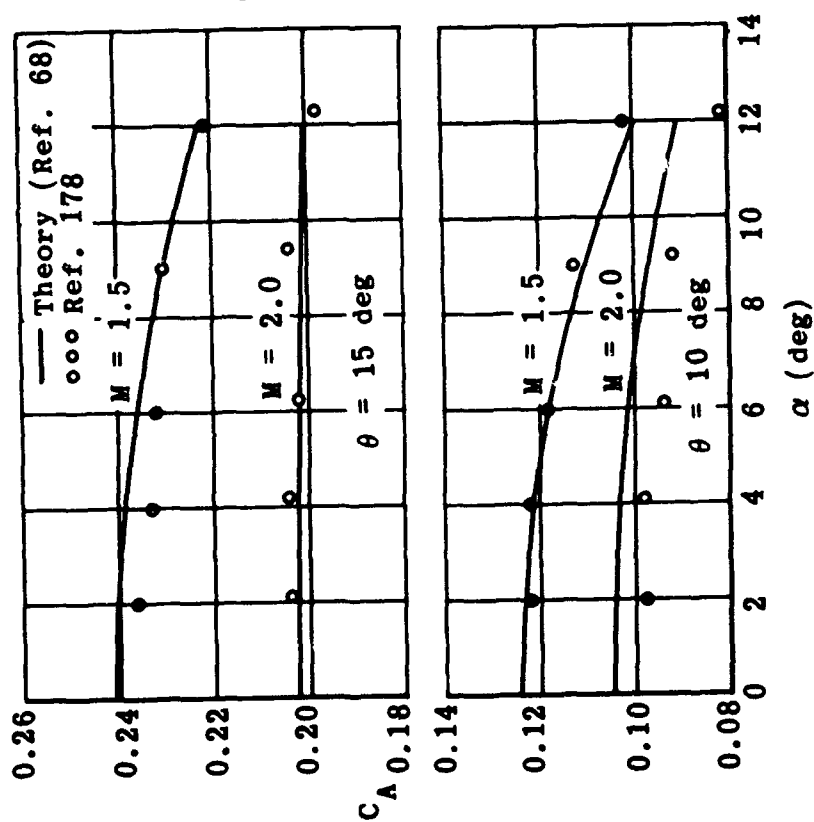
Fig. 6-1. Comparison of theoretical and experimental axial-force coefficient vs α for two cones; $\theta = 10$ and 15 deg, $M = 1.5$ and 2.0. (Source: Ref. 68)

239

Fig. 6-3   NAVWEPS Report 1488 (Vol. 3, Sec. 8)

Fig. 6-4. Calculated wave-drag coefficients versus diameter ratio for ducted cones; M = 1.6, 2.4, and 3.2; θ = 6 deg. (Source: Ref. 110)

Fig. 6-3. Experimentally determined drag of elliptical noses versus over-all fineness ratio. (Source: Ref. 93)
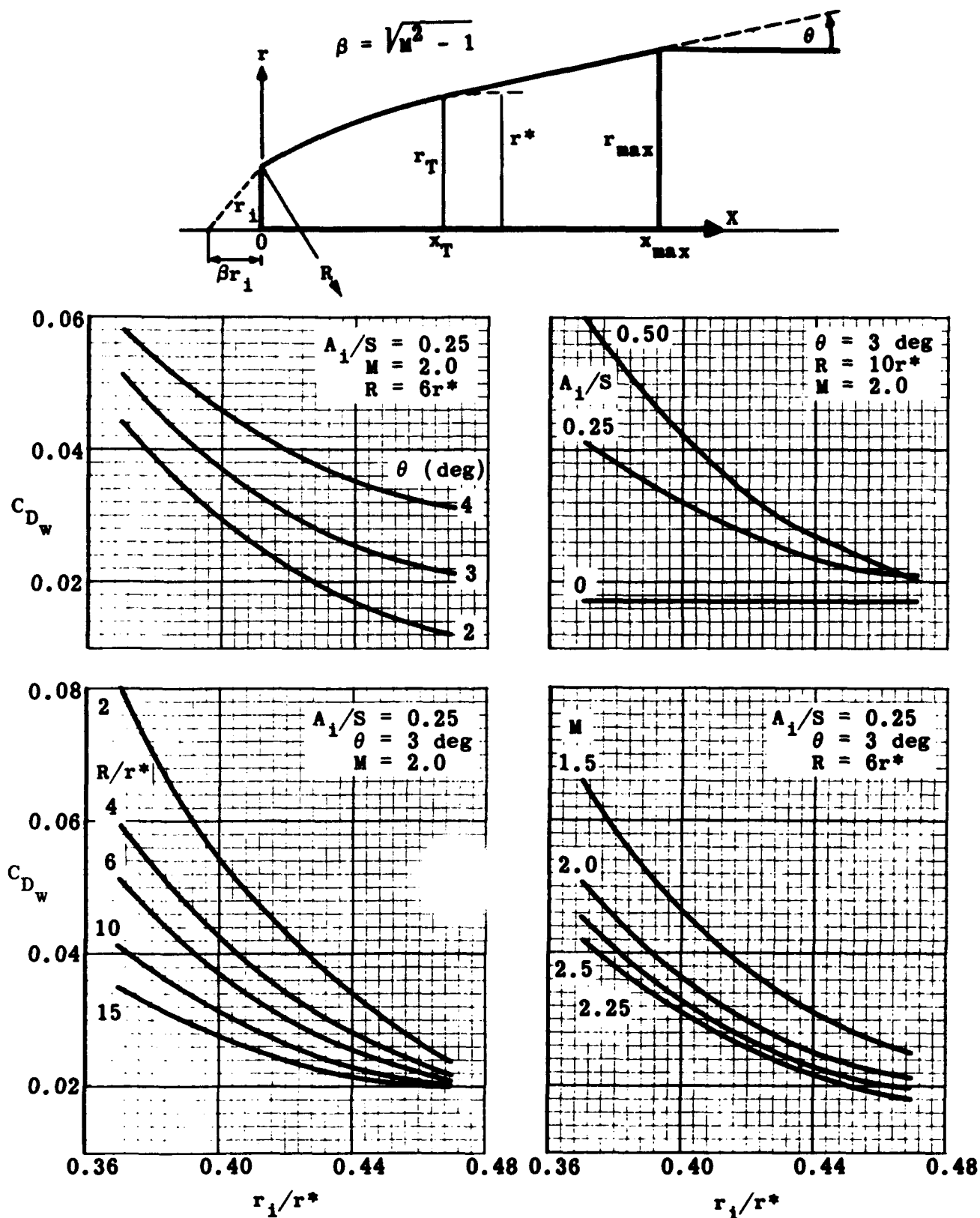
Fig. 6-5. Wave-drag coefficient versus inlet radius for ducted bodies
      in terms of cone angle, area ratio, ogive radius, and Mach number.
      (Source: Ref. 79)

Fig. 6-6   NAVWEPS Report 1488 (Vol. 3, Sec. 8)
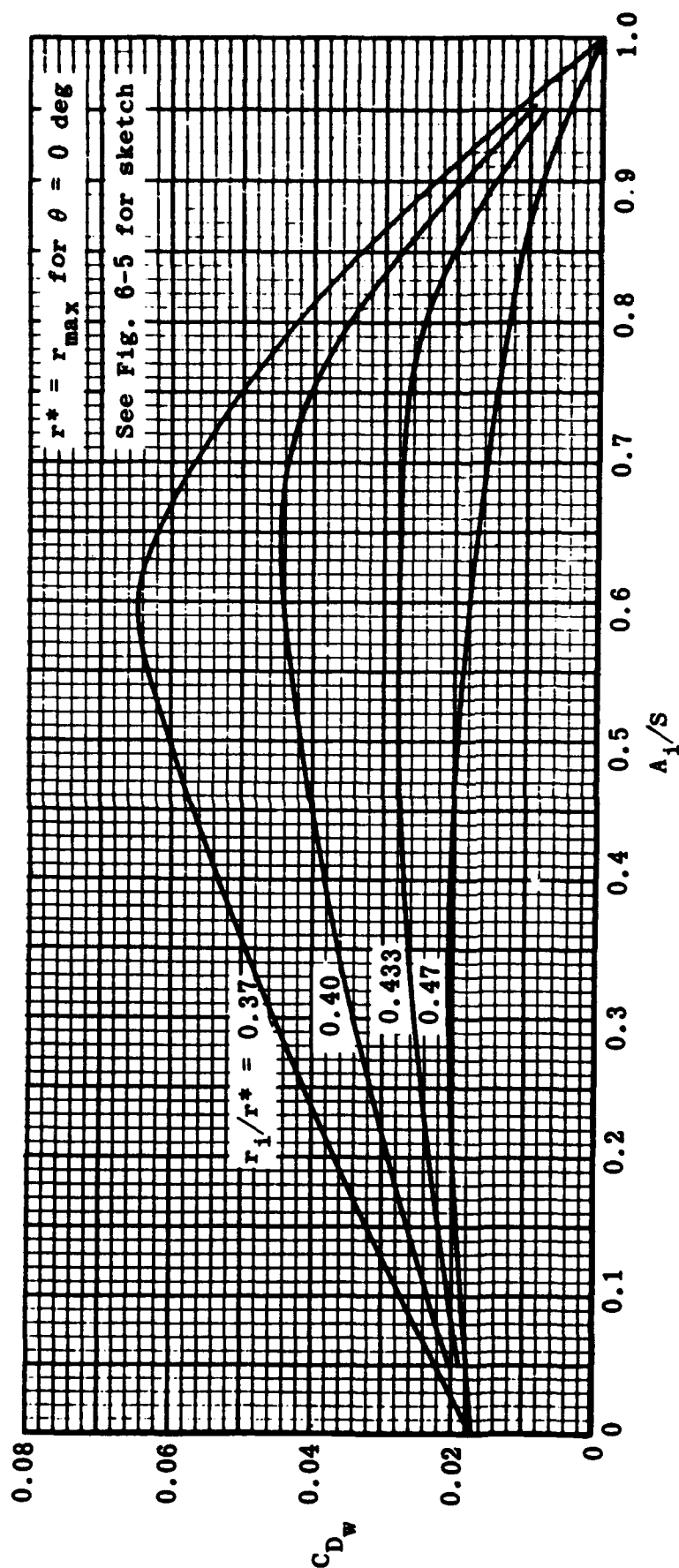
Fig. 6-6. Wave-drag coefficient of a ducted body versus area ratio in terms of inlet radius; $\theta = 3$ deg, $R/r^* = 10$, $M = 2$. (Source: Ref. 79)
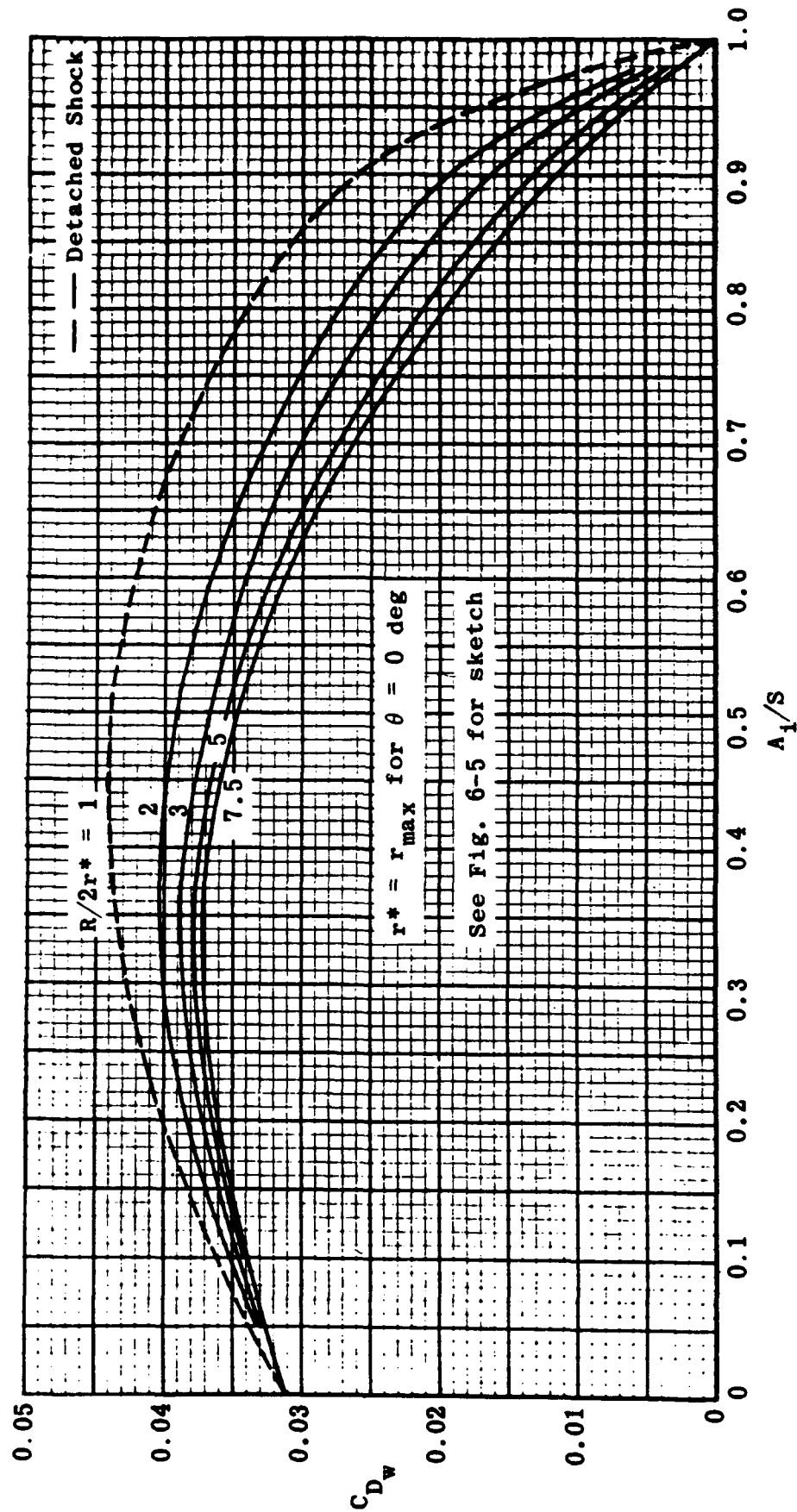
Fig. 6-7. Wave-drag coefficient of a ducted body versus area ratio in terms of ogive radius; $r_i/r^* = 0.47$, $\theta = 4$ deg, $M = 1.5$. (Source: Ref. 79)

Fig. 6-8   **NAVWEPS Report 1488 (Vol. 3, Sec. 8)**
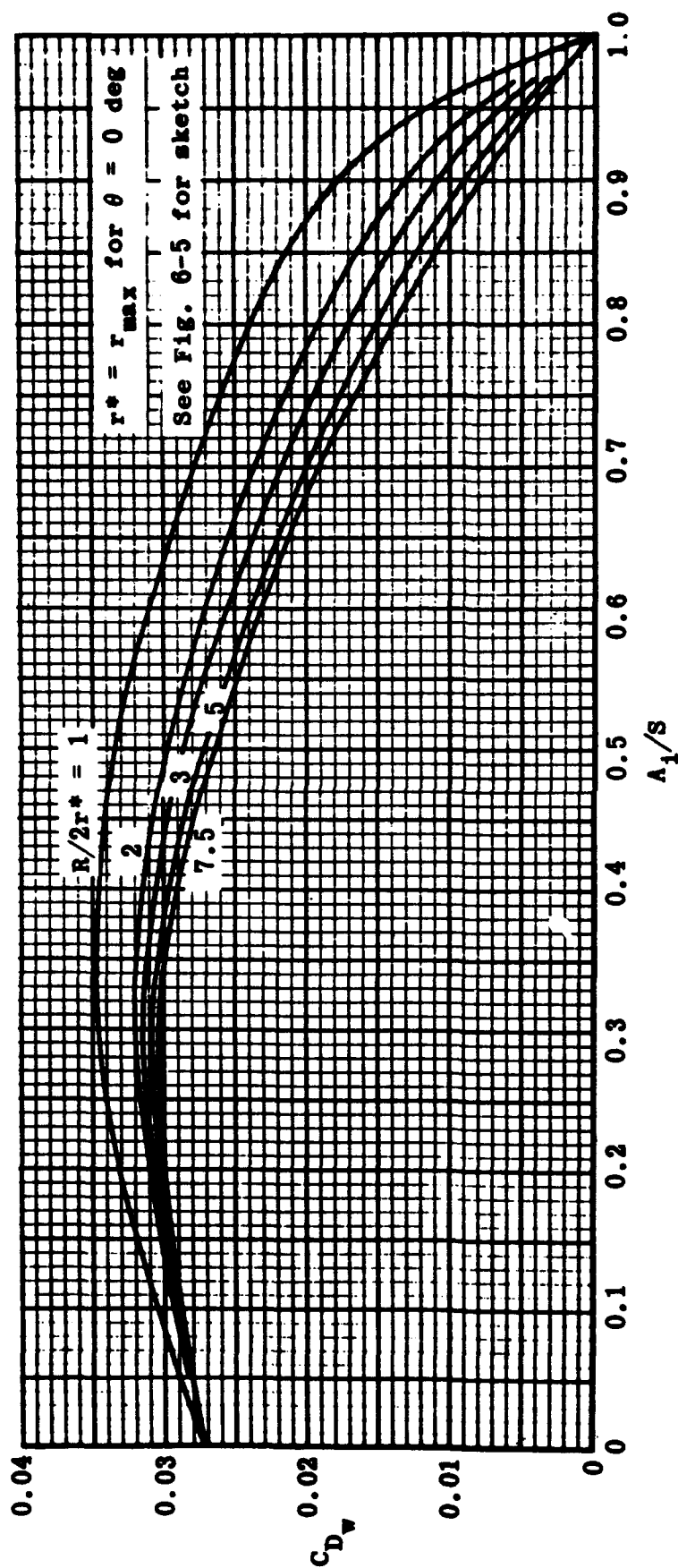
Fig. 6-8. Wave-drag coefficient of a ducted body versus area ratio in terms of ogive radius; $r_1/r^* = 0.47$, $\theta = 4$ deg, M = 2. (Source: Ref. 79)
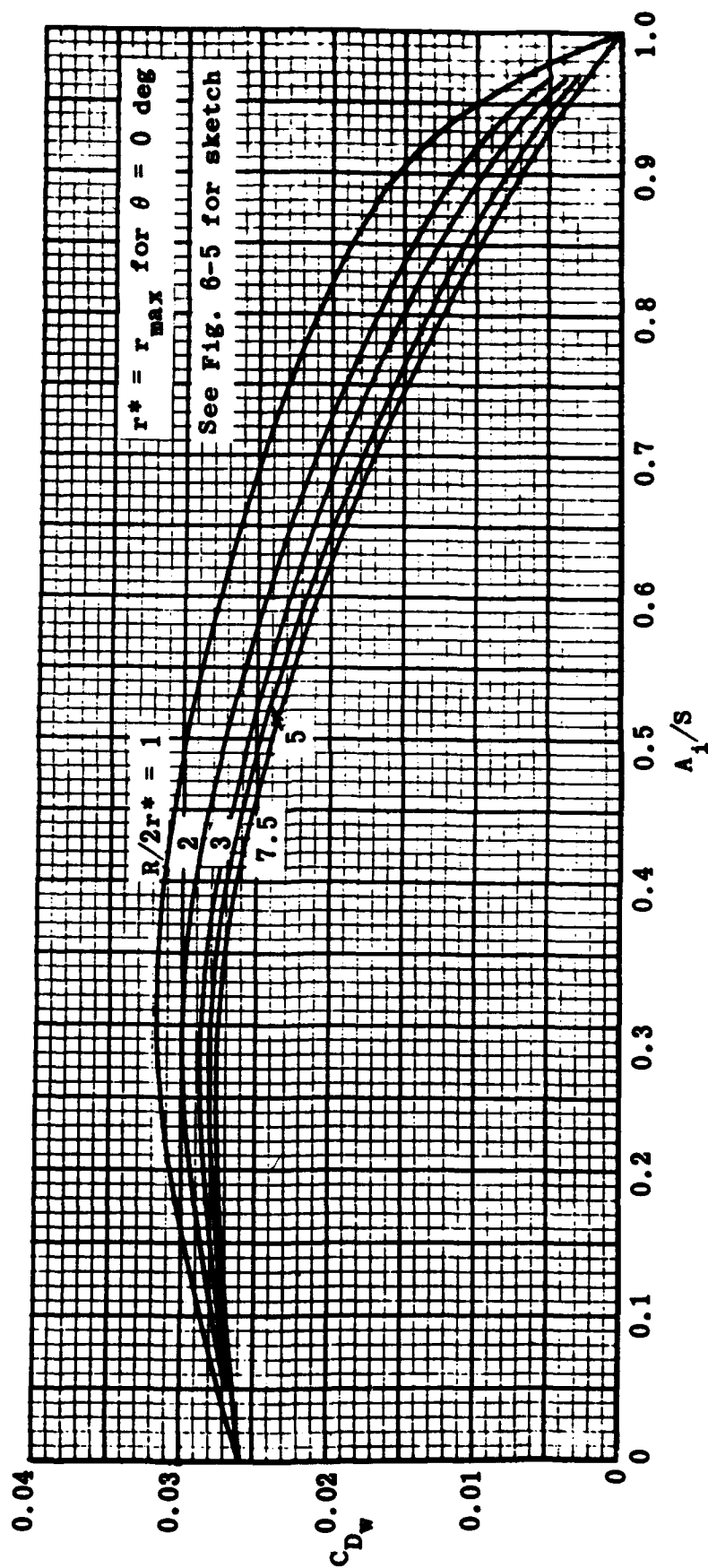
Fig. 6-9. Wave-drag coefficient of a ducted body versus area ratio in terms of ogive radius; $r_1/r^* = 0.47$, $\theta = 4$ deg, $M = 2.25$. (Source: Ref. 79)

Fig. 6-10   NAVWEPS Report 1488 (Vol. 3, Sec. 8)
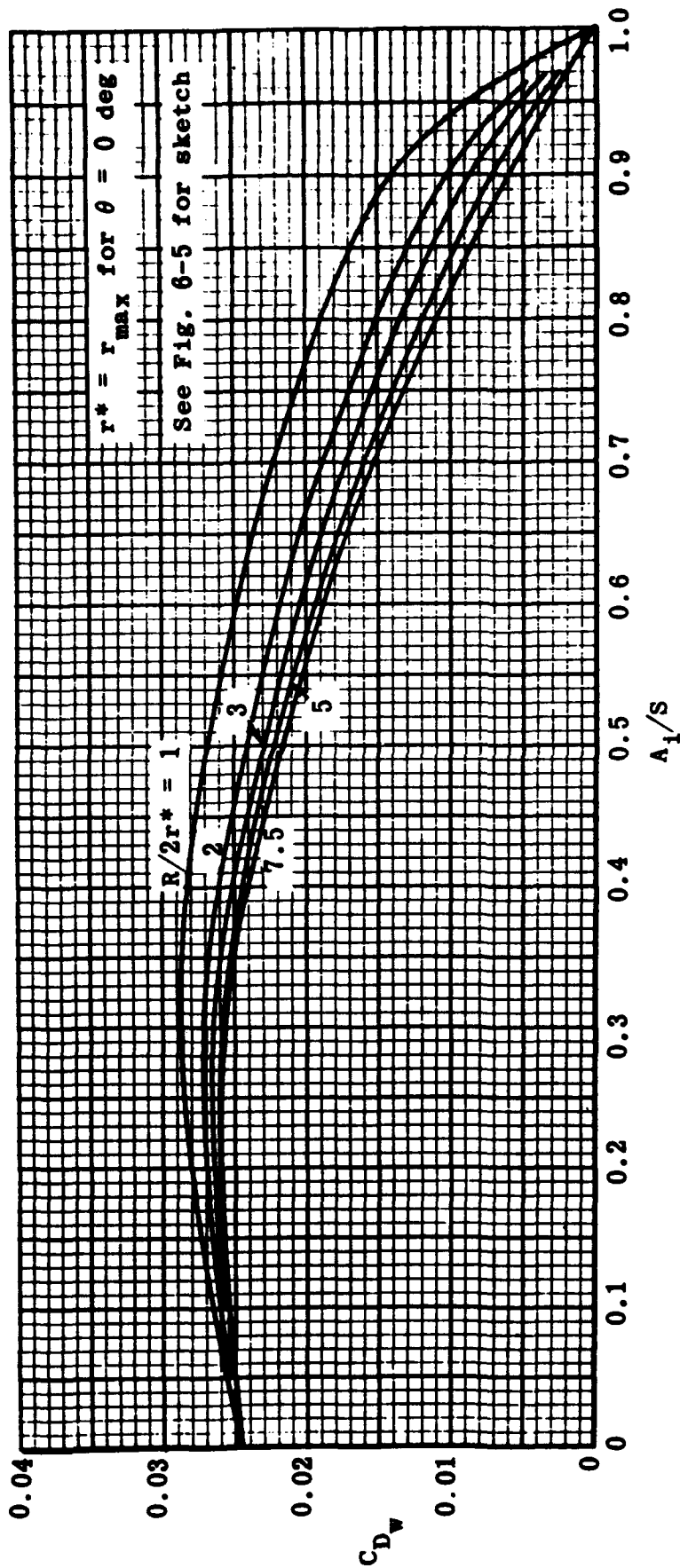
Fig. 6-10. Wave-drag coefficient of a ducted body versus area ratio in terms of ogive radius; $r_i/r* = 0.47$, $\theta = 4$ deg, $M = 2.5$. (Source: Ref. 79)
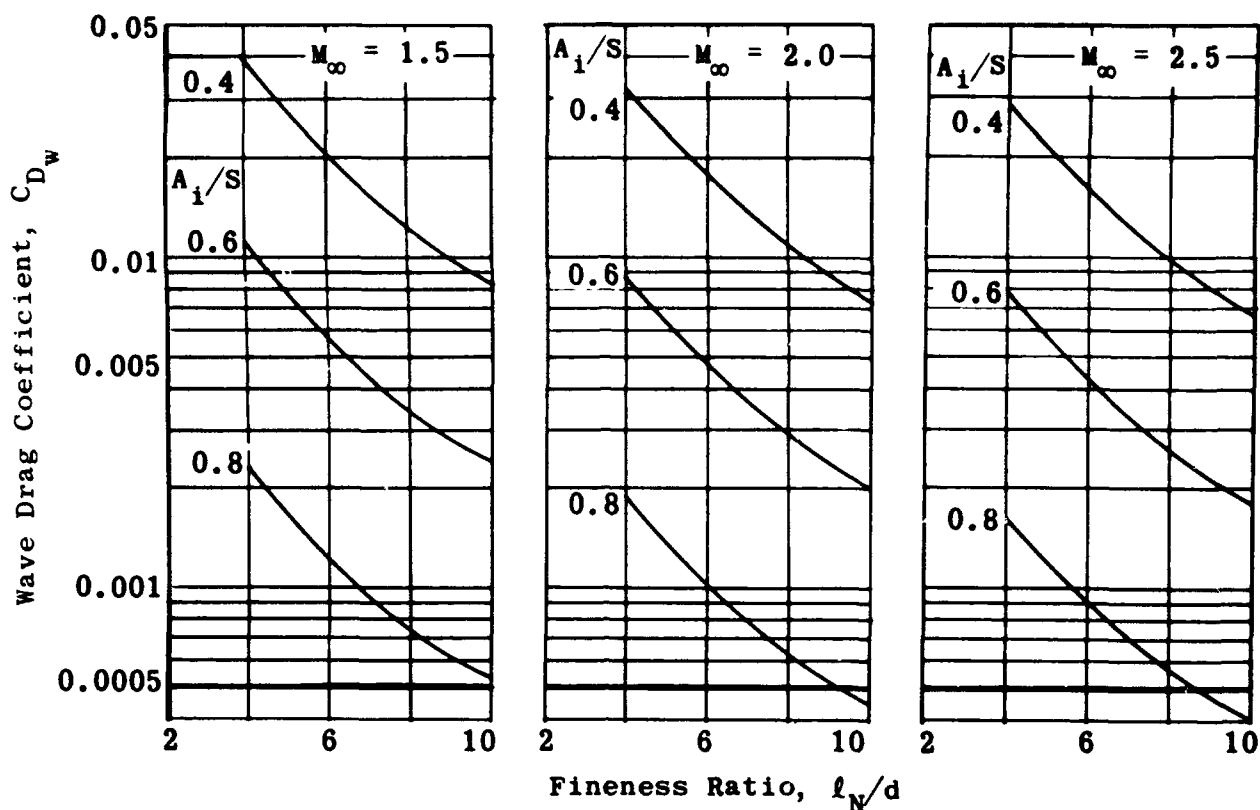
Fig. 6-11. Calculated wave drag for conical cowls versus fineness
ratio; A_i/S = 0.4, 0.6, and 0.8; M = 1.5, 2.0, and 2.5.
(Source: Ref. 75)
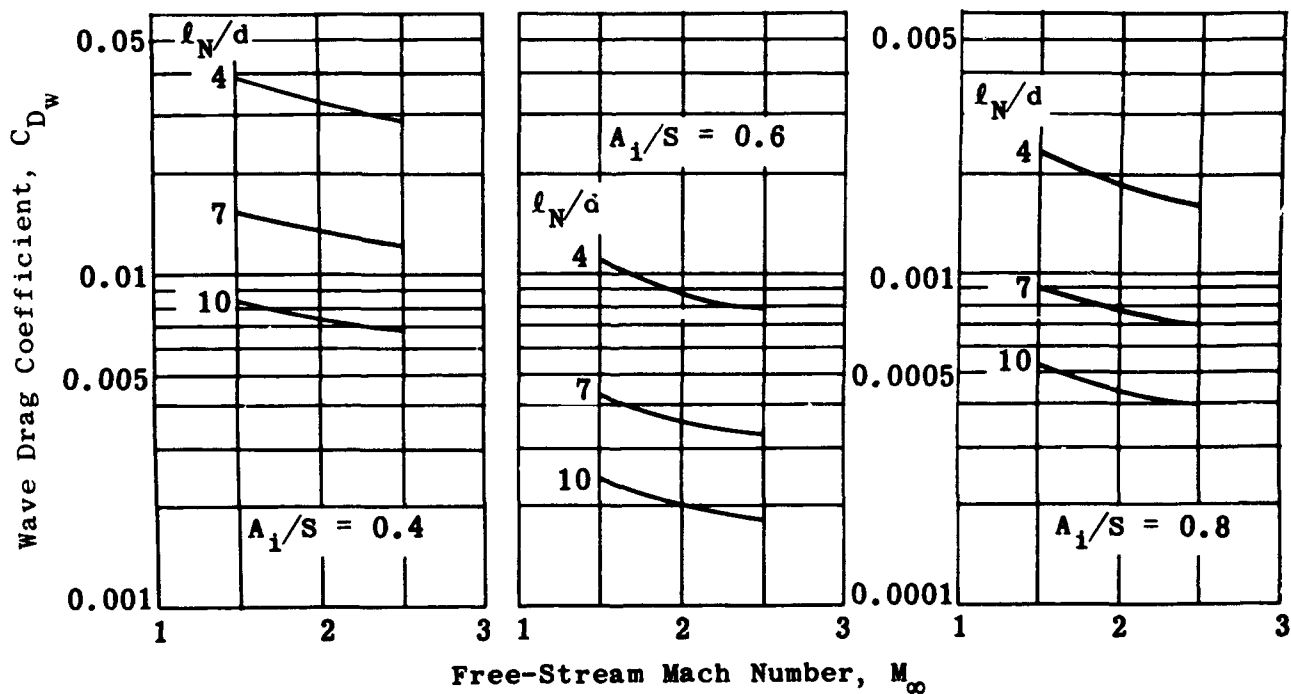
Fig. 6-12. Calculated wave drag for conical cowls versus Mach
number; A_i/S = 0.4, 0.6, and 0.8; ℓ_N/d = 4, 7, and 10.
(Source: Ref. 75)

Fig. 6-13   NAVWEPS Report 1488 (Vol. 3, Sec. 8)
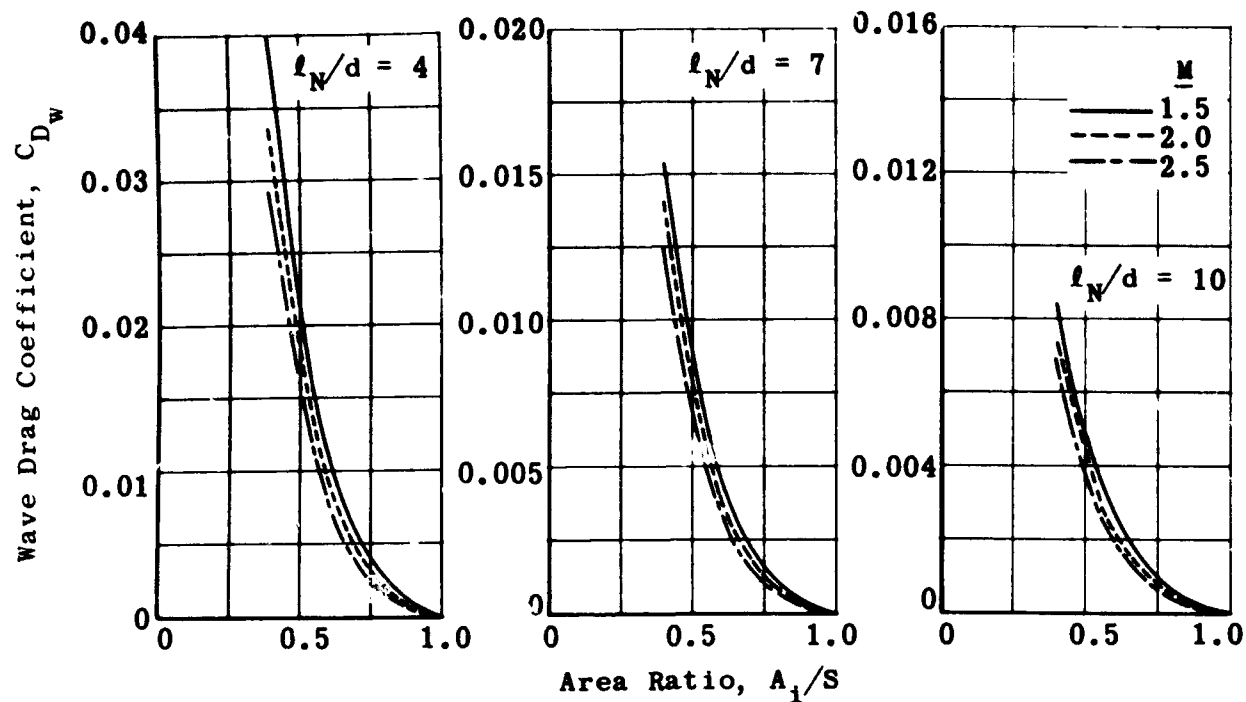
Fig. 6-13. Calculated wave drag for conical cowls versus area
ratio; ℓ_N/d = 4, 7, and 10; M = 1.5, 2.0, and 2.5.
(Source: Ref. 75)
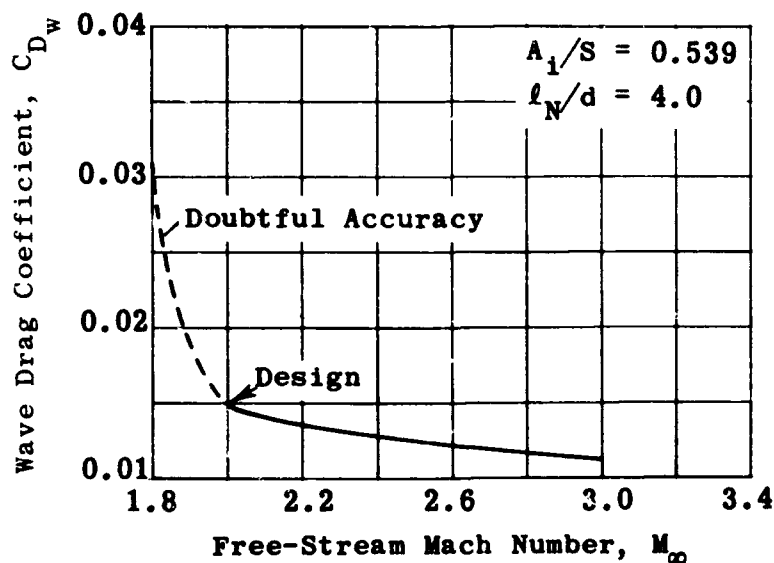
Fig. 6-14. Wave drag as a function of Mach number for a
nose inlet design for M = 2. (Source: Ref. 75)
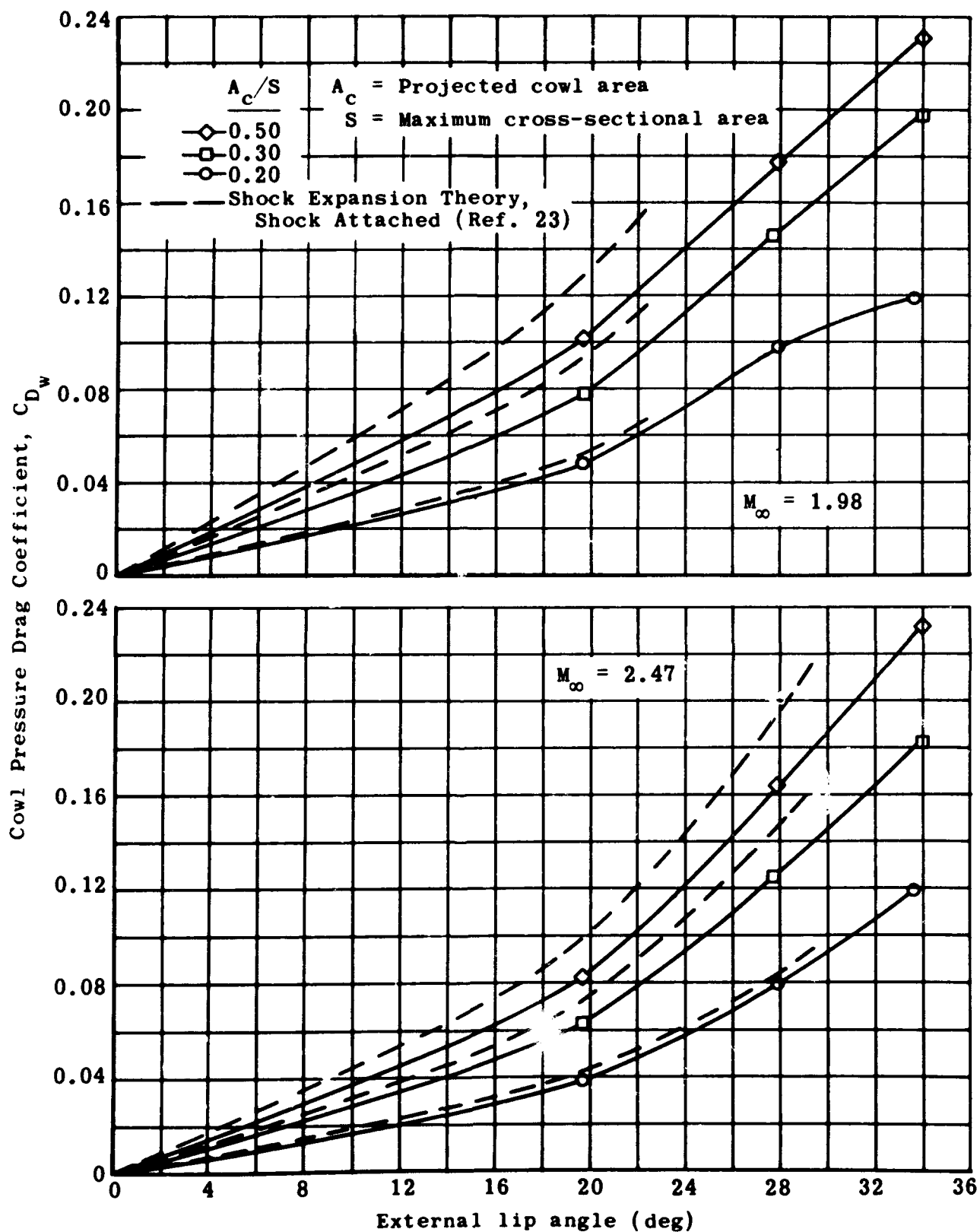
Fig. 6-15. Effect of lip angle on cowl drag; M = 1.98 and 2.47.
(Source: Ref. 80)

Fig. 6-16   NAVWEPS Report 1488 (Vol. 3, Sec. 8)
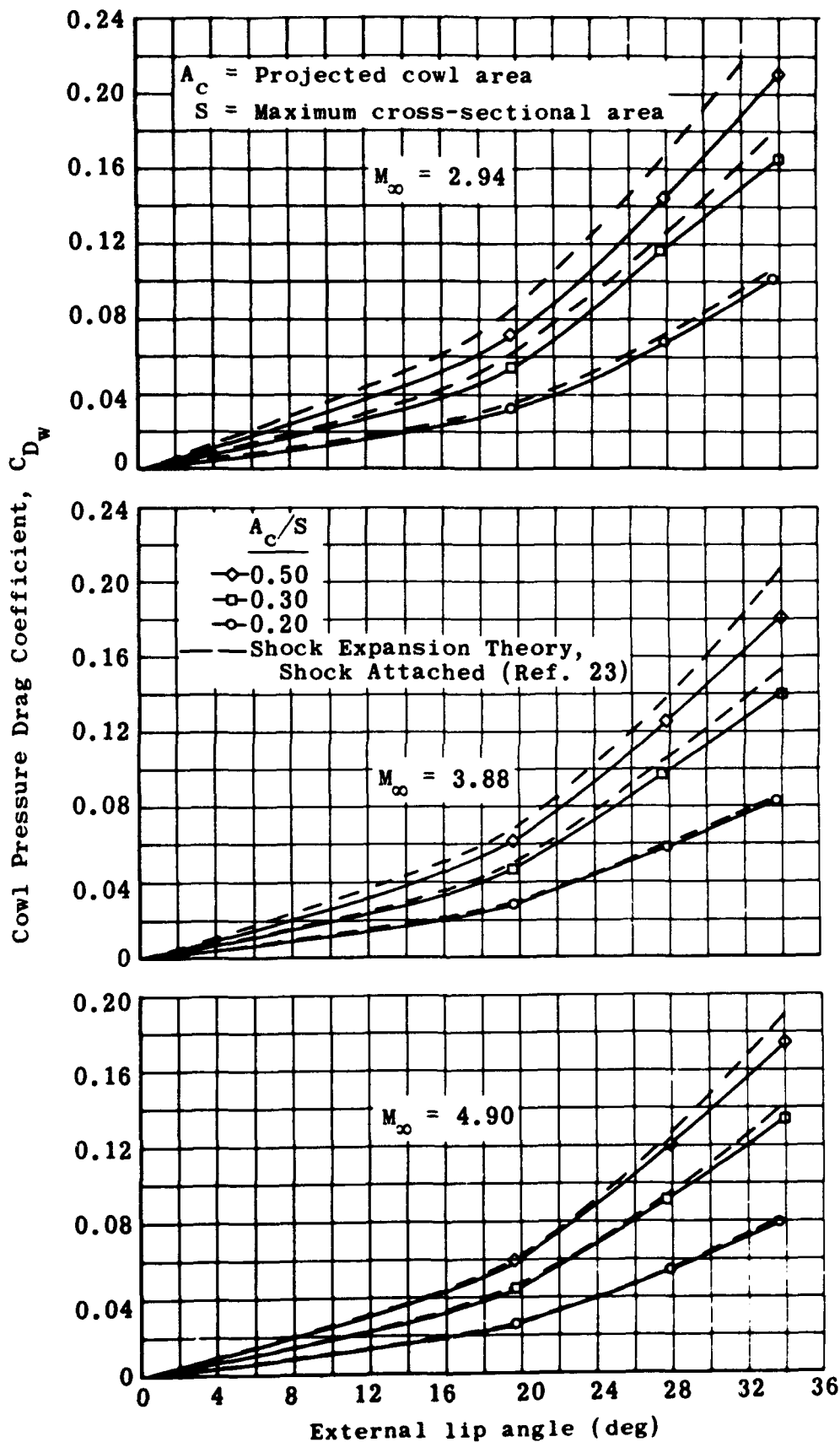
Fig. 6-16.   Effect of lip angle on cowl drag; M = 2.94, 3.88, and 4.90.   (Source: Ref. 80)
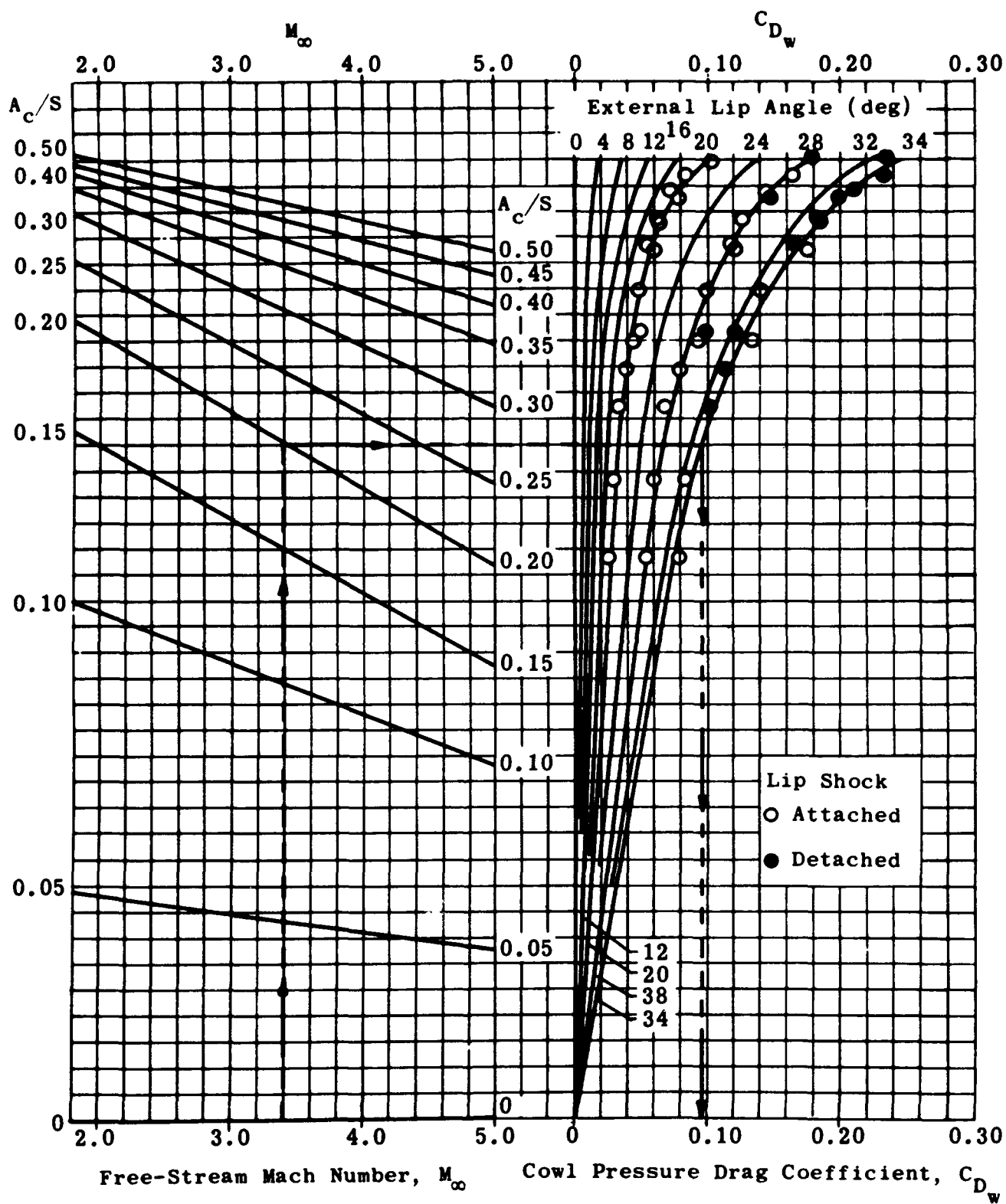
Fig. 6-17. Empirical chart for estimating cowl pressure drag
            for cowls having an approximately elliptical contour.
            (Source: Ref. 80)

Fig. 6-18   NAVWEPS Report 1488 (Vol. 3, Sec. 8)
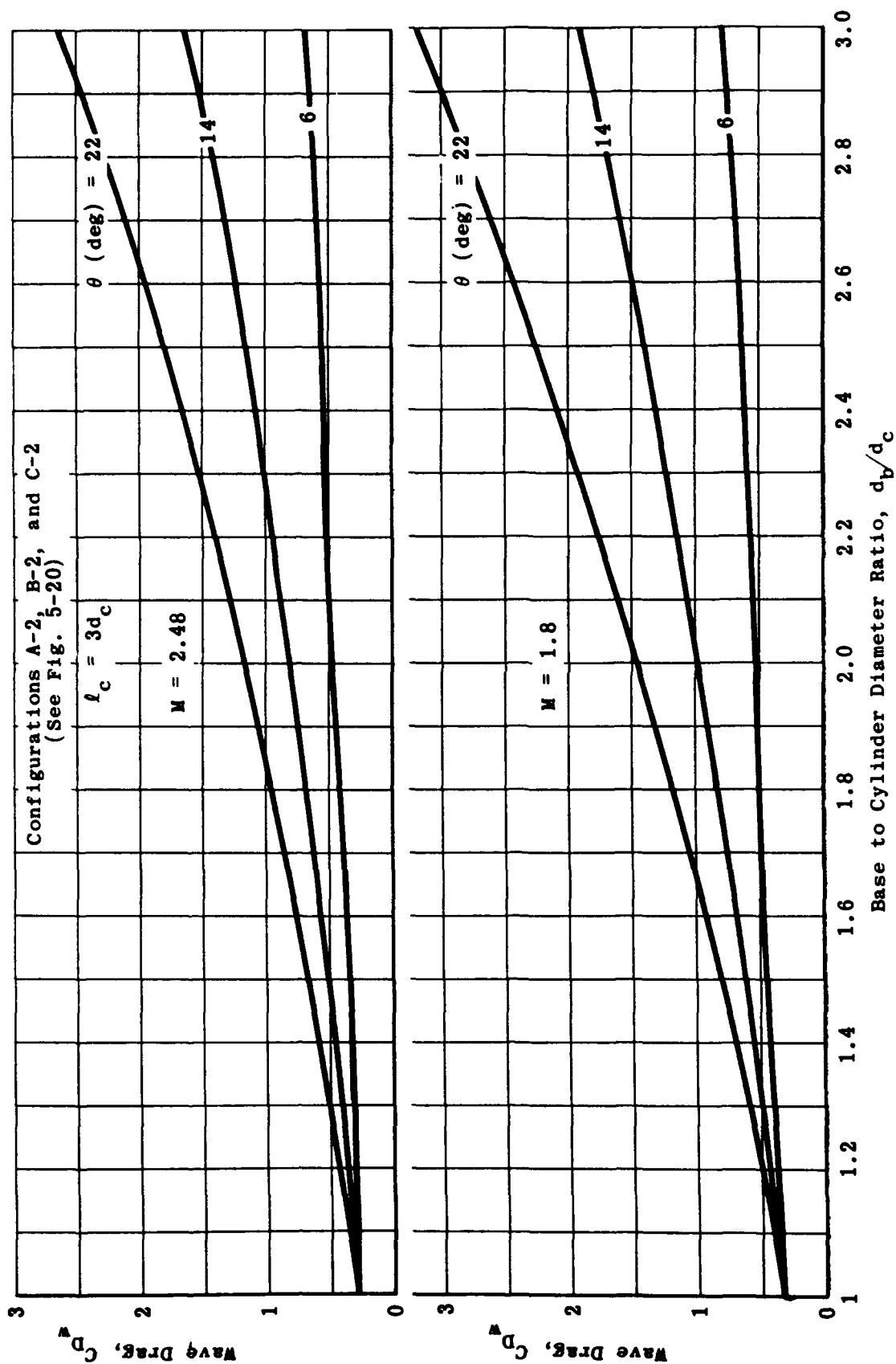
Fig. 6-18. Calculated wave drag of skirted bodies versus base-to-cylinder diameter ratio;
M = 1.8 and 2.48. (Source: Ref. 101)
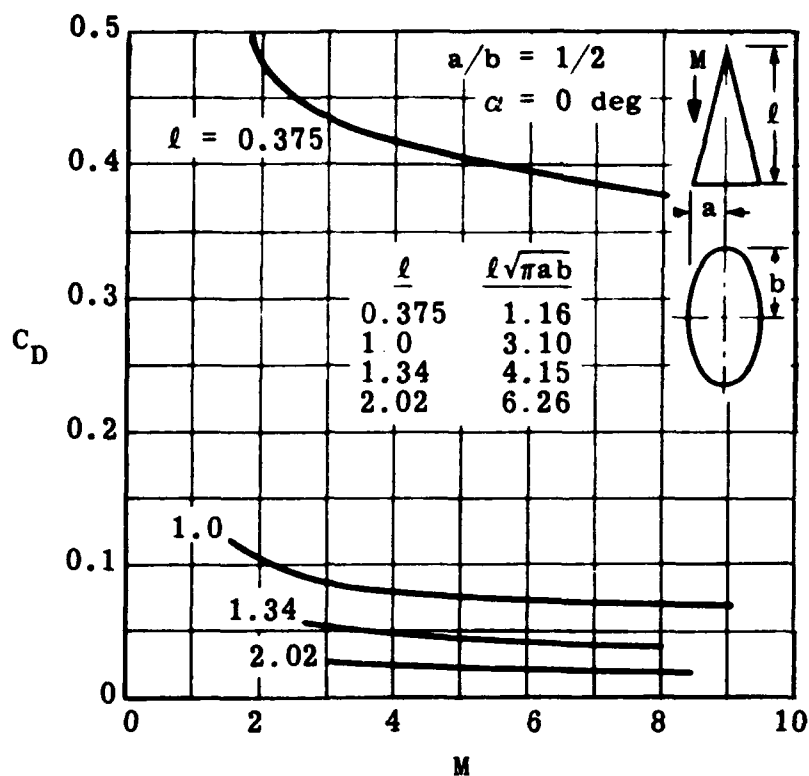
Fig. 6-19. Drag coefficient versus Mach number for elliptical
cones of equal cross-sectional area. (Source: Ref. 70)
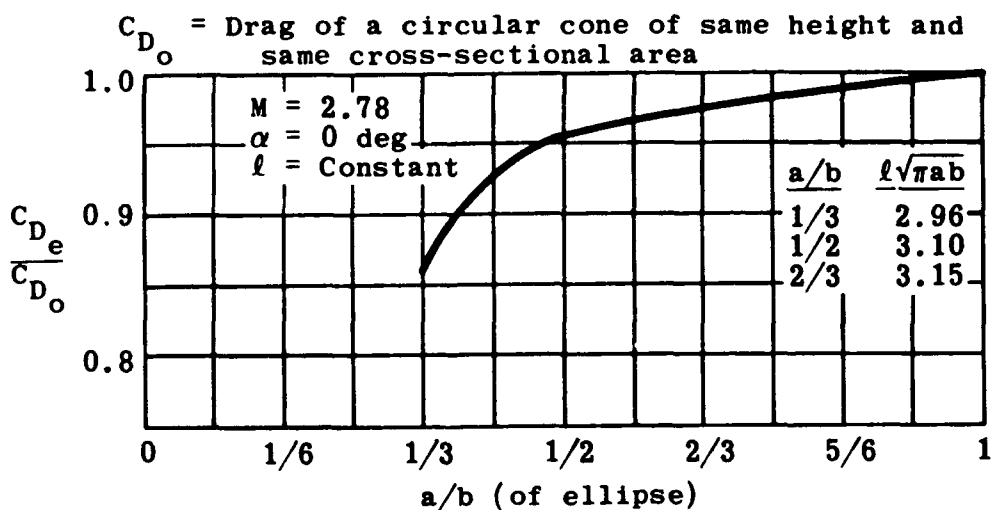
Fig. 6-20. Drag coefficient as a function of eccentricity of an
ellipse. (Source: Ref. 70)

Fig. 6-21   NAVWEPS Report 1488 (Vol. 3, Sec. 8)

C_{D_o} = Drag of a circular cone of same height and same cross-sectional area
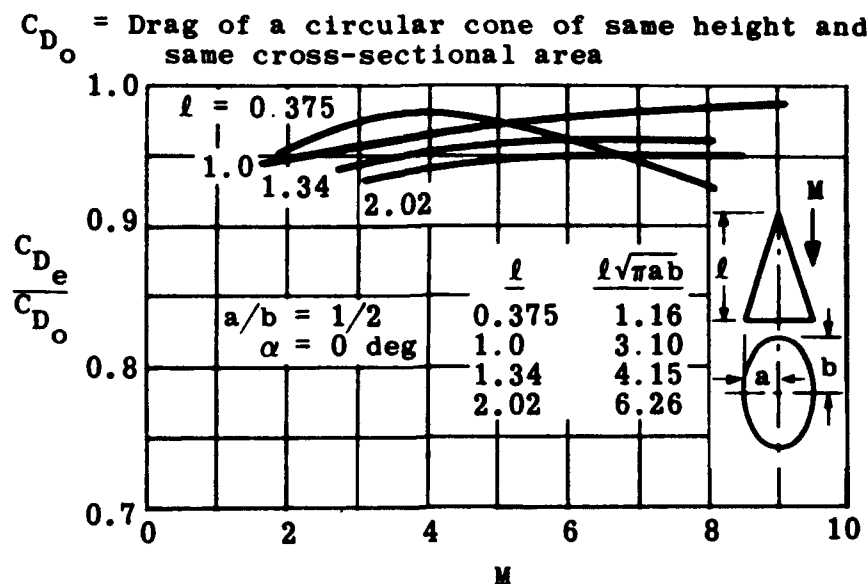
Fig. 6-21. Drag coefficient of an elliptical cone versus Mach number. (Source: Ref. 70)

C_{D_o} = Drag of a circular cone of same height and same cross-sectional area
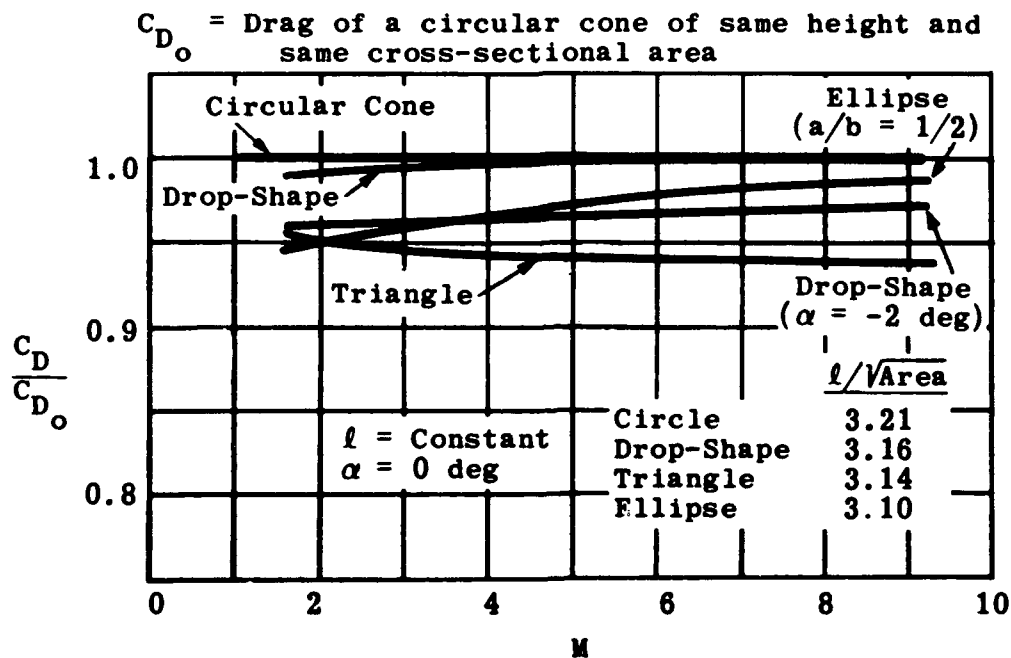
Fig. 6-22. Drag coefficient of conical bodies versus Mach number for various cross-sectional shapes. (Source: Ref. 70)

Fig. 6-24. Wave drag and position of maximum diameter for specified optimum bodies. (Source: Ref. 111)

Group 1
Given length, base diameter, and specifically located given diameter

S_b/S_s	x_s/ℓ	$C_D(\ell/d)^2$
0.25	2/3	8.32
0.125	2/3	9.99
0.25	1/3	9.78
0.125	1/3	10.74

Group 2
Given length, base area, and max area

S_b/S	x_m/ℓ	$C_D(\ell/d)^2$
0.0625	0.51	9.29
0.25	0.545	7.53
0.5625	0.63	4.75

Group 3
Given length, base diameter, and volume

S_b/S	x_m/ℓ	$C_D(\ell/d)^2$
0.0625	0.507	10.39
0.25	0.503	8.49
0.5625	0.587	5.57

S_b = Base Area
S_s = Specified Area d_s = Specified Diameter
S = Max Area d = Max Diameter

Fig. 6-23. Specifications for minimum-drag test bodies. (Source: Ref. 111)

Fig. 6-25   NAVWEPS Report 1488 (Vol. 3, Sec. 8)

Fig. 6-25. Comparison of the drag of Haack-Adams bodies and
Harder-Renneman bodies by means of Ward's equations;
$\beta(r_b/\ell) = 0.05$. (Source: Ref. 113)
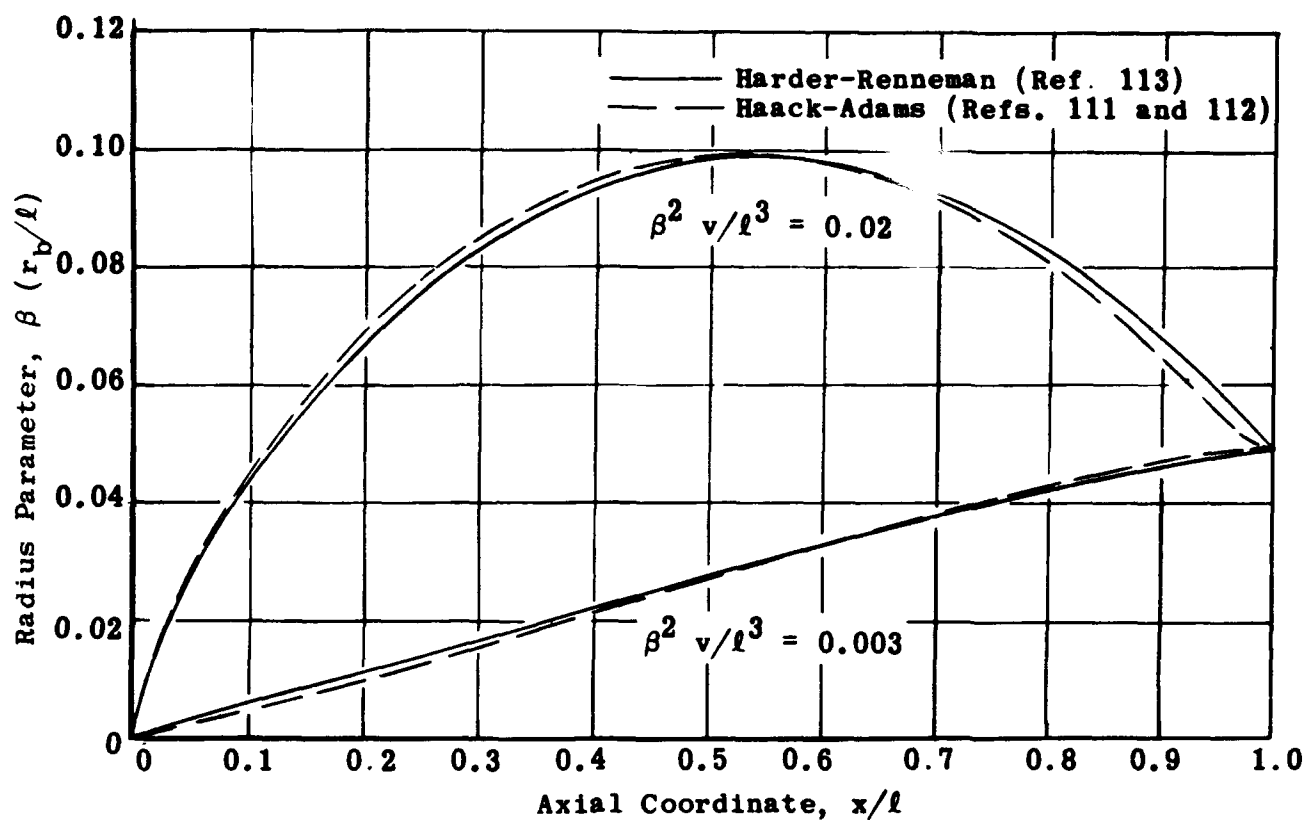
Fig. 6-26. Geometric comparison of Haack-Adams bodies and
Harder-Renneman bodies for $\beta(r_b/\ell) = 0.05$.
(Source: Ref. 113)
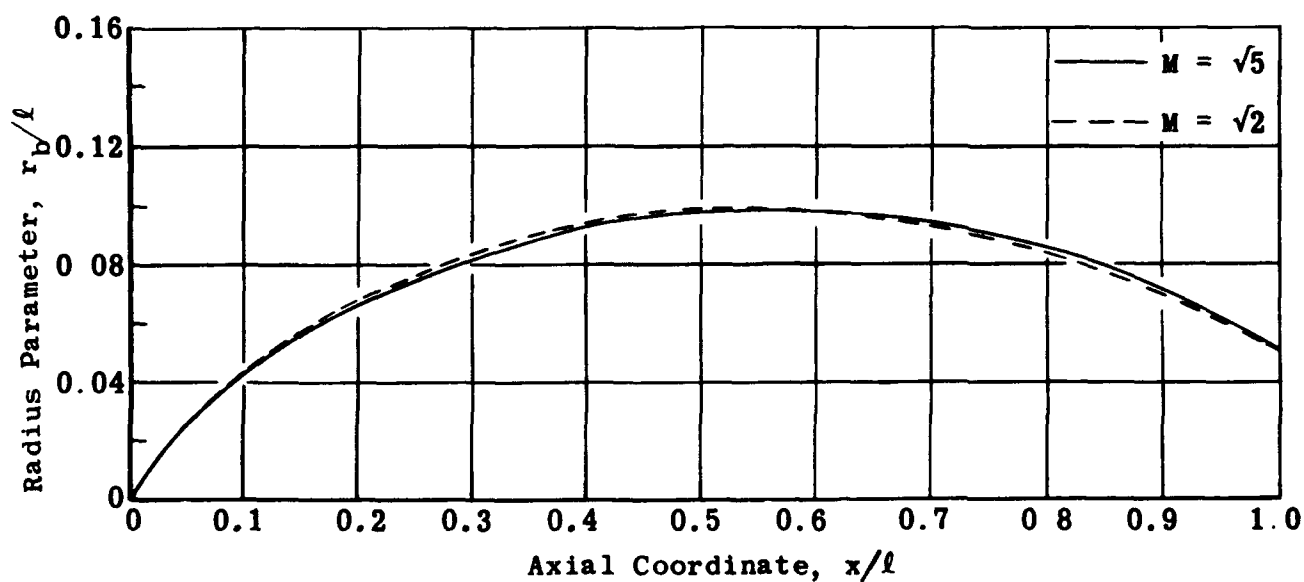
Fig. 6-27. Effect of Mach number on Harder-Renneman body
shape for $v/\ell^3 = 0.02$ and $r_b/\ell = 0.05$.
(Source: Ref. 113)

257

Fig. 6-28   NAVWEPS Report 1488 (Vol. 3, Sec. 8)
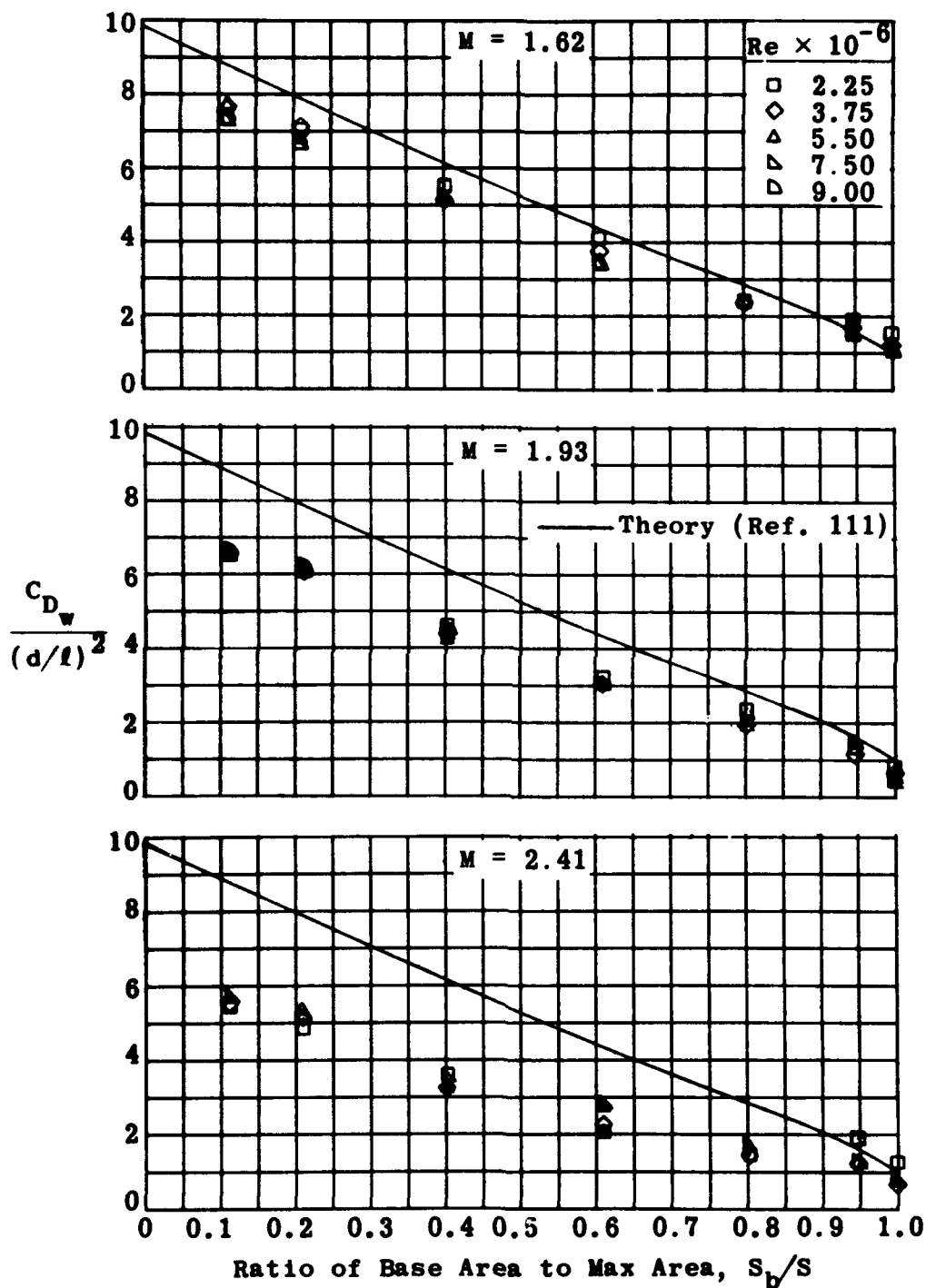
Fig. 6-28. Wave-drag parameter versus ratio of base area to
maximum area for M = 1.62, 1.93, and 2.41.
(Source: Ref. 114)
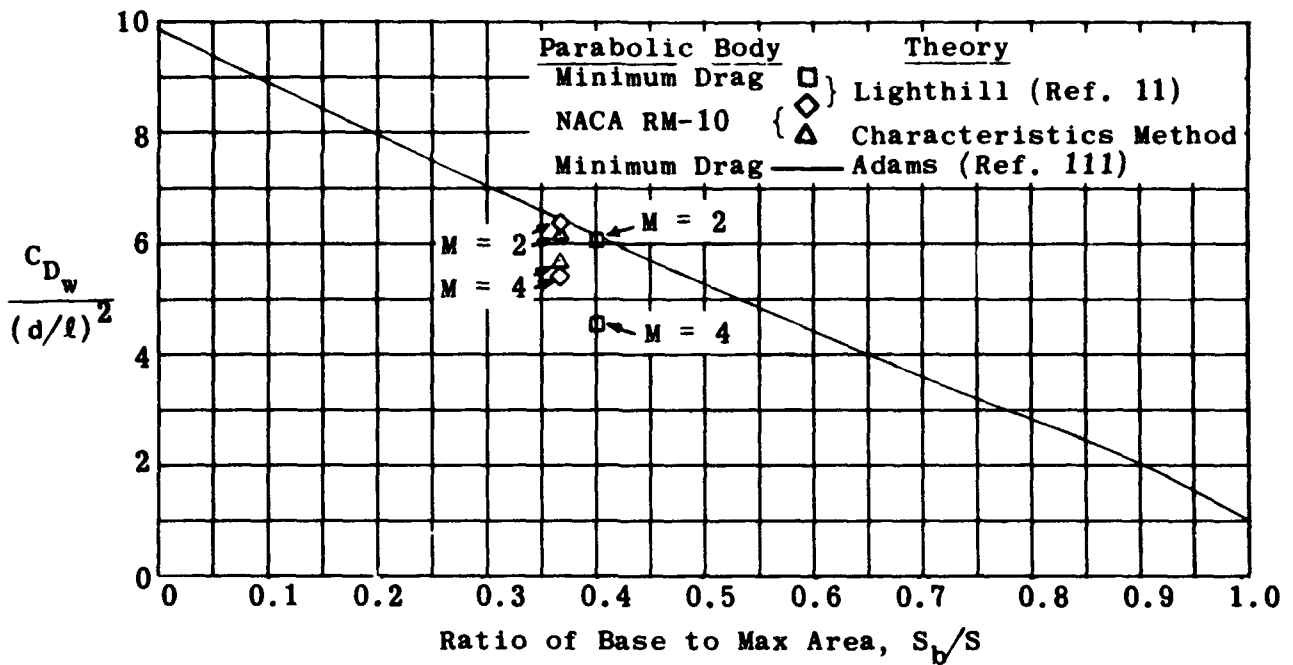
Fig. 6-29. Wave-drag parameters versus ratio of base area to
maximum area as predicted by three theories; M = 2 and 4.
(Source: Ref. 114)
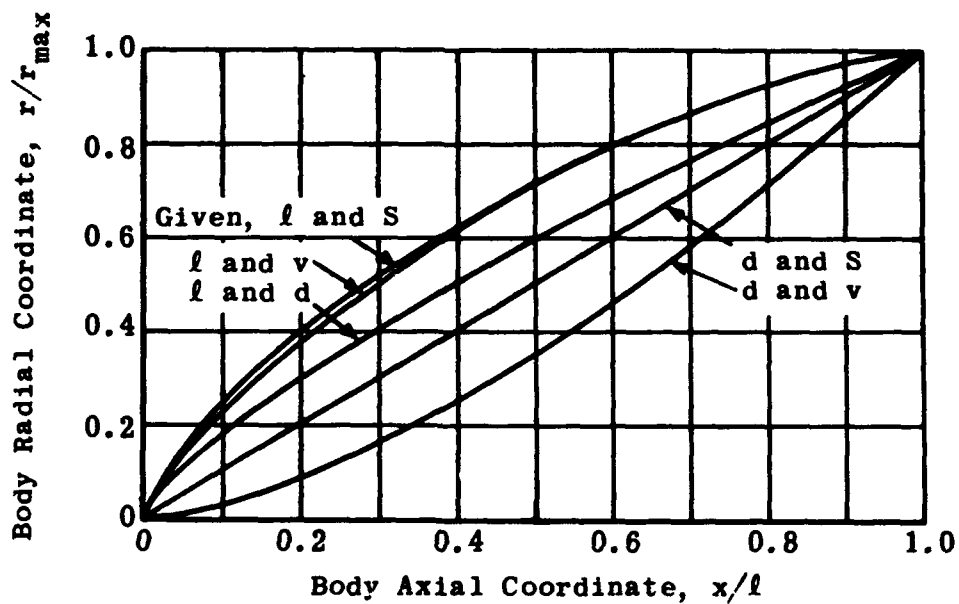
Fig. 6-30. Coordinates for minimum-drag bodies under various
conditions; $\ell/d = 5$. (Source: Ref. 42)

Fig. 6-31   NAVWEPS Report 1488 (Vol. 3, Sec. 8)
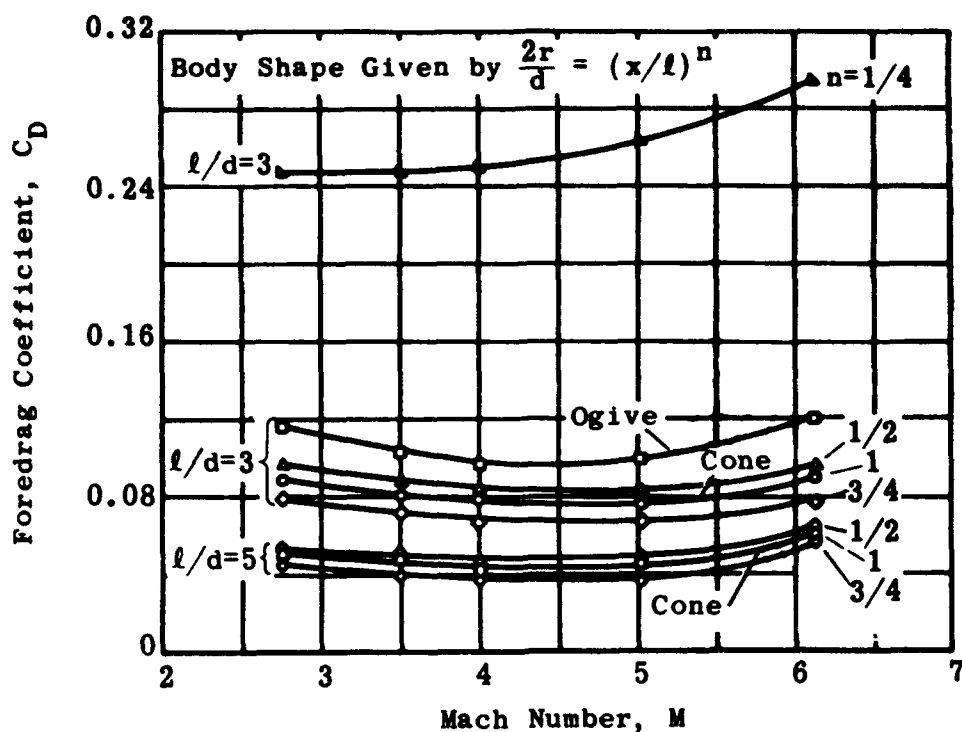
Fig. 6-31. Foredrag versus Mach number for several bodies;
ℓ/d = 3 and 5. (Source: Ref. 42)
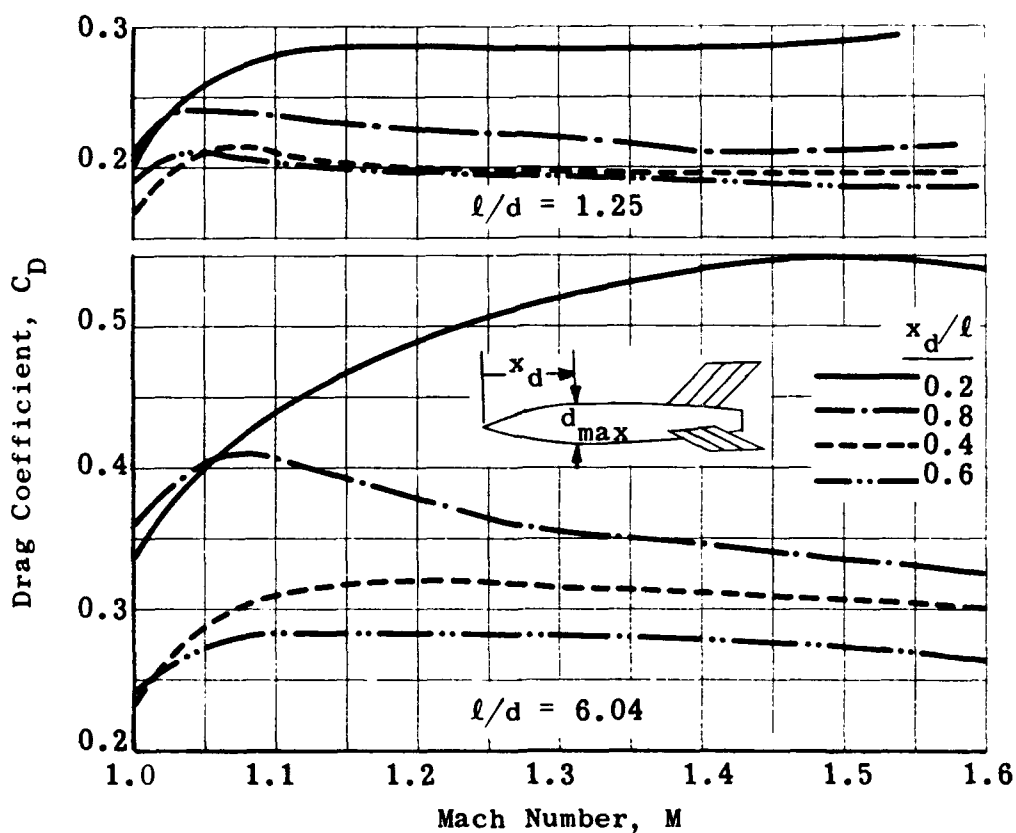
Fig. 6-32. Drag coefficient versus Mach number in terms of
position of the maximum diameter. (Source: Ref. 116)
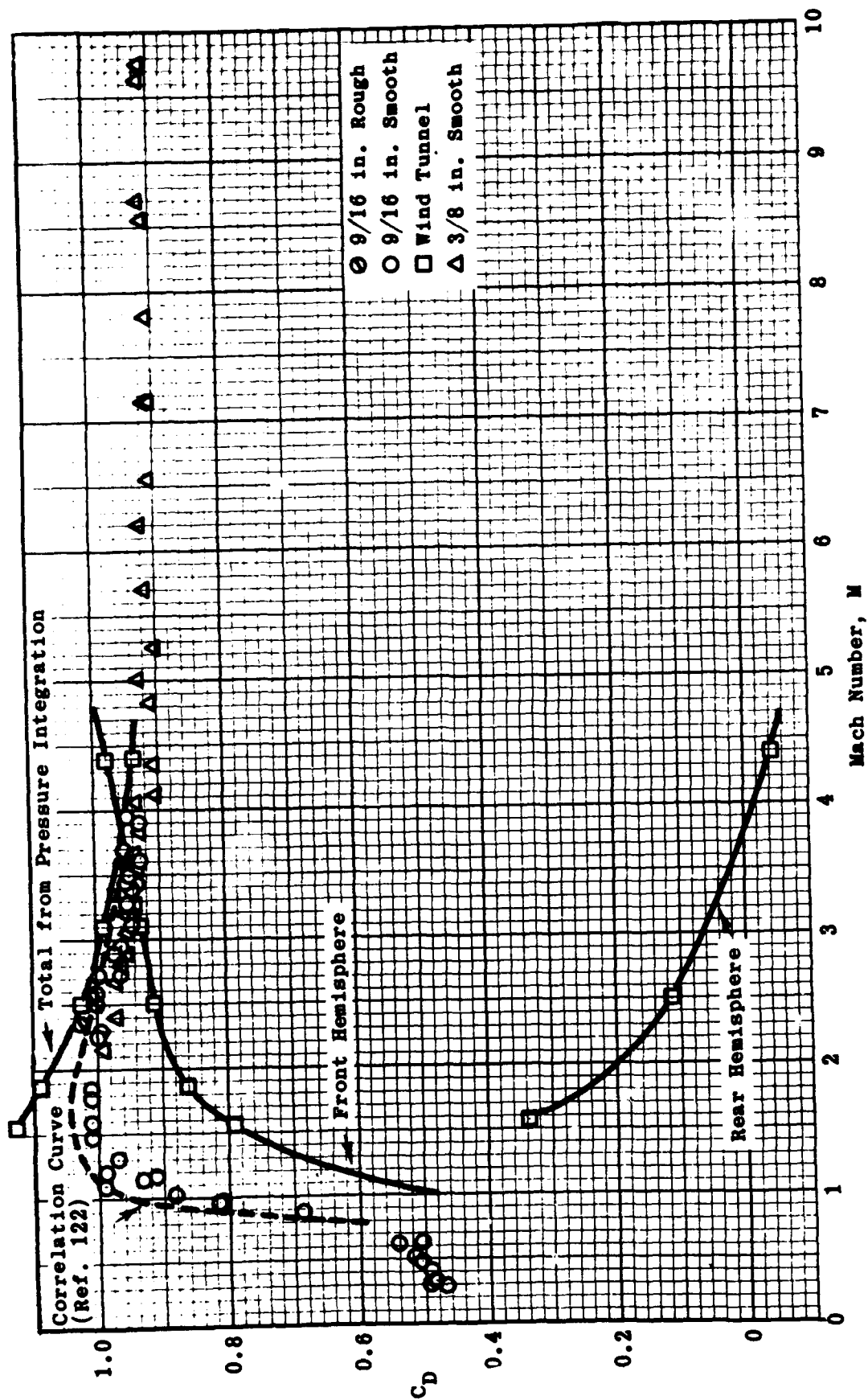
Fig. 6-33. Summary of sphere drag as a function of Mach number

Fig. 6-34   NAVWEPS Report 1488 (Vol 3, Sec. 8)
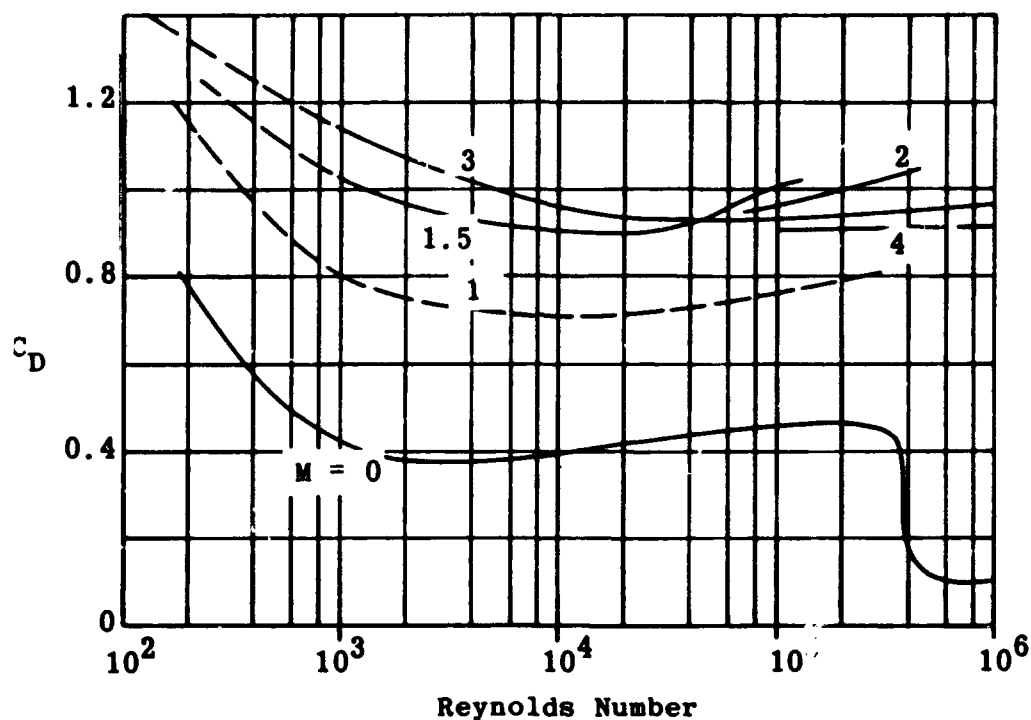
Fig. 6-34. Effect of Reynolds number on the drag of spheres
at various Mach numbers. (Source: Ref. 122)
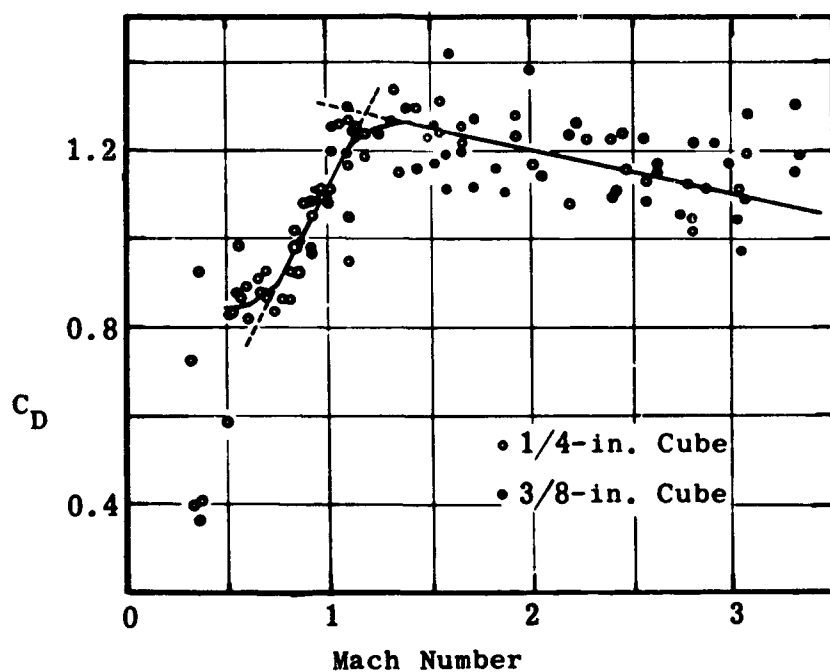
Fig. 6-35. Drag coefficient versus Mach number for
rotating cubes. (Source: Ref. 120)
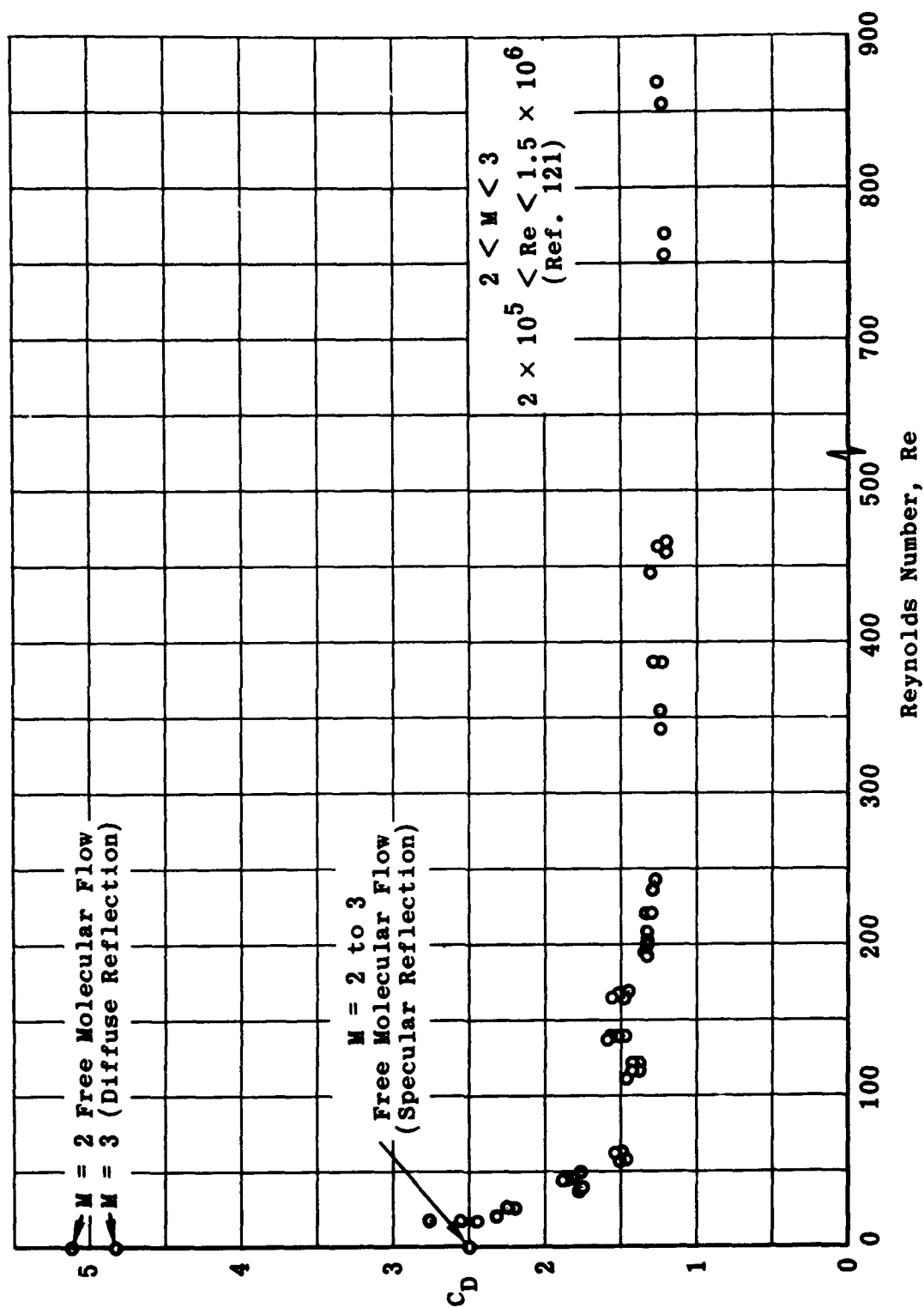
Fig. 6-36. Experimental sphere drag versus Reynolds number for low Reynolds number range.
(Source: Ref. 124)

Fig. 6-37   NAVWEPS Report 1488 (Vol. 3, Sec. 8)
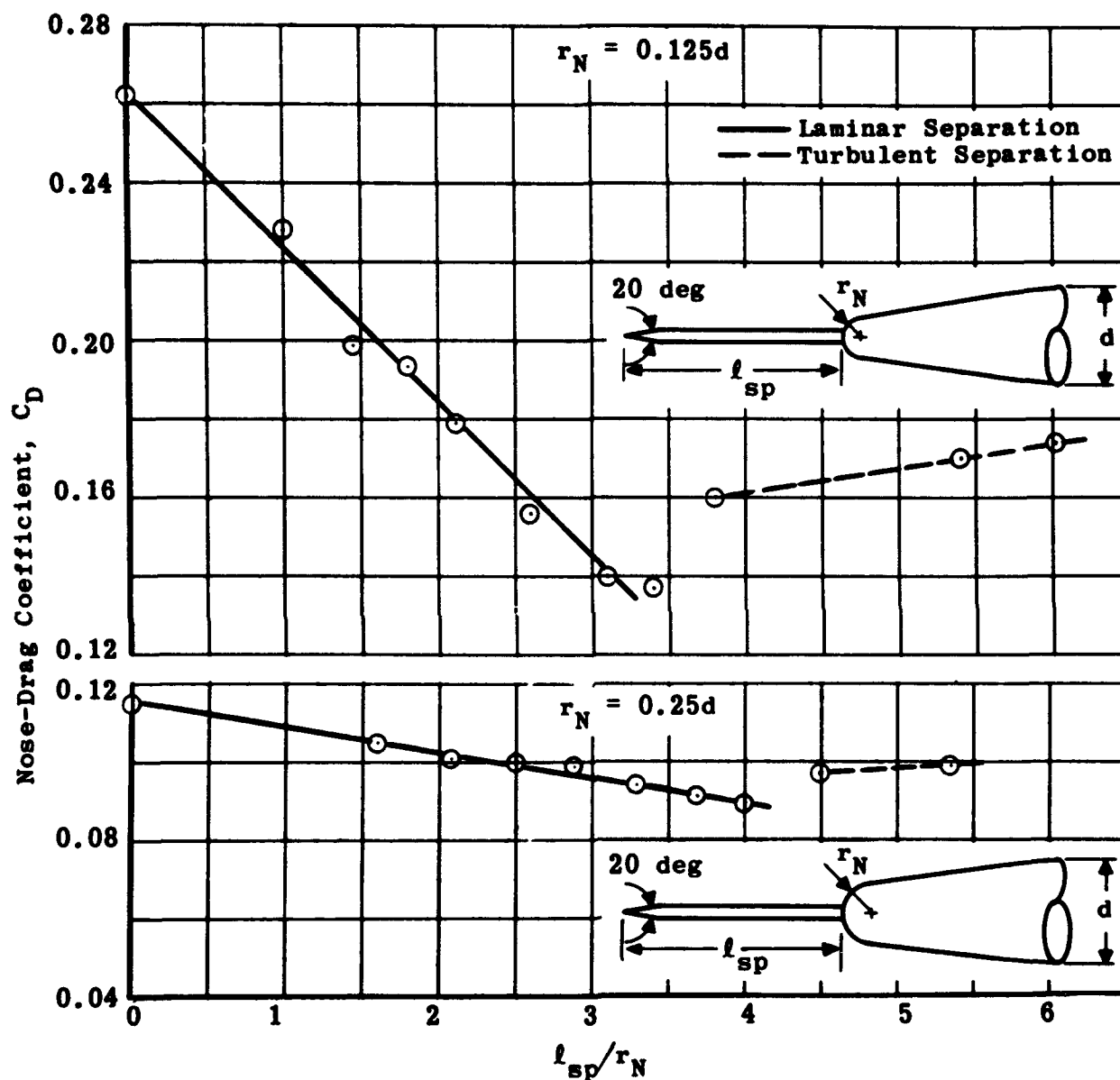
Fig. 6-37. Effect of nose spike on nose drag coefficient; M = 2.72.
(Source: Ref. 133)
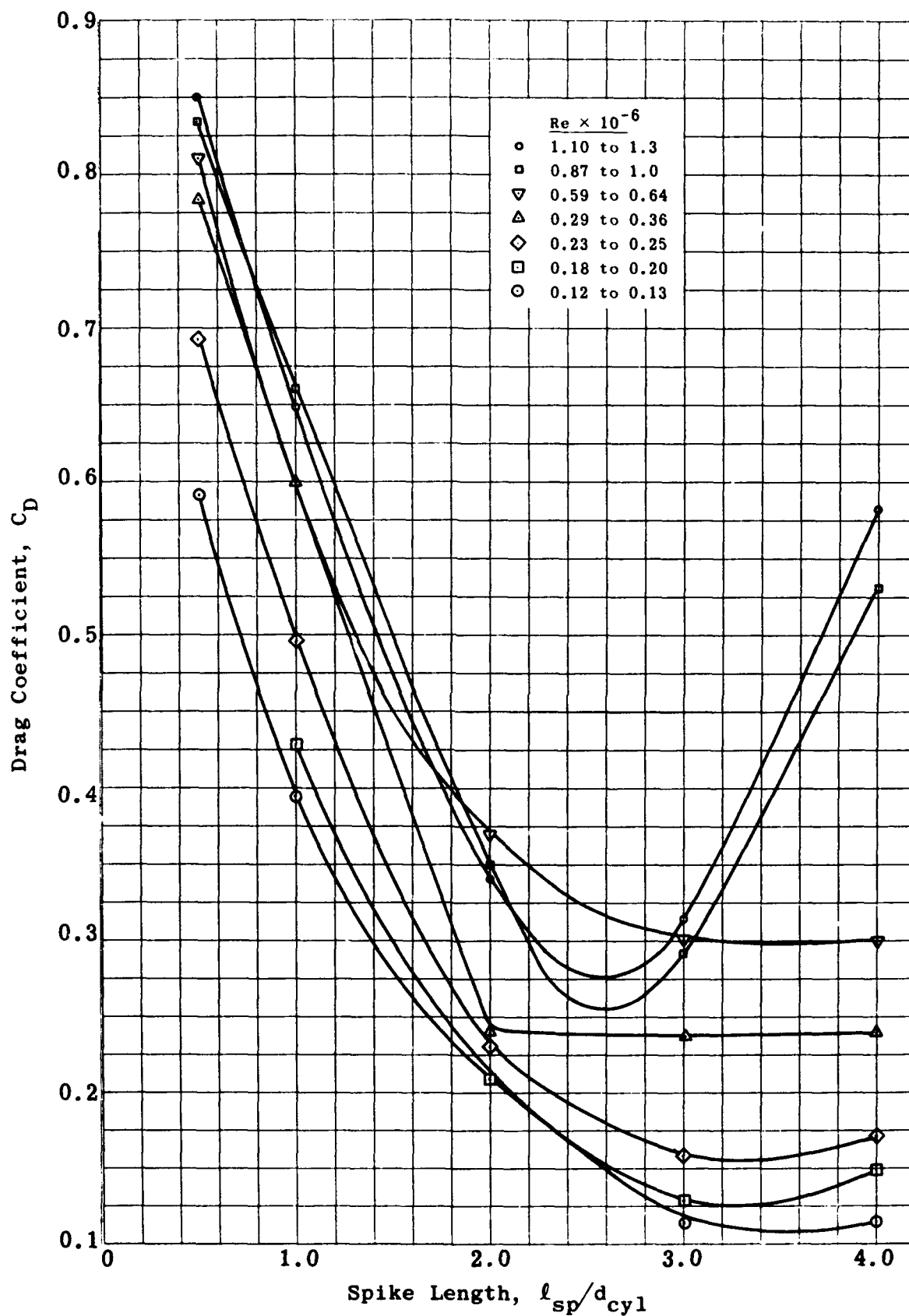
Fig. 6-38. Effect of Reynolds number and the length of a pro-
truding spike on the pressure drag of a hemisphere; M = 6.8.
(Source: Ref. 132)

Fig. 6-39   NAVWEPS Report 1488 (Vol. 3, Sec. 8)
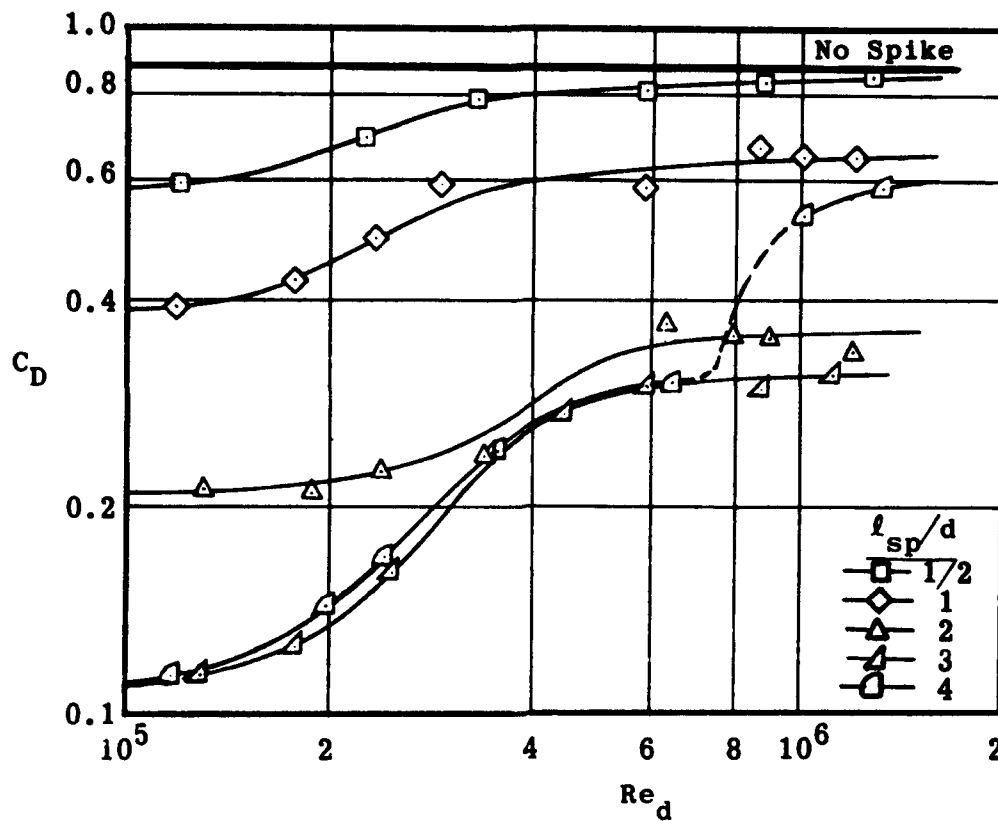
Fig. 6-39. Effect of Reynolds number on the pressure drag co-
efficient of a spike-nosed hemisphere; M = 6.8.
(Source: Ref. 132)
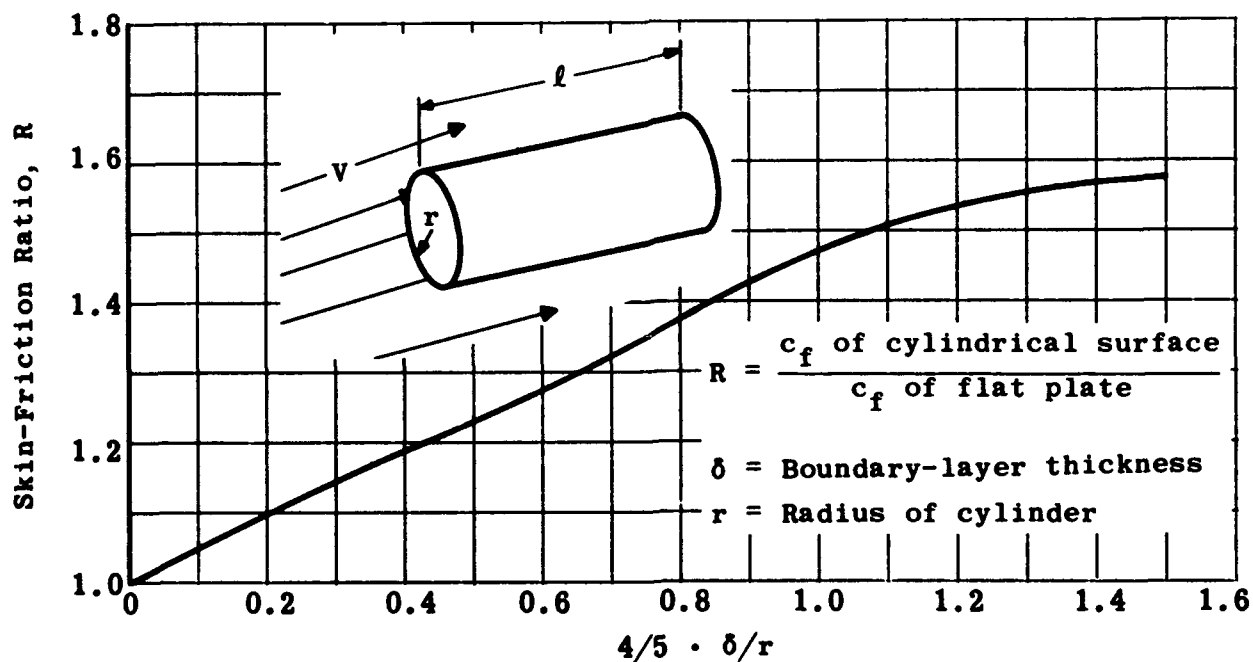
Fig. 6-40. Ratio of cylindrical skin friction to flat-plate skin
friction as a function of δ/r for incompressible flow.
(Source: Ref. 126)

$$C_f = 1.328 \ Re^{-1/2} \left(1 + 0.730 \ \frac{\gamma - 1}{2} \ Pr^{1/2} \ M^2\right)^{\frac{\omega - 1}{2}}$$

ω = Exponential factor in empirical expression of viscosity = 0.76

$Pr = 1.0$

$\gamma = 1.4$

von Karman-Schoenherr (Incompressible)

M = 10

Mean Skin-Friction Coefficient, C_f
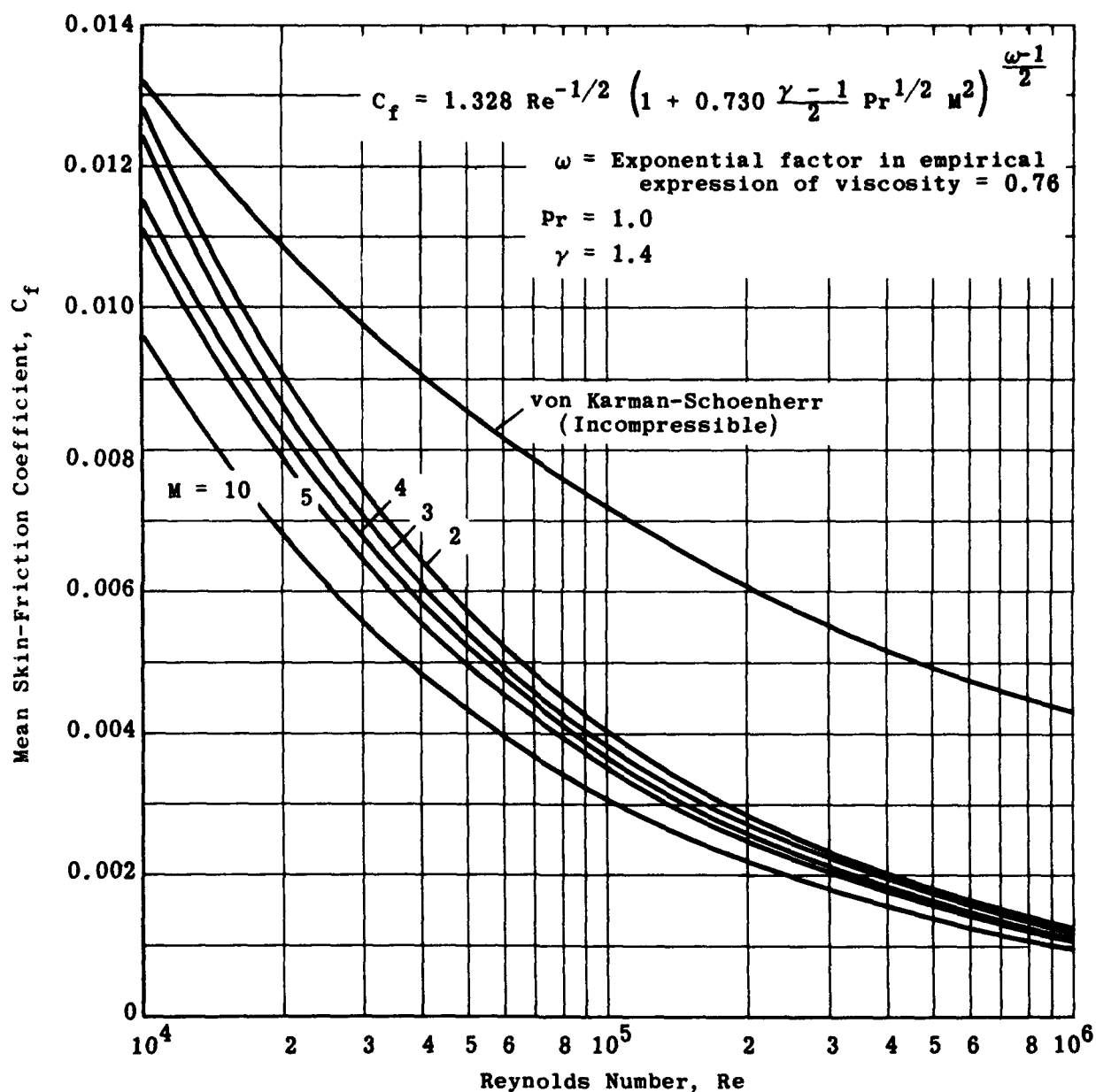
Reynolds Number, Re

Fig. 6-41. Mean skin-friction coefficient as a function of Reynolds number and Mach number for laminar boundary layer on an insulated flat plate. (Source: Ref. 135)

Fig. 6-42   NAVWEPS Report 1488 (Vol. 3, Sec. 8)

$$\frac{\sin^{-1}\lambda}{\lambda}\left(1 + \frac{\gamma - 1}{2}M_1^2\right)^{-\frac{1}{2}}\frac{0.242}{\sqrt{C_f}} = \log_{10}\left(C_f\,Re\right) - \frac{1 + 2\omega}{2}\log_{10}\left(1 + \frac{\gamma - 1}{2}M_1^2\right)$$

$\omega = 0.76$ (Exponential factor in empirical expression of viscosity)

$$\lambda = \left[\frac{2}{(\gamma - 1)\,M^2} + 1\right]^{-\frac{1}{2}}$$

$\gamma = 1.4$
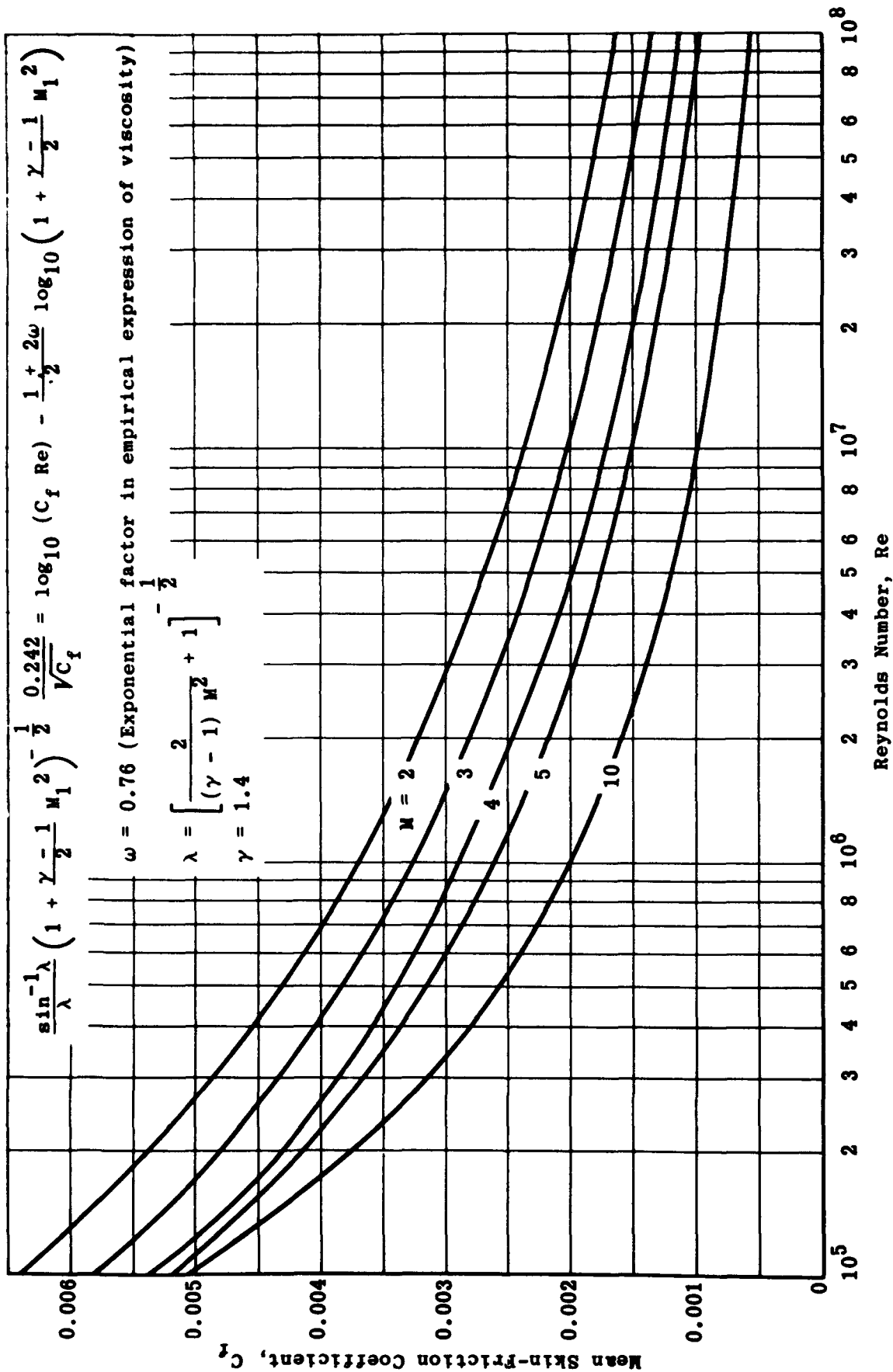
Fig. 6-42. Mean skin-friction coefficient as a function of Reynolds number and Mach number for turbulent boundary layer on an insulated flat plate. (Source: Ref. 135)

c_{f_c} = Local skin-friction per unit area of the curved surface of a cylinder

c_{f_p} = Local skin-friction per unit area of a flat plate
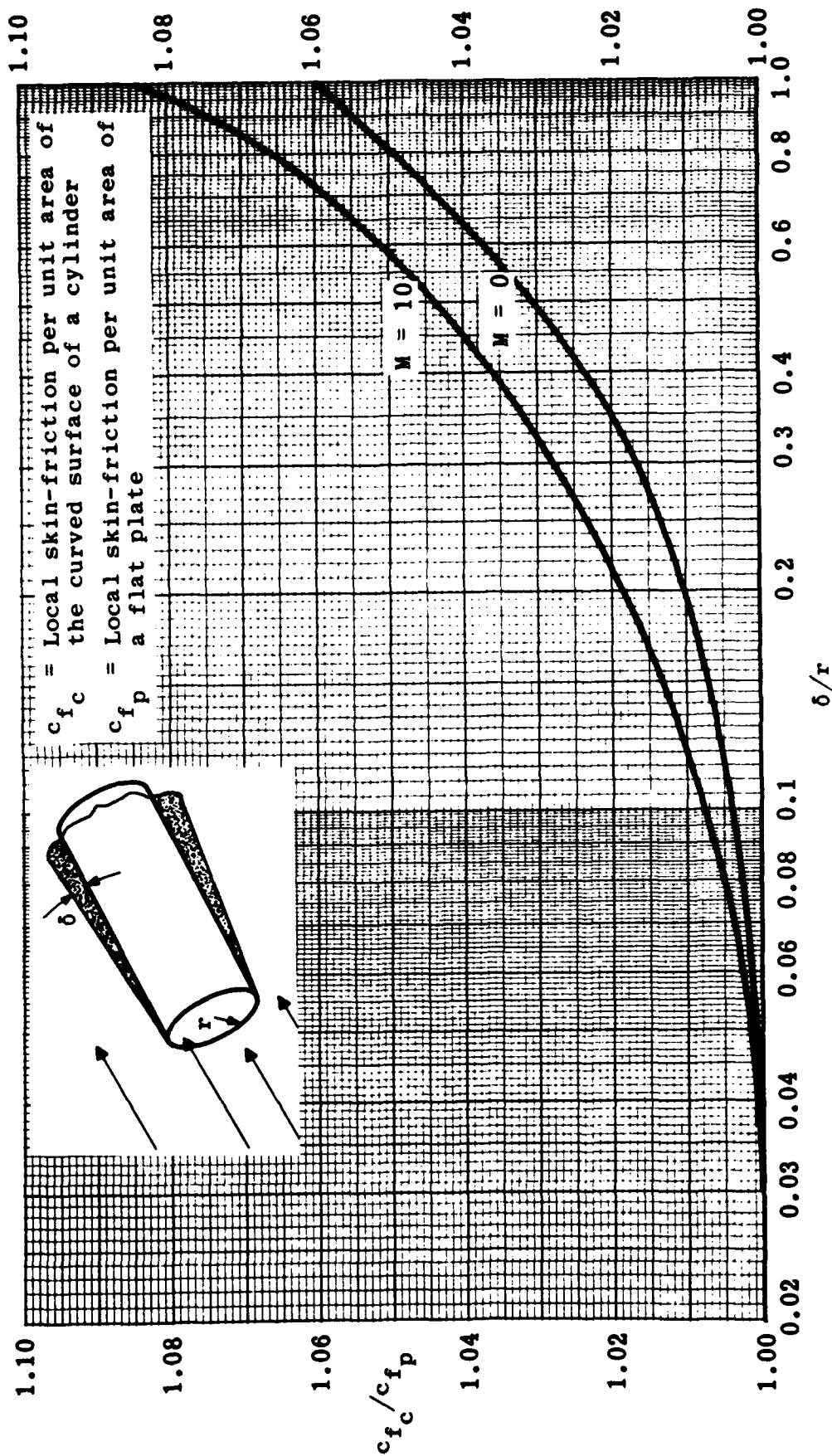
Fig. 6-43. Ratio of local skin friction on a cylinder to that on a flat plate at the same Reynolds number as a function of δ/r; turbulent boundary layer. (Source: Ref. 130)

Fig. 6-44   NAVWEPS Report 1488 (Vol. 3, Sec. 8)
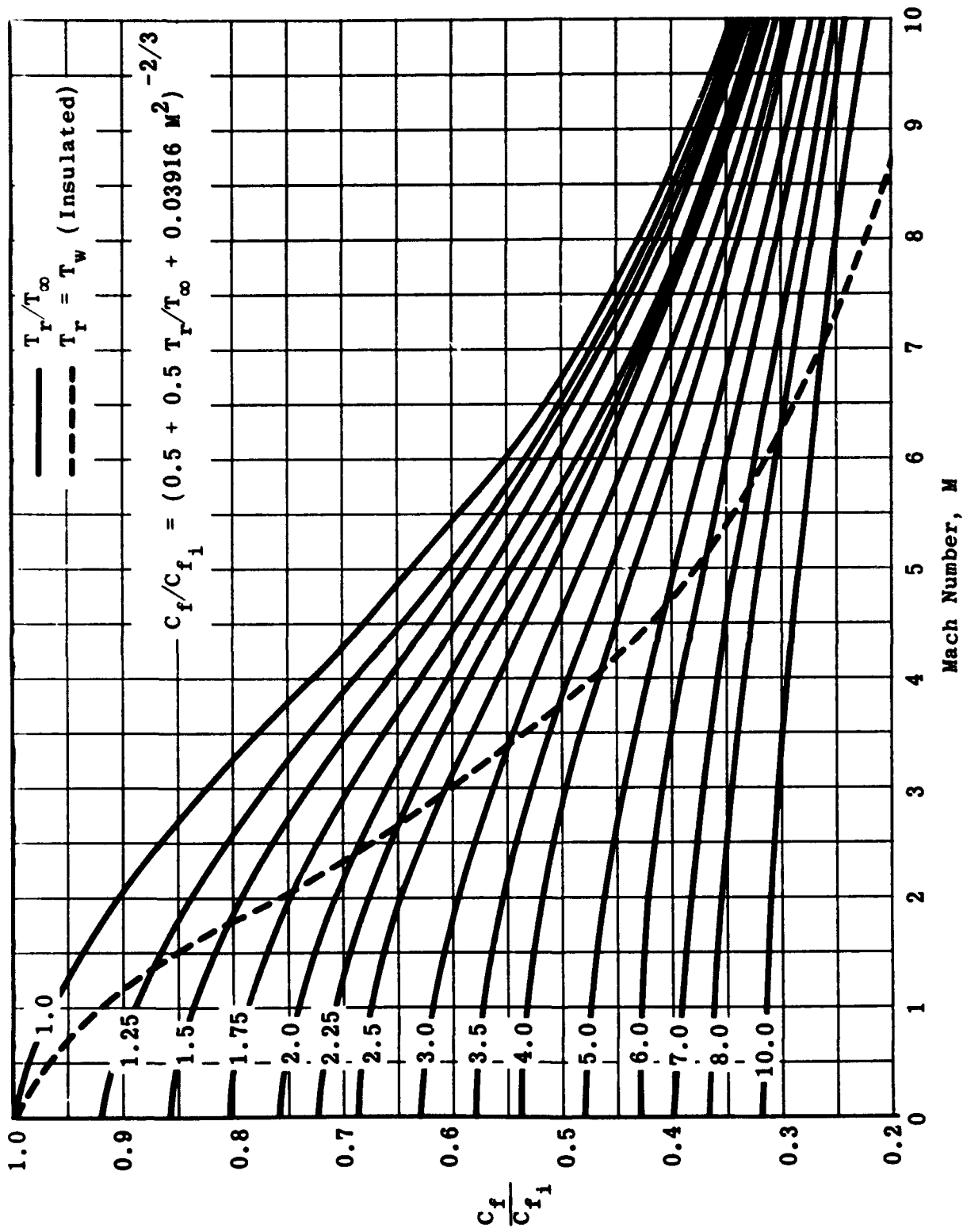
Fig. 6-44. Skin-friction ratio versus Mach number for various temperature ratios
(Source: Ref. 175)
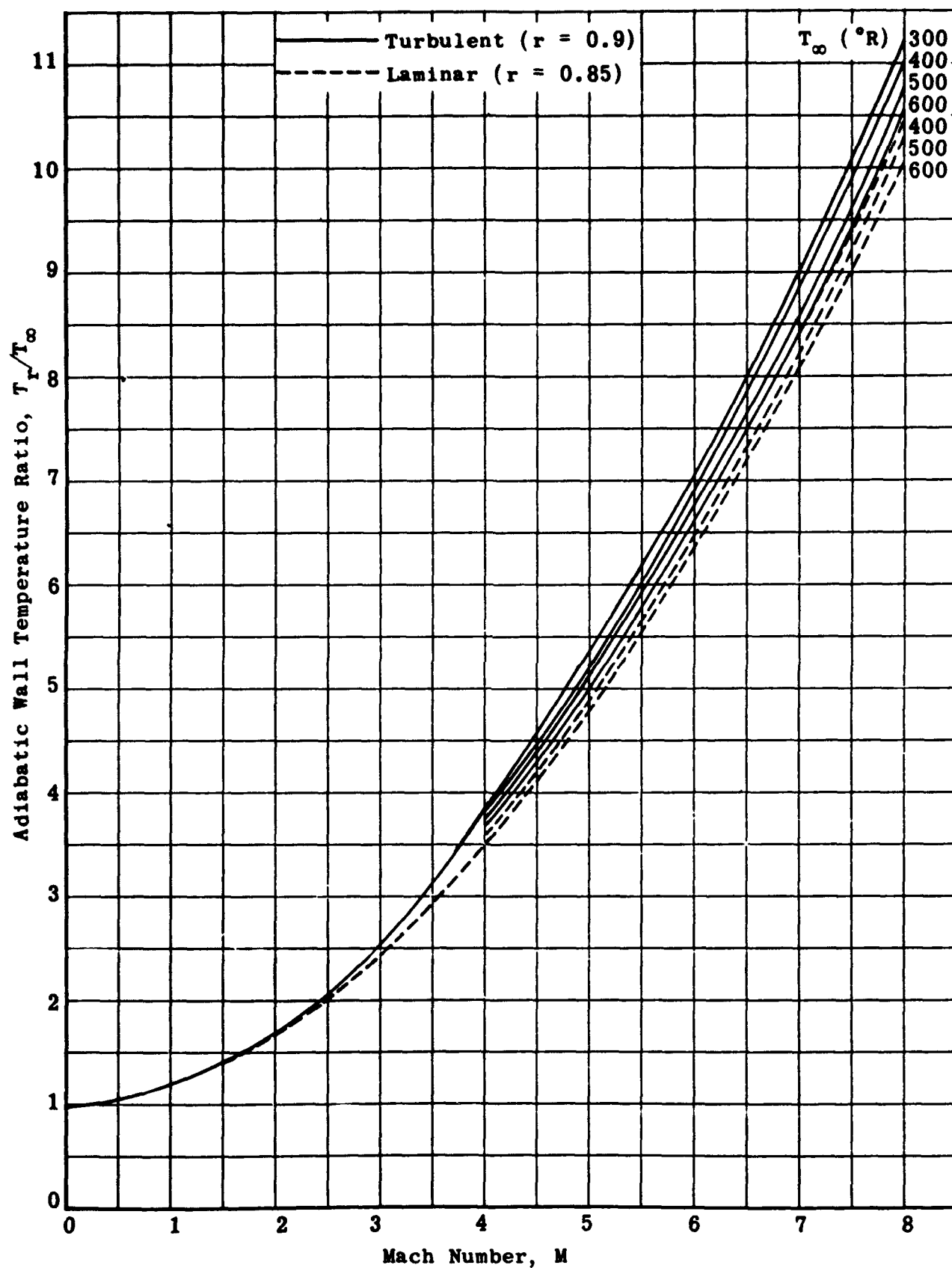
Fig. 6-45.   Variation of recovery temperature ratio versus Mach
   number; T_∞ = 300 to 600°R, laminar and turbulent flow.
   (Source: Ref. 175)

Fig. 6-46   NAVWEPS Report 1488 (Vol. 3, Sec. 8)
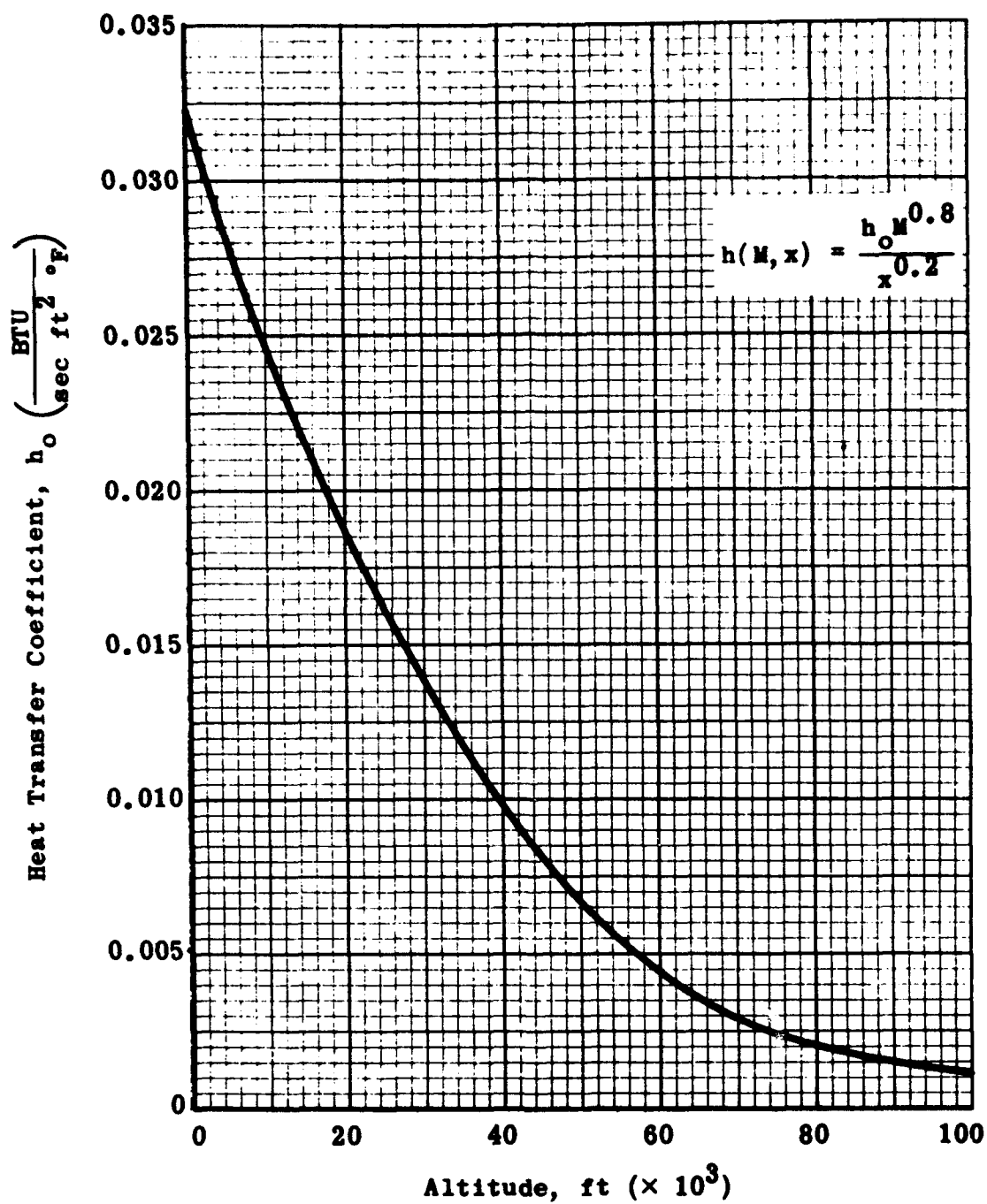
Fig. 6-46. Heat-transfer coefficient versus altitude for flat
plates. (Source: Ref. 175)
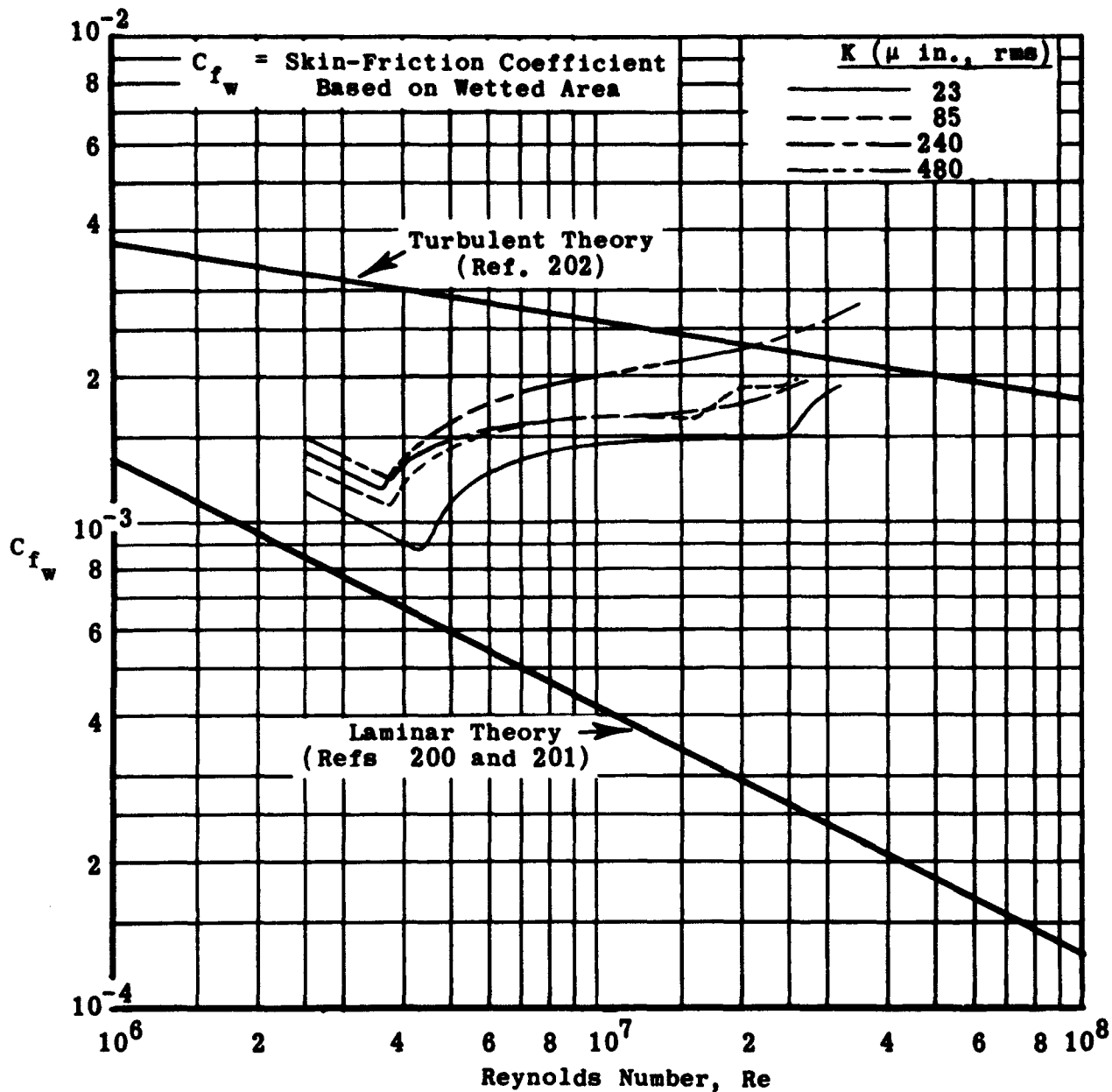
Fig. 6-47.   Influence of surface roughness on friction drag.
(Source: Ref. 173)

Fig. 6-48   **NAVWEPS Report 1488 (Vol. 3, Sec. 8)**
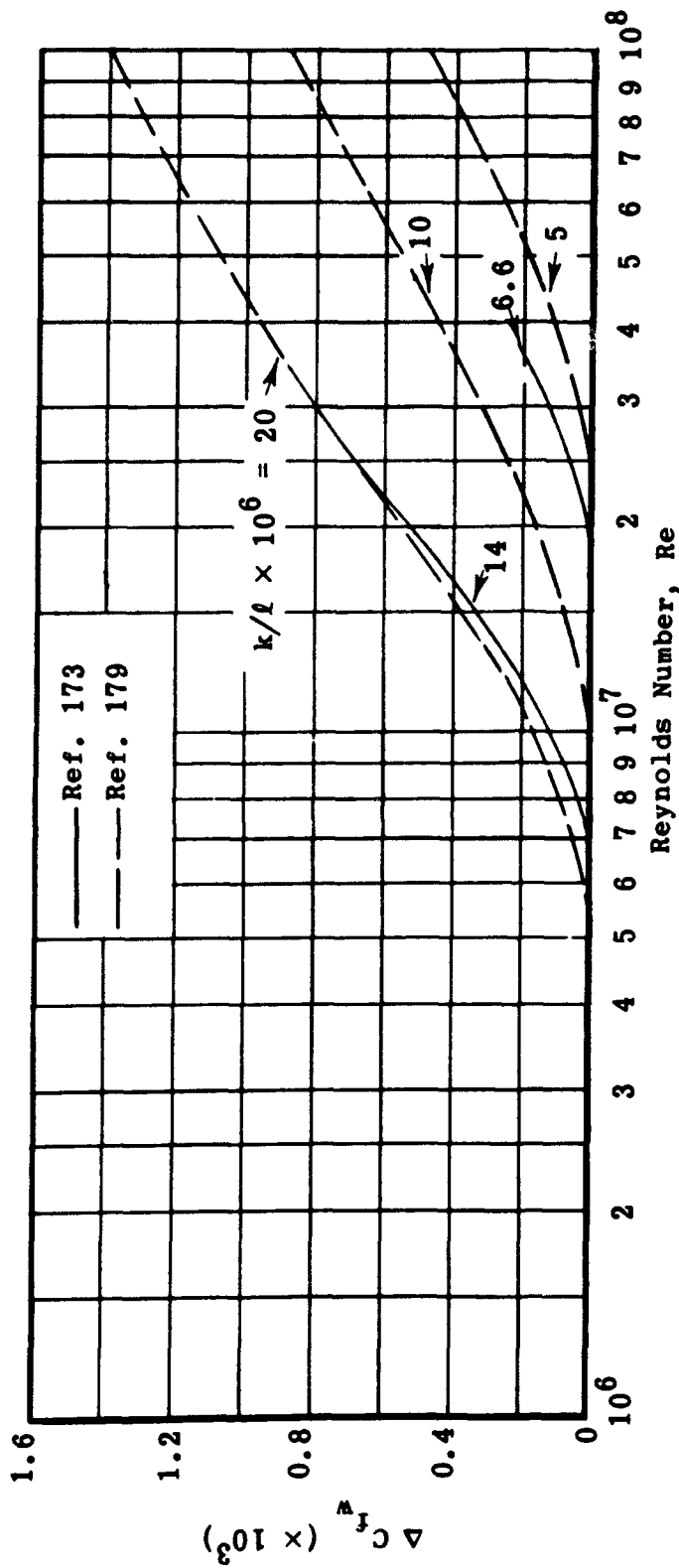
Fig. 6-48. Variation of skin friction with Reynolds number and roughness; turbulent flow.
(Source: Ref. 173)
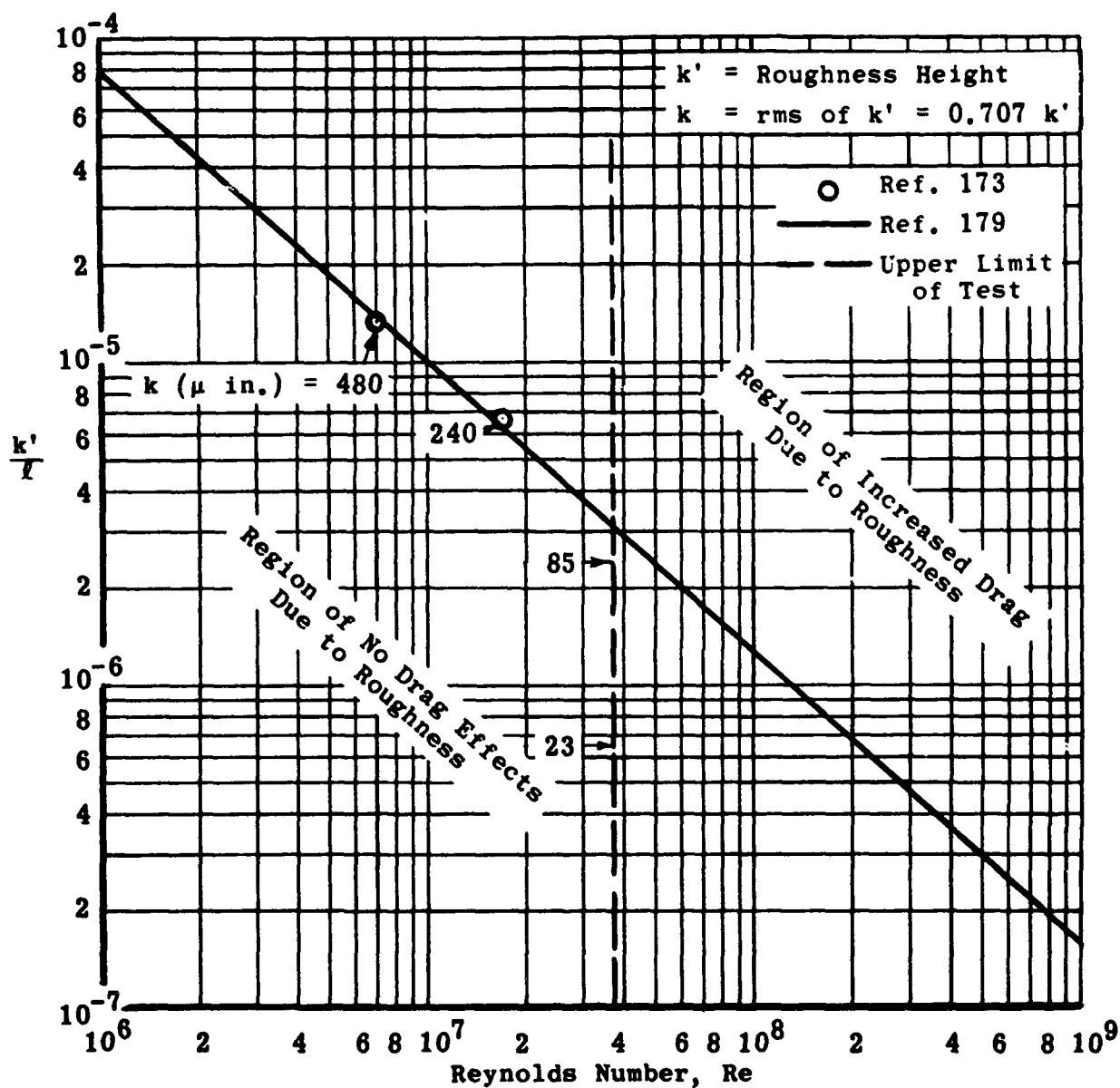
Fig. 6-49. Critical roughness height for cylinder and flat plate
    as a function of Reynolds number. (Source: Ref. 173)

Fig. 6-50   NAVWEPS Report 1488 (Vol. 3, Sec. 8)
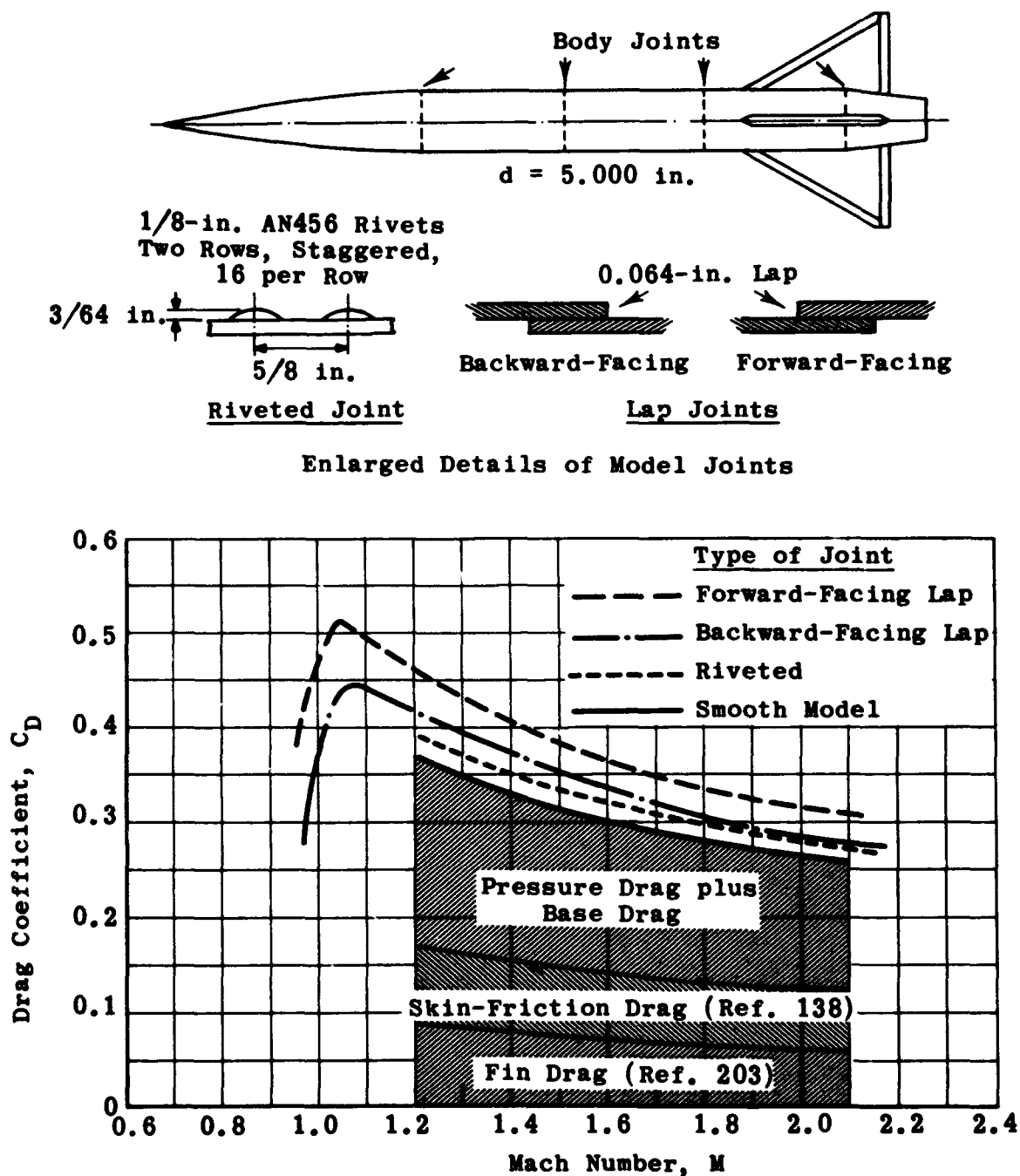
Fig. 6-50.   Effect of various types of joints on drag coefficient
             versus Mach number. (Source: Ref. 172)
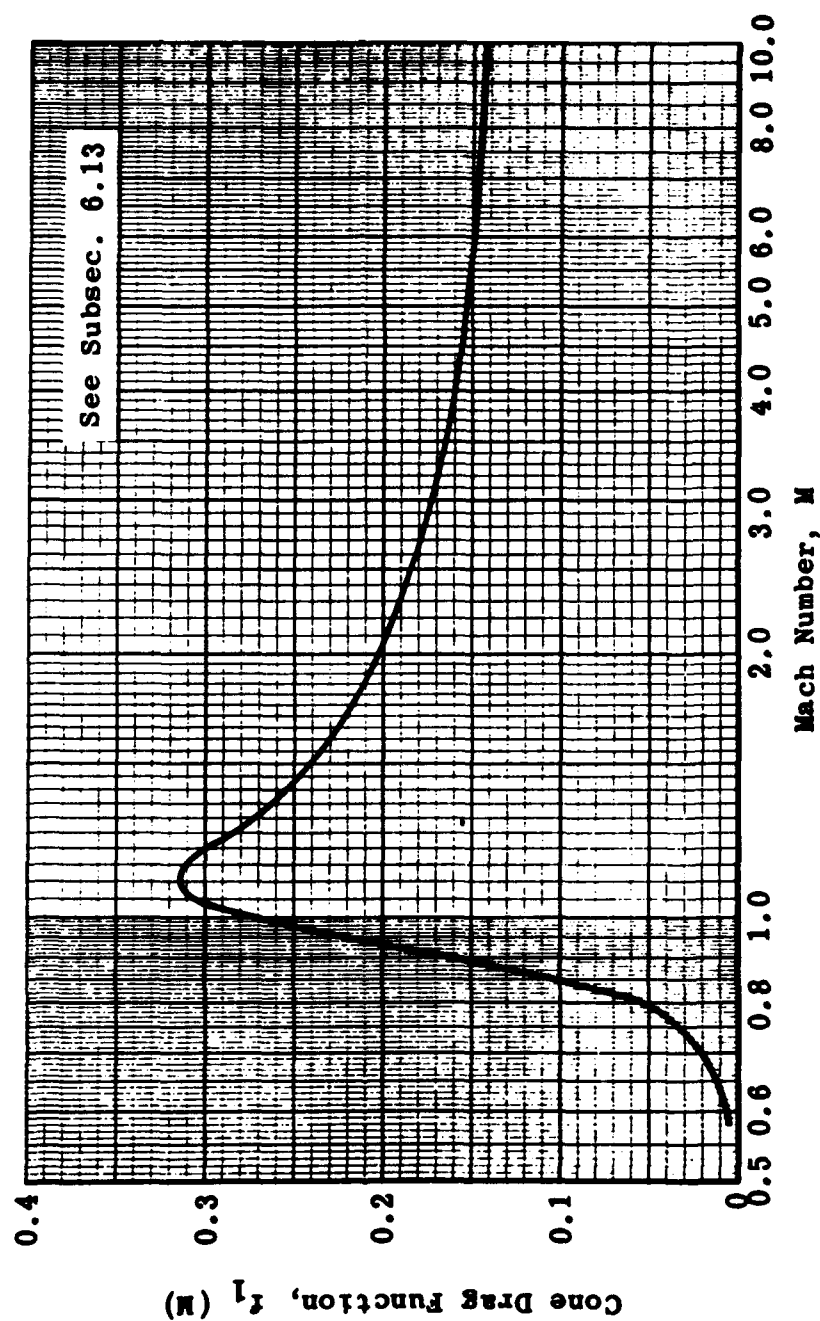
Fig. 6-51. Drag function versus Mach number for a 15-deg cone. (Source: Ref. 198)

7.   Base Drag

        For a body of revolution flying at supersonic speed, as much
as one-half the total drag of the full configuration, depending on the
over-all design and Mach number regime, may be attributed to the nega-
tive pressure (that which is lower than free stream) over the base.
Such a quantitative relation between base drag and foredrag is encoun-
tered primarily in the low supersonic regime, where the pressure on the
base may be reduced to as much as one-half that of the ambient air,
while the nose pressure may be kept relatively low by use of slender
nose shapes. As the Mach number is increased, however, there is a
limit to the drag which can be produced by the base since the under-
pressure cannot exceed one atmosphere, whereas the positive pressure
on the nose will continue to increase with Mach number. At usual flight
conditions, the base pressure becomes negligible at Mach numbers beyond
4 or 5.

        In considering the cause of this negative base pressure, the
flow phenomenon in the region of the base may be likened to a jet pump.
The external flow tends to entrain the dead air in the region immedi-
ately aft of the base and carry it downstream. There is, however, no
supply from which more air may be obtained to replace the air that is
carried away. The pump therefore has no supply and its only effect is
to reduce the static pressure at the base.

        The problem of predicting the base pressure at supersonic
speeds has received considerable attention in recent years and is well
summarized in Ref. 140. Of the several methods advanced (Refs. 141 to
150) some give results that are superior to the rest. Among these is
the theory developed by Crocco and Lees (Ref. 141) which gives a satis-
factory prediction of the qualitative effect of Mach number and Reynolds
number on base pressure. Since this theory is dependent on the flow
characteristics along the body and in the wake, quantitatively accurate
calculations cannot be made because they demand a knowledge of the loca-
tion of the boundary-layer transition, which is presently indeterminate.

        Chapman's semi-empirical method (Ref. 142) has proved satis-
factory for the prediction of the base pressure on boattailed bodies
and airfoils where the boundary layer is fully turbulent in the region
of the base. This method, discussed in Subsec. 7.1.1, utilizes accumu-
lated experimental data on non-boattailed bodies. Cortright and Schroeder
(Ref. 150) have proposed a method for estimating the base pressure on a
boattailed body having a turbulent boundary layer, but their method re-
quires a knowledge of the separation angle at the base as a function of
the local Mach number. These two methods offer reasonable agreement with
experimental measurements of boattail effects for both three-dimensional
and two-dimensional configurations. The method developed by Cope
(Ref. 144) does not appear to give as satisfactory a prediction as does
Chapman's method because the assumptions involved result in a first ap-
proximation only. Gabeaud (Refs. 143 and 146) compares his theory to
experimental data from bodies of revolution with fins; but since the
equation presented in Ref. 146 does not include any terms to cover fin
effects, the value of the method remains questionable. Kurzweg's method
(Ref. 145) gives the same values for both airfoils and bodies of revolu-
tion, and therefore its validity is also questionable.

        References 109, 140, 148, and 151 to 164 describe some of the
many experimental measurements of base pressure in wind-tunnel and free-
flight tests. The variation of base pressure with such parameters as

Reynolds number, Mach number, presence and location of fins, nose and base shapes, and jet flow will be discussed in ensuing subsections. Extensive compilations of relevant data have clarified the effects of some of the primary variables and also have provided a basis for evaluating the methods which have been advanced to predict these effects. However, there is need for additional experimental data relating to such variables as those associated with the presence of fins or jets.

In general, only bodies having turbulent boundary layers ahead of their bases will be given detailed consideration in this subsection. However, some information will be given for the laminar case, and where possible the two cases will be compared. For most practical applications the likelihood of realizing laminar flow over the entire body (of aircraft or missiles) at full-scale Reynolds numbers is remote. Moreover, the presence of wings or stabilizing fins causes boundary-layer transition even at low Reynolds numbers (see Ref. 15ʳ   One of the advantages of restricting the discussion to the turbul   ʌse is that it allows the effects of Reynolds number to be ignore   nce it has been shown (Refs. 142, 148, and 161) that once a fully tuᵣ ʋulent boundary layer exists ahead of the base, the variation of base pressure with Reynolds number is small. This is not true of base pressure in laminar flow.

7.1   Compilation of Basic Experimental Data

Since a satisfactory theory does not exist, it is necessary to rely on experimental data for the quantitative prediction of the base drag of bodies as a function of Mach number, Reynolds number, and body shape. Much of this experimental data (see preceding references) has been compiled. Figure 7-1, which was derived from several of these compilations, presents curves of the base-pressure coefficient (Eq. 7-1) as a function of Mach number for a basic body shape having the following limiting conditions.

1.   The body is one of revolution, with zero boattail angle.

2.   The fineness ratio is greater than 5.

3.   The Reynolds number is high enough $(10^6$ to $10^8)$ to ensure a turbulent boundary layer over most of the body length.

4.   The body has no fins.

These conditions are not as restrictive as they appear. It has been shown that the base pressure is not dependent on the body length when the body is long enough to allow the surface pressure to return to ambient before it reaches the base. It has also been shown that once the boundary layer ahead of the base has become fully turbulent the base pressure is almost insensitive to Reynolds number.

The base pressure coefficient plotted in Fig. 7-1 is defined as

$$C_{p_b} = \frac{2(p_b - p_\infty)}{\rho_\infty V_\infty^2} = \frac{2(p_b - p_\infty)}{\gamma \, p_\infty \, M_\infty^2} = \frac{p_b - p_\infty}{q_\infty} \qquad (7-1)$$

where

$$p_b = \text{base pressure}$$

and subscript ∞ = free-stream value

Of the several curves in Fig. 7-1, those for which equations have been derived (Ref. 204) are most recent and are based on a comprehensive compilation of test results.

7.1.1   Chapman's Semi-Empirical Theory

One of the most useful of several theories developed to account for changes in the nature of the base pressure due to changes in many of the relevant parameters is that of Chapman (Ref. 142). This theory incorporates the effects of body profile and boundary-layer characteristics.

7.1.1.1   Effect of Body Profile

This effect may be incorporated by defining the base pressure coefficient as

$$C_{p'_b} = \frac{2(p_b - p')}{\gamma \, p' \, M'^2} \tag{7-2}$$

where p' and M' are the average pressure and Mach number over a hypothetical extended profile as shown below.

Finite Profile   Finite Profile with Extended Afterbody
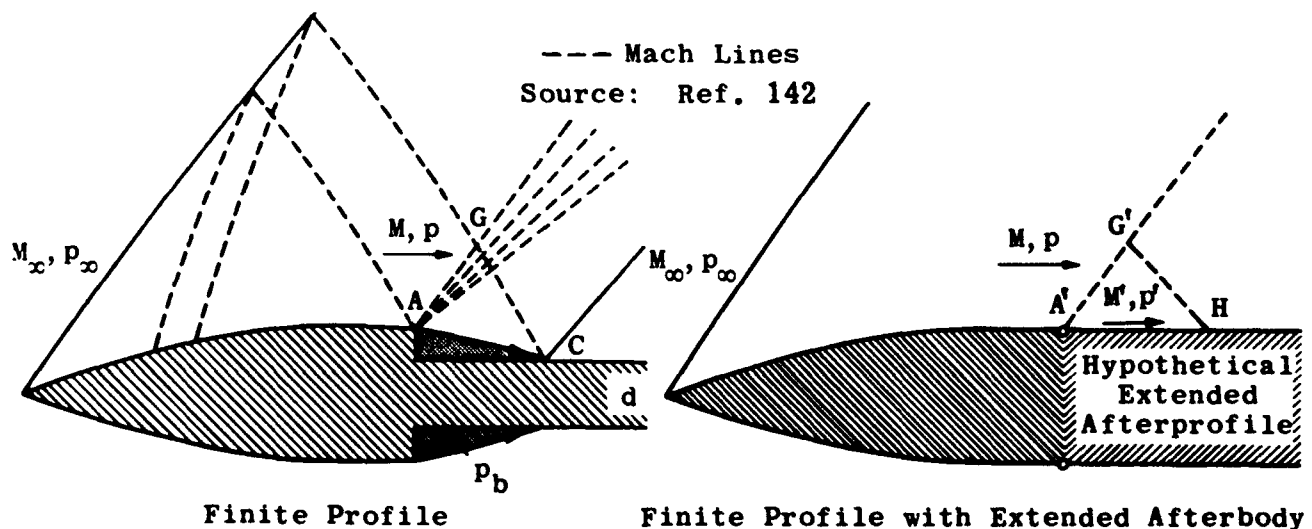
For zero boattail angles the values of p' and M' are those of the intersection G (left hand sketch). They are equivalent to p' and M' along the surface A' H (right hand sketch).

For negative boattail angles (see sketch on next page), the values of p' and M' are those at point G, the intersection of the reflected wave to C and the expansion wave from A along which the velocity vector is parallel to the free stream.
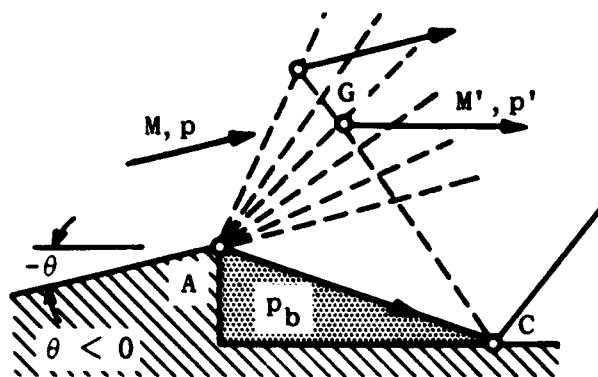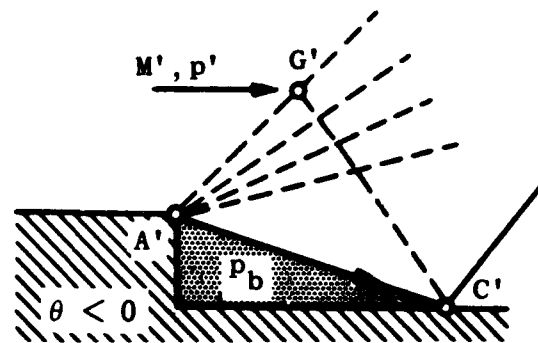
Real Flow   Equivalent Flow

For <u>positive</u> <u>boattail</u> <u>angles</u>, p' and M' (point J) may not easily be determined in the non-uniform flow ahead of the base, but may be determined approximately from conditions at G' in the equivalent flow (right hand sketch).
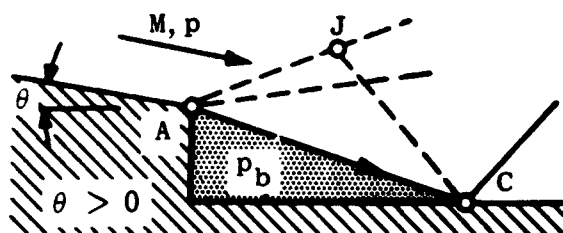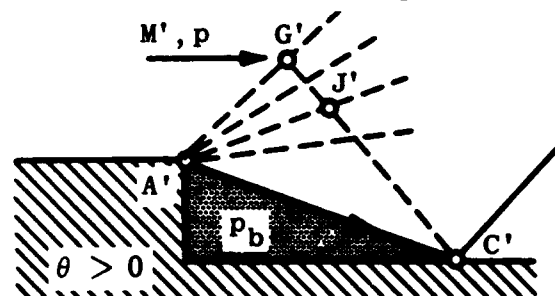
Real Flow   Equivalent Flow

The pressure and Mach number at Point A may be found by use of any of the methods discussed in Subsec. 2. For the case of cone-cylinders, the local parameters can be evaluated with the use of the tables presented in Ref. 63. The values at G must be found by the method of characteristics.

The following tabulations indicate the values of M' and p' as compared with p_∞ and M_∞ for two body shapes.

Cone-Cylinder			Cone		
M_∞	M'	p'/p_∞	M_∞	M'	p'/p_∞
1.5	1.51	0.98	1.5	1.58	0.88
2	2.02	0.97	2	2.09	0.87
3	3.03	0.95	3	3.13	0.82
7	7.02	0.86	7	7.16	0.76
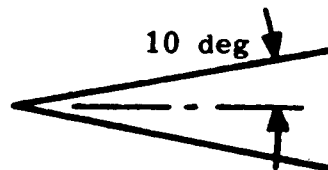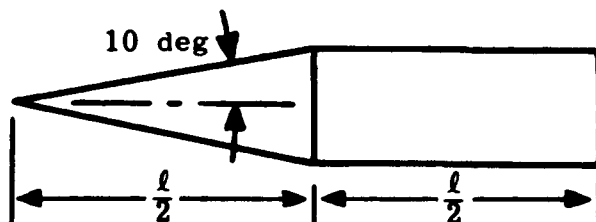
For moderate Mach numbers, when $\ell/d > 5$, the error in using the free-stream conditions instead of base conditions would not be serious.

When $C_{p'_b}$ is defined as it is in Eq. 7-2, the use of Fig. 7-1 may be extended to include all body profiles rather than the limited basic geometries from which it was computed. Figure 7-2 (from Ref. 176) shows the correlation of base-pressure data from bodies of varying fineness ratio for a wide range of local Mach numbers and local static pressures. Within the experimental accuracy, it may be seen that the effect of body shape is adequately accounted for by use of the local pressure and Mach number. The increase in scatter at high Mach numbers is probably due to the low absolute value of the measured pressures and the consequently high relative experimental errors.

7.1.1.2   Effect of Boundary-Layer Characteristics

Chapman also showed that the base pressure coefficient as defined by Eq. 7-2 could be expressed as a linear function of fineness ratio and Reynolds number at each Mach number. For laminar flow approaching the base,

$$C_{p'_b} = f_\ell \left(M', \frac{\ell}{d_b}, Re^{-1/2} \right) \tag{7-3}$$

where

d_b = diameter of the base

For turbulent flow approaching the base,

$$C_{p'_b} = f_t \left(M', \frac{\ell}{d_b}, Re^{-1/5} \right) \tag{7-4}$$

Figures 7-3 and 7-4 (from Ref. 142) show the effect of this correlation for laminar flow at $M = 1.5$ and 2.0. Figures 7-5 and 7-6 (same source) show the correlation for turbulent flow at the same Mach numbers. As has already been noted, the turbulent case is relatively insensitive to Reynolds number, especially as M increases.

7.2   Variation of Base Pressure with Radial Distance

It is generally accepted that the base pressure does not vary appreciably with radial location over the face of a flat base. Data from both free-flight and wind-tunnel tests at $1.0 < M < 2.0$ reported in Ref. 148 show no radial variation of the base pressure, whereas data plotted in Fig. 7-7 (from Ref. 159) show that there is a slight tendency for the base pressure to decrease with distance from the center of the body. Since most base-pressure measurements are made in wind tunnels, it is always difficult to separate real effects from interference effects, particularly where the absolute magnitude of the pressures are small.

7.3   Variation of Pressure in the Body Wake

       The variation of pressure within the wake of a cylindrical
non-boattailed body of revolution was studied by Love, whose findings
are reported in Ref. 140. Figure 7-8, taken from this reference, pre-
sents the pressure variation as a function of distance from the base
for Mach numbers of 1.62, 1.93, and 2.41, all at zero angle of attack.
There is very little variation of pressure across any section of the
wake. The increase of pressure with distance from the base is most
marked at the lowest Mach number.

7.4   Boattails and Their Effects on Base Pressure

       One method that is used to decrease the magnitude of drag
created by the large negative pressures at the base of a body of revo-
lution is that of boattailing. The aft portion of the body may be con-
toured with either conical or ogival shapes to provide a region of de-
creasing diameter just ahead of the base. In Ref. 150 Cortright and
Shroeder present a semi-empirical method, somewhat similar to Chapman's
method, by which the base-pressure coefficient for boattailed bodies
may be calculated in terms of the pressure, p', and Mach number, M',
just ahead of the base. In this method, the base-pressure coefficient
is expressed as

$$C_{p_b} = \frac{q'}{q_\infty} \cdot \frac{p_b - p'}{q'} + \frac{p' - p_\infty}{q_\infty} \qquad (7\text{-}5)$$

The value of p' and M' are found by use of any of the methods given in
Subsecs. 2 and 3, and p_b is found from the Prandtl-Meyer expansion for
the total angle through which the streamline turns. Good agreement be-
tween measured and predicted base pressures has been achieved by this
method. It may not be used, however, where there is flow separation
ahead of or along the boattail.

       Additional experimentally determined base-pressure coeffi-
cients are shown in Fig. 7-9 (from Ref. 140). The actual reduction of
base pressure with boattail angle compares reasonably well with theo-
retical predictions that were obtained by means of the methods of
Refs. 142 and 150.

       The decrease in base drag which results from boattailing, how-
ever, is opposed by an increase in drag which is created by the lowered
pressure over the converging afterbody. If there is excessive boattail-
ing the latter effect predominates, and the net drag consequently is in-
creased. This phenomenon is illustrated in Fig. 7-10 (from Ref. 176),
in which total afterbody drag is plotted against the ratio d_b/d for con-
stant ogival afterbody length at Mach numbers of 1.5, 3.0, and 8.0. At
Mach numbers of 1.5 and 3.0, the optimum value of d_b/d is equal to 0.6,
at which value the drag is reduced to about 60% of its value for the
non-boattailed case. At M = 8 there is no significant effect of after-
body shape, and little is therefore gained by boattailing. Base pres-
sure coefficients on a conical boattail are shown in Fig. 7-11 (from
Ref. 145) in terms of boattail angle. In this case the optimum boat-
tail angle is about 7 deg at M = 1.56; at M = 3.24 the drag is rela-
tively insensitive to boattail angle in the region of $4 < \theta < 15$ deg.

7.5   Effect of Fins on Base Pressure

The expansion wavelets emanating from fin surfaces change the wake characteristics and usually increase the base drag, i.e., decrease the base pressure. Fin effects, examined in some detail in Refs. 140 and 148, may be ascribed to fin thickness, position with reference to the base, and number of fins employed. Figure 7-12 (from Ref. 160 by Spahr and Dickey) shows the increment of base pressure in terms of distance between the trailing edge of the fin and the base of the body. These effects are shown for M = 1.5 and 2.0, thickness ratios of 5% and 10%, one plane tail panel, and cruciform tail fins.

In Fig. 7-13 (from Ref. 140) the base-pressure coefficient derived from wind-tunnel and free-flight tests of finned missiles are compared with the test data of bare bodies taken from Fig. 7-1. It may be noted from both Figs. 7-12 and 7-13 that the fin effect diminishes quite rapidly with increasing Mach number. These curves assume fully turbulent flow approaching the base.

An empirical formula derived in Ref. 204 for the additive base drag due to the pressure of fins is given by

$$\Delta C_{D_b} = t/c \left(\frac{0.825}{M^2} - \frac{0.05}{M} \right) \cdot n \qquad (7\text{-}6)$$

where

t/c = thickness-to-chord ratio of fins

n = number of fins

It is assumed that the trailing edge of the fins is flush with a non-boattailed body.

The drag increment computed from Eq. 7-6 is included with the original test data (from Ref. 140) in Figs. 7-12 and 7-13. In Fig. 7-12 the agreement with wind-tunnel test results is good, which would be expected since the data from these tests was included with that used to derive the empirical equation, Eq. 7-6. In Fig. 7-13 the agreement with free-flight data is reasonably good.

7.6   Effect of Heat Transfer on Base Pressure

The effect on the base pressure of heat transfer between the body itself and the boundary layer of the air flowing over the body is reported by Kurzweg in Refs. 145 and 163. Some of the results of these studies for both laminar and turbulent flow at M = 3.24 and 4.24 are indicated in Fig. 7-14.

The values of the drag increments shown in Fig. 7-14 are dependent on many test parameters and are quantitatively valid only for one set of conditions. However, the curves show qualitatively the magnitude of the changes in base pressure that may accompany the heating

or cooling of the body skin and the consequent changes in the temperature distribution through the boundary layer. The heat-transfer effects increase with increasing Mach number.

A second effect, allied to heat-transfer effects on base pressure and treated by Tetervin in Ref. 167, is the stabilization of the laminar boundary layer when the surface is cooled. As shown in Subsec. 7.1.1.2, base pressure is greater when laminar flow approaches the base than when fully turbulent flow at the same Mach number approaches the base. The effect of heat transfer on the Reynolds number of transition will be treated in Section 14 of the Handbook.

It may also be noted that skin-friction drag (see Subsec. 6) is increased as the body surface is cooled.

7.7 Effect of Angle of Attack on Base Pressure

An increase in the angle of attack increases base drag, i.e., makes the base pressure more negative. Figure 7-15 presents a compilation of experimental data on angle-of-attack effect.

For non-boattailed bodies without fins the base drag increases rapidly with angle of attack, the increment diminishing as the Mach number increases. For $\alpha = 10$ deg the drag increment in the range of $1.5 < M < 2$ is approximately one-third of the base drag at $\alpha = 0$ deg, whereas at $M = 3.12$ the increment at $\alpha = 9$ is about 11% of the base drag value at $\alpha = 0$ deg.

When the body has cruciform tail fins the measured increment (shown in Fig. 7-15) at $\alpha = 6$ deg is 4% of the base drag at $\alpha = 0$ deg at $M = 1.73$ and 6.5% at $M = 2$. Thus it appears that the presence of fins inhibits flow separation and the consequent increase in drag.

For boattailed bodies the drag increment is of the same order of magnitude as it is for the non-boattailed body. However, since the boattail angles are nearly optimum (i.e., 5 and 7 deg) the zero angle-of-attack base drag is much less, and the percentage increase for the boattailed body is therefore much larger. For the data shown in Fig. 7-15, ΔC_{D_b} varies from 75% to 114% at $\alpha = 6$ deg. These data indicate that the angle-of-attack effect is more sensitive to boattail length than to boattail angle.

7.8 Effect of Base Jets on Base Drag

Due in part to the limitations of testing methods, experimental data relating to the effect of jets on the external flow in the wake region of a body is somewhat meager. Free flight tests are usually confined to models of current prototype missiles, the test results of which are classified and not available for use in an unclassified handbook. In scale-model wind-tunnel tests the simultaneous simulation of the correct jet mass-flow, jet temperature, and free-stream conditions is difficult to attain. In addition wind tunnel test results are frequently clouded by unknown interference effects (e.g., from supports

and tunnel walls). A difficulty common to both types of tests is the array of parameters involved and the lack of certainty in separating the many effects.

The most significant geometric parameters for base jets are illustrated below.

Annulus Area   Base Area
(Jet On)   (Jet Off)

Incomplete Boattail

Complete Boattail
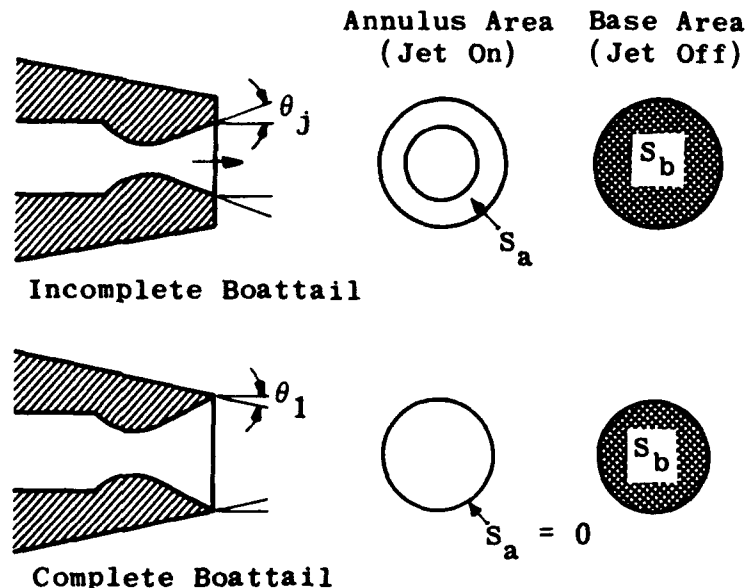
In this case the significant flow parameters are

$$\frac{p_j}{p_\infty} \, , \quad \frac{V_j}{V_\infty} \, , \quad \text{and} \quad \frac{T_j}{T_\infty}$$

where subscript j refers to the jet conditions and subscript ∞ refers to the free-stream conditions.

7.8.1   Effect of Jet Pressure Ratio on Boattail Pressure

The experimental pressure distributions on the sides of three completely boattailed configurations at zero angle of attack are presented in Figs. 7-16 to 7-18 (from Ref. 150) for jet pressure ratios ranging from no-jet flow to p_j/p_∞ = 15. The pressures were measured at ϕ = 15, 50, and 90 deg. Since the angle of attack was zero, the difference between measurements for any configuration reflects a measure of the accuracy. Varying the boattail angle or the distance from the base at which increased pressure is sensed due to the presence of the jet seems to produce no significant effect on the pressures within the accuracy of measurement. The pressure increase is clearly a function of jet pressure.

The flow mechanism whereby the jet interference takes place is illustrated in the following qualitative sketch taken from Ref. 150 and derived from schlieren photographs of the flow conditions in the region of the base of a completely boattailed body (i.e., with no annulus).

Shock Wave

Compression Region

Region of Separated Flow

Jet Boundary
and Mixing Zone

Boundary Layer

Shock Wave

Nozzle

Expansion Waves

Jet Air
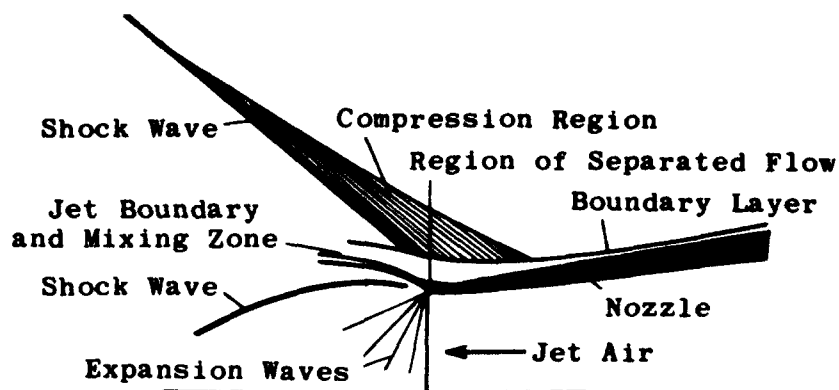
As the jet pressure ratio is increased, the issuing jet expands and
deflects the external flow, with a resultant shock wave and pressure
rise. This increased pressure propagates upstream through the subsonic
portion of the boundary layer on the body. An increased rate of bound-
ary-layer growth and compression toward the rear result in a region of
separated flow ahead of the base. Inasmuch as this interference effect
is largely one of shock-boundary-layer interaction, it would seem that
the results shown in Fig. 7-16 to 7-18 would be sensitive to the bound-
ary-layer thickness and profile at the base, i.e., to Reynolds number
and surface conditions of the body. Tests with artificially achieved
boundary-layer transition indicated that in some cases (flagged symbols
of Fig. 7-16 and 7-18) there actually was a pressure rise due to the
thickened boundary layer, but in no case did the pressure rise extend
upstream of the pressure orifice nearest the base.

In the case of the incompletely boattailed configurations,
the annular base served largely to prevent such interaction effects of
the jet on the sides of the boattail. The qualitative sketch below,
which is also from Ref. 150 and also based on schlieren photographs,
illustrates the absence of jet effects on the flow over the sides of
these boattails.

Shock Wave

Semi-Dead Air Region

Weak Compression Wave

Jet Boundary
and Mixing Zone

Boundary Layer

Shock Wave

Expansion Waves

Jet Air
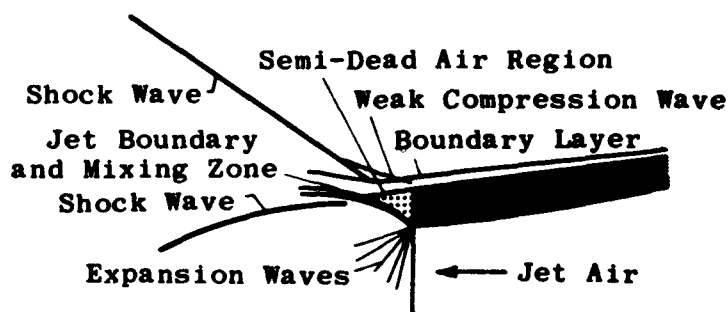
No appreciable thickening of the boundary layer is discernible even at
the highest jet pressure ratio. The fact that a strong shock wave was
formed when the jet and external streams met in the vicinity of the
annular semi-dead air region at the base would indicate, however, that
the jet might strongly affect the base pressure.

7.8.2   Effect of Jet Pressure Ratio on Base Drag

The phenomenon described above is clearly demonstrated in
Fig. 7-19 (from Ref. 150), which gives the effect of jet flow on the
pressures acting on the annular base. At this Mach number (1.9) the
jet effects are very marked.

For $0 < \dfrac{p_j}{p_\infty} < 1$, C_{p_b} increases.

For $1 < \dfrac{p_j}{p_\infty} < {\sim}3$ or 4, C_{p_b} decreases.

For $\dfrac{p_j}{p_\infty} > 3$ or 4, C_{p_b} increases.

The base pressure for both types of boattail has a peak value at $p_j/p_\infty = 1$. For the cylindrical afterbody the annular base pressure increases less rapidly than for the boattailed body and appears to approach a second maximum value at $p_j/p_\infty \sim 16$.

The effect of the jet at pressure ratios greater than unity may be explained in at least two ways. As the jet pressure ratio increases, the jet velocity increases and entrains air from the semi-dead air annulus. This entrainment tends to lower the pressure on the annular base by an amount which increases with jet pressure ratio. As the jet pressure ratio increases, however, the jet expands. The shock wave located at the point of interaction of the jet and the free stream increases in intensity and causes a pressure feedback through the subsonic mixing region between the two streams, with a resulting base pressure increase. A second qualitative explanation is that the jet displacement may act in a manner analogous to a center sting or support. Increasing the sting diameter causes the base pressure to approach the two-dimensional value. The increasing jet displacement with increasing jet pressure ratio could thus qualitatively lower the base pressure, and the strong interaction shock would again cause a reversal of trend at the high pressure ratios.

With either of these explanations it can be seen that the ratio of exit diameter to base diameter would affect the variation of base-pressure coefficient when the jet pressure is greater than the ambient pressure. This is noted in Fig. 7-19, wherein the experimental variation of base-pressure coefficient for the cylindrical body ($d_j/d = 0.5$) is much less than that for the boattailed body ($d_b/d = 0.7$). The wide separation of the two curves indicates that either the effect of the nozzle-to-base-diameter ratio is large or that there is some effect due to the increase in boattail angle (see Fig. 7-20).

7.8.3   Effect of Jet on Total Afterbody Drag

The influence of a jet on base pressure and boattail side pressure is described in the two preceding subsections. The combination of these two effects will define the effect of the jet on the total afterbody drag.

Figure 7-20 (from Ref. 150) shows the contribution to total drag of the converging portion of completely boattailed bodies having various boattail angles for a series of jet pressure ratios. The drag is reduced almost linearly with jet pressure ratio within the test range (0 to 15). In this case $d_j = d_b = 0.5d$.

Similar information is presented in Fig. 7-21 (from Ref. 150) for incompletely boattailed bodies with varying degrees of boattailing, but with $d_b/d = 0.7$ in all cases. The existence of a base annulus effectively insulates side pressure from the jet, and there is therefore no observable variation of the side-pressure drag contribution with varying jet pressure. The base drag component follows the general pattern shown in Fig. 7-19. When the pressure ratio is between 10 and 15 the base drag becomes negative, i.e., an effective thrust arises on the base annulus. The superposition of boattail drag and base drag is shown in Fig. 7-21. At the highest pressure ratio the reduction in over-all afterbody drag is of the order of 60% with a boattail angle of 6 deg and 40% with a boattail angle of 9 deg.

In Fig. 7-22 boattail pressure-drag coefficients are plotted as functions of boattail fineness ratio for all the configurations described in Ref. 150 at jet pressure ratios of 0, 3, and 15. For each curve the data points at the largest fineness ratio were obtained from the bodies boattailed to a sharp edge at the nozzle exit ($d_j = d_b = 0.5d$). The data points for zero-length boattail correspond to the cylindrical afterbody data and the intermediate points correspond to the boattails with annular bases. For the case of no-jet flow with a full base, the data indicate (within the range of the tests) the desirability of increasing the boattail fineness ratio. For an annular base the data indicate the desirability of boattailing to a sharp edge for moderate jet pressure ratios. For a jet pressure ratio as high as 15, an annular base gives minimum drag. These curves may also be used to predict optimum geometries for a fixed boattail fineness ratio if such a restriction is present. In actual application, appropriate friction drag estimates must be included.

In the lower portion of Fig. 7-22 only the pressure on the annulus was considered as adding to the boattail drag, i.e., there was zero drag over the jet opening, and hence the "no jet flow" curves should actually be considered as curves of $p_j = p_\infty$ when comparing them with those of the full base in the upper portion of the figure.

7.9   Effect of Spin on Base Pressure Characteristics

Spinning a body of revolution about its own axis at a high rate is known to alter certain of its aerodynamic characteristics (see Subsec. 5.4). Only a limited amount of unclassified data is available on this subject. The studies reported by Greene in Ref. 107 and by Schmidt and Murphy in Ref. 168 indicate that the base pressure is decreased (drag is increased) as the spin rate is increased. In the tests of Ref. 168, the over-all drag coefficient was increased by 2.6% with an increase of 0.45 in the spin rate, pd/v, where p is the rotational spin rate in radians per second. It is believed that most of this increase was due to the decrease in base pressure.

These results merely indicate trends; the absolute magnitude of the effect will be markedly influenced by the particular configuration and the flight environment. In view of the sparsity of unclassified literature, information must be obtained from the classified literature or from tests of any given configuration to determine the quantitative effect of spin.

7.10   Effect of Very Low Ambient Pressure on Base Pressure

        It is known that base-pressure characteristics will change
markedly in an environment of very low ambient pressure, i.e., a rare-
fied atmosphere. The limit of such low pressure is usually defined as
that wherein either slip flow or free molecular flow exist. The slip-
flow regime is defined by the following limitations.

$$0.01 < \frac{M}{\sqrt{Re}} < 0.1 \text{ for } Re > 1$$

or

$$0.01 < \frac{M}{Re} < 0.1 \text{ for } Re < 1$$

Section 16 of the Handbook (Ref. 170) presents a detailed treatment of
the rarefied gas regime.

        The boundaries of the continuum, slip, and molecular flow
regimes are shown in Fig. 7-23 (from Ref. 170) as functions of Mach
number and Reynolds number as well as the equivalent altitude. Since
completely laminar flow is expected to prevail when $Re < 10^5$ it is
usually necessary to consider only laminar characteristics in the slip-
flow regime.

        Kavanau (Ref. 169) has measured base (and side) pressures of
models over the following combinations of very low Reynolds numbers and
nominal Mach number.

$$159 < Re < 800 \text{ for } M \approx 2$$

$$920 < Re < 7400 \text{ for } M \approx 4$$

These data extend into the slip-flow regime since the rarefaction param-
eter $M/\sqrt{Re}$ covered the range $0.05 < M/\sqrt{Re} < 0.15$.

        With increasing altitude, and hence with lower Reynolds num-
bers, the base pressure will decrease steadily in this laminar-flow
regime because the effect of the increasing mixing rate is stronger
than the influence of an increasing ratio of boundary-layer thickness
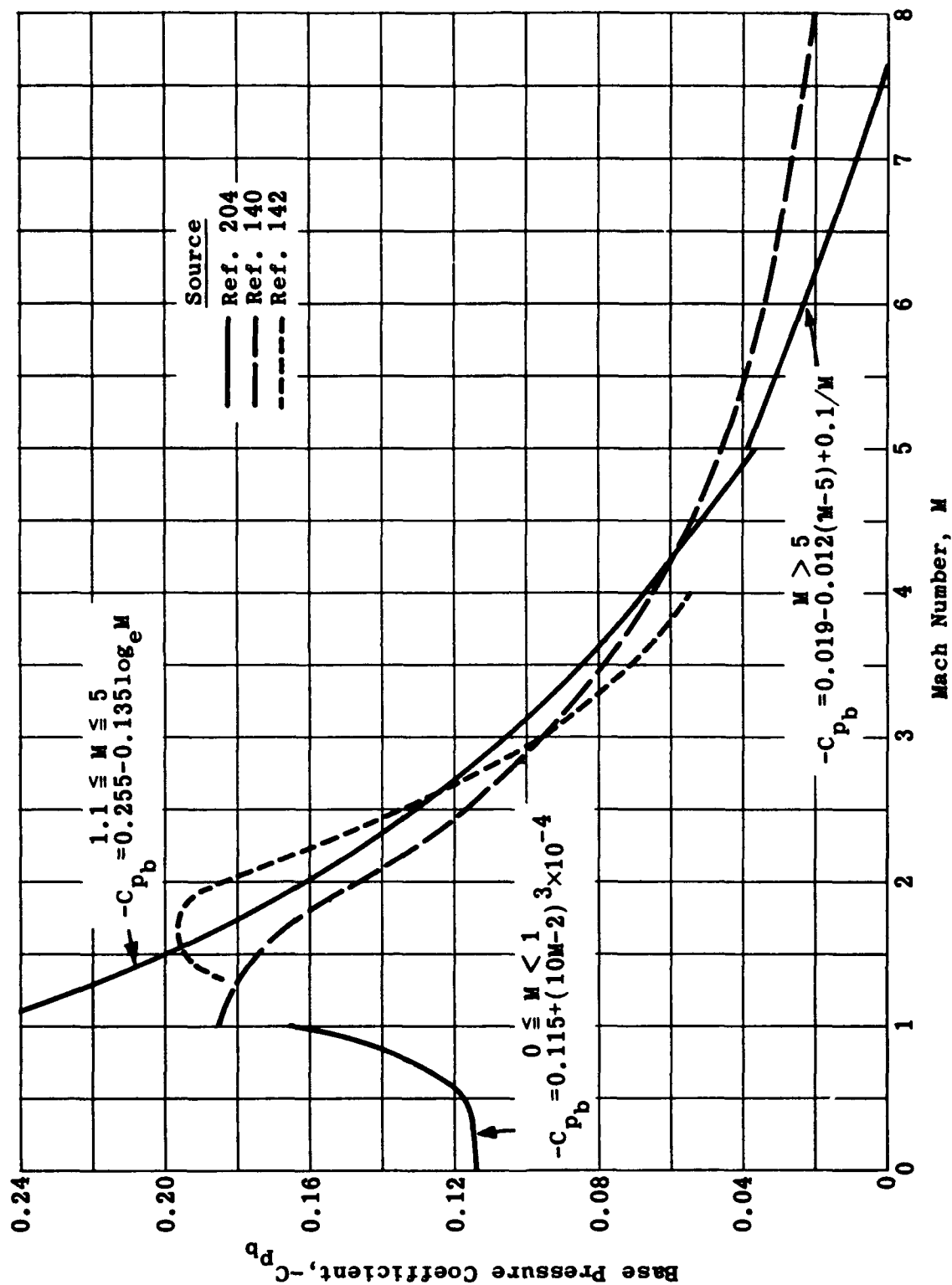to base diameter.

        The base pressure in such an environment, instead of being
radially constant, varies in a parabolic manner as indicated in
Fig. 7-25. In this figure, the local pressure has been divided by the
"area-mean-pressure" (i.e., the integrated local pressure times the
area over which it applies divided by the over-all area). The equation
for this variation and the experimental range of Mach number and Reynolds
number within which it was obtained are noted on the graph. The corre-
lation of this pressure ratio with $\sqrt{Re}/M^2$ is shown in Fig. 7-24. An
extrapolation of the data for $M = 2.84$ ties in with Kavanau's previous
test data and also generally agrees with the prediction made by Crocco
and Lees (Ref. 141).

Kavanau's quantitative measurements were made with models having a surface recovery temperature given by

$$r = \frac{T_w - T}{T_o - T} = 0.93 \tag{7-7}$$

This heat-transfer condition caused a decrease of approximately 5% in the base pressure compared to that of the insulated model. The effect of heat transfer from the model to the stream decreases the base pressure at these low Reynolds numbers, as compared to the effect of an increase in the base pressure noted previously for higher Reynolds numbers. These opposing effects may be explained by an effective Reynolds number change due to property changes in the boundary layer, together with the trend of base pressure with Reynolds numbers of the particular flow regime.

Kavanau also predicted the base pressure coefficient for free-molecule flow; his results are presented in Fig. 7-26. It can be seen that the base pressure is virtually zero for all Mach numbers greater than 2.

$$-C_{p_b} = 0.255 - 0.135 \log_e M \qquad 1.1 \leqq M \leqq 5$$

$$-C_{p_b} = 0.115 + (10M-2)^3 \times 10^{-4} \qquad 0 \leqq M < 1$$

$$-C_{p_b} = 0.019 - 0.012(M-5) + 0.1/M \qquad M > 5$$

Source
Ref. 204
Ref. 140
Ref. 142

Mach Number, M

Base Pressure Coefficient, $-C_{p_b}$

Fig. 7-1.   Base pressure on finless non-boattailed bodies of revolution; $\alpha = 0$ deg.

Fig. 7-2   NAVWEPS Report 1488 (Vol. 3, Sec. 8)
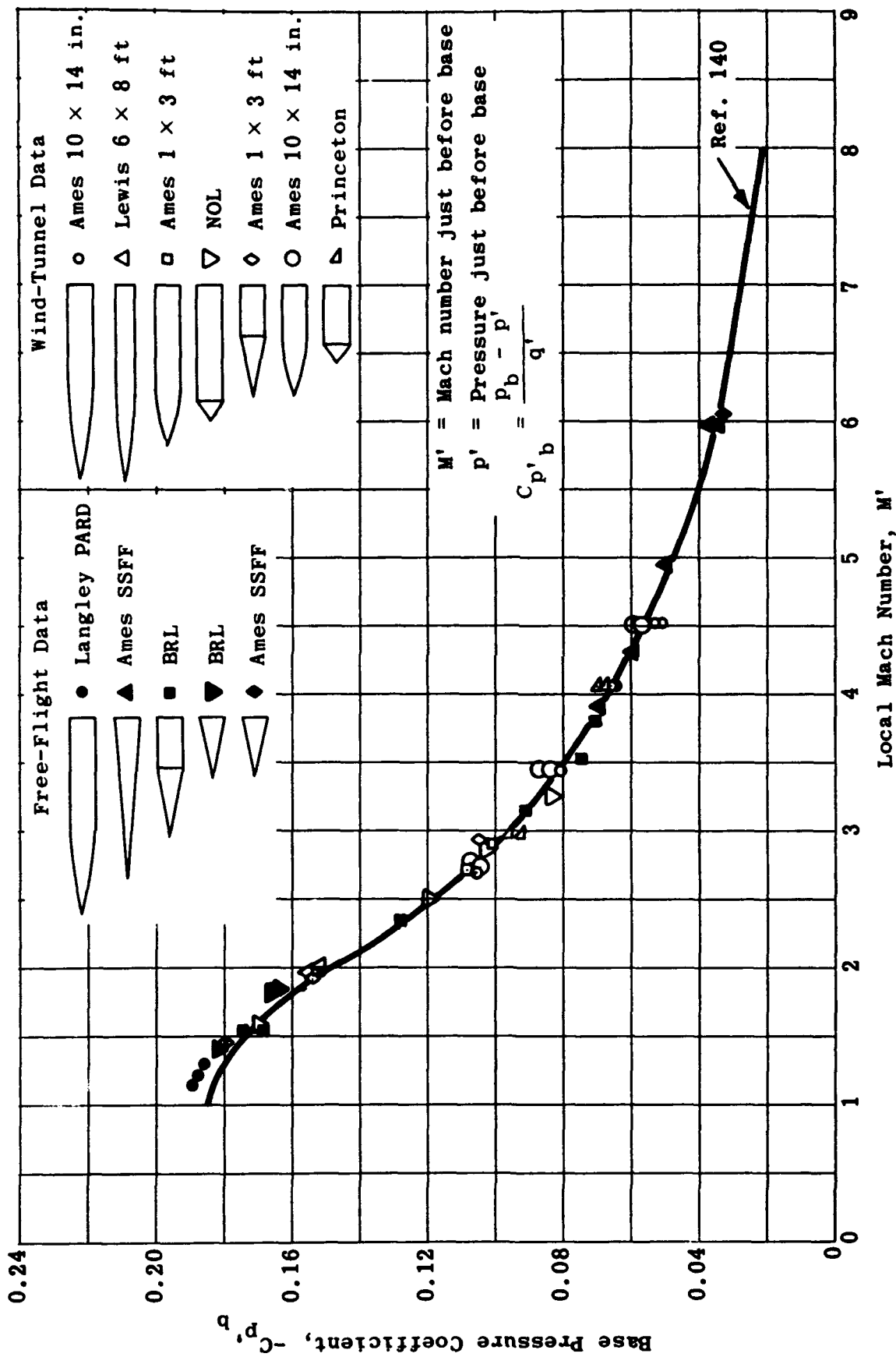
Fig. 7-2.   Base-pressure coefficient for finless bodies of revolution in terms of pressure and
Mach number ahead of the base; α = 0 deg. (Source: Ref. 176)
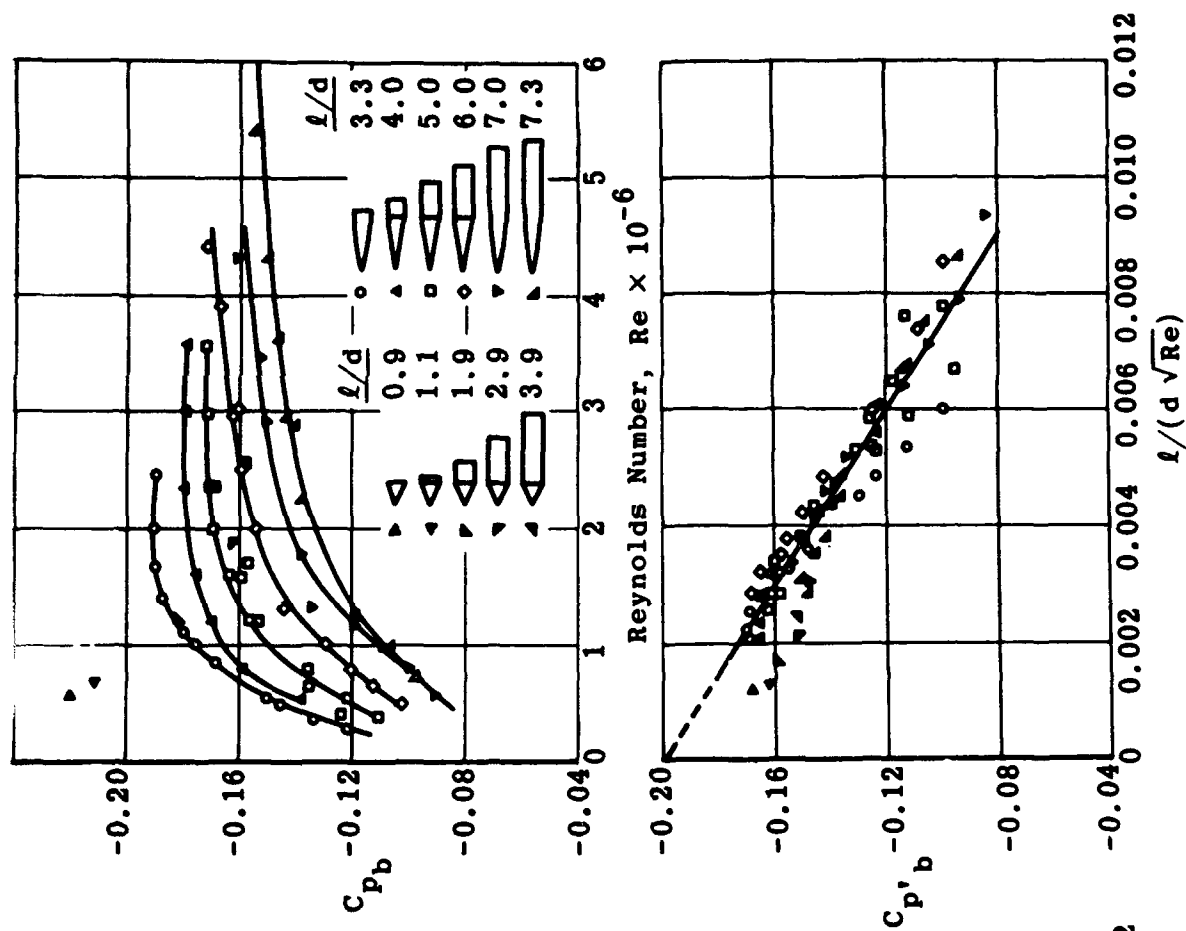
Fig. 7-4. Measured and correlated base pressures for several configurations; M = 2.0, laminar boundary layer. (Source: Ref. 142)
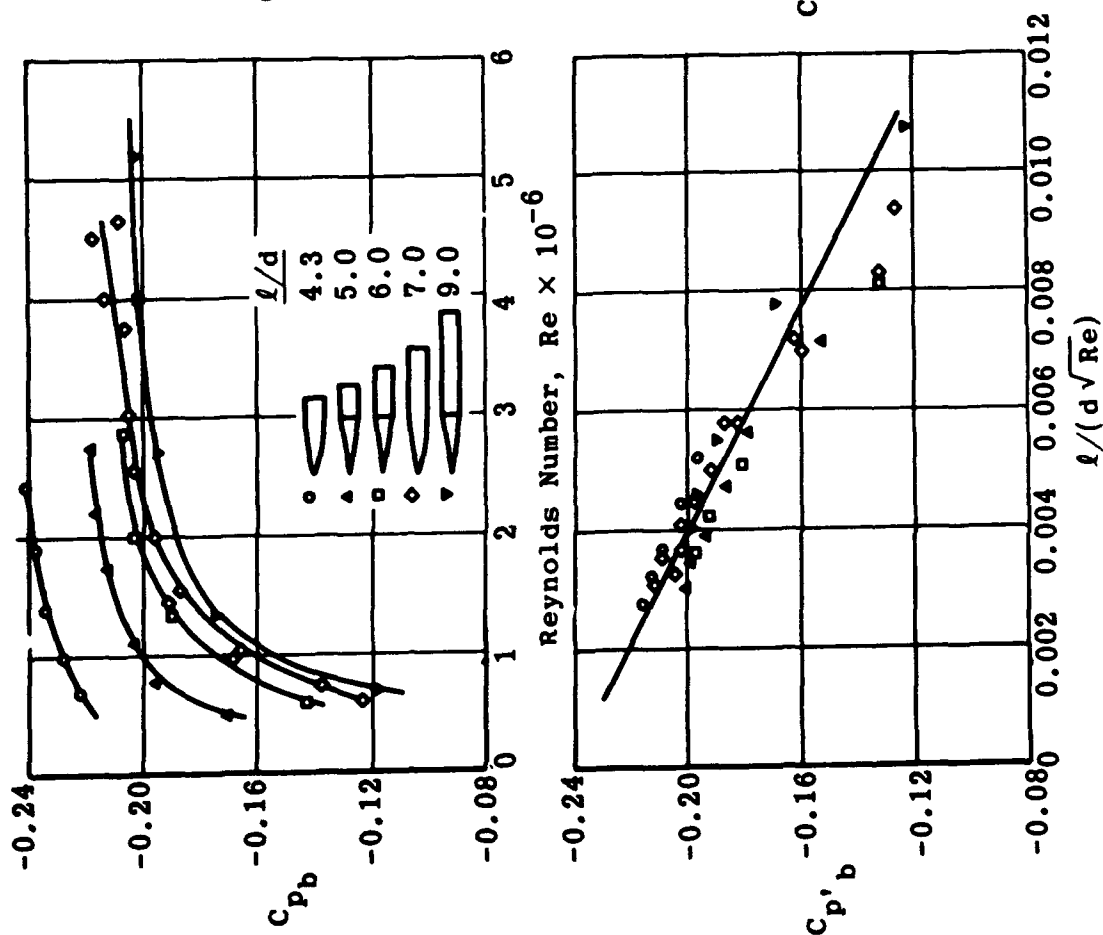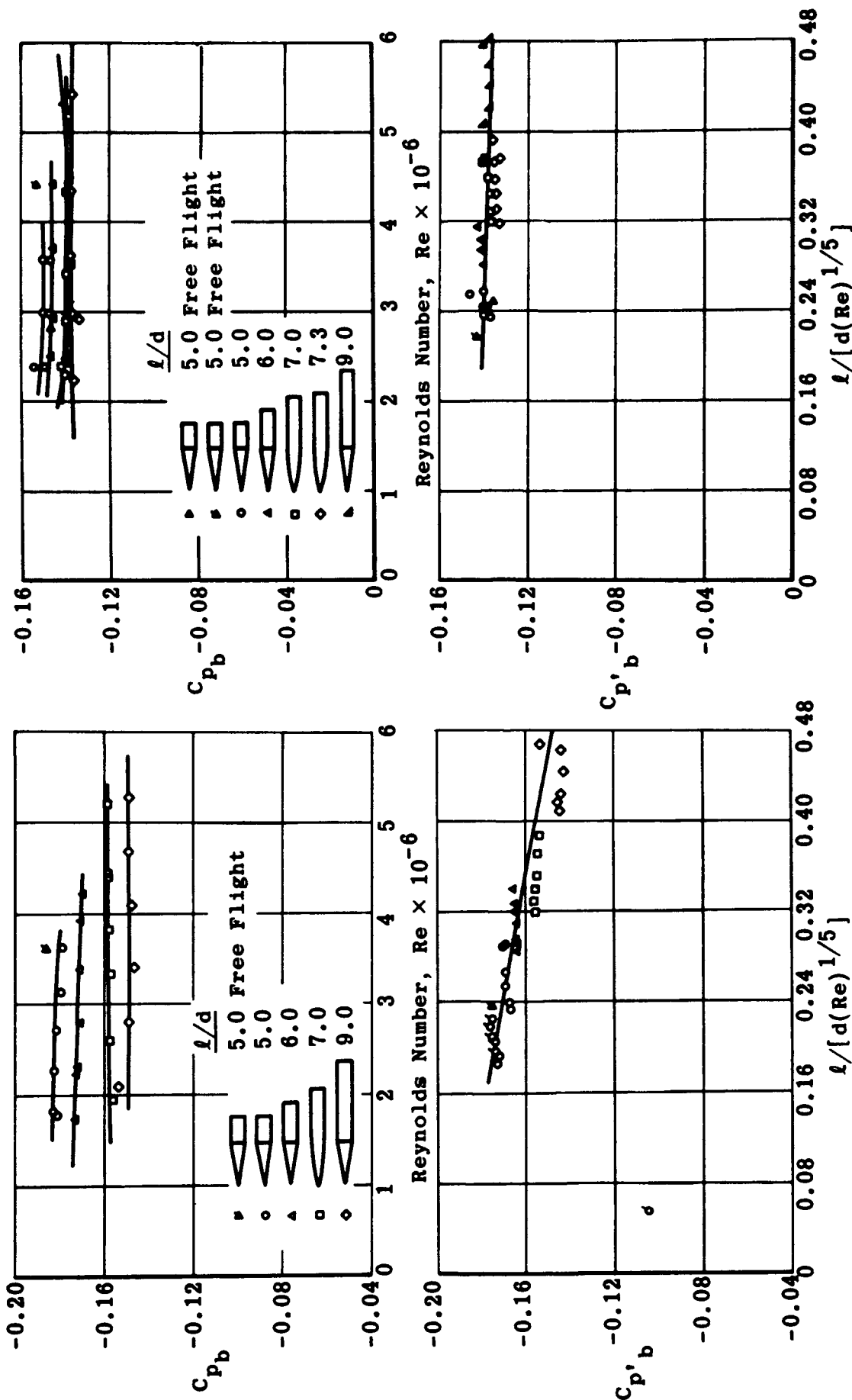
Fig. 7-3. Measured and correlated base pressures for several configurations; M = 1.53, laminar boundary layer. (Source: Ref. 142)

Fig. 7-5   NAVWEPS Report 1488 (Vol. 3, Sec. 8)

Fig. 7-6. Measured and correlated base pressures for several configurations; M = 2.0, turbulent boundary layer. (Source: Ref. 142)

Fig. 7-5. Measured and correlated base pressures for several configurations; M = 1.5, turbulent boundary layer. (Source: Ref. 142)
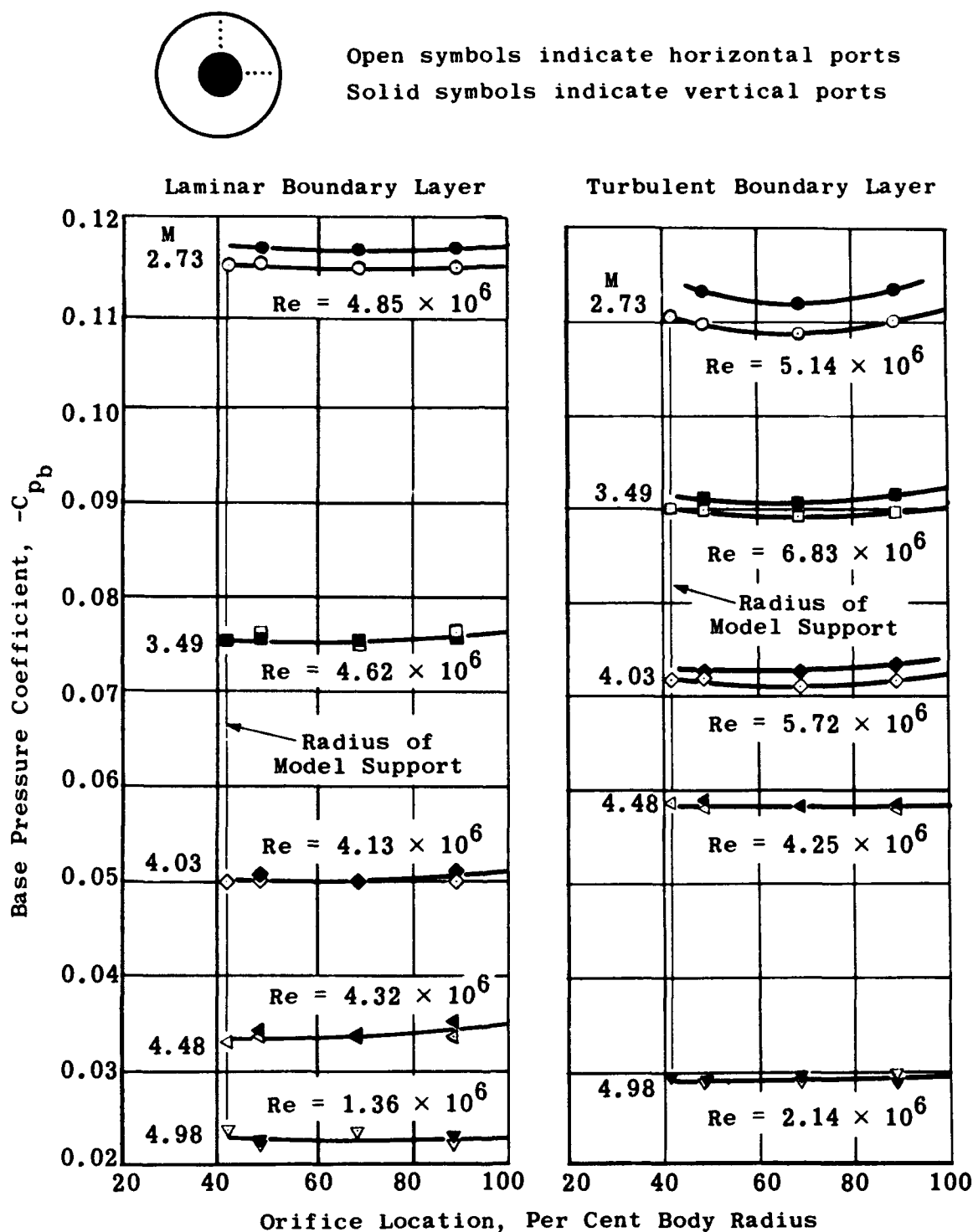
Fig. 7-7. Variation of base-pressure coefficient with radial location for laminar and turbulent boundary layers; $\ell/d = 5$. (Source: Ref. 159)
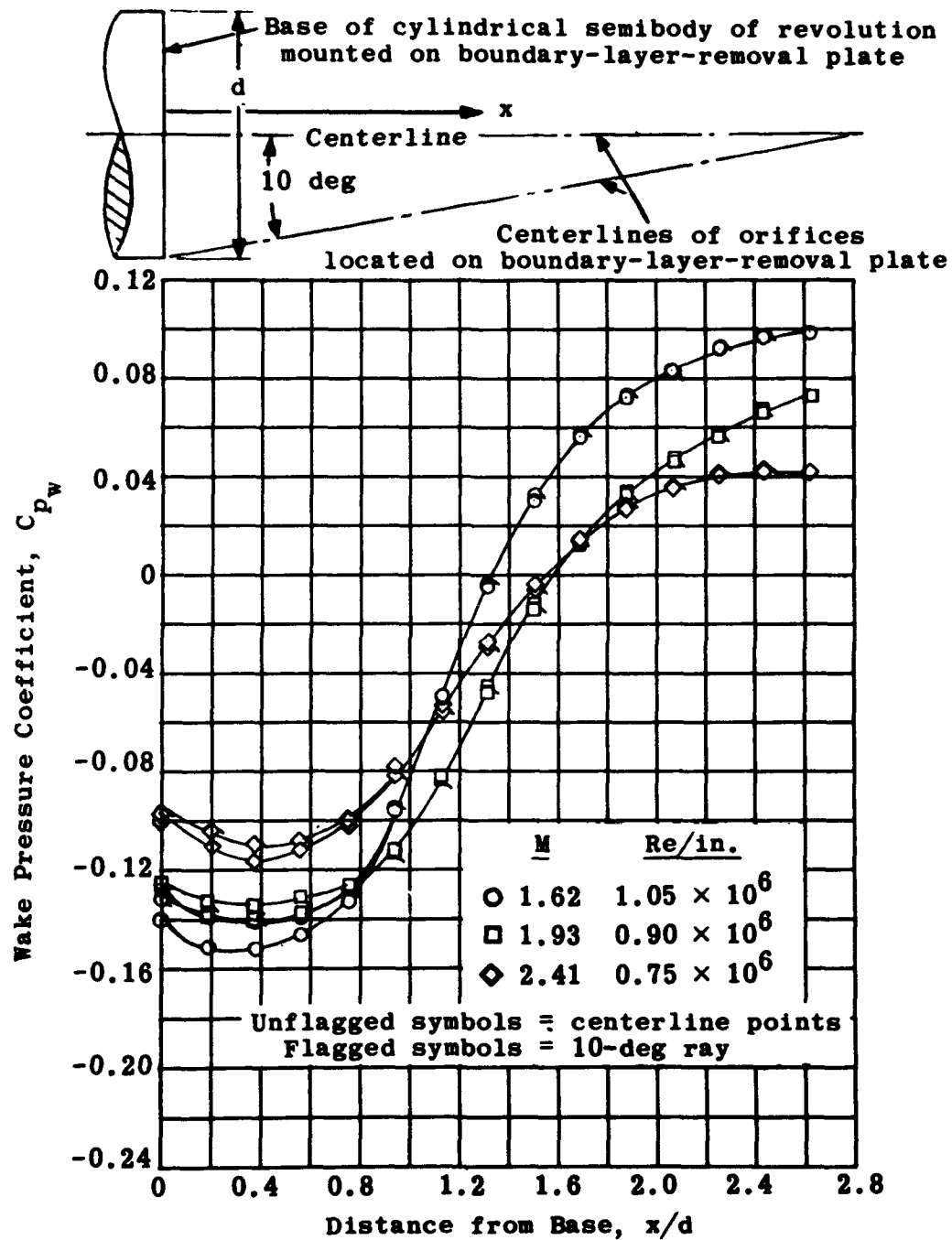
Fig. 7-8   NAVWEPS Report 1488 (Vol. 3, Sec. 8)

Fig. 7-8. Pressure variation in the wake of a cylindrical body at three Mach numbers; $\alpha = 0$ deg. (Source: Ref. 140)

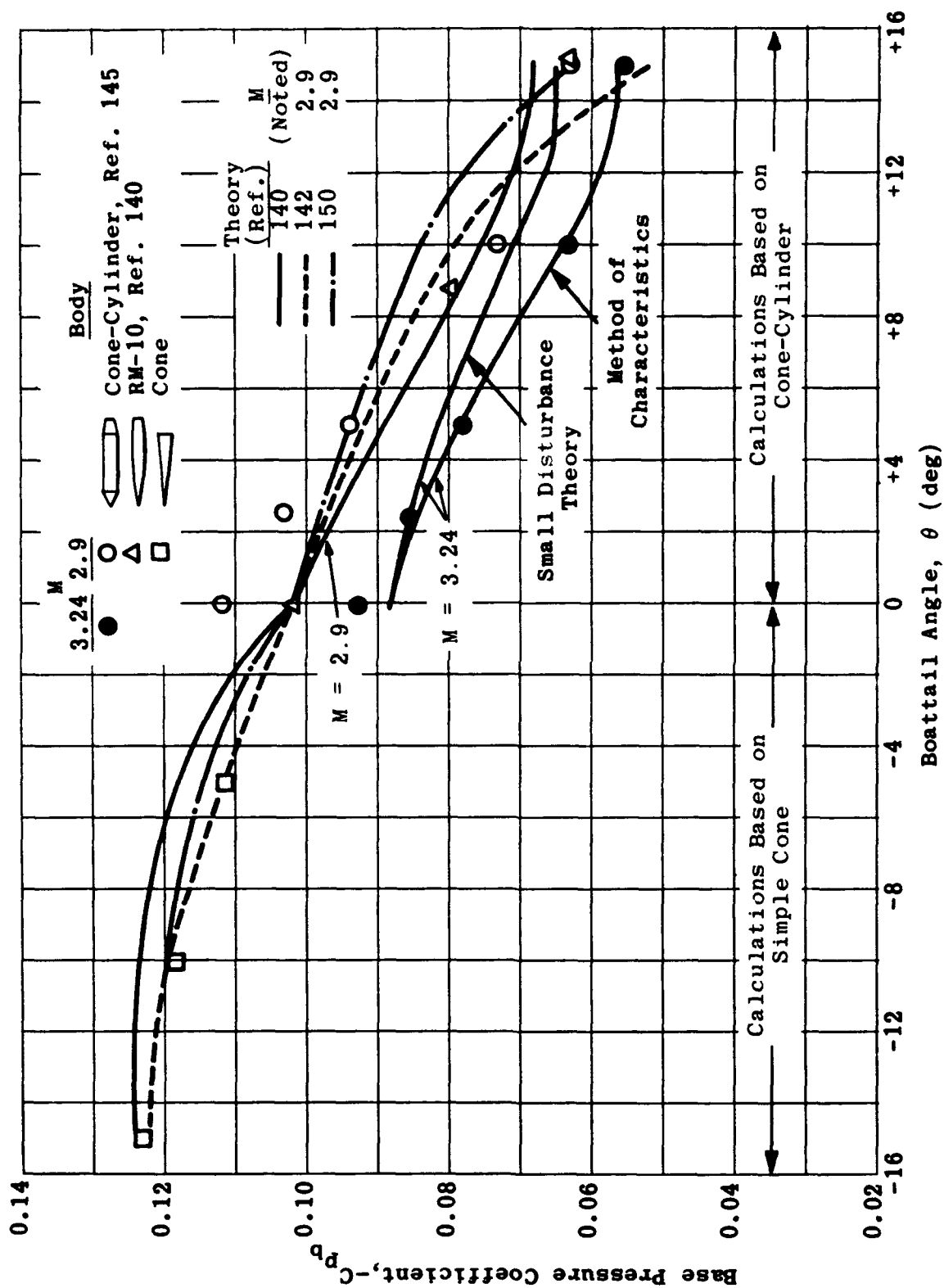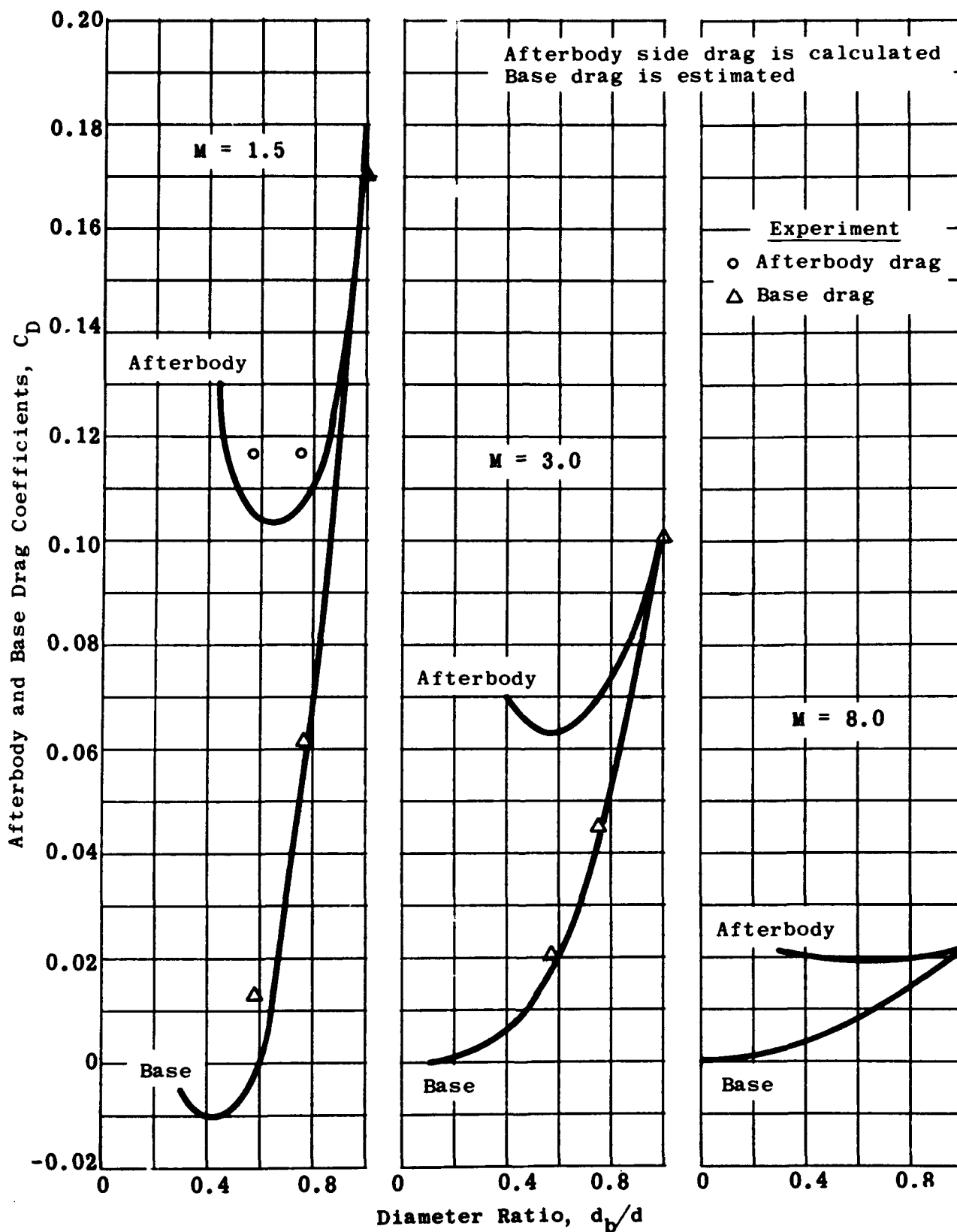Fig. 7-9. Effects of boattailing on base pressure for three configurations; M = 2.9 and 3.24. (Source: Ref. 140)

Fig. 7-10   NAVWEPS Report 1488 (Vol. 3, Sec. 8)

Fig. 7-10. Variation of afterbody drag with base diameter for constant ogival afterbody length; M = 1.5, 3.0, and 8.0. (Source: Ref. 176)
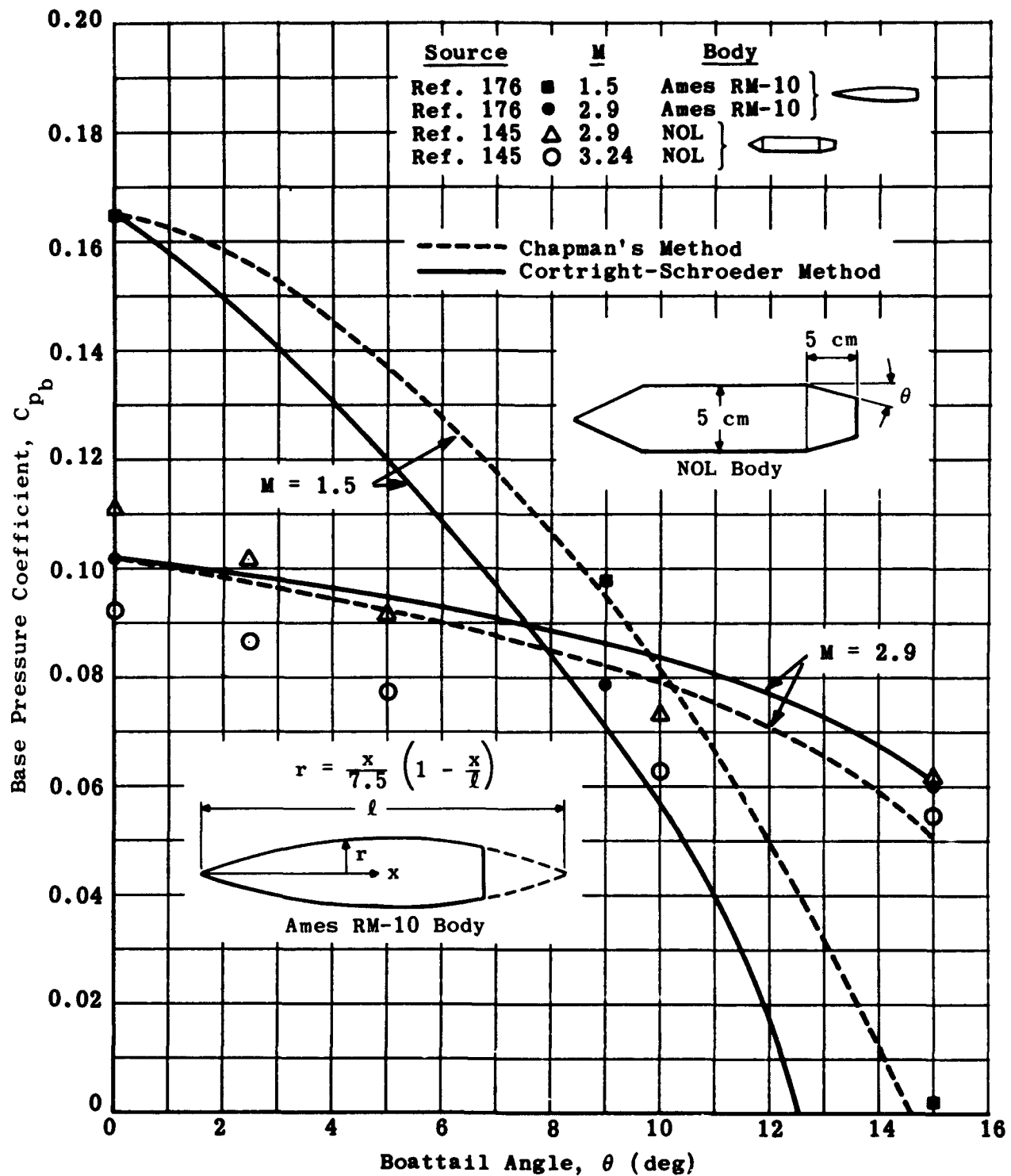
Fig. 7-11. Effect of conical boattailing on base pressure;
M = 1.5 and 2.9. (Source: Ref. 145 and 176)

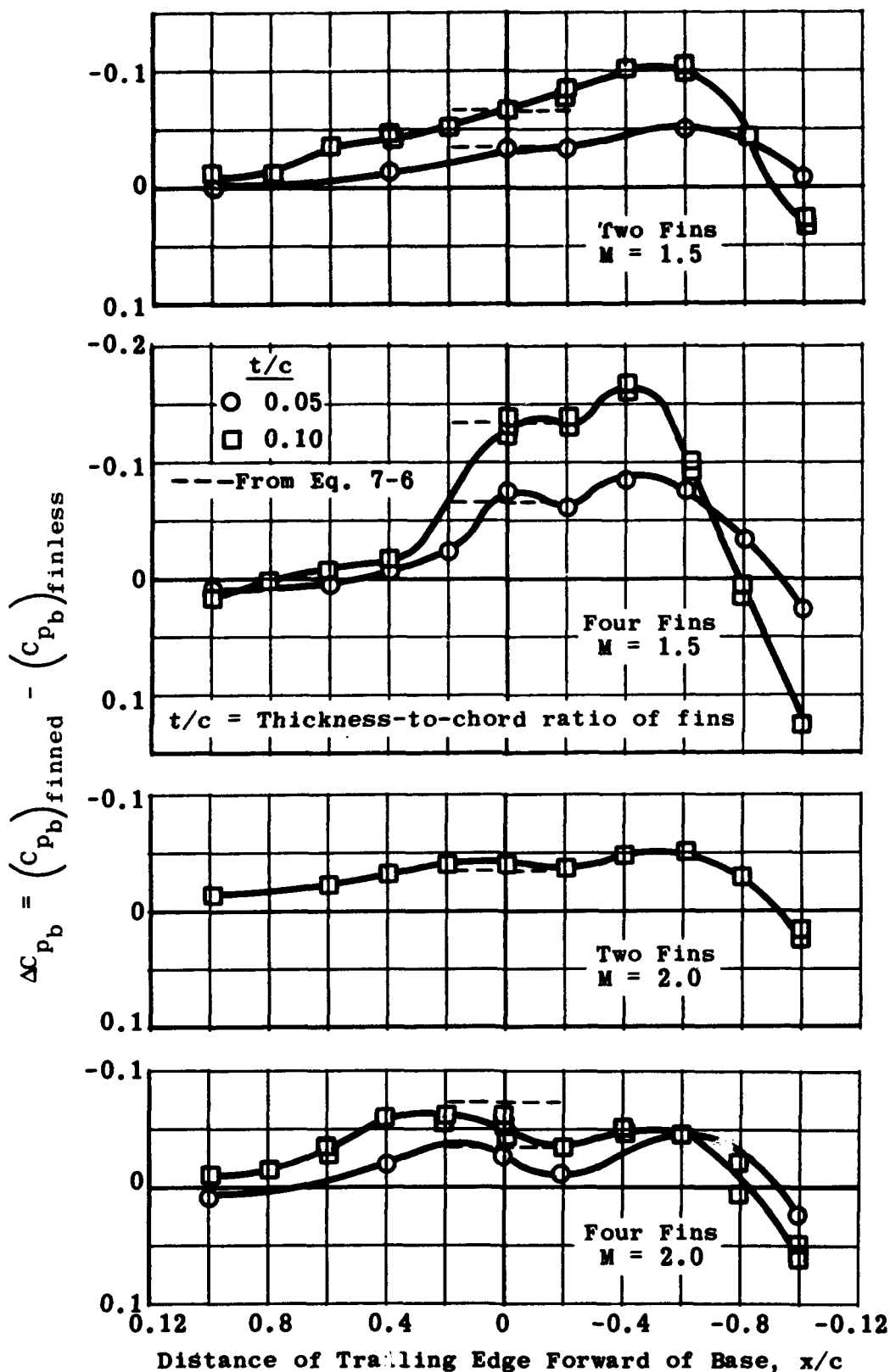Fig. 7-12   NAVWEPS Report 1488 (Vol. 3, Sec. 8)

Fig. 7-12. Effect of fins on base pressure for non-boattailed bodies;
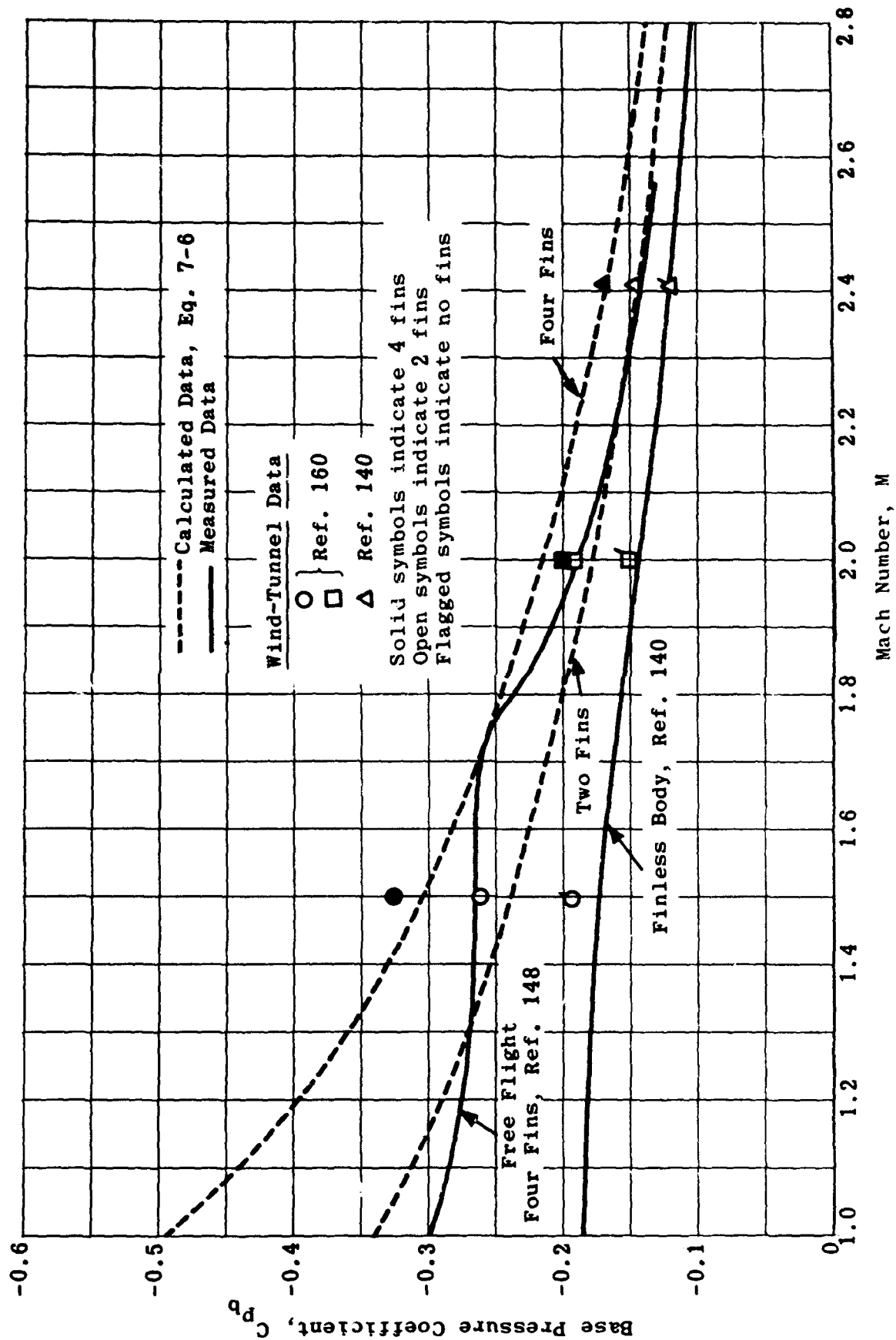M = 1.5 and 2.0. (Source: Ref. 160)

Fig. 7-13. Comparison of base pressure on finned and finless bodies as a function of Mach number.

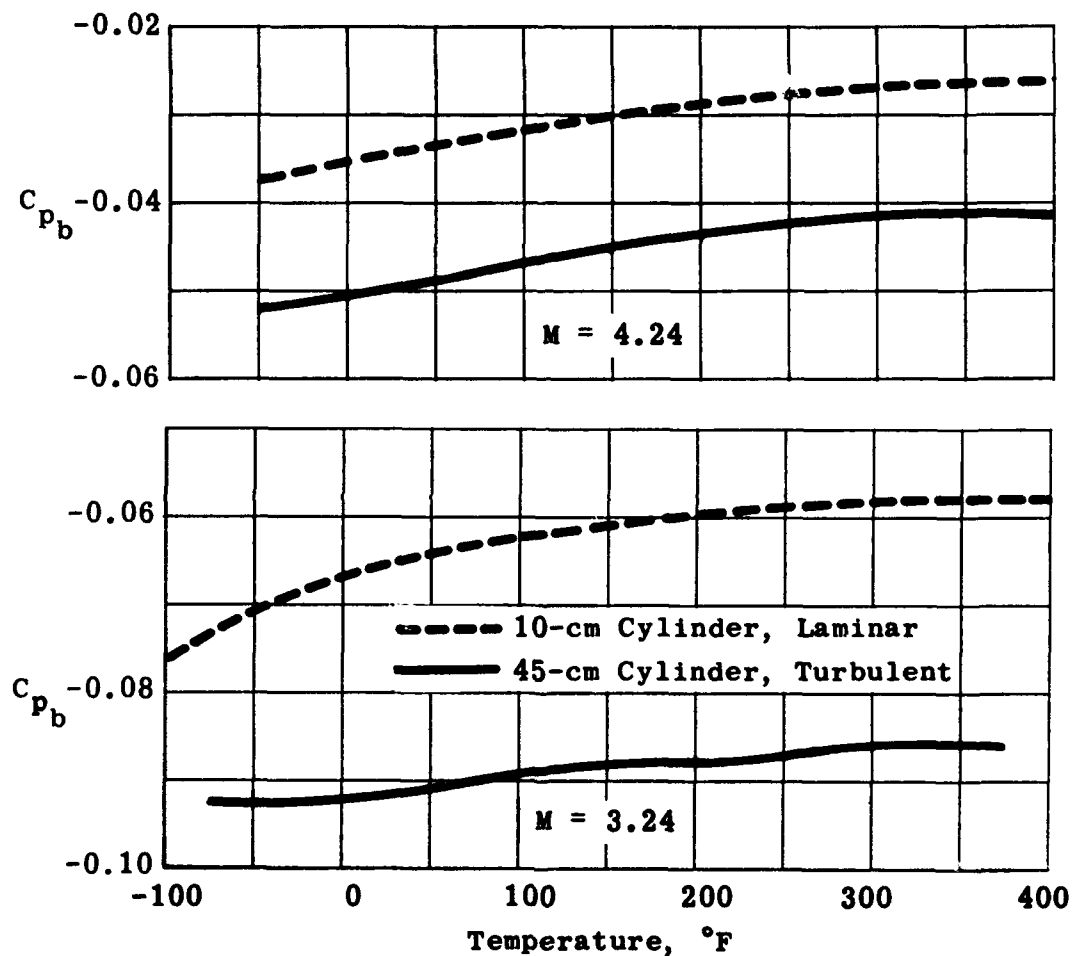Fig. 7-14   NAVWEPS Report 1488 (Vol. 3, Sec. 8)

Fig. 7-14. Effect of surface temperature on base pressure;
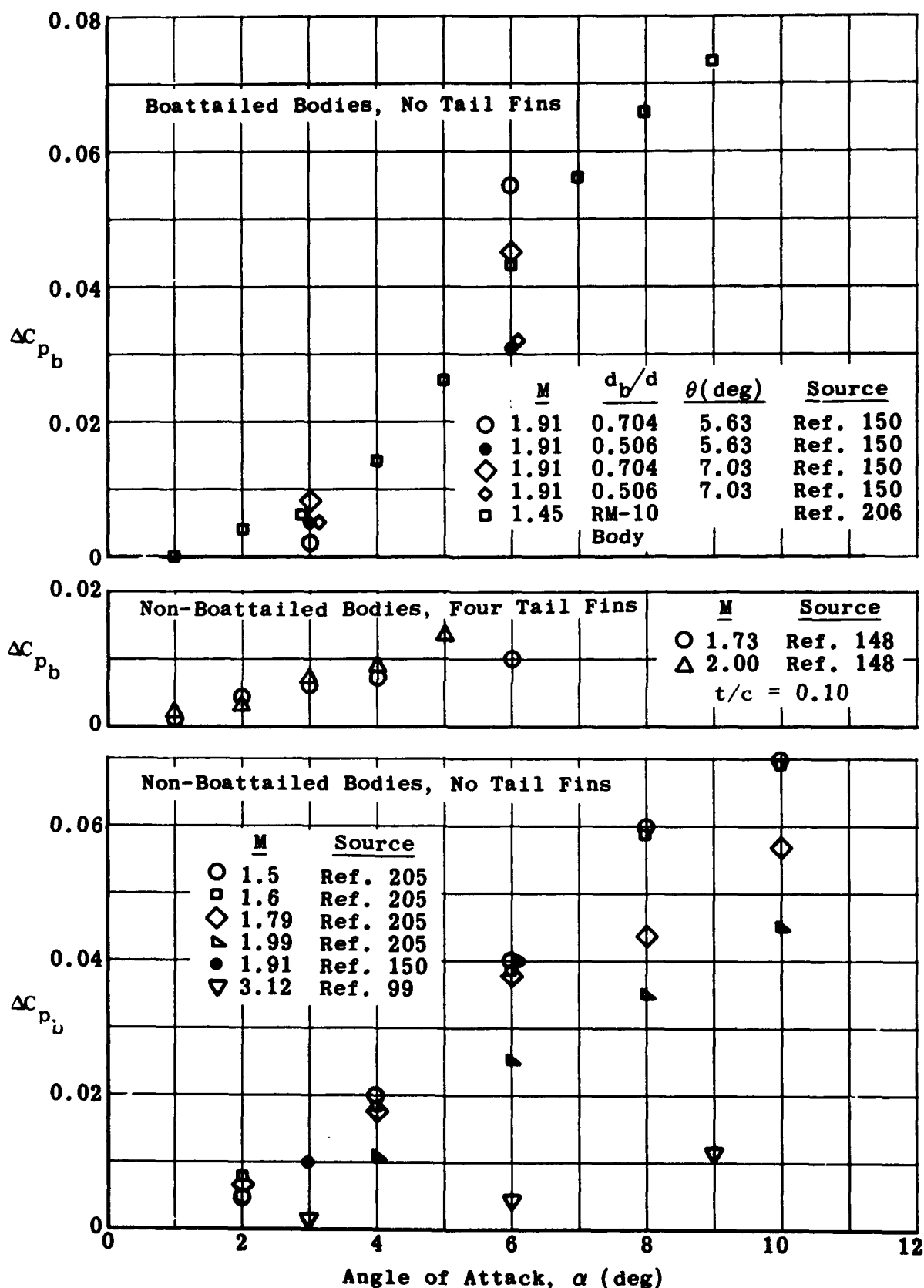M = 3.24 and 4.24. (Source: Refs. 145 and 163)

Fig. 7-15. Effect of angle of attack on base pressure for various
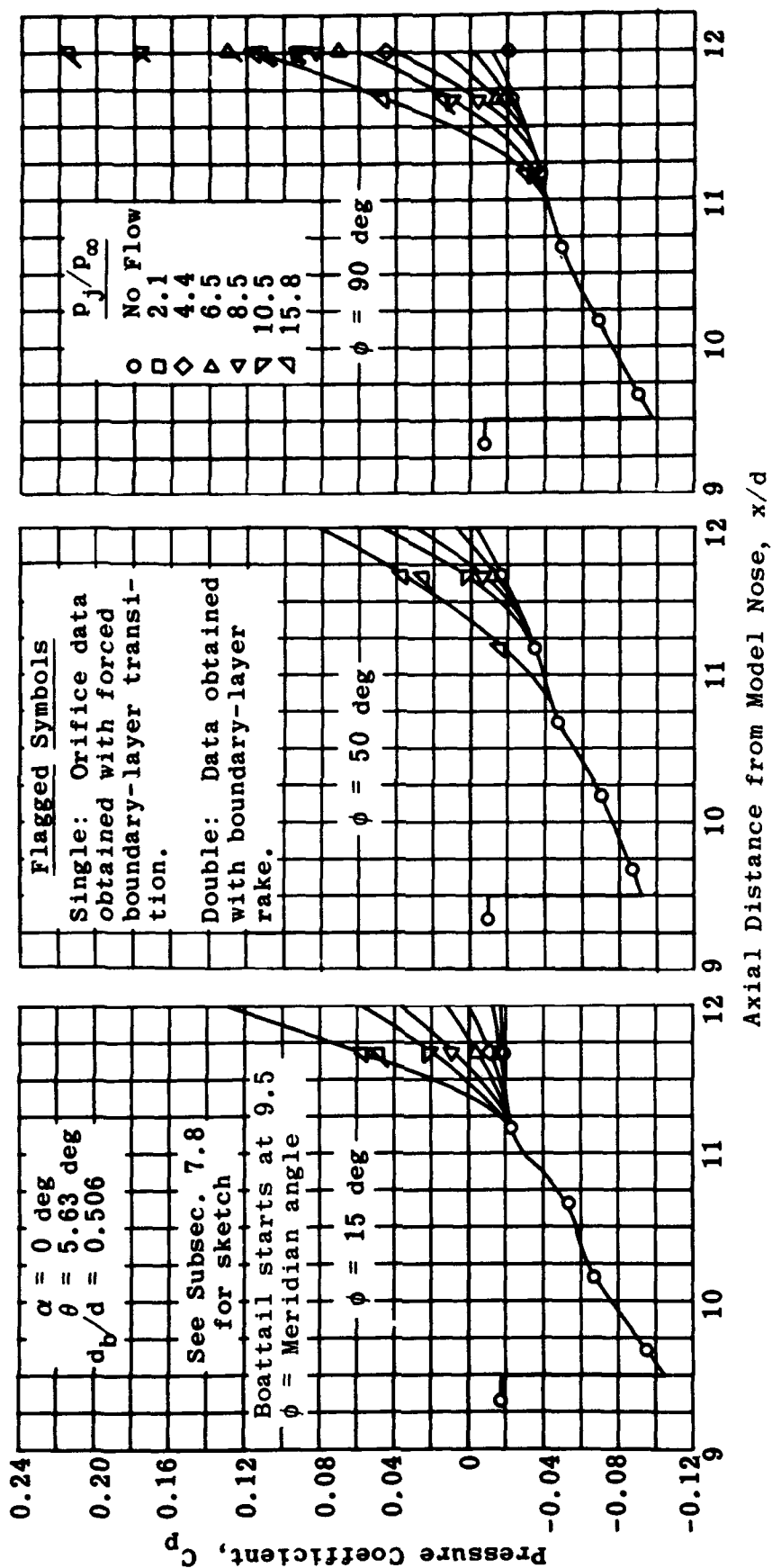bodies at Mach numbers of 1.5 to 3.12.

305

Fig. 7-16   NAVWEPS Report 1488 (Vol. 3, Sec. 8)

Fig. 7-16.   Distribution of pressure coefficients over a boattailed afterbody as a function of jet pressure ratio; M = 1.91, θ = 5.63 deg.   (Source: Ref. 150)

Fig. 7-17. Distribution of pressure coefficients over a boattailed afterbody as a function of jet pressure ratio; M = 1.91, θ = 7.03 deg. (Source: Ref. 150)

Fig. 7-18   NAVWEPS Report 1488 (Vol. 3, Sec. 8)

Fig. 7-18. Distribution of pressure coefficients over a boattailed afterbody as a function of jet pressure ratio; M = 1.91, θ = 9.33 deg. (Source: Ref. 150)
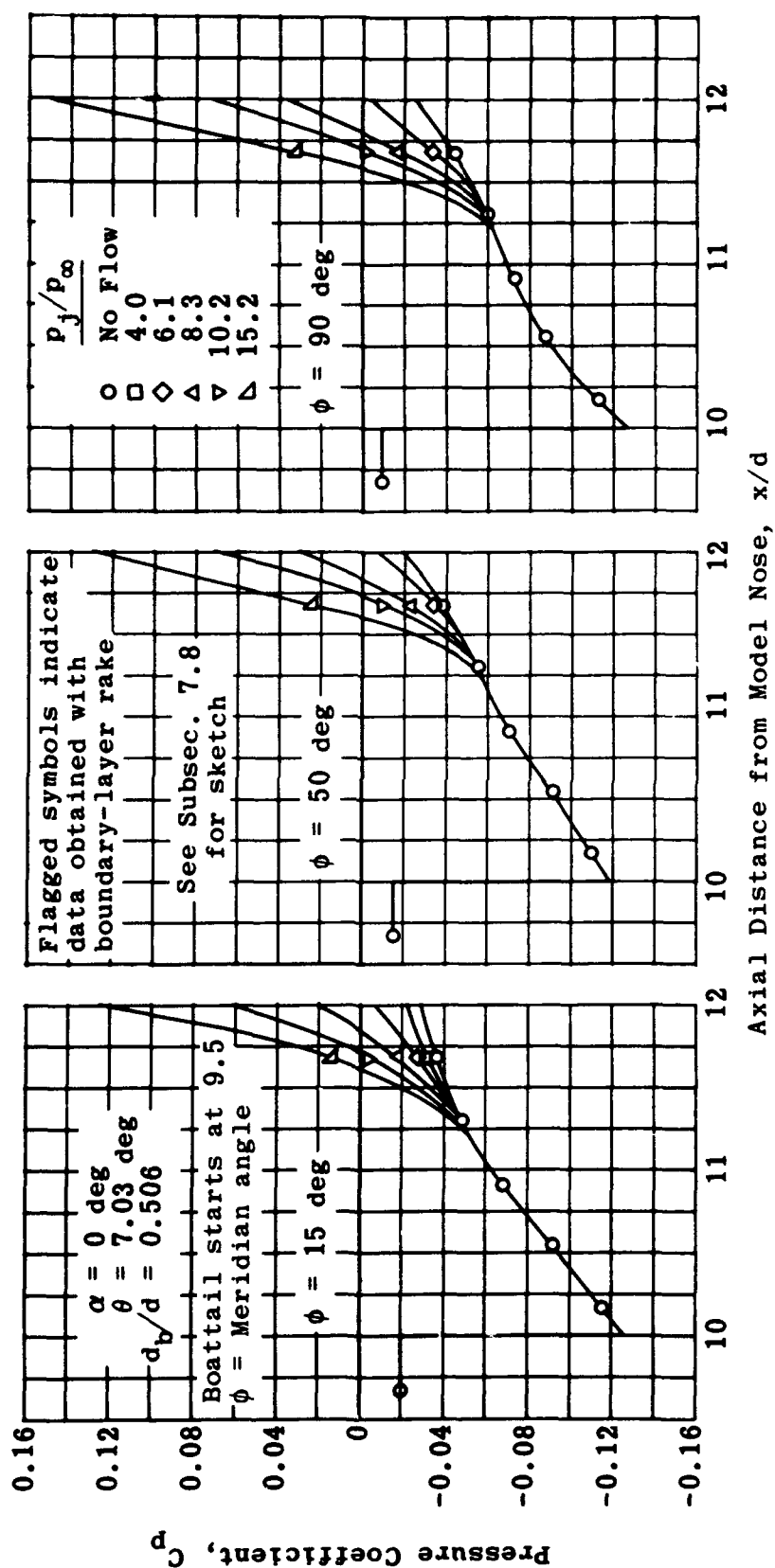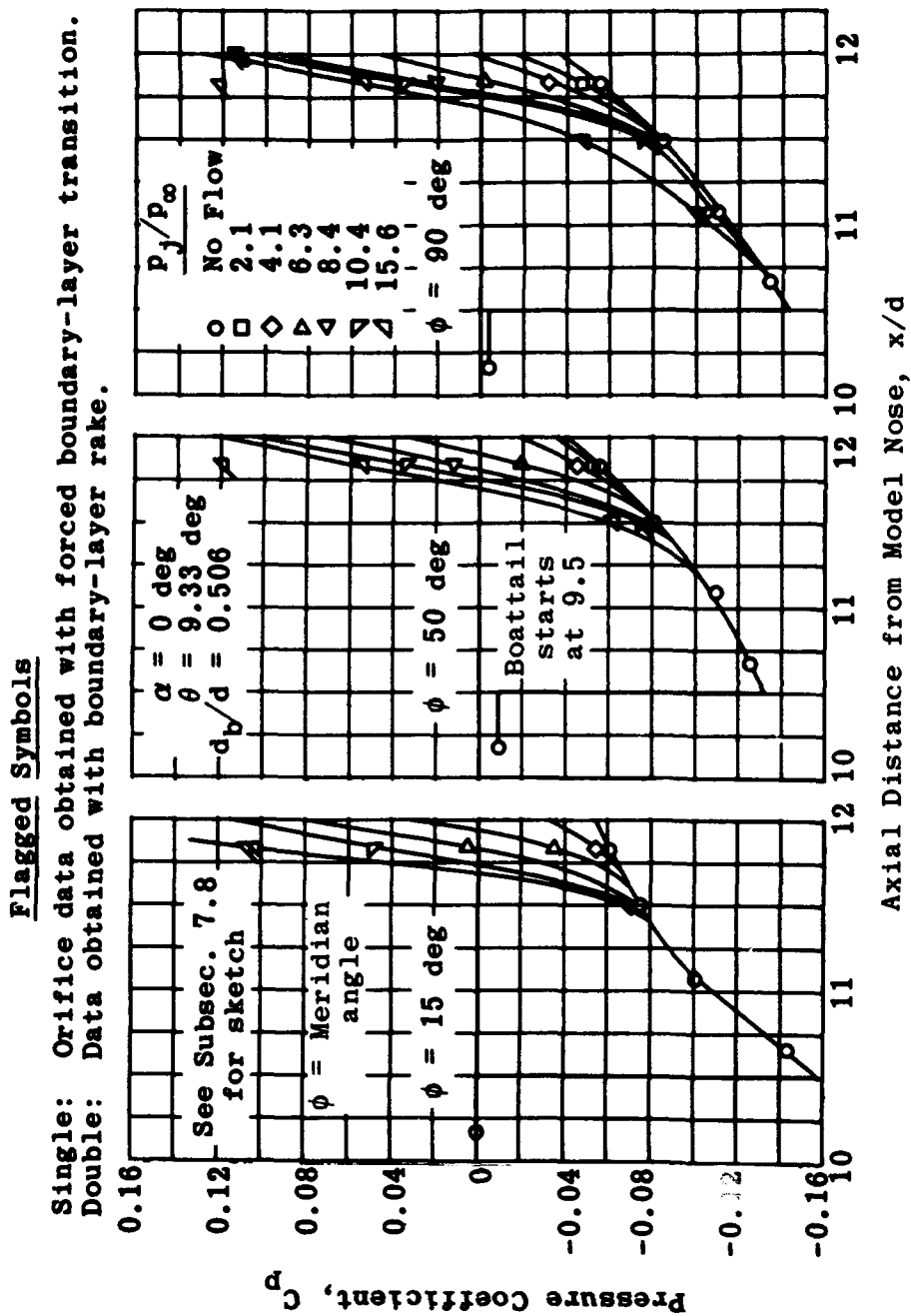
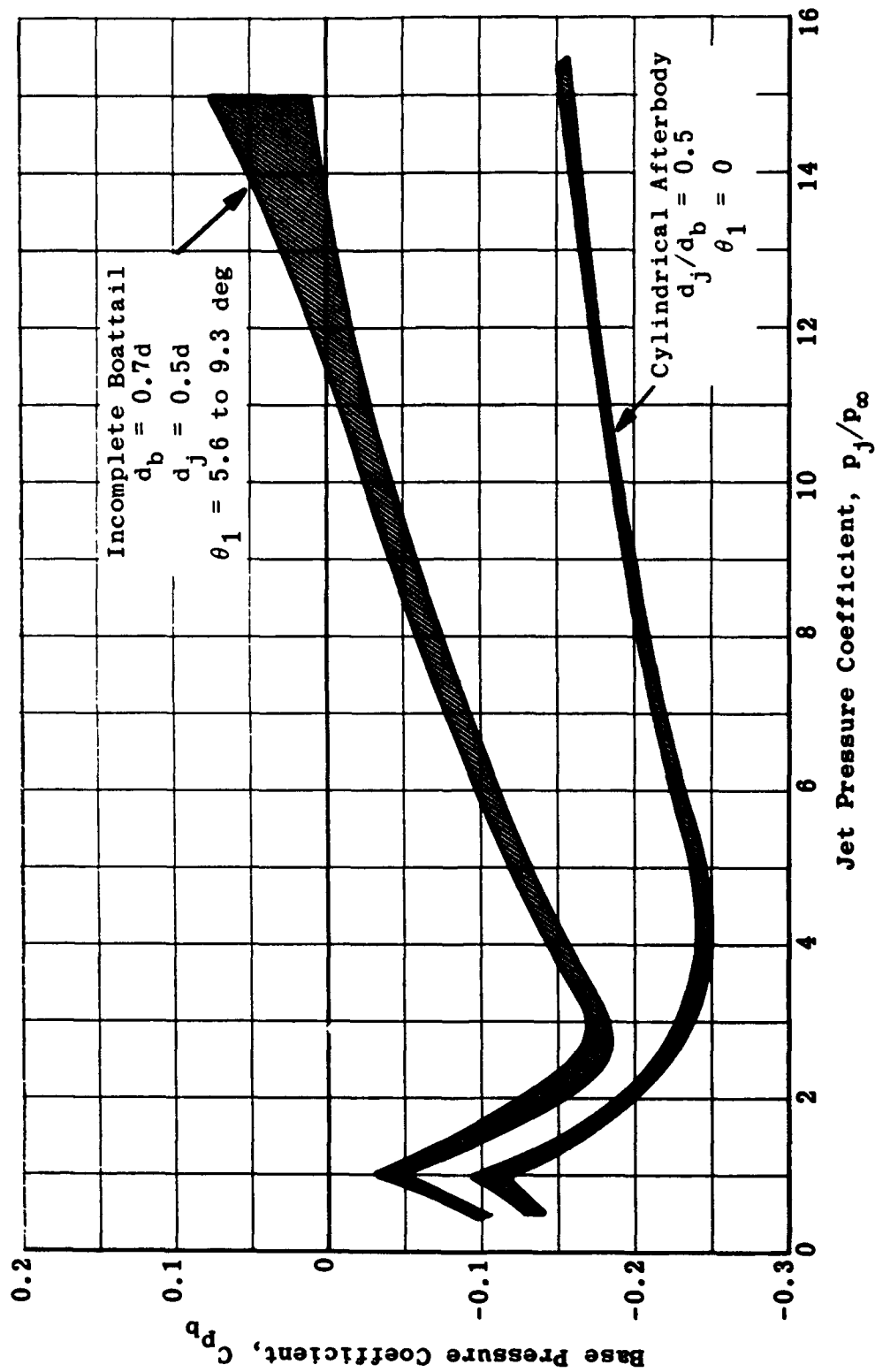**Fig. 7-19.** Envelopes of mean variations of base pressure with jet-pressure ratio at M = 1.91; α = 0 to 6 deg. (Source: Ref. 150)

Fig. 7-20   NAVWEPS Report 1488 (Vol. 3, Sec. 8)

Fig. 7-20. Variation of total afterbody drag with boattail angle in terms of jet-pressure ratio for complete boattails; M = 1.91. (Source: Ref. 150)
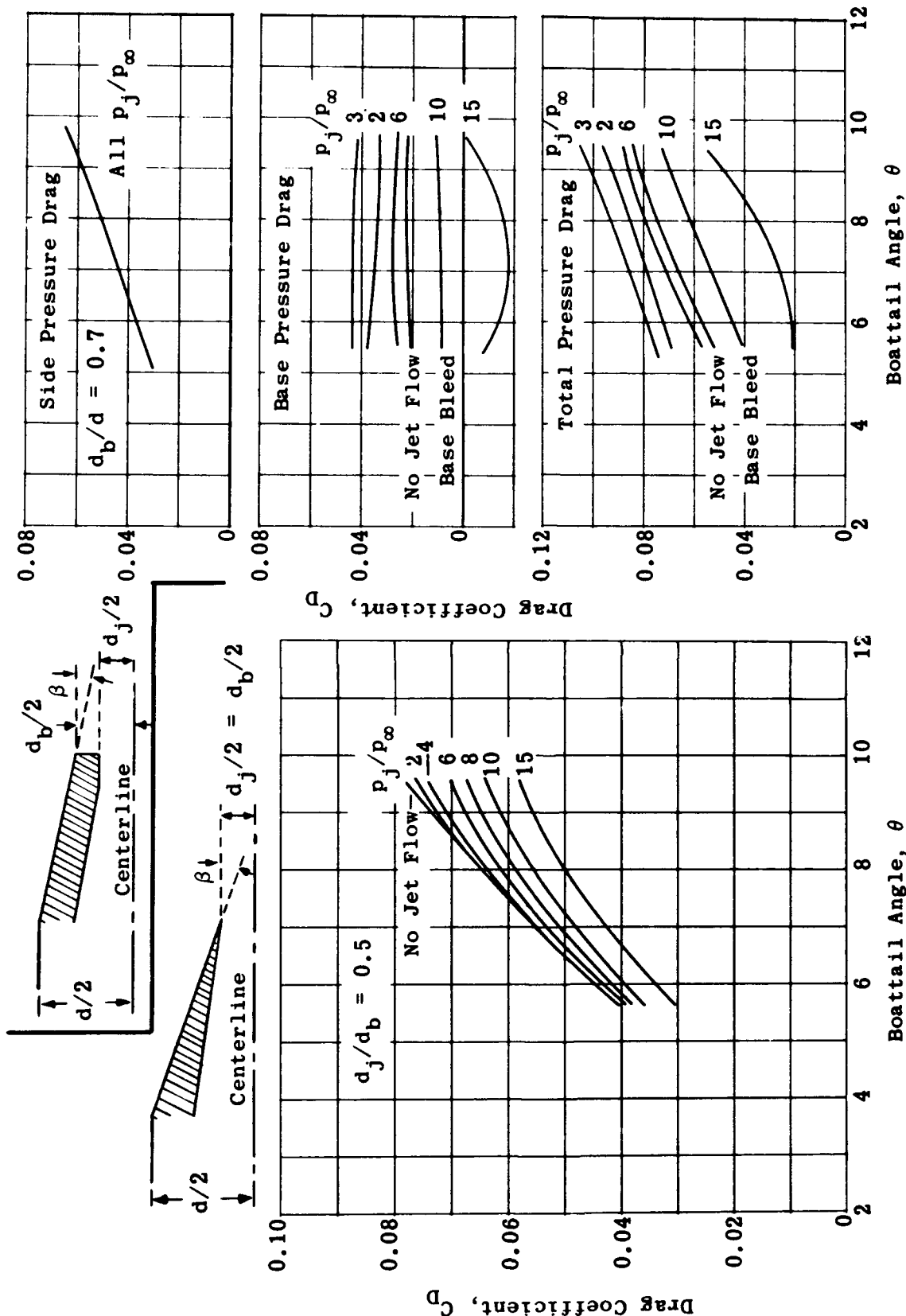
Fig. 7-21. Variation of total afterbody drag with boattail angle in terms of jet-pressure ratio for incomplete boattails; M = 1.91. (Source: Ref. 150)
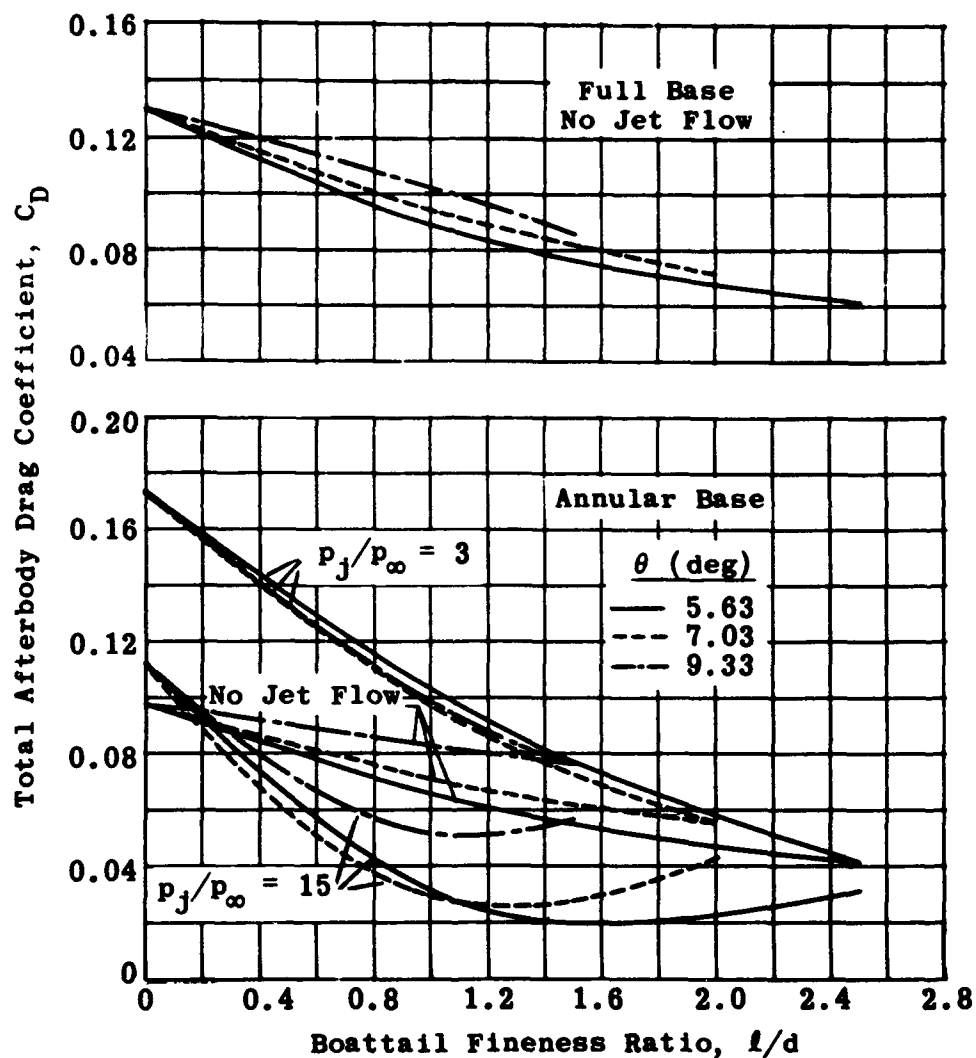
Fig. 7-22. Variation of total afterbody drag with boattail fine-
          ness ratio in terms of jet pressure ratio for full and
          annular bases; M = 1.91. (Source: Ref. 150)

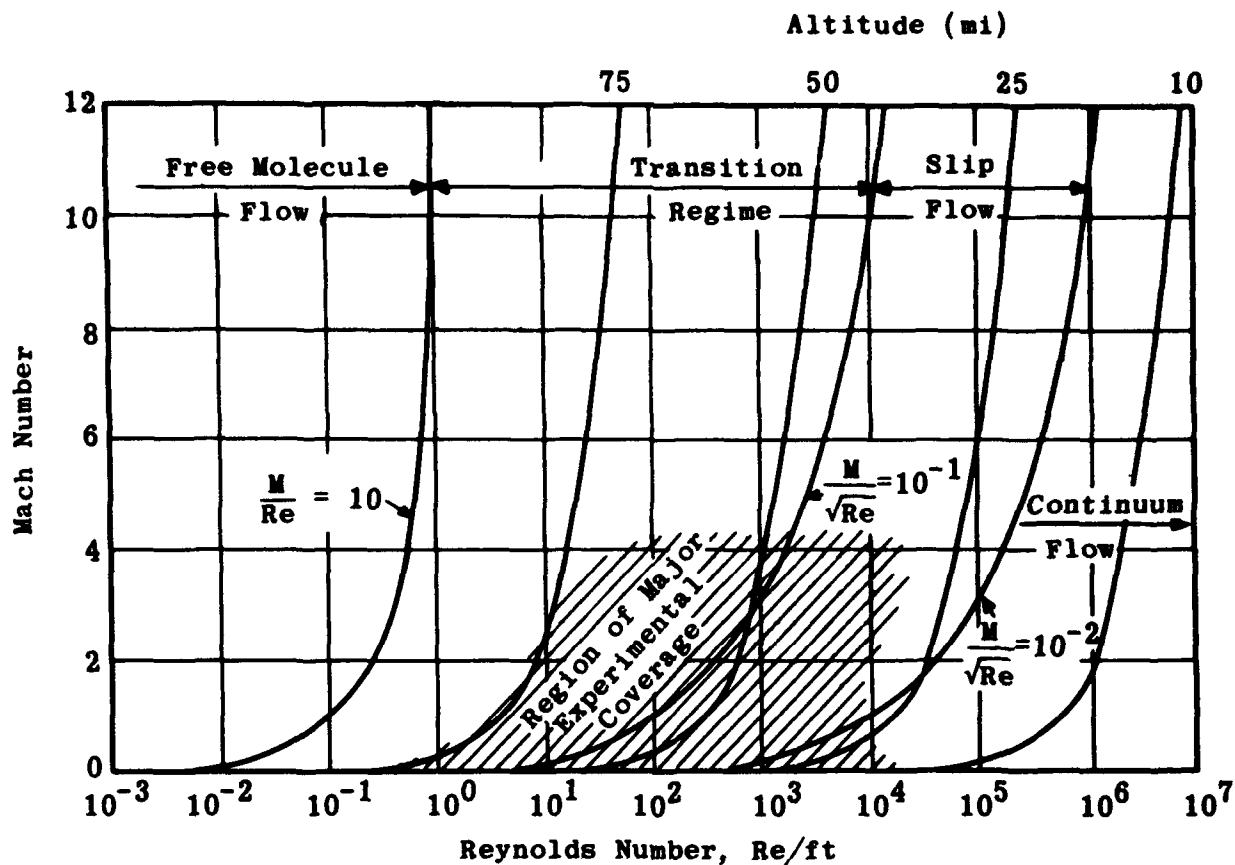Fig. 7-23   NAVWEPS Report 1488 (Vol. 3, Sec. 8)

Fig. 7-23. Boundaries of continuum, slip, and molecular flow
regimes. (Source: Ref. 170)
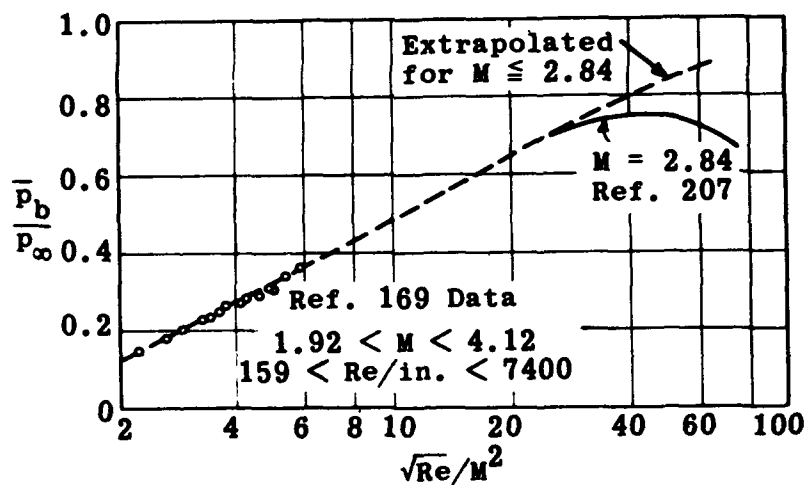
Fig. 7-24. Correlation of base-pressure distribution in the slip-
flow regime. (Source: Ref. 169)

$$\frac{p_b}{p_\infty} = \left(\frac{1}{2} - \frac{S}{\sqrt{\pi}}\right) \exp{(-S^2)}$$
$$+ \left(\frac{1}{2} + S^2 - \frac{S\sqrt{\pi}}{2}\right) \text{erfc (S)}$$
$$S = \frac{\sqrt{\gamma}}{2} M$$
$$\gamma = 1.4$$
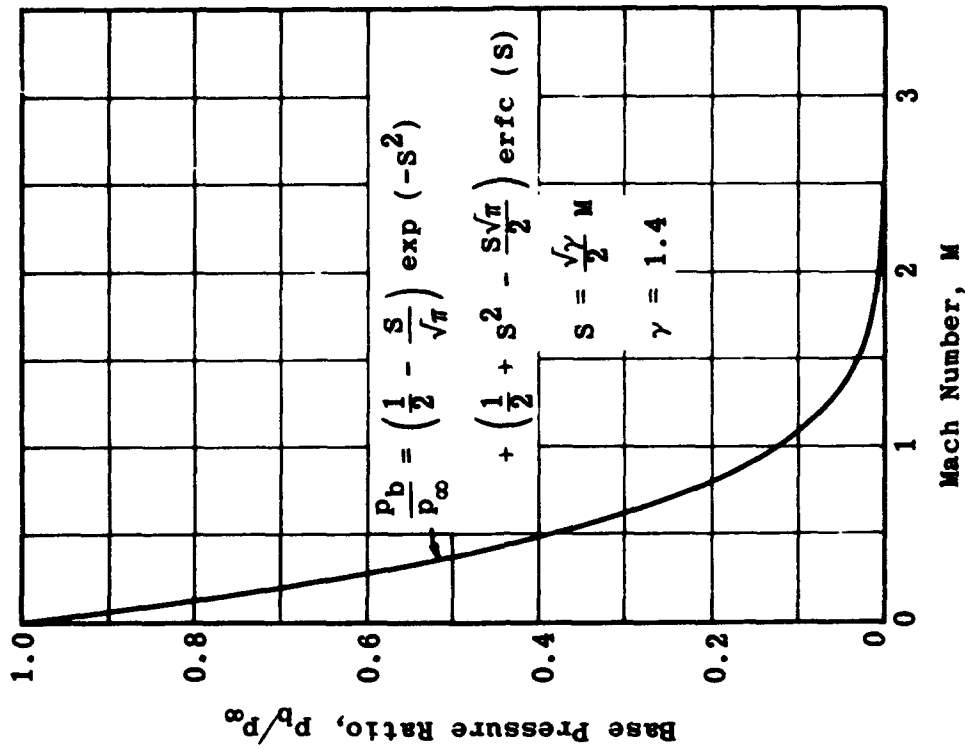
Fig. 7-26. Theoretical base-pressure coefficient in free molecular flow. (Source: Ref. 169)

$$\frac{p_b}{\overline{p}_b} = 1.59 - 1.18\left(\frac{y}{r}\right)^2$$

Experimental Data
$$1.96 \leq M \leq 4.12$$
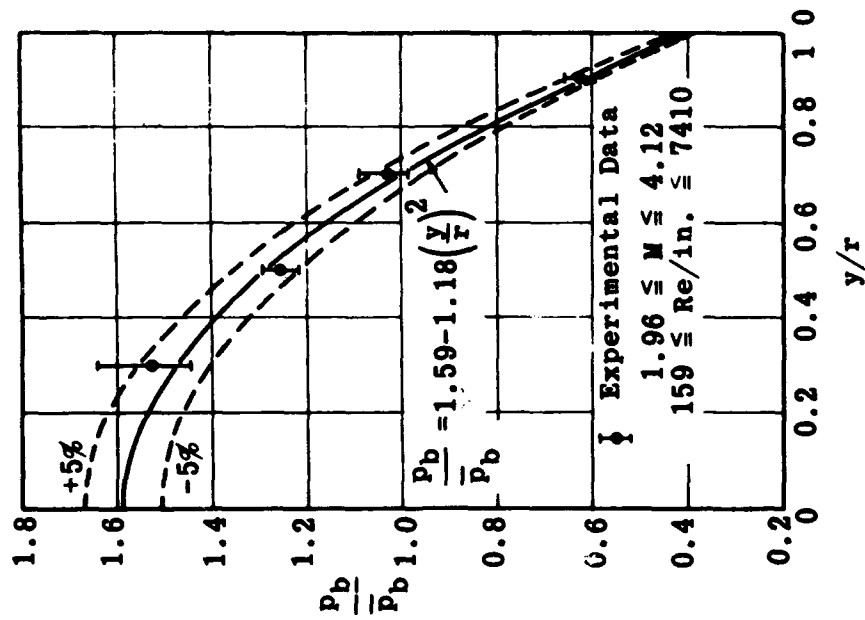$$159 \leq \text{Re/in.} \leq 7410$$

Fig. 7-25. Base-pressure distribution in the slip-flow regime. (Source: Ref. 169)

REFERENCES

1. Lighthill, M. J. "Supersonic Flow Past Slender Pointed Bodies of Revolution at Yaw," Quart. J. Mech. and Appl. Math., Vol. I, Pt. I (March 1948), pp. 76-89.

2. Van Dyke, M. D. "First- and Second-Order Theory of Supersonic Flow past Bodies of Revolution," J. Aeronaut. Sci., Vol. 18 (March 1951), pp. 161-178.

3. von Karman, T. and Moore, N. B. "The Resistance of Slender Bodies Moving with Supersonic Velocities, with Special Reference to Projectiles," Trans. ASME, Vol. 54 (1932), pp. 303-310.

4. Tsien, H. S. "Supersonic Flow over an Inclined Body of Revolution," J. Aeronaut. Sci., Vol. 12 (October 1938), pp. 480-483.

5. Sauer, R. Introduction to Theoretical Gas Dynamics (Translated by F. K. Hill and R. A. Alpher). Ann Arbor: Edwards Bros., Inc., 1947, pp. 77-81.

6. Ferri, A. Elements of Aerodynamics of Supersonic Flows. New York: MacMillan Company, 1949, pp. 210-235.

7. Brown, C. E. and Parker, H. N. A Method for the Calculation of External Lift, Moment, and Pressure Drag of Slender Open-Nose Bodies of Revolution at Supersonic Speeds. NACA Report 808, 1945.

8. Van Dyke, M. D. Practical Calculation of Second-Order Supersonic Flow past Nonlifting Bodies of Revolution. NACA TN 2744, July 1952.

9. Van Dyke, M. D. A Study of Second-Order Supersonic Flow Theory. NACA Report 1081, 1952.

10. von Karman, T. "The Problem of Resistance in Compressible Fluids," Proceedings of the Fifth Volta Congress, Rome (1935), pp. 255-264.

11. Lighthill, M. J. Supersonic Flow Past Bodies of Revolution, ARC 8321 (R and M 2003). Ministry of Supply, Aeronautical Research Council. London: Her Majesty's Stationery Office, 1945.

12. Laitone, E. V. "The Linearized Subsonic and Supersonic Flow about Inclined Slender Bodies of Revolution," J. Aeronaut. Sci., Vol. 14 (November 1947), pp. 631-642.

13. Broderick, J. B. "Supersonic Flow Round Pointed Bodies of Revolution," Quart. J. Mech. and Appl. Math., Vol. II, Pt. I (March 1949), pp. 98-120.

14. Munk, M. M. The Aerodynamic Forces on Airship Hulls. NACA TN 184, 1924.

15. Ward, G. N. "Supersonic Flow Past Slender Pointed Bodies," Quart. J. Mech. and Appl. Math., Vol. 2, Pt, I (March 1949), pp. 75-97.

16. Lamb, H. Hydrodynamics. New York: Dover Publications, 1945.

17. Tollmein, W. and Schafer, M. Rotations-symmetrische Potential-Stromungen. Archiv. Nr. 44/4, Technische Hochschule, Dresden, 1940.

18. Cronvich, L. L. "A Numerical-Graphical Method of Characteristics for Axially Symmetric Isentropic Flow," J. Aeronaut. Sci., Vol. 15, No. 3 (March 1948), pp. 155-162.

19. Kisenko, M. S. Comparative Results of Tests on Several Different Types of Nozzles. NACA TM 1066, June 1944.

20. Ferri, A. Application of the Method of Characteristics to Supersonic Rotational Flow. NACA TN 1135 (or NACA Report 841), September 1946.

21. Taylor, G. I. and Maccoll, J. W. "The Air Pressure on a Cone Moving at High Speeds - I and II," Proc. Roy. Soc. London, Series A, Vol. 139 (February 1933), pp. 278-311.

22. Kopal, Z., et al. Tables of Supersonic Flow around Cones. TR No. 1, Massachusetts Institute of Technology, 1947.

23. Eggers, A. J., Jr. and Savin, R. C. Approximate Methods for Calculating the Flow about Nonlifting Bodies of Revolution at High Supersonic Airspeeds. NACA TN 2579, December 1951.

24. Savin, R. C. Application of the Generalized Shock-Expansion Method to Inclined Bodies of Revolution Traveling at High Supersonic Airspeeds. NACA TN 3349, April 1955.

25. Rossow, V. J. Applicability of the Hypersonic Similarity Rule to Pressure Distributions Which Include the Effects of Rotation for Bodies of Revolution at Zero Angle of Attack. NACA TN 2399, June 1951.

26. Syvertson, C. A. and Dennis, D. H. A Second-Order Shock-Expansion Method Applicable to Bodies of Revolution near Zero Lift. NACA Report 1328, 1957 (Supersedes NACA TN 3527).

27. Fenter, F. W. An Approximate Method for the Calculation of the Aerodynamic Characteristics of Ogive-Cylinders near Zero Lift. Report 390, Defense Research Laboratory, University of Texas (JHU/APL Bumblebee CF-2547), January 1957.

28. Applied Physics Laboratory, The Johns Hopkins University. Handbook of Supersonic Aerodynamics, NAVORD Report 1488, Vol. 2, Sec. 5, "Compressible Flow Tables and Graphs," 1953.

29. Staff of the Ames Aeronautical Laboratory. Equations, Tables, and Charts for Compressible Flow. NACA Report 1135, 1953.

30. Ehret, D. M., Rossow, V. J., and Stevens, V. I. An Analysis of the Applicability of the Hypersonic Similarity Law to the Study of Flow about Bodies of Revolution at Zero Angle of Attack. NACA TN 2250, December 1950.

31. Ehret, D. M. Accuracy of Approximate Methods for Predicting Pressures on Pointed Bodies of Revolution in Supersonic Flow. NACA TN 2764, August 1952.

32. Tsien, H. S. "Similarity Laws of Hypersonic Flows," _J. Math. and Phys._, Vol. 25 (October 1946), pp. 247-251.

33. Hayes, W. D. "On Hypersonic Similitude," _Quart. Appl. Math._, Vol. 5 (April 1947), pp. 105-106.

34. Van Dyke, M. D. "The Combined Supersonic-Hypersonic Similarity Rule," _J. Aeronaut. Sci._, Vol. 18 (July 1951), pp. 499-500.

35. Van Dyke, M. D. "Applications of Hypersonic Small Disturbance Theory," _J. Aeronaut. Sci._, Vol. 21 (March 1954), pp. 179-186.

36. Spreiter, J. R. On the Application of Transonic Similarity Rules. NACA TN 2726, June 1952.

37. Eggers, A. J. and Savin, R. C. A Unified Two-Dimensional Approach to the Calculation of Three-Dimensional Hypersonic Flows with Applications to Bodies of Revolution. NACA Report 1249 (Supercedes NACA TN 2811), 1955.

38. Zienkewicz, H. V. A Method of Calculating Pressure Distributions on Circular Arc Ogives at Zero Incidence at Supersonic Speeds Using the Prandtl-Meyer Flow Relations. Report L.A. 024, English Electric Company, N.P.D., Luton, January 1952.

39. Bolton-Shaw, B. W. and Zienkewicz, H. V. The Rapid Accurate Prediction of Pressure on Non-Lifting Ogival Heads of Arbitrary Shape at Supersonic Speeds. Report L.A.t 034, English Electric Company, N.P.D., Luton, June 1952.

40. Ivey, H. R., Klunker, B., and Bowen, E. N. A Method for Determining the Aerodynamic Characteristics of Two and Three Dimensional Shapes at Hypersonic Speeds. NACA TN 1613, July 1948.

41. Grimminger, G., Williams, R. P., and Young, G. B. W. "Lift on Inclined Bodies of Revolution in Hypersonic Flow," _J. Aeronaut. Sci._, Vol. 17, No. 11 (November 1950).

42. Eggers, A. J., Jr., Dennis, D. H., and Resnikoff, M. M. Bodies of Revolution for Minimum Drag at High Supersonic Air Speeds. NACA Report 1306 (Supersedes NACA RM A51K27), 1958.

43. Lees, L. "Note on the Hypersonic Similarity Law for an Unyawed Cone," _J. Aeronaut. Sci._, Vol. 18 (October 1951), pp. 700-702.

44. Allen, H. J. and Perkins, E. W. A Study of Effects of Viscosity on Flow over Slender Inclined Bodies of Revolution. NACA Report 1048, 1951.

45. Allen, H. J. and Perkins, E. W. Characteristics of Flow over Inclined Bodies of Revolution. NACA RM A50L07, March 1951.

46. Hill, J. A. F. Forces on Slender Bodies at Angles of Attack. MIT NSL R-a-100-59, Massachusetts Institute of Technology Naval Supersonic Laboratory, May 1950.

47. Kelly, H. R. The Estimation of Normal Force and Pitching Moment Coefficients for Blunt-Based Bodies of Revolution at Large Angles of Attack. NOTS TM 998, Ballistics Division Aerodynamics Branch, U. S. Naval Ordnance Test Station, Inyokern, Calif., May 1953.

48.   Jones, R. T. Effects of Sweepback on Boundary Layer and Separation. NACA Report 884, 1947.

49.   Young, A. D. and Booth, T. B. "The Profile Drag of Yawed Wings of Infinite Span," Aeronaut. Quart., Vol. 3 (1951-52), pp. 211-229.

50.   Goldstein, S.,(Editor). Modern Developments in Fluid Dynamics (Vols. I and II). Oxford: The Clarendon Press, 1938.

51.   Schwabe, M. Pressure Distribution in Nonuniform Two-Dimensional Flow. NACA TM 1039, January 1943.

52.   Perkins, E. W. and Jorgensen, L. H. Comparison of Experimental and Theoretical Normal-Force Distributions (Including Reynolds Number Effects) on an Ogive-Cylinder Body at Mach Number 1.98. NACA TN 3716, May 1956.

53.   Mello, J. F. "Investigation of Normal Force Distributions and Wake Vortex Characteristics of Bodies of Revolution at Supersonic Speeds," J. Aero/Space Sci., Vol. 26, No. 3 (March 1959).

54.   Gowen, F. E. and Perkins, E. W. Drag of Circular Cylinders for a Wide Range of Reynolds Numbers and Mach Numbers. NACA TN 2960, June 1953.

55.   Kopal, Z., et al. Tables of Supersonic Flow Around Yawing Cones, MIT TR 3, Massachusetts Institute of Technology, 1947.

56.   Gowen, F. E. and Perkins, E. W. A Study of the Effects of Body Shape on the Vortex Wakes of Inclined Bodies at a Mach Number of 2. NACA RM A53I17, December 1953.

57.   Perkins, E. W. and Kuehn, D. M. Comparison of the Experimental and Theoretical Distributions of Lift on a Slender Inclined Body of Revolution at M = 2. NACA TN 3715 (Supersedes NACA RM A53E01, August 1953), May 1956.

58.   Gowen, F. E. Buffeting of a Vertical Tail on an Inclined Body at Supersonic Mach Numbers. NACA RM A53A09, March 1953.

59.   Ferri, A. Supersonic Flow Around Circular Cones at Angles of Attack. NACA Report 1045, 1953.

60.   Roberts, R. C. and Riley, J. D. "A Guide to the Use of the M.I.T. Cone Tables," J. Aeronaut. Sci., Vol. 21 (May 1954), pp. 336-342.

61.   Cronvich, L. L. Results of Experimental Studies of Pressure Distributions on Cones at Supersonic Velocities. TG-91, Applied Physics Laboratory, The Johns Hopkins University, November 1950.

62.   Van Dyke, M. D., Young, G. B. W., and Siska, C. "Proper Use of M.I.T. Tables for Supersonic Flow Past Inclined Cones," J. Aeronaut. Sci., Vol. 18 (1951), pp. 355-356.

63.   Clippinger, R. F., Giese, J. H., and Carter, W. C. Tables of Supersonic Flows About Cone Cylinders, Part I, Surface Data; Part II, Complete Flows. APG/BRL Report 729, Ballistics Research Laboratory, Aberdeen Proving Ground, July-August 1950.

64. Stone, A. H. "On Supersonic Flow Past a Slightly Yawing Cone, I,"
    J. Math. and Phys., Vol. 27 (1948), pp. 67-81.

65. Stone, A. H. "On Supersonic Flow Past a Slightly Yawing Cone, II,"
    J. Math. and Phys., Vol. 30 (1951-52), pp. 200-213.

66. Kopal, Z., et al. Tables of Supersonic Flow Around Cones of Large
    Yaw. TR 5, Massachusetts Institute of Technology, 1949.

67. Holt, M. and Blackie, J. "Experiments on Circular Cones at Yaw in
    Supersonic Flow," J. Aeronaut. Sci., Vol. 23, No. 10 (October
    1956).

68. Young, G. B. W. and Siska, C. P. "Supersonic Flow Around Cones at
    Large Yaw," J. Aeronaut. Sci., Vol. 19, No. 2 (February 1952),
    pp. 111-119.

69. Kahane, A. and Solarski, A. "Supersonic Flow About Slender Bodies
    of Elliptical Cross-Section," J. Aeronaut. Sci., Vol. 20, No. 8
    (August 1953).

70. Ferri, A., Ness, N., and Kaplita, T. T. "Supersonic Flow Over
    Conical Bodies without Axial Symmetry," J. Aeronaut. Sci.,
    Vol. 20, No. 8 (August 1953), pp. 563-584.

71. Ferri, A. The Linearized Characteristics Method and its Applica-
    tion to Practical Non-Linear Supersonic Problems. NACA TN 2515,
    October 1951.

72. Konrad, T. G. and Boyer, F. S. An Investigation of Annular Isen-
    tropic Spike Diffusers having a Design Mach No. of 5. CF-2774,
    Applied Physics Laboratory, The Johns Hopkins University,
    November 1958.

73. Dunn, E. L. Some Results of a Systematic Theoretical Pressure
    Distribution Program on Bodies of Revolution. NOTS TM 919,
    Ballistics Division, Aerodynamics Branch, U. S. Naval Test
    Station, Inyokern, Calif., April 1953.

74. Dye, F. E., Jr. A Comparison of Pressures Predicted by Exact and
    Approximate Theories with Some Experimental Results on an
    Ogival Nosed Body at a Mach Number of 2.0. CF Report 1723,
    Cornell Aeronautical Laboratory, December 1951.

75. Jack, J. R. Theoretical Wave Drags and Pressure Distributions
    for Axially Symmetric Open-Nose Bodies. NACA TN 2115, June 1950.

76. Eggers, A. J., Jr., Savin, R. C., and Syvertson, C. A. The Genera-
    lized Shock Expansion Method and Its Application to Bodies Trav-
    eling at High Supersonic Airspeeds. Report 487, Instrument
    Society of America, 1954.

77. Moeckel, W. E. Use of Characteristic Surfaces for Unsymmetrical
    Supersonic Flow Problems. NACA TN 1849, 1949.

78. Ward, G. N. "The Approximate External and Internal Flow Past a
    Quasi-Cylindrical Tube Moving at Supersonic Speeds," Quart. J.
    Mech. and Appl. Math., Vol. 1, Pt. 2 (June 1948).

79.   Kennedy, E. C. External Aerodynamic Characteristics of a Series
        of Ducted Bodies as Computed by the Linear Theory for Mach Num-
        bers 1.5 to 2.5. OAL Memo 61 and 61-1, Convair/CM 820, Septem-
        ber 1954.

80.   Samanich, N. E. Pressure Drag of Axisymmetric Cowls Having Large
        Initial Angles at Mach Numbers from 1.90 to 4.90. NASA TM
        1-10-59E, January 1959.

81.   Ferrari, C. Determination of the External Contour of a Body of
        Revolution with a Central Duct so as to Give Minimum Drag in
        Supersonic Flow, with Various Perimetral Conditions Imposed
        upon the Missile Geometry. AF Report 814-A-2, November 1953.

82.   Heaslet, M. A. and Fuller, F. B. Axially Symmetric Shapes with
        Minimum Wave Drag. NACA TR 1256, 1956.

83.   Parker, H. M. Minimum-Drag Ducted and Closed Three-Point Body of
        Revolution Based on Linearized Supersonic Theory. NACA TN
        3704, December 1956.

84.   Bromm, A., Jr. and Goouwin, J. M. Investigation at Supersonic
        Speeds of the Wave Drag of Seven Boattail Bodies of Revolution
        Designed for Minimum Wave Drag. NACA TN 3054, December 1953.

85.   Van Dyke, M. D. "The Supersonic Blunt Body Problem - Review and
        Extension," J. Aeronaut. Sci., Vol. 25, No. 8 (August 1958).

86.   Julius, J. D. Experimental Pressure Distributions over Blunt Two-
        and Three-Dimensional Bodies Having Similar Cross Sections at
        a Mach Number of 4.95. NASA TN D157, December 1959.

87.   Kendall, J. M., Jr. Experiments on Supersonic Blunt-Body Flows.
        JPL/CIT Progress Report No. 20-372, February 1959.

88.   Oliver, R. E. An Experimental Investigation of Flow over Simple
        Blunt Bodies at a Nominal Mach Number of 5.8. GALCIT Memo
        No. 26, California Institute of Technology, June 1955.

89.   Hastings, S. M., Persh, J, and Redman, E. J. Experimental Investi-
        gation of the Pressure Distribution on Axially Symmetric Flat-
        Nosed Cone Typed Bodies at Supersonic and Hypersonic Speeds.
        NOL TR 5659, October 1957.

90.   Cooper, M. and Mayo, E. E. Measurements of Local Heat Transfer
        and Pressures on Six Two-Inch Diameter Blunt Bodies at a Mach
        Number of 4.95 and at Reynolds Numbers up to 81×10^6. NASA
        TM 1-3-59L, March 1959.

91.   Henderson, A. Investigation of the Flow over Simple Bodies at Mach
        Numbers of the Order of 20. NASA TN D-449, August 1960.

92.   Potter, J. L., Shapiro, N. M., and Murphree, W. D. Normal Force
        Distributions on Right Circular Cylinders in Subsonic and Super-
        sonic Flows. OML TR 2R4F, Redstone Arsenal, September 1954.

93.   Holder, D. W. and Chinneck, A. Observations of the Flow Past El-
        liptic-Nosed Two-Dimensional Cylinders and Bodies of Revolution
        in Supersonic Airstreams. British ARC 14216 (FM-1597), August
        1951.

94. Tewfik, O. K. and Giedt, W. H. Heat Transfer Recovery Factor and
     Pressure Distributions Around a Cylinder Normal to a Super-
     sonic Rarefied Air Stream, Part I Experimental Data. Insti-
     tute of Engineering Research Report HE-150-162, University of
     California, January 1959.

95. Dennis, D. H. and Cunningham, B. E. Forces and Moments on Inclined
     Bodies at Mach Numbers from 3.0 to 6.3. NACA RM A54E03, June
     1954.

96. Kennedy, E. C. Table of Pressure Coefficients for a Series of
     Bodies of Revolution with Tangent Ogive Noses and Cylindrical
     After-Bodies at Several Mach Numbers Computed by the Linearized
     Theory. Ordnance Aerophysics Laboratory (Unpublished Report).

97. Demeritte, F. J. and Darling, J. A. Aeroballistic Research In-
     vestigation of Body-Alone Models. NOL Memo 10132, May 1950.

98. Buford, W. E. "The Effects of Afterbody Length and Mach Number
     on the Normal Force and Center of Pressure of Conical and
     Ogival Nose Bodies," J. Aeronaut. Sci., Vol. 25, No. 2
     (February 1958), p. 103.

99. Jack, J. R. and Burgess, W. C. Aerodynamics of Slender Bodies at
     Mach Number of 3.12 and Reynolds Numbers from 2×10^6 to
     15×10^6. I - Body of Revolution with Near-Parabolic Forebody
     and Cylindrial After-Body. NACA RM E51H13, November 1951.

100. Van Dyke, M. D. A Study of Hypersonic Small-Disturbance Theory.
     NACA TN 3173, May 1954.

101. Deep, R. A. and Henderson, J. H. Study of Aerodynamic Character-
     istics of Cone Cylinder Conical Frustrum Bodies by Linearized
     Theory of Supersonic Flow. Ordnance Missile Laboratory Re-
     port 6R2P, June 1955.

102. Dorrance, W. H. and Norell, R. G. "Correlation of Cone-Cylinder
     Normal Force and Pitching Moment Data by the Hypersonic Simi-
     larity Law," J. Aeronaut. Sci., Vol. 24, No. 5 (May 1957).

103. Ridyard, H. W. The Aerodynamics Characteristics of Two Series of
     Lifting Bodies at Mach Number 6.86. NACA RM L54C15, May 1954.

104. Sanger, E. and Bredt, J. A Rocket Drive for Long Range Bombers.
     Trans. CGD-32, Technical Information Branch, Navy Bureau of
     Aeronautics, August 1944.

105. Dorrance, W. H. "Nonsteady Supersonic Flow about Pointed Bodies
     of Revolution," J. Aeronaut. Sci., Vol. 18, No. 8 (August 1951),
     pp. 505-511.

106. Nicolaides, J. D. and Brady, J. J. Magnus Moments on Pure Cones
     in Supersonic Flight. NAVORD Report 6183, U. S. Naval Ordnance
     Laboratory, January 1959.

107. Greene, J. E. A Summary of Experimental Magnus Characteristics
     of a 7 and 5 Caliber Body of Revolution at Subsonic Through
     Supersonic Speeds. NAVORD Report 6110, U. S. Naval Ordnance
     Laboratory, August 1958.

108. Zienkewicz, H. V. Theoretical Wave Drag of Circular Arc Ogives
     at Zero Incidence. Report No. L.A.t. 027, English Electric
     Co., Luton, March 1952.

109. Chapman, D. R. and Perkins, E. W. Experimental Investigation of
     the Effects of Viscosity on the Drag and Base Pressure of Bodies
     of Revolution at a Mach Number of 1.5. NACA TR 1036 (Supersedes
     NACA RM A7A31a), 1951.

110. Cronvich, L. L. and Edelman, G. M. Drag Calculations for Ducted
     and Non-Ducted Cone-Cylinder Bodies. CF-1360, The Applied
     Physics Laboratory, The Johns Hopkins University, October 1949.

111. Adams, M. C. Determination of Shapes of Boattail Bodies of Revo-
     lution for Minimum Wave Drag. NACA TN 2550, November 1951.

112. Haack, W. Projectile Shapes for Smallest Wave Drag Translation.
     ATI No. 27736, Air Materiel Command, U. S. Air Force, Brown
     University, 1948.

113. Harder, K. C. and Renneman, C. On Boattail Bodies of Revolution
     Having Minimum Wave Drag. NACA TR 1271, 1956.

114. Bromm, A. and Goodwin, J. M. Investigation at Supersonic Speeds
     of the Wave Drag of Seven Boattail Bodies of Revolution De-
     signed for Minimum Wave Drag. NACA TN 3054, December 1953.

115. Parker, H. M. Minimum Drag Ducted and Pointed Bodies of Revolu-
     tion Based on Linearized Supersonic Theory. NACA TR 1213
     (Supersedes TN 3189), 1955.

116. Hart, R. G. and Katz, E. R. Flight Investigations at High-Subsonic,
     Transonic and Supersonic Speeds to Determine Zero-Lift Drag of
     Fin-Stabilized Bodies of Revolution Having Fineness Ratios of
     12.5, 8.91, and 6.04 and Varying Positions of Maximum Diameter.
     NACA RM L9I30, November 1949.

117. Whitman, G. B. "The Behavior of Supersonic Flow Past a Body of
     Revolution, Far from the Axis," Proc. Roy. Soc. London, Series
     A, Vol. 201 (March 1950), pp. 89-109.

118. Busemann, A. A Review of Analytical Methods for the Treatment of
     Flows with Detached Shocks. NACA TN 1856, April 1949.

119. Moeckel, W. E. Flow Separation Ahead of Blunt Bodies at Supersonic
     Speeds. NACA TN 2418, July 1951.

120. Hansche, G. E. and Rinehart, J. S. "Air Drag on Cubes at Mach Num-
     bers 0.5 to 3.5," J. Aeronaut. Sci. (February 1952).

121. Charters, A. C. and Thomas, R. N. "The Aerodynamic Performance of
     Small Spheres from Subsonic to High Supersonic Velocities,"
     J. Aeronaut. Sci., Vol. 12, No. 4 (October 1945).

122. May, H. and Witt, W. R. Jr. "Free Flight Determination of the
     Drag Coefficient of Spheres," J. Aeronaut. Sci., Vol. 21, No. 9
     (September 1953).

123. Hodges, H. A. "The Drag Coefficient of Very High Velocity Spheres,"
     J. Aeronaut. Sci., Vol. 24, No. 10 (October 1957).

124. Kane, E. D. "Sphere Drag Data at Supersonic Speeds and Low
     Reynolds Numbers," J. Aeronaut. Sci., Vol. 18, No. 4 (April
     1951).

125. Gazeley, C. "Boundary Layer Stability and Transition in Subsonic
     and Supersonic Flow," J. Aeronaut. Sci., Vol. 21 (January 1953).

126. Seban, R. A. and Bond, R. "Skin-Friction and Heat Transfer Char-
     acteristics of a Laminar Boundary Layer on a Cylinder in Axial
     Incompressible Flow," J. Aeronaut. Sci., Vol. 18 (October 1951),
     pp. 671-675.

127. Mangler, W. Compressible Boundary Layers on Bodies of Revolution.
     British ARC Report 9740, 1946.

128. Hasel, L. E., Sinclair, A. R., and Hamilton, C. V. Preliminary
     Investigation of the Drag Characteristics of the NACA RM-10
     Missile at Mach Numbers of 1.40 and 1.59 in the Langley 4-by
     4-Foot Supersonic Tunnel. NACA RM L52A14, April 1952.

129. Van Driest, E. R. "Turbulent Boundary Layer on a Cone in a Super-
     sonic Flow at Zero Angle of Attack" J. Aeronaut. Sci., Vol. 19
     (January 1952), pp. 55-57.

130. Eckert, H. U. "Simplified Treatment of the Turbulent Boundary
     Layer Along a Cylinder in Compressible Flow," J. Aeronaut. Sci.,
     Vol. 19 (January 1952), pp. 23-28.

131. Van Driest, E. R. "Turbulent Boundary Layer in Compressible
     Fluids," J. Aeronaut. Sci., Vol. 18 (March 1951), pp. 145-160.

132. Crawford, D. H. Investigation of the Flow Over a Spiked Nose
     Hemisphere-Cylinder at a Mach number of 6.8. NASA TN D-118,
     December 1959.

133. Jones, J. J. Flow Separation from Rods Ahead of Blunt Noses at
     Mach Number 2.72. NACA RM L52E05a, July 1952.

134. Chapman, D. R. and Kester, R. H. "Measurements of Turbulent Skin
     Friction on Cylinders in Axial Flow at Subsonic and Supersonic
     Velocities," J. Aeronaut. Sci. (July 1953).

135. Applied Physics Laboratory, The Johns Hopkins University. Hand-
     book of Supersonic Aerodynamics, NAVORD Report 1488, Vol. 3,
     Sec. 6, "Two-Dimensional Airfoils," 1957.

136. Hantzsche, W. and Wendt, H. The Laminar Boundary Layer on a Cone
     in a Supersonic Airstream at Zero Angle of Attack (Translated
     by K. G. Liebhold). RAT-6, Rand Corporation, November 1947.

137. Howarth, L. (Ed.). Modern Developments in Fluid Dynamics, High
     Speed Flow, Vol. I, Chap. X: "Boundary Layers" by A. D. Young.
     Oxford: The Clarendon Press, 1953.

138. Van Driest, E. R. "Turbulent Boundary Layer in Compressible
     Fluids," J. Aeronaut. Sci. (March 1951), pp. 145-160.

139. Hall, I. M. "Experiments on Supersonic Flow Over Flat Nosed Circu-
     lar Cylinders at Yaw," Phil. Mag., Vol. XLV (March 1954), p. 333.

140. Love, E. S. Base Pressure at Supersonic Speeds on Two-Dimensional Airfoils and on Bodies of Revolution With and Without Fins Having Turbulent Boundary Layers. NACA TN 3819, January 1957.

141. Crocco, L. and Lees, L. "A Mixing Theory for the Interaction Between Dissipative Flows and Nearly Isentropic Streams," J. Aeronaut. Sci., Vol. 19, No. 10 (October 1952), pp. 669-676.

142. Chapman, D. R. An Analysis of Base Pressure at Supersonic Velocities and Comparison with Experiments. NACA TR 1051 (Supersedes NACA TN 2137), 1951.

143. Gabeaud, A. "Base Pressures at Supersonic Velocities," J. Aeronaut. Sci. (Readers' Forum), Vol. 17, No. 8 (August 1950), pp. 525-526.

144. Cope, W. F. The Effect of Reynolds Number on the Base Pressure of Projectiles. Eng. Div. 63/44, British A.R.C., NPL, January 1945.

145. Kurzweg, H. H. "Interrelationship Between Boundary Layer and Base Pressure," J. Aeronaut. Sci., Vol. 18, No. 11 (November 1951), pp. 743-748.

146. Gabeaud, A. "Base Pressures at Supersonic Velocities," J. Aeronaut. Sci. (Readers' Forum), Vol. 16, No. 10 (October 1949), p. 638.

147. Lorenz, H. "Der Beschosswiderstand," Phy. Zeits., Vol. 18 (1917), p. 209; Vol. 29 (1928), p. 437.

148. Faro, I. D. V. Experimental Determination of Base Pressures at Supersonic Velocities. Bumblebee Report 106, Applied Physics Laboratory, The Johns Hopkins University, November 1949.

149. Cortright, E. M., Jr. and Schroeder, A. H. Preliminary Investigation of Effectiveness of Base Bleed in Reducing Drag of Blunt-Base Bodies in Supersonic Stream. NACA RM E51A26, March 1951.

150. Cortright, E. M., Jr. and Schroeder, A. H. Investigation at Mach Number 1.91 of Side and Base Pressure Distributions over Conical Boattails Without and With Jet Flow Issuing from Base. NACA RM E-51F26, September 1951.

151. Love, E. S., Coletti, D. E., and Bromm, A. F., Jr. Investigation of the Variation With Reynolds Number of the Base, Wave, and Skin-Friction Drag of a Parabolic Body of Revolution (NACA RM-10) at Mach Numbers of 1.62, 1.93, and 2.41 in the Langley 9-Inch Supersonic Tunnel. NACA RM L52H21, October 1952.

152. Love, E. S. and O'Donnell, R. M. Investigations at Supersonic Speeds of the Base Pressure on Bodies of Revolution With and Without Sweptback Stabilizing Fins. NACA RM L52J21a, December 1952.

153. Hill, F. K. and Alpher, R. A. "Base Pressures at Supersonic Velocities," J. Aeronaut. Sci., Vol. 16, No. 3 (March 1949), pp. 153-160.

154. Charters, A. C. and Turetsky, R. A. Determination of Base Pressure from Free-Flight Data. Report No. 653, Ballistic Research Laboratory, Aberdeen Proving Ground, 1948.

155. Peck, R. F. Flight Measurements of Base Pressure on Bodies of
       Revolution With and Without Simulated Rocket Chambers. NACA
       TN 3372 (Supersedes NACA RM L50I28a), April 1955.

156. Jackson, H. H., Rumsey, C. B., and Chauvin, L. T. Flight Measure-
       ments of Drag and Base Pressure of a Fin-Stabilized Parabolic
       Body of Revolution (NACA RM-10) at Different Reynolds Numbers
       and at Mach Numbers from 0.9 to 3.3. NACA TN 3320 (Supersedes
       NACA RM L50G24), November 1954.

157. Katz, E. and Stoney, W. E., Jr. Base Pressures Measured on Several
       Parabolic-Arc Bodies of Revolution in Free Flight at Mach Num-
       bers from 0.8 to 1.4 and at Large Reynolds Numbers. NACA RM
       L51F29, October 1951.

158. Ferri, A. Supersonic-Tunnel Tests of Projectiles in Germany and
       Italy. NACA WR L-152 (Formerly NACA ACR L5H08), 1945.

159. Reller, J. O., Jr. and Hamaker, F. M. An Experimental Investiga-
       tion of the Base Pressure Characteristics of Non-Lifting Bodies
       of Revolution at Mach Numbers from 2.73 to 4.98. NACA TN 3393,
       March 1955.

160. Spahr, J. R. and Dickey, R. R. Effect of Tail Surfaces on the
       Base Drag of a Body of Revolution at Mach Numbers of 1.5 and
       2.0. NACA TN 2360, April 1951.

161. Czarnecki, K. R. and Marte, J. E. Skin-Friction Drag and Boundary-
       Layer Transition on a Parabolic Body of Revolution (NACA RM-10)
       at a Mach Number of 1.6 in the Langley 4- by 4-Foot Supersonic
       Pressure Tunnel. NACA RM L52C24, May 1952.

162. Bogdonoff, S. M. "A Preliminary Study of Reynolds Number Effects
       on Base Pressure at M = 2.95," J. Aeronaut. Sci., Vol. 19,
       No. 3 (March 1952), pp. 201-206.

163. Kurzweg, H. H. New Experimental Investigations on Base Pressure
       in the NOL Supersonic Wind Tunnels at Mach Numbers 1.2 to 4.24.
       NOL Memo 10113, Naval Ordnance Laboratory, January 1950.

164. Luidens, R. W. and Simon, P. C. Aerodynamic Characteristics of
       NACA RM-10 Missile in 8- by 6-Foot Supersonic Wind Tunnel at
       Mach Numbers from 1.49 to 1.98. I - Presentation and Analysis
       of Pressure Measurements (Stabilizing Fins Removed). NACA RM
       E50D10, 1950

165. Maxwell, N. E. and Shutts, W. H. Aerodynamic Effects of Boattail-
       ing on a Body of Revolution at Mach Numbers of 1.5, 2.0, and
       2.5. Bumblebee Report CVAC/CM-645, Consolidated-Vultee Air-
       craft Corporation, March 1951

166. McIntosh, W. A., Hebert, G., and Dershin, H. The Effect of Aero-
       dynamic Heating on Skin Friction Drag. Convair Report CM-971,
       October 1959.

167. Tetervin, N. Charts and Tables for Estimating the Stability of
       the Compressible Laminar Boundary Layer with Heat Transfer
       and Arbitrary Pressure Gradient. NASA TM 5-4-59L, May 1959.

168. Schmidt, L. E. and Murphy, C. H. Effect of Spin on Aerodynamic
       Properties of Bodies of Revolution. BRL Memo 715, Ballistics
       Research Laboratory, Aberdeen Proving Ground, August 1953.

169. Kavanau, L. L. "Base Pressure Studies in Rarefied Supersonic Flow," J. Aeronaut. Sci. (March 1956).

170. Applied Physics Laboratory, The Johns Hopkins University. Handbook of Supersonic Aerodynamics, NAVORD Report 1488, Vol. 5, Sec. 16, "Mechanics of Rarefied Gases," February 1959.

171. Schlichting, H. Experimental Investigation of the Problem of Surface Roughness. NACA TM 823, April 1937.

172. Hopko, R. N. Preliminary Free Flight Investigation of the Effects of Rivets and Lap Joints on the Drag of Bodies at Zero Lift at Supersonic Mach Numbers to 2.0. NACA RM L52F09, August 1952.

173. Czarnecki, K. R., Robinson, R. B., and Hilton, J. H., Jr. Investigation of Distributed Surface Roughness of a Body of Revolution at a Mach Number of 1.61. NACA TN 3230, June 1954.

174. Monaghan, R. J. Review and Assessment of Various Formulae for Turbulent Skin Friction in Compressible Flow. RAE TN Aero 2182, Farnborough, England, August 1952

175. McIntosh, W. A., Hebert, G., and Dershin, H. The Effect of Aerodynamic Heating on Skin Friction Drag. Convair Report CM-971, October 1959.

176. Seiff, A., et al. Aerodynamic Characteristics of Bodies at Supersonic Speeds. NACA RM A51J25, November 1951.

177. Gillespie, W., Jr. Jet Effects on Pressures and Drags of Bodies. NACA RM L51J29, November 1951.

178. Dye, F. E. Pressure Distribution Tests for Basic Conical Flow Research. OAL Report 160, February 1950.

179. Schlichting, H. Boundary Layer Theory, Part II, Turbulent Flows, Lecture Series. NACA TM-1218, 1949.

180. Lees, L. "On the Boundary Layer Equations in Hypersonic Flows and Their Approximate Solutions," J. Aeronaut. Sci. (February 1953).

181. Schlichting, H. Boundary Layer Theory. New York: McGraw-Hill, 1955.

182. Truitt, R. W. Hypersonic Aerodynamics. New York: The Ronald Press, 1959.

183. Moore, F. K. Laminar Boundary Layer on a Cone in Supersonic Flow at Large Angle of Attack. NACA TN 2844, 1952.

184. Van Dyke, M. D. and Gordon, H. D. Supersonic Flow Past a Family of Blunt Axisymmetric Bodies. NASA Report 1, 1959.

185. Kennedy, E. C. Calculation of the Flow Fields Around a Series of Bi-Conic Bodies of Revolution Using the Method of Characteristics as Applied to Supersonic Rotational Flow. OAL/CM 873, 1956.

186. Heberle, J. W., Wood, G. P., and Gooderum, P. B. Data on Shape and Location of Detached Shock Waves on Cones and Spheres. NACA TN 2000, 1950.

187. Crawford, D. H. and McCauley, W. D. Investigation of the Laminar
      Aerodynamic Heat-Transfer Characteristics of a Hemisphere-
      Cylinder in the Langley 11-Inch Hypersonic Tunnel at a Mach
      Number of 6.8. NACA TN 3706, 1956.

188. Kawamura, T. "On the Detached Shock Wave in Front of a Body Moving
      at Speeds Greater than that of Sound," College of Science
      Memoirs, Series A, Vol. XXVI, No. 3, University of Kyoto
      (1950).

189. Ladenburg, R., Winckler, J., and Van Voorhis, C. C. "Interferom-
      etric Studies of Faster than Sound Phenomena Part I," Phys.
      Rev., Vol. 73, No. 11 (1948).

190. Love, E. S. A Re-examination of the Use of Simple Concepts for
      Predicting the Shape and Location of Detached Shock Waves.
      NACA TN 4170, 1957.

191. Beckwith, I. E. and Gallagher, J. J. Heat Transfer and Recovery
      Temperatures on a Sphere with Laminar, Transitional and Turbu-
      lent Boundary Layers at Mach Numbers of 2.00 and 4.15. NACA
      TN 4125, 1957.

192. Goodwin, G., Creager, M. O., and Winkler, E. L. Investigation of
      Local Heat-Transfer and Pressure Drag Characteristics of a
      Yawed Circular Cylinder at Supersonic Speeds. NACA RM A500H31,
      1956.

193. Vas, I. E., Bogdonoff, S. M., and Hammitt, A. G. An Experimental
      Investigation of the Flow over Simple Two-Dimensional and Axial
      Symmetric Bodies at Hypersonic Speeds. Report No. 382 (WADC
      TN 57-246), Department of Aeronautical Engineering, Princeton
      University, June 1957.

194. Chauvin, L. T. Pressure Distribution and Pressure Drag for a
      Hemispherical Nose at Mach Numbers 2.05, 2.54, and 3.04. NACA
      RM L52K06, 1952.

195. Lees, L. and Kubota, T. "Inviscid Hypersonic Flow over Blunt
      Nosed Bodies," J. Aeronaut. Sci. (March 1957), pp. 195-202.

196. Wagner, R. D., Jr. "Some Aspects of the Modified Newtonian and
      Prandtl-Meyer Expansion Method for Axisymmetric Blunt Bodies
      at Zero Angle of Attack," J. Aero/Space Sci. (December 1959),
      pp. 851-852.

197. Love, E. S. "Prediction of Inviscid Induced Pressure from Round
      Leading Edge Blunting at Hypersonic Speeds," ARS Journal
      (October 1959), pp. 792-794.

198. Bowers, H. M. A Simplified Method for Preliminary Design Drag
      Estimates for Ballistic Missiles. LMSD 505445, TM 57-11-06,
      May 1961.

199. Cooper, R. D. and Robinson, R. A. An Investigation of the Aero-
      dynamic Characteristics of a Series of Cone-Cylinder Configura-
      tions at a Mach Number of 6.86. NACA RM L51J09, 1951

200. Chapman, D. R. and Rubesin, M. W. "Temperature and Velocity Pro-
      files in the Compressible Laminar Boundary Layer with Arbitrary
      Distribution of Surface Temperature," J. Aeronaut. Sci., Vol. 16
      (September 1949), pp. 547-565.

201. Mangler, W. Boundary Layers with Symmetrical Airflow About Bodies
     of Revolution. Report No. R-30-18, Part 20, Goodyear Aircraft
     Corp., March 1946.

202. Rubesin, M. W., Maydew, R. C., and Varga, S. A. An Analytical and
     Experimental Investigation of the Skin Friction of the Turbu-
     lent Boundary Layer on a Flat Plate at Supersonic Speeds. NACA
     TN 2305, 1951.

203. Hopko, R. N. and Sandahl, C. A. Free Flight Investigation of the
     Zero-Life Drag of Several Wings at Supersonic Mach Numbers Ex-
     tending to 2.6. NACA RM L52D29, 1952.

204. Honeywell, E. E. Compilation of Power-Off Base Drag Data and Em-
     pirical Methods for Predicting Power-Off Base Drag. TM 334-337,
     Convair, Pomona, 1959.

205. Cohen, R. J. Aerodynamic Characteristics of Four Bodies of Revo-
     lution Shcwing Some Effects of Afterbody Shape and Fineness
     Ratio at Free Stream Mach Numbers from 1.50 to 1.99. NACA RM
     E51C06, May 1951.

206. Luidens, R. W. and Simon, P. C. Aerodynamic Characteristics of
     the NACA RM-10 Missile in 8 × 6 ft Supersonic Wind Tunnel at
     Mach Numbers from 1.49 to 1.98. NACA RM E50D10, 1950.

207. Kavanau, L. L. "Some Base Pressure at Intermediate Reynolds Num-
     bers with M = 2.84," J. Aeronaut. Sci., Vol. 21, No. 4 (1954)
     p. 257.

SUBJECT LIST OF REFERENCES

Base Drag: 63, 109, 140-164, 167-170, 176, 204

Blunt-Nosed Bodies: 85-89, 117, 119, 120, 132, 133, 139, 186, 195

Boattail Pressures: 84, 113, 114, 140, 150, 165, 205

Calculated Pressure Distributions: 25, 27, 30, 31, 38, 39, 52, 60-65, 67-69, 73, 74, 79

Center of Pressure: 79, 95, 97-99, 101, 105

Characteristics Method: 17-20, 77

Conical Flow: 21, 22, 43, 55, 59-65, 67, 68, 118, 129, 136, 178

Cross Flow: 14-16, 44-54, 56-58

Cylinders in Transverse Flow: 54, 88, 92, 94, 134

Double Cones: 72, 88, 185

Drag: 68, 75, 79, 80, 93, 101, 108-117, 120-124, 128, 178, 192, 198

Ducted Bodies: 7, 72, 75, 79, 80-83, 110

Elliptical Cones: 69, 70, 171

Experimental Pressure Distribution: 52, 60, 67, 80, 84, 165, 199

First and Second-Order Theories: 2, 8, 9

Flat-Faced Cylinders and Disks: 86, 87, 89, 92

Flow Tables: 22, 28, 29, 55, 63, 66

Flow Theories: 1-6, 8

General Texts: 5, 6, 50, 137, 178, 181, 182

Hypersonic Flow: 23, 24, 27, 30, 32-35, 37-40, 43, 91, 100, 170, 180, 182, 193, 197

Hypersonic Similarity Rule: 25, 30, 32-34, 43, 124

Jet Effects: 150, 177

Lift: 41, 79, 95, 103, 104

Linearized Theory: 1, 2, 7, 75

Low-Pressure Flow: 94, 141, 169, 170, 207

Magnus Moment: 106, 107, 168

Minimum Drag: 42, 81-84, 111-116

Newtonian Impact Theory: 40-42, 100, 196

Normal Force: 47, 52, 70, 92, 95-99, 101, 102, 105

Pitching Moment: 79, 96, 99, 102, 105

Protrusions, etc.: 171-173

Shock-Expansion Method: 23-27, 38, 39, 76

Skin Friction: 8, 44, 125-127, 129-131, 134-138, 166, 167, 171-175,
          187-191, 202

Skirted Bodies: 101

Slender-Body Theory: 1, 3, 4, 10-16, 117, 118

Spheres: 54, 85, 87, 88, 121-124, 184, 187, 191-194

Spiked Noses: 132, 133

INDEX

of tangent-ogive cylinders, 50,
175,176, 179, 180
non-steady derivatives, 170
slope, 7, 164
of cones, 21, 180, 181
of cone-cylinders, 184,
200-203, 207
of ogives, 180
of skirted bodies, 194
of tangent-ogive cylinders,
180, 182, 183
noses
blunt, 65ff, 68
conical, 55ff, 221
ducted, 61ff, 169, 223
ogival, 58, 222
spiked, 229, 264-266
numerical-graphical methods, 8,
10, 16

ogives, 58, 61ff, 222
base pressure on, 296
center of pressure of, 51, 185-187
drag of, 222, 239
normal-force coefficient for, 49,
175-177, 179, 180
normal-force slope of, 180
pitching moment, 189, 191
pressure distribution on, 23-34,
91-117
open-nosed body (see ducted body)

perturbation velocity, potential,
3ff
pitching moment, 41, 165ff, 170
angle-of-attack effect on, 50, 203
cones, coefficient of, 198
cone-cylinders, coefficient of,
199, 200, 203
of ducted bodies, 169
Reynolds number effect on, 191
of tangent-ogive cylinders, 189,
190
Prandtl-Meyer flow, 12ff
pressure distribution
base (see base pressure)
on boattails, 64, 128-132, 224,
307
on bodies, 75
blunt, 65ff, 160
ducted, 61, 62, 122, 169, 223
of elliptical planforms, 68, 87,
223
parabolic-arc, 137
skirted, 224
of varying diameter, 65
on cones, 22, 55ff, 82-84
angle-of-attack effect on, 114,
115
double, 89, 223

drop-shape, 88
elliptical, 87, 225
spherical nosed, 67, 154
triangular-shaped, 88
truncated, 148-153
on cone-cylinders, 56, 78, 80, 81
on cowls
conical, 71-73, 119, 120, 124,
125
non-conical, 124
on cylinders, 66, 68, 74, 147,
161
flat-faced, 66, 142, 143
tangent-ogive, 23, 24, 93-97,
103-117
on flat-faced cylinders and disks,
66
on hemispheres, 138
on ogives and ogive-cylinders, 58
on spheres, 66
pressure drag, 221ff
accuracy of various methods, 27
of blunt bodies, 227
of boattails, 224
of cones, 221
drop-shape cross-section, 225
ducted, 223
elliptical, 223, 225
of cowls, conical, 224
minimization of, 225
of ogives, 222
of skirted bodies, 224
protrusions, drag effect of, 237,
276

radial location effect on base
pressure, 283
Reynolds number
center of pressure, effect on,
180
critical, 46
cross-flow, 36
pitching moment, effect on, 191
pressure distribution, effect on,
101
skin friction, effect on, 267,
268
sphere drag, effect on, 262, 263
rotating cubes, 229
rotational flow, 15
characteristics method, 8
roughness effect, 236, 237, 273,
275

Schwabe's cross-flow drag on cyl-
inder, 39
secant-ogives, drag of, 239
second-order theory, 12
Fenter's modification, 12
semi-empirical method for base
pressure, 281